Detection and CCD Photometry of Eclipsing Binaries in the Large and Small Magellanic Clouds

A thesis
submitted in partial fulfillment
of the requirements for the Degree
of
Doctor of Philosophy in Astronomy
in the
University of Canterbury

by

Glenn Bayne

University of Canterbury
2003

To Christine and Shannon

Abstract

Eclipsing binary stars allow the physics of the component stars to be studied. These systems can provide a wealth of knowledge ranging from fundamental parameters such as mass, radius, and luminosity through to tests of stellar evolution and distances to the systems.

A search for eclipsing binaries in the SMC using the MOA photometric time series database yielded 169 detections. These detections were cross-referenced with the OGLE catalogue of eclipsing binaries in the SMC. A total of 35 systems were new detections with most of these lying in the outer, less dense regions of the SMC, and some outside the OGLE fields. The remainder were within the overlap region of the fields of the two surveys. In the overlap region of the two MOA survey fields, 21 systems were detected but only 2 detections were common to both fields. This implies the MOA survey is far from complete. Additionally, 14 systems ($\sim$10%) were not detected by OGLE in the MOA-OGLE overlap region implying the OGLE survey is also not complete, though to a lesser extent. The unequivocal determination of whether all systems were real eclipsing binaries was not able to be made based on the photometric light curves alone. Objects for which there was some uncertainty concerning their true nature were indicated as such.

Two of the new detections in the MOA SMC catalogue were selected for follow-up photometry, MOA J005018.4−723855 and MOA J005623.5−722123. An LMC target was selected from the MACHO LMC catalogue, MACHO*05:36:48.7−69:17:00. Observations were made from MJUO in Strömgren u, Johnson $V_{\rm J}$ and Cousins $I_{\rm C}$ filters between 1999 April and 2002 July. The McLellan 1-m telescope and CCD photometer head were used. Differential fluxes for the target stars were extracted using the ISIS-2.1 difference imaging package. To obtain flux changes with respect to a level of zero flux, DAOPHOT II was used to establish the targets' flux levels in the reference images relative to which ISIS-2.1 works.

The light curves were analysed using the Wilson synthetic light-curve code. It was not possible to make a definitive analysis of the physical nature of the three targets based on differential photometry alone. Nevertheless, it was possible to make rough estimates of the systems' apparent magnitudes and hence, via the known distance moduli and reddenings to the Magellanic Clouds, their absolute magnitudes. Coupled with additional constraints derived from Geneva models of stellar evolution for stars of reduced metallicity, it was possible to obtain astrophysically plausible parameters for the component stars comprising each target.

The LMC target MACHO*05:36:48.7−69:17:00 is located near the Tarantula nebula and very close to SN1987A. It is a well-detached, eccentric system, ($e = 0.2$) with a sidereal period of 3.853529 ± 0.000005 d and an apsidal period of 100 ± 5 years. The difference in mean epochs for the $V_{\rm J}$ and $u/I_{\rm C}$ observations resulted in an averaging of the solution parameters.

The most astrophysically plausible solution was obtained by matching the derived components to a pair of Geneva LMC models of identical age. This solution indicates a primary of $\sim 20\,{\rm M}_{\odot}$ and secondary of $\sim 14\,{\rm M}_{\odot}$ with a common age of 5×10^6 yr. Other parameters are mean effective temperatures $T_{\rm eff,1} = 33\,500$ K, $T_{\rm eff,2} = 29\,500$ K, semi-major axis $a = 33.3\,{\rm R}_{\odot}$, mean radii $\overline{R_1}/\,{\rm a} = 0.21$, $\overline{R_2}/\,{\rm a} = 0.15$ and inclination $i = 85.8\,^{\circ}$.

MOA J005018.4−723855 is a semi-detached system, period 1.839870 ± 0.000005 d, with the secondary filling its Roche lobe and with the O'Connell effect evident in the light curve. Of

the three systems, this is the most affected by blending. Third light was necessary to obtain satisfactory light-curve fits in all bandpasses. Light-curve solutions fix the mass ratio and suggest the system is undergoing case A mass transfer from the present secondary. Since the mass receptor in such a system may mimic a normal main-sequence star to within a factor of two in luminosity for a given mass and temperature, an estimate of the physical nature of this system was found by requiring the parameters to match those of a Geneva evolutionary model. This yielded $M_1 = 13.5\,\mathrm{M}_\odot$, $T_{\mathrm{eff},1} = 29\,000\,\mathrm{K}$, $\overline{R_1} = 5.9\,\mathrm{R}_\odot$, $M_2 = 20.5\,\mathrm{M}_\odot$, $T_{\mathrm{eff},2} = 20\,000\,\mathrm{K}$, $\overline{R_2} = 8.5\,\mathrm{R}_\odot$, $a = 20.5\,\mathrm{R}_\odot$ and $i = 77.6\,°$.

MOA J005623.5−722123 is a detached system, period $2.32005 \pm 0.00002\,\mathrm{d}$. Third light was necessary in the analysis of this star. Analysis of the derived solutions and comparison to the Geneva evolutionary models indicates a system 10×10^6 yr old. The most astrophysically plausible parameters for this system are $M_1 = 13.5\,\mathrm{M}_\odot$, $T_{\mathrm{eff},1} = 29\,000\,\mathrm{K}$, $\overline{R_1} = 5.8\,\mathrm{R}_\odot$, $M_2 = 15.5\,\mathrm{M}_\odot$, $T_{\mathrm{eff},2} = 29\,350\,\mathrm{K}$, $\overline{R_1} = 7.8\,\mathrm{R}_\odot$, $a = 22.65\,\mathrm{R}_\odot$ and $i = 87.8\,°$. The preferred light curve solution gives a secondary marginally hotter than the primary, yet with shallower eclipse depths. The high inclination as well as the gravity brightening in B-stars are the cause of this. During the secondary eclipse, the primary's path passes across the cooler central region the secondary, thereby leaving the hotter poles exposed. This accounts for the higher hemisphere-averaged temperature in the solution.

Acknowledgments

I would like to extend my thanks to Dr William Tobin for the huge amount of time he has given toward assisting me complete this work. This especially extends to his time in France when he has not been officially employed to supervise my work but nevertheless gave many nights to answering emails and even as going so far as to proof read my thesis in his holiday time.

The MJUO staff of Alan Gilmore, Pam Kilmartin, Steve Barlow, Nigel Frost are thanked, as are the many MOA observers both from NZ and Japan. I'm especially grateful to Alan for coming to my assistance on many occasions when I was enrolled part-time and observing on weekends. A special thanks to Steven and Nigel for the efforts in having the telescope set up for my observing runs. A special thanks to Nigel for driving back to MJUO late at night to fix a problem.

I would also like to thank my co-supervisors. Dr Ian Bond for his useful discussion on image subtraction and for supplying the MOA database to enable me to search for new targets and helping extract the data. Saskia Besier for supervising while William was away and providing guidance. Also Karen Pollard for her input and regular meetings. Finally to John Pritchard for his introduction to using the MJUO 1 metre telescope. Endless help with computer problems and assistance with analyses of the data. An additional thanks to John and Vanessa Doublier for their hospitality while I was in Santiago, Chile.

I thank John Hearnshaw and Michael Albrow for their interesting and valuable discussions and advice.

I acknowledge the assistance and support provided by the technical staff, namely Ryurick Hristev and Paul Arnold. Thanks to fellow students, Dan Pooley, Stuart Barnes, Jenny McSavney, David Ramm, Malcom Cropp. All for their help and advice.

I am grateful for the financial assistance provided to me during the course of my thesis research. The Department of Physics and Astronomy, the Dennis Moore fund and the Marsden fund. In addition, the Royal Society of New Zealand Science and Technology award, Royal Society of New Zealand - Canterbury Branch, Elizabeth Pepper Wood fund and the International Astronomical Union all of who made possible may attendance of the Extra galactic Distance Scale Workshop, Concepcion, Chile, IAU 191 Binary Formation and Evolution Merida, Mexico and IAU 193 Variable stars in the Local Group, Christchurch, New Zealand. Without the support of all of these funds, attendance at these conferences would not have been possible.

Contents

List of Figures

List of Tables

Chapter 1

Introduction

1.1 Binary stars

The field of astronomy is full of interesting if not sometimes incomprehensible objects, most of which are stars, for this is what we see with our own eyes. What is generally not considered, is that the majority of all stars are in fact in binary systems, or multiple systems with less frequency for higher multiples. The rest consist of single stars, like our Sun, which we unthinkingly consider is the norm.

Firstly, to be classified a binary star, two stars must be gravitationally bound. The class of stars labelled binaries can be divided into further sub classes:

1. Visual double stars
2. Astrometric binaries
3. Spectroscopic binaries
4. Eclipsing binaries

The binary stars let us extract information that essentially lets us understand single stars. From the binary system, mass, radius, surface temperature and distance can be determined. As always in nature, nothing is for free and the price to pay for these fundamental parameters is the increased complexity of the objects themselves. In close systems mass transfer, tidal distortion and uneven heating all add to the complexity of interpreting observations of an eclipsing binary system.

1.1.1 Visual double stars

This type of binary is normally observable and resolvable, Figure 1.1, using an optical telescope[1]. Observations and analysis of these systems give the orbital elements indicative of the orbital plane; size of the semi-major axis and shape of the orbit. To obtain the semi-major axis, very accurate parallax measurements are required, presently restricted to nearby stars. These systems may be double stars or multiple star systems.

[1]This is not the same type as optical doubles which are not gravitational bound, but separated by large distances and appear to be next to each other.

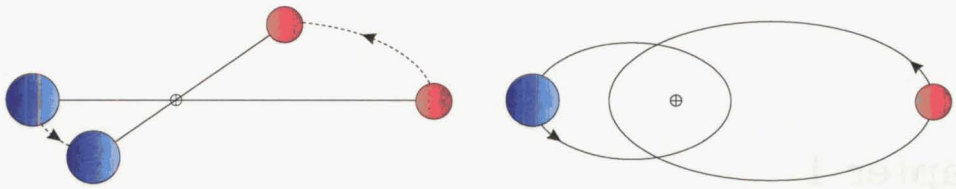

Figure 1.1: The right hand figure shows two stars in a binary system orbiting about their centre of mass, $\oplus$. The left hand figure depicts the orbital paths as seen by an observer.

1.1.2 Astrometric binaries

These are a follow on from visual double stars where only one component is visually observed. The second is detected via astrometric methods due to the gravitational influence of an unseen star on the orbital motion of the visible star. The system is similar to the one shown in Figure 1.1, with the smaller red component not visible. The faint companion can be detected by the observation of *wobbles* in the motion of the brighter star. This can imply the presence of a near solar mass sized object[2] which is interacting with the observed brighter companion star. An example is the Sirius A and B system, where the fainter companion, Sirius B is not easily observable, but the *wobble* in the motion is observed. This method can also be used for the detection of planets, generally Jovian sized. High precision astrometry is required which should become available with the next generation of astrometric telescopes in space.

1.1.3 Spectroscopic binaries

There are two types of spectroscopic binaries; 1. Doubled-lined, 2. Single-lined. If radial velocities of both components can be obtained, via their identification in the spectra, then the system is classified as a double-lined spectroscopic binary, Figure 1.2. If only one component is detectable in the spectra, maybe due to a cool fainter companion of a hot bright primary, the system is called a single-lined spectroscopic binary. In the study of eclipsing binaries for distance determination, the preferred system is the former (also well-detached). This is because in the distance modulus equation, the velocity semi-amplitudes of both components are required. Single-lined systems can be used, however the criterion is for the system to be semi-detached as the photometric mass ratio can be determined, [180].

Spectroscopic binaries can be studied at far larger distances than visual double binaries, i.e. nearby galaxies. Some of the parameters obtained from these types are; the luminosity ratio and the mass ratio. Both are difficult to determine through spectra measurements, the latter requiring the stars to have similar luminosities for best results. Radial velocity measurements[3] of the two stars gives the spectroscopic mass ratio. The amplitude of the radial velocity of both components needs to be distinguishable from noise as small, long period components can be difficult to observe due to their small radial velocity amplitudes. Such is the case for detecting planets whereby high precision radial velocity measurements are required.

Spectroscopic measurements provide the semi-major axis a, which scales the system. This value is unable to be obtained from photometric observations.

[2] In this sense small, low luminosity type star or a brown dwarf or even Jovian size planets. The object could also have a large mass, such as a black hole, although this is not the norm.

[3] The radial velocity measurement is a measure of the Doppler shift with respect to time, Figure 1.2. This is achieved by recording the spectrum of the stellar components and measuring the shift in the spectral lines.

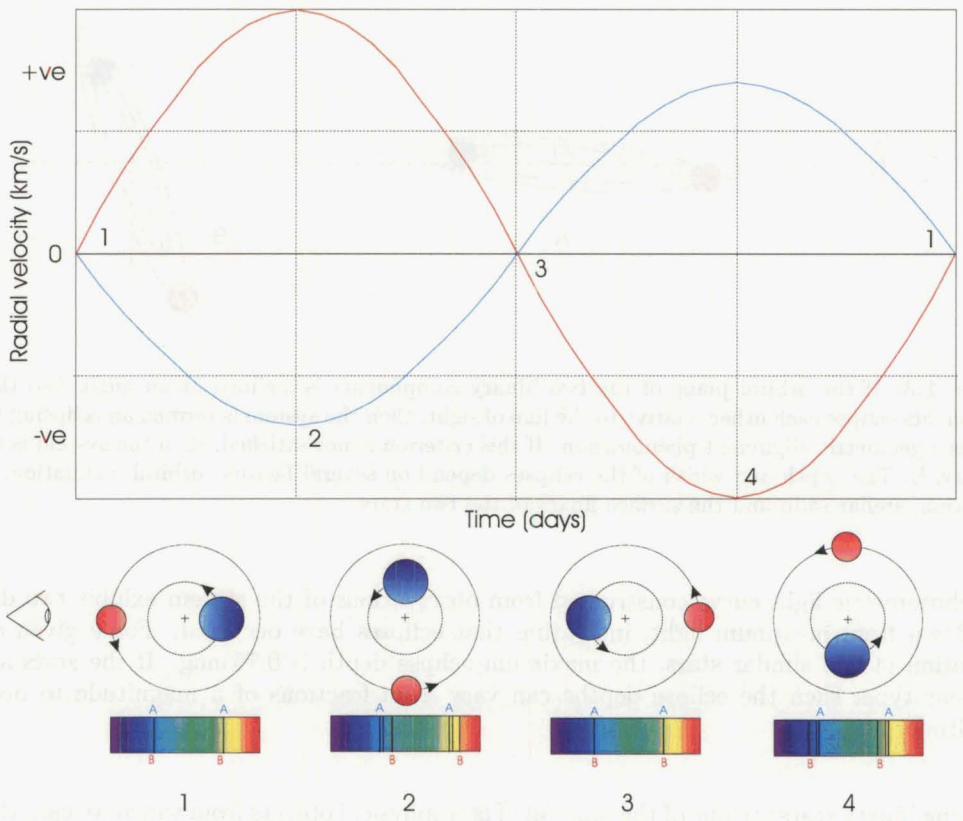

Figure 1.2: This example is for a well-detached doubled-lined spectroscopic binary whose light curve is given in Figure 1.4. The top figure shows the radial velocity curves for the two components. The red line is the smaller outer star, B (red) which has a larger orbital radius than the inner star, A (blue). The lower numbered figures correspond to the numbered sections of the orbital radial velocity curves. One cycle is shown. The observer is viewing the system from the left hand side of the page. Note the the fixed line at the zero velocity position. As a star moves away from the observer, the radial velocity is seen to increase and the spectral lines are red shifted, a positive radial velocity. As the stars are in line relative to the observer, 1 and 3, no difference in radial velocity is observed; the radial velocity is referenced here as zero. As the star moves toward the observer the spectral lines are blue shifted. The radial velocity is termed negative.

1.1.4 Eclipsing binaries

The geometric orientation of a binary systems' orbital plane, in relation to an observer, can result in one binary component eclipsing the other, Figure 1.3. Such a system is termed an eclipsing binary.

This is a special type of binary system due to the inclination of the orbital plane, with respect to an observer, resulting in eclipses of the stars' light.

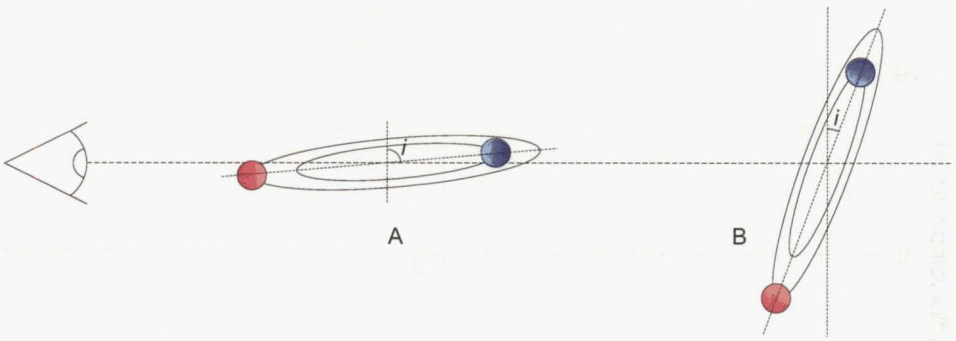

Figure 1.3: If the orbital plane of the two binary components is inclined at an angle i so that the components eclipse each other relative to the line of sight, then the system is termed an eclipsing binary, A. This a geometric alignment phenomenon. If this criterion is not satisfied, then the system is termed a binary, B. The depth and width of the eclipses depend on several factors: orbital inclination, stellar separation, stellar radii and the surface fluxes of the two stars.

The photometric light curve constructed from observations of the system exhibit two distinct dips down from maximum light, indicating that eclipses have occurred. For a given orbital inclination of two similar stars, the maximum eclipse depth is 0.75 mag. If the stars are not a similar type, then the eclipse depths can vary from fractions of a magnitude to over one magnitude.

Eclipsing binary stars are one of the handful of astrophysical objects from which we can, through careful and meticulous measurements and modelling, source information about fundamental stellar parameters. These include radii, masses, relationship between absolute and apparent magnitudes and, where possible, the distance. Knowledge of such systems extends back to the 1780's. Then, Pigott and Goodriche observed β Per (Algol) with the explanation that its periodic variability was due to two gravitationally mutually bound stars, a binary star system.

Since then, many theories and methods of binary system analysis has been developed and implemented. In the earlier half of the last century, Leavitt (1908) [84], produced a sample of 10 eclipsing binaries[4] and later the Gaposchkins worked on the first catalogue of eclipsing binary stars in the Small Magellanic Cloud. This was constructed by the study of photographic plates of the SMC over many years. In the later years with the aid of computing advances, theoretical models of binary star evolution and mass exchanges processes were developed. This resulted in a reasonable understanding of the general properties of eclipsing binary systems. Additionally, other binary types such as systems with one component either a neutron star or black hole have been studied[5].

[4]The paper was titled *Variable stars of the Algol type*, although these were in the Galaxy not in the Magellanic Clouds.

[5]If emission of x-ray wavelengths is detected from these systems then they can be termed x-ray binaries.

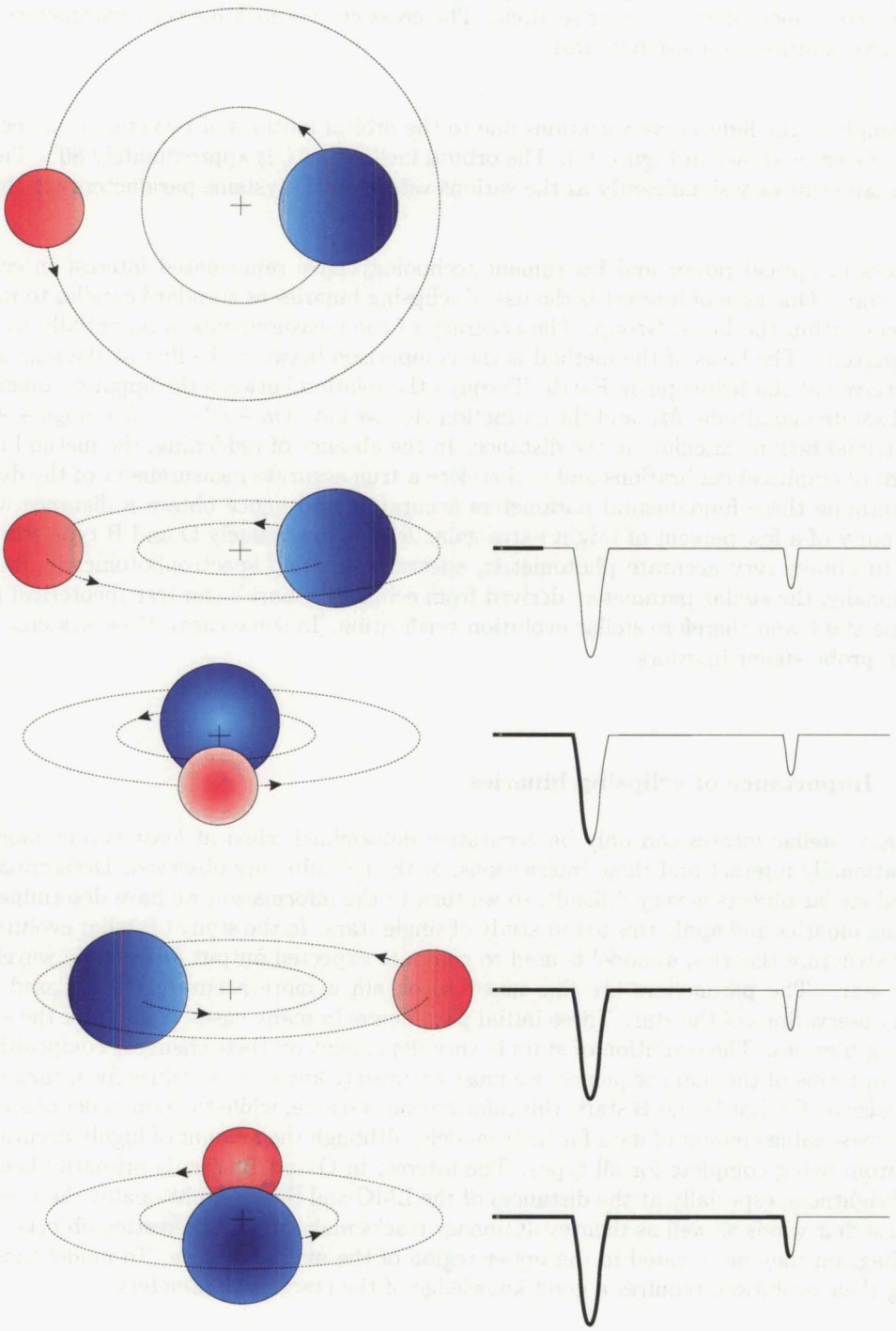

Figure 1.4: The system shown here has a circular orbit and the centre of the circular orbit is then also the centre of mass, similar principles of eclipse apply to the eccentric orbital case. The top figure is a plan view of an eclipsing binary system consisting of two stars of different diameter and temperature. A larger hotter component and a smaller cooler component. As the smaller component passes in front of the larger hotter component, the total light of the system is seen to apparently decrease, an eclipse occurs. As the two component are not obstructing each other's light, the total light is seen to be back to the same level prior to the eclipse. When the cooler smaller star passes behind the larger hotter star, an eclipse again occurs, this time the effect is less then before due to a smaller amount of light being eclipsed.

The light curves can provide, by modelling, estimations of some of the binary parameters. This is discussed in more detail in later sections. The cross correlations between parameters makes light curve solutions a non-trivial task.

An example of the light curve variations due to the orbital motions of two stars in an eclipsing binary system is shown in Figure 1.4. The orbital inclination i, is approximately 80°. The light curve shape can vary significantly as the various values of the systems parameters are changed.

Advances in optical power and instrument technology have rejuvenated interest in eclipsing binary stars. One area of interest is the use of eclipsing binaries as standard candles to measure distances within the Local Group. The accuracy of the measurements is potentially to within a few percent. The basis of the method is the comparison between the flux at the star and the flux received at the telescope on Earth. Through the relation between the apparent magnitude, m_V, absolute magnitude, M_V and the extinction A_V, we have $(m-M)_V = -5 + 5\log d + A_V$ and it is a trivial task to calculate d, the distance. In the absence of reddening, the method is independent of empirical calibrations and is therefore a true accurate measurement of the distance. To determine these fundamental parameters accurately and hence obtain a distance with an uncertainty of a few percent of bright extra-galactic systems (namely O and B type stars), one needs to obtain very accurate photometric, spectroscopic and spectrophotometric data sets. Additionally, the stellar parameters derived from eclipsing binaries can test theoretical models of single stars, and therefore stellar evolution verification. In some cases, these systems can be used to probe stellar interiors.

1.1.5 Importance of eclipsing binaries

Generally, stellar masses can only be accurately determined when at least two or more stars gravitationally interact and these interactions, or their results, are observed. Determination of isolated stellar objects is very difficult, so we turn to the information we have determined from eclipsing binaries and apply this to our study of single stars. In the study of stellar evolution and stellar structure theories, a model is used to compute expected output at multiple wavelengths of the star. The parameters are fine-tuned to obtain a more accurate result based on the actual observations of the star. These initial parameters in many cases, come from the study of eclipsing binaries. The evolution of stars is very dependent on their chemical composition and mass. In terms of the main sequence, we must accurately know these values for a range of star types (sizes). For hot O and B stars, this information is scarce, while the remainder of star types have a reasonable amount of data for their models, although the amount of highly accurate data is far from being complete for all types. The interest in O and B stars is primarily because of their brightness, especially at the distances of the LMC and SMC. Additionally, their mass loss due to stellar winds as well as their evolutionary tracks makes them interesting objects. On the H-R diagram they are located in the upper region of the main sequence. To model these stars during their evolution, requires a good knowledge of the starting parameters.

1.1.6 Properties of eclipsing binaries

To define an eclipsing binary system, seven[6] orbital elements, Figure 1.5, are required for an orbit in three dimensional space:

[6] Although six orbital elements (a, e, i, ω, Ω and T) give the size, shape and orientation of a system, in the binary case the period, P, is required as it is related to the relative orbital semi-major axis, a (with respect to the center of mass of the companion star) by the generalized form of Kepler's law $\frac{a^3}{P^2} \propto m_1 + m_2$, where m_1 and m_2 are the masses of the two stars.

1. P, orbital period, usually expressed in units of days.
2. i, inclination of the orbital plane to be the tangent plane of the celestial sphere at the star.
3. Ω, the position angle of the line of nodes joining the intersections of the orbital and tangent planes, and measured in the latter.
4. ω, the longitude of periastron, the angle between the direction of the ascending node (at which the star crosses the tangent plane while receding from the observer) and that point of closest approach of the two stars (periastron). This angle is measured in the orbital plane, in the direction of orbital motion.
5. a, the semi-major axis of the orbit.
6. e, eccentricity of the orbit. Dimensionless value between zero (circular) and unity.
7. T, the time at which the two stars pass through periastron.

To characterize the stars themselves, additional parameters of the components are required; mass m_1, m_2, effective temperature $T_{\rm eff,1}$, $T_{\rm eff,2}$, absolute orbital semi-major axes a_1, a_2 (centred on the barycentre), stellar radii R_1, R_2, Luminosity L_1, L_2 and limb darkening.

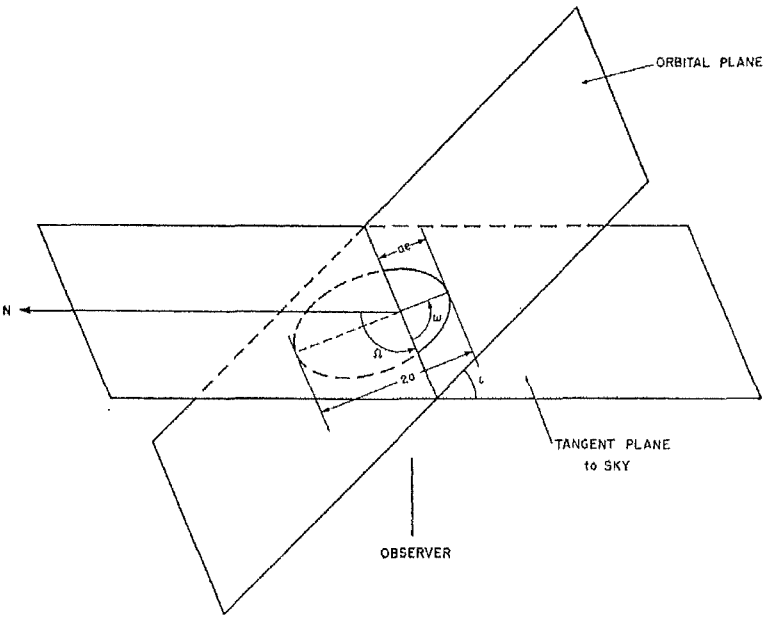

Figure 1.5: Reproduced from Batten [13]. The orbital parameters required to define a binary.

At increasing distances, the detection of binaries is dependent on their type. Detection of visual binaries, with current technology is restricted to nearby Galactic systems. Spectroscopic binaries are limited to nearby galaxies as are the eclipsing binaries, at a slightly greater distance. Different information can be obtained from each type. For extra-galactic work, namely LMC, SMC, M31 and M33, spectroscopic and photometric binaries are the only option. A summary of the parameters that can be obtained from these types is presented in Table 1.1.

Element		Visual binary	Spectroscopic binary		Eclipsing binary
			One spectrum	Two spectra	
	P	yes	yes	yes	yes
	i	yes	no	no	yes
	Ω	yes[7]	no	no	no
	ω	yes	yes	yes	yes
	a	Apparent a''	$a_1 \sin i$	$a_2 \sin i$	no
	e	yes	yes	yes	yes
	T	yes	yes	yes	yes
	m_1	if parallax	$f(m)$[8]	$m_1 \sin^3 i$	no
	m_2	is known	$f(m)$	$m_2 \sin^3 i$	no
Radius	R_1	no	can be estimated		$r_1 = \frac{R_1}{a}$, r_2
Fractional luminosity	L_1	yes	yes	yes	yes
	L_2	yes	yes	yes	yes
Spectral types		yes	yes	yes	bandpass dependent
Limb darkening	μ_1	no	no	no	in principle
	μ_2	no	no	no	in principle
Ellipticity		no	no	no	in principle

Table 1.1: For two stars, masses m_1 and m_2, in a binary system, the parameters obtained from different types of observation do not give a complete picture of the system. A mixture of photometric and spectroscopic data is required. The major semi-axis, a'' (seconds of arc), can be derived from the visual observations but it cannot be converted into absolute value of a unless the distance can be independently determined. The fractional radii, r_1 and r_2, are the radii of the stars expressed as fractions of their separation and are determined from the light curve. Note, it is possible to make measurements of the luminosity ratio.

Careful selection criteria, for example an eclipsing binary in a relatively uncrowded field with a good signal to noise ratio, can yield very accurate precision of the parameters mentioned previously. It is this property of eclipsing binaries that makes then so unique in that many of fundamental stellar parameters can be measured from the study of a single binary system. To calculate these however, many fields of physics are used, thermodynamics, radiation physics, hydrodynamics, celestial mechanics and many others.

1.1.6.1 Radii

The relative or fractional radii r_1 and r_2, where $r_{1,2} = R_{1,2}/a$ with $R_{1,2}$ the radii and a the semi-major axis, of well-detached systems can be calculated reasonably accurately from the photometric light curves, example Figure 1.9. However in the semi-detached and contact systems, the time of eclipse onset is very difficult to determine. Values of the radii are obtained from the output of a binary light curve analysis software, such as the *Wilson and Devinney* package.

1.1.6.2 Mass ratio

The mass ratio is generally determined from the spectroscopic data. A photometric mass ratio can, in special cases, be determined from photometry alone. If the spectra of the two components can be resolved, the doubled-lined case, the mass ratio, equation 1.4, is determined via the relations in equations 1.1, 1.2 and 1.3.

$$a_{1,2} = 13751(1-e^2)^{\frac{1}{2}} K_{1,2} P \ (AU) \tag{1.1}$$

$$m_{1,2} = 1.0385 \times 10^{-7}(1-e^2)^{\frac{3}{2}}(K_1+K_2)^2 K_{2,1} P \ \mathrm{M}_\odot \tag{1.2}$$

$$a_1 + a_2 = a \tag{1.3}$$

$$\frac{a_2}{a_1} = \frac{K_2}{K_1} = \frac{m_1}{m_2} \tag{1.4}$$

where K_1 and K_2 are the semi-amplitude radial velocities, in kms^{-1}, of the components of mass m_1 and m_2 (solar masses, $\mathrm{M}_\odot$) respectively. If the system is a single-lined binary then only the value of $a_1 \sin i$ can be determined and therefore only the mass function as defined in equation 1.5 can be calculated.

$$f(m) = \frac{m_2^3 \sin^3 i}{(m_1+m_2)^2} = 1.0385 \times 10^{-7}(1-e^2)^{\frac{3}{2}} K_1^3 P \ (\mathrm{M}_\odot) \tag{1.5}$$

Distance determination using eclipsing binaries requires very accurate radial velocities. An uncertainty in velocity semi-amplitude, K_1 of 10% relates to an uncertainty in mass, m_1 of 30%.

[7] Ambiguous without radial velocity observations.

[8] Where the mass function $f(m) = \frac{m_2^3 \sin^3 i}{(m_1+m_2)^2}$.

1.1.6.3 Distance

The distance, more commonly given as the distance modulus, as derived from eclipsing binary analysis, can be expressed as:

$$(m_V - M_V)_0 = m_V - A_V - M_{bol_\odot} + 5\log\left(\frac{R}{R_\odot}\right) + 10\log\left(\frac{T_{\rm eff}}{T_{\rm eff_\odot}}\right) + BC \tag{1.6}$$

The stellar radius is obtained from purely scale independent quantities, equation 1.7, which is the strength of the eclipsing binary method for distance determination.

$$\frac{R}{R_\odot} = \frac{r1.9757 \times 10^{-2}(K_1 + K_2)P(1-e^2)^{\frac{1}{2}}}{\sin(i)} \tag{1.7}$$

where A_V is the interstellar absorption (foreground plus intrinsic) obtained from the reddening e.g $E(b-y)$, which can be obtained from the standard photometry and the Strömgren c_1 colour index. The solar bolometric correction, radius and effective temperature is denoted by $M_{bol_\odot}$, $R_\odot$ and $T_{\rm eff_\odot}$ respectively. With the stellar bolometric correction, radius and effective temperature denoted by BC, R and $T_{\rm eff}$ respectively. The value r is the relative radius in units of the semi-major axis. A value of r can be obtained from the photometry of the system, however a scaling factor is required from the spectroscopic data. K_1 and K_2 are the radial velocity semi-amplitudes of the components (in $\rm kms^{-1}$), P the orbital period in days, e the orbital eccentricity and i the orbital inclination. To obtain these values and therefore obtain a value for the distance modulus, three sets of data are required. Firstly photometric, secondly spectroscopic and thirdly spectrophotometry. The latter is used for the accurate determination of the effective temperature, $T_{\rm eff}$. There are several ways to determine distances, the method of choice depending on the data sets available.

If spectrophotometry is not available, then observations in several bandpasses, for example Strömgren bandpasses, can be used to estimate the flux. When spectrophotometry is available a more simple and direct approach can be used which requires fewer assumptions. The ratio of the flux from the stars surface and the flux received at Earth is directly related to the ratio between the distance and the radius of the star, equation 1.8[9] where the two stars are denoted by subscripts 1 and 2.

$$d = R_{1,2}\sqrt{\frac{F_{*_{\rm surface,1,2}}}{F_{\rm Earth,1,2}}} \tag{1.8}$$

The flux observed from the satellite spectrophotometry can be compared to the flux derived from a Kurucz model of the stellar atmosphere. The method bypasses the need for Bolometric correction calibration and bandpass profiles. Additionally, authors have claimed the metallicity and interstellar absorption are more appropriately accounted for.

The ideal situation is to combine all three data sets thereby providing a more complete picture of the stars.

[9]This basic form of the relation assumes two very similar stars.

1.1.6.4 Effective temperature calculation

The calculation of the effective temperatures of the individual components in the binary system is one of the larger sources of uncertainty in the distance determination using eclipsing binaries. The effective temperature is calculated by fitting a model atmosphere to the observations. Therefore, for a given model, the greater the wavelength coverage and precision of the data, the more accurately the model can be fitted. It is possible to use reliable spectral classifications to limit the range of effective temperatures however the majority of eclipsing binaries observed in the Magellanic Clouds tend to be hot, bright stars, namely B type. Due to their high surface temperatures, typically 20 000 K, their peak output is in the UV. This is not transmitted by our atmosphere. Additionally, ionization occurs in the optical wavelengths resulting in very broad spectral lines, unsuitable for fitting in order to determine temperature. Therefore space based instruments are required to obtain these data. For cooler stars, fitting spectral features at optical wavelengths to a model can very good temperatures and log$g$ as demonstrated by Hill, [69].

As an example the effective temperatures of the stars comprising of HV2274 in the large Magellanic Cloud has been calculated by Ribas et al. [127] using measurements from the Hubble Space Telescope/ Faint Object Spectrograph, HST/FOS. This provided observations over the wavelength interval 1150 Å to 4820 Å, the UV wavelengths. Together with the optical photometry, atmosphere models were then fitted to reproduce the observed energy distribution. Determination of the primary temperature to $\pm$ 180 K was achieved; this also set the uncertainty for the secondary at the same value.

1.1.6.5 Apsidal motion

Apsidal motion is the rotation of the periastron or the rotation of lines of apsides[10] of an eccentric binary orbit, Figure 1.6 and hence only occurs in systems with elliptical orbits. The apsidal rotation period can vary from several years to several hundred years. The effect can be observed in both spectroscopic and photometric measurements. To clearly see the effect, it is desirable to have data sets that span a range of the same order of magnitude of the apsidal rotation period. The effect is due to either perturbations in the gravitational potential such as results from a third body, general relativistic effects or finite non-spherical mass distribution of the stars of the system. The value of the apsidal motion, indicates the deviation from Keplerian elliptic motion.

With respect to the photometric data set of an eclipsing binary with an eccentric orbit, apsidal motion is seen as a change in the times of successive primary and secondary minima. Therefore the relationship between the primary and secondary minima is not a linear function of time, but rather a more complicated function that takes account of the elliptical orbit. For an observer attempting to phase the data from a determined period and epoch, the future data sets, when combined with current data sets, will give eclipses that appear to be displaced.

The apsidal motion is slowly damped, as are many other effects, as the tidal forces circularize the orbit.

[10] Major axis of the elliptical orbit.

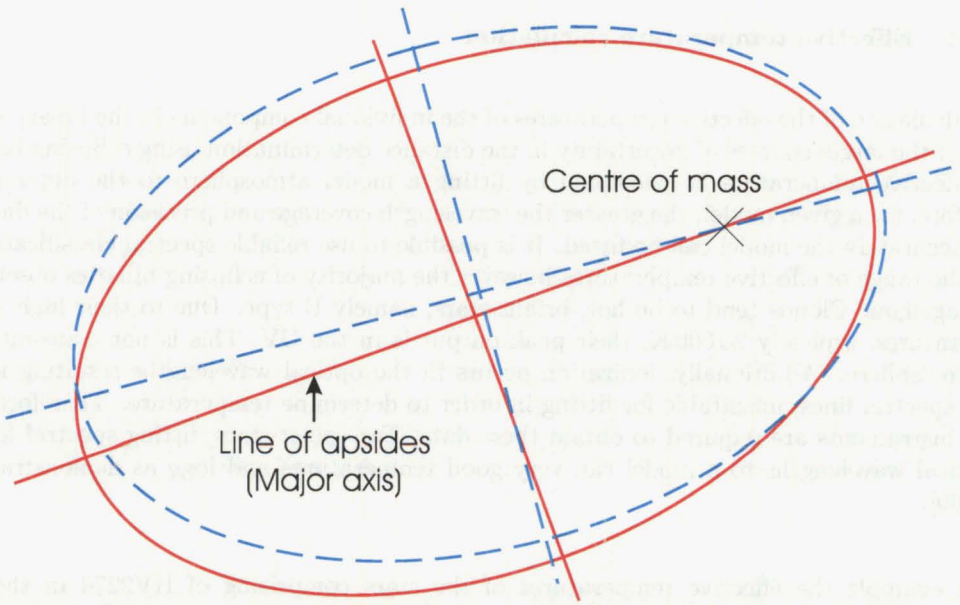

Figure 1.6: The apsidal motion is the rotation of the periastron or the rotation of lines of apsides (major axis) occurring in systems with elliptical orbits. The periods are generally far greater than that of the binary system, typically hundreds of years. The motion is observed from the photometric time series data (and also spectroscopic if available) though the relative change in phase of the eclipses relative to each other.

1.1.6.6 Forces on binary components

Though apsidal motion is one of the more easily detected variations, others are present. The formation of a binary system generally results in a set of initial conditions where the binary is not in its lowest energy state, i.e. the orbital paths are generally elliptical and therefore the stars' rotation non-synchronous (as synchronous rotation is not possible in an eccentric orbit). Over time, the components start to synchronize toward a circular orbit paths and similar stellar angular rotation speeds. This is due to the tidal torques acting on each star from the kinematics of the binary system. This is stronger the closer the two stars are. These and other features are:

- Stellar rotation axes becomes aligned perpendicular to the orbital plane of the binary
- Axial rotation periods become equal to the orbital period
- Non-spherical stars are made symmetrical with respect to the orbital plane
- Rotational flattening, resulting in the polar radius smaller than the equatorial radius
- Circularization of orbits, $e \rightarrow 0$

1.2 Classification of eclipsing binary stars

Like stellar classifications, there are many classes, if not sometimes apparently endless classifications, of eclipsing binary stars. Two main classifications are given below. Firstly, the classification groups of E, EA, EB, EW, as presented in the *General Catalogue of Variable Stars, GSC*. Secondly, the classification by Kopal [82], based on the Roche equipotentials of the binary systems'.

1.2.1 GSC classifications

These are broad ranging groups which over time, have been subdivided into small sub-groups. Their classification is based on shape of their light curve, without any further interpretation of their data. As a result, eclipse depths in each class can vary significantly depending on orbital inclination, stars relative sizes and the ratio of their surface brightness.

- **E**: Eclipsing binary systems, as outlined above

- **EA**: Algol (Beta Persei)-type eclipsing binaries. They have spherical or slightly ellipsoidal components whose light curves consist of distinct eclipses. The maximum light level between eclipses remains almost constant or varies slightly because of reflection effects, slight ellipsoidality of components, or physical variations. In some cases, secondary minima may not be detectable. Periods range from 0.2 to 10 000 days. Primary and secondary eclipse depths can vary significantly. An example is given in Figure 1.9

- **EB**: Beta Lyrae-type eclipsing binaries. These systems exhibit a continuous change in the light levels throughout their period thus making the onset of eclipses hard to determine. The secondary eclipse is always observed and is less than that of the primary. Periods are generally greater than 1 day. An example is given in Figure 1.11

- **EW**: W Ursae Majoris-type eclipsing binaries. Consist of ellipsoidal components almost in contact and therefore make the onset of eclipses hard to determine. Eclipse depths are very similar with periods generally less than 1 day. An example is given in Figure 1.13

1.2.2 Kopal's classification

This classification was introduce by Kopal [82], whose model was based on the Roche model for the surfaces of constant gravitational potential around two point masses. From the analysis of observational photometric and spectroscopic data, Kopal showed the systems could be described by three general classifications; well-detached, semi-detached and contact systems.

1.2.3 Roche lobes

In 1772, French mathematician Joseph Lagrange theorized the action of two point masses in a circular orbit on a test particle (such that the test particle was small enough that it would have no gravitational influence on the two point masses) in a reference frame rotating with the masses. The results showed that there are five positions, labelled Lagrange points $L_1 \rightarrow L_5$ (Figure 1.7), at which test particles will remain at rest relative to the point masses unless perturbed by an external force. About 90% of a star's mass is located within less than half the radius, so stars can roughly be modelled as point sources. If Lagrange's two point masses approximate an orbiting binary system, then we can now consider the gravitational and centrifugal forces on the test particle. The Roche lobes define surfaces of constant effective gravity (potential), which includes the net gravitational effect on the bodies in addition to the centrifugal force. These surfaces define what are called the Roche[11] equipotentials, and stellar surfaces will lie coincident with an appropriate equipotential. Both the Roche equipotentials and Lagrangian points are represented in a reference frame that is rotating with the binary. The limiting potential that passes through the point L_1 is called the Lagrangian surface or Roche lobe, and defines the

[11] Named after the nineteenth century French mathematician Edouard Roche.

break-point between the stars having independent atmospheres or a common envelope.

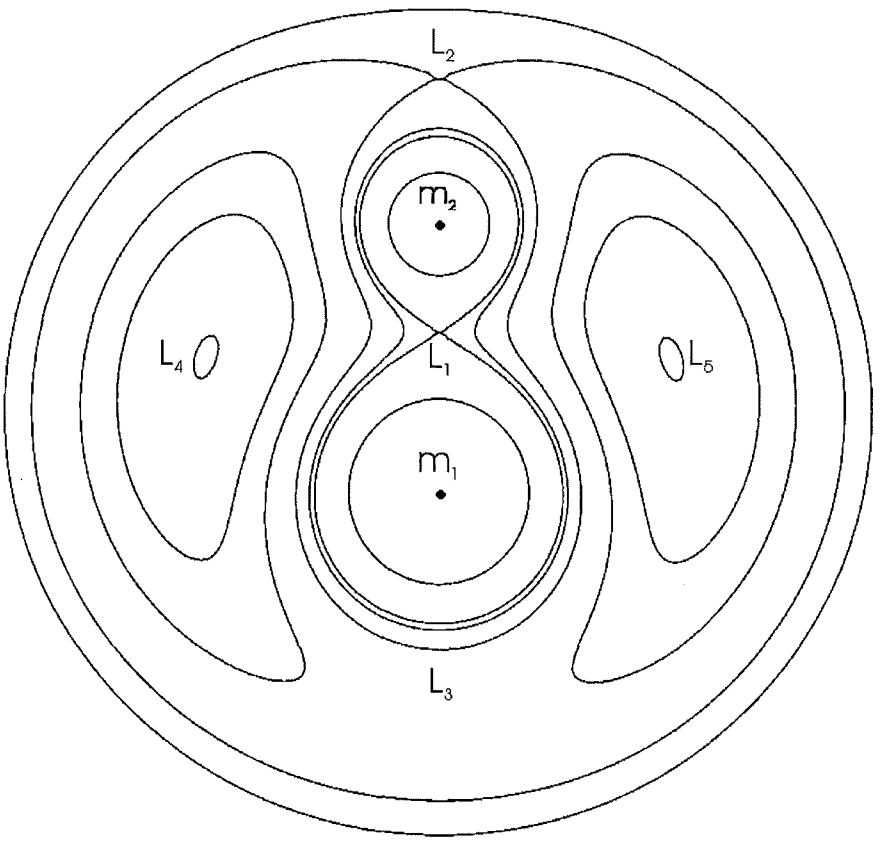

Figure 1.7: Figure reproduced from Batten, 1973 [13]. The diagram depicts a cross section of a binary orbit in the x,y plane of the surfaces of constant normalized potential. The five Lagrangian points, $L_1 \rightarrow L_5$ are depicted. Both the Roche equipotentials and Lagrangian points are represented in a reference frame that is rotating with the binary. Their positions are defined by the potentials of the stellar components, masses m_1 and m_2 where, $m_1 > m_2$ in the binary system, resulting in unique solutions for each binary system. The L_3 point indicated on the diagram is where equipotential surfaces, if drawn in, would intersect. This point provides an additional escape route, albeit a higher potential than L_2.

1.2.3.1 Well-detached binary systems

If both stars are relatively undistorted and are well within their Roche lobes, Figure 1.8, they will approximate spheres and are considered a well-detached system. These systems typically have periods greater than approximately two days, primarily due to their larger separations. A typical light curve is shown in Figure 1.9. These types of systems are preferred for study when the fundamental parameters and distance are desired due to their simple light curves and from the point of view of the astrophysics involved, although not as intriguing as a contact system.

Well-detached systems tend to be younger, less-evolved stars. As the stars deviate from the main sequence along their evolution tracks the radii of the stars generally increases. This expansion results in the star filling more of its Roche lobe. The stars in close orbits will interact with each other with various results. One is the change in classification from a well-detached system to a semi-detached system.

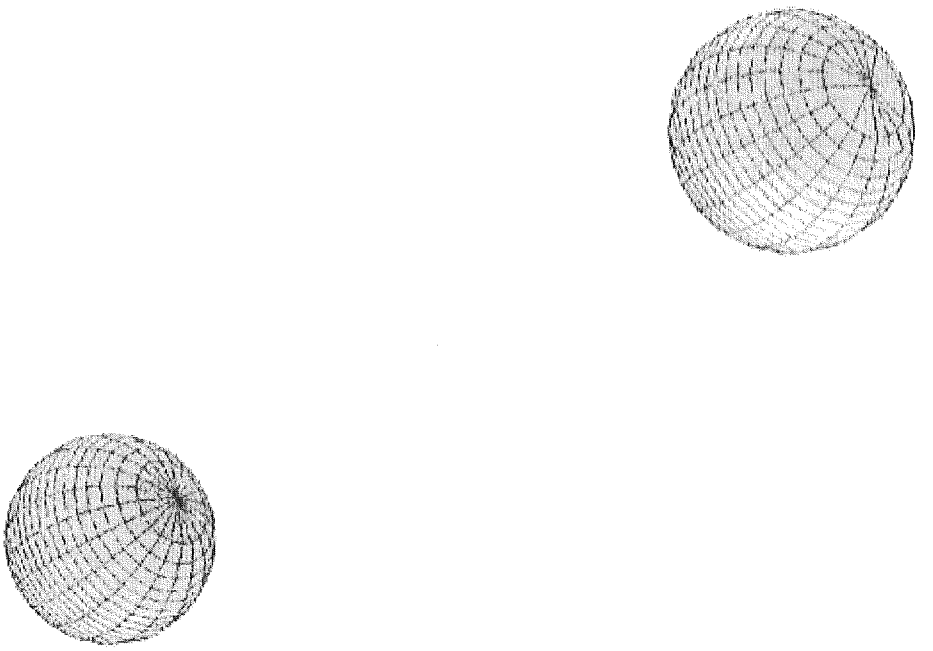

Figure 1.8: Figure reproduced from Hilditch, 2001 [73]. The stars in this well-detached system lie well within their respective Roche lobes. They can be considered spherical for modelling purposes. Orbit sizes for well-detached systems range from $1\,R_{\odot}$ and up.

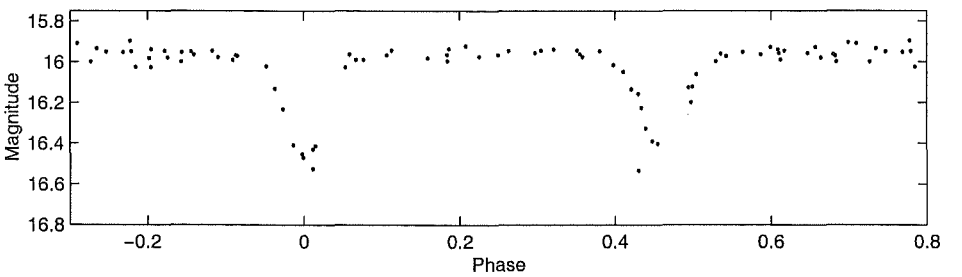

Figure 1.9: MOA J010341.5−720306. An example of a light curve from a well-detached system. This type of light curve is an EA type.

1.2.3.2 Semi-detached binary systems

These are defined as in the well-detached system case but one of the stars has filled its Roche lobe, Figure 1.10 or has begun mass transfer to the companion star via the Lagrange point L_1, Figure 1.7. The other component is still within its Roche lobe. The system provides some very interesting astrophysics to be studied however, due to the mass transfer, many more complications in modelling the system and phenomena arise. This process occurs when one component is highly evolved, generally, this implies significantly different stellar masses, radii and effective temperatures.

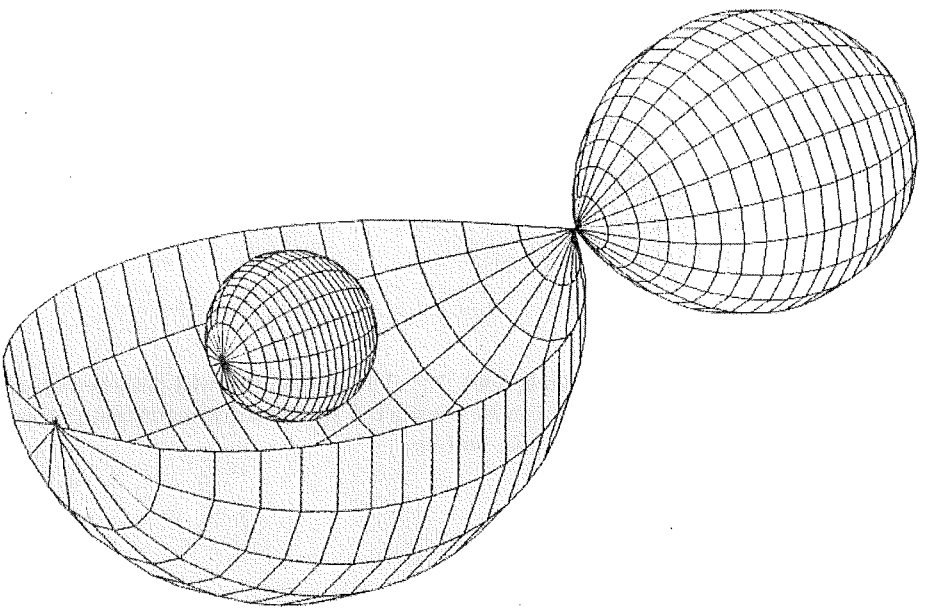

Figure 1.10: Figure reproduced from Hilditch, 2001 [73]. Semi-detached binary system. One star has filled its Roche lobe while the other is still well-detached from its Roche lobe, as seen by the cut-away outer shell representing the well-detached star's Roche lobe. Orbit sizes for semi-detached systems range from $1\,R_\odot$ and up.

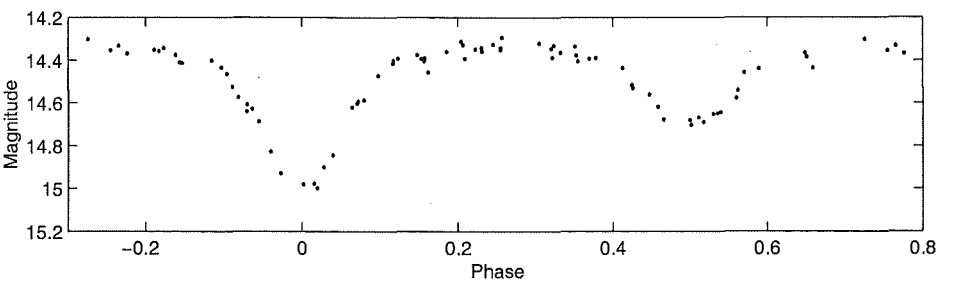

Figure 1.11: MOA J005554.4−722808. The baseline is now curved between eclipses compared to the well-detached case. This type of light curve is an EB type.

The light curve, Figure 1.11, now looks significantly different to the well-detached system,

Figure 1.9. It appears more sinusoidal than the well-detached system and the onset of eclipse is harder to determine.

Further evolution of both stars will lead to yet another classification change; to a contact system.

1.2.3.3 Contact binary systems

If both stars fill or exceed their Roche lobes, the system is called a contact system or over contact system[12]. At this stage both stellar cores are enclosed by a common envelope, Figure 1.12. It is possible for mass to be exchanged via the adjoining neck located at the inner Lagrangian point L_1. This envelope can co-rotate with the stars, with the limits being the Lagrangian points L_2 and L_3, Figure 1.7. At this stage in their evolution, the properties of the two stars can be very hard to distinguish. The sinusoidal shaped light curves, Figure 1.13, makes the calculation of the onset of the eclipses exceedingly difficult. This type of light curve can also look like a Cepheid variable, so care must be taken to distinguish the two. This was found to be the case when constructing the MOA database of eclipsing binaries in the SMC.

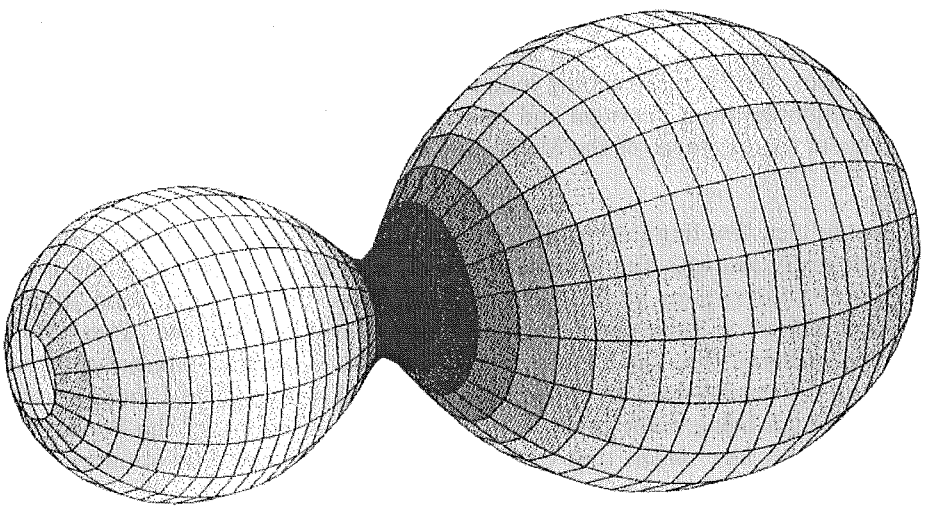

Figure 1.12: Figure reproduced from Hilditch, 2001 [73]. Contact binary. Both stars have over filled their respective Roche lobes and share a common stellar envelope about their cores. The joining region, commonly called the neck, is around the inner Lagrangian point L_1. It is through this volume that mass exchange takes place.

1.3 The Magellanic Clouds

The Magellanic Clouds are two galaxies in very close proximity to our own Galaxy, the Milky Way. They can be observed only from the Southern Hemisphere and are located near the South Celestial pole with an angular separation of $\sim 5°$. The Large Magellanic Cloud, LMC, whose optical centre is located at $5^{hr}\ 24^{m}\ -69.8°$ (J2000) is the larger, brighter and closer of the two Clouds at a distance of $\sim 50\,\mathrm{kpc}$. The Small Magellanic Cloud is located at $00^{hr}\ 48^{m}\ -72.2°$ (J2000) at a distance of $\sim 60\,\mathrm{kpc}$. Their name is a direct result of their appearance in the

[12]The moment in time at which both Roche lobes are completely full the two components are in contact. As these stars evolved over millions or billions of years this exact point in time is rare to see. Beyond this point the stellar atmospheres can appear to be one and the system is termed an over-contact binary. In this text, the term contact binary will encompass both contact and over-contact systems.

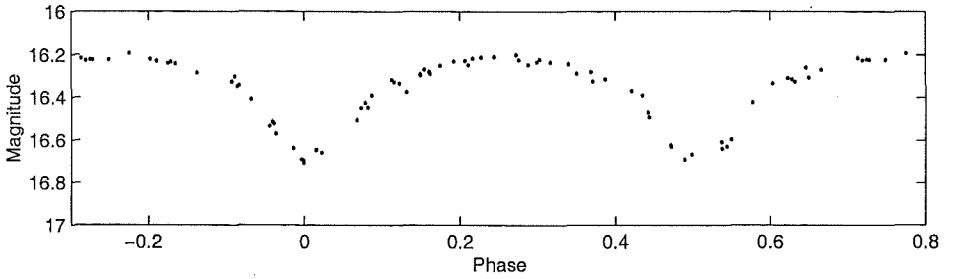

Figure 1.13: MOA J005334.4−724231 a typical contact system light curve. There is continuous variation in the base line magnitude as compared to the previous two cases, Figures 1.9 and 1.11. The light curve approximates a sinusoidal type variation. This type of light curve is an EW type.

Southern Hemisphere skies. They give the illusion of a misty thin cloud high overhead and one can fully understand from this the names that they were given. A Portuguese seafarer Magalhas who circumnavigated the globe in the 1600's had his name associated with the Clouds. In these times sea navigation relied heavily on the Clouds when journeys around the Cape of Good Hope and southern oceans were undertaken. Unlike the North Celestial pole star, a South Celestial pole star is non-existent and therefore the Clouds took the place as indicating the Southern Hemisphere's *pole*. Archaeo-astronomy indicates that for several thousands of years prior to the seafaring explorers from Portugal and Spain, the inhabitants of the Southern Hemisphere had knowledge of the existence of the Magellanic Clouds, albeit not as we know them now.

It is only in the past few hundred years have we begun to really understand what the Magellanic Clouds really are with the work of Herschel, who in 1847, published the book *Results of Astronomical Observations at the Cape of Good Hope*. In the publication, Herschel gave descriptions of objects in both the Large and Small Magellanic Clouds. Two decades later, Abbe first hypothesized that the Clouds were in fact two very close external galaxies. In the years leading to the turn of the 20th century, more detailed studies of the Clouds began with the major break-through being made by Miss H Leavitt. Her discovery of the Period-Luminosity relation for Cepheids now meant that extra-galactic distances could be obtained. This result then gave solid evidence that the Clouds were in fact extra-galactic objects.

1.3.1 The Local Group

The two Magellanic Clouds and our own galaxy, Figure 1.14 are members of the Local Group, Figure 1.15, which consists of some 40 galaxies, loosely bound but held together by their respective gravitational interactions. The group contains a variety of different galaxies, Figure 1.15, large spirals such as the Milky Way and Andromeda to small spirals such as M33 through elliptical galaxies such as NGC205 to irregular types such as the LMC and SMC. Over history, many of these galaxies have been identified, not as galaxies, but as hazy cloud-like objects in the sky as this is how the human eye perceives them. It is only with the advent of optical systems has the true nature and extent of these objects has been realized.

The majority lie within three million light years of the centre of mass of the Local Group with the remainder extending out to approximately five million light years.

The Local Group appears to contain a mass that could be and has been considered to be reasonably isolated with little interaction with the member galaxies moving in random paths. However there appears to exists a fine balance between all the interactions and a simple approach

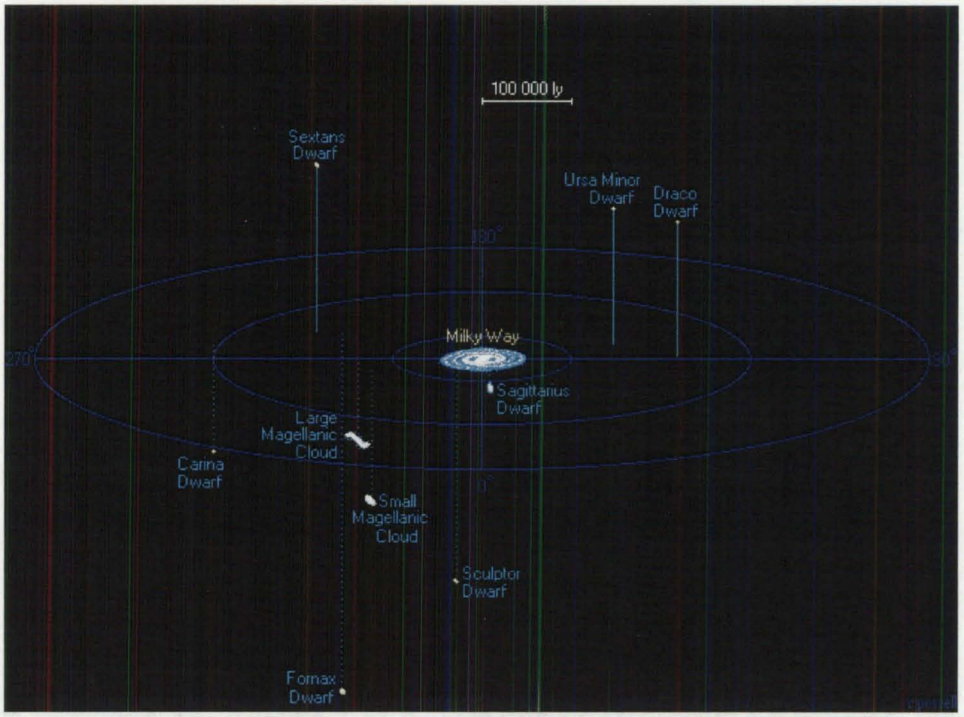

Figure 1.14: A 3-dimensional view of the Local Group within a 500 000 light year radius. The Milky Way is depicted as being at the centre of Local Group with directions based on the Galactic coordinates. Sagittarius Dwarf galaxy, at 78 000 light years, is the closest to the Milky Way followed by the LMC and SMC at 170 000 and 210 000 light years. Diagram courtesy of Richard Powell[14].

of treating each as an independent isolated system is inappropriate. This is clearly evident with the interactions of our own Galaxy and the LMC and SMC. The Local Group itself is now considered to have no obvious boundaries, and to account for all the interactions, one must allow for all nearby galaxies. This leads to the Local Group being thought of more as a local region.

1.3.2 Interest in the Large Magellanic Cloud and the Small Magellanic Cloud

The primary reason for the interest in the Magellanic Clouds, and especially the LMC, is that they are the first rung in the empirical calibration of standard candles in the extra-galactic distance scale ladder.

Some additional areas of interest with the Magellanic Clouds are:

- Their closeness to our Galaxy
- Their interactions with each other and our Galaxy
- Different structure of each galaxy
- Different chemical composition of each galaxy

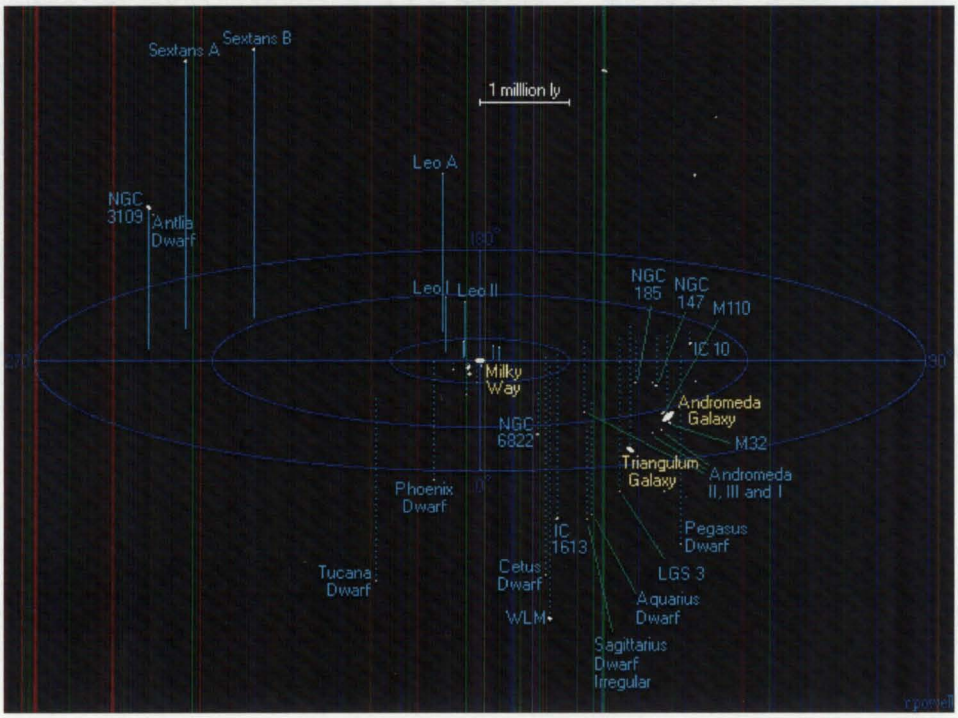

Figure 1.15: A 3-dimensional view of the Local Group. The Milky Way is depicted as being at the centre of the Local Group with directions based on the Galactic coordinates. The majority of stars lie within the Milky Way and Andromeda galaxies with dwarf galaxies typically containing a few tens of millions of stars. Solid lines indicate galaxies above the Galactic plane, dashed line are galaxies below the Galactic plane. Diagram courtesy of Richard Powell[16].

Their closeness to us means their observation can be easily achieved without the need for substantial equipment and cost. Both Clouds are irregular in shape, although the LMC does exhibit a bar-like structure covering an area of sky $\sim 3° \times \sim 1°$. This irregularity is attributed to the interactions within the Local Group. Theories, predicted properties and the physics of processes can be tested in these two galaxies. Many important results have come from the Clouds. Too numerous to mention in this brief review, refer to Westerlund [169] for a comprehensive summary and discussion of the past research.

1.3.3 Past interactions and properties of the Large and Small Magellanic Clouds

The history of the interactions that have occurred between the Magellanic system, that being the LMC and SMC, and M31 as well as our Galaxy is not entirely known. The majority of clues to their past are given by several observable features of the Magellanic system.

1. The envelope of neutral Hydrogen, HI (21 cm), around both the LMC and SMC
2. The Magellanic Stream, the bridge region of HI interconnecting the Clouds to the Galaxy
3. The bar-like structure of the LMC and the possible bar of the SMC
4. The concentration of gas and dust in the LMC around the 30 Doradus region
5. The asymmetry of dust/plasma ratios in the LMC
6. The origin of the wing in the SMC
7. Formation and evolution of super-giant shells

The exact origin of the Magellanic Clouds is not exactly known. Present day observations of stellar formation regions and gas distributions produced from past interactions can give a possible history of the Clouds. Given the present positions and velocities of the two Clouds and the Magellanic Stream, models suggest the system is on an eccentric plunging orbit around the Galaxy with a period of around 2 Gyr. The two Clouds are separated by approximately 20 kpc. Their last close encounter where the distance was only $2-7$ kpc, 200 to 400 million years ago, resulted in strong gravitational forces pulling gas out of the SMC. The result was the Magellanic Stream. Models used to reproduce the system's history lead to the following conclusions:

1. The past 10 Gyr the LMC and SMC have been gravitationally bound
2. The Magellanic Stream's source is the SMC with its formation due to tidal interactions with the LMC. Its velocity was dictated by the Milky Way once it departed the Magellanic System
3. The Magellanic system revolves around our Galaxy in an anti-clockwise direction as seen from the present position of the Sun

4. The distance between the LMC and SMC has varied markedly over time ranging from 2−7 kpc 0.2 Gyr ago up to 50 kpc 0.8 Gyr ago

5. The extra-galactic distances from the LMC and SMC to the Milky Way are ~50 kpc and ~60 kpc respectively. The closest approach to our Galactic centre occurred 50 Myr ago

6. Dynamical friction causes the distance between the SMC, LMC and our Galaxy to decrease in an oscillatory manner

Over the past ~10 Gyr many interactions are predicted to have occurred between the LMC, SMC and our own Galaxy. Evidence of these interactions is seen through bursts of star formation resulting from proto-clouds collapsing under gravitational forces. In addition, almost none of the LMC clusters are found with ages in the range of 4−10 Gyr. This results in grouped stellar populations matching those of the predicted interactions. Further evidence is seen from kinematical peculiarities of distortions in the outer regions of the galactic HI plane, [148].

1.3.3.1 The Large Magellanic Cloud

The LMC, Figure 1.16, is regarded as a flat disk inclined at an angle ~35°[132], although the inclination is often quoted over a range 33−45°. The distance modulus is 18.5 ± 0.2 mag.[17] with a total mass of $\sim 2 \times 10^{10}\,M_\odot$, luminosity, $L \approx 2 \times 10^9\,L_\odot$ (approximately 10% of the Galactic value) but making it the 4^{th} most luminous in the Local Group. It has a rotation speed, from HI observations of the order of $80\,kms^{-1}$. It exhibits a bar structure in the centre with one arm, hence its SB(s)m designation. The rotation centre is not central about the bar but ~1° northwest of the brightest region.

1.3.3.2 The Small Magellanic Cloud

The SMC inclination is 90°, however its depth is still undetermined, possibly ~10[92] to 20 kpc [94] along the line of sight, Figure 1.16. This makes its type designation and structure harder to determine. The fine structure appears very complicated and its designation of SB(s)mp shows this. The more distant of the two, the galaxy has a distance modulus of 18.9 ± 0.2 mag[18], a mass of $\approx 2 \times 10^9\,M_\odot$, and a luminosity $L \approx 2 \times 10^8\,L_\odot$ (approximately 10% of the LMC, 100^{th} of the Galactic value). Although no disk-like structure is evident, if there is one, it would have to be in the line of sight. The SMC is much less evolved than the LMC. One of the obvious differences between the two Clouds is the difference in HI, HII and molecular cloud regions.

The ionized hydrogen levels in the Clouds differ significantly. The 30 Doradus region, the giant nebula in the LMC, accounts for ~25% of the total H_α emission, a factor of two greater than the entire SMC. Most of these H_α emissions in the LMC are attributed to fine filamentary structures. The SMC, relative to the LMC, is deficient in large nebulae of high surface brightness as well as filamentary structures. It presents a smoother surface as far as the distribution of gas is concerned.

The HI regions in the LMC have a complicated structure which is shown to be well correlated with the HII regions. In the SMC the HI regions are smoother in terms of surface distribution

[17] This is a general estimate, very dependent on the method used for the distance determination.

[18] The SMC is generally considered 0.4 mag. more distant than the LMC. The depth of the SMC makes the distance determination difficult.

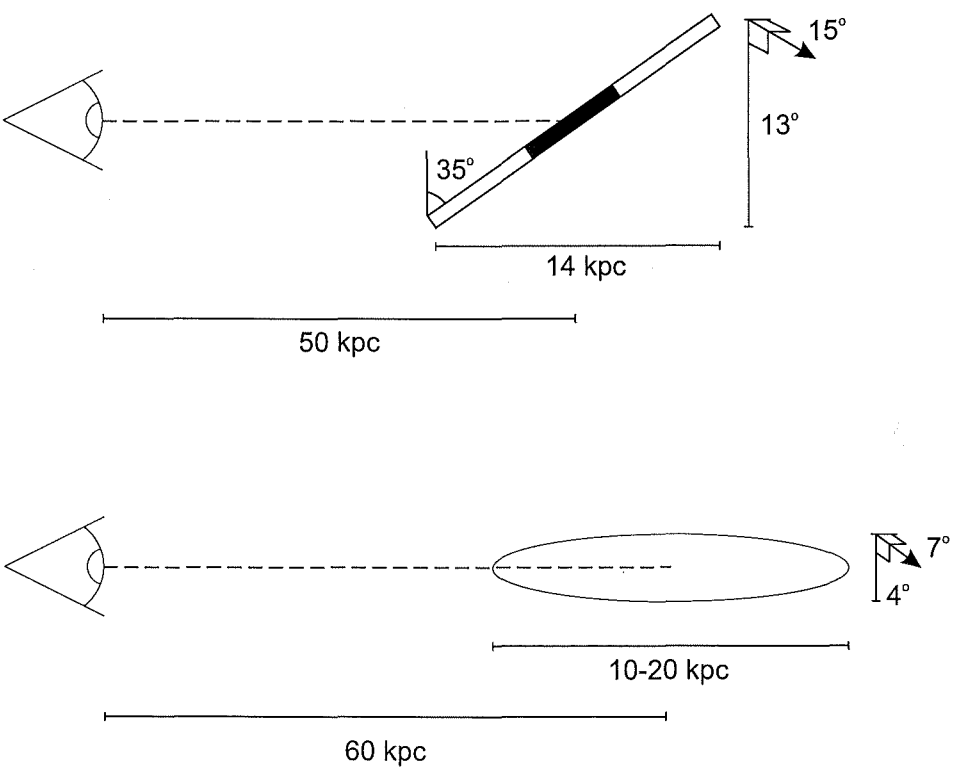

Figure 1.16: The upper and lower schematic diagrams of the LMC and SMC respectively, represent a simplified side-on view of the two Clouds with their approximate dimensions and distance. The dark region in the LMC represents the bar like structure present in the LMC.

with few complexes as seen in the LMC. It is the complexity of the neutral hydrogen region that has lead to the suggestion of an appreciable extent to the SMC, (Hindman 1964, 1967) [76], [77]. Work by Staveley-Smith et al. (1995) [141] have revealed further detailed data. It is in these regions that information about the younger generations of stars is expected to be found.

The detailed structures in both the LMC and SMC along with the filament structures are due to their interactions not only with each other but also with our own Galaxy. These are also linked to star burst formations. This has resulted in the metallicity differences compared to the Galaxy: LMC $2\frac{1}{2}$ and the SMC 10 times less than the Galactic value [113]. The differences in metallicity give different evolutionary tracks of stars as well as different stellar structure.

1.3.3.3 Molecular content

One of the methods used to determine the molecular content is to make CO, carbon monoxide, observations. This is due to the excitation of CO at low densities, typically $100\text{-}1000\,\mathrm{cm}^{-3}$, resulting in saturated lines of its main isotope. This makes the other parameters of the interstellar gas relativity undefined. As a result, a significant number of molecular transitions that require excitations are required before comment or determination of the chemical composition can be made. The comparison of the CO emissions in the Clouds show a lower value than that of our Galaxy and this is attributed to the low dust-to-gas ratios and high mean UV radiation field as well as lower C and O abundances. Therefore the comparison of the Galactic CO to H_2 abundance ratio will yield an erroneous result for the amount of molecular hydrogen in the clouds.

1.4 Distance to the LMC and SMC

1.4.1 The geometry and reddening, foreground and internal

There have been many ways in which the distances to the Magellanic Clouds have been measured. Most, if not all of these methods, are compared to each other in order to test whether each method itself does provide a reasonable figure, within uncertainty.

Over the last decade, the number of objects identified stellar type has risen dramatically and therefore the number of objects for distance determination. However there is still question over the results for the distance to the LMC, namely the short ($< 18.50\,\mathrm{mag.}$) and the long ($> 18.50\,\mathrm{mag.}$) distance. Some methods favour the short distance while others the long. It appears the uncertainties in the distances are now primarily due to the foreground and internal reddening contributions from the interstellar medium. Another contribution to the uncertainties is the actual depth along the line of sight of the Clouds. Studies of red clumps, dust in the LMC as well as the disk inclination of the LMC suggest that the disk may have a slight upward bend on the lower section closer to our line of sight [132]. This suggestion arises from studies of red clumps in regions of the LMC which have red clump distances shorter than those throughout the expected plane of the tilted disk structure.

The elongation of the SMC results in distances to targets being referenced to the optical centre of the SMC, which is difficult to determine. Due to this, the LMC is often preferred over the SMC for distance determination.

The two galaxies provide a testing ground for distance measuring methods, although some could

have additional effects due to different metallicities such as the Period-Luminosity relationship. The distance and methods used that are tested on the Clouds are then imposed on the other members of the Local Group whose distances are far greater than that of the Clouds. Secondary distance measurement methods such as Planetary Nebula, rely on an initial zero point for the distance scale, namely the distance to the LMC.

Studies by Bessell [20] show average values of reddening in the SMC and LMC are of the order of 0.06 mag. with peak variations is high as 0.3 mag., however the LMC exhibits a greater variation around the average value than the SMC. The determination of a reddening value for the target used for distance determination in the LMC is, at this point in time, one of the major sources of uncertainty. Its value can have significant effect on the result derived for the distance modulus. An error of 0.1 mag. in distance modulus relates to an error of 5% in physical distance. Ideally each measurement of the distance would have an associated measure of the reddening along the line of sight. This is the case for the eclipsing binary method.

1.4.2 Different methods of measuring the distance

There are many methods used to measure the distance (generally expressed as the distance modulus) to the LMC. The following is a brief summary of the main methods used over recent years.

1.4.2.1 Distance modulus using Cepheids

The use of Cepheids for distance determination is one of the oldest methods. The method has received several detailed studies over the years and its strengths and weaknesses are now coming under more scrutiny as we can now easily probe other galaxies with different properties. This method uses the Period-Luminosity, PL, relation, or the Period-Luminosity-Colour, PLC, relation. The PL relation is relatively insensitive to metallicity; although presently, the amount and sign is not yet known. It is however very sensitive to reddening, which in the LMC is patchy in both the foreground and internally. The opposite is true for the PLC relation. These sources of error lead to an uncertainty in the zero point, the value of which varies from paper to paper. Feast [45], [46] and [44] favours an uncertainty of 0.15 mag, or ~7.5% in distance where the uncertainty is mainly due to reddening. The HST key project[19] use a figure of 0.1 mag (~5 % in distance) for the reddening. The HST key project also identified several areas of error:

- Camera/photometric system calibration
- Reddening
- Metallicity
- Bias in the PL relation due to incompleteness of the sample

Where possible, these were taken into account giving a final result of 18.50 ± 0.10 mag. (50 kpc)[20].

Additionally, the shorter period Cepheids have a different slope on the PL relation than the longer period Cepheids. The change-over is around ten days. The cause of the period change

[19]The project is titled *Hubble Space Telescope Key Project to Measure the Hubble Constant*[53] and uses the distance to the LMC to determine the Hubble Constant, H_0.

[20]This gives a value for the Hubble constant of $H_0 = 72 \pm 8\,\mathrm{kms}^{-1}\ \mathrm{Mpc}^{-1}$.

and how it may influence the use of Cepheids for distance determination is not fully understood.

From recent data, the distance modulus for the LMC obtained using Cepheids is in the range, 18.29−18.72 mag., refer to Figure 1.17 and Table 1.4.

1.4.2.2 Distance modulus using RR Lyrae variables

For determining the distance using RR Lyrae stars, their absolute magnitude M_V must first be determined. A typical value[21] of 0.59 ± 0.03 mag. can be used but there is a possible non-linear dependence on metallicity as theory and observation only agree if this is the case. Therefore careful selection is required from outer (halo) to inner (centre) regions of galaxies to ensure the metallicity differences are accuracy accounted for. Reddening is also an issue along with temperature sensitivity on the HR diagram.

Past results from RR Lyrae have tended to favour the shorter distance scale to the LMC. Recent results are still mixed, with some tending toward an intermediate distance, such as Fabrizio's (2002) result of 18.43 ± 0.06 mag. [40], while others, Table 1.4, are still favouring the shorter distance of approximately 18.25 mag.

It still appears that the dominant contributor to the uncertainty for absolute magnitude of the RR Lyraes is the extinction.

1.4.2.3 Distance modulus using clusters

The stars in the clusters observed are fitted to features in the CMD such as the ZAMS line, AGB or HB etc. There is a sensitivity to metallicity, reddening and helium abundance. The majority of results favour the short distance while only a few tend to favour the long distance.

1.4.2.4 Distance modulus using red clump stars

The red clump in the HR diagram is used as a calibrator of stars. The red clump consists giants that are core helium burning stars, with a high metallicity equivalent to that of the horizontal branch stars. On the HR diagram, it is evident as a compact red clump and is also clearly apparent in almost all galaxies that have been studied.

The red clump is however a feature spread over a range of magnitudes and colours and the exact fit can be difficult. Errors occur from age of the cluster, metallicity, reddening and photometry. The red clump method is generally calibrated using Hipparcos measurements of nearby red clumps. Many observations of the red clump stars are being made in the near infrared, namely the H (1.6 μm) and K (2.2 μm) bandpasses. These bandpasses have some significant advantages especially the H bandpass as this wavelength can help reduce uncertainties in the extinction estimations. However a major issue arises over standards for the two bandpasses. The calibration to a standard system is far from ideal. Presently, variations in the order of 0.2 mag are easily possible from system to system. One result to come from the red clump method is the possibility of a warp in the disc of the LMC. The red clump distance of the southwestern region of the LMC on the sky appears closer than expected. One possibility is a warp and twist in the disk, [132], with features extending 2.5 kpc out of the plane.

[21] Weighted average from 10 models.

The results generally favour the short distance, OGLE 18.24 ± 0.08 mag. [156], 18.49 ± 0.03 mag. [8].

1.4.2.5 Distance modulus using blue-giant stars

The Wind Momentum Luminosity Relationship, WMLR, links the wind momentum to a function of the total photon momentum, resulting in the Flux $\propto \frac{\text{Luminosity}}{\text{Distance}^2}$. The stars are typically bright (M_V=-7.0 to -9.0 mag., spectral type B8 to A4 supergiants, $15-20\,M_\odot$, $\log(T_{\text{eff}}) \sim 4$). In the HR diagram, the Blue super-giants pass through the stage from the main sequence to the instability strip in a short period of time, typically 1000 years. During this time, the luminosity of the stars can be considered constant. The large energy and momentum density of the photosphere's radiation field leads to a Non Local Thermodynamic Equilibrium, NLTE, condition from which a stellar wind results. Observations then measure the H_α absorption/emission due to the stellar winds for which the ionization equilibria are known very accurately. This gives $\frac{\delta T_{\text{eff}}}{T_{\text{eff}}}$ to $\sim 1\%$ using the Mg lines. There is a metallicity dependence.

Another relationship that can determine the luminosity of these stars is the Flux Weighted Gravity Luminosity Relationship, FWGLR. This exploits the relationship between the gravity and H_α as a luminosity indicator, as H_α is a function of T_{eff}. The method is expected to give errors of ± 0.03 mag. for the LMC. It is possible, with use of the 8 m+ telescopes to reach 30^{th} magnitude stars.

Both these methods appear very promising for distance determination, [83].

1.4.2.6 Distance modulus using Supernovae

The most reliable type of Supernova for distance determination are the type Ia[22]. The majority of these types, with the notable exception of SN 1987A in the LMC, follow a similar trend.

In the Supernova explosion, the ejected material expands radially outwards in a shell. Measurements of the absorption line velocities in this expanding shell and the application of Baade's method can be used to derive a distance to the Supernova. However, Baade's method does make some assumptions: 1. The expanding envelope is symmetrical, 2. The emitted flux of the expanding shell is approximated by a black body. Deviations from these assumptions does lead to different values for the distance to the Supernova. The observation of light echos can be used to determine the three dimensional geometry of the circumstellar shell and thus help to constrain values on the expanding shell.

Observations of the Supernova up to 10 days after the blue maximum have little reddening effect, however after this time the dust in the host galaxy needs to be known as the effect of reddening becomes significant. This results in a change of colour over time. Another issue of using Supernovae is the sample size, as these events are not numerous for a given galaxy.

The distance derived to LMC via SN 1987A spans the range of values 18.37 to 18.67 mag., some recently calculated values are presented in Table 1.4.

[22]Thermonuclear explosion of a white dwarf, $L_{\text{max}} = 3 \times 10^9\, L_\odot$. Hydrogen is absent in the spectrum.

1.4.2.7 Distance modulus using eclipsing binaries

This is perhaps one of the most promising methods. The distance and reddening is calculated for each individual eclipsing binary. Therefore each system provides an independent distance. The data collection required is extensive and requires care at all stages.

The first accurate CCD observations of eclipsing binaries were made at ESO by Jensen, Clausen and Giménez 1988, [80], who were inspired by Graham 1983 [59]. Over the following seven years, several bright systems in both the LMC and SMC were observed, Tables 1.2 and 1.3. These systems were mainly from the Harvard catalogue, complied by Gaposhkin [56] after decades of analyses of photographic plates. A review by Hilditch, 1986 [72], presents in Table 1 of the review, some 180 eclipsing binaries in 10 nearby galaxies). After the mid 1990's, CCD microlensing surveys produced many more detections thereby providing a vast choice of systems for further study.

High quality photometric data is available for several LMC and SMC eclipsing binaries, Table 1.2 and 1.3, however high quality spectroscopy is only available for a few of these systems. Ultraviolet spectrophotometry from the now redundant IUE exists for HV 2241, HV 2274 and HV 12634 in the LMC and HV 2226 in the SMC. HST/FOS (1150 Å to 4820 Å) and HST/GHRS (R=23 000, range of 34Å centred at 1305 Å and 1355 Å, UV stellar photospheric lines for B-type stars) are available for HV 2274, Guinan 1997, [66].

The public domain of some datasets has enabled various analyses to be undertaken, in particular HV 2274. However various distances, not in agreement within uncertainties, have been reported using the same data set but different analysis methods. The re-analysis of HV 2274 Groenewegen and Salaris [63], following the method used by Guinan et al. for distance determination, [67] and [68], yielded a significant variation in results, 18.42 ± 0.07 compared to Guinan et al. 18.30 ± 0.07 [67]. Based on this result, Groenwegen and Salaris made the following comment, [63]:

It turns out that different selections of the photometric data, the set of model atmospheres and the constraints on the value of the ratio of selective to total extinction in the V-band, result in a 25% range in distances (although some of these models have a large χ^2)

The two main findings from their analysis of HV 2274 compared to Guinan et al. were:

1. Photometrically well calibrated dataset covering a large wavelength region is essential.
2. The discrepancies among theoretical model atmosphere codes is alarming and further investigation is required.

The first finding is reasonably well known, however the second was highlighted in their paper and may explain some the discrepancies seen in the eclipsing binary results to date, particularly those using the same datasets.

Tables 1.2 and 1.3 provide a summary of some of the published observations on eclipsing binaries in the Magellanic Clouds. Some of the catalogues of eclipsing binaries are presented. MACHO have a catalogue of some 6000 eclipsing binaries in the Magellanic Clouds, [32], however the numbers for each cloud are unknown at this stage.

Table 1.2: A summary of some of the more recent eclipsing binary systems studied in the LMC.

System	Author	Distance, $(m - M_V)$ or photometry
HV 982	Clausen et al. 2003, [30]	18.63 ± 0.08
	Pritchard et al. 1994, [120]	
	Pritchard et al. 1998b, [122]	
	Fitzpatrick et al. 2002, [48]	
	Fitzpatrick et al. 2000, [49]	18.50 ± 0.06
HV 2241	Niemela & Bassino 1994, [102]	18.5 ± 0.4 spectroscopic orbits
	Davidge 1987, [35]	UBV photoelectric photometry
	Pritchard et al. 1998a, [121]	18.43 ± 0.20
	Guinan et al. 1996, [65]	Calculated parameters
	Ostrov et al. 2001, [111]	VB photometry, est. 18.65, 18.80[23]
	Barge et al. 2003, [12]	
	Maloney et al. 1998, [90]	
HV 2274	Watson et al. 1992, [166]	BVI photometry
	Guinan et al. 1996, [65]	Calculated parameters
	Guinan et al. 1997, [66]	18.49 ± 0.07
	Guinan et al. 1998, [67]	18.30 ± 0.10
	Fitzpatrick et al. 2000, [49]	18.36 ± 0.10
	Ribas et al. 2002, [127]	Calculated parameters
	Groenewegen & Salaris 2001, [63]	18.46 ± 0.06
	Udalski et al. 1998, [158]	18.22 ± 0.13
	Bradstreet et al. 1994, [23]	Calculated parameters
HV 2543	Niemela & Bassino 1994, [102]	Spectroscopic orbits
HV 2765	Davidge 1987, [35]	UBV photoelectric photometry
HV5936	Jensen et al. 1988, [80]	$uvby$ photometry
	Bell et al. 1993, [18]	18.1 ± 0.3
	Guinan et al. 1996, [65]	Calculated parameters
	Bradstreet et al. 1994, [23]	
	Fitzpatrick et al. 2003, [51]	18.18 ± 0.09
	Fitzpatrick et al. 2002, [50]	
HV5943	Davidge 1987, [35]	UBV photoelectric photometry
HV12484	Tobin et al. 1993, [150]	BVI photometry
HV12578	Clausen et al. 2003, [30]	$uvby$ photometry
HV12634	Jensen et al. 1988, [80]	$uvby$ photometry
	Guinan et al. 1996, [65]	Calculated parameters
	West et al. 1992, [168]	BVI photometry
	Loudon & Budding 1993, [87]	Light curve analysis
EROS 1044	Grison et al. 1995, [61]	Detection in EROS database
	Kang et al. 1997, [81]	
	Ignasi et al. 2002, [126]	18.38 ± 0.08
	Maloney et al. 2001, [91]	

continued on next page

Table 1.2: *continued*: MACHO*05:36:48.7−69:17:00 u filter, image subtraction photometry

System	Author	Distance, $(m - M_V)$ or photometry
MACHO*05:34:41.3 −69:31:39	Ostrov 2001, [109]	Published photometry and Spectroscopic observations
SK−67° 105	Ostrov 2003, [110]	V photometry
	Haefner et al. 1994, [70]	
	Niemela & Morrell 1986, [103]	Radial velocity
	Niemela & Morrell 1999, [104]	Radial velocity, review
Catalogue	Gaposhkin, 75 eclipsing binaries in the LMC 1977, [56]	
Catalogue	EROS, 79 eclipsing binaries in the LMC 1995, [61]	
Catalogue	MACHO, 611 eclipsing binaries in the LMC 1997, [5]	
Catalogue	OGLE, 2580 eclipsing binaries in the LMC 2003, [181]	

1

1.4.2.8 Other methods

There are other less-used methods such as Mira variables (Feast 1988,[45] and 1989, [46]), but the dependence on M_V(RR) makes the method more of a secondary method.

Secondary methods, which rely on the LMC distance as a scaling factor such as Planetary Nebulae, can provide additional values to distant galaxies. Novae can be used although one has to wait for one to occur in the galaxy being observed. Additionally, only 10% of all novae follow the same Maximum Magnitude Rate of Decline relation, MMRD. They are detected via surveys and have known metallicity effects. Once again reddening determination is a complicating factor.

1.4.2.9 Summary

The graph in Figure 1.17 and the accompanying Table 1.4 show the trend and spread of the distance moduli. The currently quoted value of 18.50 ± 0.20 mag. (approximately the median) to the LMC covers the majority of the results from the various methods. The value is most unlikely to change outside of the ranges shown; instead the uncertainties will be reduced. The question of the short or long distance is now more a case of a middle distance within a range

[23] Based on two different temperature scales.

Table 1.3: A summary of some of the more recent eclipsing binary systems studied in the SMC.

System	Author	Distance, $(m - M_V)$ or photometry
HV 1620	Davidge 1998, [36]	UBV photometry
	Niemela & Bassino 1994, [102]	Spectroscopic orbits
	Pritchard et al. 1998a, [121]	Calculated parameters
HV 1620	Davidge 1998, [36]	UBV photometry
HV 1761	Duncan et al. 1993, [41]	BVI photometry
HV 1876	Jensen et al. 1988, [80]	$uvby$ photometry
HV 2226	Jensen et al. 1988, [80]	$uvby$ photometry
	Bell et al. 1991, [17]	18.6 ± 0.30
	Guinan et al. 1997, [66]	18.78 ± 0.15
	Maloney et al. 1998, [90]	Calculated parameters
HV 1433	Clausen et al. 2003, [30]	$uvby$ photometry
HV 2016	Jensen et al. 1988, [80]	$uvby$ photometry
HV 2208	West et al. 1992, [168]	BVI photometry
	Loudon & Budding 1993, [87]	Light curve analysis
HV 11284	Clausen et al. 2003, [30]	$uvby$ photometry
AzV73	Ostrov 2001, [108]	Calculated parameters
(OGLE SMC_SC5 202153)	Niemela & Bassino 1994, [102]	Spectroscopic orbits
Catalogue	Gaposhkin, 33 eclipsing binaries in the SMC 1977, [56]	
Catalogue	OGLE, 1459 eclipsing binaries in the SMC 1998, [159]	
Catalogue	MOA, 167 eclipsing binaries in the SMC 2002, [14]	

of uncertainties.

The role of the LMC as the zero point of the extra-galactic distance ladder may continue for some time to be an area of contention. The issue of variation in reddening in the LMC may continue to be a difficult obstacle to overcome. A number of groups are turning their attention to M31 as a possible new cornerstone for the extra-galactic distance scale. However many issues mentioned above need to be addressed as they will continue to be sources of error. The technology now easily allows us to study Cepheids, RR Lyrae, eclipsing binaries etc. in M31 but this is not as easy as the study of stars in the LMC and SMC as larger telescopes are required due the faintness of the targets. To go to beyond M31, even larger aperture telescopes are required which are a very limited resource. The positive aspect of the debate over the distance to the LMC is the thorough investigation and analysis of each possible method being researched.

1.4.3 Observations needed to obtain the distance modulus using eclipsing binary stars

To obtain the distance modulus of an eclipsing binary system in the LMC or SMC, up to three types of observations[25] using different specialized equipment are required. The data required are a photometric light curve for the system and a radial-velocity curve for each component in the binary. In most cases the stars observed are hot O or B types (due to their brightness), therefore some type of UV spectrophotometry is also required to characterise the stars' atmospheres, i.e. obtain a spectral classification. Accuracy is essential in all facets of the observations as they all combine in the final result.

1.4.3.1 Photometry

The data obtained from photometric observations is the basis of this work on eclipsing binaries. They provide the light curve (phased photometric time series data), from which numerous properties are determined. The light curve provides the means to determine the period and ephemeris to a high accuracy, depending on the data quality. The light curve shape can give an indication of the stage of evolution of the stars. However the photometry may be affected by the crowding of the field in which the target lies. The light curve indicates the system type, i.e. detached, semi-detached or contact system. The type of system determines the complexity of the model required to interpret the light curve.

This type of data can be collected with the use of a small aperture telescope, typically 1 to 2 metres. The work is suited to Mount John. This telescope size is sufficient for the photometry of stars in both the Magellanic Clouds. This therefore makes smaller telescopes, which may seem to be being made redundant due to new larger aperture telescope, a very useful tool. In addition, it is possible to obtain longer observing runs on smaller telescopes than on larger telescopes, which is essential for this type of work. It can take several years to collect the photometric observations to obtain sufficient phase coverage in several bandpasses.

[24] RR Lyrae stars in the LMC.

[25] Depending on the analysis method, spectrophotometry may or may not be required, but for high accuracy it is essential.

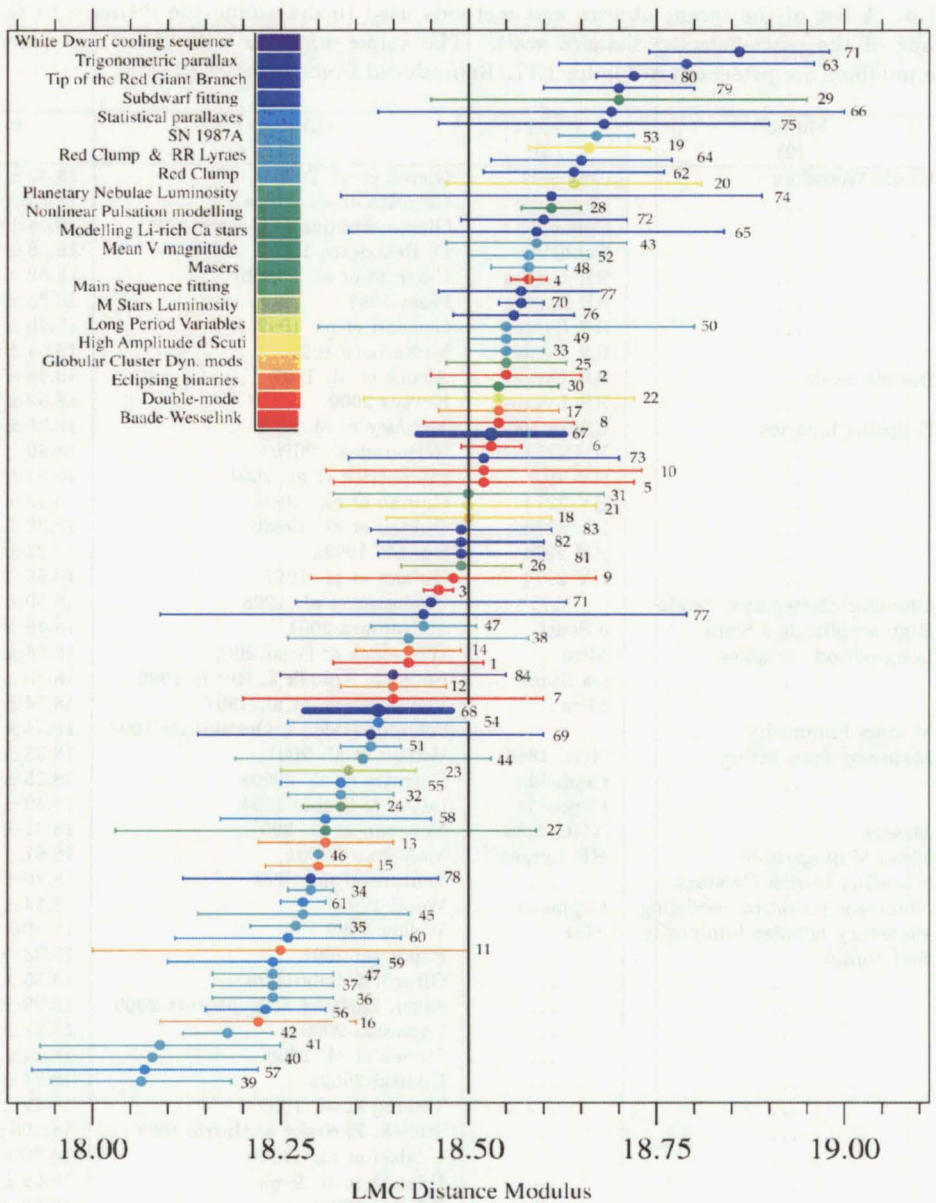

Figure 1.17: Reproduction from Benedict 2002 [19]. Recent determinations of the distance modulus of the LMC. Colours represent the various methods listed in column 2 of Table 1.4, while the numbers refer to the individual investigations, column 1. The bold lines are the results from Benedict's paper. The vertical line denotes the distance modulus adopted by the HST Distance Scale Key Project [53] and the Type Ia Supernovae Calibration Team [131]. This is approximately the median value.

Table 1.4: A list of the recent objects and methods used to determine the distance to the LMC, cornerstone of the extra-galactic distance scale. The values together with their uncertainties and reference numbers are presented in Figure 1.17. Reproduced from Benedict (2002).

No. (1)	Method (2)	Object (3)	Author (4)	$m - M$ (5)
1	Baade-Wesselink	Cepheids	Gieren et al. 2000	18.42 ± 0.10
2	...	Cepheids	Carretta et al. 2000a	18.55 ± 0.10
3	...	Cepheid	Gieren, Fouque & Gomez 1998	18.46 ± 0.02
4	...	Cepheid	Di Benedetto 1997	18.58 ± 0.024
5	...	RR Lyraes	Carretta et al. 2000b	18.52 ± 0.20
6	...	RR Lyraes	Feast 1997	18.53 ± 0.04
7	...	RR Lyraes	Cacciari et al. 1992	18.40 ± 0.20
8	...	RR Lyraes	McNamara 1997	18.54 ± 0.10
9	Double mode	RR Lyraes	Alcock et al. 1997	18.48 ± 0.19
10	...	RR Lyraes	Kovacs 2000	18.52 ± 0.21
11	Eclipsing binaries	EROS 1044	Maloney et al. 2001	18.25 ± 0.25
12	...	HV 2274	Nelson et al. 2000	18.40 ± 0.07
13	...	HV 982	Fitzpatrick et al. 2001	18.31 ± 0.09
14	...	HV 2274	Guinan et al. 1998a	18.42 ± 0.07
15	...	HV 2274	Guinan et al. 1998b	18.30 ± 0.07
16	...	HV 2274	Udalski 1998a	18.22 ± 0.13
17	...	HV 2274	Guinan et al. 1997	18.54 ± 0.08
18	Globular cluster dyn. mods	...	Chaboyer et al. 1998	18.50 ± 0.11
19	High amplitude δ Scuti	δ Scuti	McNamara 2001	18.66 ± 0.08
20	Long-period variables	Mira	Whitelock & Feast 2000	18.64 ± 0.17
21	...	Ca Stars	Bergeat, Knapik & Rutily 1998	18.50 ± 0.17
22	...	Mira	Van Leeuwen et al. 1997	18.54 ± 0.18
23	M stars luminosity	...	Schmidt-Kaler & Oestreicher 1998	18.34 ± 0.09
24	Main-sequence fitting	NGC 1866	Walker et al. 2001	18.33 ± 0.05
25	...	Cepheids	Carretta et al. 2000a	$18.55 \pm 0.04 \pm 0.04$
26	...	Cepheids	Laney & Stobie 1994	$18.49 \pm 0.04 \pm 0.04$
27	Masers	NGC 4258	Newman et al. 2001	$18.31 \pm 0.11 \pm 0.17$
28	Mean V magnitude	RR Lyraes[24]	McNamara 2001	18.61 ± 0.04
29	Modeling Li-rich Ca stars	...	Ventura et al. 1999	18.70 ± 0.25
30	Nonlinear pulsation modeling	Cepheids	Wood 1998	18.54 ± 0.08
31	Planetary nebulae luminosity	M31	Walker 1999	18.50 ± 0.18
32	Red clump	...	Popowski 2001	18.33 ± 0.07
3	...	...	Girardi & Salaris 2001	18.55 ± 0.05
34	...	...	Sakai, Zaritsky & Kennicutt 2000	18.29 ± 0.03
35	...	...	Popowski 2000	18.27 ± 0.06
36	...	...	Stanek et al. 2000	18.24 ± 0.08
37	...	...	Udalski 2000a	18.24 ± 0.08
38	...	...	Twarog et al. 1999	18.42 ± 0.16
39	...	...	Stanek, Zaritsky & Harris 1998	18.065 ± 0.12
40	...	...	Udalski et al. 1998b	18.08 ± 0.15
41	...	...	Udalski et al. 998a	18.09 ± 0.16
42	...	...	Udalski 1998b	18.18 ± 0.06
43	...	...	Romaniello et al. 2000	$18.59 \pm 0.04 \pm 0.08$
44	...	...	Cole 1998	18.36 ± 0.17
45	...	...	Girardi et al. 1998	18.28 ± 0.14
46	...	...	Beaulieu & Sackett 1998	18.3
47	Red clump and RR Lyraes	...	Popowski 2001	18.24 ± 0.08 to 18.44 ± 0.07

Table 1.4: continued. A list of the recent objects and methods used to determine the distance to the LMC, cornerstone of the extra-galactic distance scale. The values together with their uncertainties and reference numbers are presented in Figure 1.17. Reproduced from Benedict (2002).

No. (1)	Method (2)	Object (3)	multicolumn1c—Author (4)	$m - M$ (5)
48	SN 1987A	...	Carretta et al. 2000	18.58 ± 0.05
49	...	...	Romaniello et al. 2000	18.55 ± 0.05
50	...	...	Walker 1999	$18.55 \pm 0.07 \pm 0.16$
51	...	...	Gould & Uza 1998	18.37 ± 0.04
52	...	...	Panagia, ilmozzi & Kirchner 1998	18.58 ± 0.08
53	...	...	Lundqvist & Sonneborn 1998	18.67 ± 0.05
54	Statistical	RR Lyraes	Carretta et al. 2000a	18.38 ± 0.12
55	parallaxes	RR Lyraes	Popowski & Gould 1999	18.33 ± 0.08
56	...	RR Lyraes	Popowski & Gould 1999	18.23 ± 0.08
57	...	RR Lyraes	Popowski & Gould 1998	18.07 ± 0.15
58	...	RR Lyraes	Popowski & Gould 1998	18.31 ± 0.14
59	...	RR Lyraes	Gould & Popowski 1998	18.24 ± 0.14
60	...	RR Lyraes	Fernley et al. 1998	18.26 ± 0.15
61	...	RR Lyraes	Layden et al. 1996	18.28 ± 0.03
62	Subdwarf fitting	...	Carretta et al. 2000a	18.64 ± 0.12
63	...	...	Reid 1998	18.79 ± 0.17
64	...	...	Reid 1997	18.65 ± 0.12
65	Tip of the red	...	Sakai et al. 2000	$18.59 \pm 0.09 \pm 0.16$
66	giant branch	...	Romaniello et al. 2000	$18.69 \pm 0.25 \pm 0.06$
67	Trigonometric	RR Lyrae	Benedict et al. 2002	18.53 ± 0.10
68	parallax	RR Lyrae	Benedict et al. 2002	18.38 ± 0.10
69	...	RR Lyrae	Luri et al. 1998	18.37 ± 0.23
0	...	RR Lyrae	McNamara 1997	18.57 ± 0.03
71	...	Cepheids	Groenewegen & Oudmaijer 2000	18.45 ± 0.18 to 18.86 ± 0.12
72	...	Cepheids	Groenewegen & Oudmaijer 2000	18.60 ± 0.11
73	...	Cepheids	Groenewegen & Oudmaijer 2000	18.52 ± 0.18
74	...	Cepheids	Groenewegen & Salaris 1999	18.61 ± 0.28
75	...	Cepheids	Feast 1999	18.68 ± 0.22
76	...	Cepheids	Oudmaijer et al. 1998	18.56 ± 0.08
77	...	Cepheids	Madore & Freedman 1998	18.44 ± 0.35 to 18.57 ± 0.11
78	...	Cepheids	Luri et al. 1998	18.29 ± 0.17
79	...	Cepheids	Feast & Catchpole 1997	18.70 ± 0.10
80	...	Cepheids	Paturel et al. 1997	18.72 ± 0.05
81	...	HB	Carretta et al. 2000a	18.49 ± 0.11
82	...	HB	Gratton 1998	18.49 ± 0.11
83	...	HB	Koen & Laney 1998	18.49 ± 0.12
84	White dwarf cooling sequence	...	Carretta et al. 2000a	18.40 ± 0.15

1.4.3.2 Ultra Violet spectrophotometry

It is the brightest stars that are most easily observed in the Magellanic Clouds, and these are O and B type stars. They are hot, with most of their radiation emitted in the ultraviolet (~80% at 100 nm–480 nm). To determine the flux emitted by these stars for comparison with the flux received at Earth, it is necessary to obtain spectrophotometry where most flux is emitted, i.e. in the ultraviolet. These can also give an indication of the reddening of the star. Since the Earth's atmosphere is not transparent at these UV wavelengths, satellites provide the only means to collect these data. The now decommissioned International Ultra Violet Explorer satellite, IUE, recorded the first UV spectra for eclipsing binaries in the Magellanic Clouds. The Hubble Space Telescope, HST, with the FOS instrument, now provides the only means of obtaining UV spectra. Due to high demands on its time, this makes acquiring the data rather difficult.

The O and B type stars eject low density gas at high velocities, 1000 to 2000 kms^{-1}. The high temperatures ionize the ejected gas and spectra obtained from UV medium resolution spectroscopy, show the resultant resonance lines, primarily due to SiIII, IV, CIII, IV, NV ions. In the visible region of the spectrum, the spectral lines are broadened making them unsuitable for temperature determination.

1.4.3.3 Spectroscopy

Spectroscopy gives the radial velocities of the stars (assuming lines from both are resolvable) in their mutual orbits via Doppler shifts of the spectral lines. Spectroscopy of the binary system is required in order to solve for the orbital parameters, most fundamentally the absolute value of the orbital semi-major axis, a. This type of data doesn't require as many observations, in the tens rather than hundreds, as required for photometric observations used to build the light curve. However, a large aperture telescope is required (for observation of eclipsing binaries at distance of the Magellanic Clouds), typically 8 m class[26] of which at this stage, under a dozen are available. The photometric data is used in conjunction with the spectroscopic data to derive the orbital parameters from the radial velocity curve: the orbital inclination i, must be known, which is determined from photometric observations. The shape of the radial velocity curves, in theory, only has to be known for values around the maximum as from this, the values of the semi amplitude K_1 and K_2 are determined; however, a reasonable sample of the complete curve is desired to ensure the system is behaving as expected. The mass ratio can be derived from K_1 and K_2, although far from a trivial task. Kepler's equation, assuming circular orbits in this example, can be arranged to give the total mass, M, of a system, equation 1.9, containing two stars of two individual mass M_1 and M_2:

$$M = M_1 + M_2 = \frac{4\pi^2}{G}\frac{a^3}{P^2} \tag{1.9}$$

where a is the semi-major axis value, P the period, and G the gravitational constant.

The mass ratio q, equation 1.10, is defined as

$$q = \frac{M_2}{M_1},\ M_1 = \frac{1}{1+q}M,\ M_2 = \frac{q}{1+q}M \tag{1.10}$$

[26] Spectra have been recorded used a 3.9 m class telescope [71], but a 8 m class telescope gives better results and provides the most efficient use of the telescope time.

The ability to obtain this data however, is dependent on the accessibility of telescopes. The reason such large telescopes are required is because of the magnitude of the binaries, and therefore the integration times required. The times can become insurmountable, not to mention the costs, unless the collecting aperture is large enough. Typically, the required observations can be achieved in a few hours over several nights, depending on the period of the eclipsing binary system.

1.5 Current eclipsing binary programmes in the Magellanic Clouds

There are four well-established programmes (although all cooperate closely) concerning eclipsing binary stars in the Magellanic Clouds: Canterbury (New Zealand), Copenhagen (Denmark), St Andrews (Scotland) and Villanova (USA), groups. All have focused on 14^{th} and 15^{th} mag. eclipsing binaries for study. These are the brighter stars, typically O and B type.

1.5.1 The Mount John observing program

The first eclipsing binary observations were made prior to this programme by students from the University of Pennsylvania, USA. Photoelectric observations were made of several systems from which theses and papers were published, [26], [27], [85], [64]. Students studying at Canterbury continued this line of research, [97], [98], [99] and in later years, 1982, a Masters thesis by Buckley [24].

The MJUO Magellanic Cloud Eclipsing Binary programme, MJUO MCEB, was initiated in 1989 by Dr Willliam Tobin, principal investigator. The MCEB programme focused on making photometric observations of selected targets in both Clouds. The main goal was to obtain high accuracy standard photometry and multi-bandpass light curves of MCEB. This would contribute one of the data sets required for the full analysis of a binary system. The other observations, namely spectroscopic and spectrophotometry would be acquired by collaborators at other institutions.

Observations started with the acquisition of a Photometrics Ltd. cryogenic CCD system using a Thomson TH7882 CDA 384×576 pixel $23\,\mu$m square pixels CCD chip (details refer to [149] and [152]). At the time the Boller and Chivens 0.61 metre telescope was used for *BVI* photometric observations. These observations provided five complete light curves with sufficient phase coverage for analysis. The systems were LMC HV 2208, SMC HV 12634 [168], LMC HV 2274 [166], LMC HV 12484 [150] and SMC HV 1761 [41].

Toward the end of 1992 PhD. student John Pritchard [123] joined the MCEB programme. At this point a number of changes were implemented. Observations were moved to the 1 metre telescope and a custom-made photometer head was constructed. Features included a filter wheel and an offset auto-guiding system. Bandpasses were changed in order to obtain more accurate estimations of the stellar properties. The new system, currently in use, consists of Strömgren *uvby*, Johnson V_J (an approximation of) and I of the Cousins *UBVRI* system. Also reduction packages were changed from ROMAPHOT to DAOPHOT II. The reduction package change gave large advantages due to DAOPHOT's ability to handle non-circular PSFs unlike ROMAPHOT which was limited to circularly symmetric PSFs.

In 1996 the purchase of a detector system incorporating a SITe Si003ab CCD progressed the programme further. The new CCD had many advantages over the now old Thomson chip.

- Higher quantum efficiency, leads to shorter exposure times
- Larger area
- More linear chip
- More sensitive in the blue, more ideal for the filters covering these wavelengths, especially as the MCEBs studied tend to be O and B types.

In 1999 a ST4 auto-guide system was installed. This unit gave better results, more circular stars, than the previous Philips system (details in Chapter 4, section 4.1.5). The reduction package used was changed in 2001 to ISIS-2.1. This is based on image subtraction methods.

The Canterbury group works with collaborators in Copenhagen, Denmark, Jens-Viggo Clausen and in Santiago, Chile, John Pritchard and others.

1.5.2 The Copenhagen group

Some of the first photometry of eclipsing binaries in the Magellanic Clouds was collected by the Copenhagen Group, namely Jens-Viggo Clausen [80]. The group has recently acquired observing time in ESO periods 66 and 68 to obtain spectroscopy using VLT + UVES of eclipsing binaries in both the LMC and SMC. CCD *uvby* observations using the Danish 1.5 m telescope at ESO, La Silla are in progress with recent results published for 2 LMC and 2 SMC systems [30].

1.5.3 The St Andrews group

Their work using the degree field (2dF) multi-object spectrograph on the 3.9 m Anglo-Australian Telescope, AAT, to make spectroscopic observations of SMC eclipsing binaries has been successful, [71]. Plans are to obtain radial velocity measurements of over 100 SMC eclipsing binaries. Together with I band photometry from OGLE, fundamental parameters of these stars will be measured.

1.5.4 The Villanova observing program

The Villanova group is based at Villanova University, USA, and is headed by Edward Guinan. The group acquired IUE observations of 12 eclipsing binaries (1993-1995) mainly using the SWPLD camera (**S**hort-**W**avelength **P**rime **L**ow **D**ispersion, 115 nm to 200 nm). Later in 1996/97, ten of these systems were observed using HST/FOS (115 nm to 480 nm). These systems were both in the LMC and SMC. In the LMC HV 982, HV 2241, HV 2274, HV 5931, HV 12634 and EROS 1044. In the SMC HV 1620, HV 1761, HV 1876 and HV 2226. Medium resolution spectra of HV 2274 and HV 12634 were also obtained from HST/GHRS.

Chapter 2

Searching for eclipsing binaries

2.1 Searching for eclipsing binary stars

Data mining of photometric time-series databases can yield numerous types of variable stars including eclipsing binaries. This allows better target selection of potential candidates for follow-up observations. This chapter provides an overview of several large photometric time-series databases and algorithms used to search them with emphasis on the MOA SMC database.

2.1.1 Photometric databases

2.1.1.1 Microlensing surveys and their by products

Microlensing surveys have increased in numbers over the last decade as the search for dark matter[1] [2] [3] has intensified.

The present observable and detectable objects in the Galaxy do not give the total baryonic mass as expected from observations of the Galactic rotation curve. In fact the figure falls short by as much as 90 %. Dark matter has been proposed to account for this deficit as it produces little detectable radiation or absorption (using current instrumentation). It may occur in two forms, (1) baryonic matter and (2) non-baryonic particles. The latter known as WIMPS (**W**eakly **I**nteracting **M**assive **P**article**S**) are as their name suggests, weakly interacting, yet possibly numerous in numbers, therefore giving a large overall contribution to the total mass. The baryonic matter is the source of dark matter that the current microlensing surveys are focusing on. This can be almost any non/low luminous matter.

The key piece of evidence for the presence of dark matter arises from the flat Galactic rotation curve. Rotation curves for spiral galaxies are almost all determined from HI and CO gas line emission. Therefore, from the distribution of these gases, the galactic rotation curve is constructed. The curve represents the net circular rotation velocity of the galaxy. For our own Galaxy, the results have shown rotational velocities which rise rapidly from the centre of the central bulge, which is expected, but then remain flat out to the sparse regions of the

[1] Dark matter in these terms is any object that consists of baryonic matter with masses from Jovian-sized planets, $\sim 0.01\,M_{\odot}$, to brown dwarfs, red dwarfs, neutron stars and black holes of several hundred to a million solar masses.

[2] A Brown dwarf is defined as a mass which is less than $0.085\,M_{\odot}$ which therefore is below the hydrogen burning limit. The formation process is the same as a star, that is the condensation of gas and dust from the interstellar medium. This differs from a Jovian size planet, which have been detected up to $0.01\,M_{\odot}$, which are formed in the accretion disk during stellar formation.

[3] A Red dwarf is defined as a star, which therefore implies a minimum mass greater than $0.085\,M_{\odot}$. They emit feeble radiation primarily in the infrared due to the low surface temperature. Coupled with the small surface area, this makes detection very difficult.

Galaxy. Here, the curve is expected to fall as the distance from the outer bulge region increases. This is expected to be the case for a Galaxy bound only by gravity. This non-fall off strongly implies that the Galaxy has a halo of matter which is of the order of ten times that of the luminous matter in the bulge and disk. The dynamics of the motions of the stars in the Galaxy suggests that some dark matter is expected to be present in the Galactic disk, yet the majority is expected to be present in a spherical Galactic halo. Further evidence is found with the observations of stars with proper motions at right angles to the Galactic disk. Supporting evidence has come from studies of other spiral galaxies, particular those edge on such as NGC 5746 and from clusters of galaxies, particularly binary systems. The galactic rotation curves for these are similar in structure to that of our own Galaxy and this shows that our Galaxy is not a unique or special case system. Further evidence giving similar results comes from non-rotating elliptical galaxies, which appear to not have enough mass to hold together gravitationally.

These observations imply that more mass is present than we see, so therefore some form of baryonic dark matter may well be present to account for these anomalies in the observational data.

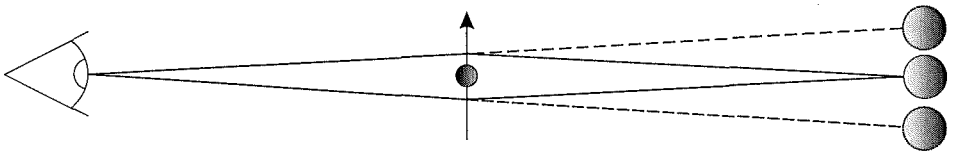

Figure 2.1: The dark matter object is transiting across the line of sight of the observer and a background star, the source. The gravitational field of the dark object bends the light from a background source as seen by an observer. The dark matter object and background source must be in near perfect alignment for this to occur. The original object is now seen in two places above and below the original position. This is a simplified view as actual observations are of arcs of light or an Einstein ring in the case of perfect alignment.

Gravitational lensing is one of the ways baryonic matter can be detected, rather than observed directly as with conventional methods. The idea behind microlensing was initiated by Einstein in his theory of General Relativity which implies that if light passes through a strong enough gravitational field (such as that found around a star) it will be slightly deflected. The first evidence that light was affected by gravitational fields was in 1917 when displacements of stars' positions were observed near the Sun during a solar eclipse, [43], [42]. In 1979, the first gravitational lenses of a Quasar were observed by Walsh [165].

A paper published by Paczynski [112] used this property of light to calculate the probability of detecting these dark matter objects in the Galactic halo. These dark matter objects could act as lenses for a background star and thus be detected by a fleeting increase in luminosity of a background star. His calculations revealed that this was indeed possible and the probability was high enough that such an event could be observed. Before this paper, most research and observations on gravitational lensing events had concentrated on distant galaxies as lenses with the distant source being Quasars. Due to the Quasars' distance, this meant that the time scale of the intensity change was very long.

For the microlensing event to occur, the alignment of the Earth, background star and the dark matter object, must be almost perfect, Figure 2.1. Depending on the precision of the alignment, the event is seen as either an *Einstein ring*, r_{E} (equation 2.1), for near perfect alignment, or segments of the ring which can also been seen as a translation of the background star:

$$r_{\mathrm{E}} = \sqrt{\frac{4GMLx(1-x)}{c^2}} \tag{2.1}$$

where M is the mass of the lens, x the ratio of the distances, observer- lens:observer-source and L the observer-source distance.

The term *microlensing* is derived from the amplification, A (equation 2.2) of the background star. The amplification gives a combined total flux greater than the single source in the non-gravitational lens situation:

$$A = \frac{u^2+2}{u\sqrt{u^2+4}} \tag{2.2}$$

where u is defined in equation 2.3:

$$u = \frac{b}{r_{\mathrm{E}}} \tag{2.3}$$

where b is the projected source-observer distance along the line of sight.

The optical depth, τ (equation 2.4) is defined as the probability that a given star is lensed when $u<1$ or $A>1.34$.

$$\tau = \pi \int_0^L \frac{\rho(l)}{M} r_{\mathrm{E}}^2(l)\,dl \tag{2.4}$$

where ρ is the dark matter density, and l the distance along the line of sight.

The probability of a microlensing event being observed is very small. Gravitational microlensing of stars in the LMC by Galactic halo objects with expected masses in the range of 10^{-6} to $10^2\,\mathrm{M}_\odot$, give an optical depth of $\tau_{\mathrm{LMC}} = 5\times10^{-7}$. Based on these figures, the time scale to maximum intensity is expected to be approximately 2 hours to 2 years for the two limit masses respectively. A Galactic Halo dark matter object of the order of a thousandth of a solar mass would produce images that would be separated by less than a milli-arc second.

The small optical depth means in order to observe a gravitational microlensing event on a realistic time scale, i.e. several months, millions of stars need to be continuously observed. To achieve these numbers, dense stellar regions need to be monitored. Therefore the Magellanic Clouds, the two closest galaxies containing the required stellar numbers, make an ideal starting point for the search of dark matter in the Galactic Halo. Additionally, to observe gravitational microlensing events, the background stars need to be surveyed for many years to obtain reliable statistics.

The actual microlensing event, observed photometrically, is seen as a brightening of the star being observed, but must not be confused with a variable source star. This can be distinguished from a stellar effect by the achomaticity of the event and hence the observations are made in two or more filters. Typically a red (600 nm to CCD cut off ~1100 nm) and blue (400 nm to

600 nm) filter are used to record the photometric time-series data. The microlensing event has a distinctive light curve, derived by General Relativity, which is superimposed on the source's ordinary photometric light curve. Most variables change luminosity depending on their temperature or are periodic, such as eclipsing binaries, whereas microlensing events are generally a single transit event and therefore independent of stellar type. The improvement of CCD technology along with faster computing power has made these types of surveys possible. Also these surveys can use the smaller class of telescopes (1 to 2.5 metres). Such a survey ideally requires a dedicated telescope, specialized data pipe-line requirements and on-line reduction methods. A survey on this scale would therefore typically take a minimum of several years to become fully operational to obtain a few detections. A more realistic time frame is the order of a decade, such as MACHO, OGLE and MOA have taken to obtain a high standard of results.

Provided the source and lens are compact objects, the event is observed as an amplification of the flux independent of wavelength. As the dark matter in the halo is expected to have a higher proper motion than the light source, the effect is transient. The duration and amplitude are a function of velocity, distance and mass of the deflecting object. Therefore it is possible to distinguish between a lens whose location is in the halo of one of the Magellanic Clouds and one that resides in the Galactic halo. For a theoretical brown dwarf in the Galactic halo, one would expect a microlensing duration of several days. The durations, according to theoretical calculations for Galactic halo events are, one day for a $10^{-7}\,M_{\odot}$ object and one month for a one solar mass object.

There are or have been a number of surveys for dark matter (Table 2.1). The early starters in the search for dark matter, namely EROS, OGLE and MACHO, concentrated on recording millions of light curves in order to detect lensing events from objects in the Galactic halo. They were joined by MOA who until 2001 continuously monitored the Magellanic Clouds. Most of the groups now target the Galactic Bulge as most events are seen in that direction. The dark matter search has now turned, for some, to planet hunting. Groups such as PLANET and DUO are concentrating on continuous coverage of microlensing events. Others, AGAPE, MEGA and WeCAPP are extending searches to M31 using unresolved stars and pixel-lensing techniques.

Table 2.1: A list of some of the groups or collaborations involved in observing microlensing events. The observations are directed toward either the Galactic bulge, LMC, SMC or M31.

AGAPE	**A**ndromeda **G**alaxy and **A**mplified **P**ixels **E**xperiment[4]
DUO	**D**isk **U**nseen **O**bjects
EROS	**E**xperience pour la **R**echerche d'**O**bjets **S**ombres
GMAN	**G**lobal **M**icrolensing **A**lert **N**etwork
MACHO	**MA**ssive **C**ompact **H**alo **O**bjects
MOA	**M**icrolensing **O**bservations in **A**strophysics
MEGA	**M**icrolensing **E**xplorations of the **G**alaxy and **A**ndromeda
OGLE	**O**ptical **G**ravitational **L**ensing **E**xperiment
PLANET	**P**robing **L**ensing **A**nomalies **NET**work
WeCAPP	**W**endelstein **C**alar **A**lto **P**ixel lensing **P**roject

The observations toward the Large Magellanic Cloud show that there are fewer microlensing events than one would expect if the missing mass of the Milky Way consisted entirely of a halo of these compact objects. The MACHO team have observed a possible 13-17 microlensing events toward the LMC over a period of 5.7 years [6]. The results indicate a halo population

[4] A number of groups refer to their observations as *experiments*, but in this thesis the term observation is used in the sense of observing and recording data with the inability to change parameters of the observed object(s). The term experiment is reserved for research where the observer can alter parameters in their laboratory to change the outcome.

in either the Galaxy or the LMC. The possibility does remain that 20% of the Galactic halo population consists of partially compact objects with mass in the range 0.15 to $0.9\,M_{\odot}$. The results of the searches to date are not conclusive enough to give the location of all the missing mass.

Observations of the Galactic bulge have detected more than 200 microlensing events in this direction, with typically an event happening at any given time. Among them are a number of binary lens events. This is about three times as many microlensing events as predicted by existing Galactic models. The optical depth is dependent on the inclination of the bar, [21], whose values range from 10° to 45° (Table 7 in Alcock 2000 [7]), bar/bulge mass and the stellar mass function all of which have large uncertainties.

These new results have meant gravitational lensing has established itself as a new tool to study the structure of the Milky Way. This method can be used to study the frequency of binary stars and also to detect planets around other stars. If the lensing stars have planets around them, the microlensing light curves deviate from the standard curve and some have sharp extra peaks. This is a signature of the planets in the microlensing light curves. To obtain a reasonable light curve from such an event, sampling in the order of a few hours is required, and thus the necessity for the various groups to collaborate.

2.1.2 Databases of stars in the Magellanic Clouds

The microlensing surveys conducted in the past decade have provided astronomers with huge amounts of data on many types of stars. The surveys of most interest are those that used the stars in the Magellanic Clouds as their source stars. The difference in metallicities of the Clouds to our own Galaxy make the Clouds a rich source of information. Over the past few years, selected variables have been extracted from these databases and this has had the result of increasing the known number of variable stars ten fold. Some of these include Cepheids, [15], eclipsing binaries [5], [159], [61], [14] and red variables [105]. Better target selection for further study is now possible as well as better statistical data for stellar type estimations.

The microlensing surveys of particular relevance to this thesis are OGLE, MACHO, EROS and MOA. A brief overview of each is given.

2.1.2.1 OGLE

The Polish **O**ptical **G**ravitational **L**ensing **E**xperiment, OGLE, started its first phase in 1992, which continued through to 1995. The operation was based at the Las Campanas Observatory, Chile, operated by Carnegie Institution of Washington. They used the 1 metre Swope telescope with a 2048×2048 Ford/Loral CCD camera. This was a successful program but had several limitations, the greatest being the availability of telescope time. To overcome this, they secured funds for a 1-metre class telescope and located it near the Las Campanas Observatory, Chile. The site was secured in August 1995, due to the long collaboration of Polish and US astronomers from the Carnegie Institution of Washington. This started phase II of the OGLE project which started observing on 6^{th} January 1997.

The results of the OGLE I project, which concentrated on observations toward the Galactic bulge, included the first microlensing event toward the Galactic bulge [160], discovery of the first microlensing by a binary object [164] and the first early warning system for the detection

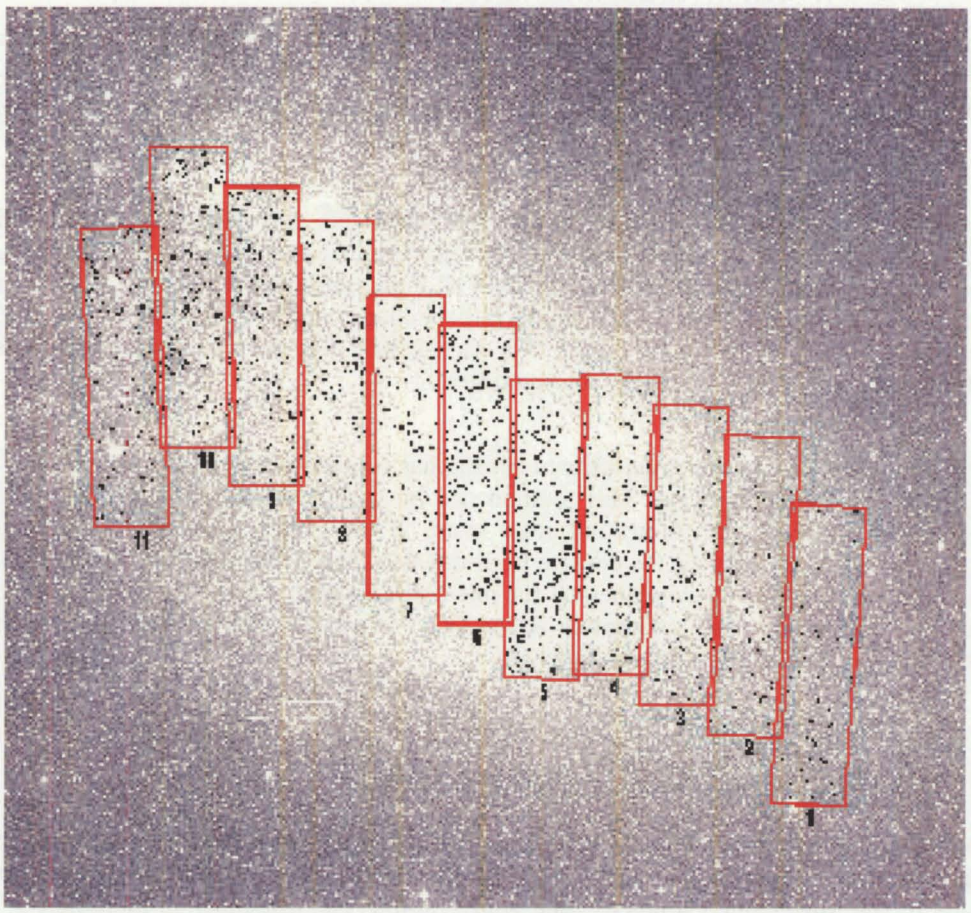

Figure 2.2: The OGLE fields superimposed on the SMC in which 1459 eclipsing binaries were found. Diagram courtesy of the OGLE group.

of microlensing events in progress [161].

The telescope's field of view of 1.5° was achieved via the use of three element correction optics. The telescope is equatorial fork mounted with a pointing accuracy of 15 arc sec (r.m.s.) ($z < 70$ degrees). A detailed analysis of the OGLE project and equipment is given by Udalski [157].

The OGLE II project [157] using the 1.3 m Warsaw telescope started observing the LMC with 20 fields covering more than 4.2 square degrees. Later, 2.3 square degrees of the central region of the SMC covered by 11 fields, Figure 2.2, were observed. A SITe 2048×2048 thinned CCD was used and observations were made with I, V and B filters with respective exposure times of 120 seconds, 180 seconds and 240 seconds for both the SMC and LMC. The majority of observations were made with the I filter. All observations were made in drift-scan mode whereby the telescope was drifting in declination at a few arc seconds per time second. The charges were clocked across the CCD at the same rate. This resulted in a single image having 8192 lines, with the image size now 8192×2048 giving 34 MBs of raw data. The only drawback of the drift-scan method is the reduced seeing resolution due to telescope tracking error but with a median value of 1.1 arc sec, this was not a severe problem. The number of stars surveyed in the SMC is 2×10^6, 2.3 sq degrees; LMC 7×10^6, 4.2 sq degrees.

The third phase of the OGLE project, OGLE III, began on the 11^{th} June 2001 using a new CCD camera. The camera consists of 8 thinned SITe 2048×4096 CCD chips giving a total array of 8192×8192 pixels at a scale of 0.26 arc sec per pixel. This gives a total field of view of 35×35 minutes with a 98 second readout time for the camera.

2.1.2.2 MACHO

The MACHO project, **MA**ssive **C**ompact **H**alo **O**bjects, is a collaboration between scientists at the Mt. Stromlo and Siding Spring Observatories, the Centre for Particle Astrophysics at the Santa Barbara, San Diego, and Berkeley campuses of the University of California, and the Lawrence Livermore National Laboratory. The project started observations from the Mount Stromlo Observatory, Canberra, Australia in June 1992. The project used the 1.27 m telescope in conjunction with a purpose built CCD camera. The camera consisted of two arrays of 2×2 Loral 2048×2048, $15\,\mu\text{m} \times 15\,\mu\text{m}$ pixel CCDs in two focal planes, thus allowing simultaneous imaging via a diachronic beam splitter. Two bandpasses were used, red 590 nm to 780 nm and blue 450 nm to 590 nm. Using a 300 second exposure time, the resulting 64 Mb image was read out in 70 seconds. This gave a 0.5 square degree field coverage at 0.63 arc sec per pixel. The facilities were unfortunately destroyed by a bush fire in early 2003.

The MACHO group have constructed a database containing 8 million stars in the LMC and 10 million stars in the direction of the Galactic bulge. They have also produced a catalogue of eclipsing binary stars in the LMC [5]. The catalogue contains 611 binaries along with a new decimal classification scheme based two properties of the systems:

1. The sum of the relative radii $(r_1 + r_2)$ and
2. The surface brightness ratio, $J_s : J_p$

The motivation for this new system was due to the difficulty encountered when attempting to distinguish between EA and EB type light curves (defined in the *General catalogue of Variable Stars* [133]), due to the continuous change of the flux from primary eclipse to secondary eclipse.

They found 64 of the 611 binaries had eccentric orbits. One of these was selected for further study in this thesis, namely MACHO*05:36:48.7−69:17:00, (Figure 2.3). The catalogue is magnitude limited to 18^{th} magnitude, and a variation in eclipse of greater than 0.2 magnitudes. The stars also have $V - R < 0.3$, on the main sequence. These criteria select bright binaries down to spectral type AO.

2.1.2.3 EROS

EROS, **E**xperience pour la **R**echerche d'**O**bjets **S**ombres, is a search for dark matter which belongs gravitationally to our Galaxy, with the detection method being microlensing. Like OGLE, EROS has to date two major phases, EROS I and EROS II. EROS I started in 1990 based at La Silla European Southern Observatory, ESO, with two complementary programmes. A 0.4 m $f/10$ telescope in conjunction with a CCD array was used for the observations. The detector array consisted of 16 edge-buttable Thomson THX 31157 chips, in a 2×8 arrangement. Each chip was 579×400 pixels, with a pixel size of $23\,\mu$m square, giving 1.21 arc sec per pixel. A full description is given by Arnaud et al [9], [10]. The other programme used the photographic Schmidt ESO telescope. The telescope equipped with the CCD camera was used to search for

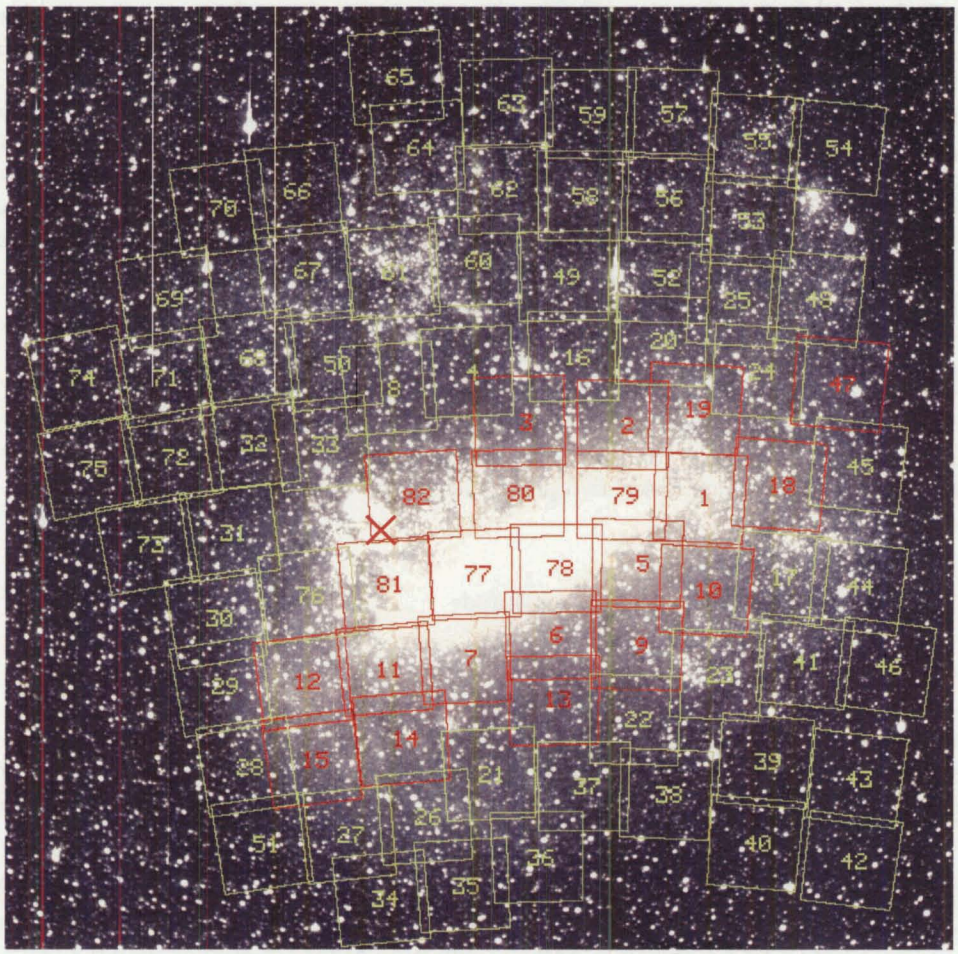

Figure 2.3: The MACHO field for the LMC in the R bandpass. The red field regions are the primary search areas and the green regions are the secondary search areas. The selected target, MACHO∗05:36:48.7−69:17:00, is indicated by ×. Diagram courtesy of the MACHO group.

short duration microlensing events, however none were found. The Schmidt telescope recorded 350 photographic plates, in red and blue broad band filters, which were digitized. These contained approximately 6 million stars and two possible microlensing events were identified.

The analysis of the EROS I CCD data from the season of 1991-92 yielded a catalogue of 79 Eclipsing Binaries, Grison [61], [62] and Cepheids, Beaulieu [15], [16], both in the bar of the LMC. The eclipsing binary catalogue doubled the number of known systems in this region from the previous catalogues of Gaposhkin[5][55], [56] and [54], [115]. The stars were very well sampled in phase, with typically 1000 points per filter, red and blue. This resulted in very well sampled light curves, although not all images were taken in photometric conditions. These two catalogues were amongst the first produced from the by-products of the searches for dark matter via microlensing events. This opened the way for a new source, not just for eclipsing binary detection, but for variable star detection in general. The catalogue had the range of depth of 15^{th} to 18^{th} magnitudes. Based on this fact alone, this made the majority of the systems possible to be observed from MJUO.

2.2 The MOA project

The MOA collaboration kindly made available their LMC and SMC data for the 1997 season to search for Eclipsing Binaries. Once suitable candidates were identified, follow up observation were to be made, details of which are given in Chapter 4.

2.2.1 The MOA collaboration

The MOA Project (**M**icrolensing **O**bservations in **A**strophysics) was the source of the database which was used to search for Eclipsing Binaries. The project is a joint New Zealand and Japanese collaboration based at the University of Canterbury Mount John University Observatory (MJUO), New Zealand.

The primary science goals are:

1. To search for sub stellar objects below the hydrogen burning limit in the Galactic halo.
2. Collaborative studies of microlensing events toward the Galactic bulge including a search for distant planets.
3. A variable star survey.
4. Photometric study of type Ia supernovae with red-shift < 0.1 and declination $< 60°$.

The location of MJUO was ideal due to the ongoing availability of telescope time, cost and of course the sky position of the LMC, SMC and Galactic centre. The long dark winter nights, 12-14 hours are also an advantage. Collaboration with other groups in Chile and Australia results in a possible opportunity to observe a microlensing event for almost a 24 hour period. The major disadvantage with the New Zealand site is the seeing which is typically 2.5 arc sec, and on the best nights approximately 1.2 arc sec. However for photometric surveys such as microlensing, a high accuracy of the photometry is not essential as the microlensing events are

[5] Gaposhkin varied the romanization of his name, using both Gaposchkin and Gaposhkin at various times.

based on the change in the light curves which are often large. No attempt is made to extract accurate stellar information, therefore broad band filters are satisfactory.

2.2.1.1 Telescope and CCD array

A 61 cm Boller and Chivens Cassegrain reflector with modified $f/6.25$ optics was used to conduct the observations. This gave a 1.3° square field of view with 2 models of CCD camera used. MOA-cam1, 1996 to 1997, consisted of 9 CCD chips, all 1024×1024, $12\,\mu\text{m} \times 12\,\mu\text{m}$ pixels giving a sky coverage of 0.645 arc sec per pixel. MOA-cam2, 1998 to current, consists of three 2048×4096 SITe CCDs, $15\,\mu\text{m} \times 15\,\mu\text{m}$ pixels giving a sky coverage of 0.81 arc sec per pixel. Both cameras used two bandpasses, both broad band, red 600 nm to the CCD cut off, i.e. where the silicon becomes transparent, at approximately 1100 nm and blue 385 nm to 630 nm.

The telescope was moved in a 4 phase cyclic motion as indicated in Figure 2.4. Each position gives a small overlap of the previous position for alignment purposes. This results in 4 possible positions for each chip, therefore each observation has an associated CCD chip number $(1 \rightarrow 9)$ and a cyclic phase number $(0 \rightarrow 3)$. This is seen in Tables 2.3 and 2.5. This layout is termed the mosaic and has its own coordinate system denoted by X, Y. Each CCD has its own coordinate system denoted by x,y. This is explained in detail later in section 2.2.3.

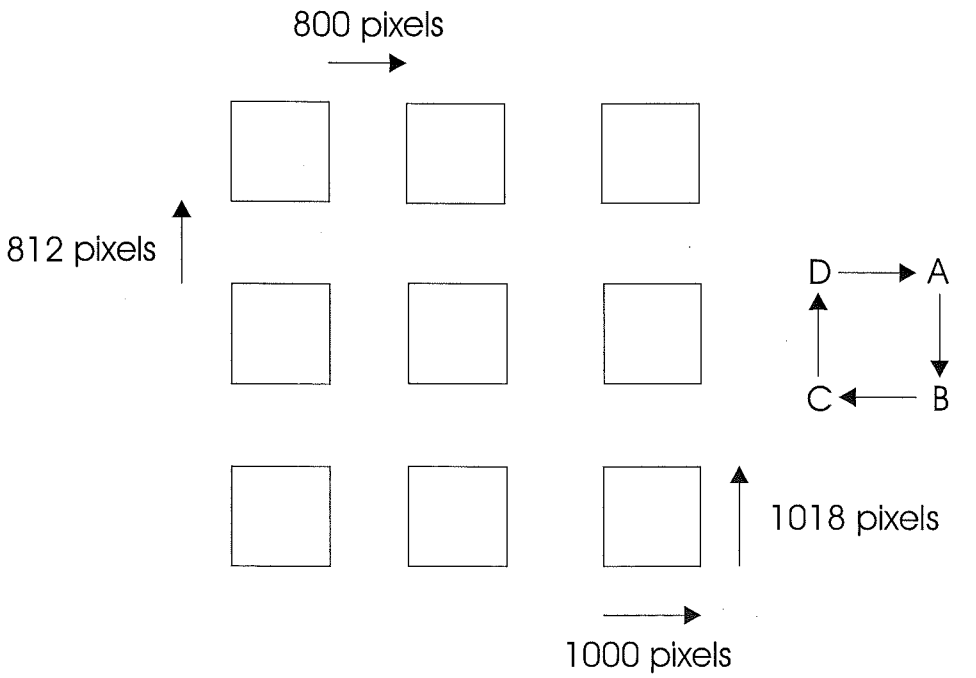

Figure 2.4: MOA-cam1 consisted of 9 CCD chips arranged as shown. The telescope was stepped through a 4 phase cyclic motion (ABCD) to cover the desired field area.

2.2.1.2 Data acquisition software and processing

After correcting for the instrumental effects of dark current and flat fielding, the CCD frames were analyzed using the DoPhot photometry software in the fixed position warm start mode [137]. The templates for the warm starts were constructed by selecting all frames of the best

seeing observations for a given field. These frames were then reduced using DoPhot, [93]and [137], without the warm starts to resolve as many individual stars as possible. Using the overlap between adjoining frames, a mosaic of star positions across the whole field was constructed. After eliminating double counting in the overlapping regions, a catalogue of (X,Y) star positions across the field was constructed.

All individual observation frames were then analyzed individually by first matching to the coordinate system in the catalogue. Star positions were then extracted from the catalogue and transformed to local CCD coordinates (x,y) to produce an input list to DoPhot for the fixed position warm starts. The subsequent photometry was then normalized to a common photometric scale using constant stars and renormalisation techniques similar to those of Honeycutt [78].

2.2.2 The MOA database

The databases supplied by the MOA group for the purposes of this thesis consisted of MOA-cam1 observations of the LMC and SMC fields. The LMC field area is $1° \times 3°$ covered by a mosaic of 3 field frames, nlmc1, nlmc2 and nlmc3[6]. The number of stars surveyed was approximately 1 million down to 18^{th} magnitude. The SMC was observed in 2 fields, smc1 and smc2, covering a $1° \times 2°$ field of view, with a total of approximately 400 000 stars, also down to 18^{th} magnitude. All observations supplied by MOA were of their April to December 1997 observations. The stars observed in each field frame were divided into groups of 2000 for easier data handling. A typical photometric light curve consisted of approximately 90 points of raw data for each of the blue and red filters.

The datafile structure for the SMC and LMC fields divided into groups is as follows:

- smc 1 `smc1.group0` to `smc1.group109`
- smc 2 `smc2.group0` to `smc1.group97`

- lmc 1 `nlmc1.group0` to `nlmc1.group200`
- lmc 2 `nlmc2.group0` to `nlmc2.group192`
- lmc 3 `nlmc3.group0` to `nlmc2.group162`

Due to archiving errors, not all groups contained data. This was due to two reasons; Firstly, data was lost for the SMC fields. Secondly, group files were accidentally written that contained no data (phantom groups). This occurred in the LMC data with groups `nlmc1.group133, 164, 166` $\rightarrow$ `200`. The fields have two *slot*-like gaps in the otherwise square field, Figure 3.1. This was due to a problem with the camera's cyclic motion, as the same features are seen in the three LMC fields.

2.2.3 The MOA data files

The fields observed by MOA in the SMC and LMC contained approximately 400 000 and 1 000 000 stars respectively. The observations for each star typically contained 90 data points

[6]The n prefix to the lmc is an in-house data labelling notation.

per filter, but in the case where a star was in the overlapping region of the chips, approximately 180 data points per filter were recorded.

The stars detected in each field using DoPhot were assigned a star identification number, ID. The photometric data, in groups of 2000 stars, was written to an ASCII file. An example of this file is given in Table 2.3 along with an explanation of the entries in Table 2.2. These files were labelled as smc{field number}.group{group number}, example, `smc1.group12`. For the LMC the prefix smc is substituted with nlmc.

Table 2.2: Data structure for the group files in the MOA database.

Column	Description
1	Star identification number for the star in this field
2	Observation number
3	Field in which the star is located
4	The phase of the 4 step telescope motion (0-3)
5	Filter colour
6	The CCD chip number on which the star was measured
7	Julian date of mid-exposure
8	DoPhot classification type
9	X pixel position of the star measured along the mosaic field
10	Y pixel position of the star measured along the mosaic field
11	The direct magnitude obtained after reducing the CCD image with DoPhot or raw instrumental magnitude
12	The formal error determined by DoPhot associated with the magnitude[7]
13	The corrected magnitude after establishing a common photometric scale over all images
14	The uncertainty in 13 given by the quadratic sum of the Poisson error and the calibration error [8]

For easy identification of a particular star, a catalogue file was written which contained each star's position in its respective field on the CCD frames (in mosaic coordinates). This saved having to search through many of the group files to locate a star's position. An example of the catalogue file is given in Table 2.5 with an explanation of the column entries given in Table 2.4.

Catalogue files were produced which additionally contained the Right Ascension, RA, and Declination, Dec, of the stars. The conversions were done by MOA's Japanese collaborators.

To identify stars in both the CCD and mosaic coordinate systems used by MOA, transformation equations were used. The transformation coefficients X_o,Y_o, a, b, c and d are required to convert between CCD (x,y) and mosaic (X,Y) coordinates. The transformation coefficients are tabulated for each of these positions in Tables 2.6 and 2.7 for the smc1 and smc2 fields respectively. Given (x,y) on a CCD chip, the corresponding mosaic coordinates (X,Y) are given by:

[7]This is essentially determined by photon counting statistics.

[8]Ideally this should only be limited by Poisson noise statistics in the uncertainties. However there are a number of other sources of error (flat-fielding, calibration etc). The error in column 14 was an attempt to quantify these factors. The determination of the uncertainties empirically was attained by plotting χ^2 using the formal error against magnitude. It was then found that: realistic error $\approx$ factor $\times$ photon noise uncertainty. The factor ranges from $\sim$2 for bright stars (mag. $\sim$12 on the instrumental MOA magnitude scale) to $\sim$1 for faint stars (mag. $\sim$6). Most of the stars are considered faint and therefore the scaling factor is generally $\sim$1, which gives very similar numbers in columns 12 and 14.

Table 2.3: Sample data from the MOA database file `smc1.group0`. The explanations of the columns are given in Table 2.2.

1	2	3	4	5	6	7	8	9	10	11	12	13	14
1961	L150	smc1	1	red	1	2450572.907188	11	609.99	971.97	−8.326	0.033	−8.190	0.033
1961	L150	smc1	1	blue	1	2450572.911111	11	611.94	974.81	−7.316	0.054	−7.255	0.054
1961	L150	smc1	2	red	1	2450572.915058	11	601.23	58.47	−8.212	0.034	−8.105	0.034
1961	L150	smc1	2	blue	1	2450572.918993	11	603.82	61.57	−7.314	0.055	−7.339	0.056
1961	L151	smc1	1	red	1	2450573.133356	11	596.08	962.40	−8.319	0.026	−8.122	0.026
1961	L151	smc1	1	blue	1	2450573.137280	11	598.13	962.33	−7.252	0.059	−7.117	0.059
1961	L151	smc1	2	red	1	2450573.141181	11	586.18	49.59	−8.341	0.030	−8.151	0.031
1961	L151	smc1	2	blue	1	2450573.145104	11	588.28	47.82	−7.346	0.048	−7.221	0.049
1961	L152	smc1	1	red	1	2450573.850544	11	618.24	971.29	−8.376	0.035	−8.230	0.035
1961	L152	smc1	1	blue	1	2450573.854456	11	618.87	975.17	−7.475	0.048	−7.439	0.048
1961	L152	smc1	2	red	1	2450573.858356	11	608.30	58.92	−8.324	0.036	−8.196	0.037
1961	L152	smc1	2	blue	1	2450573.862269	11	610.82	62.98	−7.454	0.049	−7.426	0.049

Table 2.4: The data format for the `smc1.catalog` and `smc2.catalog` data files.

Column	Description
1	ID number for the star in this field
2	The phase of the 4 step telescope motion ($0 \rightarrow 3$)
3	The CCD chip number on which the star was measured
4	Local ID number of the star on the CCD chip
5	DoPhot classification type
6	X pixel position of the star measured along the mosaic field
7	Y pixel position of the star measured along the mosaic field
8	DoPhot Magnitude of the star
9	Formal magnitude error as determined by DoPhot

Table 2.5: The data format for the `smc1.catalog` and `smc2.catalog` data files. Shown is a sample of data from `smc1.catalog`.

1	2	3	4	5	6	7	8	9
52512	3	2	708	1	3563.56	1375.89	−8.9410	0.0130
52513	3	2	709	3	3220.25	1375.03	−8.8650	0.0180
52514	3	2	710	2	2841.34	1373.84	−9.6790	0.0000
52515	3	2	711	1	3257.61	1379.47	−8.8660	0.0190
52516	3	2	712	3	3361.62	1380.66	−8.5970	0.0260

$$X = X_\circ + a \times x + b \times y \tag{2.5}$$

$$Y = Y_\circ + c \times x + d \times y \tag{2.6}$$

In the mosaic there are 9 chips, each of which can have one of 4 phases (0, 1, 2, or 3) in the 4-step cyclic motion. The mosaic coordinates for the eclipsing binaries were given in the group and catalogue files. Although not essential for the period searching work, the CCD coordinates were required to construct the finding charts for each Eclipsing Binary detected. The images supplied for constructing the finding charts were raw CCD images with their respective CCD x,y coordinates. Therefore, a transformation from the mosaic coordinates to the CCD coordinates was required. Equations 2.5 and 2.6 were solved for x and y.

$$x = \frac{X - X_\circ - by}{a} \tag{2.7}$$

$$y = \frac{-c(X - X_\circ) + (Y - Y_\circ)}{a(d + \frac{cb}{a})} \tag{2.8}$$

2.3 Searching photometric time sequences for eclipsing binaries

The Eclipsing Binary systems, as mentioned in Chapter 1, exhibit a periodic variation. This section will review some of the methods for finding a periodic variation in a photometric time series.

Table 2.6: Coordinate transformation coefficients for the MOA smc1 field.

Cycle phase	Chip number	$X_\circ$	$Y_\circ$	a	b	c	d
0	1	928.20	−20.47	0.999209	−0.015020	0.015846	1.001660
1	1	0.00	0.00	1.000170	−0.005631	0.006923	1.001890
2	1	3.81	915.48	0.999827	−0.005272	0.006795	0.999869
3	1	924.33	891.07	0.998704	−0.015049	0.015796	0.999470
0	2	2715.95	−6.79	1.000100	−0.008542	0.008083	1.001870
1	2	1789.86	−1.21	0.999174	0.000629	−0.000777	1.001900
2	2	1792.77	914.09	0.998810	0.001253	−0.000512	0.999457
3	2	2711.36	905.13	0.999692	−0.008560	0.008499	0.999763
0	3	4514.40	4.67	1.000150	−0.000670	−0.000049	1.002150
1	3	3587.35	−5.49	0.999223	0.008679	−0.008930	1.001960
2	3	3589.77	910.24	0.998984	0.009084	−0.008464	0.999577
3	3	4509.30	917.61	0.999709	−0.000862	0.000642	1.000110
0	4	903.04	1814.79	0.999621	−0.003833	0.004252	0.999966
1	4	−9.70	1836.56	1.002390	0.004886	−0.004944	1.000390
2	4	−2.62	2749.30	0.999556	0.005746	−0.005223	0.999294
3	4	899.78	2723.33	0.997530	−0.003205	0.004545	0.999055
0	5	2697.87	1832.59	1.000000	0.000000	0.000000	1.000000
1	5	1789.07	1838.13	0.998988	0.009124	−0.008866	1.000170
2	5	1791.89	2750.51	0.999078	0.009592	−0.008751	0.999169
3	5	2692.95	2741.57	0.999964	0.000164	0.000427	0.999327
0	6	4501.02	1840.14	0.999901	−0.004395	0.004294	0.999850
1	6	3591.43	1829.50	0.999235	0.004473	−0.004539	0.999869
2	6	3594.36	2741.91	0.999173	0.004873	−0.004133	0.999191
3	6	4496.26	2749.84	1.000060	−0.004641	0.004841	0.999560
0	7	899.91	3646.38	0.997423	−0.003468	0.005140	0.998238
1	7	6.13	3668.90	0.999563	0.005872	−0.004323	0.998623
2	7	9.23	4581.43	0.999869	0.005053	−0.004599	0.999327
3	7	894.74	4554.81	0.997675	−0.003411	0.005215	0.999034
0	8	2694.14	3660.60	0.999882	−0.003401	0.004128	0.998171
1	8	1802.15	3666.18	0.998891	0.005706	−0.004723	0.998408
2	8	1805.47	4578.31	0.999125	0.005903	−0.004747	0.998903
3	8	2689.46	4569.32	1.000050	−0.003404	0.004389	0.998785
0	9	4491.62	3668.05	0.999874	−0.002486	0.002612	0.998415
1	9	3598.78	3657.08	0.998999	0.006491	−0.006052	0.997958
2	9	3602.50	4569.04	0.999220	0.006516	−0.005647	0.998757
3	9	4487.26	4577.60	1.000150	−0.002644	0.003411	0.998828

Table 2.7: Coordinate transformation coefficients for the MOA smc2 field.

Cycle phase	Chip number	X_o	Y_o	a	b	c	d
0	1	929.52	−21.25	0.999451	−0.014603	0.014600	1.000730
1	1	0.00	0.00	1.001950	−0.005276	0.007207	1.001010
2	1	3.02	920.95	1.001630	−0.005059	0.007084	0.999302
3	1	924.35	899.24	0.998952	−0.014648	0.014529	0.999043
0	2	2718.04	−9.07	1.000300	−0.008075	0.007667	1.001120
1	2	1791.55	−2.09	0.999766	0.001194	−0.000673	1.001410
2	2	1793.86	919.13	0.999558	0.001294	−0.000523	0.998904
3	2	2712.26	911.96	0.999897	−0.008152	0.008047	0.999216
0	3	4517.33	2.70	1.000150	−0.000807	0.000013	1.001110
1	3	3590.36	−6.14	0.999459	0.008520	−0.008004	1.001240
2	3	3591.83	915.24	0.999150	0.008969	−0.007607	0.999042
3	3	4510.61	924.41	0.999778	−0.000414	0.000771	0.999669
0	4	905.16	1811.50	0.999875	−0.003701	0.004401	0.999733
1	4	−7.57	1833.67	1.002110	0.005121	−0.004337	0.999973
2	4	−2.41	2753.06	0.999714	0.004919	−0.005068	1.001210
3	4	899.84	2729.74	0.998626	−0.003962	0.004280	1.000900
0	5	2700.79	1828.87	1.000000	0.000000	0.000000	1.000000
1	5	1791.35	1836.25	0.999533	0.008957	−0.008945	0.999858
2	5	1793.08	2754.67	0.999602	0.008806	−0.008785	1.000980
3	5	2694.36	2747.53	1.000040	−0.000200	0.000443	1.001040
0	6	4504.18	1836.73	0.999994	−0.004547	0.004404	1.000030
1	6	3594.21	1827.63	0.999389	0.004306	−0.003664	0.999864
2	6	3596.06	2746.39	0.999447	0.004164	−0.003303	1.000880
3	6	4497.97	2756.33	1.000160	−0.004961	0.004945	1.001200
0	7	900.84	3644.75	0.998522	−0.004381	0.004936	0.999824
1	7	6.68	3667.93	0.999569	0.004255	−0.004091	1.000350
2	7	7.23	4588.57	0.999997	0.003522	−0.004480	1.001000
3	7	893.33	4564.43	0.998874	−0.005091	0.004926	1.000540
0	8	2696.72	3658.41	0.999831	−0.004684	0.004217	0.999742
1	8	1803.68	3665.59	0.999337	0.004165	−0.004722	0.999817
2	8	1804.75	4585.41	0.999528	0.004073	−0.004705	1.000950
3	8	2689.39	4578.35	1.000170	−0.004613	0.004413	1.000630
0	9	4494.31	3666.32	1.000020	−0.003579	0.002651	0.999919
1	9	3600.73	3656.68	0.999303	0.004952	−0.005290	0.999721
2	9	3602.16	4576.64	0.999601	0.005013	−0.004874	1.000270
3	9	4487.75	4587.10	1.000310	−0.003763	0.003425	1.000540

2.3.1 Review of search algorithms

Searching the vast photometric time series databases for eclipsing binaries, which are in the fractional percent range, requires good robust algorithms, not to mention reasonable computer speed. The light curves need to be identified as variable and then phased to produce a distinguishable eclipsing binary light curve. A brief overview of several available computer based search algorithms is given.

The algorithms take the raw data and apply a test statistic to determine variability (this is the fast part) and then fit possible periods or equivalently frequencies in an attempt to phase the data (this is the time consuming part). There are many algorithms that will perform these functions, however most are designed for evenly spaced data sets, which in the field of astronomy, are a rarity. Over the last 20 years several search algorithms for unevenly spaced data sets have been designed and implemented, each with there own pros and cons.

A prerequisite before using a search algorithm, is to match the shape/variability of the phased data with the algorithm's ability to detect this shape/variability. Therefore a basic knowledge of the light curve parameters are required in advance in order to optimize the search. Failure to do so, can result in very long processing time or discarding of the required light curves. The two important factors in the selection of a suitable search algorithm are:

1. The shape of the signal to be detected.
2. The distribution of observations in time.

Many periodic variables follow an approximately sinusoidal variation such as Cepheids, while others have non-periodic, or very long period, variations. Eclipsing binaries however, have a distinct type of light curve, yet these vary depending on whether the systems are in contact or well detached. In contact binaries, the resultant light curves are very close to that of a sinusoidal variation as shown in Figure 1.9. In the semi-detached case, again the light curves start to depart from, but still approximate a sinusoidal variation. Therefore in these two cases, a database search based on the fitting of a sinusoid via Fourier methods would in fact find a vast majority of these cases. Now consider the well-detached eclipsing binary, which is the target type for this thesis, of which a typical light curve for such a system is shown in Figure 1.13. The two main features and are the sharp distinct eclipses that occur, almost approximating a delta like function in some cases. The other features are the flat base line. These features result in the sinusoidal method being not appropriate for the detection of this category of star. This will be discussed later. The other main point with eclipsing binaries is that the eclipses need not be of equal depth if for example, the components have different temperatures. This in itself gives the light curve a shape that departs from the basic sinusoidal shape.

The second factor of the distribution of observations in time has a large significance because of the constraints faced in astronomical observations. The data collection times are not periodic due to several factors such as weather, allocation of observing times, phases of the objects, Moon phases etc. This gives data with unequally spaced observations, many of which are clumped with large gaps between them. Classically, the use of Fourier series analysis has been for equally spaced data, but the analysis of unevenly spaced data introduces new challenges.

2.3.2 The methods available

Many methods for period detection are now available. A,few of the methods considered for this work are discussed in the following sections.

2.3.2.1 Discrete Fourier Transform, DFT

There have been several methods that have exploited the Discrete Fourier Transform, DFT, in the analysis of time series sampled unevenly, such as the power spectrum or CLEAN [39], [128] algorithms. Here we consider a data set of observations $x(t_k)$, where k=1,...,n, which only consist of a pure harmonic oscillation with no noise. Then for a given frequency ω, the DFT can be expressed as two scalar products:

$$(x, \sin \omega t) \equiv \sum_{k=1}^{n} x(t_k) \sin \omega t_k \quad \text{and} \tag{2.9}$$

$$(x, \cos \omega t) \equiv \sum_{k=1}^{n} x(t_k) \cos \omega t_k \tag{2.10}$$

For an even sampling, the scalar product of the sine and cosine functions are orthogonal.

$$(\cos \omega t, \sin \omega t) = 0 \tag{2.11}$$

This is the Fast Fourier Transform case, FFT. However in the case of uneven sampling, this scalar product is no longer orthogonal, i.e:

$$(\cos \omega t, \sin \omega t) \neq 0 \tag{2.12}$$

Graphically, we see in Figure 2.5 that if the Fourier transforms are shown as a projection onto the direction of the cosine and sine functions in space of functions of time, then the resultant x, for the orthogonal case, is when $\gamma = 90°$, however when $\gamma \neq 90°$ then the projection depicted by x' no longer forms a right-angled triangle therefore not satisfying Pythagoras theorem.

The amplitude squared, A^2, corresponds to the vector norm $||x||$ of x, which corresponds to the power $P(\omega)$ such that:

$$A^2 \equiv ||x||^2 = (x, x) \tag{2.13}$$

but since $\gamma \neq 90°$, then the resultant x' gives

$$P(\omega) \equiv ||x'||^2 \neq (x, x) \neq A^2 \tag{2.14}$$

so the true power becomes

$$P(\omega) \equiv (x, \sin \omega t)^2 + (x, \cos \omega t)^2 \neq ||x||^2 \neq (x, x) \tag{2.15}$$

Because of this result, the values of the estimated amplitudes of the power spectrum peaks are questionable making this method not the most desirable to use. This is because the non-orthogonality of the sine and cosine projections in the space of functions of time. The power, $P(\omega)$, and squared amplitude, A^2, values correspond to different norms due to the non-orthogonality, resulting in a disparity of their values.

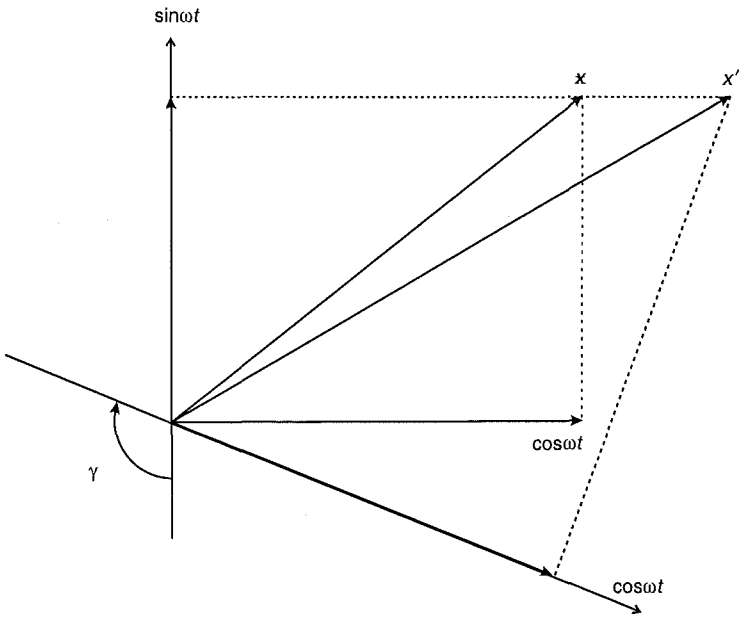

Figure 2.5: The least-squares fit of the test frequency to the observed data for an orthogonal (even sampling) and non-orthogonal (uneven sampling) case. In the orthogonal case, in geometric terms, the Fourier transforms are orthogonal projections onto the direction of the cosine and sine functions in the space of functions of time, $\cos\omega t$ and $\sin\omega t$ respectively, γ=90°, for the projection of a function x. In the non-orthogonal case, $\gamma \neq$90°, the sine and cosine are not orthogonal vectors, the resultant is given by the projection of the function x'. Therefore the amplitude squared does not correspond to the power $\| x \|^2 \neq \| x' \|^2$.

2.3.2.2 Lomb-Scargle

The Lomb-Scargle method is based on a modification of the DFT and is constructed as follows. If we consider a signal contained in an arbitrarily sampled data set $X(t_j)$ where $j = 1, 2, ..., N_o$, then the discrete Fourier transform, DFT, has the form:

$$FT_X(\omega) = \sum_{j=1}^{N_o} X(t_j) e^{-i\omega t_j} \tag{2.16}$$

It therefore follows that the periodogram is defined as:

$$P_X(\omega) = \frac{1}{N_o} \|FT_X(\omega)\|^2 \tag{2.17}$$

$$P_X(\omega) = \frac{1}{N_o} \left| \sum_{j=1}^{N_o} X(t_j) e^{-i\omega t_j} \right|^2 \tag{2.18}$$

Expanding

$$P_X(\omega) = \frac{1}{N_o}\left[\left(\sum_{j=1}^{N_o} X_j \cos(\omega t_j)\right)^2 + \left(\sum_{j=1}^{N_o} X_j \sin(\omega t_j)\right)^2\right] \tag{2.19}$$

In a continuation of the above methods, the orthogonality issues were addressed by Lomb in his 1976 paper [86]. Scargle argued that the previous two methods of:

1. Least squares fitting of sine and cosine functions of various periods to folded data.
2. Periodogram analysis.

are, with his modifications, equivalent methods. In this he showed that the sine and cosine terms can be made orthogonal by adding in an additional term in the form of a phase shift which was dependent on the frequency such that the periodogram can be made invariant to time translation, i.e. time independent. This is done by the addition of a constant term τ. Briefly, the periodogram is expressed and constructed as follows:

First, compute the data's mean and variance:

$$\bar{x} = \frac{1}{N_o}\sum_{j=1}^{N_o} x(t_j) \tag{2.20}$$

$$X(t_j) = x(t_j) - \bar{x} \tag{2.21}$$

$$\sigma^2 = \frac{1}{(N_o - 1)}\sum_{j=1}^{N_o} X(t_j)^2 \tag{2.22}$$

Secondly, for each angular frequency $\omega = 2\pi f > 0$, the offset time τ is computed as:

$$\tau = \frac{1}{2}\arctan\left[\frac{\sum_{j=1}^{N_o}\sin(2\omega t_j)}{\sum_{j=1}^{N_o}\cos(2\omega t_j)}\right] \tag{2.23}$$

which makes the periodogram time independent or equivalently is an additional parameter in the least-squares fitting which results in the method's correlation term being zero, i.e. the result obtained if the harmonic content of a data set at a given frequency was estimated by a linear least-squares fit to the model

$$X(t) = A\cos(\omega t) + B\sin(\omega t) \tag{2.24}$$

Lastly, the spectral power as a function of ω (Lomb-Scargle normalized periodogram), $P_N(\omega)$, is defined as:

$$P_N(\omega) \equiv \frac{1}{2\sigma}\left[\frac{\left(\sum_{j=1}^{N_o} X(t_j)\cos(\omega t_j - \tau)\right)^2}{\sum_{j=1}^{N_o}\cos^2(\omega t_j - \tau)} + \frac{\left(\sum_{j=1}^{N_o} X(t_j)\sin(\omega t_j - \tau)\right)^2}{\sum_{j=1}^{N_o}\sin^2(\omega t_j - \tau)}\right] \tag{2.25}$$

Scargle pointed out that the other main result of the method was that for arbitrary sampling, a confidence level can be used to detect the significant periodicities due to the statistical property of the periodogram having an exponential probability distribution when X is pure Gaussian random noise.

The Lomb-Scargle method involves fitting three functions, a sine, cosine and constant function; this last is generally estimated from the average value of the data. However the constant term is not orthogonal to either of the sine or cosine functions and therefore results in a fit which is not a realization of the initial least squares fit. This in turn causes the estimated amplitude of the power spectrum to be biased by the constant function term.

Press and Rybicki [118] present a method of using a FFT like algorithm to approximate the periodogram. This reduces the number of operations for N data points from 10^2N^2 to the order of $10^2N\log N$. Although only an approximation, it can be used where accuracy is not critical.

2.3.2.3 The relation between the orthogonality and the least-squares fitting

In Figure 2.6 the signal is depicted by the resultant x, whose components derive from the relation between the model of the signal and the residuals between the two.

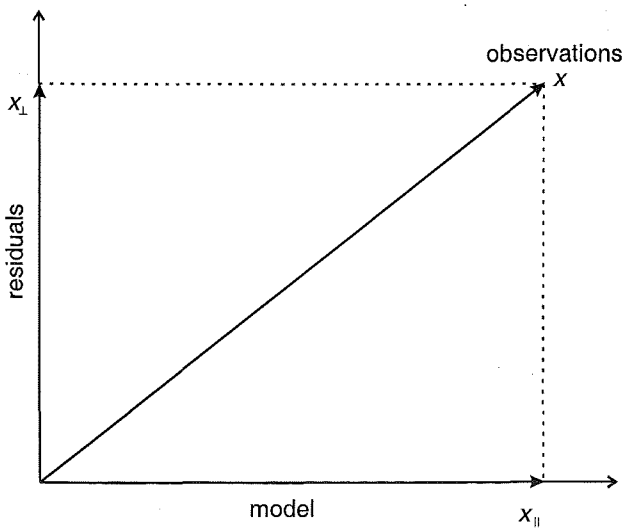

Figure 2.6: The least-squares fit of the test frequency to the observed data is depicted by the vector x. The decomposition of the model given by the fitting algorithm is $x_{\|}$, with the residuals given as $x_{\perp}$. The better the fit, the smaller the angle between x and $x_{\|}$ and hence a small residual value $x_{\perp}$.

Most methods for period searching use a test frequency in an attempt to model a fit to an observed signal, x. In doing so, the observed signal is decomposed into its model, $x_{\|}$ and

residuals, $x_\perp$. The least-squares fit is achieved by the projection of model functions onto an orthogonal base. These model parameters must therefore have the model, $x_\parallel$, and residuals, $x_\perp$, orthogonal, i.e. they satisfy Pythagoras's relation:

$$||x_\parallel||^2 + ||x_\perp||^2 = ||x||^2 \tag{2.26}$$

This is shown in Figure 2.6. Therefore, for a given test frequency, the power is split between the two components $x_\parallel$ and $x_\perp$. When the residual is a minimum, the test frequency is approximately equal to the fundamental frequency in the data set. At other test frequencies, the residuals are higher indicating the that they do not match the fundamental frequency in the data set. We can therefore base our test statistics around this idea. The plots of $x_\parallel$ and $x_\perp$, or their functions, against the frequency, ω, are the so called periodograms.

If the orthogonality relation in this case is true, it does not however mean that the model functions are themselves orthogonal at different frequencies. This therefore leads to correlations between values in the periodogram which results in aliasing and power leakage effects.

2.3.2.4 Date Compensated Discrete Fourier Transform, DCDFT

The Date Compensated Discrete Fourier Transform is a variant of the DFT, but defined to allow for the uneven data spacing and also a weighting function for the corresponding data. Ferraz-Mello [47] showed that for uneven sampling, the Lomb-Scargle method is equivalent to fitting three functions, sine, cosine and a constant term. However, only the sine and cosine terms are orthogonal which results in a correlation existing between the constant term and the estimate of the amplitude. As a result, this estimate is now biased. Improvement on the Lomb-Scargle method is made by constructing orthonormal functions so that the sine, cosine and constant function are all orthogonal. This is done by the use of the Gramm-Schmidt orthogonalization procedure. This procedure is however, very computationally heavy and therefore not suited for large data sets, greater than 10^4 data points. However for small data sets, it can be reasonably efficient. The DCDFT allows the use of harmonic filtering to aid in the removal of either un-wanted signals or aliasing effects. The method also gives better determination of the periodogram spectral intensity. As a result, better filtering can be used as well as better detection of the true frequencies.

2.3.2.5 Wavelet

Wavelet analysis has in recent years found its forte in the area of detecting varying periodicities in signals. This type of analysis is required for stars that are variable and/or have stellar atmospheres variation. However, wavelet analysis is not the method of choice in the detection of eclipsing binaries, as the output needs to be studied and the method requires large computational times per star. Foster [52] and Szatmáry [147], give a description of the application of this analysis technique to astronomical data. Scargle [135] gives an overview of the early papers in the technique as applied to astronomical data.

2.3.2.6 Spline

This method is based on using cubic B-splines to model a curve, in this case a variable star light curve. The cubic B-spline uses sections of a cubic function which approximate the curve over an interval. In this case the interval is the phased period and the phased light curve shape is the function being approximated. The sections within the interval are separated by values called knots to which a piecewise cubic polynomial is fitted. The coefficients of the polynomial

must have the first two derivatives continuous at the knots. This ensures a smooth, continuous function. The more knots that are in the interval, the more computational time is required.

A least-squares fitting programme based on Cubic B-splines was developed by Akerlof [1] to analyze the periodicity of variable stars' light curves in the MACHO database. The method is used on datasets $N<10^4$ as the number of computations varies as N^2, where N=number of data points. The coding efficiency is of particular importance due to the N^2 computational time, especially in the fitting procedure. The method works well, although it is time consuming to program. However with increasing computer speeds, the actual running time on small data sets as in MOA, approximately 100 to 150 data points, may not be such an issue.

2.3.2.7 Phase Dispersion Method, PDM

The Phase Dispersion Method is based on the binning and phase folding of data. The method works well with uneven data sets and with limited data. The user specifies a series of trial frequencies for which the data is to be folded. The full phase range (0,1) of each test frequency is divided into a specified number of bins. The variance within these bins is then calculated which gives a measure of the scatter around the mean light curve defined by the means of the data in each bin. The PDM statistic is then calculated by dividing the overall variance of all the samples by the variance of the original, unbinned, dataset. This process is repeated for each test frequency. The PDM statistic is then compared to the Fisher-Snédécor F distribution to determine the significance of the detection. If the test frequency is the true frequency, then the PDM statistic will approach a local minimum compared to adjacent frequencies. If the test frequency is not the true frequency, then the overall sample variance will be approximately equal to the variance of the original dataset, therefore the PDM statistic will approach a value of 1. The method had been used by Noda [105], to search the MOA database for variables. The search yielded some 78 eclipsing binaries in the LMC and 136 in the SMC, as well as Cepheids, 78 in the LMC and 38 in the SMC. These numbers are smaller than those from searching the same database using the Grison method discussed below.

An overview of the initial calculations of the PDM statistic, Θ_{PDM}, is given: Consider a set of data for test frequency f, over which the phase (0,1) is divided into r bins. Let n be the total number of observations, $\bar{x}$ their average and n_i, $\bar{x}_i$ the number of observations in the i^{th} bin and their average respectively. Also x_{ij}=$x(t_{ij})$ is the j^{th} individual observation in the i^{th} bin at time t_{ij}. Three statistics, s_k, k=0,1,2, can then be defined:

$$(r-1)s_1^2 = \sum_{i=1}^{r} n_i(\bar{x}_i - \bar{x})^2 \tag{2.27}$$

$$(n-r)s_2^2 = \sum_{i=1}^{r}\sum_{j=1}^{n_i} n_i(x_{ij} - \bar{x}_i)^2 \tag{2.28}$$

$$(n-1)s_0^2 = \sum_{i=1}^{r}\sum_{j=1}^{n_i} n_i(x_{ij} - \bar{x})^2 \tag{2.29}$$

where the degrees of freedom are given as $(r-1)$, $(n-r)$ and $(n-1)$ respectively. For arbitrary, but not necessarily random x, these statistics satisfy the relation

$$(n-1)s_0^2 = (r-1)s_1^2 + (n-r)s_2^2 \tag{2.30}$$

Their properties in the case of a signal purely containing Gaussian white noise with zero mean and unit variance:

$$\mathrm{E}[x_{ij}] = 0,\ \mathrm{Var}[x_{ij}] = \sigma^2 \equiv 1,\ \mathrm{Cov}[x_{ij}, x_{kl}] = \delta_{ik}\delta_{jl} \tag{2.31}$$

where E is the expectation value, Var is the Variance and Cov is the Covariance. The probability distribution for such a case is given in equation 2.29, with the degrees of freedom as mentioned previously. For the pure noise case, s_1^2 and s_2^2 are independent but not s_0^2. Their properties are given in equations 2.32, 2.33 and 2.34.

$$\mathrm{E}[s_1^2] = \mathrm{E}[s_2^2] = \mathrm{E}[s_0^2] = \sigma^2 \equiv 1 \tag{2.32}$$

$$\mathrm{Var}[s_1^2] = \frac{2}{r-1},\ \mathrm{Var}[s_2^2] = \frac{2}{n-r},\ \mathrm{Var}[s_0^2] = \frac{2}{n-1}, \tag{2.33}$$

$$\mathrm{Cov}[s_1^2 s_2^2] = 0,\ \mathrm{Cov}[s_1^2 s_0^2] = \mathrm{Cov}[s_2^2 s_0^2] = \frac{2}{n-1}, \tag{2.34}$$

The s^2 values are unbiased estimates of σ^2 as we do not know the expected value of σ. To verify the assumptions of equations 2.32, 2.33 and 2.34 the ratios of the s_k^2 values must be considered rather than the individual values of s^2. These ratios give the three statistics, Θ_{PDM}, Θ_{LS}, Θ_{AoV} for the Phase Dispersion Method, Lomb-Scargle and Analysis of Variance respectively.

$$\Theta_{\mathrm{PDM}} = \frac{s_2^2}{s_0^2},\ \Theta_{\mathrm{LS}} = 1 - \frac{s_1^2}{s_0^2},\ \Theta_{\mathrm{AoV}} = \frac{s_1^2}{s_2^2} \tag{2.35}$$

These are termed test statistics and these are given in equation 2.36 in the terms of equation 2.26.

$$\Theta_{\mathrm{PDM}} \equiv \frac{\|x_\perp\|^2}{\|x\|^2},\ \Theta_{\mathrm{LS}} \equiv \frac{\|x_\parallel\|^2}{\|x\|^2},\ \Theta_{\mathrm{AoV}} \equiv \frac{\|x_\parallel\|^2}{\|x_\perp\|^2} \tag{2.36}$$

The AoV test statistic, Θ_{AoV}, is the ratio of two independent χ^2 random variables, therefore it obeys a Fisher-Snédécor F distribution. This is also the case for multi-harmonic methods such as the Grison method. Analyzing the method, Schwarzenberg-Czerny [139], commented that the comparison of the PDM statistic to the Fisher-Snédécor F distribution is not correct. Rather, the PDM statistic follows a beta distribution. The result of using the incorrect distribution is a decreased sensitivity to minor but significant signals in the dataset.

2.3.2.8 Analysis of Variance, AoV

The Analysis of Variance period detection follows very closely the Phase Dispersion Method as it too is based on the binning and phase folding of data. The difference is in the AoV statistic which is defined in equation 2.35.

This properties of the AoV statistic is very well known and follows a Fisher-Snédécor F distribution. The result is a very robust period searching algorithm that can handle large datasets. It has been used by groups such as EROS and OGLE to search for variable stars with reasonable success. It has been shown to be better than the PDM in variable detection [138].

2.3.2.9 Grison algorithm

This is the method that was adopted for the MOA database search. A more detailed description is given in section 2.5. Grison's algorithm uses a Fourier method in conjunction with harmonics that are used in a least squares fit of the data set. For a given test frequency, a set of orthogonal basis functions are calculated such that they are the linear combinations of the preceding ones. This is achieved by applying the Gramm-Schmidt procedure and therefore satisfying the orthogonality requirements. In doing so, the statistical behaviour of the periodogram is preserved. The use of harmonics enables a least-squares fit to most periodic light curves and is ideal for eclipsing binaries. The computation cost however rises as the number of harmonics is increased. Typically, the fundamental plus the first three harmonics will enable a fit to most curves. Above this, more harmonics add large amounts of computing time with little gain in the fit.

2.4 Which method to use?

Reimann [125] gives a description and comparison of several methods for which data from the MACHO database was the test-bed, here reproduced in Table 2.8. The stars used for testing were Cepheid type variables and eclipsing binaries. The eclipsing binaries were a mixture of contact type light curves to semi-detached type light curves. None however were of a detached nature.

Table 2.8: Frequency estimation methods as used by Reimann [125] to detect the period of an eclipsing binary, P=2.47133 d, similar to MOA J005206.7−725122, P=1.8218 d (refer appendix G). The scaled speed ranges from 1, fastest to 10, slowest. The data consisted of 300 data points unevenly sampled over 400 days, to which 20,000 test frequencies in one step, then an additional 4000 test frequencies were fitted.

Method	Scaled run-time(1-10)	Parameters
Lomb-Scargle Cosine	1.6	Modelled by least squares fit
Fourier decomposition(2)	2.9	2 term expansion (5 parameters)
Fourier decomposition(4)	6.0	4 term expansion (9 parameters)
Fourier decomposition(6)	10.0	6 term expansion (13 parameters)
Periodic cubic B-spline(5)	4.7	5 knots over the phase interval
Periodic cubic B-spline(9)	5.5	9 knots over the phase interval
Periodic cubic B-spline(13)	5.8	13 knots over the phase interval
Lafler Dispersion method	1.1	
Renson Dispersion method	1.3	
Supersmoother	6.0	

Although not tested, Reimann's analysis predicted the PDM to be somewhere between the Lafler and Renson dispersion methods and the Supersmoother. The PDM makes more assumptions about the shape of the curve as bins are allocated which influences the result. The speed of the dispersion methods is high, but as we will see, they are not ideal.

Table 2.9 gives the results of the frequencies detected in the data, for the top four best estimates. It was found that the Cosine (Scargle) method did not estimate the fundamental frequency until its fourth estimate. This result is not surprising since the method uses a sinusoid to fit the light curve. The best performers were the 4-term Fourier method, the 9-knot spline and the Supersmoother. The aforementioned Fourier and spline method give very similar results with both estimating the fundamental ω, first sub-harmonic $\frac{\omega}{2}$, first harmonic 2ω and the second sub-harmonic of the first harmonic $\frac{2\omega}{3}$. The Supersmoother also gave a good result that was

equal to the Fourier and Spline methods.

Reimann conducted several tests using an eclipsing binary light curve that was adjusted so as to increase its noise level, then the various methods were tested to fit the data. The initial light curve resembled a bright, non-blended eclipsing binary that one may detect in the SMC. The worst case scenario could be considered as a typical light curve of what would be expected from the MOA database in terms of brightness and blending. The test however did not account for a very noisy case in which an answer on whether the light curve was in fact an eclipsing binary could not be made immediately.

Table 2.9: Data in this table is reproduced from Reimann [125]. Frequency estimation methods as used by Reimann to detect the period of an eclipsing binary P=2.47133, similar to MOA J005206.7−725122, P=1.8218 d, Appendix G. The 1^{st}, 2^{nd}, 3^{rd} and 4^{th} estimates of the fundamental frequency, ω, by the methods are given for the dataset in terms of the fundamental, ω, harmonics and sub-harmonics. For the test light curve, all but one method detected the actual frequency on the first estimation. Note: the + 1 or $+\frac{1}{2}$ values correspond to pseudo-aliases.

	Identification of the fundamental			
Method	1^{st}	2^{nd}	3^{rd}	4^{th}
Lomb-Scargle Cosine	2ω	2ω+1	-2ω+1	ω
Fourier decomposition(2)	ω	2ω	2ω+1	$\omega+\frac{1}{2}$
Fourier decomposition(4)	ω	$\frac{\omega}{2}$	2ω	$\frac{2\omega}{3}$
Fourier decomposition(6)	ω	$\frac{\omega}{2}$	$\frac{\omega}{3}$	2ω
Periodic cubic B-spline(5)	ω	2ω	2ω+1	$\omega+\frac{1}{2}$
Periodic cubic B-spline(9)	ω	$\frac{\omega}{2}$	2ω	$\frac{2\omega}{3}$
Periodic cubic B-spline(13)	ω	$\frac{\omega}{2}$	2ω	$\frac{\omega}{3}$
Renson Dispersion method [9]	ω	$\frac{\omega}{2}$	$\frac{\omega}{3}$	$\frac{\omega}{4}$
Supersmoother	ω	$\frac{\omega}{2}$	$\frac{\omega}{3}$	2ω

These results gave guidance on which methods to pursue. The Phase Dispersion Methods, namely Lafler and Renson, performed very poorly, as did the Cosine (Scargle) method. Their poor performance was due to their high variance when encountering noise in the the data. In the MOA data, the noise levels, also systematics due to blending, will be a critical factor, especially for fainter systems. Therefore it would be inappropriate to considered these methods. The spline method gave a satisfactory performance under the higher noise levels than the Supersmoother method, but although the estimations contained more error, they were more consistent than the Supersmoother. The best result was obtained from the 4 and 6 term Fourier method which performed well under noisy conditions. This was followed by the 2 term Fourier method. Reimann indicated that the 2 term Fourier decomposition method (5 parameters) is the minimum model that should be used to identify an eclipsing binary. This is primarily due to the shape of their light curves. Using 4 terms (9 parameters) results in an even better fit, where the gains are seen in the reduction of oscillations in the light curve fit. These can be reduced further by using more terms, such as 6 terms (13 parameters), however the penalty is doubling computational time. The results show little increase in accuracy for this increase in time therefore using 6 terms (13 parameters) gains little over using 4 terms.

The Fourier decomposition method generally detects the following harmonics in the order of that given below:

- Fundamental frequency, ω

[9] Reimann stated that the Renson and Lafler methods gave near identical result, therefore he only gave the Renson method results.

- First sub-harmonic frequency, $\frac{\omega}{2}$
- First harmonic frequency, 2ω
- Second sub-harmonic of the first harmonic frequency, $2\frac{\omega}{3}$
- etc ...

Although a fit can be made within reason to any well-sampled eclipsing binary, due to the high complexity, the penalty is high processing time. Additionally, the more terms/parameters that are introduced in the Fourier decomposition method, the more harmonics or sub-harmonics are detected rather than the fundamental frequencies. This hinders rather than assists in the detection of the true period, as more time is required to physically view the phased light curves and possibly calculate the fundamental period from the given harmonic and sub-harmonic frequencies.

When using a Fourier Decomposition method, the number of parameters must be chosen so that the light curve can be modelled sufficiently well at its fundamental period (converge quickly to a good approximation) yet avoid some of the problems mention above.

In a quantitative analysis of period search algorithms, Schwarzenberg-Czerny [140] concluded with two main points:

1. The method using smooth functions such as the Lomb-Scargle spectrum, power spectrum, the multi-harmonic Fourier periodogram, and those χ^2 methods involving a smooth model are generally more sensitive than those which rely on phase binning. This is because the phase binning methods use step functions rather than smooth functions.
2. It is important that the resolution of the model functions match the structures in the detected signal. Too high or too low resolution, results in a loss of detection sensitivity.

In conclusion it would appear that the best type of method to use for the detection of eclipsing binaries in the MOA catalogue would be a Fourier method such as that given by Grison [60]. The data is expected to contain some bright eclipsing binaries, however many would most likely be several orders of magnitude fainter and contain some noise. Also the seeing at the MJUO site averages about 2.5 arc sec so this means that the method must be able to perform well under noisy conditions.

The Grison algorithm was seen to have worked well in the EROS programme, so this gives confidence in its capabilities.

2.5 The Grison algorithm

2.5.1 Features of the Grison algorithm

The method is designed for astronomical data which is almost always unevenly spaced and is ideal for finding the period in most periodic light curves.

This section is intended to discuss the main features of how the Grison algorithm works and how it differs from other period searching algorithms. It is not intended to give a full in depth description of the mathematical working of the algorithm, instead the reader is referred

to Grison's paper [60] for a full treatise on the method. Appendix F contains the coded mathematical method used as this differed slightly from the equations in Grison's paper as the test frequency variable was required to be included in the code. It additionally contains the C programming code for the algorithm used to search the MOA LMC and SMC database. Details of the parameter set and changes are discussed in more detail in Chapter 3.
Firstly a brief overview is given, followed by a more detailed description of each step in the algorithm.

The Grison period finding algorithm is based primarily on a Fourier Method. The algorithm uses a range of user specified test frequencies which are used to attempt a least squares fit of the data. These are stepped through one by one. During processing, each frequency in turn is assigned as a fundamental frequency. This is then fitted to the data and its first harmonic calculated. The combination of the two is then fitted and the next harmonic calculated. This continues to the n^{th} harmonic thereby giving:

- Fit 1: fundamental
- Fit 2: fundamental + 1^{st} harmonic
- Fit 3: fundamental + 1^{st} harmonic + 2^{nd} harmonic
- Fit 4: fundamental + 1^{st} harmonic + 2^{nd} harmonic + 3^{rd} harmonic

In section 2.4 the advantage of a Fourier method was given. Another advantage of the Fourier approach is that a significance test can be applied to the end result which gives a probability on the detection (significance) of the detected (in this case the quality of the least-squares fit) frequency in the data being real or not. This is very useful when the user is searching through millions of light curves; a task which is very commonplace now days.

The Modified Periodogram (power spectrum), $\mathrm{MP}_k(\omega)$, given by Scargle [134] was taken in a general form of:

$$\mathrm{MP}_k(\omega) = \sum_{i=1}^{k} A_i \cos(i\omega t - \tau_i) + B_i \sin(i\omega t - \tau_i) \tag{2.37}$$

In order to solve the equation, a solution for the value of A_i and B_i is required to be found. This is achieved by the Gramm-Schmidt procedure applied to the Fourier terms in order to find a set of orthogonal functions which are a linear combination of the previous ones. This results in a general least-squares model which is a linear combination of k pairs of functions (Φ_i^c, Φ_i^s). For dataset's containing N observational data measurements $x(t_j)$, the datasets mean, $\bar{x}$, is defined as:

$$\bar{x} = \frac{1}{N} \sum_{j=1}^{N} x(t_j) \tag{2.38}$$

If we considered a set of data with zero mean and variance σ^2 which is estimated by s^2, then:

$$X(t_j) = x(t_j) - \bar{x} \tag{2.39}$$

and the estimated variance s^2:

$$s^2 = \frac{1}{N-1}\sum_{j=1}^{N} X(t_j)^2 \tag{2.40}$$

The general least-squares model, M_k, is then defined as:

$$\mathrm{M}_k = \sum_{i=1}^{k} A_i \Phi_i^c + B_i \Phi_i^s \tag{2.41}$$

Refer to Grison's paper [60], for the details on the functions.

The method gives an estimate for the coefficients as:

$$A_i = \frac{\sum_{j=1}^{N} X_j \Phi_k^c(t_j)}{\sum_{j=1}^{N} \Phi_k^c(t_j)^2} \tag{2.42}$$

$$B_i = \frac{\sum_{j=1}^{N} X_j \Phi_k^s(t_j)}{\sum_{j=1}^{N} \Phi_k^s(t_j)^2} \tag{2.43}$$

This gives a definition for the modified periodogram, $\mathtt{MP}_k$, as:

$$\mathtt{MP}_k = \frac{1}{2ks^2}\left[\sum_{j=1}^{N} X(t_j)^2 - \left(\sum_{j=1}^{N} X(t_j) - \mathrm{M}_k\right)^2\right] \tag{2.44}$$

For the orthogonal case, we now define the general least-squares model called the Periodogram P_k, such that:

$$\mathrm{P}_k = \frac{1}{2ks^2}\sum_{i=1}^{k}\left[A_i^2 \sum_{j=1}^{N} \Phi_k^c(t_j)^2 + B_i^2 \sum_{j=1}^{N} \Phi_k^s(t_j)^2\right] \tag{2.45}$$

This gives the probability of false detection, Pr as:

$$\Pr(k) = 1 - \left(\int_0^{\mathrm{P}_{k\max}} f_{\mathrm{F}_{2k,N-1}}(x)dx\right)^{N_i} \tag{2.46}$$

$$\text{where } \int_0^{\mathrm{P}_k max} f_{\mathrm{F}_{2k,N-1}}(x)dx = 1 - I_{\frac{(N-1)}{N-1+2k\mathrm{P}_k \max}}\left(\frac{N-1}{2}, k\right) \tag{2.47}$$

where N_i is the number of independent frequencies; I the incomplete beta function; $\mathrm{F}_{2,N-1}$ the Snédécor distribution and f_{F} its probability density function.

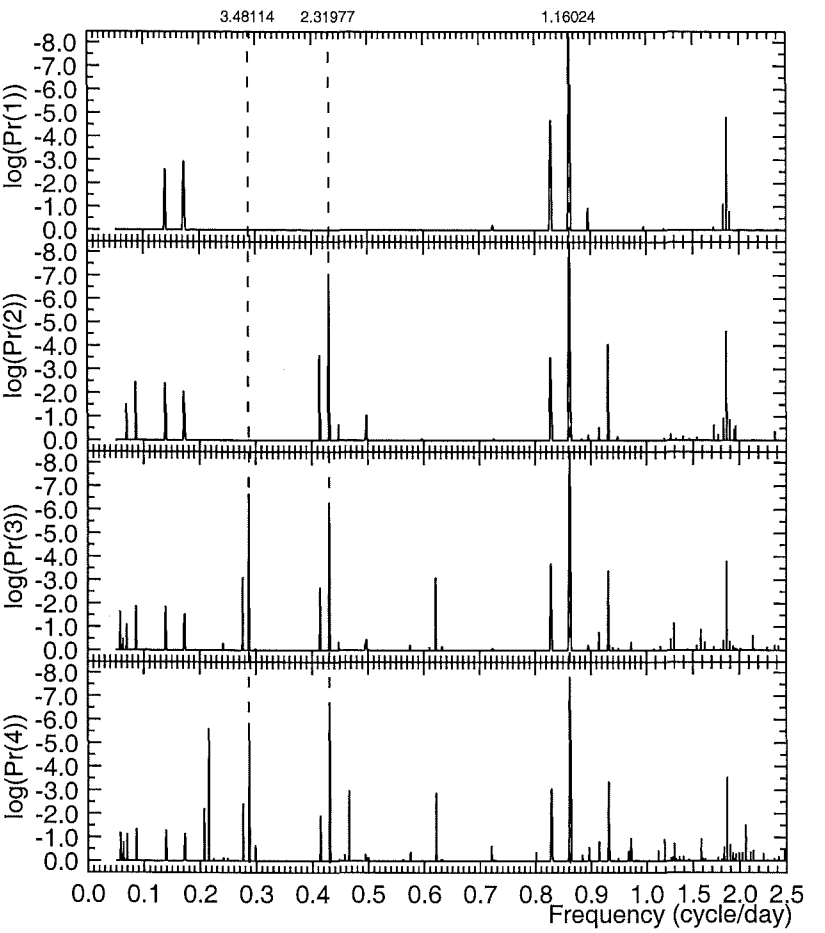

Figure 2.7: Probability of false detection plots for the target MOA J005623.5−722123. The highest peak corresponds to the lowest value of $\log_{10}(\Pr(k))$, $k = 1,2,3$ and 4. This implies that the corresponding frequency is not a false detection but a real signal. The three periods indicated are the most probable periods.

The initial input requires a range of frequencies to test for periods. Care must be taken to allow for an appropriate resolution or the actual periods can easily be missed. The number of test frequencies is proportional to the processing time. Therefore the search range can require careful selection. The orthogonal set of functions constructed are used to solve for the coefficients A_i and B_i in order to use the probability of detection property of the periodogram. If we do not adopt this approach, this property is completely lost. It is this part of the algorithm that is the most CPU intensive. From these solutions, a probability of false detection is calculated. This is achieved by identifying the frequency corresponding to the largest value of the periodogram for each harmonic, where each harmonic is the addition of the previous. That is $\Pr_4 = \Pr_3 + \Pr_4$, $\Pr_3 = \Pr_2 + \Pr_3$, $\Pr_2 = \Pr_1 + \Pr_2$, $\Pr_1 = \Pr_1$.

The lowest value of each $\log_{10}(\Pr(k))$ is assigned as $\mathrm{P}_k\mathrm{max}$, i.e. the highest peak in a plot of $\log_{10}(\Pr(k))$ versus frequency, ω, is deemed to be a possible period. In terms of the probability of false detection, the lower the value of $\log_{10}(\Pr(k))$, the greater the probability that the detection is not false, i.e. a small value for the probability of false detection.

The peak value is then used to phase the data. At this stage, it is not known whether the period is the true fundamental or merely a harmonic. Therefore, further tests are required.

The possibly also exists that the period is not a true signal, rather noise or an alias peak. The implications of this possibility and ways to estimate the true period are discussed in Chapter 3.

Chapter 3

Results of searching for eclipsing binaries

In this chapter the results of searching the MOA database for eclipsing binaries are presented and discussed. The eclipsing binaries that had previously been detected are the 100 or so systems in both Clouds listed in Gasposchkin catalogue [56]. A search of the database of photometric time-series observations acquired by the French EROS Collaboration, in the mid to late 1990's, resulted in the detection of a further 79 new eclipsing binaries in the LMC. Until then, these were the only catalogues available until the results of searches in other microlensing survey databases were published. A majority of the eclipsing binaries detected in the EROS catalogue were not ideally suited to follow-up observations, mainly due to crowding in the fields as these were in central region of the LMC. During the EROS programme, P. Grison developed an algorithm to search through the EROS database for eclipsing binaries and Cepheids.

3.1 The SMC fields surveyed in the MOA database

The SMC region surveyed by MOA incorporated the central, dense areas of the SMC as well as areas of lower stellar density around the periphery of the central region. This was due to the field sizes and placements. The SMC was divided into two fields, smc1 and smc2, which were essentially 1° square and overlapped in the central region of the SMC. This ensured that most of the dense regions of the SMC were covered for the microlensing survey. The size of the fields arises from the MOA-cam1 size and the adopted cyclic observing sequence. In Figure 3.1 the fields have an irregular shape with two *slots* in them. This is due to an error in the cyclic motion of the telescope. The same feature is apparent in the LMC fields.

The 1° square field outlines are defined by the coordinates listed in Table 3.1.

Table 3.1: The coordinates (J2000) for the corners of the MOA fields, smc1 and smc2 in the SMC.

	smc1		smc2	
Field corner	RA	Dec	RA	Dec
South West	$00^h41^m21^s$	$-73°37'44''$	$00^h52^m17^s$	$-73°00'50''$
South East	$00^h55^m18^s$	$-73°36'28''$	$01^h05^m43^s$	$-73°00'35''$
North East	$00^h54^m51^s$	$-72°36'07''$	$01^h05^m20^s$	$-72°00'10''$
North West	$00^h41^m36^s$	$-72°36'30''$	$00^h52^m33^s$	$-72°00'22''$

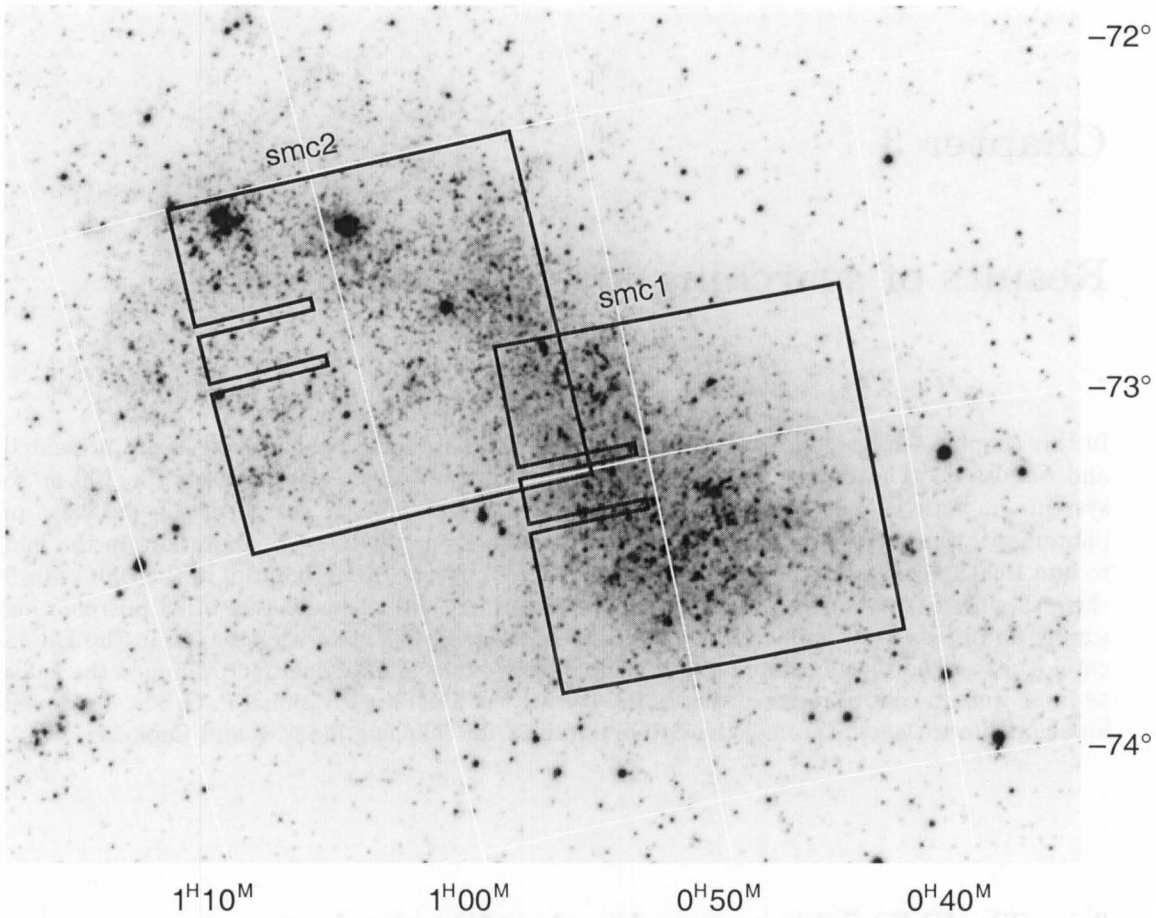

Figure 3.1: MOA smc1 and smc2 fields superimposed over a image of the SMC from the Canterbury Sky Atlas (Doughty, Shane and Wood 1972). J2000 coordinate grid.

3.1.1 Coding of the Grison algorithm

The mathematical algorithm which is termed here the Grison algorithm was coded in the C programming language. Modifications such as an addition of the test frequency variable ω were added to the code so that various test frequencies could be assessed. The C code and modifications are presented in Appendix F.

The photometry for the input was imported from the MOA data files and then processed. The output from the program had to be in an easy to read/view form as many phased light curves needed to be viewed by eye. It was decided that a file in PostScript format would be used. This had several advantages:

- Portable graphical format, printer friendly
- The output data is listed in the PostScript code and is readily accessible
- The phasing could be calculated in the PostScript code
- The files are small, especially once compressed (gzipped)

The other output was an ASCII data file called `starfile[MOA ID].dat` which contained the values of the Julian Date and magnitudes of the red and blue filter data. Although not

immediately essential, it was a useful format to have in case the use of other software packages such as MIDAS required an easy-to-read format.

In very simple terms, the main procedure in the algorithm attempts to fit a series of test frequencies to the data and select the best fitting one as the most likely period for that data set.

The actual true frequency[1] is estimated by fitting a series test frequencies[2] in the hope of hitting upon the true frequency of the data set. Therefore the range of these frequencies is pre–selected before the period finding algorithm is initiated. The purpose of the search was to locate new eclipsing binaries with periods in the range of 0.4 days to 20 days that could be used for follow up observation at the Mount John University Observatory. Therefore the test frequencies were selected to cover this range of values.

Care must be taken to have the test frequency steps fine enough to detect the true frequencies but not too fine as to oversample the frequency interval and therefore take an excessive time to process. The sampling resolution is therefore a critical quantity. The shorter period binaries are more sensitive to the increments in the test frequencies than those with longer periods. This is due to small variations in the periods, which repeat more over a fixed interval and therefore any small variations compound more rapidly. Therefore the sampling rate was altered to allow for this.

The search range of 0.4 days to 20 days was first sampled using 7000 equally-spaced test frequencies. The first group of the smc1 data, `smc1.group0`, was used as the test data set. This, like the other groups, contained 2000 photometric light curves. The average number of data points in the light curves for each of the red and blue filters was typically 90. The group did however contain brighter than average stars, but this made the initial evaluations easier as the signal-to-noise levels were high.

3.1.2 Initial results and modifications of the test data

All of the initial test group was processed and the PostScript output results viewed. This enabled the periodic variables to be identified and ensured the coding of the algorithm was functioning correctly. In this data group several eclipsing binaries were detected as well as Cepheids and other variables. This therefore made the group an excellent test bed for testing different selection criterion.

The PostScript output was of great use as the values could be viewed graphically which made selection a much faster process. Additionally, in the PostScript file, small changes to the calculated period could be made to ensure the resolution was sufficient

3.1.2.1 Initial numbers

The initial search of the database processed approximately 10 000 light curves. This was in order to determine if the search parameters were reasonable and also to identify any problems

[1] The true frequency implying that the data can be phased to that frequency to reveal its periodic variation; of course not all data sets will have a true frequency. Some are constant or are simply noisy data sets.

[2] This directly relates to a period as period $= \frac{1}{\text{frequency}}$.

that might occur due to noisy light curves. The two main parameter values to be addressed were:

- The test frequency resolution
- Determination of a detection threshold for the probability of false detection

One of the problems with Fourier methods is that they will always find a period, as there is always one peak higher than the rest in the periodogram plots, whether it be purely noise or a real signal. The algorithm gives the results in the form of a period with probability of false detection in an effort to make the results more intelligible. When a strong signal is present in the periodogram, strong side bands are also present, which are the aliases of the main peak. These side bands are stronger when the light curve resembles a sinusoidal shape with little associated noise. The shapes of the various eclipsing binary light curves differ greatly and as a result the detection of particular shapes depends on the number of harmonics added. For sinusoidal-type curves, a single frequency generally detects the fundamental very effectively. The additional harmonics have a tendency to detect false periods, which are generally attributed to the noise in the data and stray data points that do not phase correctly.

Detached systems have light curves very different from the contact type. The baseline is very flat which results in a very poor fit from the fundamental frequency as the eclipse profiles are generally sharp rather than rounded (sinusoidal-like). As more harmonics are added the shape resembles more that of the light curve and the real period is detected. In these systems, generally the second, with sometimes the third, harmonic was required to detect the true period. It was common for the detected period to be a fraction, generally half, of the real period. This is because, with similar primary and secondary eclipse depths, the data repeats with twice the orbital frequency. Such cases were identified during examination of the PostScript plots and the detected period was doubled.

3.1.2.2 Test frequencies

The range of test frequencies is very critical to the operation of the search algorithm as it sets two critical factors:

- The sampling resolution
- The computation time to search the database is proportional to the number of test frequencies

The initial testing found that the largest peak in the probability of false detection did not always give the true period. This was the case for periods over ten days. Sometimes the value was a fraction of the period, other times it was a completely incorrect value. It was also found after investigation of the test frequencies and the probability of false detection data that the resolution of the test frequencies was such that some of the peaks were being missed and as a result the frequency was only being partially detected. This resulted in the determination of the peak being deemed insignificant and therefore rejected.

In addition, the resolution at lower periods, 0.4 to 1.0 day, was unnecessarily high, resulting in oversampling of these frequencies. Although not a problem, the processing time of each photometric sequence was unnecessarily long.

As the period increases, the sensitivity of the frequency of the true period decreases and a coarser interval between the test frequencies is used. At the lower periods the opposite is true. Different sampling steps were therefore used over two frequency ranges selected from 0.4 days to 2 days 2 days to 20 days. The former was sampled using 500 test frequencies and latter using 3000 test frequencies.

3.1.2.3 Determination of a detection threshold for the probability of false detection

A cut-off value for the log(probability of false detection) was set at -0.25. This was set after viewing about a thousand light curves in order to obtain an idea of the value to use. One had to be careful not to cut out any noisy eclipsing binaries, specifically well-detached systems by setting the value too high. Since we were trying to detect well-detached systems, this would have been detrimental to the final goal. Another issue encountered was the number of so-called variables that were not variables. These tended to be noisy light curves where a strong signal had been detected in the data.

3.1.2.4 Alteration to the PostScript output

From these results, the PostScript code was altered so that the probability of false detection plots[3] for Pr_1, Pr_2, Pr_3 and Pr_4 were shown. The highest peak indicates the probability that the respective frequency is the most likely frequency. This is not necessarily the correct frequency (or period). Taking the highest peak in each plot however, did not give four different, most probable frequencies. In many cases, the most probable frequency was the same frequency in each of the probability of false detection plots. Therefore, to aid in the selection of the correct frequency, the highest peak in the first plot, $\log(\mathrm{Pr}_1)$ was selected, then the highest peak in the second plot, $\log(\mathrm{Pr}_2)$ was selected other than that selected in the $\log(\mathrm{Pr}_1)$ plot. Similarly for $\log(\mathrm{Pr}_3)$, thereby giving three different frequencies as the most probable frequencies. The data were then phased and plotted, Figure 3.2. This enabled the phased plots to be examined by eye to determine if the the system was an eclipsing binary and to check if the periods detected were reasonable. The Pr_4 value was not used as aliasing effects become stronger and more than likely, the highest peak often not being the actual frequency.

The sampling ensures that the actual period is estimated as shown in the phasing of the data, but further refinement is required to get a more precise value. This is more efficient than using a fine sampling rate. Also the uncertainty needs to be calculated and this is done at the period-refining stage.

3.1.3 The first search

The first search was then initiated with the criteria of $\log(\mathrm{Pr}_k) < -0.25$. It was thought that several thousand, perhaps 5 000 to 10 000 light curves might be detected as variables, however the figure was about 40 000. This was 10% of the SMC database, too many to look at. Therefore more filters were needed to narrow the selection criteria.

A number of the 40 000 light curves were looked at in order to determine the functionality of the code on the noisy light curves. It was found that these made up the bulk of the 40 000

[3] $\log(\mathrm{Pr}_k)$ vs frequency, where k=1,2,3 and 4.

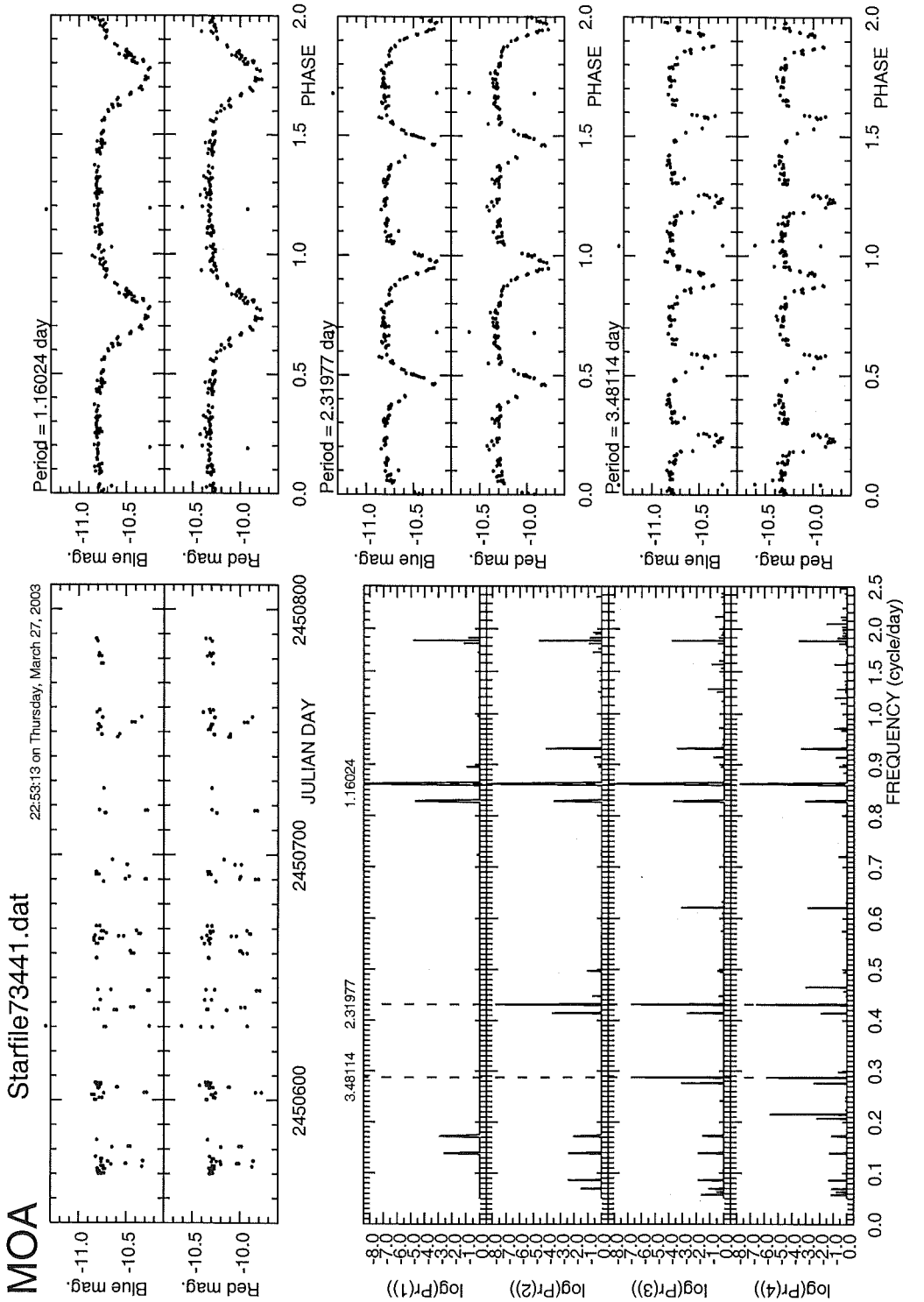

Figure 3.2: Periodogram plot of an eclipsing binary in the smc1 field from the `smc2.group36` data set. The MOA number 73441 is an internal catalogue number. The IAU designation for this system is MOA J005623.5−722123. The two top left boxes (when viewed in landscape orientation) display the raw data as extracted from the MOA database. The data were passed to the Grison algorithm and the 4 periodograms, lower 4 boxes on the left, are produced. The peaks indicate a probability that the respective frequency is the most likely frequency. The frequency of the highest peak (most probable period) in the first plot $\log(\mathrm{Pr}_1)$ is selected. The highest peak in the second $\log(\mathrm{Pr}_2)$ plot other than that selected in the $\log(\mathrm{Pr}_1)$ plot is selected and similarly for $\log(\mathrm{Pr}_3)$. The data phased to these three frequencies are then plotted, three plots to the right, for both blue and red filters. This then enables viewing of the three most probable detected frequencies. In this case, the centre period is correct as the primary and secondary eclipses are present in 1 cycle (0 - 1 in phase). Note the other two are a ratio $\frac{1}{2}$, top and $\frac{3}{2}$, bottom, of the correct period. The PostScript file is then written to disk. Note the phasing of the data is performed in the PostScript file, thereby allowing easy alteration at a later date if required.

detections. A revision of the code and selection criteria was required.

Due to these results, several other cut factors had to be added into the program to reduce the number of light curves that had to be looked at by eye on the computer screen.

3.1.3.1 Modifications to code and selection criterion

There are several ways to further reduce the number of light curves that have to be viewed by eye:

- Use statistical filters
- Ratios of the detected frequencies
- The system's colour−magnitude values

The use of a statistical filter prior to the actual fitting of any test frequencies would not only reduce the number of stars to pass through the algorithm, but also decrease the processing time as most of this occurs in the test frequency fitting stage.

The following statistics/values for each light curve's red and blue filter were calculated in the order given below:

- The minimum and maximum values
- The mean for the red and blue data
- All points > 4.0 Standard Deviations from the mean were excluded
- Recalculate mean and Standard Deviation for the red and blue data
- Recalculate minimum and maximum values

These were then used to make the following selections:

1. Exclude all points > 4.0 Standard Deviations from the mean.
2. Select the light curve which contain > 50 data points in the red and blue filters.
3. Select the light curves whose difference between the maximum and minimum values in the red and blue is > 0.25 magnitudes.

Selection criterion 1 ensured that sufficient data points where available so that a reasonably sampled light curve would result upon the data being phased. Criterion 2 cut the outlying points that were generated from spurious results brought about from bad seeing or data reduction errors. These can have effects on the frequency fitting, especially at higher harmonics. Criterion 3 was to ensure the light curve had sufficient variation that follow-up observations would be worthwhile, as this was one of the search requirements.

If the data passed these initial criteria it was then passed to the Grison algorithm, the test frequency fitting stage. This initial cut had the advantage that it was very fast to do, in the order of a few seconds for 2000 light curves, whereas to pass through the algorithm to detect the three most-likely periods took about 45 seconds per photometric sequence.

3.1.3.2 Ratios of the detected frequencies

Another criterion was based on the way the Fourier method produces results. Since harmonics are being added, one expects that the highest peaks in each of the probability of false detection plots will be related in terms of a factor or ratios. This is seen in the periods detected in the Fourier decomposition models, Table 2.9.

After the passing through the period finding stage but before the light curve was written to a PostScript file for viewing, a final set of selections was applied.

Viewing of the results showed that the variable stars, namely eclipsing binaries and Cepheids, had their strongest detected periods in ratios of; $\frac{1}{3}$, $\frac{1}{2}$, $\frac{2}{3}$, $\frac{3}{2}$, 2.0 or 3.0, with errors of ± 0.003. A large proportion of the other light curves that did not have these ratios were generally noisy data or long period variables, with variation greater than 100 days, and these were not of interest as they have a small probability of being eclipsing binaries. However if they were, their stellar velocity components would be exceedingly hard to measure and therefore they would be of little interest to our goal. Therefore a ratio of simple integers (± 0.003) for the detected periods was added to the selection criteria.

In addition, the longer period variables and noisy data with no apparent or detected frequency, suffered from aliasing effects which resulted in periods being reported around integer values, i.e. 1, 2 and 3 days ± 0.002 day. If periods occurred with these values of 1, 2, or 3 (within an uncertainty of ± 0.003 day) they were rejected. This was due to aliasing effects in the periodogram which give spurious signals around the length of day. It should be noted however that the possibility exists that systems have periods with these values. If they do, then they are discarded. Multiple observations on one night could help resolve the issue, however such observations were not available for MOA data. From an observational view, it is preferable not to have targets around the integer day value as recording data for the complete light curve would be a very long process as the cycle takes a long time to evolve in phase.

To quantify these numbers, the results from a single group of 2000 stars were passed through the algorithm with various settings (determined previously). Initially, all 2000 light curves were passed through and the short period variable light curves, mostly eclipsing binaries and Cepheids, recorded. This therefore gave an idea of the numbers and types of variables present. In this selection was a range of types of eclipsing binaries from detached to contact, with periods from 0.5 days to 6.4 days. This range gave a good test of the algorithm and the initial selection criteria. The following additional criteria were then applied:

- case 1 - Only stars with a variability > 0.25 magnitudes between the minimum and maximum and with more than 50 data points
- case 2 - As for case 1 with the addition that the probability of false detection parameter must be < -0.25
- case 3 - As for case 2 with the addition that the period is not an integer value 1, 2 and 3 days ± 0.003 day

- case 4 - As for case 3 with the addition that the ratios of at least one pair of the three detected periods must be $\frac{1}{3}$, $\frac{1}{2}$, $\frac{2}{3}$, $\frac{3}{2}$, 2.0 or 3.0, with errors of ± 0.003

- case 5 - As for case 4 but requiring the ratios of all three period pairs to be as in case 4

It is important to minimize the number of light curves to view in the test group yet still detect all the eclipsing binaries in the group. It must be remembered that there are 400 000 stars in the SMC catalogue and 1 000 000 stars in the LMC catalogue. The results of applying these additional criteria are reported in Table 3.2. All eclipsing binaries in the group of 2000 stars are detected under each criterion.

Table 3.2: Application of the selection criteria to the initial 2000 photometric sequences shows a reduction in the number of light curves to view. All eclipsing binaries initially identified were found in all cases. This helped reduce the total number of light curves required to be viewed by eye.

Criterion	Number of stars detected to view	Estimated number to view	
		LMC	SMC
none	2000	1000000	400000
case 1	1004	502000	200800
case 2	295	147500	59000
case 3	232	116000	46400
case 4	107	53500	21400
case 5	49	24500	9800

Therefore case 5 was added to the selection criteria and dramatically reduced the number of so-called periodic variables detected. The remaining stars that passed all of these criteria were then passed to the PostScript file to be written to disk along with the associated ASCII files.

3.1.3.3 Processing time

The processing time for a single light curve was typically 45 seconds on a Pentium II 350 MHz personal computer with 128 Mb RAM. Although not optimal, the code ran sufficiently fast to produce a reasonable total processing time. Since the algorithm is based on a Fourier method, it is the cosine and sine calculations that take the majority of the time, namely the orthogonality based calculations. An implementation of approximations of trigonometric functions could improve the speed, but the estimated values from the approximations would need to be examined to ensure the orthogonality conditions were still meet. Also the number of test frequencies and resolution has a direct relation to the process time. Doubling the number of test frequencies will result in an increase of the processing time by a factor of approximately two.

The search was conducted on several computers, stand-alone desktop and dedicated servers, each with their assigned groups to process. The procedure was automated and therefore left to run in the background. The total computational time[4] on each machine was not recorded, but the processing of all the SMC stars took less than 2 months[5]. This included the above refinements and the runs were fragmented in time.

[4]With reference to actual CPU time and running time.
[5]Not all of this time was purely processing time, some was bug fixing.

3.1.3.4 Missed eclipsing binaries

The search through the MOA database was based on a specific goal in mind, to find new detected eclipsing binaries for follow-up study. The initial criteria for this goal meant the search was not so rigorous as to detect all eclipsing binaries. Therefore it must be noted that the catalogue is not entirely complete. The initial search criteria were based on variations greater than 0.25 mag., therefore any eclipsing binaries with eclipse depths less than this were overlooked. Such an example is MOA J005258.0−723704 whose inclusion is solely due to the light curve being in the initial data group, `smc1.group0`, which, as mentioned previously, had all 2000 light curves manually viewed for data assessment purposes.

3.1.3.5 Long period variables

Long period variables were detected even though the search range limit was 20 days. These arose from an incorrect period being fitted which managed to pass through the selection criteria. These required manual alteration of the estimated period in order to obtain the actual period. For longer period variables, greater than 40 days, periodicity and variability was obvious from their raw data itself which spanned approximately 220 days, therefore showing several cycles.

3.2 Small Magellanic Cloud search results

3.2.1 Search results

From the 400 000 light curves contained in the two fields smc1 and smc2 some 5 000 possible variable stars were selected and their associated PostScript files viewed. The majority were not, within this analysis, the desired periodic variables that fitted within our criteria. A reasonable proportion were either long period variables or Cepheids.

A short list of approximately 350 possible eclipsing binaries was made. Some targets looked as though a refinement of the period would be needed in order to phase the data well. However it become apparent that this was not the case, within the period criteria. These were discarded. The second group of possible eclipsing binaries were the Cepheids who exhibit a near sinusoidal type light curve. Given the approximate distance to the SMC and the period-luminosity relation, the Cepheids were removed. Several light curves still remained whereby a definite decision could not be made as to whether the light curves were from eclipsing binaries or not. These were included in the published catalogue and commented as possibly not being eclipsing binaries. Follow-up observations will be required to confirm or invalidate the classification of these systems.

The targets identified as eclipsing binaries are presented in Table 3.3. The table consists of a total of 167 eclipsing binaries.

Table 3.3: Eclipsing binaries detected in the MOA SMC database.

Designation and coordinates (J2000) Name MOA J	Extra digit[6]	$\mathbf{B_M}$ $\boldsymbol{R_M}$ (max.)	**Period** (days)	**Primary Epoch** HJD −2450680	**OGLE name** ***Remarks***
00 42 25.5	6	16.88	1.3368	0.655	SMC_SC3 8986
−73 29 29	*.8*	*17.50*	±0.0002	±0.007	
00 43 06.1	2	16.83	21.25	1.166	SMC_SC3 28139
−73 11 04	*.5*	*17.01*	±0.05	±0.005	
00 43 10.8	3	15.96	7.903	1.959	
−73 23 39	*.7*	*15.60*	±0.003	±0.006	
00 43 42.0	2	16.42	1.56853	1.540	SMC_SC3 71563
−73 20 44	*.3*	*16.98*	±0.00007	±0.002	
00 44 06.9	2	17.42	2.43682	0.914	
−72 43 32	.8	*17.96*	±0.00003	±0.001	
00 44 08.7	4	13.39	6.052	0.336	SMC_SC3 139376
−73 14 17	*.6*	*14.12*	±0.002	±0.005	*probably eccentric*
00 44 08.8	7	17.05	0.8601	0.566	SMC_SC3 139681
−73 15 25	*.7*	*17.42*	±0.0002	±0.008	
00 44 11.6	6	15.86	11.85	0.046	SMC_SC3 134555
−73 17 37	*.6*	*16.22*	±0.01	±0.003	
00 44 22.0	7	15.59	0.84545	0.19	SMC_SC3 139427
−73 14 49	*.2*	*16.23*	±0.00004	±0.02	
00 44 56.5	3	15.07	2.1630	0.53	SMC_SC3 197942
−73 17 06	*.6*	*15.49*	±0.0003	±0.02	
00 45 01.6	3	15.70	2.6420	1.025	SMC_SC3 189215
−73 26 10	*.6*	*16.40*	±0.0003	±0.002	
00 45 03.6	9	16.06	0.80883	0.092	SMC_SC3 217672
−73 03 36	*.7*	*16.60*	±0.00002	±0.006	
00 45 28.6	4	16.49	16.93	16.119	SMC_SC4 29281
−73 03 02	*.2*	*16.80*	±0.02	±0.002	
00 45 38.2	5	15.95	0.76256	0.759	SMC_SC4 35694
−72 56 17	*.9*	*16.68*	±0.00003	±0.009	
00 46 13.2	2	15.94	3.712	1.86	
−72 57 55	*.4*	*16.00*	±0.001	±0.01	*Cepheid?*
00 46 19.6	5	12.80	0.37663	0.375	SMC_SC4 88435
−72 50 56	*.6*	*12.65*	±0.00001	±0.008	
00 46 22.4	5	17.02	1.02929	1.055	SMC_SC4 85856
−72 55 04	*.6*	*17.61*	±0.00002	±0.006	
00 46 32.7	8	15.27	1.7411	0.581	SMC_SC4 53898
−73 26 38	*.6*	*15.93*	±0.0001	±0.004	
00 46 33.1	6	15.12	1.08984	0.47	SMC_SC4 56804
−73 22 16	*.4*	*15.63*	±0.00005	±0.01	
00 46 34.0	4	16.18	3.7015	1.30	
−73 06 00	*.3*	*16.10*	±0.0002	±0.02	*Cepheid?*
00 46 34.6	5	15.72	0.85467	0.345	SMC_SC4 56829
−73 24 35	*.9*	*16.30*	±0.00003	±0.003	
00 46 59.0	8	16.22	2.3835	1.592	SMC_SC4 113885
−73 14 57	*.6*	*16.90*	±0.0004	±0.004	*eccentric*
00 47 02.6	7	16.31	4.547	3.363	SMC_SC4 111053
−73 18 57	*.3*	*16.50*	±0.001	±0.003	
00 47 25.5	1	14.38	1.3558	0.224	SMC_SC4 103706
−73 27 16	*.1*	*15.05*	±0.0001	±0.003	

continued on next page

Table 3.3: *continued*: Eclipsing binaries detected in the MOA SMC database.

Designation and coordinates (J2000) Name MOA J	Extra digit[7]	$\mathbf{B_M}$ $\boldsymbol{R_M}$ (max.)	**Period** (days)	**Primary Epoch** HJD −2450680	**OGLE name** ***Remarks***
00 47 29.5	9	14.42	1.12508	0.41	
−73 25 01	*.9*	*15.05*	±0.00005	±0.01	
00 47 32.1	4	16.16	0.82372	0.412	SMC_SC4 121084
−73 09 08	*.8*	*16.73*	±0.00002	±0.005	
00 47 38.2	3	16.78	1.6264	0.095	SMC_SC4 113857
−73 15 18	*.9*	*17.10*	±0.0002	±0.005	
00 47 50.1	2	14.82	1.02310	0.830	SMC_SC4 153178
−73 27 27	*.5*	*15.50*	±0.00007	±0.006	
00 48 04.3	7	16.52	3.322	1.881	SMC_SC4 163724
−73 17 03	*.5*	*16.95*	±0.005	±0.002	
00 48 09.5	0	17.42	1.41219	0.735	SMC_SC4 175831
−73 06 04	*.4*	*18.00*	±0.00005	±0.006	
00 48 26.0	0	18.02	0.7902	0.005	SMC_SC5 39026
−73 07 24	*.7*	*18.40*	±0.0005	±0.006	
00 48 28.9	3	16.32	43.6	30.434	SMC_SC5 26819
−73 12 34	*.9*	*16.32*	±0.1	±0.004	
00 48 45.3	9	16.82	0.91365	0.819	
−72 38 29	*.3*	*17.54*	±0.00004	±0.006	
00 48 47.4	7	12.72	1.8411	0.515	SMC_SC5 11416
−73 24 58	*.5*	*13.51*	±0.0002	±0.005	
00 48 56.9	3	15.57	3.6080	1.176	SMC_SC5 32412
−73 11 40	*.0*	*16.11*	±0.0005	±0.001	
00 48 59.9	2	15.29	1.4115	0.563	SMC_SC5 26631
−73 13 28	*.9*	*15.95*	±0.0005	±0.007	
00 49 02.9	7	16.64	1.24618	0.412	SMC_SC5 16658
−73 20 55	*.7*	*17.30*	±0.00008	±0.005	
00 49 13.2	1	16.26	0.98910	0.968	
−72 58 23	*.3*	*16.81*	±0.00005	±0.008	
00 49 15.4	0	?	0.90460	0.570	SMC_SC5 95337
−73 22 05	*.5*	*16.71*	±0.00005	±0.005	B_M *unreliable*
00 49 19.9	1	16.20	1.5190	1.345	SMC_SC5 100485
−73 17 55	*.5*	*16.89*	±0.0003	±0.003	
00 49 20.0	5	15.92	2.1939	0.389	SMC_SC5 106039
−73 13 37	*.4*	*16.49*	±0.0002	±0.003	
00 49 20.2	5	16.70	1.05780	0.211	
−73 00 01	*.5*	*16.93*	±0.00002	±0.004	
00 49 24.8	3	15.66	0.81831	0.280	SMC_SC5 90597
−73 25 46	*.6*	*16.28*	±0.00003	±0.005	
00 49 28.4	4	16.58	138.6	94.420	SMC_SC5 145588
−72 49 42	*.5*	*15.78*	±0.4	±0.006	
00 49 31.3	0	16.58	2.3779	1.349	SMC_SC5 129722
−73 01 27	*.2*	*16.99*	±0.0001	±0.005	
00 49 40.5	7	15.09	8.050	3.545	SMC_SC5 129441
−73 00 23	*.3*	*15.70*	±0.001	±0.002	*eccentric*
00 50 10.4	3	15.72	2.0739	0.38	
−72 37 36	*.3*	*16.38*	±0.0002	±0.02	
00 50 11.2	7	17.10	0.76888	0.152	SMC_SC5 230776

continued on next page

Table 3.3: *continued*: Eclipsing binaries detected in the MOA SMC database.

Designation and coordinates (J2000) Name MOA J	Extra digit[7]	**B_M** ***R_M*** (max.)	**Period** (days)	**Primary Epoch** HJD −2450680	**OGLE name** ***Remarks***
−72 44 44	*.2*	*17.69*	±0.00005	±0.003	
00 50 14.3	3	17.53	1.7968	0.055	SMC_SC5 208422
−73 00 12	*.6*	*18.10*	±0.0002	±0.001	
00 50 18.4	0	14.12	1.8399	1.084	
−72 38 55	*.2*	*14.78*	±0.0002	±0.006	
00 50 21.2	9	17.61	1.29792	1.449	SMC_SC5 170506
−73 25 36	*.7*	*18.12*	±0.00005	±0.004	
00 50 27.9	1	13.23	4.6067	0.064	SMC_SC5 202153
−73 03 16	*.9*	*14.00*	±0.0002	±0.003	
00 50 40.5	2	15.42	2.4015	2.268	SMC_SC5 185154
−73 12 56	*.2*	*16.00*	±0.0005	±0.006	
00 50 58.6	6	16.73	1.28358	0.648	SMC_SC5 283079
−73 04 36	*.7*	*17.30*	±0.00004	±0.004	
00 51 07.0	9	13.62	7.116	4.229	SMC_SC5 316708
−72 43 28	*.2*	*14.20*	±0.001	±0.009	
00 51 07.6	8	15.77	1.19112	0.021	SMC_SC5 311526
−72 47 28	*.7*	*16.28*	±0.00002	±0.005	
00 51 16.7	3	15.20	1.8089	0.363	SMC_SC5 266015
−73 13 02	*.4*	*15.70*	±0.0001	±0.006	
00 51 18.6	9	14.08	1.8717	0.953	SMC_SC5 243188
−73 30 15	*.7*	*14.75*	±0.0002	±0.004	
00 51 24.5	3	14.87	0.56565	0.03	
−72 40 14	*.6*	*15.50*	±0.00008	±0.01	
00 51 28.0	1	15.42	3.4955	0.538	SMC_SC6 17345
−73 15 17	*.9*	*16.04*	±0.0003	±0.005	*eccentric*
00 51 34.7	9	15.21	3.2915	2.501	SMC_SC5 311566
−72 45 46	*.1*	*15.83*	±0.0005	±0.002	*eccentric*
00 51 34.9	6	16.04	1.2766	0.732	SMC_SC6 11806
−73 17 11	*.6*	*16.63*	±0.0001	±0.006	
00 51 35.5	4	16.94	0.88824	0.599	SMC_SC6 55836
−72 54 32	*.9*	*17.42*	±0.00004	±0.004	
00 51 35.6	8	16.32	1.3028	0.485	SMC_SC6 22883
−73 12 45	*.4*	*16.87*	±0.0001	±0.005	
00 51 40.2	4	14.62	2.3240	0.856	SMC_SC6 17316
−73 13 20	*.7*	*15.10*	±0.0005	±0.007	
00 51 43.0	0	16.82	2.4282	0.10	SMC_SC6 23618
−73 09 27	*.7*	*17.26*	±0.0002	±0.01	
00 51 57.8	5	16.47	1.5422	1.190	
−73 24 58	*.0*	*16.99*	±0.0002	±0.004	
00 52 06.2	1	14.47	7.320	3.039	SMC_SC6 67221
−72 45 14	*.3*	*15.05*	±0.002	±0.002	
00 52 06.7	0	16.04	1.8218	1.487	SMC_SC6 61502
−72 51 22	*.0*	*16.53*	±0.0001	±0.003	
00 52 08.2	0	15.80	2.3122	2.215	SMC_SC6 29212
−73 06 32	*.2*	*16.42*	±0.0005	±0.007	*possibly eccentric*
00 52 12.1	0	16.51	1.7186	1.228	SMC_SC6 67902
−72 44 53	*.3*	*17.19*	±0.0001	±0.003	

continued on next page

Table 3.3: *continued*: Eclipsing binaries detected in the MOA SMC database.

Designation and coordinates (J2000) Name MOA J	Extra digit[7]	**B_M** ***R_M*** (max.)	**Period** (days)	**Primary Epoch** HJD −2450680	**OGLE name** ***Remarks***
00 52 13.3	2	15.95	0.83630	0.318	SMC_SC6 61653
−72 48 42	*.4*	*16.49*	±0.00003	±0.003	
00 52 19.2	8	14.17	2.5785	1.387	SMC_SC6 158118
−72 41 51	*.2*	*14.80*	±0.0005	±0.004	
00 52 27.9	3	16.52	0.83368	0.59	SMC_SC6 158653
−72 41 35	*.1*	*16.91*	±0.00005	±0.01	
00 52 31.4	1	16.12	1.66845	1.233	SMC_SC6 163076
−72 39 09	*.0*	*16.65*	±0.00005	±0.003	
00 52 34.6	3	16.62	3.373	0.422	*possibly eccentric*
−73 33 05	*.0*	*17.02*	±0.001	±0.007	
00 52 34.7	0	16.50	1.8865	0.679	SMC_SC6 148139
−72 50 00	*.2*	*16.80*	±0.0001	±0.005	
00 52 38.4	3	15.10	5.9535	1.252	SMC_SC6 162962
−72 39 27	*.7*	*15.62*	±0.0008	±0.001	
00 52 42.3	3	15.61	2.1692	1.119	SMC_SC6 158178
−72 41 26	*.7*	*16.28*	±0.0001	±0.002	*eccentric*
00 52 46.9	8	17.52	1.08820	0.066	SMC_SC6 142123
−72 53 33	*.6*	*18.05*	±0.00005	±0.004	*possibly eccentric*
00 52 53.3	3	15.67	1.53890	0.764	
−72 09 50	*.4*	*16.35*	±0.00003	±0.006	
00 52 58.0	9	14.14	6.357	2.064	SMC_SC6 167473
−72 37 04	*.0*	*14.83*	±0.002	±0.007	*probably eccentric*
00 53 00.1	6	14.22	0.72149	0.23	
−73 11 23	*.1*	*14.99*	±0.00002	±0.01	
00 53 29.1	3	16.47	2.4571	1.08	SMC_SC6 242137
−72 38 53	*.2*	*16.90*	±0.0001	±0.01	*detected SMC1 & SMC2*
00 53 29.9	2	15.62	1.6142	0.037	
−72 42 28	*.9*	*16.25*	±0.0004	±0.006	SMC_SC6 237514
00 53 34.4	9	15.02	0.80633	0.75	
−72 42 31	*.6*	*15.71*	±0.00002	±0.01	
00 53 40.2	9	15.51	3.410	0.675	SMC_SC6 246676
−72 36 44	*.3*	*16.09*	±0.002	±0.006	
00 53 40.4	3	15.11	3.4168	1.965	SMC_SC6 221543
−72 52 22	*.1*	*15.70*	±0.0005	±0.004	*eccentric*
00 53 42.2	9	14.94	1.4752	0.33	SMC_SC6 180084
−73 23 20	*.1*	*15.53*	±0.0001	±0.01	
00 53 49.1	6	16.10	1.2300	1.138	SMC_SC6 296901
−72 52 12	*.4*	*16.50*	±0.0001	±0.007	
00 53 55.9	1	16.09	2.2199	1.202	
−72 04 58	*.9*	*16.76*	±0.0002	±0.005	
00 54 00.0	0	15.52	4.7272	0.413	SMC_SC6 291695
−72 56 58	*.0*	*16.08*	±0.0007	±0.002	
00 54 12.7	1	16.72	0.49668	0.01	SMC_SC6 311582
−72 42 07	*.8*	*17.15*	±0.00001	±0.02	
00 54 16.5	9	15.72	3.030	1.272	SMC_SC6 296738
−72 54 24	*.0*	*16.20*	±0.002	±0.004	
00 54 16.7	8	15.87	1.6034	0.976	SMC_SC6 315786

continued on next page

Table 3.3: *continued*: Eclipsing binaries detected in the MOA SMC database.

Designation and coordinates (J2000) Name MOA J	Extra digit[7]	**B_M** ***R_M*** (max.)	**Period** (days)	**Primary Epoch** HJD −2450680	**OGLE name** ***Remarks***
−72 39 09	*.3*	*16.45*	±0.0001	±0.005	
00 54 17.1	7	15.46	1.1007	1.07	
−72 37 10	*.7*	*15.78*	±0.0001	±0.02	
00 54 22.7	1	16.42	2.1532	1.030	SMC_SC6 306609
−72 46 06	*.3*	*16.95*	±0.0002	±0.006	
00 54 32.1	3	16.93	2.4081	0.937	SMC_SC7 32419
−72 56 39	*.3*	*17.51*	±0.0002	±0.002	
00 54 33.1	1	14.89	5.7110	0.577	SMC_SC7 13487
−73 10 40	*.1*	*15.56*	±0.0005	±0.005	
00 54 34.6	1	16.52	1.6415	1.586	SMC_SC6 315873
−72 40 51	*.0*	*17.10*	±0.0001	±0.006	*detected SMC1 & SMC2*
00 54 38.2	6	13.57	3.6264	0.234	SMC_SC7 66175
−72 32 06	*.0*	*14.10*	±0.0003	±0.003	
00 54 39.4	5	16.57	1.8227	1.743	SMC_SC7 70994
−72 26 35	*.8*	*17.11*	±0.0001	±0.003	
00 54 43.0	8	16.87	3.4352	0.460	SMC_SC7 42474
−72 49 23	*.7*	*17.41*	±0.0005	±0.006	
00 55 01.4	0	15.87	2.5853	0.95	SMC_SC7 18319
−73 06 42	*.7*	*16.48*	±0.0005	±0.02	
00 55 52.0	0	15.24	1.2704	0.839	
−72 02 29	*.3*	*15.99*	±0.0002	±0.009	
00 55 54.4	8	14.08	3.1886	2.069	SMC_SC7 142073
−72 28 08	*.3*	*14.77.*	±0.0001	±0.003	
00 56 11.6	1	13.72	4.482	1.770	
−72 18 24	*.2*	*14.52*	±0.002	±0.004	*eccentric*
00 56 15.6	1	15.94	1.3182	0.407	
−72 13 24	*.8*	*16.55*	±0.0001	±0.008	
00 56 23.5	9	14.02	2.3195	1.936	
−72 21 23	*.7*	*14.78*	±0.0001	±0.003	
00 56 24.2	1	14.74	1.6202	1.580	
−72 01 44	*.9*	*15.50*	±0.0002	±0.003	
00 56 53.7	3	17.07	1.5241	0.156	SMC_SC7 255917
−72 37 18	*.5*	*17.62*	±0.0001	±0.005	
00 56 56.4	5	13.94	2.6316	0.093	SMC_SC7 243913
−72 49 06	*.1*	*14.60*	±0.0002	±0.008	
00 57 03.0	3	16.08	1.5837	1.042	
−72 22 46	*.3*	*16.70*	±0.0001	±0.004	
00 57 15.8	0	16.83	1.90675	0.689	SMC_SC7 240244
−72 50 10	*.2*	*17.30*	±0.00006	±0.003	
00 57 26.4	0	15.32	4.330	2.345	SMC_SC8 30634
−72 36 45	*.5*	*16.04*	±0.002	±0.002	*eccentric*
00 57 27.5	5	14.63	1.1452	1.030	SMC_SC8 49526
−72 19 59	*.5*	*15.32*	±0.0001	±0.006	
00 57 31.1	6	16.64	1.03002	0.352	SMC_SC8 22435
−72 46 16	*.6*	*17.20*	±0.00004	±0.003	*possibly eccentric*
00 57 42.2	0	16.11	2.4284	0.172	SMC_SC8 18970
−72 48 14	*.4*	*16.60*	±0.0001	±0.003	

continued on next page

Table 3.3: *continued*: Eclipsing binaries detected in the MOA SMC database.

Designation and coordinates (J2000) Name MOA J	Extra digit[7]	$\mathbf{B_M}$ $\boldsymbol{R_M}$ (max.)	**Period** (days)	**Primary Epoch** HJD −2450680	**OGLE name** ***Remarks***
00 57 43.3	2	14.98	1.4238	0.545	SMC_SC8 52831
−72 18 14	*.3*	*15.61*	±0.0002	±0.003	
00 58 21.3	7	15.52	3.111	1.873	*probably eccentric*
−72 01 07	*.2*	*16.25*	±0.002	±0.005	
00 58 21.9	9	13.43	5.845	2.31	SMC_SC8 90965
−72 35 15	*.8*	*14.10*	±0.002	±0.01	
00 58 22.3	5	16.25	1.05184	0.626	
−72 40 09	*.0*	*16.68*	±0.00002	±0.004	
00 58 24.4	0	14.89	1.47120	0.938	
−72 05 32	*.5*	*15.60*	±0.00003	±0.003	
00 58 51.8	0	16.10	2.408	2.362	SMC_SC8 107328
−72 17 50	*.8*	*16.69*	±0.001	±0.004	
00 58 55.8	4	17.29	1.4832	1.621	SMC_SC8 79914
−72 43 54	*.8*	*17.82*	±0.0001	±0.004	
00 59 02.5	2	14.90	1.32475	0.372	SMC_SC8 135992
−72 42 21	*.1*	*15.63*	±0.00002	±0.003	
00 59 11.4	3	17.24	1.29380	0.380	
−72 01 47	*.6*	*17.92*	±0.00003	±0.003	
00 59 28.6	3	14.61	1.09878	0.594	SMC_SC8 132613
−72 43 47	*.0*	*15.30*	±0.00004	±0.004	
00 59 30.2	7	15.32	3.3070	2.768	
−72 02 53	*.1*	*15.98*	±0.0005	±0.008	
00 59 34.2	2	13.29	1.12302	0.325	SMC_SC8 129157
−72 46 57	*.4*	*14.00*	±0.00002	±0.008	
00 59 36.1	5	13.60	1.9496	0.47	
−72 15 57	*.3*	*14.32*	±0.0003	±0.01	
00 59 47.8	1	17.52	32.30	28.92	SMC_SC8 183352
−72 44 26	*.4*	*17.12*	±0.03	±0.02	
00 59 54.3	5	16.83	1.55703	0.416	SMC_SC8 186844
−72 41 39	*.4*	*17.40*	±0.00002	±0.008	
01 00 15.9	7	13.46	3.313	0.243	SMC_SC8 209964
−72 12 44	*.7*	*14.15*	±0.002	±0.008	
01 00 23.7	3	15.58	2.6135	0.246	SMC_SC9 30310
−72 26 20	*.1*	*16.28*	±0.0003	±0.004	*probably eccentric*
01 00 36.8	0	15.95	1.8637	0.803	SMC_SC9 47495
−72 06 46	*.8*	*16.66*	±0.0002	±0.005	
01 00 41.0	8	15.61	3.1590	0.751	SMC_SC9 41849
−72 13 12	*.1*	*16.20*	±0.0007	±0.002	
01 00 42.4	7	14.56	1.5953	0.589	
−72 24 57	*.1*	*14.91*	±0.0002	±0.009	
01 00 50.8	6	16.14	1.4868	1.398	
−72 20 17	*.8*	*16.67*	±0.0001	±0.005	
01 00 52.3	3	16.12	1.63250	0.988	SMC_SC9 13423
−72 45 05	*.6*	*16.61*	±0.00004	±0.002	*possibly eccentric*
01 00 57.2	9	18.02	3.1640	1.568	SMC_SC9 14011
−72 44 52	*.6*	*18.38*	±0.0003	±0.004	
01 01 36.8	5	15.42	1.6766	0.755	

continued on next page

Table 3.3: *continued*: Eclipsing binaries detected in the MOA SMC database.

Designation and coordinates (J2000) Name MOA J	Extra digit[7]	B_M R_M (max.)	**Period** (days)	**Primary Epoch** HJD −2450680	**OGLE name** ***Remarks***
−72 04 15	*.0*	*15.87*	±0.0003	±0.009	
01 01 40.0	9	14.84	5.275	0.446	
−72 03 44	*.2*	*15.43*	±0.002	±0.003	
01 02 25.5	6	14.72	2.4968	1.443	SMC_SC9 134245
−72 07 45	*.0*	*15.47*	±0.0004	±0.005	*(3/4)P*
01 02 28.1	3	14.72	2.539	1.611	SMC_SC9 111281
−72 37 48	*.6*	*15.36*	±0.001	±0.009	
01 02 41.2	6	14.94	5.454	3.754	SMC_SC9 129557
−72 14 25	*.5*	*15.50*	±0.001	±0.005	
01 02 46.1	8	14.13	1.9710	0.747	SMC_SC9 163575
−72 24 44	*.0*	*14.90*	±0.0004	±0.003	*probably eccentric*
01 03 00.5	7	15.16	3.1305	1.821	SMC_SC9 173156
−72 08 30	*.1*	*15.83*	±0.0007	±0.004	
01 03 19.8	8	15.81	1.1666	1.158	SMC_SC9 175441
−72 06 12	*.1*	*16.36*	±0.0001	±0.008	
01 03 21.3	3	12.77	2.206	0.300	SMC_SC10 33878
−72 05 38	*.2*	*13.50*	±0.001	±0.009	
01 03 22.6	9	14.43	3.477	3.167	
−72 03 22	*.0*	*15.15*	±0.001	±0.004	
01 03 28.9	0	14.62	2.6985	0.690	SMC_SC10 37156
−72 01 28	*.3*	*15.31*	±0.0002	±0.003	*possibly eccentric*
01 03 41.5	5	15.41	2.5810	2.257	SMC_SC10 37223
−72 03 06	*.8*	*16.10*	±0.0002	±0.008	*eccentric*
01 03 46.4	4	15.30	0.92025	0.549	SMC_SC10 17256
−72 28 29	*.8*	*15.95*	±0.00007	±0.007	
01 03 49.2	2	13.96	3.962	0.426	SMC_SC10 19653
−72 28 07	*.0*	*14.70*	±0.003	±0.007	
01 03 54.3	1	14.33	1.7299	0.157	SMC_SC10 33925
−72 04 18	*.3*	*15.09*	±0.0002	±0.007	
01 04 01.6	1	15.50	2.1284	1.78	SMC_SC10 3097
−72 46 41	*.7*	*16.11*	±0.0002	±0.01	
01 04 14.9	5	14.43	8.788	1.495	SMC_SC10 70439
−72 09 18	*.7*	*15.00*	±0.005	±0.005	
01 04 16.6	1	17.19	0.92599	0.364	SMC_SC10 75073
−72 00 46	*.1*	*17.78*	±0.00003	±0.005	
01 04 29.9	9	14.94	3.510	1.577	SMC_SC10 61625
−72 23 28	*.7*	*15.57*	±0.001	±0.005	
01 04 34.1	1	15.70	1.2701	0.542	SMC_SC10 59402
−72 27 25	*.7*	*16.31*	±0.0003	±0.006	
01 04 56.6	4	15.62	1.8266	1.879	SMC_SC10 100613
−72 16 09	*.9*	*16.18*	±0.0002	±0.004	
01 04 59.0	9	16.12	1.42940	1.408	SMC_SC10 78731
−72 50 08	*.2*	*16.72*	±0.00005	±0.003	
01 04 59.6	7	16.07	129.0	118.18	SMC_SC10 78655
−72 50 26	*.2*	*15.31*	±0.2	±0.01	
01 05 01.3	7	16.44	2.2635	0.677	SMC_SC10 108195
−72 00 41	*.1*	*17.08*	±0.0003	±0.003	

continued on next page

Table 3.3: *continued*: Eclipsing binaries detected in the MOA SMC database.

Designation and coordinates (J2000) Name MOA J	Extra digit[7]	$\mathbf{B_M}$ $\boldsymbol{R_M}$ (max.)	**Period** (days)	**Primary Epoch** HJD −2450680	**OGLE name** ***Remarks***
01 05 17.0	7	16.50	2.70966	0.040	SMC_SC10 83754
−72 43 10	*.4*	*17.05*	±0.00002	±0.002	
01 05 20.5	4	16.11	14.40	5.398	SMC_SC10 88122
−72 37 59	*.5*	*16.23*	±0.02	±0.007	

1

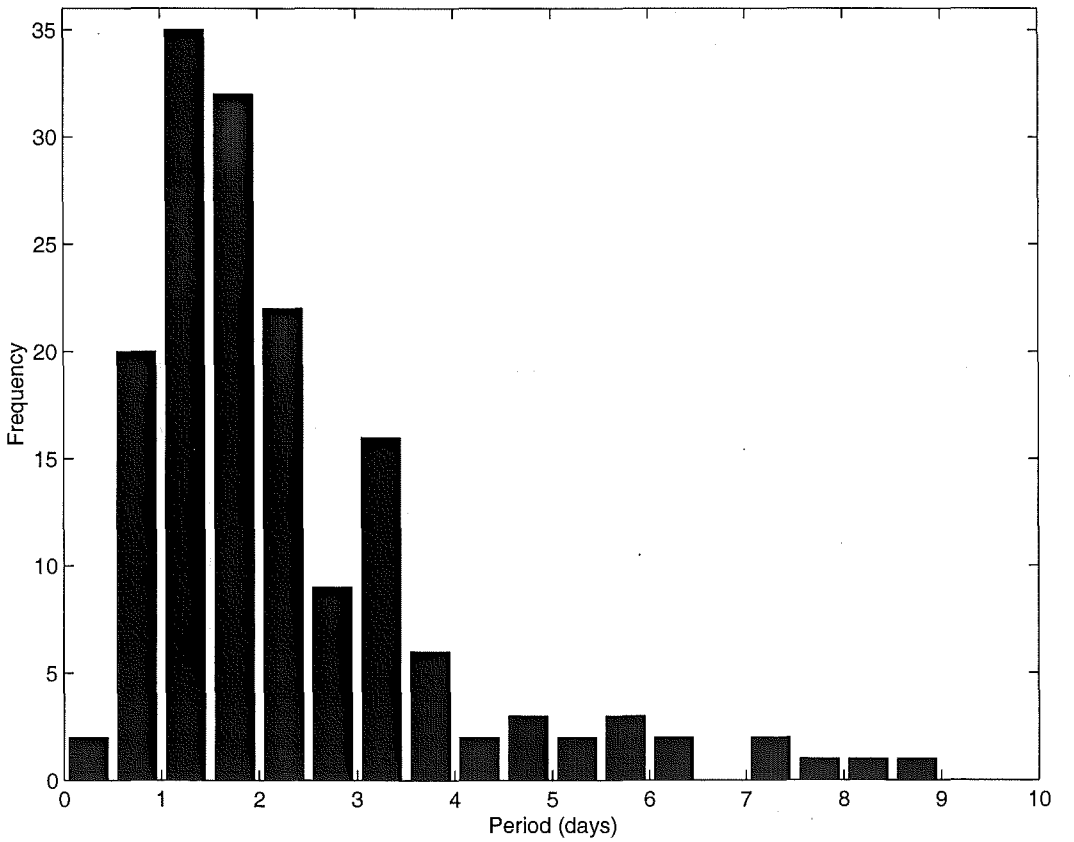

Figure 3.3: Histogram showing the periods of the detected eclipsing binaries in the MOA SMC catalogue in 0.5 day bins. There an 8 additional eclipsing binaries with periods outside this range: 11.85 d, 14.4 d, 16.93 d, 21.25 d 32.3 d, 43.4 d, 129 d, 132 d.

Figure 3.3 shows the range of periods of the detected eclipsing binaries for the SMC fields. The highest number of periods are located in the 1.0 to 1.5 day range. The majority of the periods are in the shorter ranges with a rapid fall off toward the longer periods.

[7]IAU-approved designations are formed from coordinates truncated to the level at which there is no ambiguity between sources. The extra digit column provides additional significant figures (e.g. for spacecraft pointing). For example, the system MOA J004310.8−732339 has J2000 coordinates $00^{\rm h}43^{\rm m}10\overset{\rm s}{.}83$, $-73°23'39\overset{''}{.}7$.

3.2.2 Period refinement

The PostScript files generated from the search were used for the period refinement. The original periods from the search algorithm output were accurate enough to phase the data, but in general, not the optimum period. It was easy to edit the PostScript files so that they displayed three light curves phased to slightly different periods, Figure 3.4, so a comparison could be made. The periods were adjusted so that the best phasing of the data was achieved as determined by viewing these light curves. This was then deemed to be the optimum period for the system.

The uncertainty calculations of the period posed a problem. Several ways were tried to obtain an uncertainty estimate statistic that could be applied to all the systems. These included using the FWHM of the peaks in the probability of false detection plots and the periodogram plots. The results however, gave estimates for the short and long period systems in an inconsistent manner. The same applied to the noisy data versus the better signal-to-noise data. A blanket approach was also considered for the period binned into a certain range, but again this was not satisfactory as a number of systems had uncertainties either too small or two large for the type and quality of their respective data sets. The best solution was to determine the uncertainty by eye. Since the total number of detections was 167, it was considered that the time spent pursing an automated method that may or may not work, would be better spent analysing the data in a case-by-case fashion. The procedure adopted was as follows: The uncertainty in the period is when the phasing is such that one can visually see a slight smearing between the original phased data and the phased data with the period plus the uncertainty added or subtracted. This change is identified when the points in the phased light curve start to distort the curve from the optimal case, as illustrated in Figure 3.4.

This method is dependent of the person viewing the light curves as opinions as to when the light curve has smudged from the original can be open to debate. However, the above definition worked very successfully. Here subtle changes are seen more easily as the changes are amplified over many cycles. Several of the uncertainties were independently verified or cross checked to ensure the uncertainties were of a reasonable value.

Although this is a more time consuming process than a blanket approach, it ensures that all data sets have been treated and analysed to give accurate as possible values of the periods with a reasonable estimate of their uncertainty.

3.2.3 Ephemeris calculations

The ephemeris calculations required a primary and secondary eclipse to be specified for each light curve. The distinguishing feature that determines this is the depth of the eclipses[8]. The deeper eclipse is termed the primary, the shallower eclipse depth the secondary. This was determined purely by viewing the light curve. Generally, both eclipses had different depths, making this a simple exercise. However, several cases arose when the depths were very similar. The eclipse minima were then determined by a fitting procedure, which provided an easy way of handling noisy data. The viewing of the profile fits is used in determining the primary and secondary designations. The fitted values gave an uncertainty for the fit. If the two fits fell within the two uncertainty ranges, then they effectively have the same depth.

This can therefore pose a slight problem as the choice of the formally deeper eclipse as the

[8]Photometrists and spectroscopists can have different ways of determining this. Photometrically it is determined by the eclipse depth, the greater one being the primary eclipse at which the star eclipsed is also called the primary. This is based solely on the temperature. Spectroscopically it can be specified from spectral line or radial velocity data. The two approaches may not always agree.

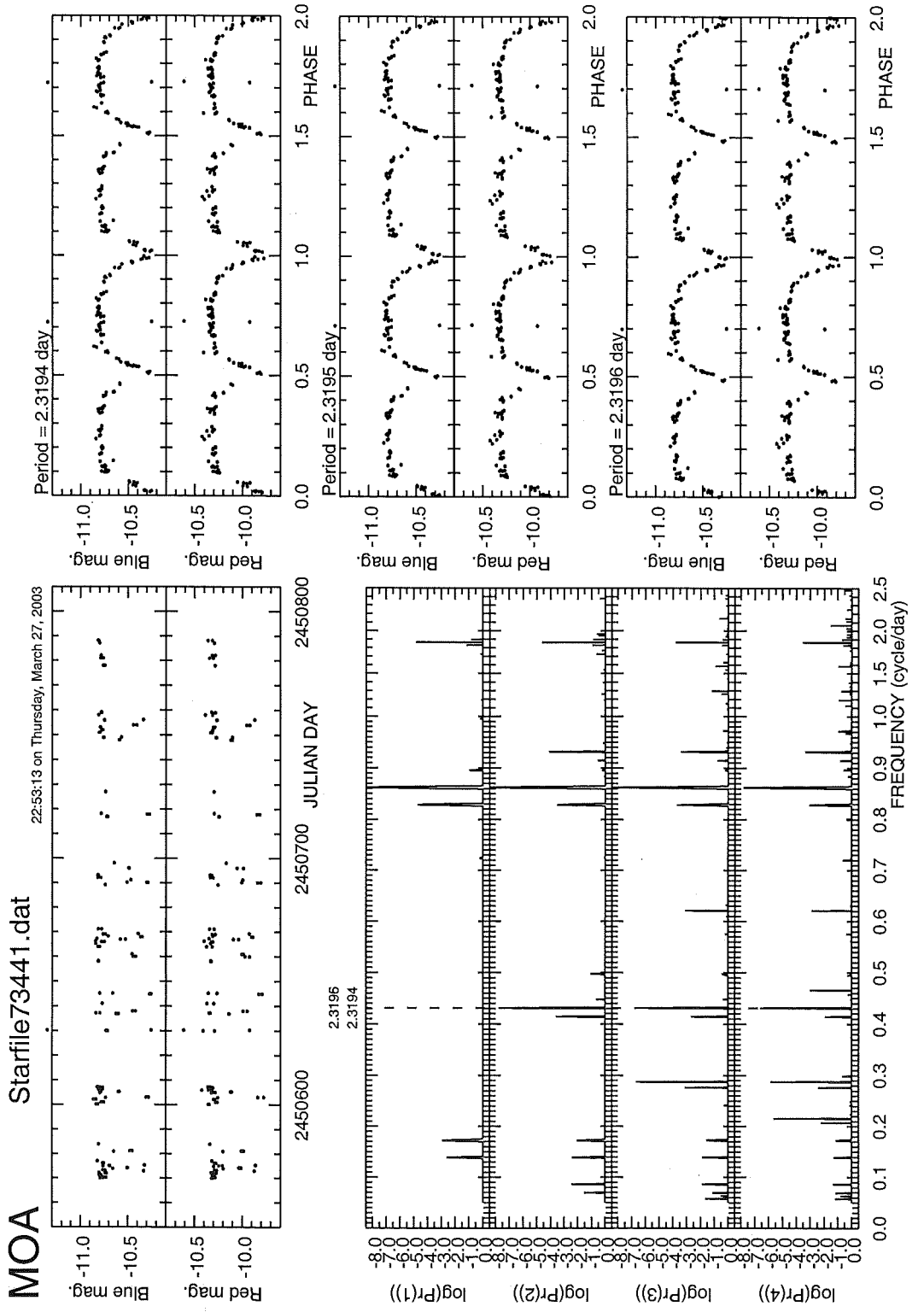

Figure 3.4: Periodogram plot of an eclipsing binary in the smc1 field from the `smc2.group36`, MOA J005623.5−722123. The three phased light curves shown in the left hand side boxes show the detected period (centre) 2.3195 days, the detected period minus the period uncertainty (top) 2.3194 days, the detected period plus the period uncertainty (bottom) 2.3196 days. Inspection of the top and bottom phased light curves to the centre one, reveals the phased light curves are beginning to deviate from the initial detected period. Therefore the uncertainty for the light curve, is the difference between the centre and the top and bottom periods, in this case ± 0.0001 day.

primary is little more than a guess. If the primary eclipse in such a case has been misidentified as determined by later observations, this will mean that the phasing is incorrect by a factor of 0.5 for a circular orbit.

A number of the binary orbits are not circular and therefore elliptical. These are termed eccentric systems. Such systems don't have the secondary eclipse at 0.5 phase but rather at some other phase value which is dependent on the eccentricity and orientation of the system. For eccentric systems, the epoch of secondary minimum is calculated and presented as in section 3.2.4 and Table 3.5.

Prior to commencing the calculation of the ephemerides, the light curves were cleaned of any stray points. These were points that were obviously incorrect. The `starfile[MOA ID].dat` files were loaded into MIDAS for the ephemerides determination, along with their periods. The `starfile[MOA ID].dat` files were written to disk prior to any exclusions being made on the basis of points more than 4.0 Standard Deviations (S.D.) from the mean. This was to preserve the raw data as extracted from the database. A similar cut removed most stray points with the exception being points that did not phase properly. Care was taken to remove as few points as possible so as not to misrepresent the true nature of the data set, not make it look better than it actually is.

A Gaussian curve was fitted to each eclipse. The variable parameters of the Gaussian fitting parameters were depth, FWHM and phase position. The parameters were adjusted until the fitting uncertainties were minimized. This then constituted the best fit to the eclipse.

The MOA observations for these data spanned the interval May (HJD 2450570) to December (HJD 2450790) 1997. A mid epoch Heliocentric Julian Date, HJD, of 2450680 was used in phasing the light curves. The light curve and its associated fitted Gaussian were adjusted, positioning the minima of the primary eclipses so that the zero phase of the ephemeris lay as close as possible to HJD 2450680.

The uncertainties in the primary and secondary epoch times are determined by the uncertainty in the fit of the Gaussian to the eclipses. The range of the uncertainties of the fitted Gaussian values were greater than the fitting differences of the periods and their uncertainties.

The light curves for both the red and blue filters are presented for all 167 eclipsing binaries in appendix G.

3.2.4 Eccentric systems

A total of 20 systems were deemed to be eccentric to varying degrees. The eccentricity was determined by a comparison of the epochs of the primary and secondary eclipses. The uncertainties given by the fitting routine were used to calculate an uncertainty in the phase difference between the two eclipses and this uncertainty was compared with how much the phase difference differed from 0.5. The stars in the catalogue were determined as possibly, probable or certainly eccentric (the later termed eccentric) systems according to the criteria given in Table 3.4. Examples are presented in Figures 3.5, 3.6 and 3.7 respectively.

Although this is not a standard definition of whether the orbit of an eclipsing binary is eccentric, it does provide an operational categorization of the question.

Table 3.4: The criteria used to determine the eccentricity categories for the eclipsing binary systems based on their binary orbits.

Eccentricity criterion	Conditions
Possibly eccentric	2 S.D. $< \|\|\frac{\text{uncertainty}}{\text{difference from 0.5}}\|\| <$ 3 S.D.
Probably eccentric	3 S.D. $< \|\|\frac{\text{uncertainty}}{\text{difference from 0.5}}\|\| <$ 4 S.D.
Eccentric	$\|\|\frac{\text{uncertainty}}{\text{difference from 0.5}}\|\| >$ 4 S.D.

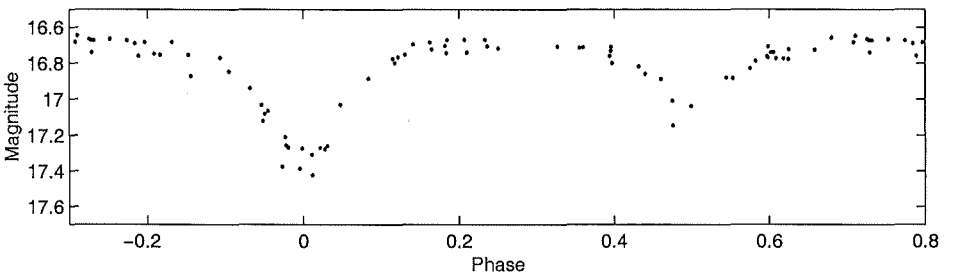

Figure 3.5: MOA J010052.3−724505. An example of a light curve of a possibly eccentric eclipsing binary as defined in Table 3.4.

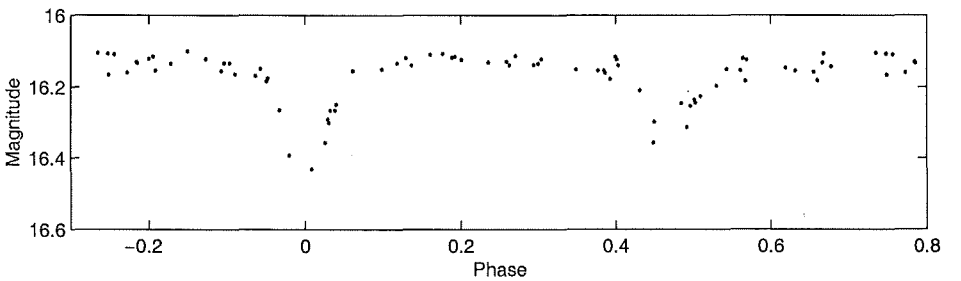

Figure 3.6: MOA J010023.7−722620. An example of a light curve of a probably eccentric eclipsing binary as defined in Table 3.4.

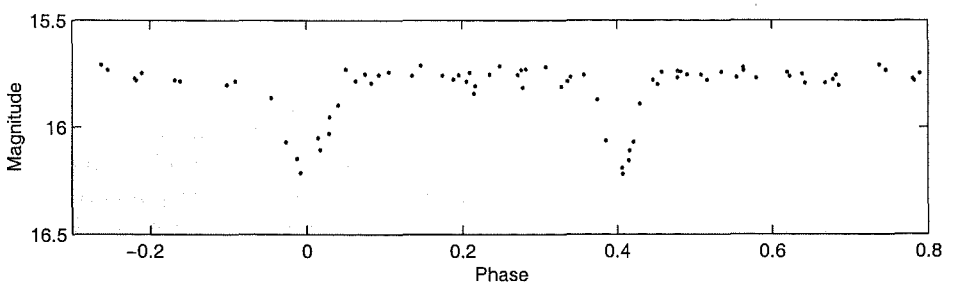

Figure 3.7: MOA J005726.4−723645. An example of a light curve of an eccentric eclipsing binary as defined in Table 3.4.

A number of eccentric eclipsing binary systems, as defined in Table 3.4, for the MOA SMC catalogue are presented in Table 3.5. Within the new detections one probably eccentric and two eccentric systems were identified.

3.2.5 Finding charts

The finding charts, samples presented in Figures 3.13 and 3.14, were constructed from FITS files provided by the MOA group for each field at each phase and chip number. Using the transformations equations 2.7 and 2.8, Tables 2.6 and 2.7, the catalogue stars were identified on the frames. The plate scale on the CCD chip was 0.64 arc sec per pixel in the East-West columns and similarly in the North-South rows. Therefore a 1 arc minute square field equated to approximately 94 pixels square.

A MIDAS routine was written to extract the region from the appropriate chip with the target at the centre of the extracted field. It was soon realized that the cuts values, and hence the contrast of the extracted images, varied depending on the frame the image was extracted from. Therefore for each frame, a list of cut values were determined so the extract images all appeared to have similar contrast levels. This made the comparison of the finding charts easier and the brightness of the stars and the crowding of the surrounding field are able to be compared on a more uniform basis.

The right ascension and declination of each star was given in the `smc1.catalog` and `smc2.catalog` files provided by the MOA group. The MAgellanic Catalogue of Stars, MACS [38] catalogue, which has a limiting magnitude $B \leqslant 16.3$ mag was used to check the accuracy of the quoted co-ordinates in the two catalogue files. The bright stars at or above the MACS limiting magnitude were selected, 31 in total, and the MACS and MOA coordinates compared. The comparison of the r.m.s. uncertainties were made and calculated as 0.11 s in right ascension and 0.6 arc sec in declination.

Since the coordinates were of a reasonable accuracy, the Digital Sky Survey, DSS, was used to provide a check on the MOA finding charts. The Second Generation survey images were used, red and blue. A 1 arc minute square field centered around these coordinates was extracted from the DSS. Each finding chart was then compared to those from the MOA FITS files to assess accuracy. A diagonal line from corner to corner was drawn and it was found that the star diameters all fell on the cross over point, so the MOA charts were therefore passed as acceptable. A sample of the finding charts are presented in Figures 3.13 and 3.14.

The complete set of finding charts for the blue and red filters for all 167 eclipsing binaries is presented in Appendix G.

3.2.6 Magnitudes and naming

The MOA instrumental magnitudes, $B_{\mathrm{MOA}}^{\mathrm{instr}}$ and $R_{\mathrm{MOA}}^{\mathrm{instr}}$, which are given in the database were used in analysing the time-series photometry. Throughout the analysis, the actual magnitude in a standard system was not required until the comparison of the MOA stars to the MACS stars were made. Therefore the transformation was done at a late stage. Muraki et al. [100] calculated the transformation from the MOA instrumental scale to the scale of the HST Guide Star Catalogue (GSC) for both $B_{\mathrm{MOA}}^{\mathrm{instr}}$ and $R_{\mathrm{MOA}}^{\mathrm{instr}}$ to give B_{M} and R_{M} respectively. These were determined as follows:

Table 3.5: Eccentric systems identified in the MOA SMC catalogue. The definition of the Remarks column is given in Table 3.4.

MOA name	Secondary Epoch HJD −2450680	OGLE name	Remarks
MOA J004408.7−731417	3.505 ±0.005	SMC_SC3 139376	probably eccentric
MOA J004659.0−731457	0.547 ±0.004	SMC_SC4 113885	eccentric
MOA J004940.5−730023	5.690 ±0.002	SMC_SC5 129441	eccentric
MOA J005128.0−731517	2.134 ±0.005	SMC_SC6 17345	eccentric
MOA J005134.7−724546	1.074 ±0.002		eccentric
MOA J005208.2−730632	1.740 ±0.007	SMC_SC6 29212	possibly eccentric
MOA J005234.6−733305	2.176 ±0.007	SMC_SC5 311566	possibly eccentric
MOA J005242.3−724126	1.866 ±0.002	SMC_SC6 158178	eccentric
MOA J005246.9−725333	0.594 ±0.004	SMC_SC6 142123	possibly eccentric
MOA J005258.0−723704	5.705 ±0.007	SMC_SC6 167473	probably eccentric
MOA J005340.4−725222	0.443 ±0.004	SMC_SC6 221543	eccentric
MOA J005611.6−721824	0.281 ±0.004		eccentric
MOA J005726.4−723645	4.088 ±0.002	SMC_SC8 30634	eccentric
MOA J005731.1−724616	0.925 ±0.003	SMC_SC8 22435	possibly eccentric
MOA J005821.3−720107	0.430 ±0.005		probably eccentric
MOA J010023.7−722620	1.466 ±0.004	SMC_SC9 30310	probably eccentric
MOA J010052.3−724505	0.150 ±0.002	SMC_SC9 13423	possibly eccentric
MOA J010246.1−722444	1.775 ±0.003	SMC_SC9 163575	probably eccentric
MOA J010328.9−720128	2.074 ±0.003	SMC_SC10 37156	possibly eccentric
MOA J010341.5−720306	0.852 ±0.008	SMC_SC10 37223	eccentric

$$B_{\rm M} = B^{\rm instr}_{\rm MOA} + 24.82^{+0.18}_{-0.27}$$

$$R_{\rm M} = R^{\rm instr}_{\rm MOA} + 25.10^{+0.26}_{-0.36}$$

The uncertainties in the magnitude calibration were not considered when constructing the catalogue as the magnitudes are used purely as a guide for future study, rather than as exact figures. The values of the magnitudes quoted for the MOA catalogue stars were determined by viewing a printed copy of the PostScript data file and ruling a line through the top of the data. Where the data was noisy with a reasonable scatter in the data, the midpoint of the top band was taken. The values obtained from this method are those given in Table 3.3.

A more useful and accurate calibration is given by the transformation of the MOA $B_{\rm M}$ and $R_{\rm M}$ to Johnson colours as given by Reid [124][9]:

$$\begin{aligned} (B-V)_{\rm Johnson} &= \underset{\pm 0.006}{0.646} + \underset{\pm 0.010}{1.036}\times(B_{\rm M}-R_{\rm M}) \\ (R-I)_{\rm Johnson} &= \underset{\pm 0.006}{0.321} + \underset{\pm 0.010}{0.612}\times(B_{\rm M}-R_{\rm M}) \end{aligned}$$

These transformations are more useful than the straight magnitude calibration for comparing colours with other objects.

When naming newly-detected systems, caution needs to be taken as the plethora of naming systems developed in the past makes cross referencing of targets very difficult. Obscure internal catalogue names and numbering systems do not help. Neither does mis-classification in a name. Therefore naming a newly detected system as MOA 123 EB, for example, can be misleading, especially if the target later turns out not to be an eclipsing binary after all.

The naming of the MOA targets generated some interesting debate. The internal catalogue numbers are specific to each observed field. OGLE's SMC catalogue used their own internal referencing to identify their detected systems. The labels were based on their field identification number and the star's identification number in that field e.g. OGLE SMC_SC4 35694. However without the details of the labelling systems, the actual coordinate location is an unknown. The EROS group used a running number system. It started at 1000 and was incremented for each addition target e.g. EROS 1066. Initially, a similar format was to be used for the MOA catalogue, however the IAU recommendations for naming celestial objects give a format of MOA JHHMMSS.S−ddmmss, using the system's J2000 equatorial coordinates truncated to a level where there is no ambiguity between sources. This was satisfactory, but in doing so the accuracy of the position is lost as the last significant figure in both the right ascension and declination is discarded. Therefore, in the tables where the names are given, instead of an additional column with the full coordinates, a column containing the extra digits is given.

3.2.7 Completeness and comparison of the MOA catalogue to the OGLE catalogue

The level of completeness of the catalogue proved difficult to predict. Numerous factors need to be considered such as seeing, periods, phase coverage, reduction techniques etc. When comparing detections, the most significant factor for the MOA database would most likely be the seeing at the observatory. This is especially critical for observations toward the dense stellar

[9] Originally in terms of $B^{\rm instr}_{\rm MOA}$ and $R^{\rm instr}_{\rm MOA}$ but presented here in this form for ease of use.

regions of the SMC. The blending of fainter targets in bad seeing would most likely lead to a reduction in the number of systems detected. Figure 3.8 gives the histogram of the MOA R_{M} values in the catalogue. The majority of the stars lie in the 16 to 17 mag. range, with the numbers rapidly reducing after 17.5 mag. Additionally, the use of templates, as explained in section 2.2.1.2, limits the number of stars detected on the MOA CCD frames.

At the time of searching the MOA database, OGLE published their catalogue of eclipsing binary stars for the SMC [159]. The OGLE and MOA field had overlapping regions as both groups' primary goal was to search for microlensing events near the central region of the SMC due to the high star density. OGLE used 11 fields, all containing some partial overlap region, Figure 3.15. MOA settled for two relatively large fields that covered a similar area. Both MOA and OGLE fields were based on camera size and operational method. There was some area where there was no overlap.

In order to gauge the completeness of the MOA SMC catalogue it was compared with the OGLE catalogue of SMC eclipsing binaries. In order to compare only similar objects, the following selections were made:

- Stars with periods $\geqslant 0.40$ day and $\leqslant 20.00$ days
- Stars detected in overlap region between the smc1 and smc2 regions are only counted once
- Only those OGLE stars that lie within the MOA fields are selected
- The magnitudes are cut off at 17.5 mag.

The final condition has a large impact on the numbers stars selected, especially for the OGLE catalogue. However to go beyond this cut off value is of little use as the MOA detection efficiency is already decreasing rapidly.

Taking these criteria, a selection of 514 OGLE systems results. These are therefore deemed to be potentially detectable by the MOA search. With 130 MOA systems within the common area to both surveys, this gives 384 systems that were not detected by MOA.

The MOA magnitude distribution is skewed toward the brighter stars, but only by a few stars. Otherwise, the distribution is reasonably symmetrical. This is unlike the OGLE distribution, Figure 3.9, which appears as an obviously skewed distribution. Both distributions reduce rapidly near the detection limit, as expected, and is very noticeable for OGLE (1459 detections), but not so for MOA (169 detections). With similar observations and detections, one would expect the MOA distribution to approximate the OGLE distribution.

Furthermore, in the MOA database, the overlapping region between the smc1 and smc2 fields resulted in the detection of 23 eclipsing binaries. It was found that in their overlapping region, only 2 out of 23 detections were in both of the fields. It was thought that the detection method might have been the issue for the discrepancies in the overlap region. However a manual search of the database catalogue file within this region based on the cross-matching of coordinates showed that the 21 systems for which there was no double detection were in fact present in the photometric sequences for only one of the two fields. This gives confidence in the search method but raises questions concerning the completeness of the MOA survey. This indicates that the MOA survey is far from complete. Similarly, the OGLE catalogue is not complete. According to Udalski 1998, [159], *The average completeness of the catalog is about 80%*. The

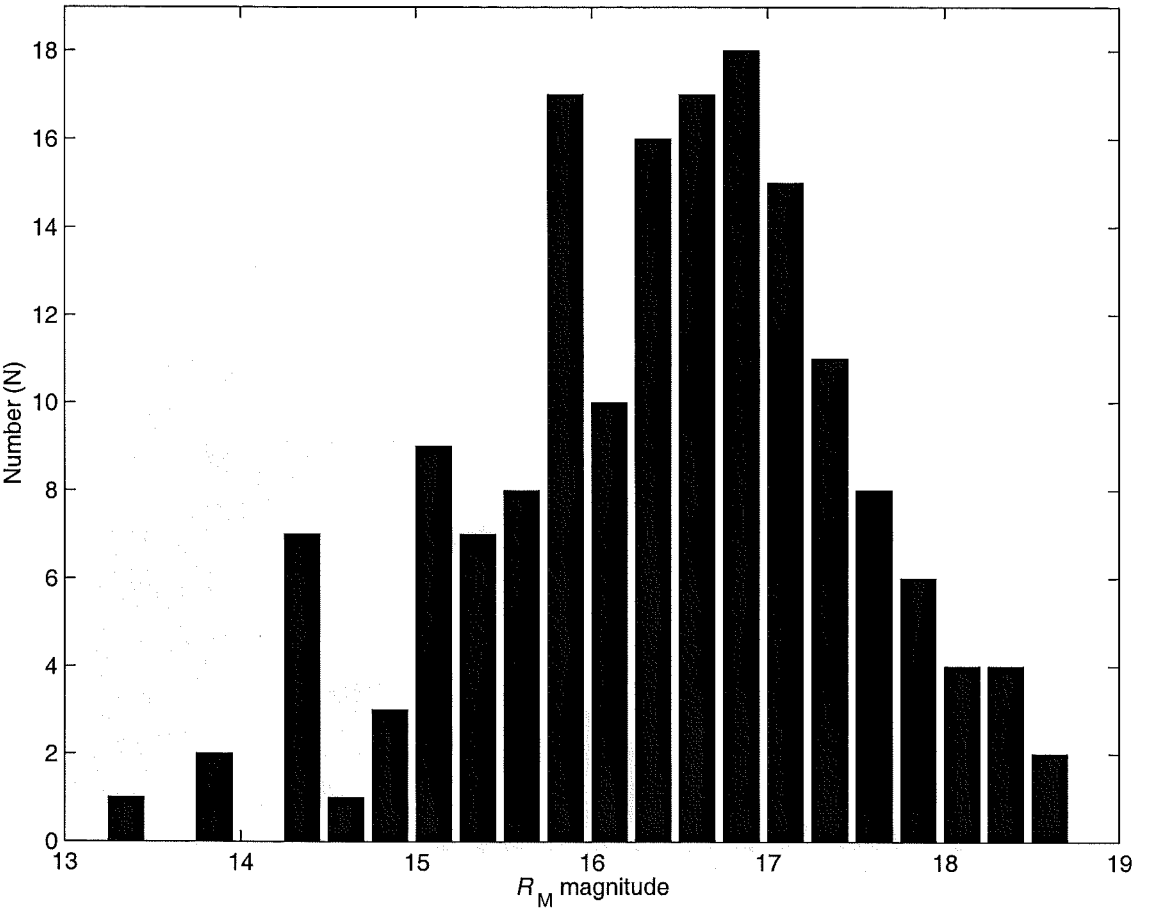

Figure 3.8: Histogram of the MOA R_M value from the SMC eclipsing binary star catalogue. The total number of stars is 167.

estimate was based on the cross-matching of stars in the overlap region of the fields. A total of 170 stars were detected, of which 136 were paired, 80%. It was noted that this is a lower limit due to the effect of stars only being detected once due to their close proximity to the edge of the fields and non-perfect pointing of the telescope. If the same method is applied to the MOA catalogue the figure is ~10%.

3.2.7.1 New eclipsing binaries

The OGLE and MOA systems within the common area were cross matched. The coordinates of the MOA and OGLE stars were of reasonable accuracy that they could be matched on these alone, however there were a few cases where the differences were inexplicably large compared to the average. As a result the systems were matched by selecting the MOA coordinate position and selecting all OGLE target with an area around them. The systems were then compared firstly by light curve, then period and finally magnitude to obtain a match.

The DSS and MOA finding charts were compared to make sure that they were in agreement. If all of these criteria were satisfied, then a match was considered to be positively made, if not the target was considered a new detection.

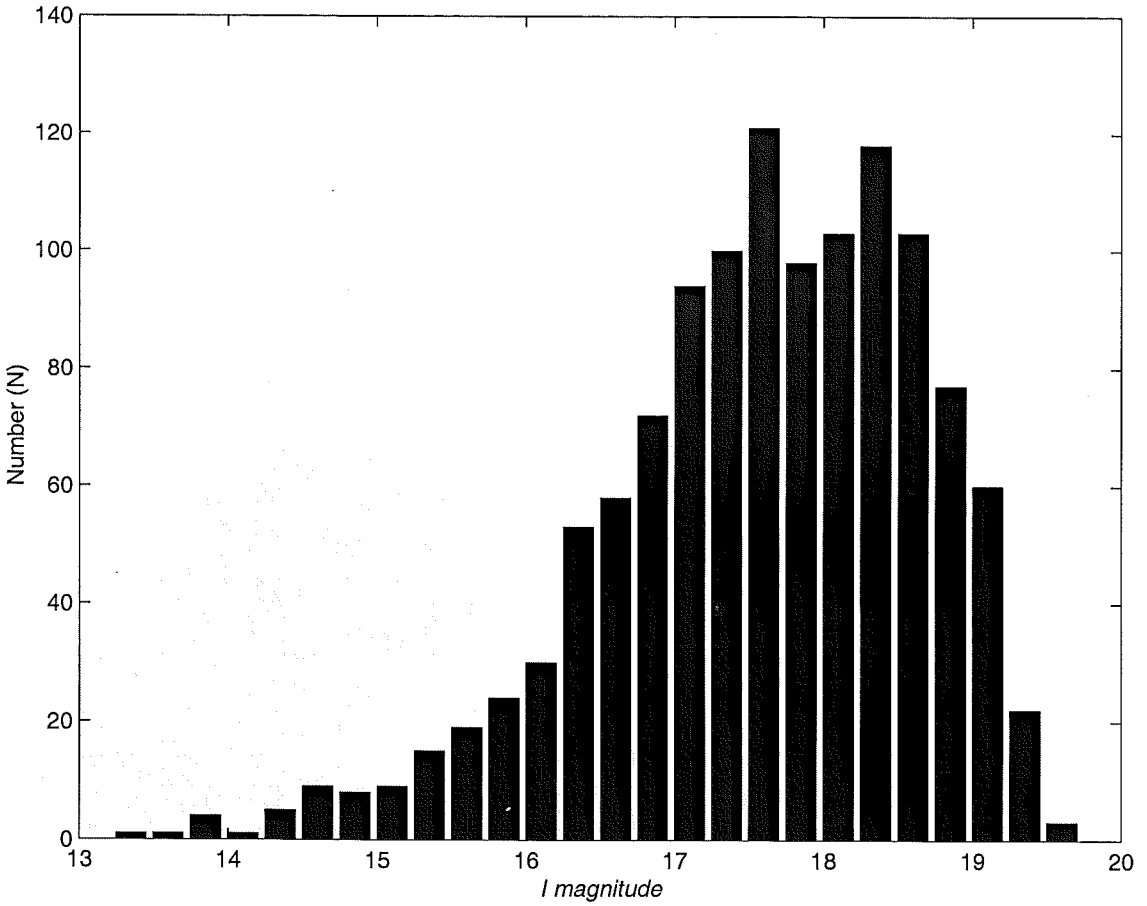

Figure 3.9: Histogram of the OGLE I band values of all 1242 stars that lie within the MOA fields. The total number of stars in the OGLE catalogue is 1459. There are 64 stars that are located in the overlapping regions which have been included.

A total of 35 new eclipsing binary detections were identified, Figure 3.10. These did not appear in the OGLE, Harvard or Cordoba catalogues. Results of the cross matching indicated 21 new detections lie within the common area of the OGLE and MOA regions surveyed, and 14 lie outside, Figure 3.15. Samples of the light curves in $B_{\rm M}$ and $R_{\rm M}$ are presented in Figures 3.11 and 3.12.

The 35 new detections were published in the Monthly Notices of the Royal Astronomical Society, MNRAS [14], appendix G. The finding charts and light curves of all 167 eclipsing binaries were placed on the CDS server[10].

[10]ftp://cdsarc.u-strasbg.fr/MNRAS/331/609

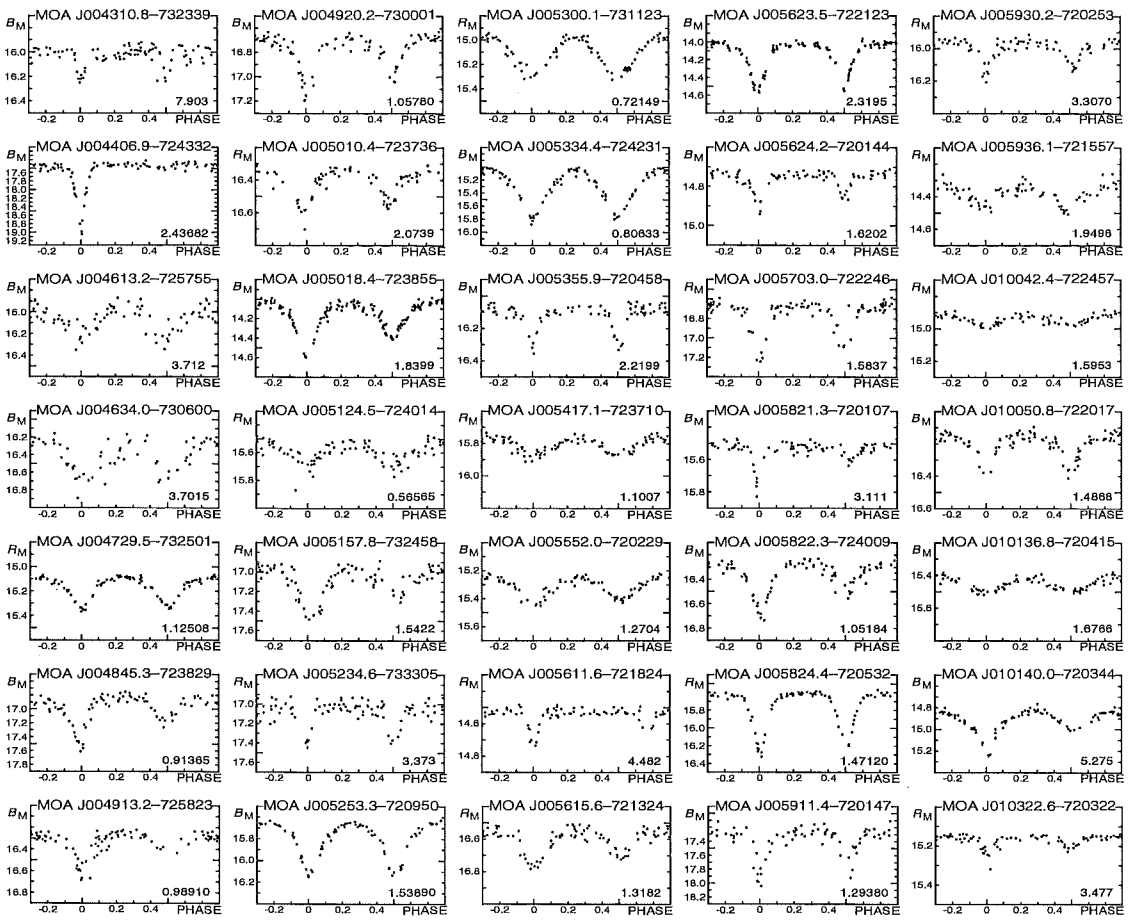

Figure 3.10: The light curves of the 35 new detections in the MOA catalogue of eclipsing binaries in the SMC. The light curves are presented in either the blue or red bandpasses ($B_{\rm M}$ and $R_{\rm M}$).

3.2.7.2 Discrepancies between OGLE and MOA

The comparison of the two catalogues presents the interesting fact that several new detections were in regions covered by both MOA and OGLE. They show a wide range of types of eclipsing binaries and periods. Given that the OGLE catalogue detects eclipsing binaries two magnitudes fainter than MOA and the average seeing is better, it is a surprising result.

Both surveys used DoPhot for the initial image analysis. The search algorithms used varied: MOA, Grison method for detection; OGLE, AoV method. A photometric analysis of the raw images using a image subtraction method, such as ISIS[3],[2] could result in a higher detection rate. The problem, however, is that there are a huge number of parameters which have to be set between the data recording through to analysis and searching that make it difficult to make a direct connection to the source of the discrepancies. As a result, a cross-match between all catalogues would be required to get a more complete picture of the true numbers of eclipsing binaries and the completeness of the catalogues.

Part of the analysis of the OGLE II observations was to review all previous data using an image subtraction method, called Difference Imaging Analysis, DIA [183], [184]. In theory, this should find all variables stars above a selected variation level. This will provide an interesting comparison between the use of DoPhot versus DIA for variable star detection as the image

subtraction methods give better photometry especially in crowded fields. MOA is currently using an image subtraction method, but is yet to apply this to older data analysed using DoPhot. If this is done, it would be interesting to apply the same period search algorithm to the database to see if more detections are made.

3.3 Eclipsing binaries in the Large Magellanic Cloud

The MOA LMC database contains approximately 1 000 000 time sequences. The search method applied to the MOA SMC database has been applied to the MOA LMC catalogue. The number of light curves that require manual examination is yet to be finalised, but this examination and the production of a catalogue is beyond the scope of the thesis. An initial estimate places the number of expected eclipsing binaries in the order of 500, based on SMC results. MACHO have published their catalogue of eclipsing binaries in the LMC [5], 611 detections, and more recently OGLE have announced 2580 eclipsing binaries in the LMC [182].

MACHO have reported a catalogue of some 6000 eclipsing binaries in the Magellanic Clouds, [32]. The number in each cloud are unknown at this stage. The MACHO group is attempting make an estimation of the statistical distributions of orbital elements for these systems, [4]. Additionally, they are searching for companions to the eclipsing binaries, i.e. Jupiter mass objects, [114].

Chapter 4 onward discusses the detailed photometric studies of two eclipsing binaries detected by the search of the MOA database as well as a system from the MACHO survey.

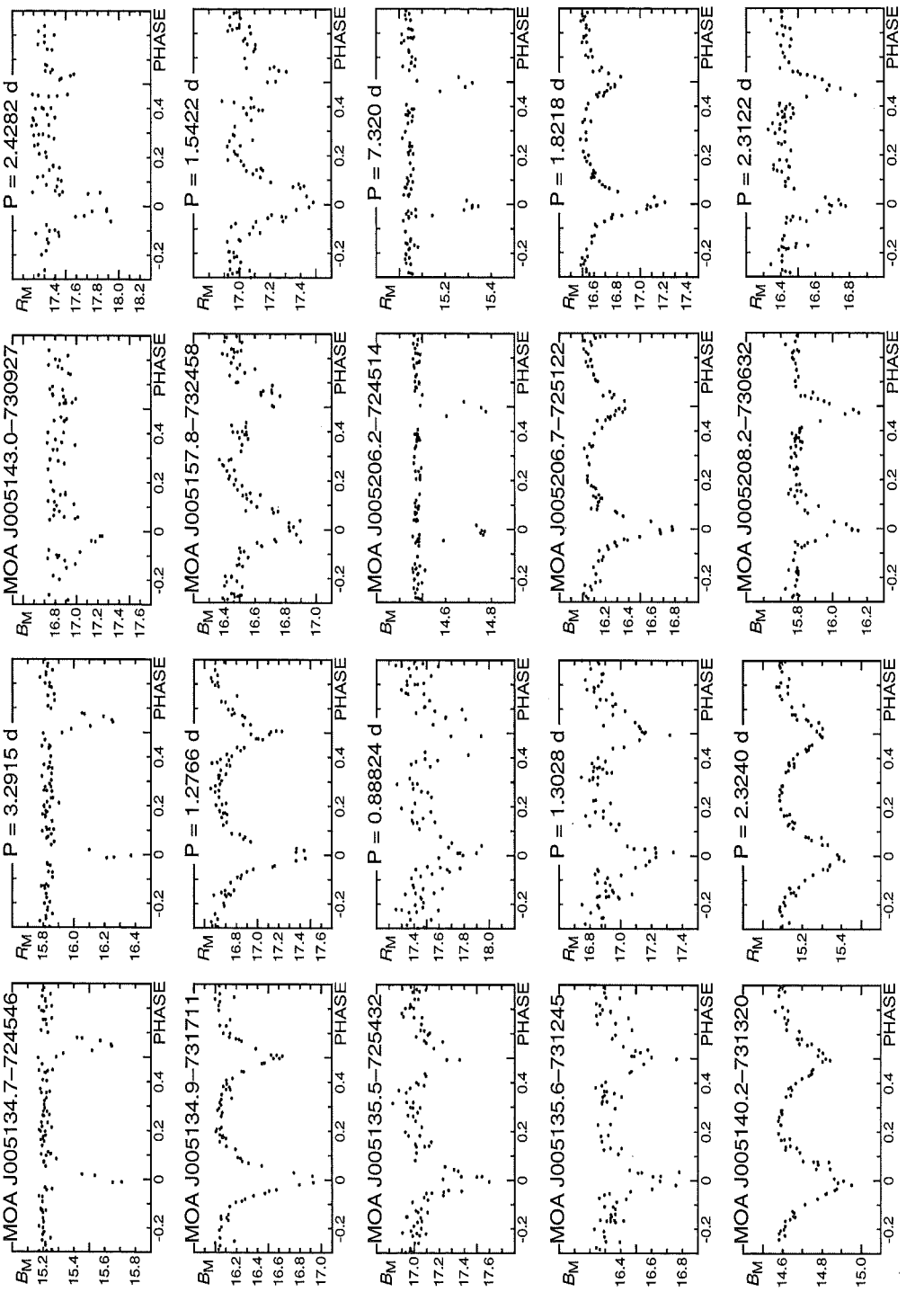

Figure 3.11: A sample of the light curves produce for the MOA catalogue of eclipsing binaries in the SMC. The light curves are presented for both the blue and red bandpasses (B_M and R_M). The phase is shown from -0.3 to 0.8 to show both eclipses clearly. Light curves for all the eclipsing binaries are presented in Appendix G. The light curves are constructed using data supplied by MOA.

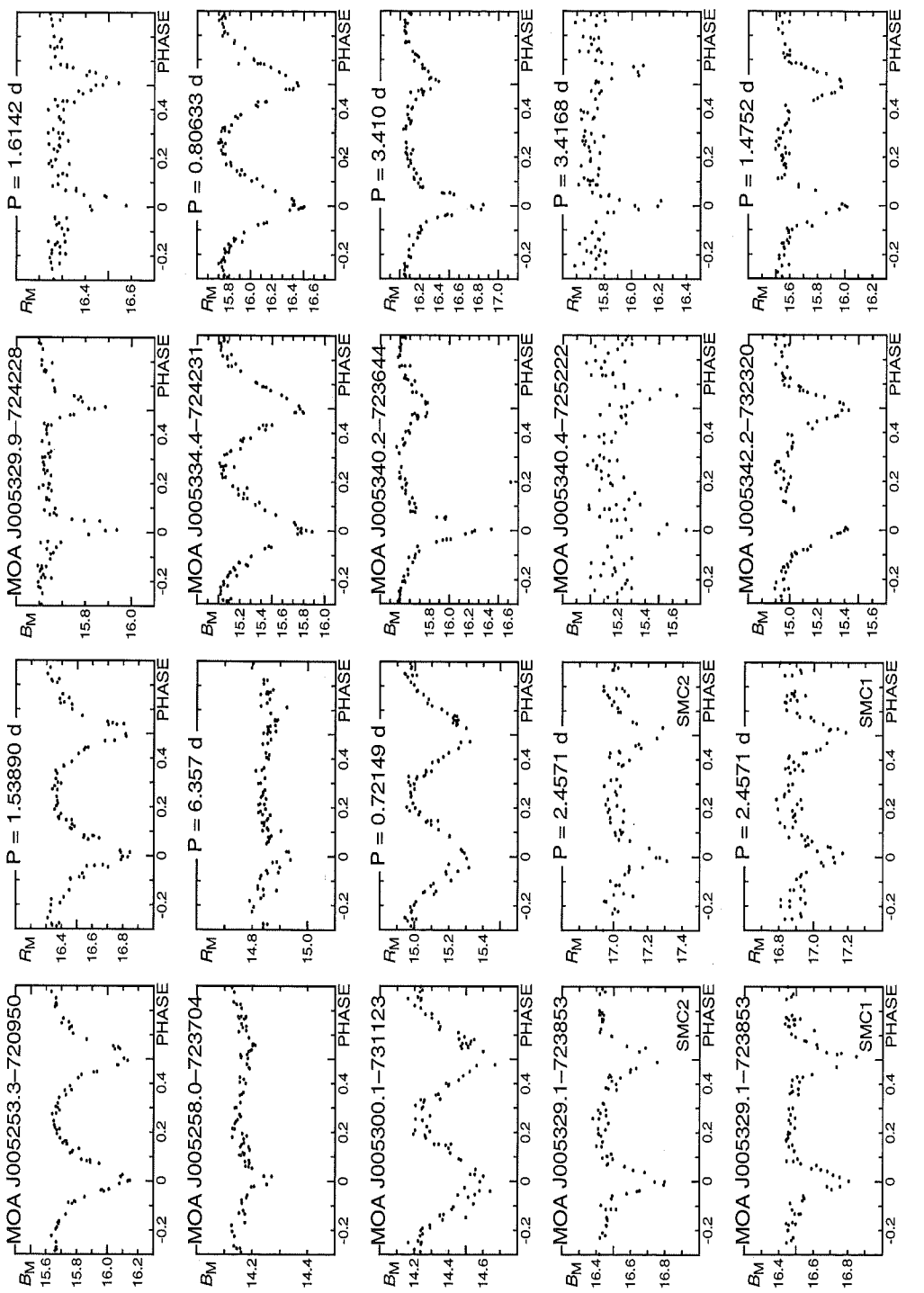

Figure 3.12: A sample of the light curves produce for the MOA catalogue of eclipsing binaries in the SMC. The light curves are presented for both the blue and red bandpasses (B_M and R_M). The phase is shown from -0.3 to 0.8 to show both eclipses clearly. Light curves for all the eclipsing binaries are presented in Appendix G. The light curves are constructed using data supplied by MOA.

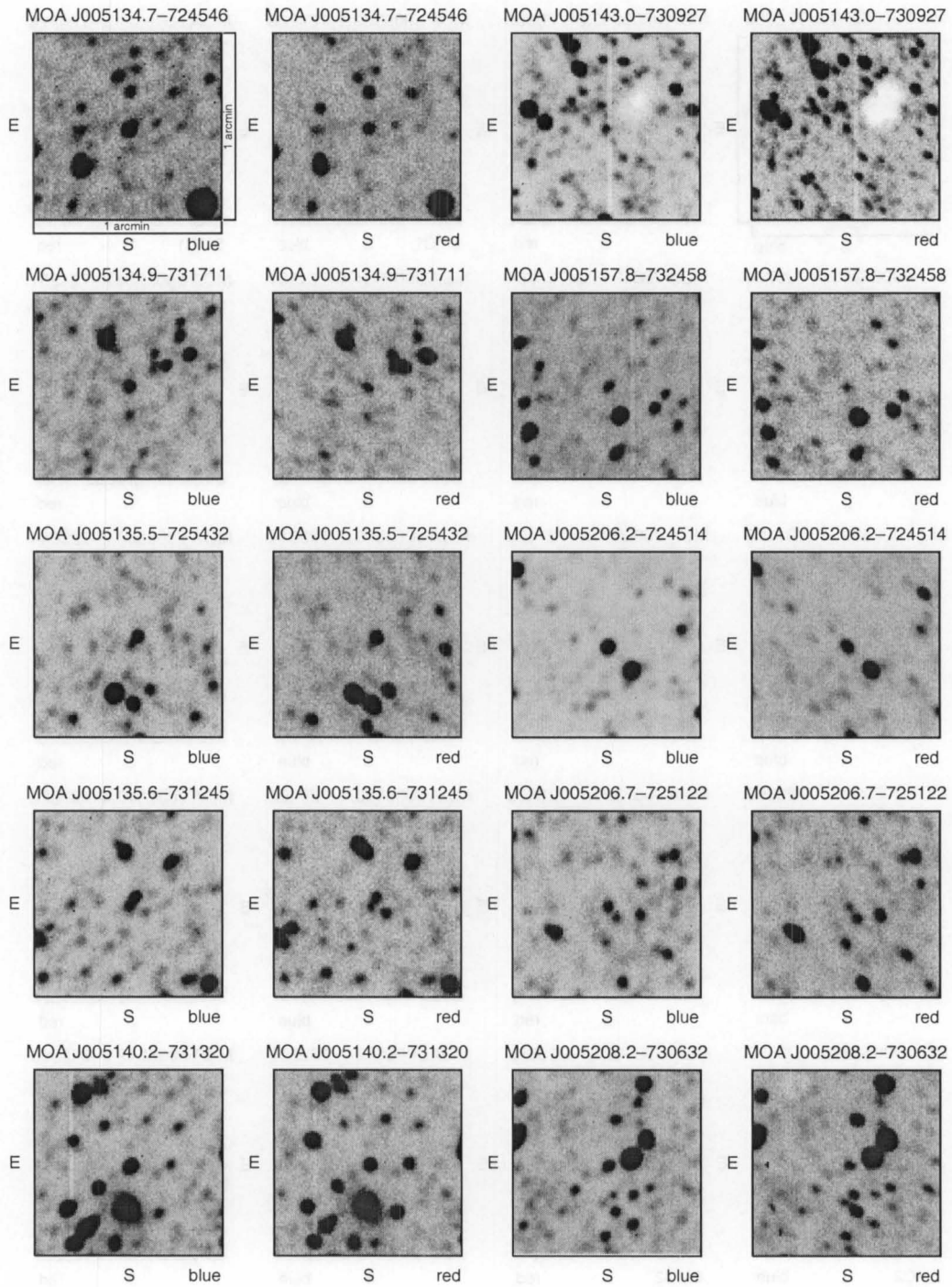

Figure 3.13: A sample of the finding charts produced for the MOA catalogue of eclipsing binaries in the SMC. The eclipsing binary is located in the centre of the finding chart; each chart is 1 arc min square. The chart is presented for the blue and red bandpasses ($B_{\rm M}$ and $R_{\rm M}$). The remainder are presented in Appendix G. The charts were extracted from the raw MOA FITS images from each chip from one cyclic motion. The finding charts and coordinates were matched with fields extracted from DSS with the MOA coordinates which were cross checked against the MACS catalogue where possible.

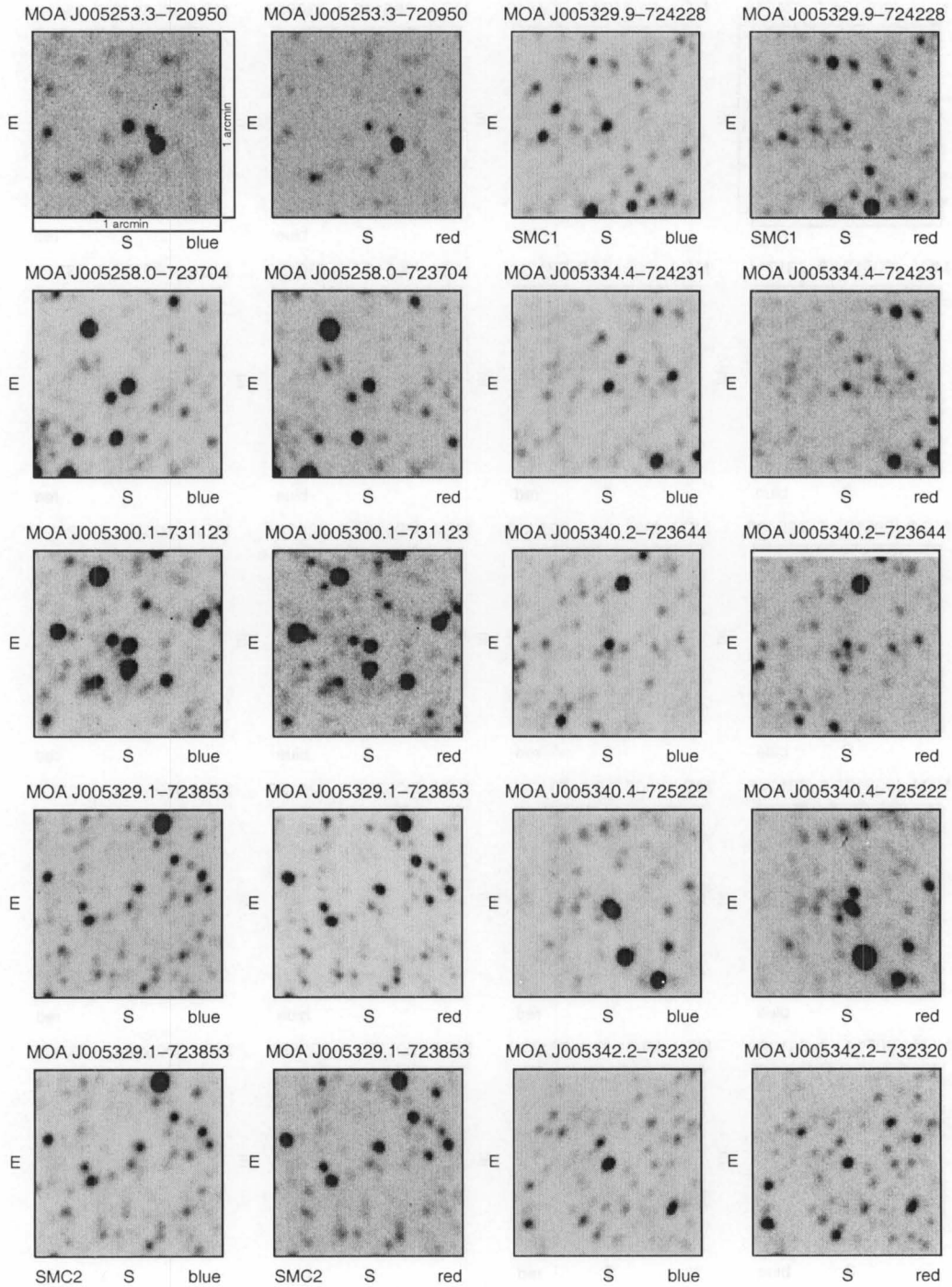

Figure 3.14: A sample of the finding charts produced for the MOA catalogue of eclipsing binaries in the SMC. The eclipsing binary is located in the centre of the finding chart; each chart is 1 arc min square. The chart is presented for the blue and red bandpasses ($B_{\rm M}$ and $R_{\rm M}$). The remainder are presented in Appendix G. The charts were extracted from the raw MOA FITS images from each chip from one cyclic motion. The finding charts and coordinates were matched with fields extracted from DSS with the MOA coordinates which were cross checked against the MACS catalogue where possible.

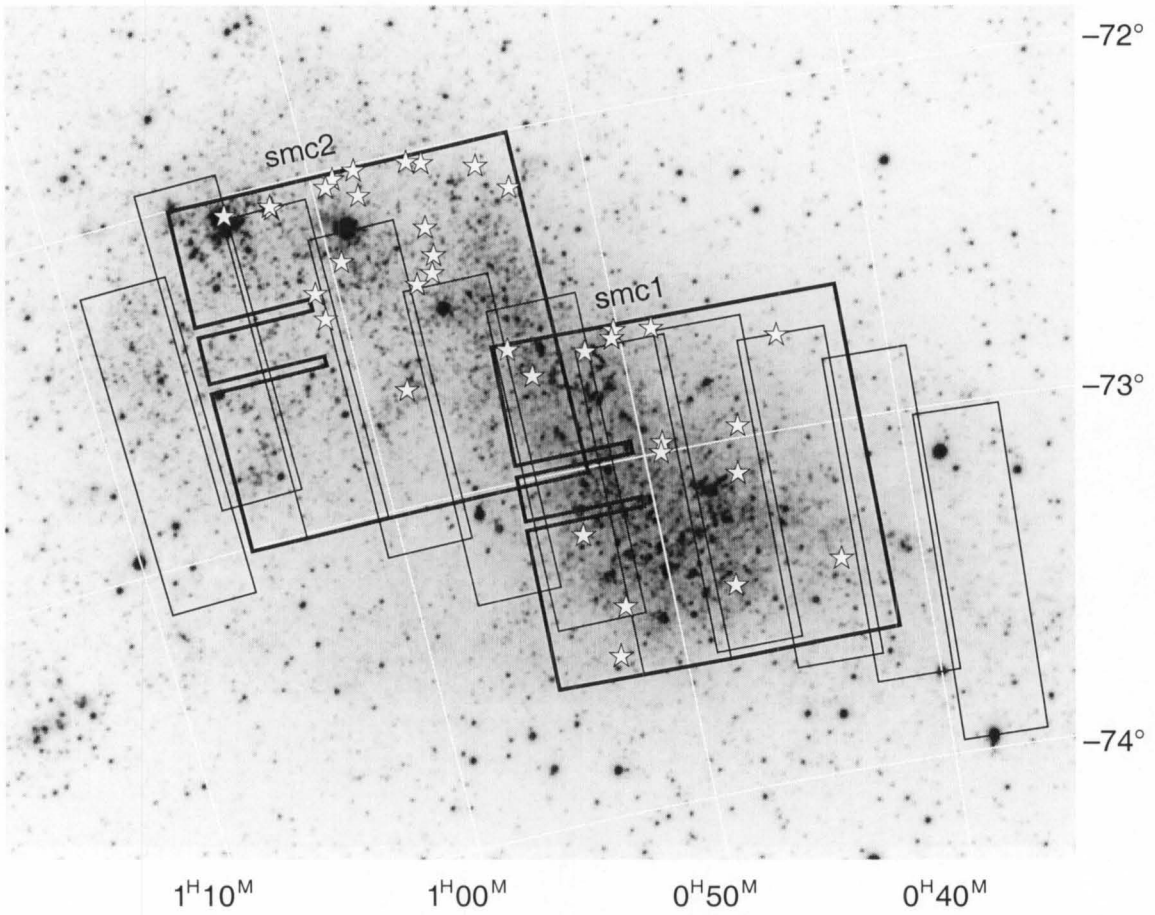

Figure 3.15: MOA smc1 and 2 fields superimposed over an image of the SMC from the Canterbury Sky Atlas (Doughty, Shane and Wood 1972). The OGLE fields are shown along with the 35 new eclipsing binaries detected in the MOA database. J2000 coordinate grid.

Chapter 4

Acquisition of photometry

This chapter presents an overview of the equipment and procedure involved in obtaining data from the MJUO 1 metre telescope through to a point where data reductions can start. Observations acquired for the research span from 1998 to 2002. The initial year and a half of observations were made on a part-time basis, 2-3 nights per run. After this, once I became a full-time student, longer periods were possible, about a week in length depending on telescope availability.

4.1 MJUO facility

The Mount John University Observatory (longitude 174° 34″ 23.4′ E latitude −43° 12″ 25.3′ S) is located beside Lake Tekapo, South Island, New Zealand at an elevation of 1030 metres above sea level.

4.1.1 1 metre telescope

The McLellan 1 metre telescope was constructed by technical staff in the then Department of Physics at the University of Canterbury during the period 1980-1985 (for further details the reader is referred to Tobin and Evans (1996) [151]. First light was achieved in March of 1986. The design is based on Dall-Kirkham optics; ellipsoidal concave primary and a spheroidal convex secondary mirror. Two interchangeable secondary mirrors allow for two focal ratios, $f7.7$ and $f13.5$, the latter for spectroscopy and the former for photometry. To operate the telescope at $f7.7$ requires two additional lenses to be inserted in the chimney baffle of the telescope in order to correct off-axis aberration.

From time-to-time the mirror is removed and is re-aluminised on site due to dust or water marks from moisture on the surface.

4.1.2 Photometer head and filters

The photometer head unit contains the auto-guide camera and filter wheel assembly, as seen in Figure 4.1 and is attached directly onto the telescope. The CCD and dewar are connected to the bottom of the photometer head. The system is designed so the CCD chip lies in the Cassegian focal plane for the focal ratio $f7.7$.

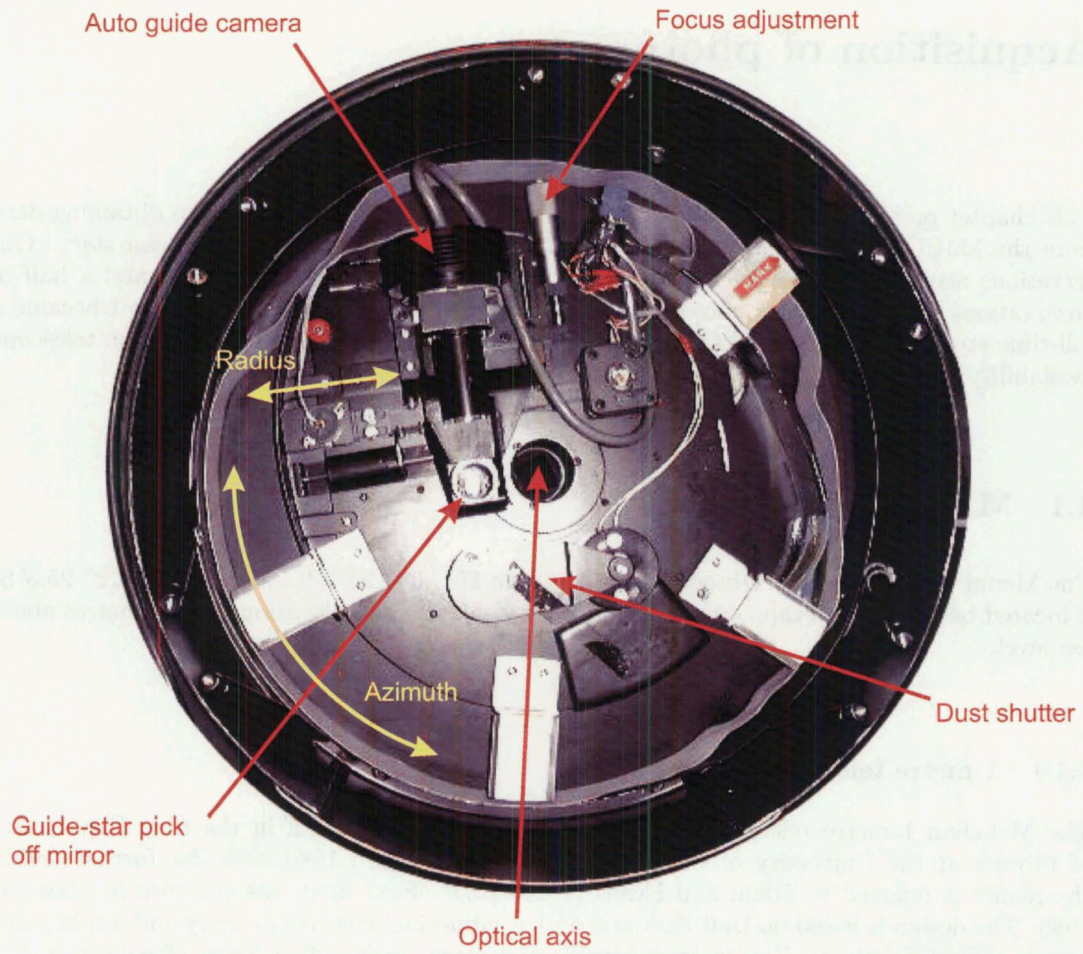

Figure 4.1: A plan view of the photometer head. The off-axis auto-guide camera, ST4, is indicated. The focused light passes through the centre of the photometer head along the optical axis as indicated and then continues through the filter wheel, immediately below, past the CCD shutter and lastly falls on the CCD chip. The auto-guide camera, as well as other items, are mounted on an internal circular platform can which rotate 370° about the optical axis. The auto-guide camera can move in and out in radius and also in azimuth (position angle 0 to 370°), hence the term off-axis guiding. This provides a sizable area in which a suitable guide star can be located. The guide camera positioning, in relation to the cryogenic CCD, is determined from sky survey prints using on overlay grid, Figure 4.2, as the guide star lies well outside the CCD field of view area.

The photometer head was purpose-built by the technical staff in the Department of Physics and Astronomy at the University of Canterbury [153]. Implemented in 1993, little change has been made to the original design, apart from the auto-guide camera. The key function of the photometer head is to enable the user to make filter changes and guide camera positioning from a remote location, i.e. the data room. This makes for efficient use of time and lowers the chance of human errors occurring.

The two major components are the filter wheel and auto-guide unit. There are several filter wheels, each with specific filters permanently loaded for certain types of observational requirements. The only filter wheel used for this research consisted of 8 filters labelled 0→7 whose bandpasses are given in Table 4.1 and graphically in Figure 4.3. The transmission values over their individual bandpasses are presented in Appendix B.

Table 4.1: The filters loaded in the filter wheel. The H_α filter was not used for any of the observations.

Position	Filter	Mean Wavelength (nm)
0	Clear-glass	...
1	Strömgen u	346.6
2	Strömgen v	410.0
3	Strömgen b	465.9
4	Strömgen y	548.2
5	Cousins I_C	794.6
6	H_α	...
7	V_J	550.5

The advantage of this system is the filters are not disturbed throughout the run (apart from surface cleaning at the start). This means less chance of dust contamination and the filters are rotated into the same positions for each exposure.

The V filter[1] is made to emulate the V of the Johnson-Cousins $UBVRI$ photometric system, which is negligibly different from the V of the Johnson UBV system. It is constructed of 2 mm Schott GG495 filters glass, oiled to 3 mm of BG39. In addition, it has a 2 mm clear-glass plate. This is to ensure that the filter is approximately the same thickness as the other filters thereby obviating the need to refocus the telescope when filters are changed.

4.1.3 Vignetting of the image

The photometer head and components were originally designed for a Thomson CCD chip with dimensions 384×576 pixels, 24μm pixels, (9.2 mm × 13.8 mm). The CCD became redundant with the purchase of a Photometrics series 200 CCD system incorporating a SITe 003ab 1024×1024pixel, 24μm pixels, (24.6 mm square) CCD. The design of the photometer has filter-wheel and optic-axis tube dimensions which are too small for the size of the new chip. Consequently, the image on the SITe CCD is partially obscured, particularly around the edges, Figure 4.4. Additionally, the original shutter supplied with the SITe system was too tall to fit between the CCD mounting plate and the photometer head (if a spacer were inserted, then the CCD and offset guide camera would no longer be in a common focal plane). This causes more light to be blocked from the source, although minimal compared to the filters.

To rectify this problem and achieve full use of the chip, new filters, shutter and filter wheel are required as well as increasing the diameter of the centre region which the light passes through in

[1]This filter is referred to as V_J throughout the thesis to avoid confusion with the Strömgen v.

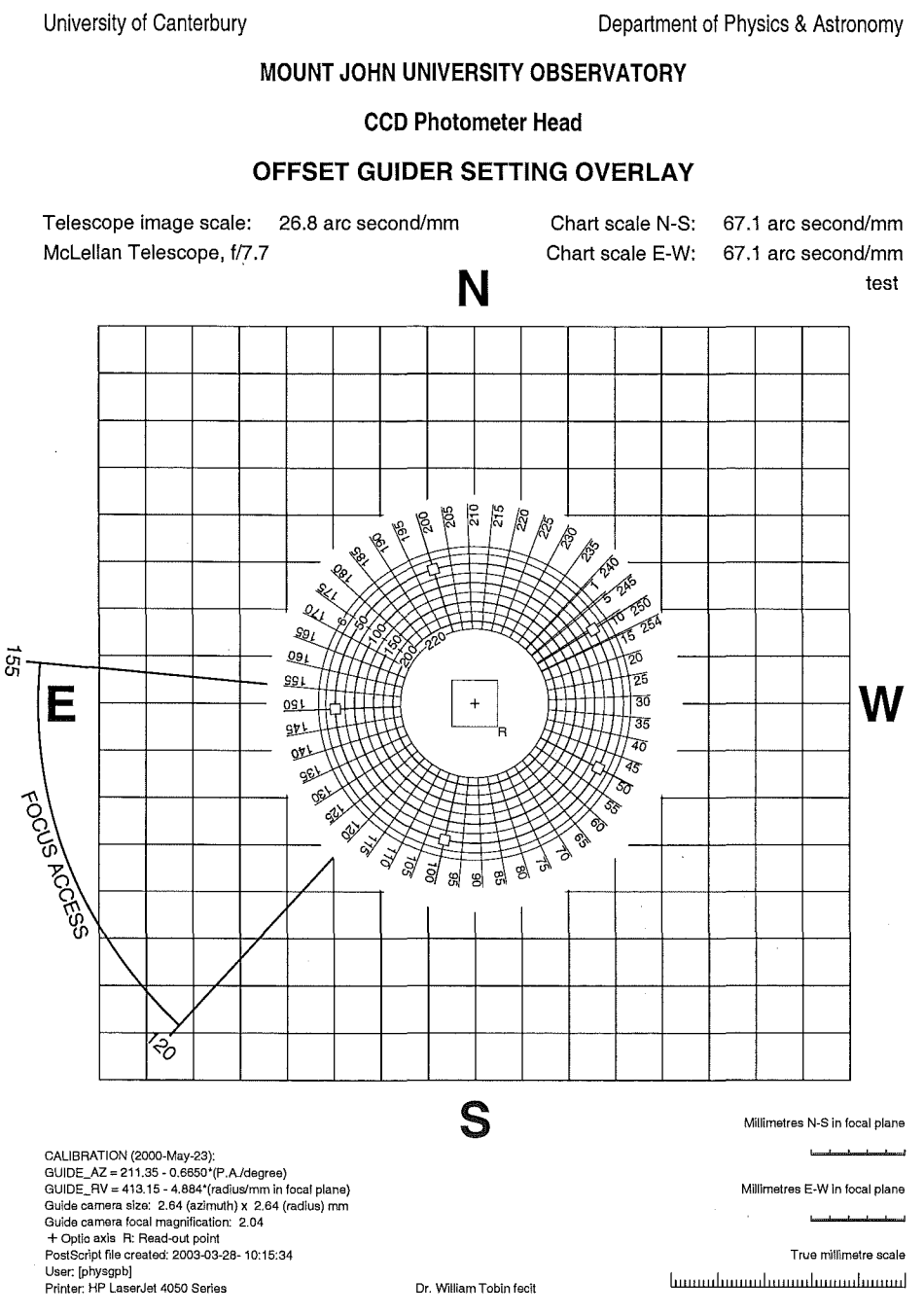

Figure 4.2: The overlay used for the photometer head and auto-guide system. The centre square is the full extent of of the SITe chip, though only a lesser portion is usable due to vignetting. The R denotes the readout point on the CCD. The chart is used to determine the auto guide camera position for a given star. To see the star on the science CCD, a considerable movement is required away for the target.

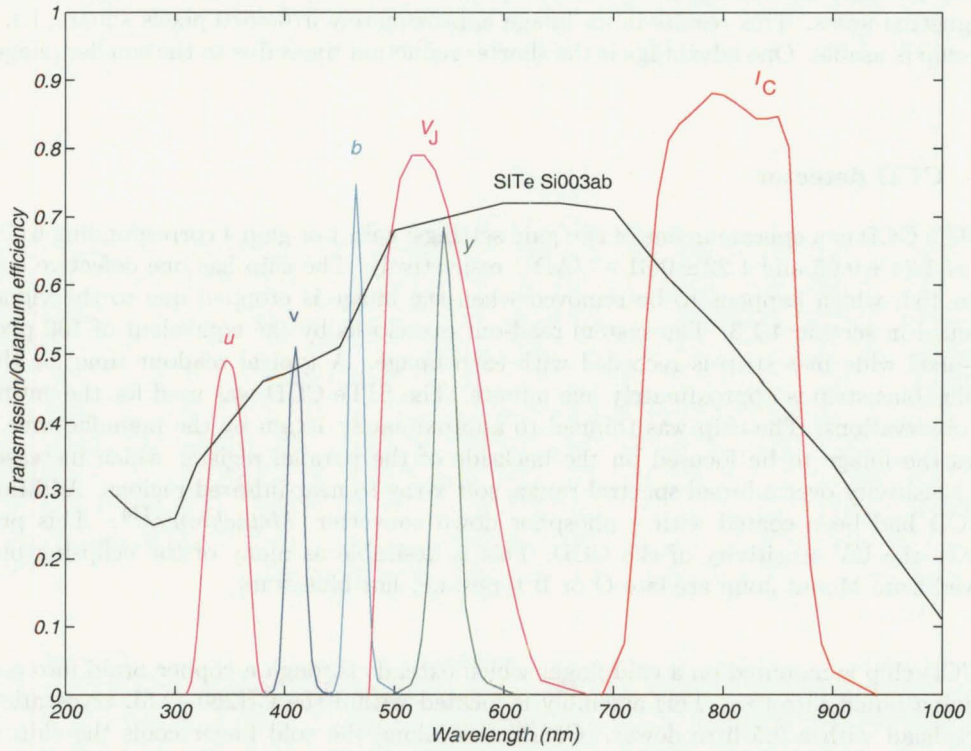

Figure 4.3: The transmission of the filters as a function of wavelength. Produced from data in Pritchard [123].

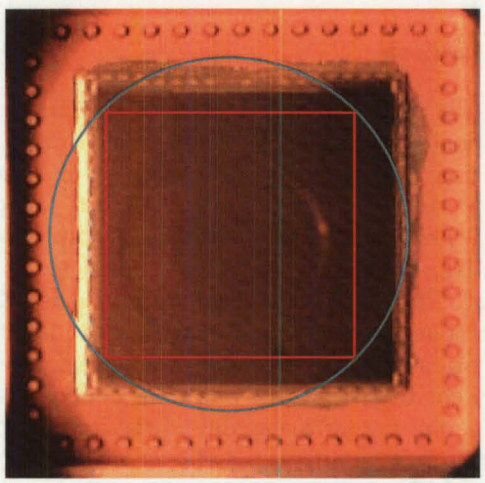

Figure 4.4: The SITe CCD chip is surrounded by the gold coloured region. The two images superimposed on the CCD chip are the unvignetted footprints of the filter (red square) and the optic axis tube (green circle). The light path is through these two objects. Only cones of rays whose central ray passes through the common area of the red and green regions reach the chip unobstructed. Outside of the common area, the light path is obstructed resulting in a vignetted image. The flat field image in Figure 4.10 and the contour plot Figure 4.11, clearly shows the light as *seen* by the detector.

the photometer head (in other words a new photometer head). However for the purpose of the photometry undertaken at MJUO for this project, it is sufficient to crop the image to eliminate the vignetted areas. This results in an image approximately 570×570 pixels square, i.e. 31 % of the chip is usable. One advantage is the shorter reduction times due to the smaller image size.

4.1.4 CCD detector

The SITe CCD can operate in one of two gain settings; gain 1 or gain 4 corresponding to inverse gains of 4.74 ± 0.05 and 1.22 ± 0.01 e^-/ADU respectively. The chip has one defective column, column 153, which happens to be removed when the image is cropped due to the vignetting mentioned in section 4.1.3. The system read-out overclocks by the equivalent of 100 pixels so a 100-pixel wide bias strip is recorded with each image. A typical readout time for the full chip plus bias strip is approximately one minute. The SITe CCD was used for the entirety of these observations. The chip was thinned to approximately 10 μm by the manufacturer. This enables the image to be focused on the backside of the parallel register which increases the chip's sensitivity over a broad spectral range, soft x-ray to near-infrared regions. Additionally, the CCD had been coated with a phosphor down converter, *Metachrome*^{TM}. This product improves the UV sensitivity of the CCD. This is desirable as many of the eclipsing binaries observed from Mount John are late O or B types, i.e. hot blue stars.

The CCD chip is mounted on a cold finger which extends through a copper braid into a dewar containing liquid nitrogen. This assembly is located within the CH260−2.5L cryostatic CCD camera head with a 2.5 litre dewar. Conduction along the cold finger cools the chip whose temperature is set via a heating resistor and thermostat. The range of operation is from −70° to −130°C. The normal operating temperature is −95°C, which is the coldest temperature for which the thermostat maintains the chip temperature constant irrespective of the orientation of the cryostat. The cryogren boil off rate of 1 litre per 18 hours[2] is sufficient to enable a full winter's night observation without the need to refill the dewar[3].

4.1.5 ST4 auto-guide camera

The telescope guiding for the initial observations were performed by using an offset guiding system contained in the photometer head with a slowed Philips video camera unit as the guide star detector. The image was display on a monitor and the observer was required to make minor adjustments to the telescope position to ensure the guide star remained at the predetermined position. This system had two main drawbacks; Firstly, manual guiding wasn't the most efficient or effective; secondly, the guide star had to be very bright in order to be detected by the Philips unit. The system was replaced with a S-BIG[4] ST4 CCD. The unit and software allowed for continuous auto-guiding throughout the night to the sub pixel level. In addition, far fainter guide stars could be used than with the old system. The results in image quality were immediately seen. Under similar conditions, a non-auto-guided (manually guided) image generally has an apparent poorer seeing due to the image moving about a central point. A *round* stellar image may result but it is spread over more pixels. The auto-guided images have a tight bound under which the guide star moves, giving a small stellar diameter, hence apparent better seeing. A majority of the non-auto-guided images were rejected however a number were taken in poor conditions so a definitive answer as to the cause of any particular high seeing value is not easy, since it is likely a combination of both factors. Figure 4.5 shows

[2]Under a vacuum of 10^{-4} torr. The vacuum is generally less than this and therefore a figure of 1 litre per 6 hours is more typical.

[3]Depending on the target position and telescope orientation, some liquid nitrogen is lost via the vent duct, so the level needs to be monitored and refilled if required.

[4]Santa Barbara Instrument Group.

the two extremes. The settings used for the ST4 auto-guide unit are given for reference in Appendix E.

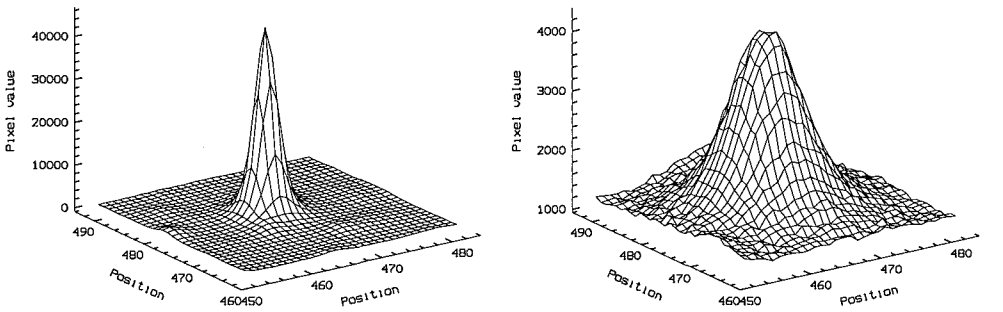

Figure 4.5: A 30 × 30 pixel view of MACHO*05:36:48.7−69:17:00, in the V_J bandpass, in two different conditions with the same airmass 1.15. The left hand side FWHM seeing is 2.59 arc sec, auto-guiding. The right hand side is without auto-guiding, seeing 7.08 arc sec.

4.2 Photometric observations

4.2.1 CCD requirements

The CCD has generally replaced photographic film or plates as the detector of choice for observational astronomical research. Although photographic media are still occasionally used to provide the colourful pictures for which the field of Astronomy and Astrophysics is so well known, the CCD has become the common tool of the professional astronomer. With reduced production costs, it is now also affordable for the amateur astronomer. Since the CCD's inauguration to Astronomy [79], major improvements have been made, including size and cost. Although the CCD is not the perfect detector, it has many advantages as given:

1. Linear response.

2. High quantum efficiency.

3. Area array detection.

4. Low intrinsic noise.

5. Digital readout to PC.

6. Good response to visible spectrum ~380 nm → ~1100 nm (silicon limit).

The disadvantages of the CCD can be overcome, to some extent, with some additional work:

1. Pixel-to-pixel sensitivity variations cause standardization problems.

2. Large file sizes, 1024×1024 ($1k \times 1k$) of CCD array requires 4.2 Mb of storage space.

3. The spectral sensitivity varies with the direction of the incoming light.

4. Sensitive to cosmic rays.

5. The quantum efficiency and dark current depend on temperature.

6. Calibration problem, uniformly illuminated dome flats, hard to obtain skyflats.

4.2.2 Bias

A Bias frame was not recorded as this is included in the dark frame and is removed from the science image in the dark frame subtraction. The CCD chip did however have a bias strip located between columns $1024 \rightarrow 1124$. This strip is in the form of on over-read strip and is present in every frame recorded. The bias level should have negligible changes if the gain and fat zero settings on the CCD amplifiers are not changed. Also the bias frames are specific to a particular controller configuration, however all the observations under taken all used the same controller configuration. Variations in the initial observations did occur when a gain setting of 1 rather than 4 was used. The bias frames' purpose is to remove any amplifier structure which might be present in the data. This is achieved by the shutter staying closed and the exposure time set to zero. The chip is then read out. Ideally, a sequence of exposures should be done every observing night to maintain a series of regular calibrations of the system.

4.2.3 Shutter calibrations

The time taken for the shutter to open and close can affect the signals recorded, especially during the acquisition of *dome* flats if exposure times are short. To see if this was of concern, a series of short exposures were performed under *dome* flat field conditions using the 1200 watt lamp. An image of the shutter was observed for exposures less than ~ 1.5 seconds. The shortest exposure time, excluding darks as the shutter is not opened, was 11 seconds for a Strömgren *v dome* flat and 400 seconds for the science images using the I_C filter. In both of these cases the counts recorded per second are very different. The science image exposure is very long compared to the shutter opening time and therefore has a negligible effect. The flat field image however, has a high count over a short time. The shutter shadow is seen in an exposure of 0.9 seconds, Figure 4.6. This is clearly seen in the profile, Figure 4.7.

At an exposure time greater than 1.5 seconds, the shutter shadow is greatly diminished and the profile tends toward a flatter surface.

The exposure times for all flat field images were based on reaching a preset number of counts. Since the shutter affects them in the same way and the exposure times are of a far greater length than the shutter opening time, the effect was considered minimal in this case, therefore no corrections were applied. In retrospect, it might have been better to arrange for longer Strömgren *u* dome flat-field exposures Figure 4.7, but since the targets were always placed at the same point on the CCD, and the flat-field procedures were standardized, there should be no effect on differential photometry except for a small zero-point shift.

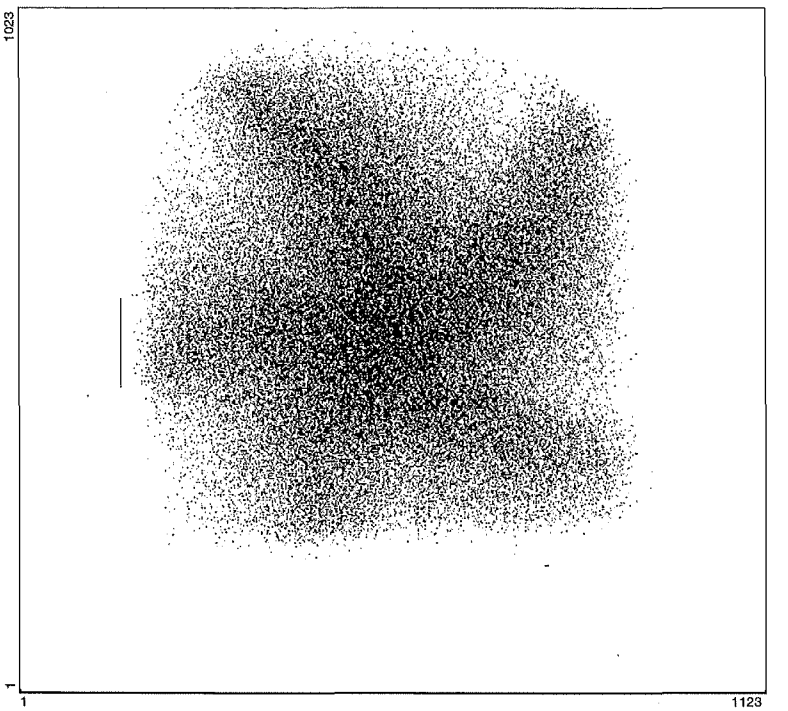

Figure 4.6: The shutter map for the MJUO SITe CCD photometer head, represented as a negative image. The exposure time is 0.9 seconds. The shutter leafs are clearly visible. The vertical line to the left of the image is the defective column on the CCD.

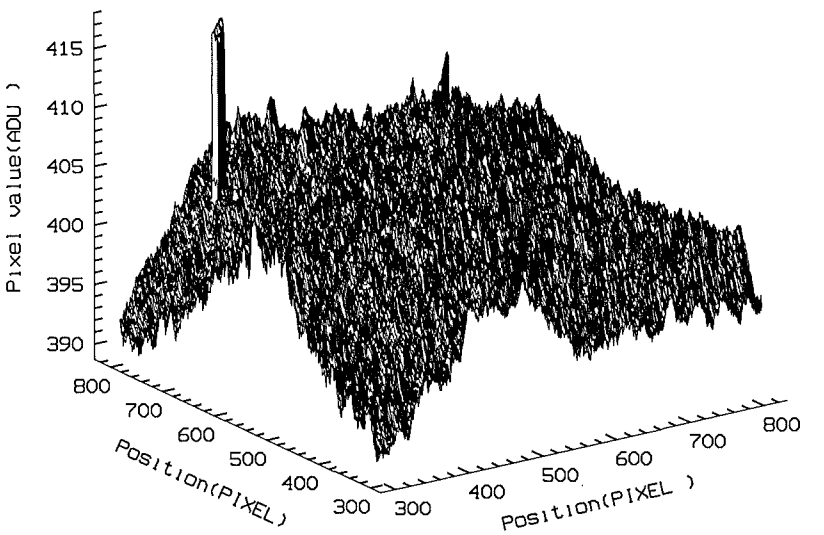

Figure 4.7: The surface profile of Figure 4.6 as viewed from the bottom left corner. The surface profile for the shutter map is plotted for the central 510 pixels square area. The mean dark level over this central region is 340. The effect for a 0.9 s exposure is ~15%. For a 11 s exposure (Strömgren *u* filter *dome* flat), ~1.2% and a 31 s exposure (V_J filter *dome* flat) ~0.44%.

4.2.4 Darks

When the information obtained from the bias image is combined with that of the dark frame, one can obtain the detector characteristics of the CCD when it is not illuminated. This information is of vital importance as we must know the basic properties of the CCD and amplifiers before we can illuminate it. The term dark current is in reference to the thermal current in the CCD without any illumination. CCDs are sensitive to the thermal generation of electrons, which cause a signal and associated noise. Therefore, CCDs are required to be cooled, generally to the order of $-100°C$[5] for scientific grade CCDs. This helps reduce the dark current, but there is always a residual component. Therefore this needs to be measured and subtracted from any science or *dome* flat images.

Dark frames can be used to identify *hot* and *warm* pixels as these can be the order of the background count in the science image. An alternative is to produce a bad pixel mask to identify the pixels in question. This was not done in this case. To account for the dark current, three dark images were obtained at the start of each night. These were recorded prior to the *dome* flat fields before the start of the night's observations and with all lights off in the dome. The CCD was exposed for 10 seconds with the shutter closed. The average result was a count of approximately 340, this is neglecting the cosmic rays during this period, Figure 4.8. To remove the cosmic rays so the dark could be used to subtract off the science image, a median of the three darks, was calculated by a script in MIDAS, Figure 4.9.

4.2.5 Flat fielding

The fluxes of the stars need to be calibrated for the variation of the optical throughput of the telescope and filters and the quantum efficiency of the detector. These variations depend both on wavelength and on the position of the object on the detector. To correct them, the CCD was

[5]Temperatures above $-70°$ have additional noise due to the thermal current. If the temperature is below $-130°$, the performance is degraded due to poorer charge transfer efficiency.

Figure 4.8: A dark frame, `f2046001.fits` of 10 seconds exposure time, represented as a negative image. The small black regions are cosmic rays. There is a chip defect, column 153 on the left hand side of the image. The Bias strip is also evident on the right hand side.

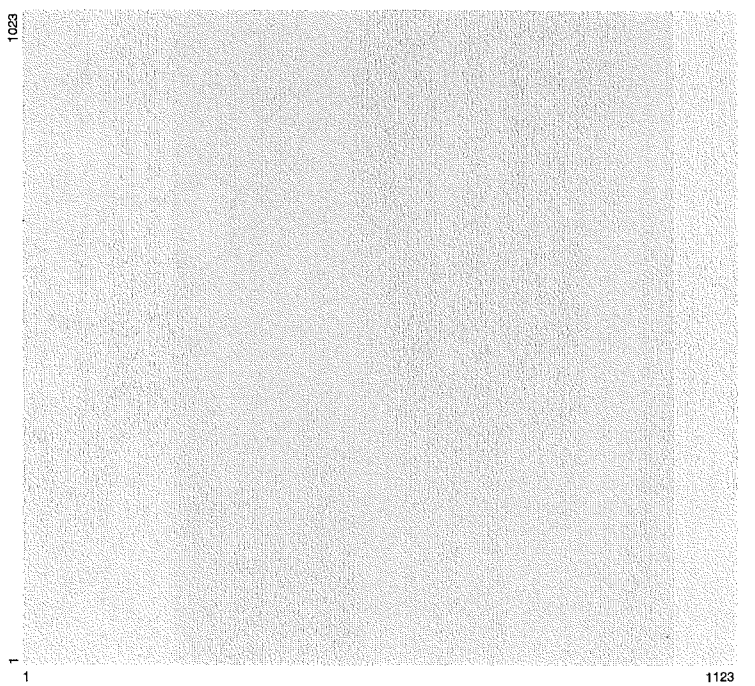

Figure 4.9: A median dark frame constructed from the median values of three dark frames, exposure time for each frame was 10 seconds. The image is represented as a negative. The cosmic rays have been removed by computing the median of the three frames.

exposed to a uniform source of illumination, and subsequent dark-corrected science images were divided by this dark-correct flat field image or sensitivity map. However, the sensitivity may not be correctly mapped by this flat field due to scattered light in the telescope optics. Any flat field error was therefore made into a constant effect by placing the target at a predetermined location, to within 2 pixels, on the chip for each observation. The auto-guide unit was then started. The flat field correction is made during the data reduction stage.

Two sources of flat fields are available; the *dome* flat fields and the *sky* flat fields. At MJUO, the *dome* flat field is the preferred choice. This is due to convenience and generally guaranteed availability, unlike the *sky* flat field which relies on an appropriate region of sky being available at the right time and clear skies. Additionally, the sky must have the right brightness which only gives a small window of opportunity during twilight each night.

The *dome* flat fields were obtained by illuminating a circular quartz cloth mounted on the inside of the dome. Surrounding this is a black low-reflective surface in an effort to reduce extraneous light scattering into the telescope. Two lamps were used to illuminate the quartz cloth; one a 1200 watt theatrical lamp the other a 5 watt halogen torch lamp. The flat field images for each filter required different exposure times, Table 4.2, due to the spectral power of the lamp, the chip sensitivity and the filter transmission. The exposures times were adjusted to give a photon count of around 75% of the linear operating range of the detector ($\sim 60\%$ of the saturation level) in the plateau region on the vignetted chip.

Some filters also required neutral density filters in front of the 1200 W lamp to reduce the light throughput because the lamp's intensity was too great[6].

Table 4.2: The filters' flat field exposure times are based on acquiring a mean count of approximately 40 000 in the plateau region on the vignetted chip.

Filter	Lamp	Neutral Density filter	Exposure time (seconds)
Strömgren u	1200 W	...	34
Strömgren v	1200 W	...	11
Strömgren b	1200 W	1, (0.5 transmission)	24
Strömgren y	1200 W	2, (0.25 transmission)	24
I_C	5 W	...	160
V_J	5 W	...	31

Dome flat fields were acquired at the start and end of the night. Three images per filter were acquired for each of the filters used on that particular night. These typically took 30 minutes to acquire and archive.

The flat field image, Figure 4.10 clearly shows the vignetting effect as explained previously in section 4.1.3. The *dome* flat and science images were cropped to a size that was unaffected by the vignetting. The size of the cropped region was based on the analysis of flat fielding images. Using MIDAS, contours of various levels were over layed on an image, Figure 4.11.

Cross sections of the flat field image across rows, (Figure 4.12) and columns (Figure 4.13), show the effect very clearly. Additionally, they show a slight gradient in the flat field. The effect of the vignetting means that approximately 31 % of the effective chip area is usable. The vignetting was examined for a number of flat field images for different nights and different

[6]The transmission of the 0.3 neutral density filter is $10^{-0.3}$.

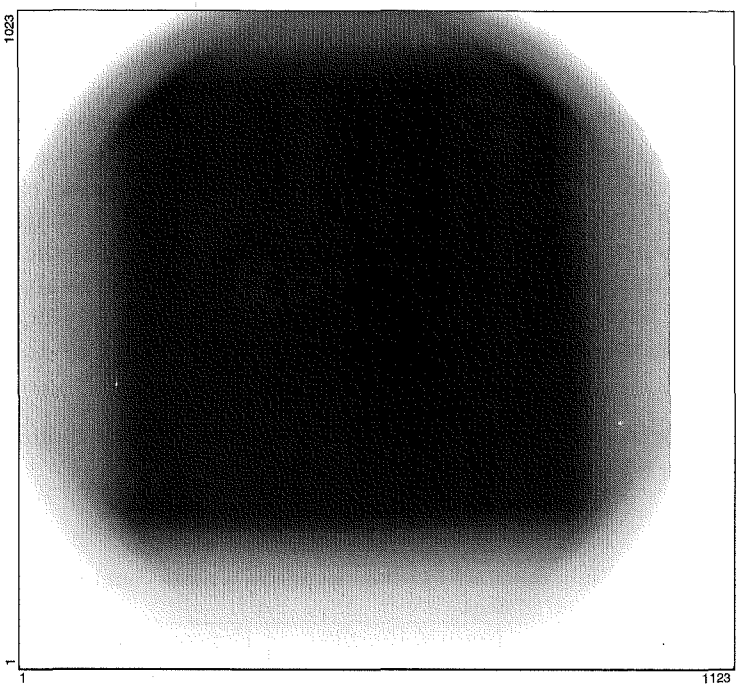

Figure 4.10: A flat field frame, `f2046010.fits` showing the effect vignetting has on a CCD image, negative representation. This effect is seen best in the flat field images due to the high photon flux levels. In the science images, the stars appear to gradually reduce in brightness toward the edges.

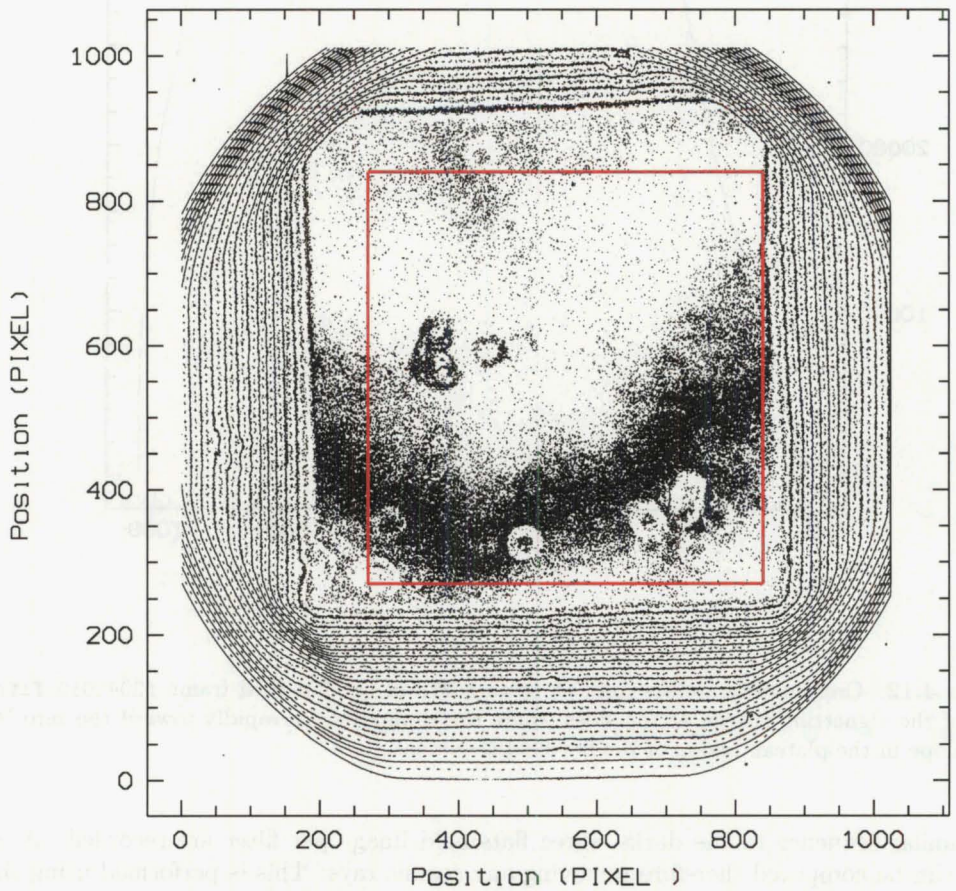

Figure 4.11: Contour plot of the flat field frame `f2046010.fits`. The red box is the plateau region of the flat field that was considered free of the vignetting effect after considering several flat field images from all filters. All images were cropped to the box which is bounded by rows 270 and 840 and columns 270 and 840. Visible on the frame are round *doughnut* shaped features. These features are images of dust particles located on the underside of the CCD dewar window. These are divided out during the flat fielding stage of the reduction process.

filters. The area shown in Figure 4.11, was considered the optimum region unaffected by the severe vignetting.

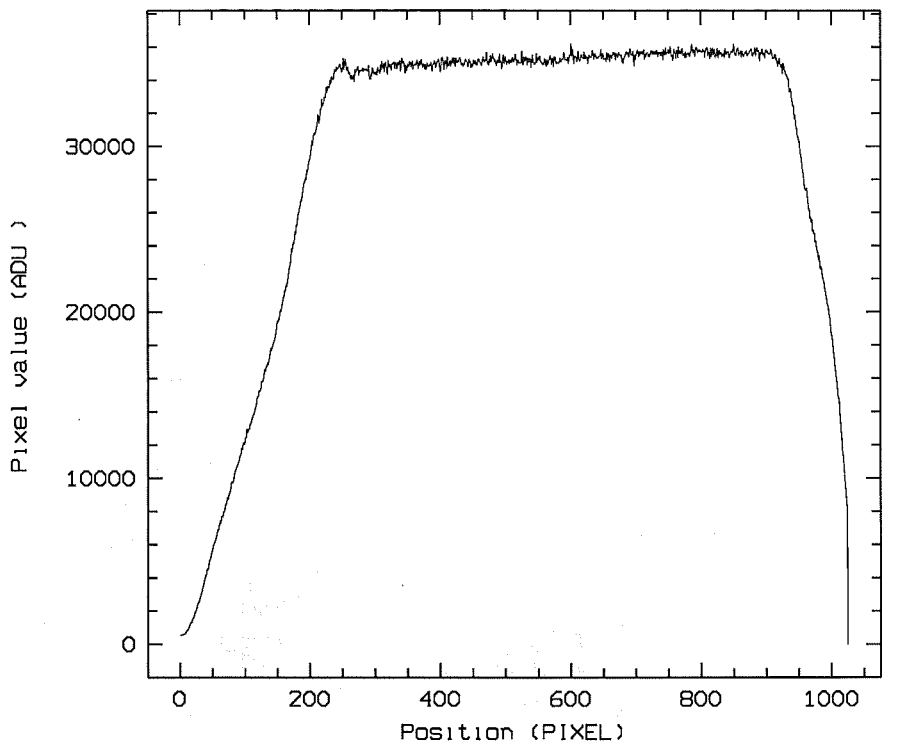

Figure 4.12: Cross section across rows at column 270 of the flat field frame `f2046010.fits`. The effect of the vignetting is seen at the sides where the counts reduce rapidly toward the zero level. A slight slope in the plateau region of the flat field is evident.

In a similar sequence to the darks, three flats field image per filter are recorded. A median frame can be computed therefore removing any cosmic rays. This is performed using the flats fields acquired at the start of the night. The mean of the flat field in the usable region was computed using MIDAS in a procedure which first scales the individual flats to the same average signed level. A median frame was constructed using MIDAS by selecting the median pixel value from the corresponding three frames, thereby removing any cosmic rays. The three frames used were from the flat fields recorded at the start of each night's observations. The calculated median frame was divided by its mean to obtain the image which was the normalized flat field correction image. The science image was then divided by this image.

In Figure 4.11, dark *doughnuts* shaped rings are present on the contour plot. These are due to dust spots on the outer or inner face of the quartz window of the dewar. The outer face is easily cleaned and this was done so at the start of each observing run along with the filters. These stayed clean throughout the run as the system filter-wheel bay is reasonably well sealed. The underside of the dewar window however is under vacuum with the exposed CCD chip directly below. Over time, dust within the cryostat has migrated and adhered to the inside of the quartz window. This could not be easily cleaned, for obvious reasons. The *donuts* divide out when the flat fielding correction is applied. Subtracted flat field images acquired at the start of the observational programme, the middle and end show minor differences in dust spot location.

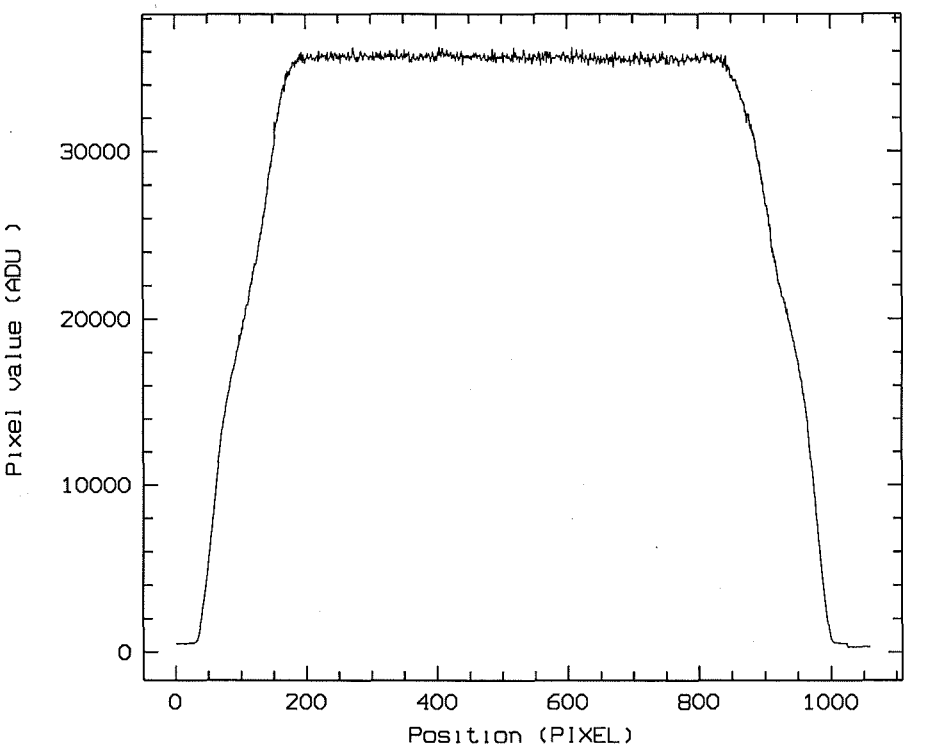

Figure 4.13: Cross section across columns at row 840 of the flat field frame `f2046010.fits`. The effect of the vignetting is seen at the sides where the counts reduce rapidly toward the noise level.

Movement of the dust spots was not seen on a nightly basis and therefore all *doughnuts* are divided out. The movement of the dust spots most likely happens during instrument changes rather than during an observing run.

4.2.6 Observations

Observations were planned around the phases of the eclipsing binaries. All targets were positioned, as mentioned in section 4.2.5 at a predetermined location on the CCD. All dark correction and flat fielding corrections were performed in Christchurch, after the observing run. Observations in the Moon phases half Moon – new Moon – half Moon and in all types of wind and seeing conditions were undertaken. Although not all data was usable, this did help to determine the level at which data is deemed unusable due to the conditions. The phase coverage for the targets is not entirely complete due numerous factors such as the weather, Moon phase and available observing time. Within the time constraints on thesis work, it was not possible to obtain more observations.

4.2.7 Data acquisition and storage

The Data acquisition system at the Mount John University Observatory ran on a personal computer, 550MHz CPU, 128MB RAM running a Redhat distribution of the Linux operating system. A schematic diagram of the system is given in Figure 4.14. During the night's observing, this machine is dedicated to data acquisition and data storage. The PC contains the data storage disks and a CDROM reader/writer. After the image is acquired the data is written to a *user's* hard disk and then to a separate *archive* hard disk. At the end of each observer's run, the observer writes their data to CDROM. An observatory technician similarly writes a copy of the data to CDROM for archive purposes. Archive copies are stored at Mount John and in the Department in Christchurch.

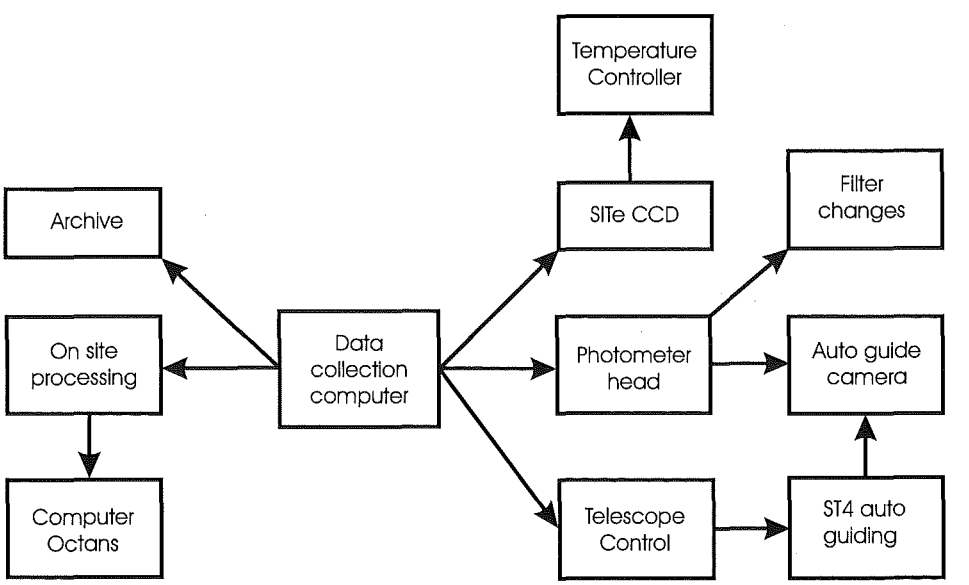

Figure 4.14: Schematic diagram of the photometry instrumentation and data collection. The data collection computer, named Hydrus, stores all recorded images for the night.

4.2.8 Image quality

Image quality is measured by the seeing parameter and influenced by a number of effects some of which can be minimised. Seeing values can vary significantly over short time periods, often less than one hour and this is seen in the nightly seeing data. At high airmass, refraction of star light through the atmosphere, especially with moderate upper level winds present, caused problems with the auto-guiding. The stellar images were seen to *jump* about therefore causing the auto-guide unit to make large corrections, which did not necessarily keep the average position of the stellar profile peak at the same location on the CCD chip. The auto-guide settings were adjusted to account for this.

The airmass can be simply defined, as $z = \sec\theta$, where θ is the zenith distance (angle from the perpendicular) and z is the path length along the perpendicular to the outer atmosphere. The Magellanic Clouds are visible all year from MJUO with varying airmass, Table 4.3 and Table 4.4.

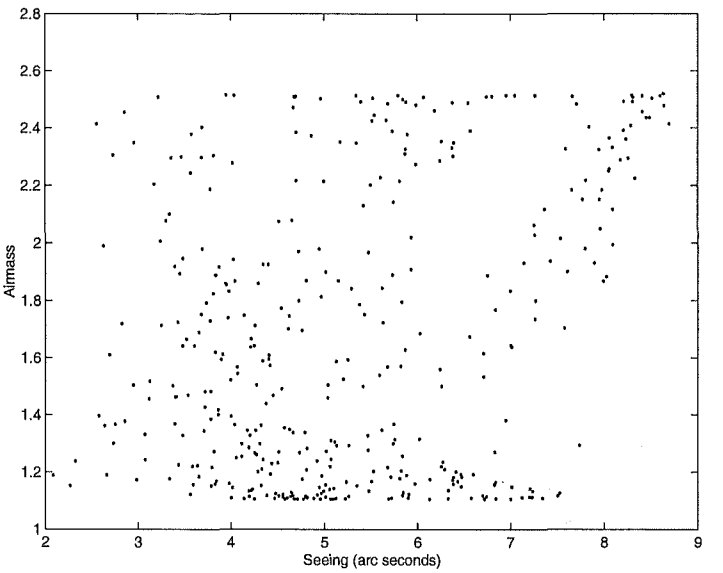

Figure 4.15: FWHM seeing of MACHO*05:36:48.7-69:17:00 V_J filter. No tight correlation is seen between the airmass and the seeing.

Generally, the higher the airmass, the worse the seeing, as there is a greater chance of the light to be perturbed during its path through the atmosphere. However, no tight correlation was seen between airmass and seeing, Figure 4.15. This has been found on many occasions from the MJUO site. The upper winds are the dominant factor for the site and no direct method of measuring these is available to the observer.

Other factors such as optical systems, atmospheric conditions, exposure times, filters, dust and moisture on the mirror and thermal venting of air from the dome to the outside etc. all need consideration although some are very difficult to quantify.

4.3 Target selection

The Observatory's geographical position is ideal for observations of the Magellanic Clouds, as they are visible all year round. The physical spacing of the two galaxies and their closeness

to the South Celestial Pole results in quite significant differences in airmass throughout each night's observations. It is therefore very convenient to have targets in both the SMC and LMC, not only from an observational point of view but also from a astrophysical point of view due to the different physical and chemical properties of the two galaxies.

The primary objective for the eclipsing binary programme at the Department of Physics and Astronomy at the University of Canterbury is to obtain photometric measurements of eclipsing binary systems as accurately as possible, to better than one percent, with the long term goal of using this data in conjunction with spectroscopic and spectrophotometric data to obtain a distance to the system and to test evolutionary models. With this objective in mind, the following constraints are placed on target selection as follows.

1. Ideally a new detection or not previously observed with high accuracy.
2. Located in a relatively clear, uncrowded field, little blending.
3. Bright enough to allow observations from MJUO using the 1 metre telescope.
4. Have sufficiently deep eclipses so that the primary and secondary are clearly. distinguishable from the baseline noise.
5. Preferably be detached systems for easier comparison with single-star evolutionary models.

4.3.1 SMC targets

The two SMC targets, MOA J005018.4−723855 and MOA J005623.5−722123 were selected from the MOA catalogue of eclipsing binary stars [14]. The data for these stars, as given in Table 4.3, were calculated from the MOA database as both of these targets were new detections.

Table 4.3: Data for the two SMC targets from the MOA catalogue [14].

MOA J005018.4−723855	
Right Ascension (J2000)	$00^h\ 50^m\ 18^s.40$
Declination (J2000)	$-72°\ 38^m\ 55^s.2$
Ephemeris, T0	2450681.083
Ephemeris, Period	1.8399 d
Blue mag.	14.05
Red mag.	14.75
Primary eclipse depth blue	0.60
Primary eclipse depth red	0.60
Airmass min.	1.11
Airmass max.	2.30
MOA J005623.5−722123	
Right Ascension (J2000)	$00^h\ 56^m\ 23^s.59$
Declination (J2000)	$-72°\ 21^m\ 23^s.7$
Ephemeris, T0	2450681.934
Ephemeris, Period	2.3195 d
Blue mag.	14.00
Red mag.	14.95
Primary eclipse depth blue	0.45
Primary eclipse depth red	0.35
Airmass min.	1.11
Airmass max.	2.30

The light curves and finding charts, as extracted from the MOA database and presented in the MOA SMC catalogue, are shown in Figures 4.16 and 4.17 for MOA J005018.4−723855 and

MOA J005623.5−722123 respectively. These data collected by MOA, were available in the blue and red broad-band MOA bandpasses, $B_{\rm M}$ and $R_{\rm M}$.

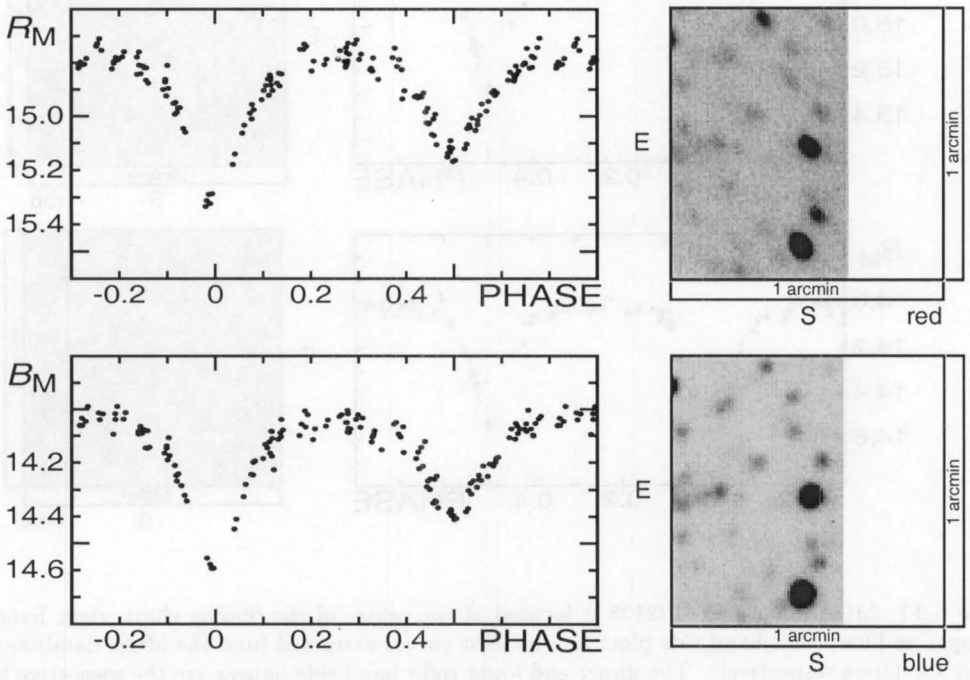

Figure 4.16: MOA J005018.4−723855 is located at the centre of the finding chart, right hand side. The upper and lower left hand side plots are the photometric times series extracted and phased from the MOA database in the $B_{\rm M}$ and $R_{\rm M}$ filters respectively. The upper and lower right images are the respective finding charts.

4.3.2 LMC target

The LMC target was selected from the MACHO catalogue of eclipsing binaries in the LMC [5]. The target selection criteria were the same as for the SMC targets. The data was sourced from the MACHO catalogue, Table 4.4, as were the light curves in Figure 4.18.

Table 4.4: Data for the LMC target from the MACHO catalogue [5].

MACHO*05:36:48.7−69:17:00	
Right Ascension (J2000)	$05^h\ 36^m\ 48^s.7$
Declination (J2000)	$-69°\ 16^m\ 59^s.95$
Ephemeris, T0	2449073.3806
Ephemeris, Period	3.853434 d
Blue mag.	14.87
Red mag.	14.64
Primary eclipse depth blue	0.48
Primary eclipse depth red	0.48
Airmass min.	1.10
Airmass max.	2.52

The light curves of MACHO*05:36:48.7−69:17:00 in Figure 4.18 are reproduced from the MACHO catalogue paper. The Digital Sky Survey, DSS, was used to construct a finding chart

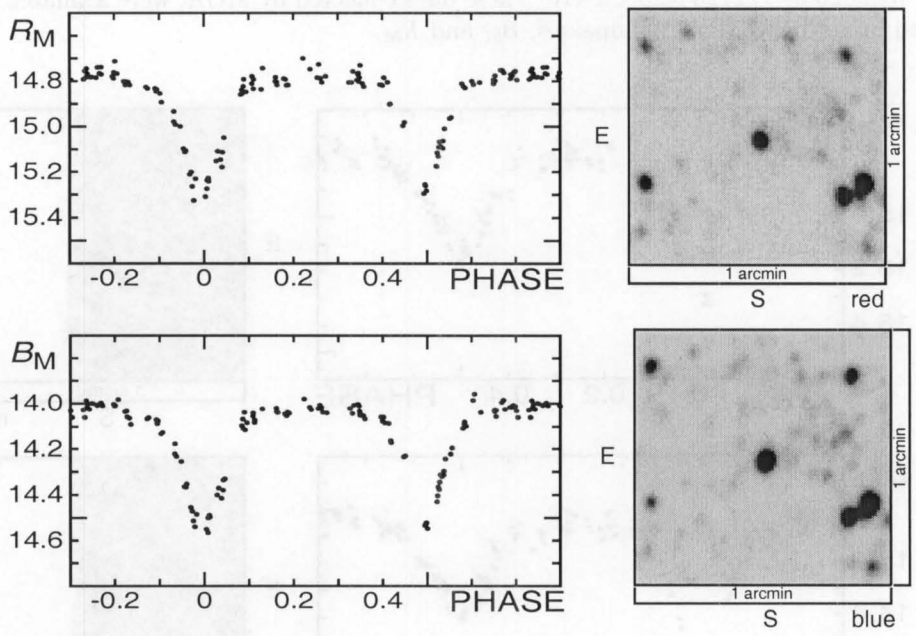

Figure 4.17: MOA J005623.5−722123 is located at the centre of the finding chart, right hand side. The upper and lower left hand side plots are the light curves extracted from the MOA database in the B_M and R_M filters respectively. The upper and lower right hand side images are the respective finding charts.

for the target. The second generation data was used, as it is deeper than the first generation survey. Only the red bandpass data was available for this region as the blue bandpass had not yet covered this region. The finding charts presented in Figure 4.18 are from MJUO observations.

4.4 Summary of observations

The first system to be observed was MACHO*05:36:48.7−69:17:00. Observations started on 26th April 1999 (JD 2451263) and concluded on 26th July 2002 (JD 2452481). This target was the first observed and as a result, has more complete coverage than the MOA targets. Initially observations were only in V_J, hence the larger number of these observations. The observations of both MOA targets started on 11th July 2000 (JD 2451782) and concluded on 11th July 2002 (JD 2452466) for MOA J005018.4−723855 and 9th July 2002 (JD 2452464) for MOA J005623.5−722123.

The observations were planned to obtain sufficient phase coverage of the light curves, however suitable weather conditions did not always allow this. The observational coverage, Heliocentric Mean Julian Date, HMJD as a function of phase, are presented in Figures 4.19, 4.20 and 4.21 for each system in the three filters Strömgren u, V_J and I_C.

Observations of the two MOA systems were started at a later stage as the search through the MOA database was initiated after the observations on the MACHO target started. These systems were observed using the Strömgren u, V_J and I_C Figures 4.19, filters. The observation interval for both systems spanned a similar range as shown graphically in Figures 4.20 and 4.21. The number of observations and the adopted exposure times are reported in Table 4.5.

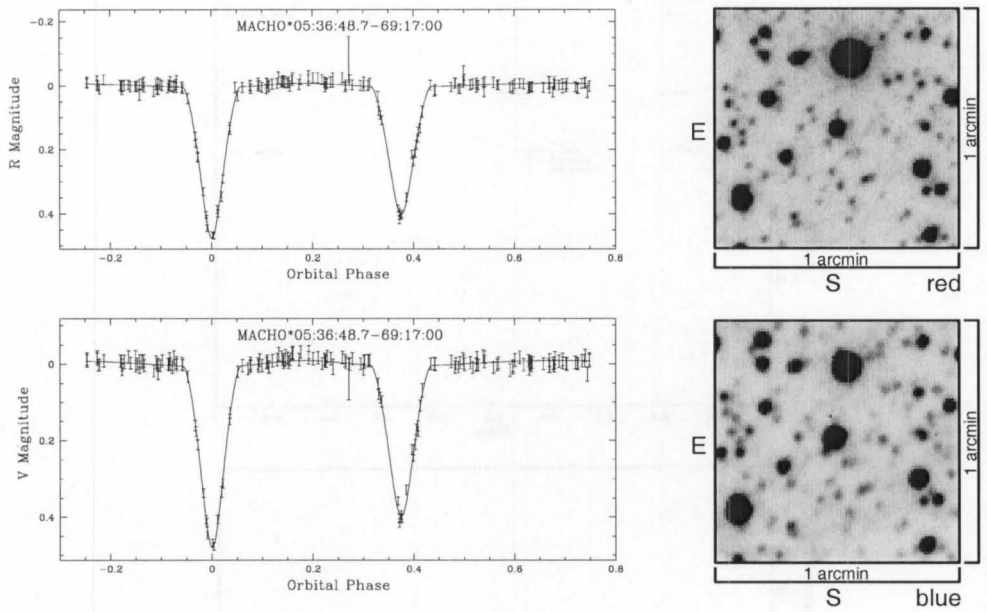

Figure 4.18: MACHO*05:36:48.7−69:17:00 is located at the centre of the finding chart, right hand side. The left plots are the MACHO light curves [5]. The finding chart on the right side are from MJUO observations. The top finding chart is in the I_C bandpass. The lower is in the V_J bandpass. The Tarantula nebula is located approximately 20 arc minutes to the North East of the target. SN1987A is located approximately 10 arc minutes the the North East.

Table 4.5: The exposure times for the science images in both Clouds. The Strömgren v, b and y filters were used in the initial observations of MACHO*05:36:48.7−69:17:00 but not for the two MOA systems MOA J00501840−7238552 and MOA J00562359−7221237.

Filter	Exposure time (seconds)	Total number of observations		
		MACHO*05:36:48.7 −69:17:00	MOA J005018.4 −723855	MOA J005623.5 −722123
Strömgren u	1200	176	168	211
Strömgren v	1200	52	...	...
Strömgren b	1200	34	...	...
Strömgren y	1200	27	...	...
I_C	400	163	193	240
V_J	700	410	183	230

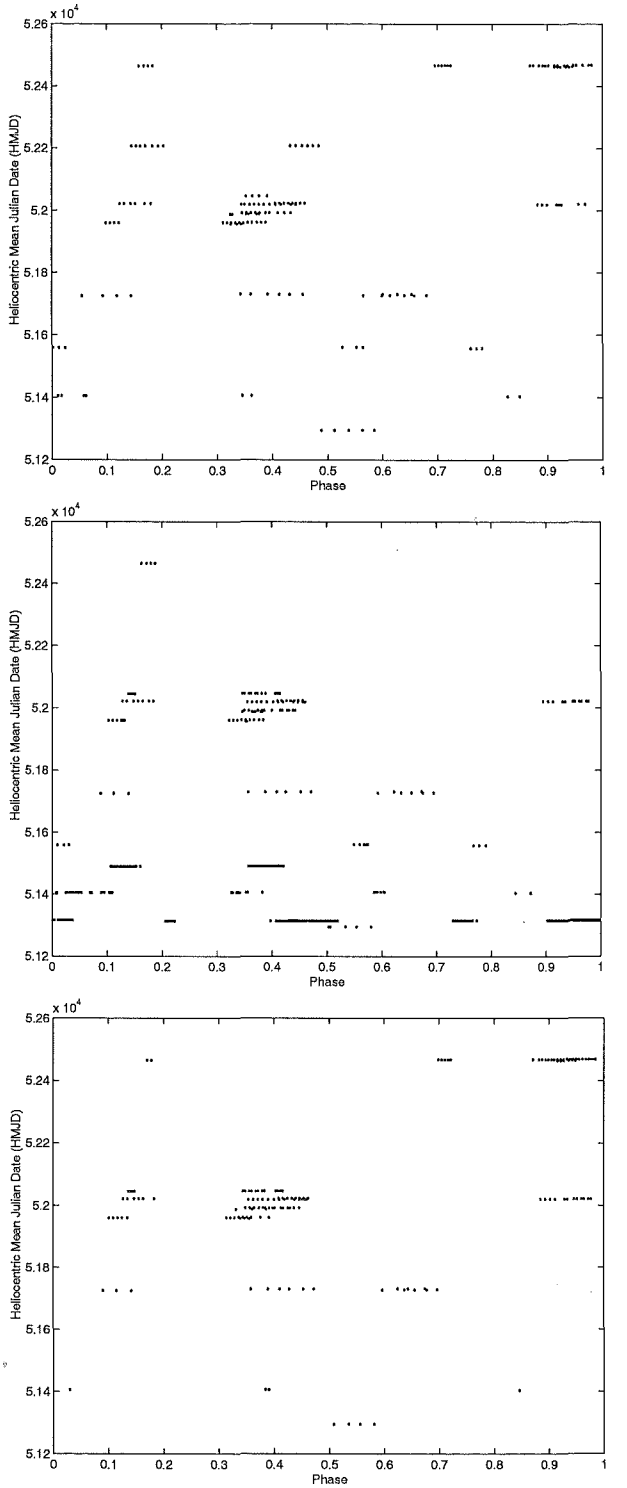

Figure 4.19: The observations for MACHO*05:36:48.7−69:17:00. These show the HMJD of the observations as a function of the phase for Strömgren u, V_J and I_C top, middle and bottom respectively. The observations span a range of 1268 days which corresponds to ~316 periods.

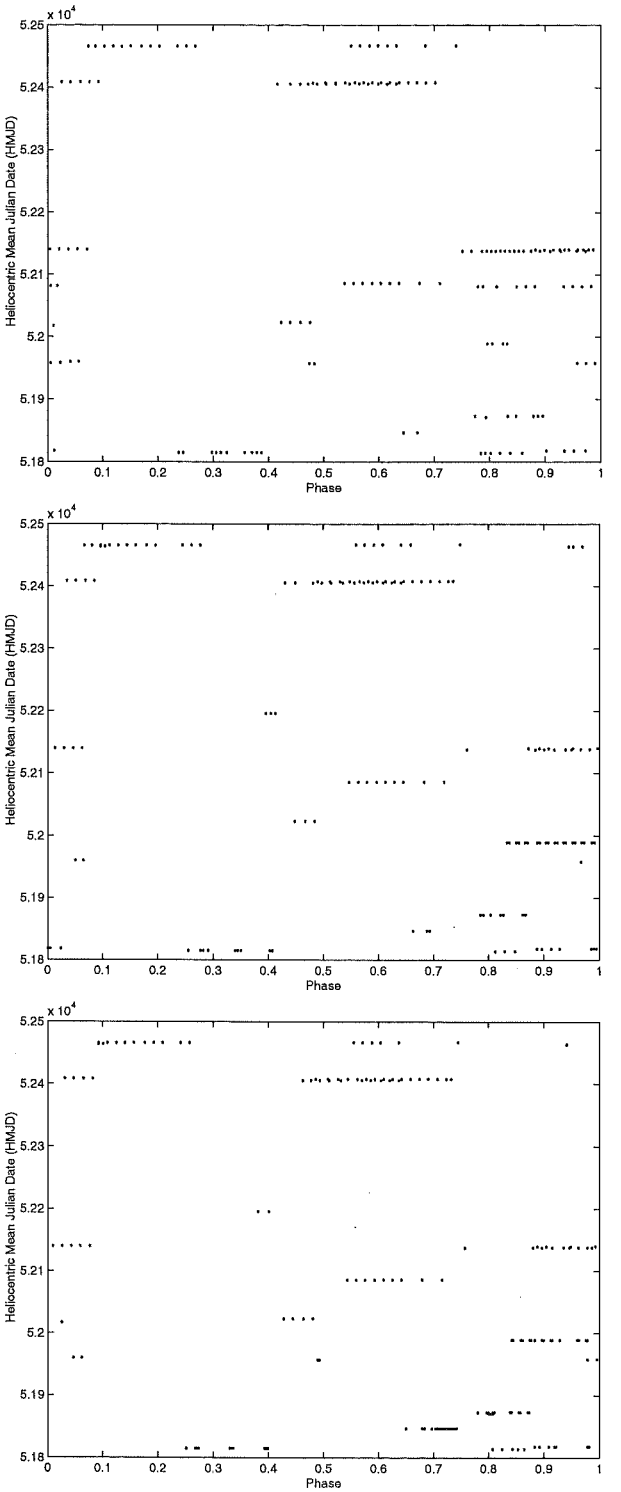

Figure 4.20: The observations for MOA J005018.4−723855. These show the HMJD of the observations as a function of the phase for Strömgren u, V_J and I_C top, middle and bottom respectively. The observations span a range of 618 days which corresponds to ~371 periods.

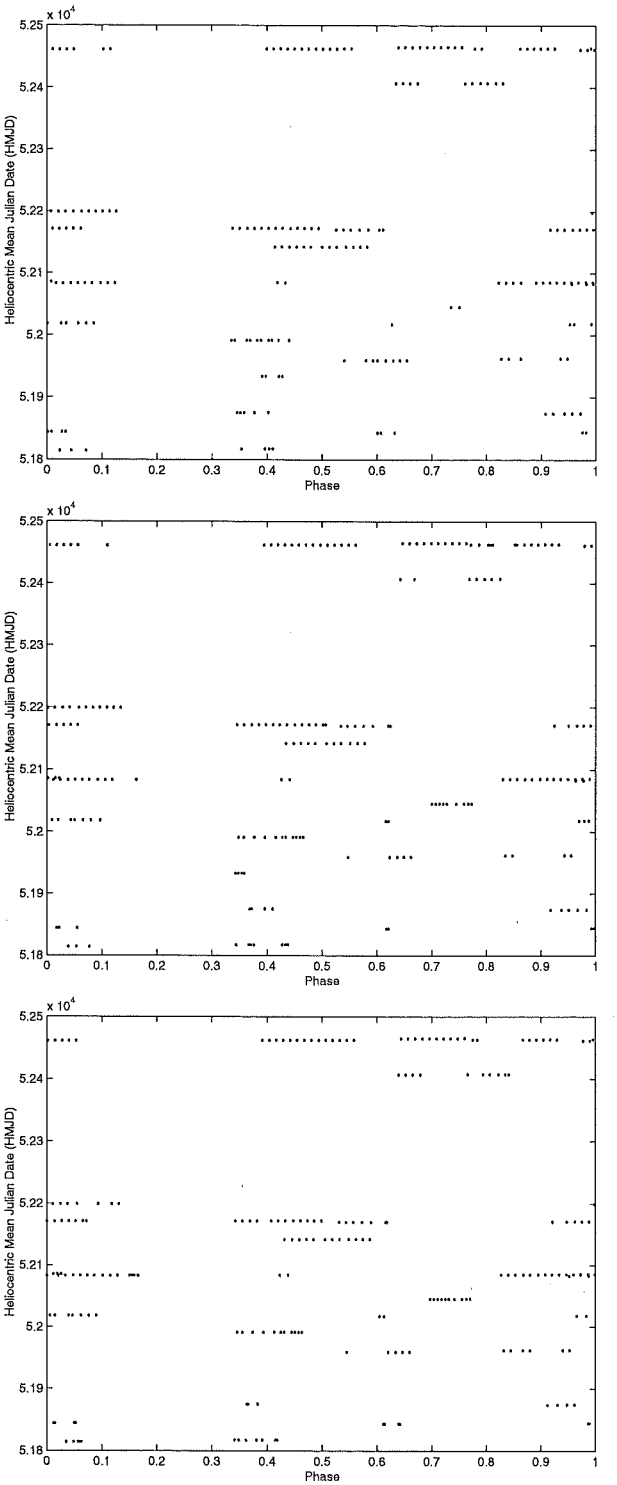

Figure 4.21: The observations for MOA J005623.5−722123. These show the HMJD of the observations as a function of the phase for Strömgren u, V_J and I_C top, middle and bottom respectively. The observations span a range of 682 days which corresponds to ~294 periods.

Chapter 5

Data reduction

The reduction of the science images is required in order to determine the flux received on Earth from the target star. Chapter 4 described the details and considerations of recording a stellar image with a CCD, now the images are examined in detail. The flux measurement needs to be free of any contaminants, i.e. dark current, quantum efficiency fluctuations, nearby stars etc. The data reduction process is an attempt to account for these and produce estimates of flux value for the star.

5.1 Data reductions

5.1.1 Crowding of the fields

The majority of new detections come from microlensing projects which need to observe crowded fields in order to increase the probability of the detection of a microlensing event. Ideally, the denser the field the better. Unfortunately, for accurate photometry, as required here in the order of $\sim$1%, the task becomes very difficult. If one is fortunate to locate an isolated target on the outskirts of the main search field where the stellar densities are reducing, the crowding issue can be avoided. The problem for accurate photometry is one of overlapping, or blending, of nearby stars with the target. Almost any target will have some form of contribution from a background star. In a sparse field this background star is extremely faint, so much so, that it blends into the background count unnoticed. In a crowded field, nearby stars overlap, either in front or behind, and add a considerable count to the total flux received from the target star position. In this case, the nearby stars must be accounted for and subtracted when determining the total flux of the target. The blended star or stars, may be, with some luck, non-variable (although with modern CCDs the non-variable star is becoming a rarity); if not, this is a further complication. The seeing often blurs these overlapping stars into one, as seen in Figure 5.1 and therefore the blended stars may only be clearly visible on the very best frames that are obtained during the observations of the target or from a larger telescope with higher resolution and better seeing.

5.1.2 Data reduction packages

Traditional methods have used software such as the DoPhot package for photometric extractions. The program uses a profile-fitting technique which determines the flux of a star on a given image by integrating over the star's profile. The program relies on the total flux from each component being known relative to a zero point. The difficulty arises when trying to determine each component's contributions to the flux levels, especially, as mentioned previously, when the blending of nearby profiles occurs in very crowded fields. This can lead to errors especially in the determination of eclipse depths and magnitudes which compound during the light curve analysis. Due to this, the general trend has been to avoid photometry in crowded fields.

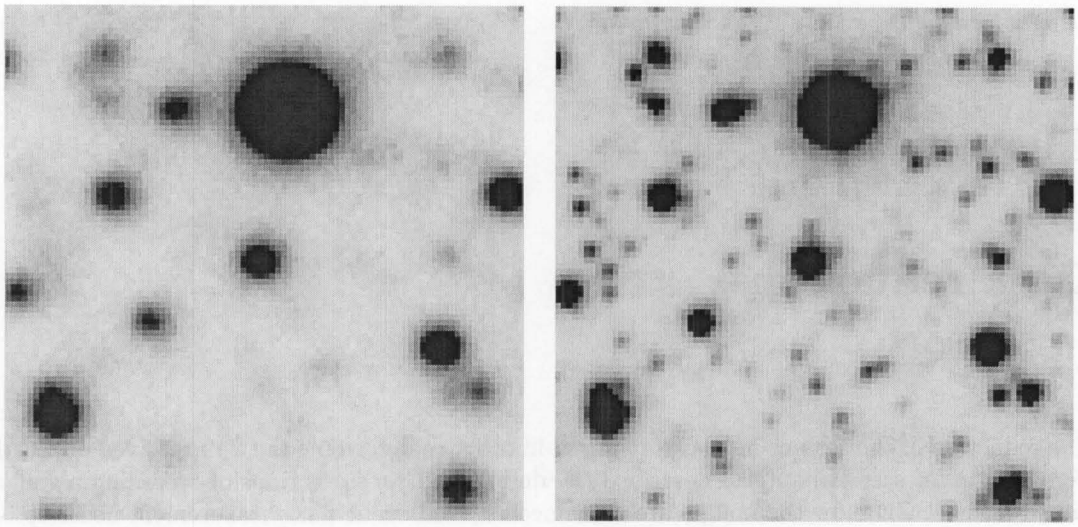

Figure 5.1: The two image are of the MACHO*05:36:48.7-69:17:00 taken under different conditions with the I_C filter. The fields are 1 arc min square with the target located in the centre. The left image, seeing ~3.7 arc sec, is a typical image acquired from MJUO. It appears there is only one star, the target, with no nearby stars. The right image, seeing ~1.8 arc sec, was acquired under good conditions. The presence of three nearby stars of significant brightness, is now apparent.

The MOA project, prior to their use of image subtraction reduction methods, used DoPhot. The initial input templates constructed used the best seeing frame to identify the positions of as many stellar objects as possible. However, if a variable star, microlensing event or nova had an initial brightness below the detection threshold of the templates and then increased in brightness beyond the detection threshold, they would not be detected, as they have not been identified on the template frame.

Many of the stars present in the CCD images will be of a variable nature. The variations can provide much information as to the stars' physical nature. We therefore want to select only the variables by subtracting the non-variable stars from the crowded frame relative to some reference frame i.e. work in flux differences, as proposed by Crotts [33]. The flux differences between frames, the AC signal (as termed by Wozniak 2001, [178]), varies about some arbitrary value as set by the reference frame. Many of the traditional photometry tools, such as those that use profile fitting techniques, e.g. DoPhot, estimate the DC signal, that is the total flux of the stars. However, because of difficulty in estimating the blending, it may be illusory to think that the zero flux level has been established correctly. Thus there is an advantage, if possible, in using only the AC signal. However, current light curve analysis codes assumes DC signals, but the AC variations can be calibrated to DC ones, albeit imperfectly. This can be a more realistic approach than assuming the DoPhot light curve is *the* definitive result.

5.1.3 The Image Subtraction method

The image subtraction method has several names; Difference Image Photometry, Difference Image Analysis, DIA, Pixel lensing and of course Image Subtraction. In this work the term Image Subtraction is preferred because the software used, ISIS-2.1, is dubbed Image Subtraction by its author, Alard.

The subtraction process requires the user to specify a reference frame on which the subtractions are based. This therefore defines the zero flux level. The actual phase of variability and total flux of the star are irrelevant (assuming the star isn't saturated). Before the two frames can be

subtracted, the seeing in both frames must be exactly matched. This is one of the more difficult and critical steps in the subtraction process, as the deviation of the convolution kernel needs to be determined with very high accuracy (i.e. as near as possible, exactly match the two PSFs). An early implementation of the subtraction method by Tomaney and Crotts, [154], [34], and Phillips and Davis [116], used the ratio of the Fourier transforms of a bright star on each frame. This was based on direct PSF matching, where a PSF model was constructed for each image, and used deconvolution techniques to find a kernel in Fourier space. This approach suffered from the problem of noise dominating at higher frequencies. Improvements in the method were made, but the optimal solution for the kernel is not found by this method. This gave results of varying quality for the convolution kernel and therefore for the subtraction process as well. This approach was used by MACHO in the re-analysis of their data [7].

A variation of the image subtraction method developed by Tomaney and Crotts was written by Alard and Lupton [3]. Their approach finds the optimal kernel solution, in real space, to give the best possible subtracted image. It is achieved by a least squares analysis using all pixels in both frames. In addition the method simultaneously fits a differential background. The result from the subtracted frame produces residuals that approach the level of the photon noise.

Another main difference between the Tomaney and Crotts approach compared to the Alard and Lupton approach is the choice of reference frame. The reference will be one of two options; 1. The worst frame or 2. The best frame.

If the worst frame is taken then all frames are degraded to this level. In doing so, the signal to noise ratio is reduced. Alard and Lupton used the best frame as their reference frame. However, by taking this approach, greater difficulty is encountered when aligning the frames to the best seeing frames.

The science images are all acquired at the telescope under slightly different conditions. Therefore a simple subtraction doesn't work. The following steps need to be considered in order to obtain the flux difference from the frames:

- A reference frame consisting of one or several frames must be constructed
- To subtract the frames, the alignment must be an exact match for each frame, therefore each frame must be scaled and transformed to a reference of some description
- Flux levels must be scaled, as must the background and any spatial variation in the background
- Once corrected the frames can then be subtracted to leave the variable images
- Some type of photometry needs to be done to retrieve the flux values relative to the reference level
- The light curve is constructed using the subtracted frames

The ISIS-2.1 package allows for the points mentioned.

5.1.3.1 Image subtraction

The following is a brief introduction to the Image subtraction method. Many image subtraction methods are based on very similar foundations, namely the optimal kernel solution method

introduced by Alard and Lupton, with slight variations in mathematical detail. A thorough detailed description of this process is presented by Alard and Lupton [3], Alard [2], Zebrun [183] and Bond [22].

Firstly, we consider two images $Im(x,y)$, current image, and $Ref(x,y)$, the reference image, acquired under different background conditions, $Bkg(x,y)$. The two image are related by a convolution kernel, $K(u,v)$ as given in equation 5.1:

$$Im(x,y) = K(u,v) \otimes Ref(x,y) + Bkg(x,y) \tag{5.1}$$

To solve the equation, the convolution kernel at a given location (x,y), is decomposed into a linear combination of basis functions, equation 5.2.

$$K(u,v) = \sum_n a_n(x,y) K_n(u,v) \tag{5.2}$$

Therefore the coefficients are spatially dependent and can be modelled as a linear combination of basis functions in the form of a two-dimensional polynomial. The coefficients in equation 5.3, are found by standard linear techniques.[1]

$$a_n(x,y) = \sum_{i,j} b_{i,j} x^i y^j \tag{5.3}$$

where i and j are polynomial indices dependent on the function index n.

These basis functions for the kernel are constructed from 2-dimensional Gaussian functions modified by polynomials, equation 5.4. This allows a very complicated kernel shape.

$$K_n(u,v) = e^{-\frac{(u^2+v^2)}{2\sigma_k^2}} u^i v^j \tag{5.4}$$

Regardless of the spatial variations of the kernel, the integral of the kernel across the chip is constant. This is required to ensure constant flux scaling (sum of the local kernel), as flux conservation for photometry is, of course, extremely important. Therefore at a given position (x,y), a set of basis functions needs to be constructed, which are simply linear combinations of the previous kernel basis functions, such that the sum of the all the basis vectors are zero, except the first, equation 5.5.

$$K'_n = K_n - K_0 \begin{cases} K'_0 & = K_0 \\ \sum\limits_{1,N} K'_n & = 0 \end{cases} \tag{5.5}$$

Therefore the kernel for a given position (x,y), is defined as given in equation 5.6.

[1] The equation $\mathbf{A}x=\mathbf{b}$ is solved for the coefficients x.

$$K(u,v) = a_0 K_0(u,v) + \sum_{1,N} a_n(x,y) K'_n(u,v) \tag{5.6}$$

where the coefficient a_n is a function of (x, y) and the function $K'_n(u, v)$ renders the integral zero for all but the first basis functions.

It is found that 3 Gaussians with polynomials of order 2 to 6 are sufficient to give residuals of the subtracted image in the order of $\sqrt{2}$ × photon noise.

The code for the image subtraction method used in this thesis was obtained from Alard's website[2] as *freeware*. The software installed was provided with a tutorial on the basic working of the package, although little in the way of detailed instructions was provided. Appendix A provides a description of the software and configuration files that are used to run the package. It also contains the settings used for the following reduction results.

5.1.3.2 Bug fixes

The ISIS-2.1 package was initially installed on an older version of Redhat Linux, 6.1, and compiled. The data output was compared to the test data supplied in the package as a check of the installation. In this instance, the installation was successful. At a later stage, the package was installed on another machine running a more recent version of the operating system, Redhat Linux 7.0. This time the output data was not in agreement with the test data. The problem was tracked to the version of the C compiler `gcc` being sourced and the use of the optimization switches by the code at the time of compiling the C code for installation. In the main package directory, the `install.csh` file sets the optimization switch for the environmental variable COPTS to `-O2`. The optimization is primarily to reduce running time, which is always needed in data reductions. In this case however, it is thought that the optimization is changing the program order in such a way that the functionality of the program is lost. As a result, the optimization was turned off using the `-O` switch and this rectified the problem and the test data now matched the output data. The optimization switches for `gcc` are described in detail in the manual file for `gcc`, available at the command prompt in Linux.

Another problem was encountered whilst running the script `detect.csh`. This produced a *segmentation fault* error which terminated the program immediately. This was due to the way the memory was being cleared in the `main.c` file in the subroutine `abs`. The end of the `main.c` file is a *for loop* that frees the memory, however this sometimes failed and crashed the program. The line was commented out to prevent this from happening. The program tries to keep all files open at once and this may contribute to the error. The operating system limit is 512 file handles, so a crash is expected if the number of files opened by ISIS-2.1 exceeds this.

5.1.4 Preparation prior to running ISIS-2.1

Before passing the science images to ISIS to process, the raw images need to be prepared. The corrections for the CCD, as mentioned in chapter 4, were made. The flow diagram in Figure 5.2 shows steps taken.

For each night's observations, a log file was produced for each target and filter combination. This listed the raw science images and the relevant dark and flat field images. From this, the

[2] C. Alard's website for downloading ISIS-2.1; http://www2.iap.fr/users/alard/package.html

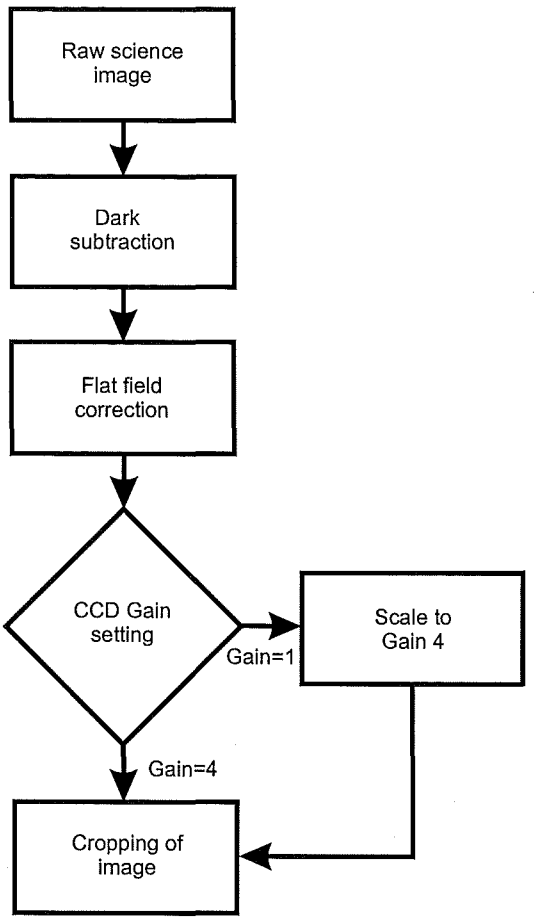

Figure 5.2: Flow diagram of the pre-processing of science images before they are passed to the ISIS image subtraction package for further reduction.

science images had the corrections applied, cropped and placed in directories for their respective filter and target where they were to be reduced by ISIS-2.1. An ASCII file named `dates` was constructed, containing the image file name and the respective Heliocentric Modified Julian Date, HMJD, of mid exposure. The HMJD was calculated using MIDAS, from the exposure times stored in descriptors located in the FITS headers of the science images. There were four different versions of FITS headers over the course of the observations, therefore making the task non-trivial as many had to be manually checked. The `dates` file was used by ISIS-2.1 to load the required images. In addition, another ASCII file was written containing the target name, filter, exposure time and CCD gain. This was a check to ensure that the individual directories contained science images for the same target and filter.

5.1.5 Selecting and building the reference frame

Selecting or constructing the reference frame is the most important step in the image subtraction process. This is because all other frames are compared to it i.e. a kernel is found that is the deconvolution of the current image frame and reference frame. There are two options available in selecting a reference frame, but the over-riding factor is the quality of the frame. The reference frame can be one frame, or a stack of frames. If only one frame is used then it must be *the best of the best.* The advantage to stacking images is the improvement of the signal to noise ratio, equation 5.7, however 4 images must be stacked in order to double the signal to

noise. The important point is that the quality of these stacked frames must be very similar. If one frame is of slightly poorer quality, then the final result is worse than if the image was excluded and a reduced signal to noise ratio in the reference frame is used. So if one frame is markedly superior to the rest, then only one frame should be assigned as the reference frame.

$$\text{Signal} : \text{Noise} \propto \sqrt{\text{Number of images}} \tag{5.7}$$

The ISIS-2.1 package contained a script called `seeing.csh` which determines the seeing, FWHM, in units of pixels of all the images listed in the `dates` file. In addition the seeing values for the cuts in the x and y directions are given. It was unclear how reliable this data was and if it could be used to assist in the selection of a reference frame and to discard bad frames.

The test data for the reduction process were the MACHO*05:36:48.7−69:17:00 V_J filter observations. This comprised some 400 observations of varying quality including pre and post auto-guide images. Each of these images was viewed and assigned a quality factor. This was done in order to check the values obtained from the `seeing.csh` script. The values were given in pixels[3] rather than arc seconds, but is somewhat arbitrary as the conversion is a constant, pixel value × 0.64. In most cases the values gave a reasonable estimate of the seeing as compared to the notes taken from visual inspection. This assisted in sorting the images by quality and resulted in the selection of several reference frame candidates. However in some cases, generally the u filter, the returned seeing values were anomalously low. In these cases, seeing values were obtained by fitting a Gaussian PSF to a selection of stars.

Approximately 20 images were selected for each star and each filter. They were examined based on their low seeing values (excluding the obviously incorrect very low values), generally within 0.3 pixels of the lowest value. The best reference frame candidates had typically values of approximately 3 pixels corresponding to 2 arc sec. This list quickly reduced as several were immediately seen to be of inferior quality. The final selection was made using the MIDAS `blink/image` command with the contrast levels matched as closely as possible.

Single reference frames were selected for some of the targets and filters, others were constructed from multiple stacked frames. The stacking procedure was done within ISIS-2.1. A file called `ref_list` contains the list of files to be used in the construction of the reference frame. The ISIS-2.1 subroutine `ref.csh` produces the reference image, `ref.fits`.

5.1.6 Running ISIS-2.1

A full description of the configuration files and running of the routines is given in Appendix A. The following is a brief description in order to make the results more comprehensible.

The ISIS-2.1 program requires the user to name an image to which all images are astrometrically transformed. The transformation can be one of or a combination of translation, scaling or rotation. If only one frame is selected as the reference frame, then this is also the astrometric frame. Where multiple frames were used to construct the reference image, one frame was required to be the astrometric transformation frame. This was taken to be the very best seeing frame based on the values obtained from the `seeing.csh` script. Often seeing values differ only

[3] f = 7.7 m, pixel size 24 μm square, conversion to arc seconds $\frac{180}{\pi} \times 60 \times 60$ = 206 264, giving $\frac{24 \times 10^{-6} \times 206\,264}{7.7}$ = 0.64 arc sec per pixel.

by a tenth or less of a pixel. No visible difference was obvious to the eye.

The seeing values obtained from the `seeing.csh` script spanned a large range, ~3 to ~13.5 pixels. A seeing value greater than 12.75 pixels was considered a very bad frame and marked for possible rejection. At this level of seeing, images were very blurred. This agreed with the quality factor assigned during the visual determination of image quality. All frames were initially passed to ISIS-2.1 in order to determine how poor a image ISIS-2.1 could process.

The ISIS-2.1 program is structured into 6 main subroutines which call many other sub-subroutines. These main 6 can be run separately, which is initially very advisable so the output can be examined. Figure 5.3 shows the subroutines executed.

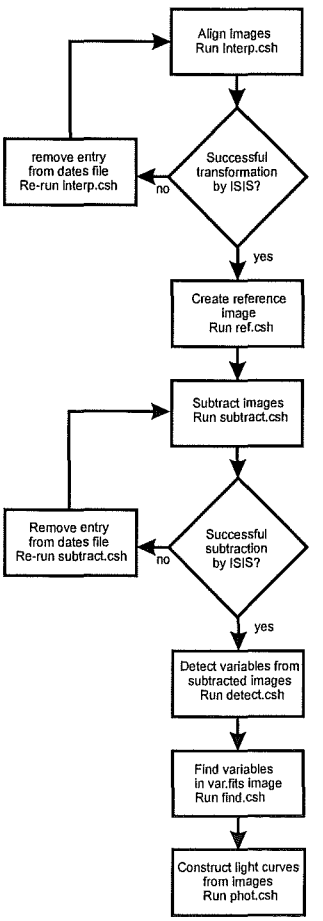

Figure 5.3: Flow diagram of ISIS-2.1 image subtraction software package.

The first script to run is `interp.csh` which aligns the images relative to the specified astrometric frame, Figure 5.5. At this stage, ISIS-2.1 selects areas called *stamps* around non-saturated bright stars in order to derive the kernel. Their size and number is set in the `default_config` file. A log file `log_interp2` is created by ISIS-2.1 which gives a summary of the transformations for each frame. An unsuccessful transformation is seen in the log file in two ways. Residuals from the transformation can be high, but this is not always the case. Alternatively, the number of stars used for the transformation is very low, typically less than 10 (`ndata` variable), whereas normally several hundred are used. An example in presented in Table 5.1. Therefore if the transformation was unsuccessful, the image entry in the `dates` file is removed. Additionally,

Table 5.1: An example of the expected output from the `log_interp` log file created while running the `interp.csh` subroutine, image registration and interpolation. A badly aligned science image `pf1937027.fits` is shown on the first line. Here the residuals (which are given in pixels) appear satisfactory but the number of stars detected, `ndata` = 5, and number used for the transformation, `nrest`, is very low, only 4. This is an indication of a badly aligned frame. The second line shows the astrometric alignment frame `pf1988038.fits`, note the zero residuals (this is due to the alignment frame being aligned with itself, so if the alignment process has been made correctly the residuals should be zero) and 500 stars selected on the frame to align the images. The remaining five entries are typical of the acceptable images processed.

sigmax:	0.097158	sigmay:	0.195752	ndata:	5	nrest:	4	pf1937027.fits
sigmax:	0.000000	sigmay:	0.000000	ndata:	500	nrest:	499	pf1988038.fits
sigmax:	0.104201	sigmay:	0.091162	ndata:	434	nrest:	410	pf2406032.fits
sigmax:	0.199937	sigmay:	0.160327	ndata:	387	nrest:	335	pf2406035.fits
sigmax:	0.137226	sigmay:	0.122202	ndata:	425	nrest:	379	pf2406038.fits
sigmax:	0.174857	sigmay:	0.178268	ndata:	413	nrest:	381	pf2406041.fits
sigmax:	0.283782	sigmay:	0.297025	ndata:	349	nrest:	342	pf2406044.fits

images that have large transformations were checked. The large shift was found to be due to either: 1, an error in positioning of the star; or 2, cloud cover had obscured most stars and ISIS-2.1 was attempting to align images on only the few bright stars in the frame that were visible. The images in both of these cases were rejected and removed from the `dates` file.

If these images were left in the `dates` files, they caused serious problems at later stages. Because of the large translations due to the alignment, the images could be rotated or have only a small portion of the image showing. This presents two possible outcomes. Firstly, if the image undergoes a large translation, then the remainder of the frame is blanked out, at the zero level. A problem now occurs at the subtraction and variable detection stage. The effective subtractable area is reduced. An example of this is given in Figure 5.4. The reduction depends on the amount of translation. Secondly, if a large rotation has occurred or the image is the wrong field, then the alignment takes place on a few stars. However, the first problem will most likely occur but in addition, the majority of stars are not aligned. Once `detect.csh` is run, all the stars then appear to have varied as the fluxes are different. Therefore, the subtracted image looks very similar to the reference image. This follows on to the variable detection, as a majority of stars (depending on the severity of the alignment error) all appear as variables, hence giving a completely incorrect reduction result. This is very important at the telescope, as the target needs to be positioned at the same pixel location on the chip (at least within a few pixels) for each exposure otherwise the area over which the image subtraction is effectively working is dramatically reduced. The observations for this work had this procedure of target placement, but it was due to flat field issues not for the reasons mentioned above, because they had not been appreciated at the time.

The running of `ref.csh` produces the reference frame, Figure 5.6, as specified. This is either from a single frame or from several frames. The reference frame is aligned to the astrometric frame during this procedure.

The subroutine `subtract.csh` is the main part of the image subtraction process and the most CPU intensive. The deconvolution kernel image is written to disk in the form of a FITS file, Figure 5.7 and provides a view of the quality of the subtraction process. This together with the output from the subtraction log file `log_subtract`, Table 5.2, can be used to monitor changes made to the parameters in the configuration files. This was employed when initially deciding on the parameters to set for the reduction process. Due to the large numbers of parameters it is not cost effective, in terms of time, to try all combinations.

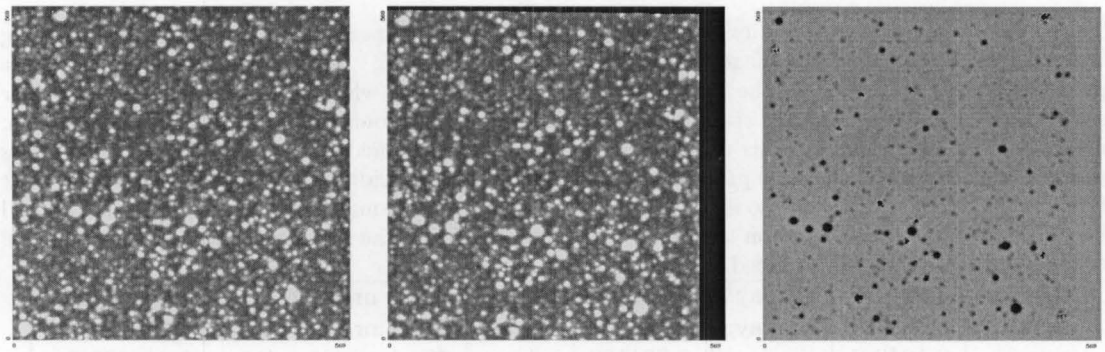

Figure 5.4: MOA J005018.4−723855, V_J filter. The science image, `pf1937027.fits` is shown on the left. Due to the target not being at the same position as on the reference frame, the alignment frame shows a translation and rotation, `interp_pf1937027.fits`, centre image. This mapping follows through to the variable frame, `var.fits` (right image), as the usable image size is now reduced. Therefore, if a star position varies considerably, the `var.fits` frame will show only a small proportion of the original reference frame. This also applies to very bad seeing frames, where only a few stars are used for the alignment process and therefore severe mis-alignment can occur.

Table 5.2: An example of the output from the `log_subtract` log file created while running the `subtract.csh` subroutine, image registration and interpolation, on the same files as in Table 5.1. The first line contains the badly aligned science image `pf1937027.fits`. The mean is the mean sigma of all the *stamps* selected to derive the kernel solution. The scatter is the scatter of the sigma distribution. The very high mean and scatter are indicative of a bad image and also a bad alignment from `interp.csh`. The astrometric alignment image shows small residuals, as it is only slightly different from the stacked reference image (this being one of them). The remaining entries show typical values from the subtraction process.

mean:	85.028904	scatter:	88.145050	pf1937027.fits
mean:	0.414364	scatter:	0.048695	pf1988038.fits
mean:	1.030358	scatter:	0.647718	pf2406032.fits
mean:	0.705696	scatter:	0.127018	pf2406035.fits
mean:	0.855175	scatter:	0.309573	pf2406038.fits
mean:	0.851066	scatter:	0.305975	pf2406041.fits
mean:	0.842125	scatter:	0.323073	pf2406044.fits

After the subtraction subroutine is complete the frames are stacked and the variables detected using the routine `detect.csh`. It produces the two images `var.fits`, mean of the absolute normalized deviations, Figure 5.8 and `abs.fits`, mean absolute deviation. The `var.fits` file, Figure 5.8, is used to then determine the maximum intensity value and position (in x,y frame coordinates) of the variable target by using some FITS viewing program, e.g. MIDAS or GAIA.

The `find.csh` routine, locates all stars whose maximum intensity value is greater than the value set by the parameter SIG_THRESH in `process_config`. In this case, only the target star is of interest. Therefore SIG_THRESH is set just below the value obtained for the target. This therefore gives a list of intensities along with their associated positions, greater than or equal to the target. This is written to the log file `phot.data`. The value of SIG_THRESH could be set to zero, however all stars would be selected. The `phot.data` file is then edited to contain only the variable target, which is identified by its coordinates on the `var.fits` frame.

The photometry script `phot.csh` is now run to build the light curve(s) of the star(s) listed in the `phot.data` file from the subtracted images. The output for each frame gives the flux

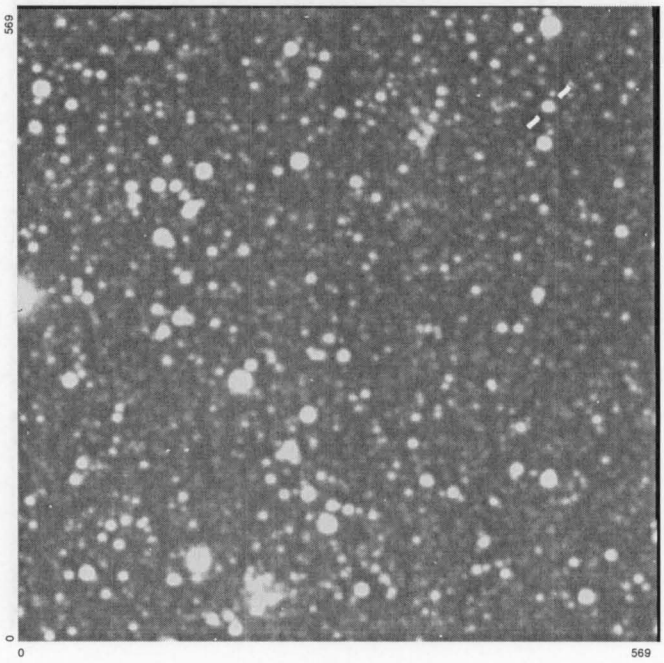

Figure 5.5: The image shown here is of MOA J005018.4−723855, V_J filter, `pf2406038.fits`, after the `interp.csh` alignment procedure. A border is apparent about the edges of the frame due to the alignment process. The image has been translated by 3 pixels to the left and 2 pixels down. Also the image has been rotated anti-clockwise by about a degree. The target, upper right, is indicated by two diagonal bars.

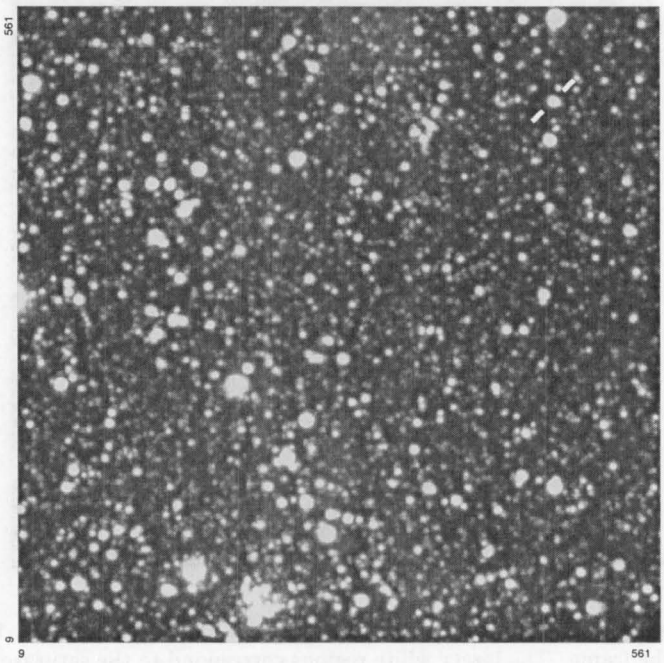

Figure 5.6: The image shown here is the stacked reference image for MOA J005018.4−723855, V_J filter. The reference image was constructed using the images, `pf1988038.fits`, `pf1988039.fits` and `pf1988043.fits`. The signal to noise ratio has increased by $\sim \sqrt{3}$ =1.732 by stacking the three frames. The target, upper right, is indicated by two diagonal bars.

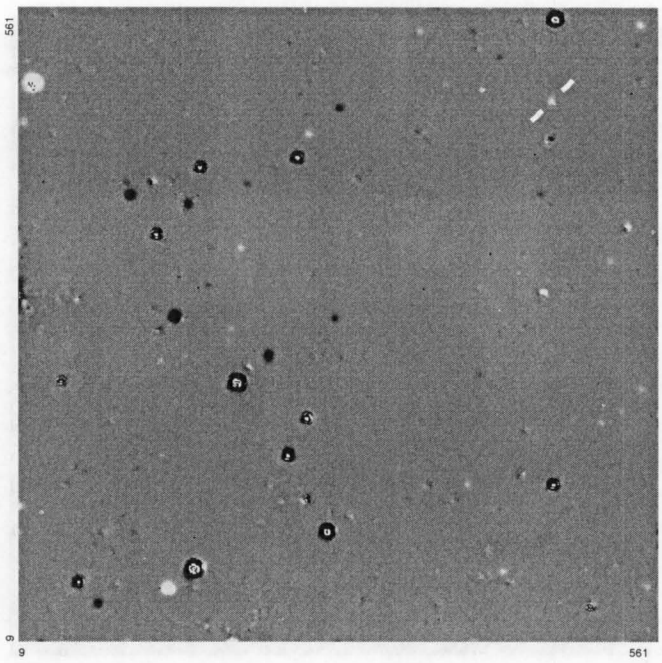

Figure 5.7: The image shown here is the convolution of MOA J005018.4−723855, V_J filter, `conv_pf2406038.fits` reference image and a typical science image. The larger dark regions with white centres, and vice versa, are saturated stars on the frames. The remaining black or white spots indicate variable non-saturated stars.

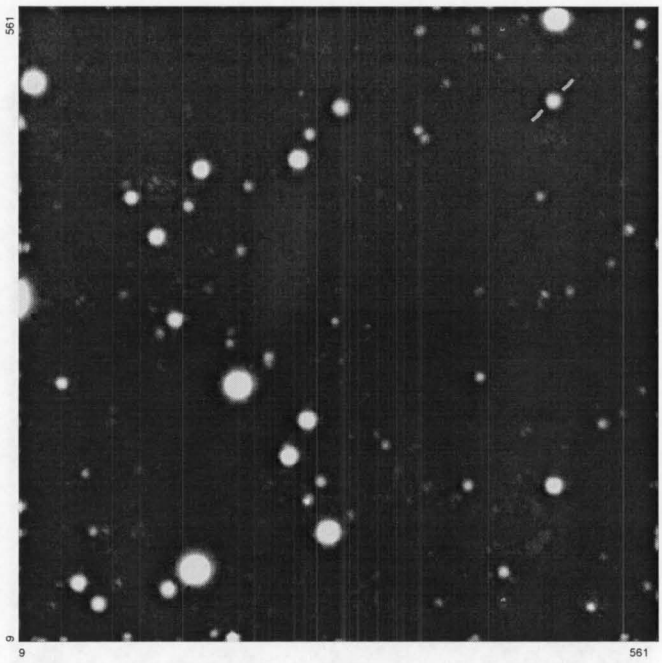

Figure 5.8: The image shown here is the `var.fits` for MOA J005018.4−723855, V_J filter. This shows the variable stars in the frame. The larger white regions correspond to the saturated stars. The smaller white or black region are variable stars. The white or black regions are values above and below the zero respectively. The reference frame defines the zero level. The white regions, residual areas, around the border of the `var.fits` frame are due to the fact that convolution has been used twice; once to build the reference and another time to make the subtraction. Due to this effect, variables cannot be detected if they are located less than the kernel size from the image edge.

difference between itself and the reference frame. The reference frame corresponds to the zero of these differences.

The light curve can then be phased and displayed; MIDAS and MATLAB were used for this.

A note of caution should be sounded concerning ISIS-2.1. It was found to append **or** overwrite files. It is therefore prudent to delete all files, except the images to be processed in the images directory, before commencing the next run. If this is not done, and parameters changed, the results could be meaningless or at least very confusing as old versions of some files were used.

The ISIS-2.1 routines were run in a script to minimize user input. Prior to running the `find.csh` subroutine, the `var.fits` and `abs.fits` files were checked in order to determine the SIG_THRESH value as previously mentioned.

The ISIS-2.1 reductions were run on a computation server. Run times therefore varied depending on loadings. A run-time of approximately 1 minute per image was typical. Since all the images for a given filter and target were reduced together, times of approximately 3 hours were common. The number of files produced by ISIS-2.1, especially the FITS files, requires a minimum amount of disk space present before starting. Typically an additional 3.5 MB is required for each 1 MB of image. The memory requirement, RAM, should be greater than the size (MB) of the total number of images. This is due to all files being held open during the variable detection process, when running `detect.csh`.

5.1.7 Photometry in ISIS-2.1

The photometry, flux extraction, in ISIS-2.1 is performed via fitting a PSF to the stars on the frame. The limits of the PSF are defined by four parameters, whose values and sensitivity all affect the final value of the flux in varying ways. With reference to the PSF of the image, an approximate value for the radius of the annulus which estimates the background is required. This is defined using two parameters; 1. `rad1_bg`, the inner radius of the annulus. 2. `rad2_bg`, the outer radius of the annulus. These were set to 15 and 20 respectively.

The radius of a circle within which the pixels of the object will be fitted by the PSF in order to estimate the flux is given by the parameter `rad_phot`. The radius for the flux normalization is given by the parameter `rad_aper`. Both parameters are very important and sensitive, especially `rad_phot`, as they have a strong influence on the value of the estimated total flux, Figure 5.9. The issue of where the PSF fitting stops and the background begins is discussed in section 5.8.4. Figure 5.9 shows the amount of flux from increasing values of `rad_phot` which peaks at values of 6 and 7 (slightly more positive values at `rad_phot` = 7). A value slightly less than the peak value was chosen as too larger value can increase the contribution from the nearby background field stars. The value of `rad_aper` is recommended to be set to 2 increments higher than `rad_phot`. Therefore the values for `rad_phot` and `rad_aper` were set at 5 and 7 respectively.

5.2 Check stars

In CCD photometry small fields, as in this case, generally suffer the same atmospheric perturbations. Hence when using reduction packages such as DAOPHOT ([142], [143], [146], [144], [145]) a variable-comparison is required to remove such effects. In image subtraction however the correction for the differential background on the reference frame is the equivalent proce-

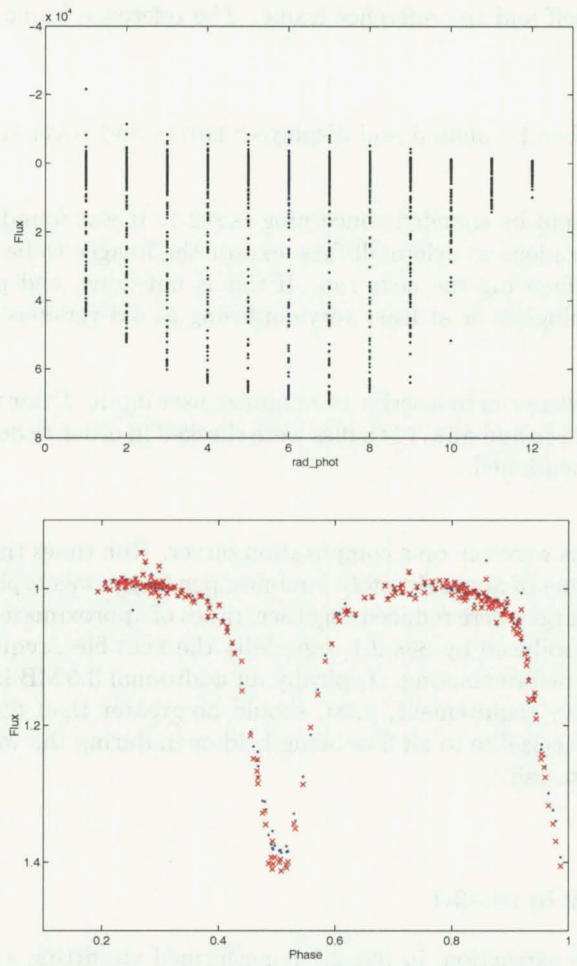

Figure 5.9: Photometry extraction on a given frame for a given star using various values of `rad_phot` gives various estimates of the total flux, top figure. The values of `rad1_bg` , `rad2_bg` and `rad_aper` were fixed at 15, 20 and 7 respectively. The lower figure shows the difference using two different values of `rad_phot`, 3 and 5, (indicated by • and × respectively), with other parameters values set as before. The eclipse depths are greater for the larger value of `rad_phot`. Therefore if comparing light curves from difference bandpasses, if is essential to have a reasonable value of `rad_phot` set. Note, the light curve has not been *cleaned* of rough points, i.e. those at phase ~0.3.

dure. The following is a check to ensure this procedure satisfactorily accounts for the required corrections.

Check or comparison stars can be used to reduce the nightly variations in the signal due to atmospheric effects. If a check star exhibits a variation in light from its usual flat light curve due to atmospheric conditions then the variable star will experience a similar effect[4]. Subtracting the constant star from the variable star should ideally remove these effects. Several check stars can be added together to increase the signal to noise, however, the variation in the eclipsing binary light curve is far greater than the noise in a single check star, therefore this was not pursued. In this case, the check stars were used as an indicator of the quality of the photometry.

Several check stars were identified on each frame by using the respective `var.fits` image. When

[4]Similar in terms of the light path is different for the check and variable, but the scale of variations are considered larger than the difference in the path differences.

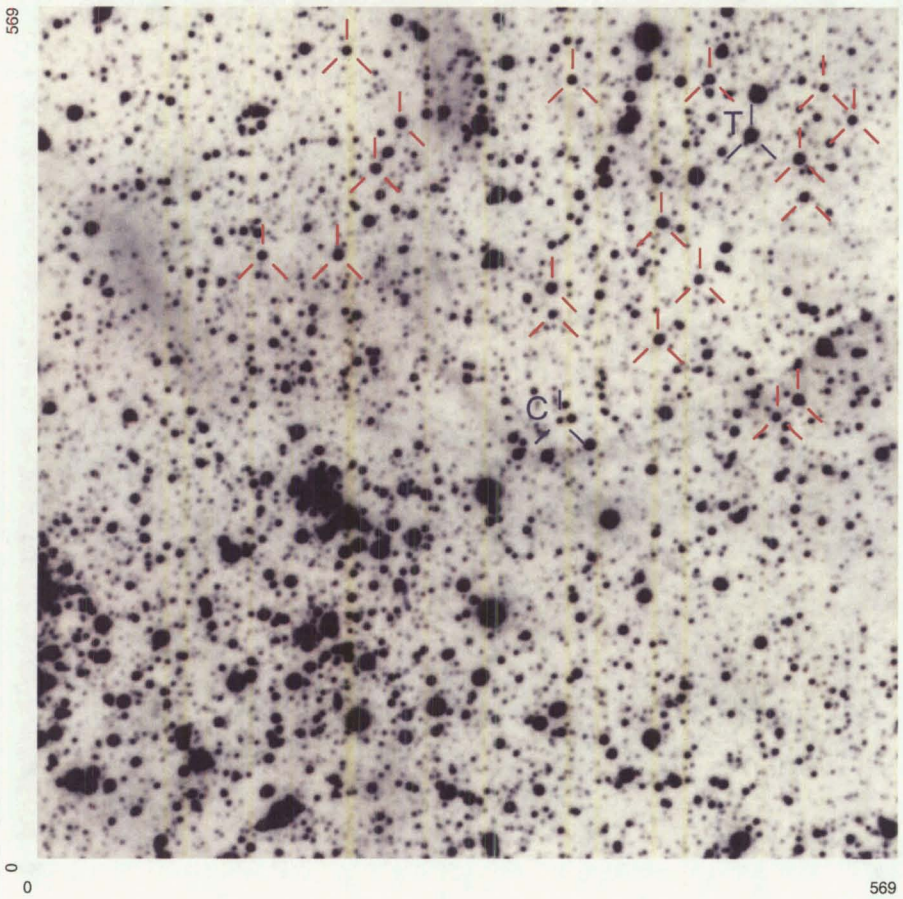

Figure 5.10: The reference frame for MACHO*05:36:48.7−69:17:00, V_J bandpass, with target (T) and check stars. The selected comparison star is indicated (C).

blinked with the reference frame, the constant stars disappear as they are only present in the reference frame. Several stars of similar flux values on the reference, which itself is designated as the zero flux level, were identified as possible constant stars. The light curves for these were then extracted using ISIS-2.1. Photometry was obtained by setting the variable threshold parameter to the limit of the faintest star that was considered a constant. The `detect.csh`, `find.csh` and `phot.csh` routines were run on the original frame to obtain the positions. The resulting `phot.data` file was edited to contain only the possible constant stars of interest. The `detect.csh` was edited to take the `ref.fits` rather than the `var.fits` file. Photometry was then obtained from the subtracted frame `var.fits` for the possible constant stars. Their respective light curves were output and plotted using the same methods as for the variable stars.

Their light curves were then examined for any variation that wasn't noise and also compared to the variable star light curve. The scatter of the base level of the variable was compared to the scatter in the check star. A variability level was set to aid in the determination of whether a check star was indeed a constant. The check stars' level was similar to that of the background. The variable detection had trouble identifying these stars on the variable frame. In most cases a small residual was the only remnant. This helped to serve as a check for a constant star.

The reference frames of the possible check star candidates in each bandpass were viewed in order to select stars with similar colour to that of the variable. Most stars were unsuitable as

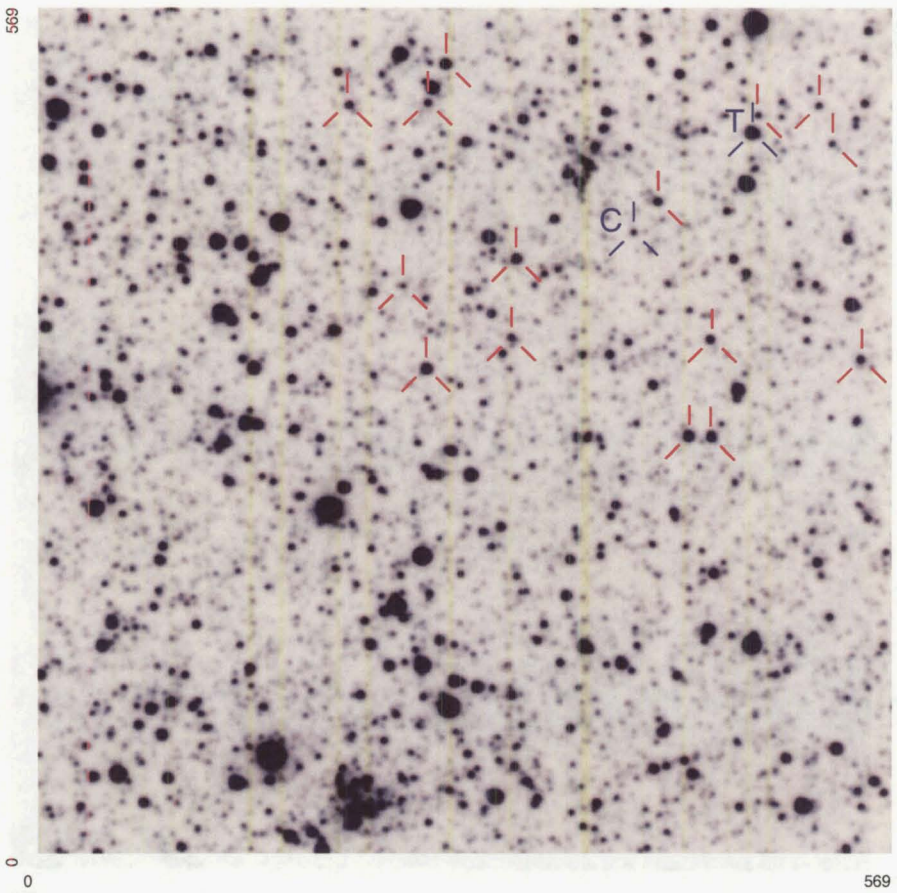

Figure 5.11: The reference frame for MOA J005018.4−723855, V_J bandpass, with target (T) and check stars. The selected comparison star is indicated (C).

their flux decreased markedly in the u bandpass, ~300 to 380 nm indicating the stars were too cool. Stars which had similar brightness in each frame or brightness ratio as the target would be considered good candidates.

A number of check stars in the order of 15 to 20 were selected. Most were selected to be within the quarter of the chip (one quarter, 285×285 pixels, of the extracted format) that contained the target star. This selection was made in order to reduce any variation present across the chip. The selected constant stars are given for MACHO*05:36:48.7−69:17:00, MOA J005018.4−723855 and MOA J005623.5−722123 in Figures 5.10, 5.11 and 5.12 respectively.

The light curves of the check stars were then plotted with the variable. This enabled the data of poorer quality nights to be examined in order to determine if any correlations existed. The data of the V_J bandpass for MACHO*05:36:48.7−69:17:00 showed regions of phase that had distinct variations, most likely from poor quality nights. These variations were also shown in the constant star light curves. Plotting the flux versus HMJD clearly showed the large variations. This enabled the data to be cut by specifying a 3 sigma cut level.

The check star light curves were analysed and the *most constant* light curve was selected based on its low sigma value.

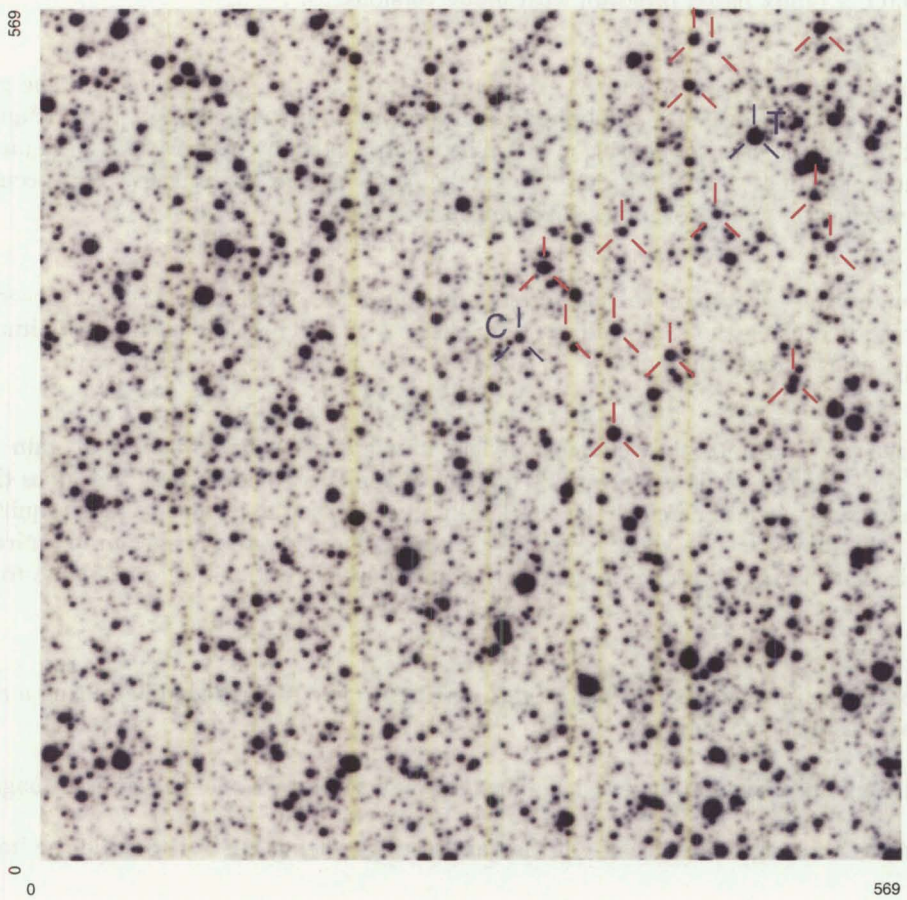

Figure 5.12: The reference frame for MOA J005623.5−722123, V_J bandpass, with target (T) and check stars. The selected comparison star is indicated (C).

Figure 5.13 shows the light curve of the check star for MACHO*05:36:48.7−69:17:00 V_J bandpass as indicated in Figure 5.10. The photometry of the comparison star is shown in the top left of Figure 5.13. The variable − comparison is shown in the top right of figure 5.13. Points greater than 3 sigma were removed as these were most likely rogue points, details on the top right plot, Figure 5.13. The mean and sigma were then recalculated, as indicated on the top left plot, Figure 5.13, details top right plot. The variation in the comparison star light curve is seen, top right plot, to coincide with region of high scatter in the variable light curve. The light curve of the variable is plotted, bottom left with the variable − comparison plotted in the bottom right, Figure 5.13. Although a slight difference is evident, it does not account for all the scatter in the variable light curve. The scatter in the variable is of greater amplitude than the scatter in the comparison for the same phase.

5.2.0.1 Gain differences

During the observational programme, several data acquisition programs were used.

- PM3000, with FORTH based software
- VWIN, a Windows based program

- MOJO, a Linux based program with many versions

This unfortunately led to an operator error with regards to the data recording. The gain was originally set to 4, however several observational sessions later a software upgrade defaulted the gain back to 1 in the user configuration file. The result was many observations were made with gain 1 and not gain 4. Therefore there are two gain settings for the images. This occurred for 5 observing runs between November 1999 and March 2001.

For each night's observations, the dark frames and *dome* flats, pre and post science observations, were all recorded using the same gain setting, either 1 or 4. Therefore each night's images can be reduced using one setting only.

Since fluxes are scaled to the reference image, it might seem irrelevant what gain is used. However the software needs to know how many electrons were collected as this gives the noise properties of the image. Therefore the CCD gain, in this case the inverse gain, is required. The software only allows for one value for all the images. Therefore the images are required to be processed with the same gain (inverse gain). Three possible options were available to achieve this:

1. Process the images grouped by the gain settings in two separate batches using a reference image of the same gain.
2. Multiply all pixels in images with gain 1 by 3.89 to be equivalent to gain 4 images.
3. Process all images irrespective of the gain settings letting ISIS-2.1 to scale the images.

Using two groups with different gain settings posed problems. Firstly, two different reference images were required. This meant the one would not be the best and therefore the quality would be reduced. Secondly the results had to be combined at the end. Because the zero point for the flux is based on the flux level of the reference, this meant that the two final light curves had to be offset by a constant in order to agree with each other.

The second option was implemented. This simply required an extra step in the pre-processing stage where the image pixel values are multiplied by the value 3.89, which is the difference in the conversion factor where $\frac{\texttt{inverse gain 1}}{\texttt{inverse gain 4}} = \frac{4.74}{1.22} = 3.89$. This ensures all images are scaled so the correct number of electrons are derived when this value is used on all images. The other factor to be considered is the saturation levels. If the a star is saturated or saturated once multiplied by the conversion factor, then the relevant pixel values are set to 65535, the saturation value.

Option 3 would be the easiest to implement as no changes would be required. However it cannot be used as one gain setting is required in the ISIS-2.1 reduction process and is considered constant for all images. The noise properties would therefore not be scaled properly. By mixing the gain 1 and gain 4 images and processing together, a gain would nevertheless required to be specified. This would inevitably be the gain of the reference frame. For all frames not with this gain, ISIS-2.1 treats these as having a strong variation in their background and makes the appropriate correction. Due to this, the light curve of the mixed gains and that where all images have been scaled to have the same gain, look very similar, Figure 5.14. Clearly due to the very similar results, the number of electrons collected is not what is limiting the precision of the photometry. This result gives an indication that ISIS-2.1 performs the background variation correction satisfactorily.

5.3 LMC eclipsing binary MACHO*05:36:48.7−69:17:00

5.3.1 Strömgren v, y and b filters

Initial observations were conducted using the Strömgren u, v, b, y filters, and the V_J and I_C filter, Tables 5.3 and 5.4. After several runs, it was decided to omit the Strömgren v, b, y filters. Standard photometry was not the primary goal, rather the building of the light curve to obtain the flux differences with a high internal precision. This, together with the long exposure times (1200 seconds each) of the Strömgren v, b, y filters, made data recording using these of little value compared to the effort required. Additionally, the b and y filters were of dubious quality as the physical condition of the these two filters showed deterioration. Observations with them gave ring structures around stars, possibly an indication a type of de-lamination of the filter's interference layers. The ring structures were noted by Pritchard [123]. Therefore it was considered more appropriate to use the Strömgren u, Johnson V_J and Cousins I_C filters which are primarily made of glass. This selection gave the greatest wavelength coverage and therefore the greatest handle on the stellar temperatures.

Table 5.3: The number of observations made in the Strömgren filters v, b and y not used in the data reductions. All observations are for the MACHO*05:36:48.7−69:17:00.

Strömgren filter	Total number of observations
v	52
b	34
y	27

Table 5.4: The number of observations made in each of the filters Strömgren u, Johnson V_J and Cousins I_C for MACHO*05:36:48.7−69:17:00. Not all observation were used in the reduction process, mainly due to poor weather conditions, resulting in several for each filter being discarded. These numbers were further reduced in the light curve analysis.

Filter	Total number of observations	Number of observations used in the reductions	Number of frames used for the reference
u	176	165	2
V_J	410	391	1
I_C	163	155	3

5.3.2 u, V_J and I_C filters

The greatest number of observations was completed using the V_J filter, a total of 410, nearly twice that of any other filter for its associated target, Table 5.4. Initial cuts for bad frames were made from the seeing and interp log files (See appendix C for a listing of the images used in the reduction process). A majority of the images were acquired pre-autoguide and also in rather bad seeing conditions. Although high in quantity, the quality is not the most desirable.

The results of the reductions of MACHO*05:36:48.7−69:17:00 using ISIS-2.1 are presented in figure 5.15. Here the reference frame and resulting `var.fits` frame is given. The variable frame shows the target, as indicated, along with several other variables. Only the target light curve was constructed using `phot.csh`.

5.4 The MOA targets

Observations of the two MOA targets, MOA J005018.4−723855 and MOA J005623.5−722123, were recorded in the u, V_J and I_C filters, (Tables 5.5 and 5.6). Both are located in the SMC.

5.4.1 MOA J005018.4−723855

Reasonable phase coverage in all filters was achieved for this target. The images, were on average, recorded in better conditions than those of MACHO*05:36:48.7−69:17:00.

Table 5.5: The number of observations made in each of the filters Strömgren u, Johnson V_J and Cousins I_C for the MOA J005018.4−723855 target. The discarded frames could not be processed by ISIS-2.1. These numbers were further reduced in the light curve analysis.

Filter	Total number of observations	Number of observations used in the reductions	Number of frames used for the reference
u	168	154	5
V_J	183	146	3
I_C	193	159	3

The reduction results using ISIS-2.1 are presented in figure 5.16. Given are the reference frames the variable frames for each filter. The target is indicated in each frame. The I_C bandpass image showing the larger amount of variable, residuals, mostly due to the contrast level (cuts level) used to clearly indicate the target. Similar residual are seen in the u filter but to a lesser extent.

5.4.2 MOA J005623.5−722123

Complete phase coverage of this target was not achieved, with a gap between 0.0 to 0.15 phase. This results in half of the primary eclipse not being present. However reasonable phase coverage of the remaining curve was achieved. This was the case for all filters and was due to timing of observation schedules and weather.

Table 5.6: The number of observations made in each of the filters Strömgren u, Johnson V_J and Cousins I_C for the MOA J005623.5−722123 target. The discarded frames could not be processed by ISIS-2.1. These numbers were further reduced in the light curve analysis.

Filter	Total number of observations	Number of observations used in the reductions	Number of frames used for the reference
u	211	200	11
V_J	230	207	11
I_C	240	220	1

Figure 5.17 presents the reduction results using ISIS-2.1 showing the reference frames and respective variable star frames `var.fits`. The target is indicated in all frames. The variable star frame for the u bandpass has a white speckle appearance due to the contrast level (cuts level) used to indicate the target position.

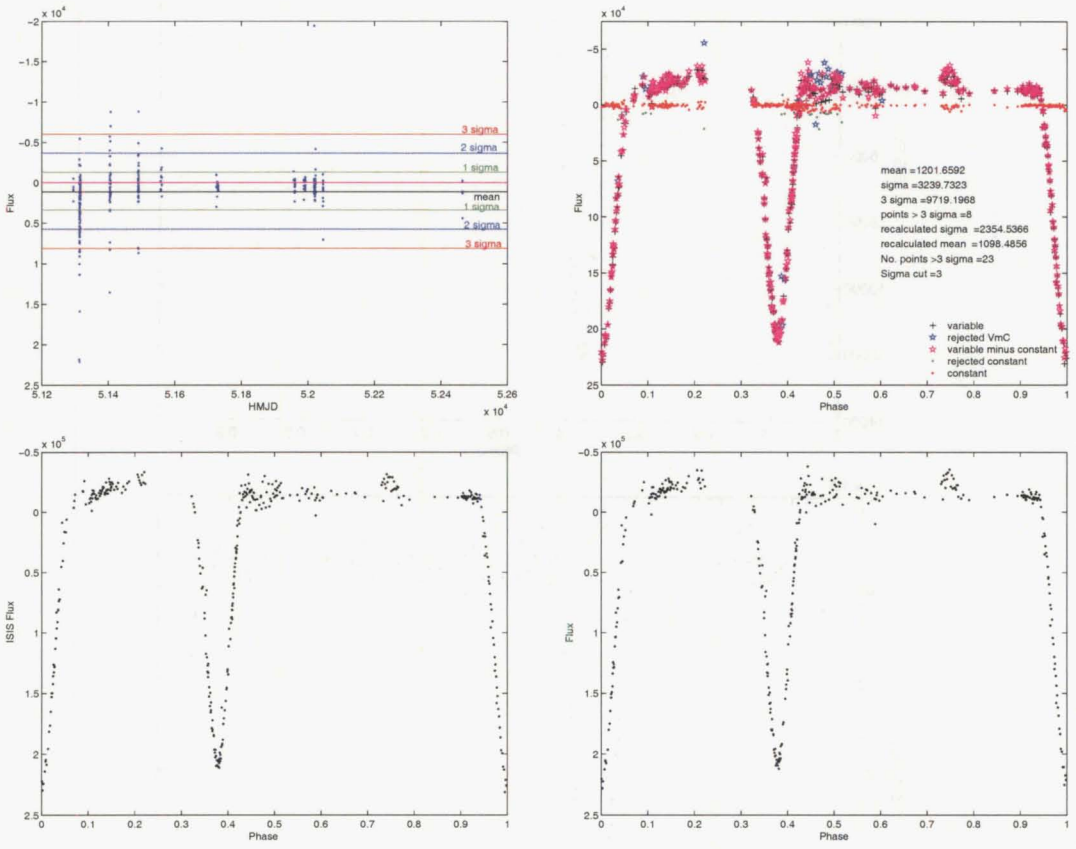

Figure 5.13: Light curve of the comparison star for MACHO*05:36:48.7−69:17:00 V_J bandpass. The top left figure shows the data collected on each night for the comparison star. A nightly spread is evident in the data as the conditions changed over the course of the night. An initial removal of points over 3 sigma was made followed by the recalculation of the mean and 1, 2 and 3 sigma levels as indicated. The zero flux level is also indicated. The top right figure has the comparison star (phased to the period of the variable) and variable star over plotted together with the variable minus comparison. Points greater than 3 sigma are indicated together with the values of the mean and sigma for the comparison star. Variations in the comparison star light curve coincide with variations in phase of the variable star. This indicates that the atmospheric conditions have distorted both light curves. This effect is then removed from the original light curve, bottom left, leaving a light curve given in the bottom right figure. The scatter in the variable is of greater amplitude than the scatter in the comparison for the same phase and therefore is not fully removed.

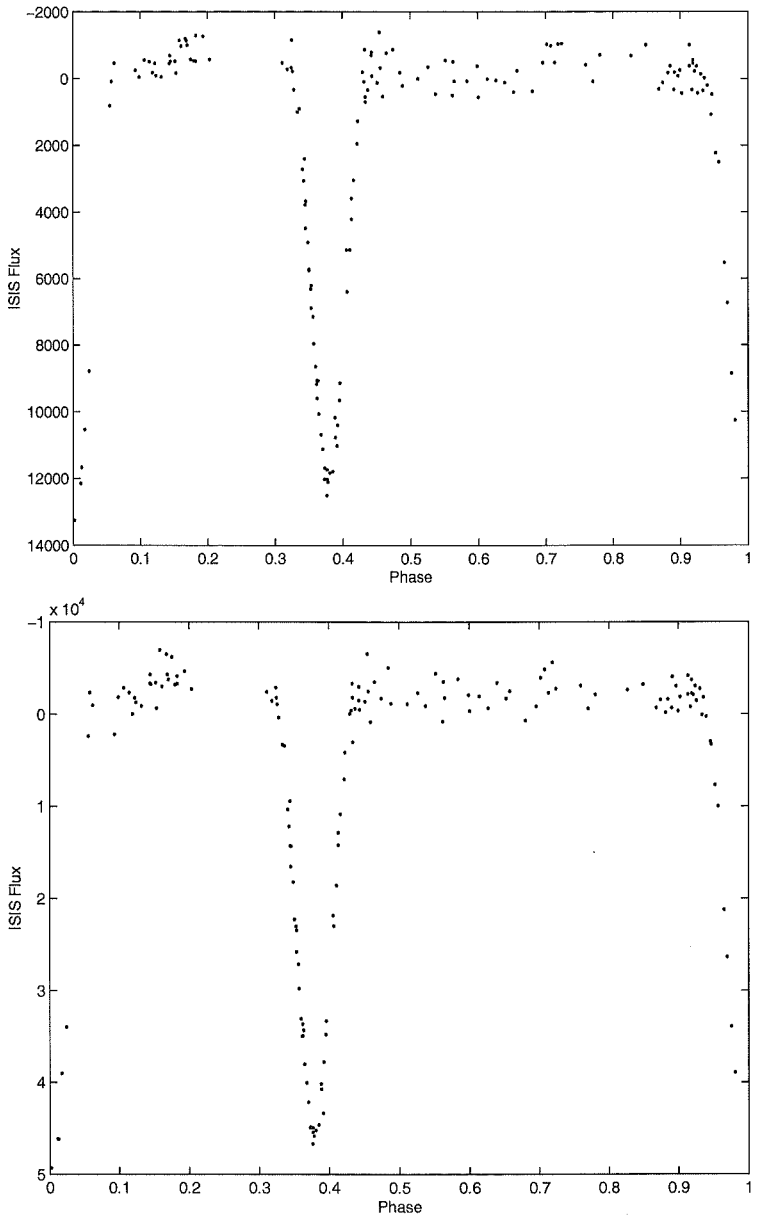

Figure 5.14: The two raw light curves are of MACHO*05:36:48.7−69:17:00, u filter as given by ISIS-2.1. The top light curve was constructed using frames with varying gain settings, either 1 or 4, with the reference frame having a gain of 1. The lower light curve was constructed using frames scaled to have apparently the same gain. For those with gain 1, the individual pixel value was increased by 3.89. The reference frame used, originally gain 1, was also scaled to be equivalent to having a gain of 4. In comparison to the mixed-gain light curve, differences are more easily seen in the flat sections of the light curve as well as the gradient of the steep sides of the eclipses.

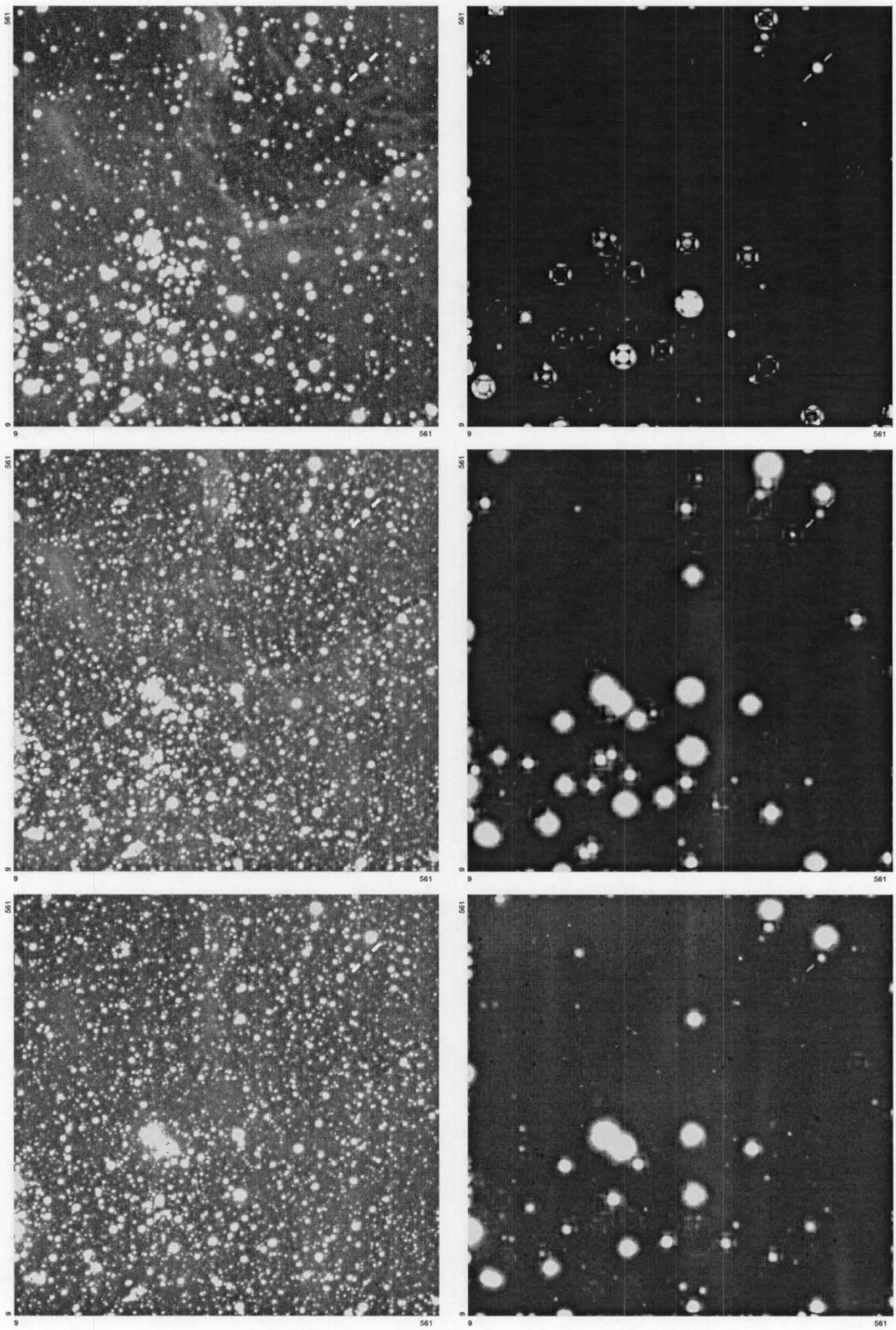

Figure 5.15: The images on the left, from top to bottom, are the MACHO*05:36:48.7−69:17:00 reference image for the filters u, $V_{\rm J}$ and $I_{\rm C}$. The images on the right are the corresponding frames showing the variable stars (`var.fits` frames) with the smaller circular white regions are the variable stars. The large circular white regions in the images on the right side are due to the saturated stars in the reference frame not subtracting cleanly, thereby leaving large residuals. The images on the left show these stars as having large diameters. Saturated stars are not analyzed but because of this poor subtraction are seen in the variable frames. Other residuals are also present around the stars, both saturated and non-saturated. These are in the form of small square shapes whose edges, namely the mid sections of the sides, are visible.

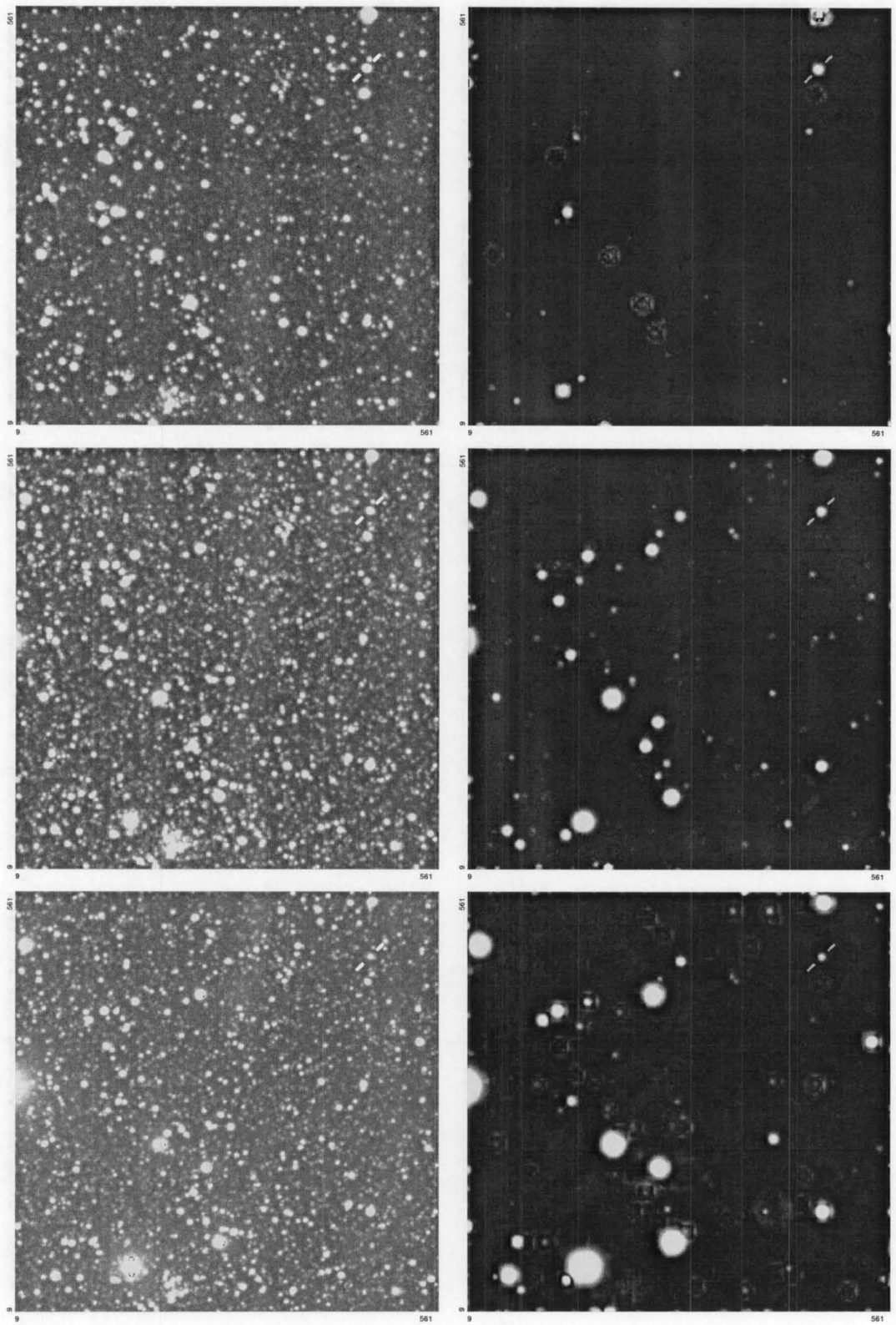

Figure 5.16: The images on the left, from top to bottom, are the MOA J005018.4−723855 reference image for the filters u, V_J and I_C. The images on the right are the corresponding frames showing the variable stars (`var.fits`). The smaller circular white regions are the variable stars. The large circular white regions in the images on the right side are due to the saturated stars in the reference frame not subtracting cleanly, thereby leaving large residuals. The images on the left show these stars as having large diameters. Saturated stars are not analyzed but because of this poor subtraction are seen in the variable frames. Other residuals are also present around the stars, both saturated and non-saturated. These are in the form of small square shapes whose edges, namely the mid sections of the sides, are visible.

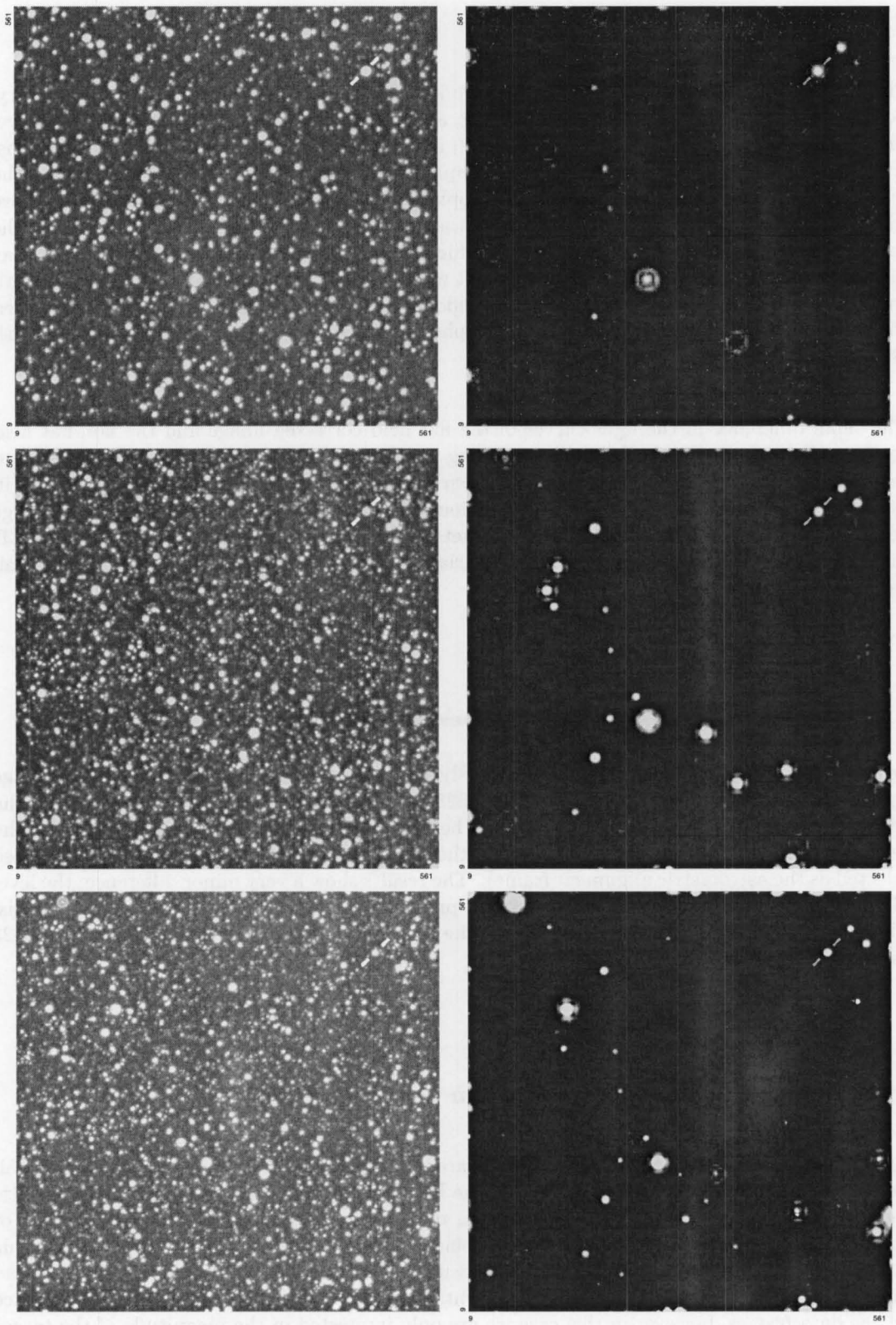

Figure 5.17: The images on the left, from top to bottom, are the MOA J005623.5−722123 reference image for the filters u, $V_{\rm J}$ and $I_{\rm C}$. The images on the right are the corresponding frames showing the variable stars (`var.fits`). The smaller circular white regions are the variable stars. The large circular white regions in the images on the right side are due to the saturated stars in the reference frame not subtracting cleanly, thereby leaving large residuals. The images on the left show these stars as having large diameters. Saturated stars are not analyzed but because of this poor subtraction are seen in the variable frames. Other residuals are also present around the stars, both saturated and non-saturated. These are in the form of small square shapes whose edges, namely the mid sections of the sides, are visible.

5.5 To flat field or not?

Flat fielding is considered as an important step in the image reduction process for photometry. To ensure that the flat fielding was improving, as it should, the quality of the end light curve, the data for all targets and the bandpasses u, V_J and I_C, were reduced with flat field corrections, and then without flat field corrections. A sample light curve is presented in Figure 5.18. The results for all bandpasses indicated that the application of the flat field correction does improve the quality of the light curve although not dramatically. This is seen as a reduction in the scatter of the data points in the light curves which is more apparent at the maximum light level rather than on the steep sides of the eclipses. It would be interesting to make a comparison with the theoretical signal:noise based on the flat regions of the light curves in Figure 5.18, compared with the RMS in the same region. However photon statistics required are not available with ISIS-2.1 and were therefore not pursued.

The small difference in the light curves of the flat field corrected image and the non-flat field corrected images are due the flat field containing small variations across the field (on the plateau region), Figures 4.10 and 4.11. This is also seen in the cross sections of the flat field frames in figures 4.12 and 4.13. This is unlike the previous PM3000 CCD system which exhibited large flat field variations across the chip. The target was maintain in the same place on the CCD for each exposure, thereby minimizing the variation across the flat field, although only small variations in this case.

5.5.1 Reference frame selection and construction

Selection of the reference frame, as previously mentioned, is a critical stage in the image subtraction process. The target MOA J005623.5−722123 has 11 frames used to create the reference image in both the u and V_J filters. The data was reduced using just one image for the reference frame in I_C, the very best based on the seeing values from `seeing.csh` (this was also selected as the astrometric alignment frame). The results show a very minor difference, the level of which is insignificant and has a very small probability of affecting the light curve analysis. Figure 5.19 and 5.20 shows this result for the u and V_J filters of MOA J005623.5−722123 respectively.

5.6 Zero point flux determination using DAOPHOT II

The values obtained from the data reductions are in terms of flux differences, i.e. the AC signal. To convert the flux differences to fluxes, i.e. the DC signal, the number of counts that comprise the stellar profile on the reference image need to be accounted for. The background must of course be properly taken into account, this being the difficult part of the equation. To do this a profile fitting programme, DAOPHOT II was used. DAOPHOT II estimates the point spread function, PSF,[5] on the CCD chip. More conventionally, the reduction package is used to reduce all the data frames, however in this case we are only interested in the magnitude of the target variable on the reference frame.

[5]The point spread function is a function that models the light distribution as detected on the chip. The spread of the image is due to the atmosphere and optics. Since stars are effectively points, the function is called the Point Spread Function, PSF.

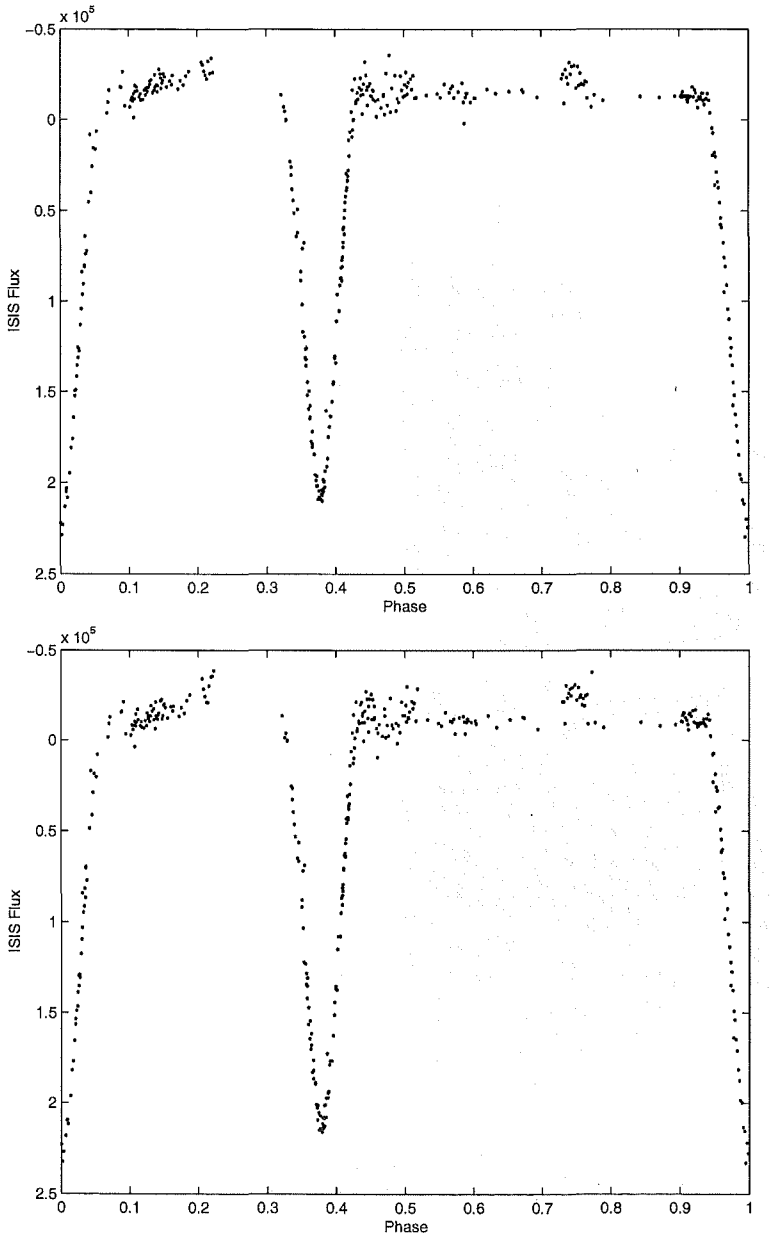

Figure 5.18: Both raw light curves are of MACHO*05:36:48.7−69:17:00, V_J filter. The flat field correction has been applied to data in the top light curve. The lower has not had the flat field correction. The top light curve has a slightly tighter data grouping, more visible on the flat than the eclipse sections of the light curve.

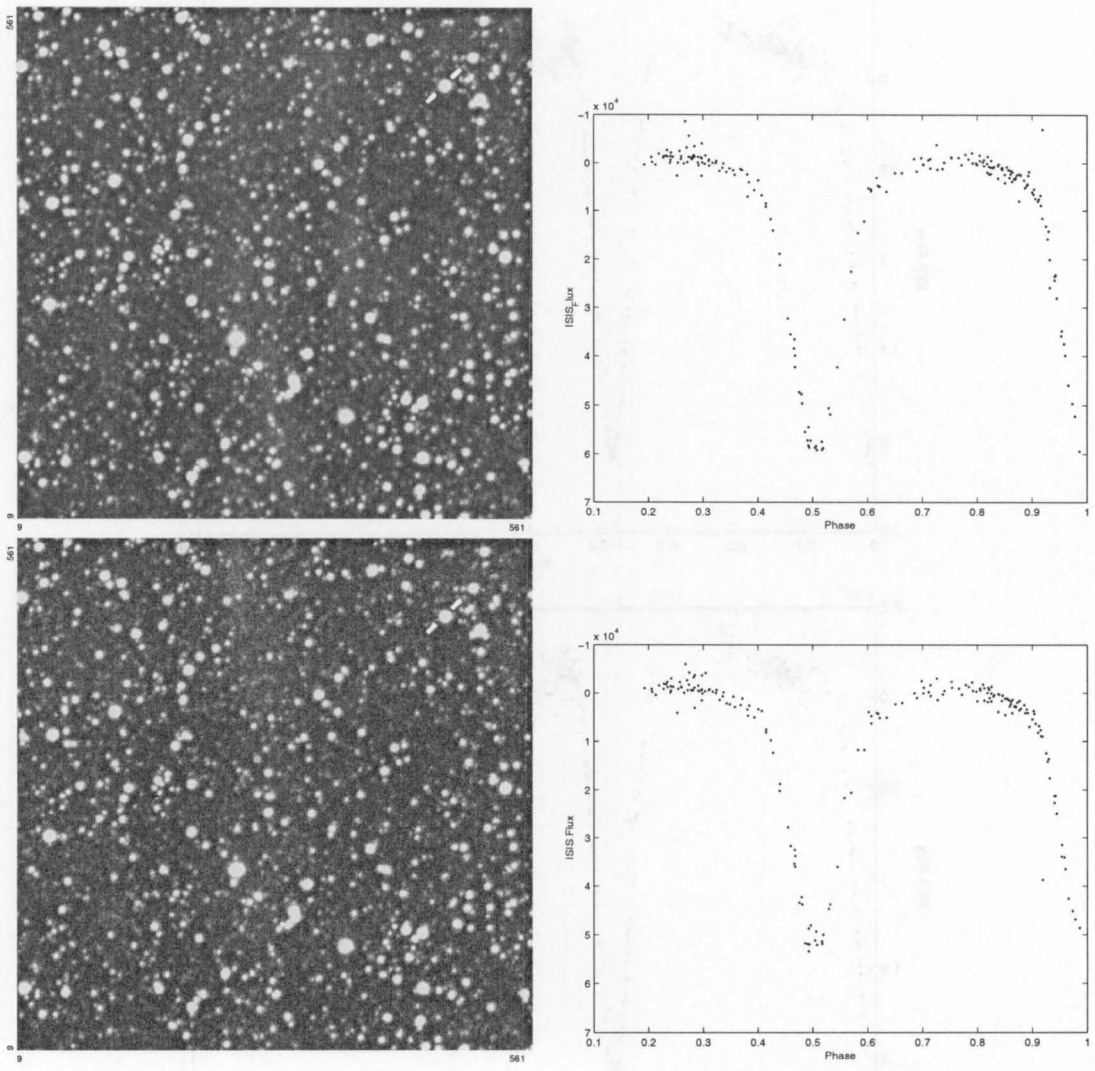

Figure 5.19: The images on the top and bottom are raw reference frames and light curves of MOA J005623.5−722123, u filter. The top left image is the reference image created using 11 stacked images; to the right the resulting light curve from the reduction process. The bottom left image is the reference image created using only 1 image, very best seeing based on values from `seeing.csh` (also the astrometric alignment frame). To the right is the resultant light curve. There is a slight difference between the two light curves, with the difference more noticeable at the bottom of the eclipses. This effect was not as apparent in the V_J filter case, Figure 5.20.

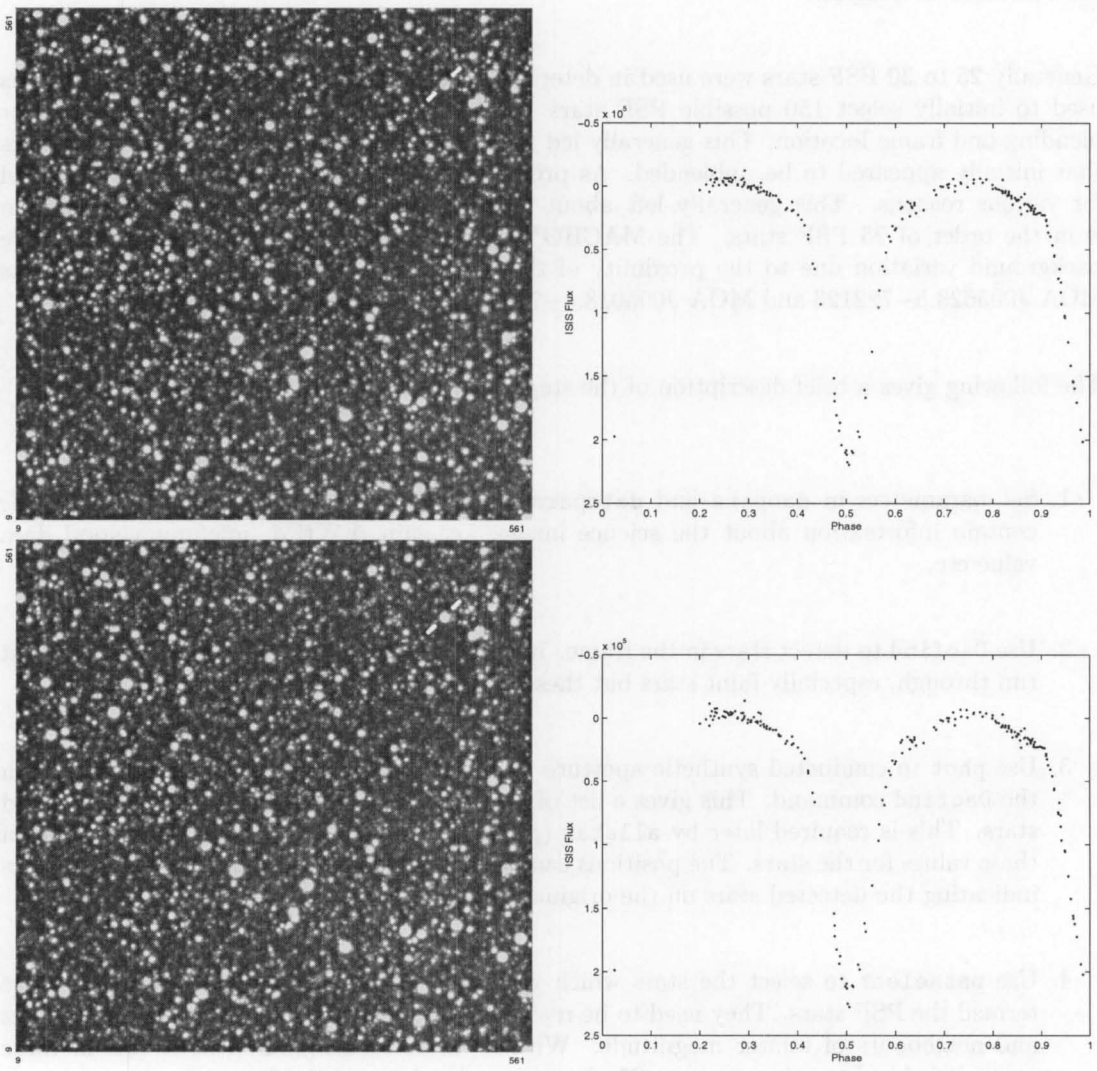

Figure 5.20: The images on the top and bottom raw light curves and reference frames of MOA J005623.5−722123, V_J filter. The top left image is the reference image created using 11 stacked images; to the right the resulting light curve from the reduction process. The bottom left image is the reference image created using only 1 image, the one with the very best seeing based on values from `seeing.csh` (also the astrometric alignment frame). To the right is the resultant light curve. There is very little difference between the two light curves.

5.7 DAOPHOT II

DAOPHOT II attempts to use the best features of both the analytical and empirical methods in the determination of the PSF. This includes the use of look-up tables in order to improve the quality and speed in determining the PSF. The following is a simple breakdown of the steps used to construct the PSF for the reference frames. The software package IRAF[6] was used for the DAOPHOT II analysis.

Generally 25 to 30 PSF stars were used in determining the PSF. The `psfselect` function was used to initially select 150 possible PSF stars. These were then interactively inspected for blending and frame location. This generally led to a sample of approximately 30-40 PSF stars that initially appeared to be unblended. As processing was continued, some were eliminated for various reasons. This generally left about 30 PSF stars. The recommended minimum is in the order of 25 PSF stars. The MACHO*05:36:48.7−69:17:00 frames had considerable background variation due to the proximity of the Tarantula nebula. The two MOA targets MOA J005623.5−722123 and MOA J005018.4−723855 had relatively cleaner backgrounds.

The following gives a brief description of the steps used in the reduction process.

1. Set parameters in `daopars` and `datapars` for use by several sub-programmes. These contain information about the science image, i.e. gain, FWHM, maximum good data value etc.

2. Use `Daofind` to detect stars in the frame. Inevitably not all stars are detected on the first run through, especially faint stars but these are detected later in additional passes.

3. Use `phot` to conducted synthetic aperture fitting photometry on the stars detected with the `Daofind` command. This gives a list of positions and magnitudes for all the detected stars. This is required later by `allstar` (profile fitting algorithm) as an initial guess of these values for the stars. The positions can be written to a file and used to overlay marks indicating the detected stars on the original frame.

4. Use `pstselect` to select the stars which will be used to construct the PSF. These are termed the PSF stars. They need to be reasonably isolated stars with similar magnitudes and neighbours of fainter magnitude. With a variable background, as it was in these cases, it is ideal to select at least 25 plus stars spread across the frame.

5. Use `psf` to construct the 1^{st} generation PSF for the original frame.

6. Use `allstar` to group and fit the PSF to the detected stars in the frame simultaneously. This command takes the photometry file and the list of PSF stars and fits a PSF to the stars simultaneously. The output is a more accurate photometry file and a frame of the original frame with the fitted stars subtracted.

7. Use `Daofind` on the subtracted image, output from `allstar`, to detect any faint stars missed on the first pass, especially those around the PSF stars, i.e. the PSF neighbours.

[6] Although generically called IRAF, the version used had a GUI interface and was called PYRAF.

8. Use `phot` on the subtracted image from `allstar` using the positions found by `daofind`.

9. Run `pconcat` to concatenate the original photometry position list with the just-previously computed one using the subtracted frame.

10. Use `prenumber` to renumber the concatenated photometry file.

11. Run `allstar` to group and fit the PSF to multiple stars simultaneously, using the first PSF.

12. Use `substar` to subtract from the reference frame all the stars contained in the output file from `allstar` **except** the PSF stars.

13. Use `psf` to compute the second generation PSF using the subtracted frame from `substar`.

14. Use `allstar` to group and fit the PSF to multiple stars simultaneously on the **original** frame, using the second generation PSF. The output is improved photometry.

If the residuals were still high, as was the case in all filters/targets, then steps 8–14 were repeated until the residuals, especially around the target were in the order of ~1% of the original flux level for the target.

The command allstar produces `.mag` files containing the photometry for each star identified in the frame. The relevant photometry values for the target were then extracted. A summary for each filter/target in presented in Table 5.7.

The magnitude and error calculated by DAOPHOT II is given by:

$$magnitude = 25 - 2.5log\left(\frac{(\text{total flux} - \text{background flux})}{\text{exposure time}}\right) \tag{5.8}$$

The reference value of 25 in equation 5.8 is arbitrary.

5.8 Reduction results

5.8.1 MACHO*05:36:48.7–69:17:00

The blending of nearby stars with the target is seen in an image (Figure 5.28) obtained from ESO, which was acquired by the 2p2 wide field image camera. This was used to image the Tarantula nebula in several bandpasses to constructed a colour composite image and fortunately contained MACHO*05:36:48.7–69:17:00. The nearby stars became evident during the DAOPHOT II reduction process. Three nearby stars, immediately resolvable from the reference image, were detected along with one other that was faint but near the target. All of these stars were subtracted relatively cleanly. Additional passes were made in order to reduce the residuals, even though the majority of the frame had subtracted very well. The nebulosity from the nearby Tarantula nebula is clearly seen in the subtracted images, Figure 5.21. This shows the greatly

Table 5.7: The results of profile fitting on the reference frames of each filter and target using the DAOPHOT II package contained in IRAF. The Id no. is the identification number assigned by DAOPHOT II. In addition, the x and y are the pixel position of the target star on the relevant reference frame. The flux value is the total flux including the background value. The background value is also given in the table. The magnitude and associated error is that as determined by DAOPHOT II using equation 5.8.

Target	Filter	Id no.	Position x	Position y	flux	Exp. time (s)	Background	Magnitude	Mag. error
MACHO*05:36:48.7−69:17:00	u	2581	463.812	481.508	122 663.2646	1200	155.294	20.070	0.004
	V_J	3813	467.294	479.196	529 841.2880	700	1276.729	17.805	0.004
	I_C	5240	468.484	481.508	198 055.1491	400	1963.097	18.274	0.007
MOA J005018.4−723855	u	1524	466.800	480.324	82 843.4288	1200	357.2384	20.407	0.009
	V_J	2462	471.478	480.249	448 120.0090	700	1952.398	17.989	0.003
	I_C	2036	472.825	476.522	191 888.1660	400	3062.949	18.315	0.012
MOA J005623.5−722123	u	2861	468.111	476.950	121 668.8472	1200	111.4909	19.986	0.004
	V_J	4468	468.074	479.168	386 049.8870	700	1016.810	18.149	0.005
	I_C	3669	478.514	481.518	162 578.3826	400	1565.735	18.488	0.012

varying background level of the frame. Initially only a linear PSF was considered, however it became apparent at an early stage that this was insufficient as a systematic variation in residuals was seen across the frame. Therefore a quadratic variation of the PSF was used. This was possibly due to this background variation, although it could be an effect of the telescope optics. All bandpasses subtract to a similar level, the data values are presented in Table 5.7. The CHI values of the target in all three bandpasses Figure 5.25, were reasonable, together with acceptable values of the reported DAOPHOT II magnitude error.

The nearby blended field stars are shown, in close up, in Figure 5.28. The profiles of the field stars within an approximately 30 arc second square field around the target with and without the target are given in Figure 5.30. The three brighter field star in the close vicinity of the target contribute a few percent to the total flux. This becomes significant in all the other frames, as these three stars are generally undetermined. There is a question as to whether the subtracted image, namely the `var.fits` image of the target contains any other stars. The `var.fits` image gives all variable stars. Therefore if one of the blended stars is variable, then this will add to the total flux of the target star.

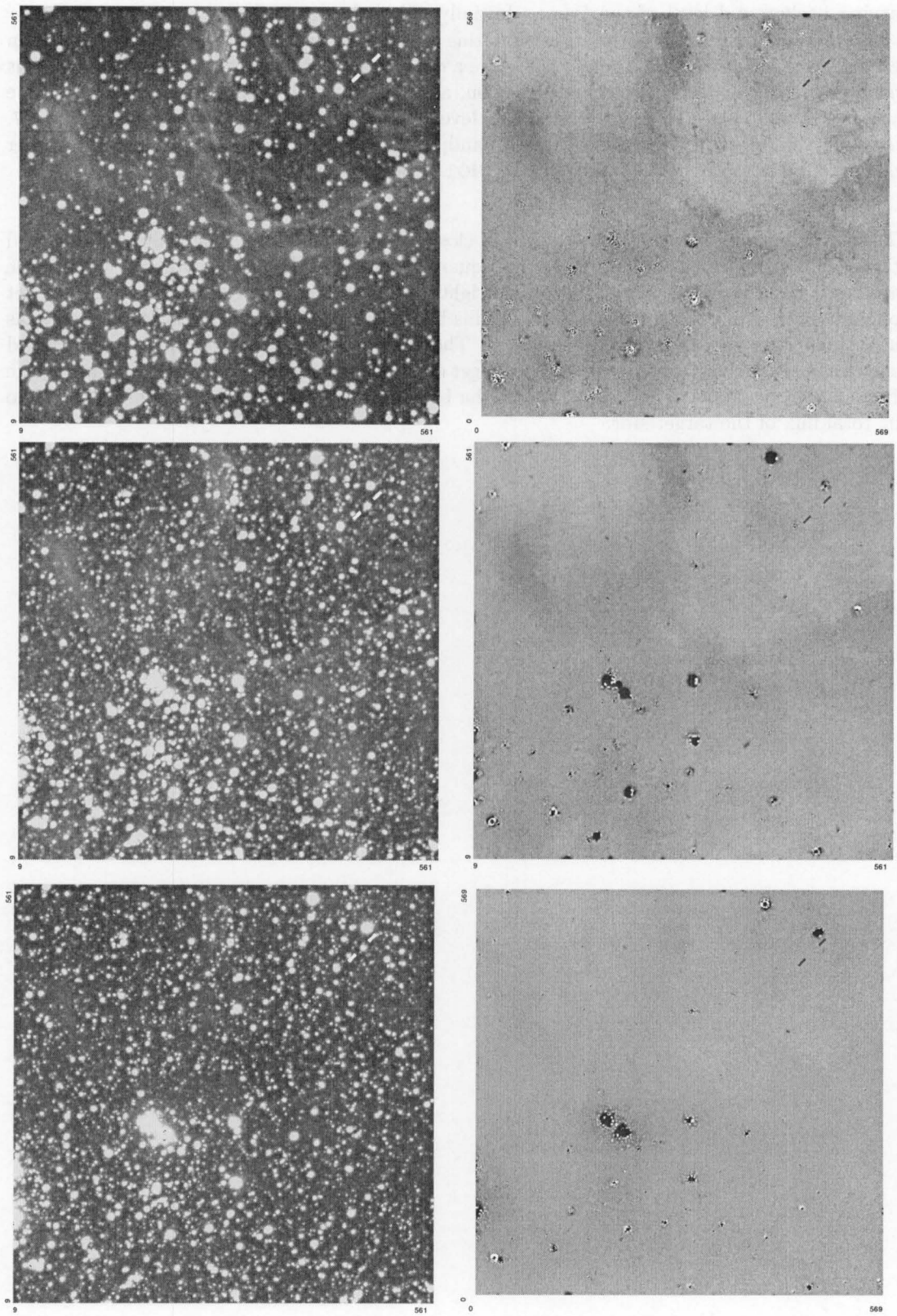

Figure 5.21: The images on the left, from top to bottom, are the MACHO*05:36:48.7−69:17:00 reference images for the u, V_J and I_C filters respectively. The images on the right are the corresponding DAOPHOT II subtracted images. The target star position is indicated on each frame. The saturated stars on the frames have not been successfully subtracted, as expected, and therefore are evident by the high residuals in localized regions. There are 3 slightly blended stars, i.e. the peak of their profiles just separate from the target's profile. Another star was blended to a greater extent and harder to extract.

5.8.2 MOA J005018.4−723855

The target is blended with a star to the right of the centre of the stellar profile as well as nearby star, left of centre, Figure 5.31, although not as severely. The brightness of the blended star makes this target the most affected by blending of the three. Initially a linear PSF was used in the subtraction of the stars on the reference frame, however variations across the frame, bottom left to top right resulted. Therefore a quadratic variation for the PSF was adopted as in the MACHO*05:36:48.7−69:17:00 subtraction. The use of the quadratic variation for the PSF for the target indicated the effect is due to the telescope optics. Several passes were made to obtain a clean subtraction of the stars, Figure 5.22, giving an acceptable level of the residuals. The CHI values of the target in all three bandpasses Figure 5.25, were reasonable, together with acceptable values of the reported DAOPHOT II magnitude error.

5.8.3 MOA J005623.5−722123

There are three nearby stars in the top right quadrant from the target, Figures 5.23 and 5.28. Using a quadratic PSF, as with the other two targets, the stars were subtracted from the reference frame. Several passes were required to reduce the residuals in the u bandpasses however the subtraction in not entirely clean, Figure 5.23 top right panel. The I_{C} bandpasses subtraction was better than the u bandpasses although a high CHI value is given relative to other subtracted stars on the I_{C} reference frame, Figure 5.26.

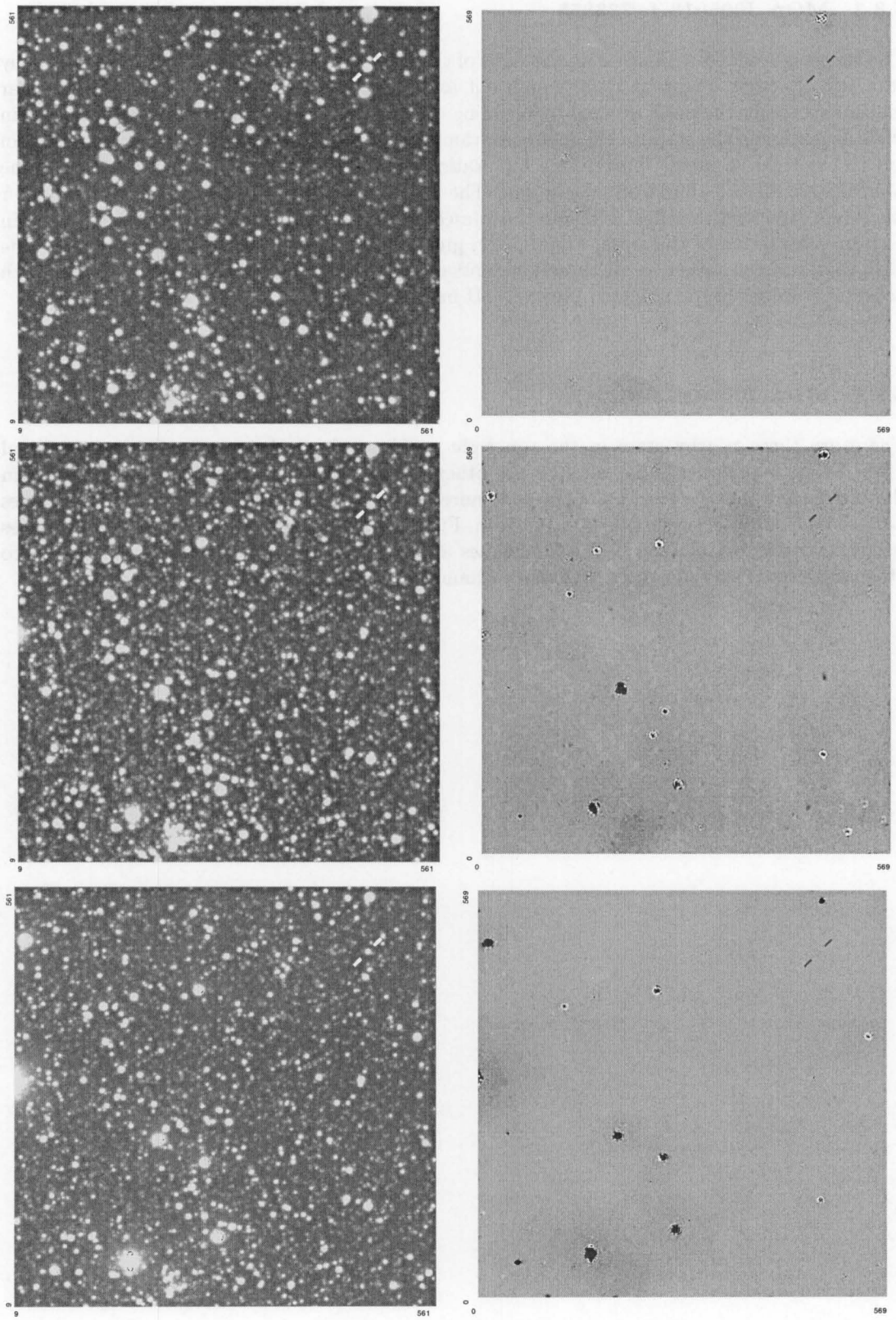

Figure 5.22: The images on the left, from top to bottom, are the reference images for the MOA J005018.4−723855 u, V_J and I_C filters respectively. The images on the right are the corresponding DAOPHOT II subtracted images. The target star position is indicated on each frame. The saturated stars on the frames have not been successfully subtracted, as expected, and therefore are evident by the high residuals in localized regions. There is one well blended star to the right of the centre of the target's profile.

5.8.4 Extracting fluxes

The application of DAOPHOT II to the reference frames provided the zero-level fluxes of the targets stars, as well as a background value. These extracted flux values were calculated after all[7] nearby and detectable blended stars were removed. The resultant flux value was then used to set the zero point for the ISIS-2.1 light curves, thereby giving the light curve in terms of light. The light curves were then compared to the original MOA light curves and light curves obtained from the MACHO database for the LMC and both SMC targets. The MOA and MACHO data agreed well, as one would hopefully expect since both used a similar resolution and initial reduction process. The light curves constructed using the reduced data gave deeper eclipses in all cases. This gave two options.

- There was a systematic error in the data reduction procedure, either during the ISIS-2.1 reductions or the DAOPHOT II reductions.
- The MOA and MACHO data had over estimated the amount of flux from the target star.

Either one or both these options could be possible. Given the number and magnitude of close and nearby stars, and in addition the very similar system data collection configurations and data reduction procedures used by MOA and MACHO, an over estimation could be possible. However it is well known that it is difficult to obtain measures of total flux from area detectors. The difficulty is most easily understood from aperture photometry of an isolated stellar image. If the aperture is too small, it is clear that not all the flux lies within it. As the aperture gets bigger more of the PSF is enclosed, and the enclosed flux increases. Unfortunately, a larger aperture also includes a larger area of background, which of course is subtracted away, and background noise (or uncertainty), which is not. Once the aperture attains a certain size, these background fluctuations become bigger than any increase of the enclosed flux due to a fuller sampling of the PSF and the integrated flux begins to show random fluctuations which may be positive or negative.

It is therefore necessary to stop flux integration at some finite radius and accept that it only includes a certain, unknown fraction of the total flux. Photometry via PSF fitting suffers from the same problem because the PSF to be fitted cannot be determined accurately beyond the radius at which background fluctuations become dominant.

The AC signal derived from ISIS-2.1 therefore represents differences measured within some radius, which in fact was 5 pixels. The DAOPHOT II fluxes were obtained on some other assumption so it is not surprising that they did not provide reference fluxes that were consistent with the ISIS-2.1 AC signals.

The solution to this dilemma was to use DAOPHOT II to remove all stars except the target from the reference frame, and then use ISIS-2.1 to obtain photometry of this difference image containing only a single star in exactly the same way as for the difference images used for the AC photometry. The computer procedure was as follows:

- In DAOPHOT II select the last (in this case the solution) subtracted frame that contains no stars, `nostars.fits`. This contains the background plus saturated stars.
- Edit the last `allstar` output file `ref.als.[number]` and remove the target star (identified previously by position).

[7] Although not possible to exactly account for and extract all nearby stars, these were reasonably removed.

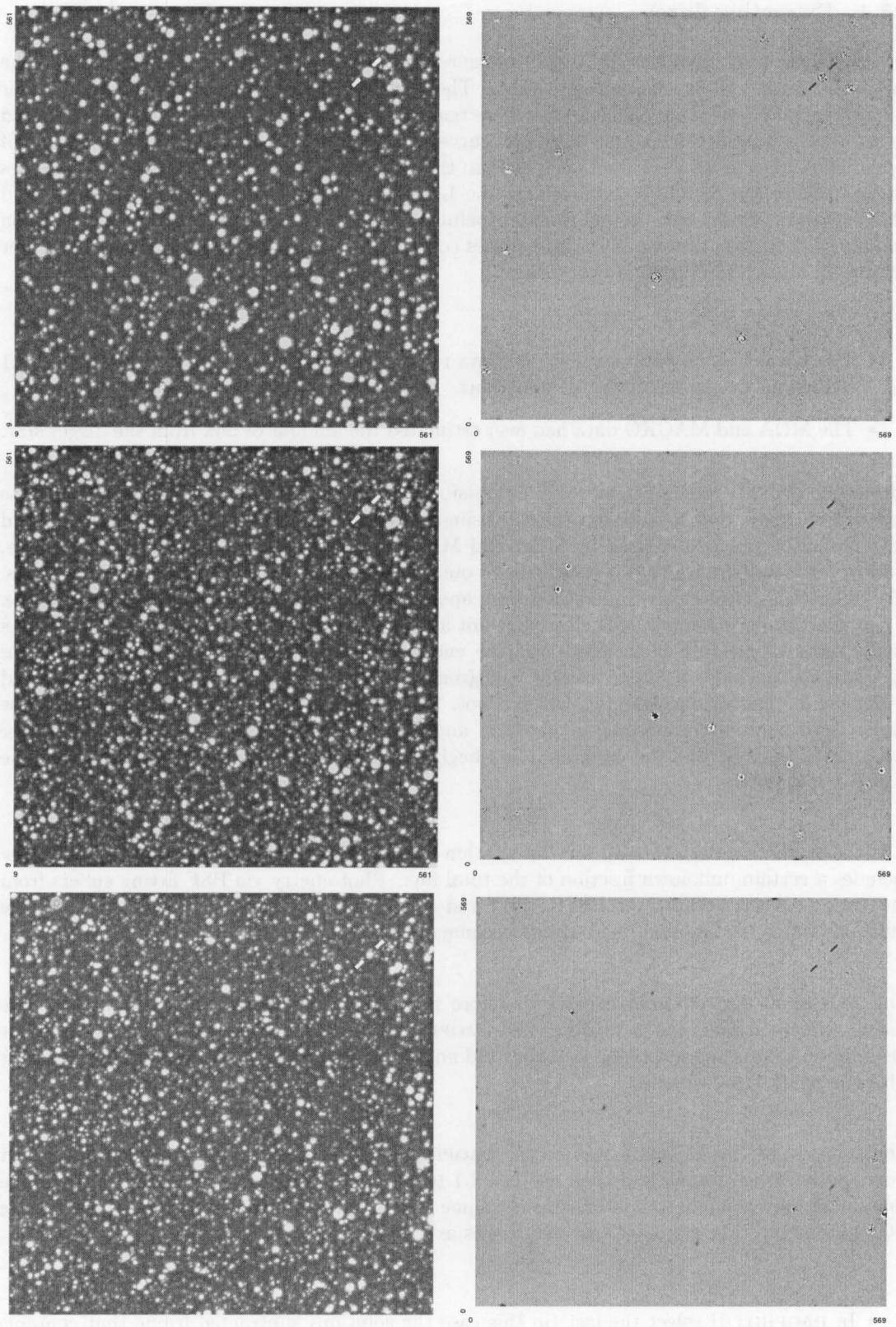

Figure 5.23: The images on the left, from top to bottom, are there reference images for the MOA J005623.5−722123 u, V_J and I_C filters respectively. The images on the right are the corresponding DAOPHOT II subtracted images. The target star position is indicated on each frame. The saturated stars on the frames have not been successfully subtracted, as expected, and therefore are evident by the high residuals in localized regions. There are slightly blended stars in the upper right quadrant from the centre of the target's profile. The subtraction of these stars where not as clean as the other two targets, more noticeably in the u bandpass, upper right figure.

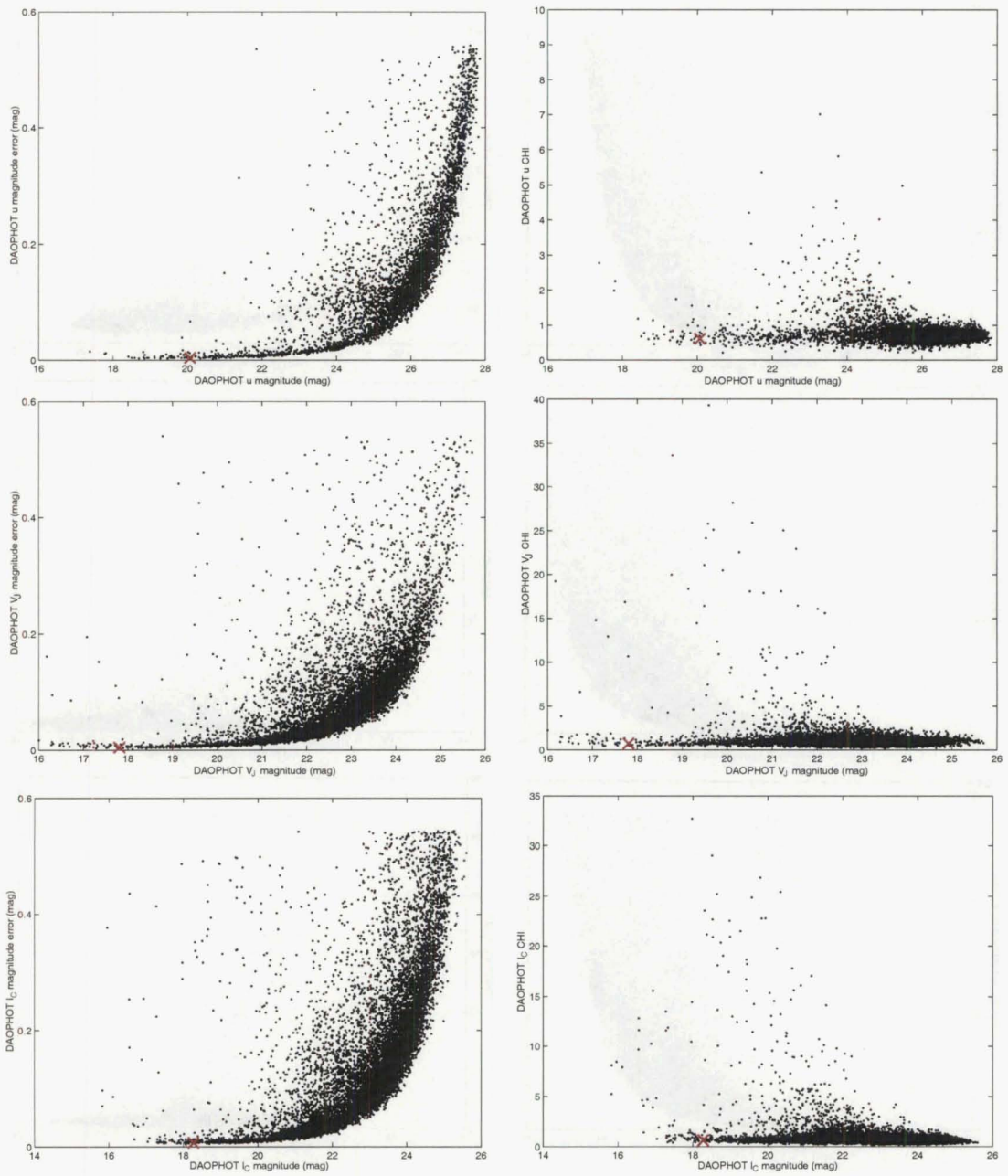

Figure 5.24: The plots on the left are the extracted magnitude errors as reported by DAOPHOT II for the reference frames of MACHO*05:36:48.7−69:17:00, u, V_J and I_C filters, top, middle and bottom respectively. All detected and fitted stars are plotted with the target indicated, ×. The saturated stars which are shown in the subtracted frames have high errors. The plots on the right are the CHI values from DAOPHOT II. The CHI values are a *goodness* factor computed by DAOPHOT II of the fit. The smaller the value the better the fit.

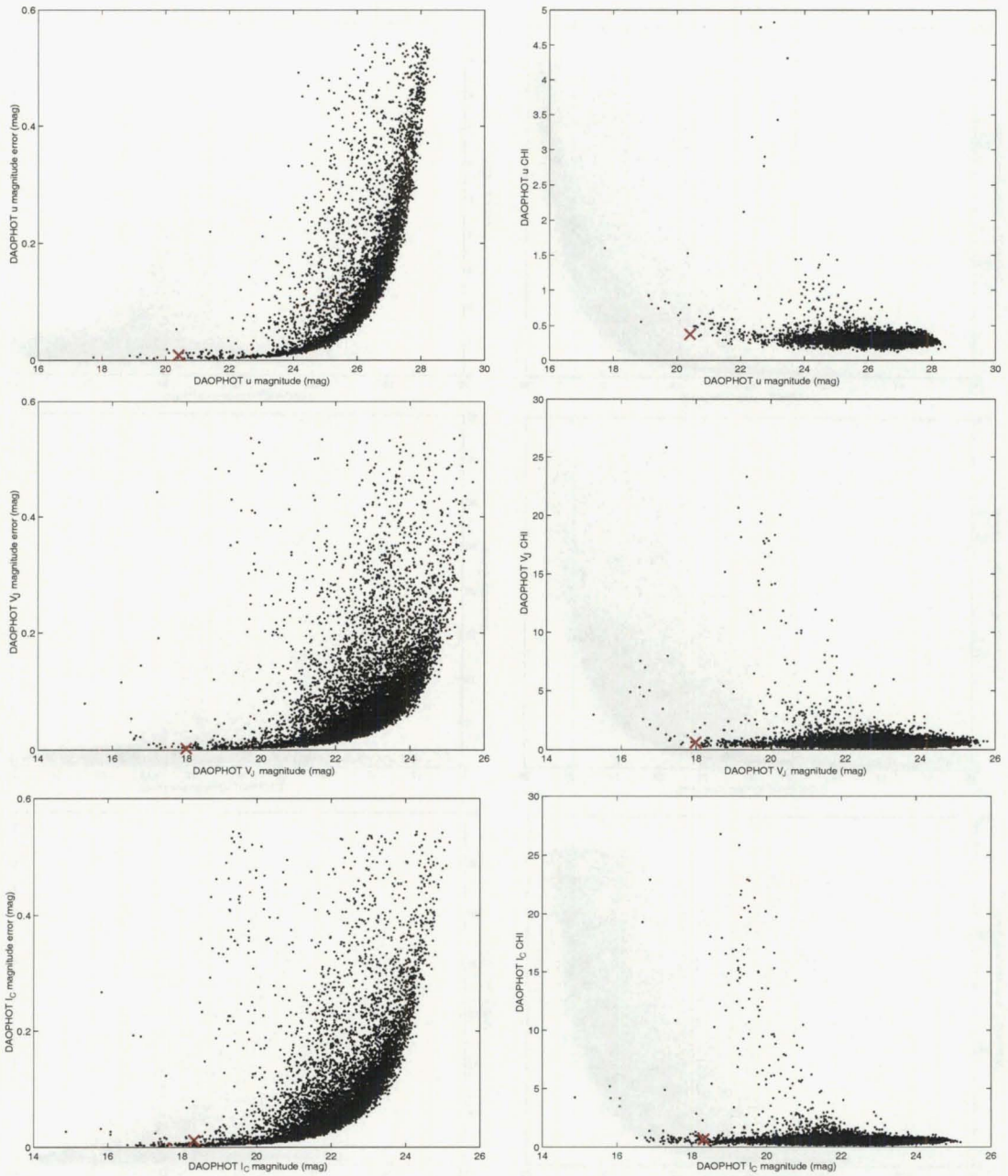

Figure 5.25: The plots on the left are the extracted magnitude errors as reported by DAOPHOT II for the reference frames of MOA J005018.4−723855, u, V_J and I_C filters top, middle and bottom respectively. All detected and fitted stars are plotted with the target indicated, ×. The saturated stars which are shown in the subtracted frames have high errors. The plots on the right are the CHI values from DAOPHOT II. The CHI values are a *goodness* factor computed by DAOPHOT II of the fit. The smaller the value the better the fit.

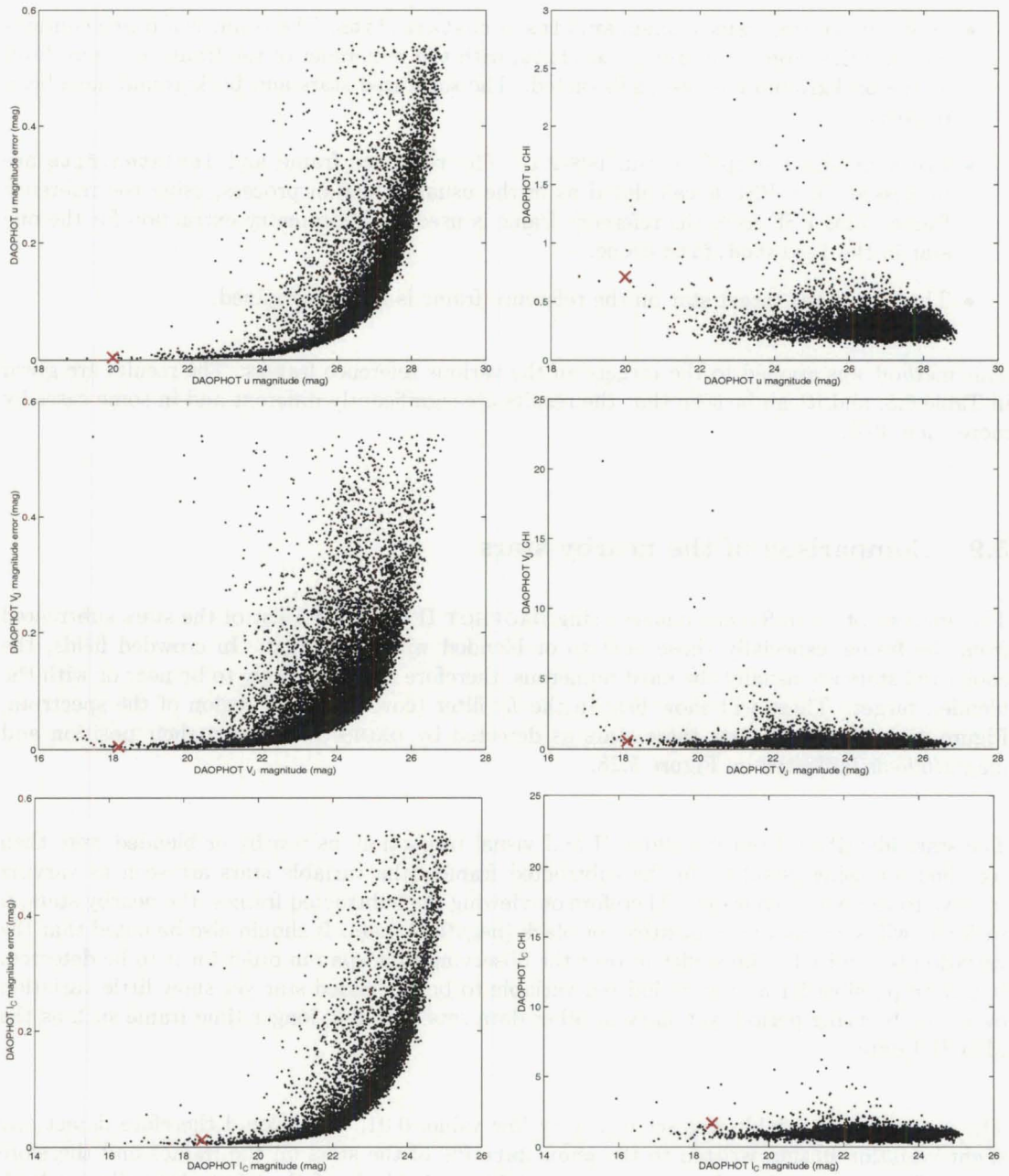

Figure 5.26: The plots on the left are the extracted magnitude errors as reported by DAOPHOT II for the reference frames of MOA J005623.5−722123, u, V_J and I_C filters, top, middle and bottom respectively. All detected and fitted stars are plotted with the target indicated, ×. The saturated stars which are shown in the subtracted frames have high errors. The plots on the right are the CHI values from DAOPHOT II. The CHI values are a *goodness* factor computed by DAOPHOT II of the fit. The smaller the value the better the fit.

- Run `substar` with the input frame set to the reference and the input star list from the just edited `ref.als.[number]` file. This will produce an image of the reference frame with all stars subtracted, as previously, but with the exception of the target star, the background and the saturated stars. The image is `onestar.fits`.
- Subtract the two frames; `onestar.fits` − `nostars.fits`. The result is a frame containing only the target star, `isolated.fits`, with the remainder of the frame at a zero level as the background has been subtracted. The saturated stars and background have been removed.
- Use a modified script[8] to run ISIS-2.1. The reference frame and `isolated.fits` are processed. The PSF is calculated as in the usual reduction process, using the reference frame. This PSF from the reference frame is used for photometry extraction for the one star in the `isolated.fits` frame.
- The flux of the target star on the reference frame is now determined.

This method was applied to the targets on the various reference frames. The results are given in Table 5.8, and it can be seen that the results are significantly different and in some cases by more than 30%.

5.9 Comparison of the nearby stars

The analysis of the reference images using DAOPHOT II produces a list of the stars subtracted from the frame, especially those next to or blended with the target. In crowded fields, the cooler red stars are usually the most numerous, therefore the most likely to be near or with the blended target. These will show best in the I_C filter (covers the red region of the spectrum, Figure 4.3). Table 5.9 lists these stars as detected by DAOPHOT II given their position and magnitude as indicated on Figure 5.28.

The stars identified, from DAOPHOT II and visual inspection, as nearby or blended were then searched for using ISIS-2.1. In the subtracted frames, the variable stars are seen as varying relative to the reference frame. Therefore on viewing the subtracted frames, the nearby stars, if variable, will show as white (positive) or black (negative) stars. It should also be noted that the variation is required to be sufficient over the observing time span in order for it to be detected. It can be possible for a long period red variable to be a blended star yet show little variation over the observing period, yet show in other data sets spanning longer time frame such as the MACHO data.

The SIG_THRESH variable was set to a very low value, 0.01. This would therefore detect any slight variation in flux written to the `phot.data` file of the stars on the frames and therefore detect if the nearby blended stars were variables. Analysis of the `phot.data` file for both MACHO*05:36:48.7−69:17:00 and MOA J005018.4−723855 revealed none of the nearby stars, thus they were considered constant. One star was detected as variable for MOA J005623.5−722123, far right star (487.817,480.052). The expanded region around the target is shown in Figure 5.28. However, as seen from Figure 5.29, the variation is small and combined with its distance from the target, the effect, if any, can be considered negligible. There is a well blended star that merges with MOA J005018.4−723855. The DAOPHOT II reduction of the MOA J005018.4−723855 reference frame suggests, from residuals and DAOPHOT II error estimates, the stars flux is not fully separated from the target. This could produce difficulties in the fitting of models to the light curve in the analysis. Fortunately, the *Wilson-Devinney* package allows

[8] A description of the details are presented in Appendix D.

Table 5.8: The fluxes as calculated by DAOPHOT II and their uncertainties, $+\delta$ and $-\delta$, as derived from the magnitude error in DAOPHOT II. The middle columns give the fluxes calculated by ISIS-2.1 with their uncertainties using a frame with only the target star and zero at all other locations. The far right column is the percentage difference of the fluxes (DAOPHOT II − ISIS-2.1). All fluxes calculated by DAOPHOT II are smaller than the ISIS-2.1 values. This results in deeper eclipses in the light curves.

Target	Filter	DAOPHOT II flux	δ DAOPHOT II fluxes		ISIS-2.1 fluxes	$\pm\delta$ ISIS-2.1 flux	Difference	% difference
			$+\delta$	$-\delta$				
MACHO*05:36:48.7−69:17:00	u	122 663.2646	413.6301	415.3572	146 435.0531	436.6868	−23 771.7885	−19.4
	V_J	529 841.2880	1943.7200	1944.1044	652 964.3188	897.2349	−123 123.0308	−23.2
	I_C	198 055.1491	1260.1855	1268.3314	221 494.1179	522.2068	−23 438.9688	−11.8
MOA J005018.4−7238552	u	82 843.4288	680.9272	686.5950	110 396.2798	393.5101	−27 550.851	−33.3
	V_J	448 120.0090	1231.1050	1234.5114	600 462.0772	911.2627	−152 342.0682	−34.0
	I_C	191 888.1660	2075.4832	2098.5486	223 377.7770	511.0956	−31 489.611	−16.4
MOA J005623.5−722123	u	121 668.8472	447.0100	448.6598	153 348.3635	457.9582	−31 679.5163	−26.0
	V_J	386 049.8870	1769.0663	1777.2319	533 532.3439	833.6885	−147 482.4569	−38.2
	I_C	162 578.3826	1769.7794	1789.4482	195 531.2939	505.4222	−32 952.9113	−20.3

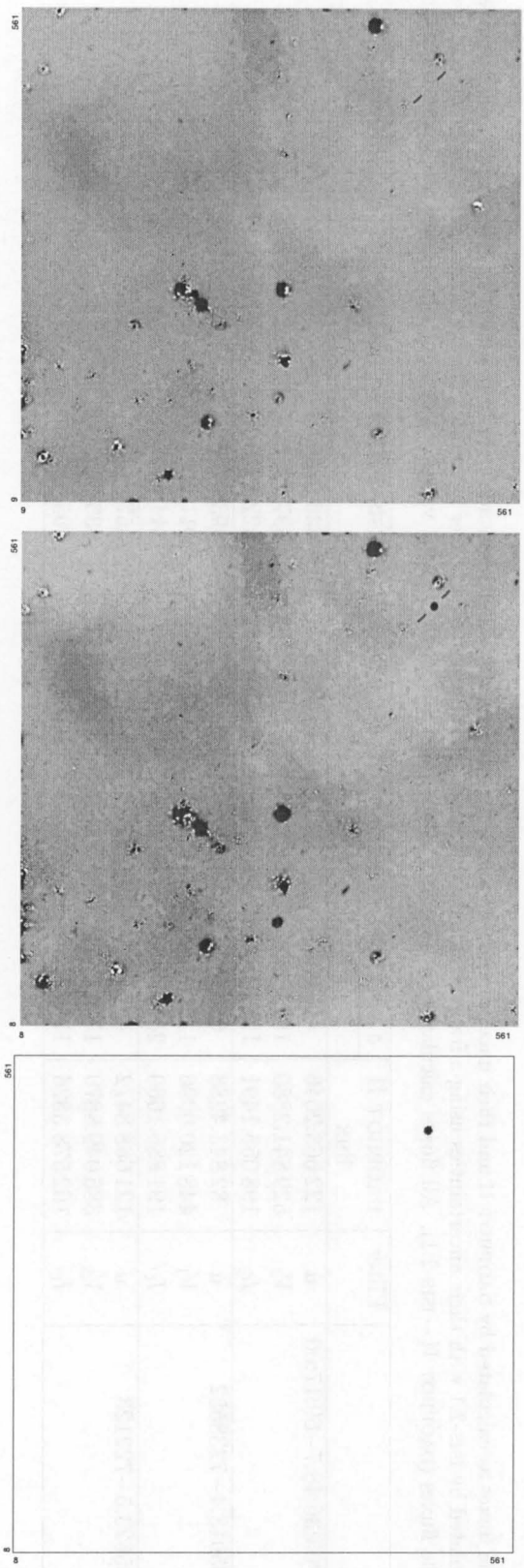

Figure 5.27: The frames shown are for MACHO*05:36:48.7−69:17:00 V_J filter with the target indicated. The top frame is the subtracted frame using DAOPHOT II, with only the background, saturated stars and some small residuals present. The middle frame is created by running `substar` on the reference frame but editing out the target stars from the `ref.als.[number]` file, therefore subtracting all stars, except the target star. The bottom frame is the middle frame minus the top frame. This gives only the target star with the all other regions zero. The bottom frame is then passed to ISIS-2.1 for the flux extraction using the PSF as derived from the reference frame in ISIS-2.1 as used in the reduction process.

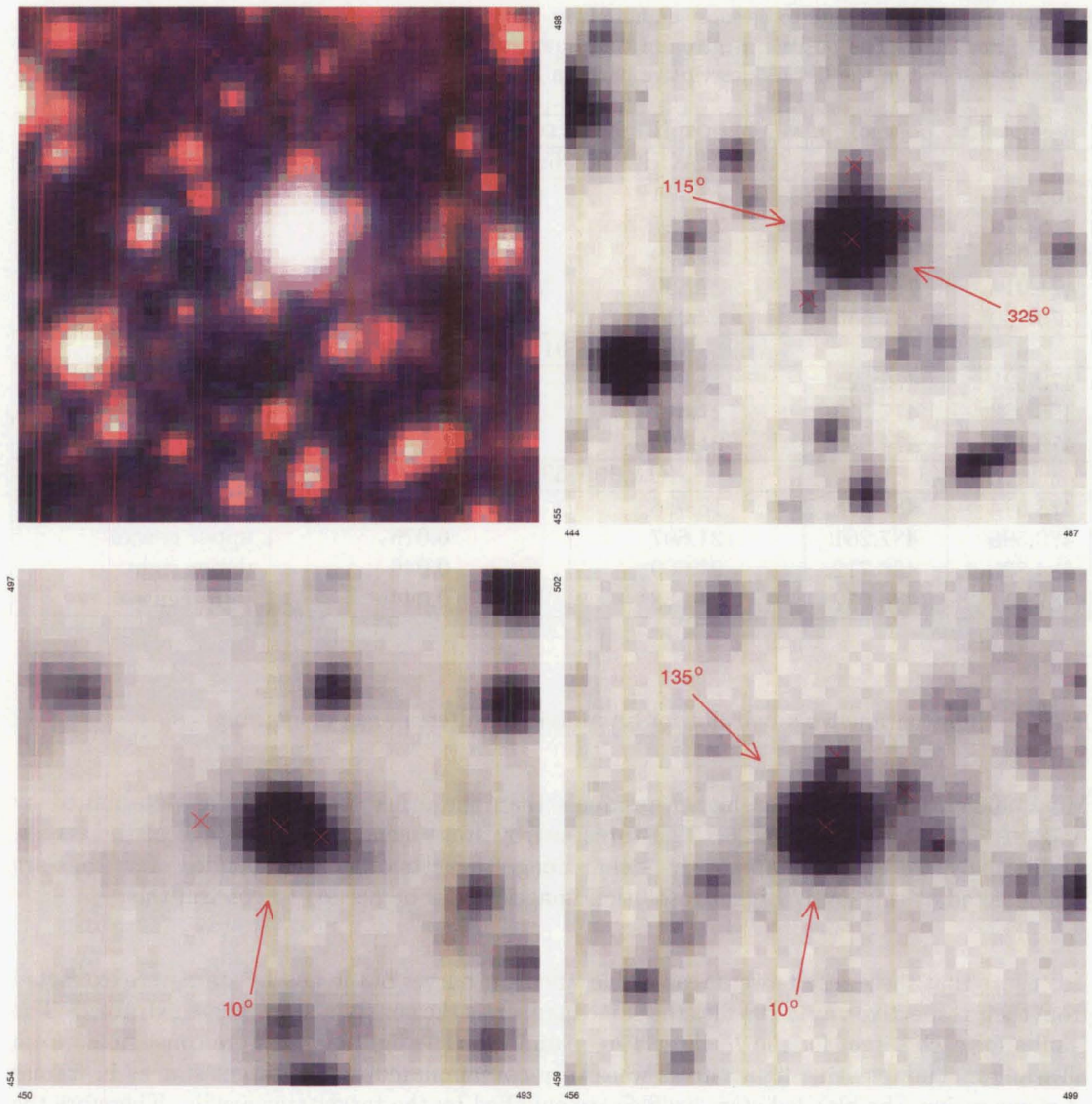

Figure 5.28: The frames show the target stars and the nearby stars within a 27.5 arc seconds square with the target located at the centre. The top two frames contain MACHO*05:36:48.7−69:17:00. The top left frame is from the ESO 2p2 wide field camera, colour composite image. The top right frame is the reference frame used for the reductions, I_C filter. The higher resolution and better seeing frame from ESO shows at least 5 smaller stars, near the target. Three of these are visible near the target as seen in the reference frame. The fourth, lower right, is most likely too faint to be detected in the wings of the target star. The star located to the middle left of the target in the 2p2 image is too faint to be seen in the reference image and contributes to the background. The bottom left and right images are of MOA J005018.4−723855 and MOA J005623.5−722123 respectively, both in the I_C filter, indicating the nearby stars. Both these stars exhibited possible blended stars, more so MOA J005623.5−722123. This was evident in the DAOPHOT II plots shown in Figure 5.26. The shape of MOA J005018.4−723855 indicates at least two stars are blended which extend from the centroid of the target to the outer right region. Profile plots of the targets showing the nearby stars for the angles indicated are presented in Figures 5.30, 5.31 and 5.32.

Table 5.9: Stars that are nearby and/or blended with the target as depicted in Figure 5.28. The photometry file from the DAOPHOT II analysis provides the positions and estimated magnitudes, relative to the target star's magnitude, for these stars. Most are cooler red stars as compared to the hotter blue binaries, as these tend to be most numerous in crowded fields. Therefore the data presented is for the I_C filter (red). The position is given in coordinates of the reference frame with the position of the target as the first in the list. A descriptive position is given relative to the target star.

position x	position y	DAOPHOT II mag.	DAOPHOT II mag. error	Descriptive position
MACHO*05:36:48.7−69:17:00				
468.484	479.611	18.274	0.007	target
465.219	474.707	21.867	0.064	lower left
468.946	486.054	21.840	0.073	upper centre
471.014	475.005	22.850	0.082	lower right
473.660	481.545	22.018	0.047	upper right
MOA J005018.4−723855				
472.825	476.522	18.315	0.012	target
465.993	477.315	21.611	0.035	left centre
478.178	474.659	21.195	0.050	right centre
MOA J005623.5−722123				
478.514	481.518	18.488	0.012	target
479.596	487.261	21.607	0.076	upper centre
484.830	484.712	21.609	0.046	upper right
487.817	480.052	21.638	0.044	right centre

for a 3^{rd} light parameter albeit not for an individual filter, i.e. all or nothing.

MOA J005623.5−722123 has higher residuals than the other two targets as determined by DAOPHOT II in the Figure 5.26. The three nearby stars blend into the wings of the target. Additionally, the *square* shape of the stellar image suggests other well blended stars that are not detected at this level. Higher resolution images would be needed to confirm this.

To ensure that these results were reasonable, the light curves of the nearby stars were extracted from their respective `var.fits` files the same manner as the constant stars where extracted. The results for each target for the I_C filter were examined. The light curves were constructed from all frames. The resulting light curves were very contaminated by the target star as in frames of worse seeing, the blended stars profiles are engulfed by the target star profile. Therefore the light curves resemble a target star light curve.

If the nearby stars that blend with the target in poor seeing conditions are variable, the amount can be considered minimal. To obtain a definite answer, more photometry in better seeing conditions are required in order for the photometry to be extracted for these stars.

5.10 Estimation of magnitudes

Magnitudes for the targets were calculated by MOA (SMC targets) and MACHO (LMC and SMC targets). As a check of the reduction process, estimates of the magnitudes from the DAOPHOT II reductions were obtained. In DAOPHOT II the magnitudes are calculated as given in equation 5.8, with an arbitrary value of 25 used in the equation to calibrate the magnitudes, i.e. defines a zero point. Therefore an estimate of the zero point for each frame needs to be

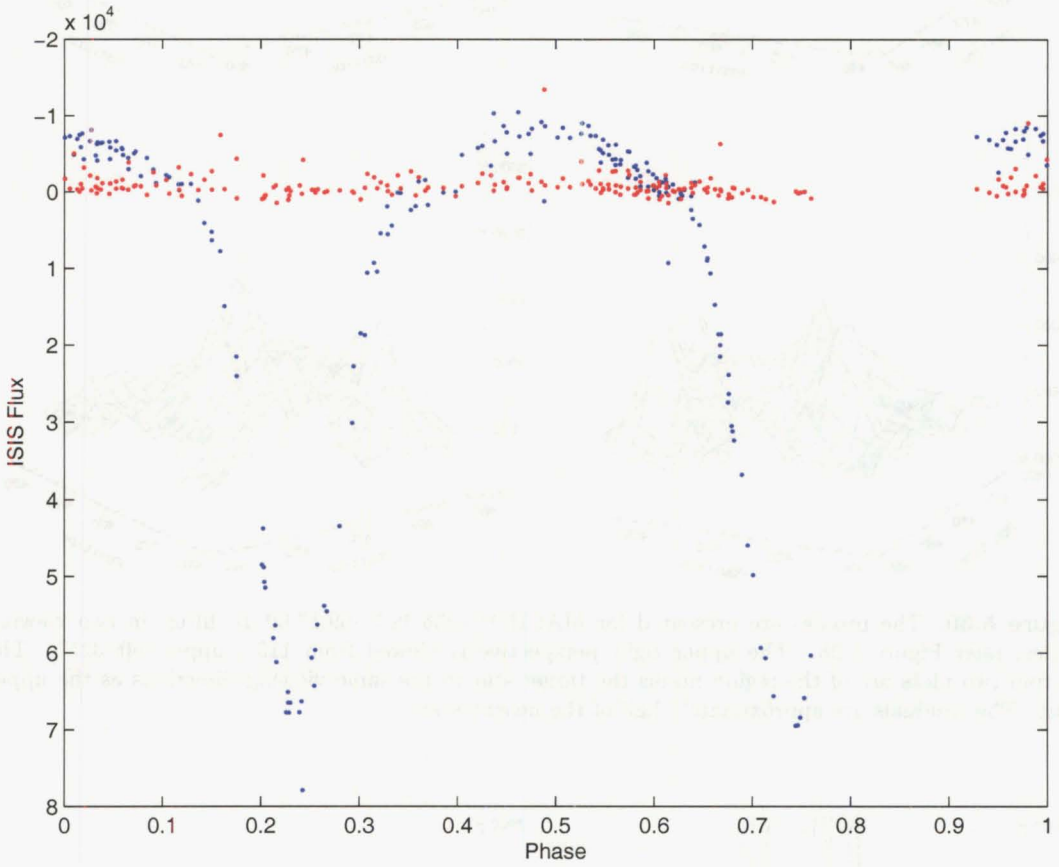

Figure 5.29: The light curve for MOA J005623.5−722123, and a nearby star, far right (487.817,480.052) in Figure 5.28. The effect of the nearby star on the target star can be considered negligible due to the small variation in flux and its distance from the target. The wings of the stellar profile slightly overlap, Figure 5.32, but two stars are easily separated in the reduction process.

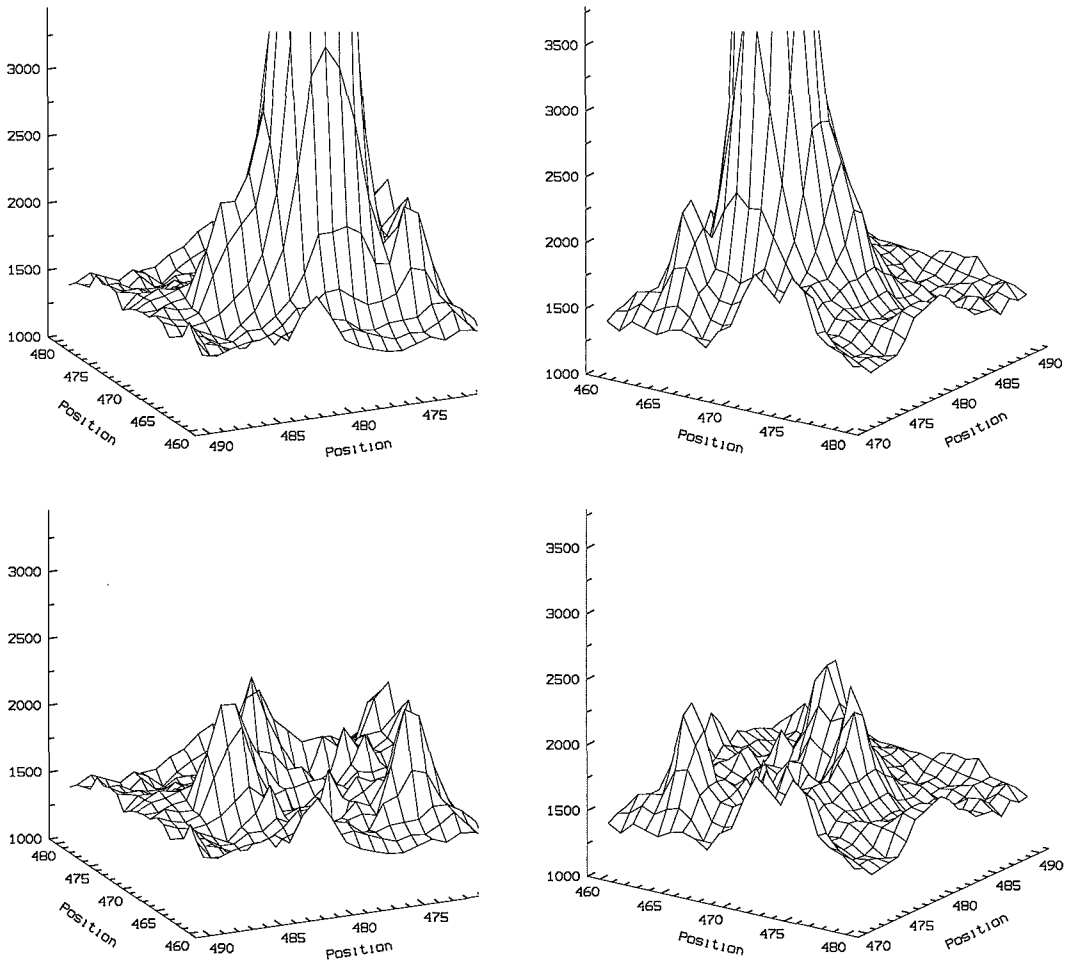

Figure 5.30: The profiles are presented for MACHO*05:36:48.7−69:17:00 I_C filter, in two viewing angles, refer Figure 5.28. The upper right perspective is viewed from 115°, upper left 325°. The bottom two plots are of the region minus the target star in the same viewing directions as the upper plots. The residuals are approximately half of the nearby stars.

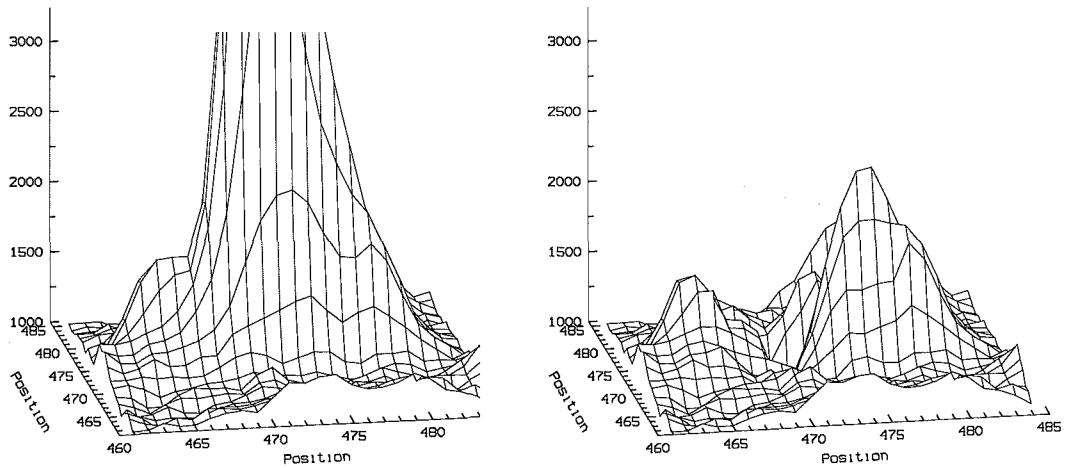

Figure 5.31: The profiles are presented for MOA J005018.4−72385 I_C filter, refer Figure 5.28. The left perspective is viewed from 10°. The right plot is of the region minus the target star in the same viewing direction as the left plot.

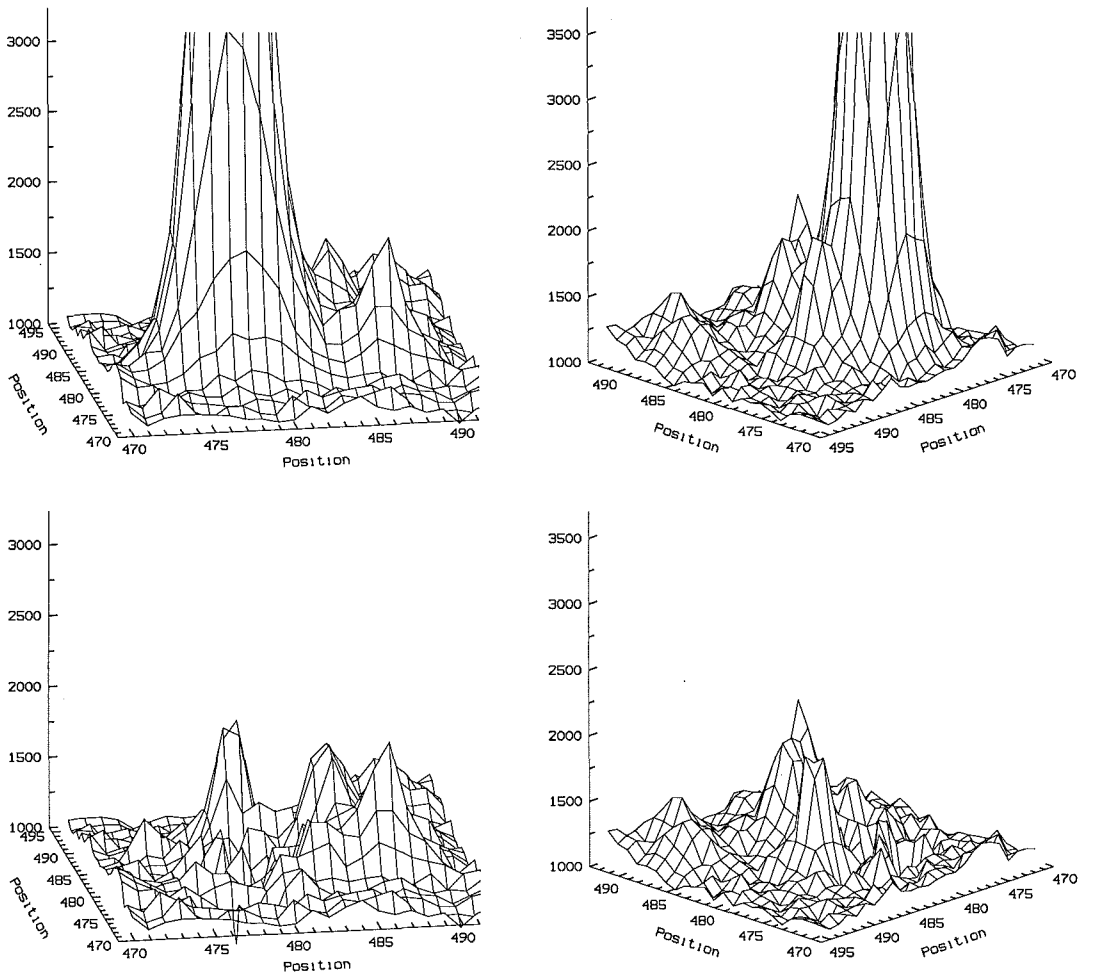

Figure 5.32: The profiles are presented for MOA J005623.5−722123 I_C filter, in two viewing angles. The upper right at 10°, the upper left 135°, refer Figure 5.28 with the viewing direction indicated by the arrow. The lower left and right plots are of the region minus the target star in the same viewing direction as the right plot.

obtained so a comparison can be made to the MOA and MACHO values. This can be obtained by plotting the stars in each frame on the Colour-Magnitude, CM, diagram. The position of the red clump and it respective magnitude gives the offset when compared to calibrated value. The CM diagram was constructed using the V_J and I_C bandpass data, thereby giving $V_J - I_C$ versus V_J and $V_J - I_C$ versus I_C, Figure 5.33. The red clump magnitude for a similar region of the LMC was adopted from Udalski 2000 [162], and for the SMC Udalski 1998 [163]. The LMC Udalski red clump magnitude agreed with Alves et al. [8]. The values derived from Udalski are in V and I of BVI photometric system, (here referred to as V_{OGLE} and I_{OGLE} to avoid confusion with MJUO V_J and I_C or MACHO bandpasses). These are only approximate to the MJUO V_J and I_C bandpasses. The effects of age and metallicity dependence [31], [155] have not been considered in the values extracted from Udalski [162] and [163].

The following are the red clump magnitudes for the LMC and SMC the V_{OGLE} and I_{OGLE} bandpasses respectively.

$$\mathrm{LMC}_{V_{OGLE}} = 19.2\,\mathrm{mag}.$$

$$\mathrm{LMC}_{I_{OGLE}} = 18.2\,\mathrm{mag}.$$

$$\mathrm{SMC}_{V_{OGLE}} = 19.4\,\mathrm{mag}.$$

$$\mathrm{SMC}_{I_{OGLE}} = 18.4\,\mathrm{mag}.$$

The difference between the red clump magnitude from the literature and these data, then gave the offset for the magnitude in equation 5.8. The target magnitudes were then adjusted. The MACHO group have published an out of eclipse magnitude from their calibration of their data for the MACHO*05:36:48.7−69:17:00 target. The out of eclipse magnitudes for the MOA targets, MOA J005018.4−723855 and MOA J005623.5−722123, were calculated. A comparison of the published out of eclipse magnitudes and magnitudes via the red clump estimation are presented in Table 5.10. Note the CM diagrams are constructed from the reference frame which in **not** necessarily the zero point, but some arbitrary value. It transpired that the arbitrary zero flux value was reasonably close the the out of eclipse maxima in all cases. The values derived are only as an approximation to give a starting point for the light curve analysis.

V_{OGLE} and I_{OGLE}

Table 5.10: The red clump magnitudes as estimated from the Colour-Magnitude (CM) diagrams in Figure 5.33, are compared to values obtained for the red clump from Udalski, LMC [162], SMC [163]. The difference then gives the offset which should be similar to the offset of the magnitudes derived from the Colour-Magnitude diagrams for the targets and the published out of eclipse magnitudes. The magnitudes were derived from the reference frames whose position in phase was not necessarily out of eclipse. This provides an approximate check for the photometry and reduction process with regards to the estimated magnitudes. Due to the differences in the filters between MJUO $V_{\rm J}$, MOA $B_{\rm M}$, MACHO V and $V_{\rm OGLE}$ as well as MJUO $I_{\rm C}$, MOA $R_{\rm M}$, MACHO R and $I_{\rm OGLE}$, the magnitudes are only estimates.

Target	MJUO Red clump mag. from CM diagram		OGLE Red clump mag. LMC [162], SMC [163]		Difference (Red clump$_{MJUO}$ − Red clump$_{OGLE}$)		MJUO Magnitude[1] of target from CM diagram		MACHO/MOA[2] Calibrated magnitude		MJUO Estimated magnitude	
	$V_{\rm J}$	$I_{\rm C}$	$V_{\rm OGLE}$	$I_{\rm OGLE}$			$V_{\rm J}$	$I_{\rm C}$			$V_{\rm J}$	$I_{\rm C}$
MACHO*05:36:48.7 −69:17:00	22.4	21.5	19.2	18.2	3.2	3.3	18.3	17.8	$15.3_{\rm MACHO_V}$	$_{\rm MACHO_R}$	15.1	14.5
MOA J005018.4 −723855	22.5	21.7	19.4	18.4	3.1	3.3	18.0	18.3	$14.1_{\rm MOA_{B_M}}$	$14.8_{\rm MOA_{B_M}}$	14.9	14.7
MOA J005623.5 −722123	22.8	22.0	19.4	18.4	3.4	3.6	18.1	18.5	$14.0_{\rm MOA_{B_M}}$	$15.0_{\rm MOA_{B_M}}$	14.7	14.9

[1]The magnitudes are calculated from the reference frames which are **not** the out of eclipse magnitudes, but close to them.

[2]Out of eclipse magnitudes but with different bandpasses than the MJUO data.

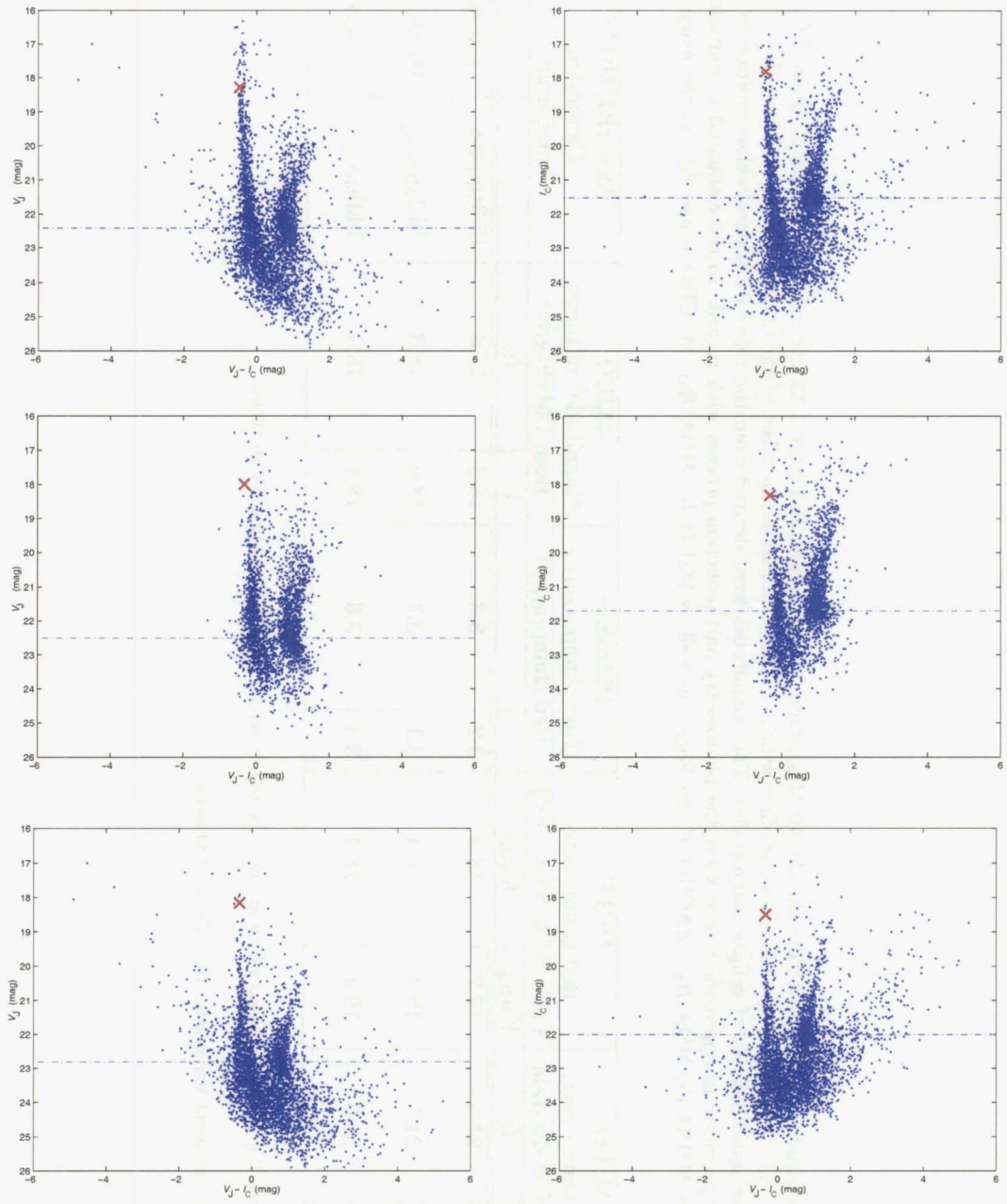

Figure 5.33: The top two Colour-Magnitude diagrams are for MACHO*05:36:48.7−69:17:00, the middle two MOA J005018.4−723855 and the bottom two MOA J005623.5−722123. The positions of the target in the diagrams is indicated by ×. An estimation of the red clump magnitude is indicated by the horizontal dashed line.

Chapter 6

Light curve analysis

The analysis of the reduced light curves is presented in this chapter. The analyses are not complete, in the sense that spectroscopic data, which would fix the size of the systems, was not available. Bounds are presented for the binary parameters including the most astrophysically plausible solutions.

6.1 Brief history of the development of eclipsing binary computer models

Early work involving photometric light curve analysis was undertaken by Henry Russell [130], [129]. Russell modelled eclipsing binaries by means of truncated Fourier series in an effort to solve the system. The light curves, however, needed to be altered, or to use his term, *rectified*, in order to remove *ellipticity* and *reflection* effects. This transformed the system to a spherical model for which look-up tables were then used. As progress in the field was made, it become apparent the systems were in fact far more complicated and Russell's model only gave an approximation to the true system: in many cases the models were markedly incorrect. The simplifications did not suffice and it became apparent that a more vigorous analysis was required if the model solutions were to be more in-line with physical reality. Progress was hindered by the large computation requirements of the models. They had become, for hand calculations, exceedingly long and complicated, and too much to do without the aid of a computer.

The topic had a resurgence about the early 1970s as computers become more readily available to researchers which meant that more sophisticated models could now be run. The programs modelled the systems and computed synthetic light curves and velocity curves. Models based on spherical stars, EBOP (Nelson, Davis and Etzel[101], Eztel [96]), followed on from calculations in the previous years. Ellipsoidal geometry was allowed for in later versions of EBOP, but initially treated by Wood (1971) [177] in a program called WINK. The other approach to the problem was to use Roche lobe geometry as a basis for the modelling program. This was achieved by Lucy (1968) [89], [88], with the addition of reflection effects and gravitational distortions by Hill and Hutching (1970) [75], Wilson and Devinney (1971) [174], and Mochnacki and Doughty (1972a,b), [98], [99]. These codes, with the exception of Wood, used computationally heavy methods of numerical quadrature using many points distributed over the stellar surface. At this time computational speed was a very important. Wood implemented of ellipsoidal approximations of a star's shape, enabled a double-Gauss quadrature scheme thereby dramatically reducing the computational cost. Additionally, it only required a few 100 points distributed over the stellar surface as opposed to 10 000 of the previous methods. Improvements were made by Wilson and Devinney 1976 to their code [175]), by incorporating modifications to calculate tidal distortion and the reflection effect on binary star velocity curves. Initial advances were made by Hill with the implementation of the LIGHT code in 1979, [74] which incorporated a light curve solver called CURFIT from Bevington, [25]. Also around this time, advances were made by Wilson and Devinney 1979 [170], [171], [176] and [172] by using a least-squares method to fit the

observed and modelled light curves. Their programs, referred to as the Wilson-Devinney code, continued to evolve over the years. From this point, the modelling field has expanded using least-squares minimization and Roche-lobe models. The Wilson-Devinney code is now one of the most widely-used programs for synthetic light curve modelling. Its success lies in its ability to be easily added to, so allowing for different scenarios or new parameters. Since its initial development, several improved least-squares based algorithms have been developed to achieve solutions in more difficult systems involving non-linear least-squares problems. Hill revised the LIGHT code and in 1993 released LIGHT2. Another code available is ELC developed by Orosz and Hauschildt [107]. This is similar to the Wilson-Devinney code but uses the NEXTGEN model atmospheres. We selected the Wilson-Devinney code over other available synthetic light-curve codes such as EBOP, Budding's, WINK and ELC. We chose the Wilson-Devinney code because of its generality and our previous experience with it.

6.2 Wilson-Devinney code

A version of the Wilson-Devinney code was modified by Pritchard for his thesis [123] and then further. The version incorporates Kurucz model atmospheres [96] in addition to the black-body and Carbon-Gingerich atmosphere approximations of the standard version of the code. The modifications were derived from the atmosphere subroutine (ATM) of the Calgary group (Milone, priv. comm.). The ATM subroutine interpolates the Kurucz atmosphere models at the local temperature for each grid element on the surface of the model stars whilst adopting the global mean gravity of the star. Pritchard extended the ATM routine to interpolate the Kurucz atmosphere models at the local temperature *and* gravity for each grid element, and to interpolate within tabulated values of the ratios of the flux at the emergent angle relative to the normal emergent flux (thereby eliminating the limb-darkening approximation) for each grid element. This version was termed *WD95K92jdp*, hereafter *WD95*.

The *WD95* software runs under the MIDAS package and incorporates various graph-plotting routines, thus giving a more user-friendly handling of the I/O files. This interface was written by Pritchard.

The *WD95* program comprises two main sub-programs. First, `LC`, for a given set of input parameters, generates a synthetic light curve and, if required, radial velocity curves. Second, `DC`, which computes differential corrections to the parameters in order to give better agreement between the synthetic light curve and observed light curve (and radial velocities). `DC` does not compute corrections for all parameters, but only those in a subset specified by the user. The code allows for the entire data set to be used in the solution i.e. all bandpasses and radial velocities (if available). The advantages are a solution derived with less free parameters and the need to avoid an averaging of values if each light curve (bandpass) is processed individually which can also discard information about each solution.

The program allows for different physical constraints to be imposed on the system e.g. detached, semi-detached, over-contact and x-ray binary. These types of systems are set via a `Mode` parameter as outlined below.

The program is run in one of 8 `Modes`, depending the eclipsing binary system's type. Some modes have degenerate parameters, such as the secondary luminosity being coupled to the temperatures, as in a detached binary model, `Mode 2`, for example.

- `Mode` -1: x-ray binaries

- `Mode 0`: non-constrained models, nonphysical models; solutions can easily be obtained
- `Mode 1`: over-contact binaries, with both stars of identical effective temperature
- `Mode 2`: detached binaries
- `Mode 3`: over-contact binaries, no secondary temperature constraint unlike mode 1
- `Mode 4`: semi-detached binaries, with star 1 filling its Roche lobe
- `Mode 5`: semi-detached binaries, with star 2 filling its Roche lobe
- `Mode 6`: double contact binaries, with both stars accurately filling their Roche lobes

Systems examined in this work were modelled using the detached binary, semi-detached binaries, with star 1 filling its Roche lobe and semi-detached binaries, with star 2 filling its Roche lobe models, (`Mode 2`, `Mode 4` and `Mode 5`).

The *WD95* code allows up to 30 parameters to be changed by the differential correction routine, `DC`. The number of parameters set as variable depends on the system (`Mode`) used. In certain systems, some parameters are redundant, e.g. the luminosity of the secondary component is coupled to the luminosity of the primary and the effective temperature of the two components.

To generate a fitted light curve the parameters relevant to the type of binary must be set variable with an incorporated model stellar atmosphere, refer above. The parameters that can be adjusted which are relevant to this work, i.e. the only input data are the light curves in three bandpasses. The parameters are listed below in order of their appearance in the setup file:

- **Spots**: If required, an arbitrary number of spots can be set. These are specified by a spot latitude, longitude, radius and temperature. The spots can be used to deal with the O'Connell effect[1] by means of obtaining a better fit between the model and observations. The origin of this effect is not known and therefore the interpretation of the use spots is unclear. They were not used in this work.
- **Longitude of periastron,** ω: A value of 90° corresponds to a primary eclipse at periastron.
- **Orbital inclination,** i: In units of degrees.
- **Phase of primary conjunction**: Zero offset for the ephemeris with which the observations have been phased.
- **Eccentricity,** e: Set to 0 for circular.
- **Mass ratio,** q: Secondary/primary (M_2/M_2). This parameter is weakly correlated to the light curves. The exception is the semi-detached case where the relative size of the Roche lobe provides the location of the inner Lagrangian point L_1. Therefore it provides a well defined mass ratio from the light curve and geometric information of the system.
- **Orbital semi-major axis,** a: In units of $R_\odot$ of the relative orbit.
- **Effective temperature,** $T_{\rm eff}$: Set for each component $T_{\rm eff,1}$ = primary, $T_{\rm eff,2}$ = secondary. The different depth of the eclipses in each bandpass provide information on the relative surface brightness. Observations in several bandpasses can provide information on the absolute temperature scale, however for the hot B-stars in this study, observations over the wavelength range of 350 nm ($I_{\rm C}$) to 790nm ($V_{\rm J}$), these correlations are very weak. Therefore the primary temperature is fixed and the secondary temperature solved for.

[1]The out-of-eclipse light levels between the primary and secondary eclipse are higher than between the secondary and primary eclipse, [37] and [106].

- **Surface potential,** Ω: Surface potential of the primary star, Ω_1 and the secondary star, Ω_2.
- **Stellar luminosity,** L: Can be fixed or variable for each component in each bandpass.
- **Gravity darkening component**: Set for each component, a value of 1 is used for radiative envelopes as in this case. This implies that the bolometric flux $\propto$ local gravity.
- **Bolometric albedo coefficient**: Set for each component it specifies the local ratio of re-radiated bolometric energy to received bolometric energy. For a radiative envelope, as in this case, it is set to 1.
- **Axial to orbital rotation rate ratio**: The ratio of the axial rotation rate to the mean orbital rotation rate for each component. For circular orbits, the both have synchronized, therefore the ratio is 1. For eccentric systems, the axial and orbital rotation ratios are synchronized at the periastron rate (Claret 1995, [29]). The axial to orbital rotation rate is given by Avni, [11], equation 6.1.

$$\frac{\omega_{axial}}{\bar{\omega}_{orb}} = \frac{\omega_{peri}}{\bar{\omega}_{orb}} = \sqrt{\frac{1+e}{(1-e)^3}} \tag{6.1}$$

- **Limb darkening coefficient**: Set for each component in each bandpass. These were set as calculated by Pritchard [123].
- **Third light**: This can be set either constant or variable for all the bandpasses. It is not possible to vary it for only one bandpass.

6.3 Light curves

Data points of very poor quality were removed during the ISIS-2.1 reduction process as these were not able to be processed. Further removal of poor quality data after the reduction process was undertaken at the light curve analysis stage. These data were evident during the phasing of the light curve. Points with seeing values greater than 7 arc secs were removed as the uncertainties on the these points were high and so the measurements were considered unreliable. The *cleaned* light curve was then passed to the *WD95* code.

6.3.1 Light curve solutions

It is possible to find many solutions from *WD95* analysis whose parameter sets produce light curves that match the observations. This is especially the case when only the photometric light curves are available without radial velocity data. The parameter space surrounding the most probable and astrophysically plausible solutions were explored for each target. By making some initial assumption, it is possible to obtain bounds for the systems.

However, this still leaves a large number of possible solutions. As a further constraint to obtain an astrophysically-plausible idea of the nature of the stars, we require the *WD95*-derived properties to match Geneva evolutionary models (Geneva grids of stellar evolution models, here termed Geneva models) where possible.

The Geneva group has made publicly available[2], its extensive homogeneous database of stellar evolution models. The models cover a range of masses 0.1 to 120 $M_\odot$ as well as metallicities

[2]http://obswww.unige.ch/~mowlavi/evol/stev_database.html

Z=0.001 to 0.1 (LMC Z = 0.008 ([m/H] = −0.3), [136] and [95], SMC Z = 0.004 ([m/H] = −0.5), [28] and [95]). The models generally cover a range of evolutionary phases from the main sequence up to either the end of carbon burning for massive stars, the early asymptotic giant branch phase for intermediate-mass stars, or core helium flash for low-mass stars. Fortran codes for the calculation of isochrones are also available.

6.3.2 Convergence of a solution

The question of when a particular solution has converged can be difficult to determine especially for cases such as these where only photometric data is available. In parameter space, several local minima can occur, however the global minimum, i.e. the deepest minimum, is the desired one provided it is very clearly the deepest one. If the minima are all of similar depths then more information is required to decide which solution best describes the physical system. Distinguishing between several local minima and a global minimum can be difficult, therefore convergence criteria are required. The convergence criteria, however, must allow the algorithm to *escape* the local minima in order arrive at a global minimum, or another if all solutions are of similar depth.

The *WD95* code outputs the *suggested parameter correction* and the *standard error* for each parameter that is flagged to be optimized. Ideally, as convergence on a solution occurs, the suggested parameter correction should begin to become smaller and smaller as compared to the standard error with each iteration. Eventually, the suggested parameter correction will become negligibly small. However, this is not usually the case as a solution may approach a local minimum where indeed, the suggested parameter corrections are smaller than standard errors. However further iterations start to lead away from this minimum to converge upon another local minimum. To establish when convergence has been achieved, the requirement set is for all the suggested parameter corrections to be simultaneously smaller than the respective standard error **and** this to continue to be the case for one further iteration. The solution is assigned the parameter set of the first iteration. This was the criterion used by Pritchard [123], who also investigated the use of the Method of Multiple Subsets, MMS [173]. This breaks the parameters which are strongly correlated into small subsets of weakly-correlated parameters. These subsets are solved until the suggested parameter corrections are negligibly small. The differential corrections are applied to all subsets in turn until the convergence criterion is achieved for all of them. Pritchard found MMS had the tendency to remain in local minima rather than continue on to a global minimum which is possible if the former criterion is adopted.

Using the modified *WD95* code with a model atmosphere procedure based on the ATLAS9 code, Graczyk (2003), [58], adopted the following convergence criterion. The solution was considered to have converged if:

The suggested parameter corrections are less than 0.75 times the standard error (1.0 times in the case of eccentricity and argument of periastron) on two consecutive iterations.

Although slightly more restrictive than the criteria used in this work, it was found that in many cases, the suggested parameter corrections were less than 0.75 times their standard error.

6.4 Scaling of parameters

The analysis of the acquired differential photometry enables the period to be accurately determined. However the mass ratio, $q = M_2/M_1$, and semi-major axis, a, of the system are usually unknown. However, estimates can be made of the individual masses, M_1 and M_2, and the semi-major axis when the magnitude at maximum light and stellar evolutionary models are used to restrict the solutions to astrophysically plausible ones, as outlined in the following sections.

A light curve model is calculated by *WD95* to fit the observed light curve for a given value of the semi-major axis, a. As this is unknown (since only photometry is available), it was therefore usual to assign a an initial arbitrary value of 15 or $20\,R_\odot$. Since the systems most likely consist of early type B-stars and have periods of a few days these seem reasonable starting values. If the value of the semi-major axis is now changed, the resultant fitted light curve will correspond to the same relative dimensions, i.e. R_1/a, R_2/a and e[3].

The difference between the depth of each eclipse and bandpass give an indication of the temperature differences between the stars. The effective temperatures, $T_{\rm eff,1}$ and $T_{\rm eff,2}$ are not well defined by the observed photometric light curves and hence the geometric parameters defining the light curve solution from the *WD95* fit are relatively insensitive to changes in effective temperature. Solutions for a range of effective temperature, $T_{\rm eff,1}$, were solved for, where defining a value of $T_{\rm eff,1}$ then sets $T_{\rm eff,2}$.

Adopting a value of $T_{\rm eff,1}$, and hence $T_{\rm eff,2}$, together with q for a value of a now defines a model of a fixed size and surface flux. Therefore the luminosity can be calculated, for example in units of watts in the $V_{\rm J}$ bandpass. In the implementation of the *WD95* code, the absolute $V_{\rm J}$ magnitude, $M_{V_{\rm J}}$ is calculated. The implementation of the *WD95* code used was modified for use with the EROS LMC catalogue and therefore reports the apparent magnitude one would expect for a distance modulus to the LMC of 18.35 mag. and reddening of $E(B-V) = 0.08$ mag., adopting:

$$A_V/E(B-V) = 3.2 \tag{6.2}$$

It was preferred not to modify the *WD95* code but to relate the reported apparent magnitude to the corresponding absolute magnitude manually. Therefore for the $V_{\rm J}$ bandpass, for example:

$$V_{\rm J} = M_{V_{\rm J}} + DM + A_{V_{\rm J}} \tag{6.3}$$

Substituting gives:

$$V_{\rm J} = M_{V_{\rm J}} + 18.35 + 3.2 \times 0.08 \tag{6.4}$$

Therefore for the LMC:

$$V_{\rm J} = M_{V_{\rm J}} + 18.61 \tag{6.5}$$

or

$$M_{V_{\rm J}} = V_{\rm J} - 18.61 \tag{6.6}$$

The *WD95* code reports the apparent magnitudes as derived from the models, for each bandpass for both components combined and for each individual component. These values are, as outlined

[3]Due to numerical noise the values will, in practice, not be exactly the same.

above for the M_{V_J} bandpass, for a model at a distance modulus of 18.35 mag. and reddened (E(B-V)) by 0.08 mag. Since targets are contained in both the LMC and SMC, the analysis was conducted in terms of absolute magnitudes M_{V_J}. The approximate maximum light magnitudes as derived from the V_J bandpass were 14.5, 14.9 and 15.1 mag. for MACHO*05:36:48.7−69:17:00, MOA J005623.5−722123 and MOA J005018.4−723855 respectively. The total absolute magnitude for each system was then calculated using the distance modulus and reddening E(B-V), for the LMC of 18.50 mag. and 0.13 mag. and for the SMC 18.90 mag. and 0.09 mag. respectively (Westerlund (1997) [169]). These estimated M_{V_J} magnitudes are therefore −4.4, −4.4 and −4.1 mag. for MACHO*05:36:48.7−69:17:00, MOA J005018.4−723855 MOA J005623.5−722123 respectively.

Using the starting value of $a = 15.0$, a set of initial solutions was obtained for a range of mass ratios and effective temperatures. These solutions were then compared to Geneva models of a similar metallicity to obtain astrophysically plausible solutions. The solutions from the Geneva models are expected to differ to those of the initial set of solutions. The best matching solution from the set of solutions was then selected and scaled to match the Geneva models by the scaling factors as outlined below.

The difference between the estimated and calculated (from *WD95* models) values of M_{V_J} (denoted by est and mod respectively) are used to derive a scale factor, equivalent to the relative increase in apparent brightness ($l_{\rm est}/l_{\rm mod}$) needed for the model to match the observed magnitude of the system, equations 6.7 and 6.8.

$$M_{V_{J,\rm est}} - M_{V_{J,\rm mod}} = -2.5 \log \left(\frac{l_{\rm est}}{l_{\rm mod}} \right) \tag{6.7}$$

therefore

$$\text{scaling factor} = \left(\frac{l_{\rm est}}{l_{\rm mod}} \right) = 10^{-0.4 \times (M_{V_{J,\rm est}} - M_{V_{J,\rm mod}})} \tag{6.8}$$

The result of equation 6.8 is the scaling factor. The brightness of the system is increased by this factor; the square root of this factor, the linear dimension factor, then scales $R_{1,2}/R_\odot$ and a. Kepler's third law gives:

$$(M_1 + M_2)P^2 = a^3 \tag{6.9}$$

If the separation is increased by the linear dimension factor, then each individual mass is increased by:

$$(\text{scaling factor})^{\frac{3}{2}} \tag{6.10}$$

Using these scaling factors, a further constraint can be added between the semi-major axis a, and the effective temperature $T_{\rm eff,1}$ (and therefore $T_{\rm eff,2}$) for a given mass ratio, q, since an approximate value of maximum light is known. Using a particular q and $T_{\rm eff,1}$, the system can be scaled, namely changing a, to give the appropriate magnitude at maximum light. Plotting the solutions for a given a and q as a function of $T_{\rm eff,1}$ (and therefore $T_{\rm eff,2}$) on the HR diagram, gives two lines, one for the primary and one for the secondary. The secondary can be expressed

as a function of $T_{\rm eff,2}$, although it is coupled to $T_{\rm eff,1}$. As will be discussed further below, model parameters are adjusted until one or both of the component stars match the physical properties of Geneva model stars for the same mass and temperature.

6.5 MACHO*05:36:48.7–69:17:00

The eccentricity of this system is clearly apparent from the light curve with the secondary eclipse minima located ~0.4 in phase from the primary minima and different widths for the eclipses, Figure 6.2. The shape of the light curve indicates a detached system comprising two very similar stars due to the similar eclipse depths in the u, V_J and I_C bandpasses. As mentioned previously, this target was selected from the MACHO database, therefore giving access to MACHO data spanning an approximate ten year interval. This gave a longer baseline than the 3 years of the MJUO observations to detect possible apsidal motion that might be expected in an eccentric system.

A number of initial observations were made in the V_J filter at the start of the observing period, with u and I_C started at a later time. This gave a mean epoch of observation 440 days later for u and I_C observations. It soon became clear in the analysis of the MJUO data that apsidal motion might be an issue. The addition of the MACHO data to the MJUO data confirmed that this was indeed the case due to the difficulties of the phasing of the light curve on a simple linear ephemeris.

To investigate and determine the apsidal period, the span of the data was divided into approximately yearly intervals, Table 6.1. Light curve solutions for each interval were determined, giving the values of the inclination, i, eccentricity, e, longitude of periastron, ω and times of primary, $T_{E,1}$, and secondary, $T_{E,2}$ minima, Tables 6.1 and 6.2. Solutions were also determined for a common mean eccentricity.

The derived longitudes of periastron as a function of time are plotted in Figure 6.1 (upper panel). The resultant apsidal period derived from Figure 6.1 is 100 ± 5 yrs. Two values of the longitude of periastron were determined for V_J, $\omega = 196.6°$, and u, I_C, $\omega = 200.9°$, corresponding to the mean epochs of each set of observations.

Table 6.1: Times of minima for MACHO*05:36:48.7–69:17:00 using the MACHO and MOA data divided into approximately yearly intervals. $T_{E,1}$ and $T_{E,2}$ are the primary and secondary eclipse times respectively.

Minima calculated from observations	$T_{E,1}$ (HJD)	$T_{E,2}$ (HJD)
MACHO	2449115.7687	2449117.2161
	2449535.8072	2449537.2500
	2449917.3118	2449918.7542
	2450318.0755	2450319.5201
	2450722.6960	2450724.1438
	2451262.1891	2451263.6416
MJUO V_J	2451589.7409	2451591.2003
MJUO u and I_C	2452025.1908	2452026.6548

The value for the anomalistic period was determined using the relations given in Gimenez & Garcia-Pelayo 1983, [57]. The anomalistic period, P_a, is defined as the time between two consecutive periastron passages and the sidereal period, P_s, equation 6.11 (derived via equations 2 and 15 in Gimenez & Garcia-Pelayo 1983), defined as the time between two consecutive primary or secondary minima.

$$P_s = P_a(1 - \frac{P_a}{U}) \tag{6.11}$$

where U is the period of the apsidal motion. The time $T_{E,j}$, of the j^{th} (primary $j = 1$, secondary

Table 6.2: Ephemerides for MACHO*05:36:48.7−69:17:00

Epoch, T_0	HJD 2452024.946 ± 0.002
Sidereal period, P_s	3.853529 d ± 0.000005
Anomalistic period, P_a	3.853935 d ± 0.000005
Apsidal period, U	36 600 d ± 1700 (100 yr ± 5)
Longitude of periastron, ω at T_0	200.9° ± 1.2
Rate of advance of periastron, $\dot{\omega}$	3.6°/yr ± 0.2

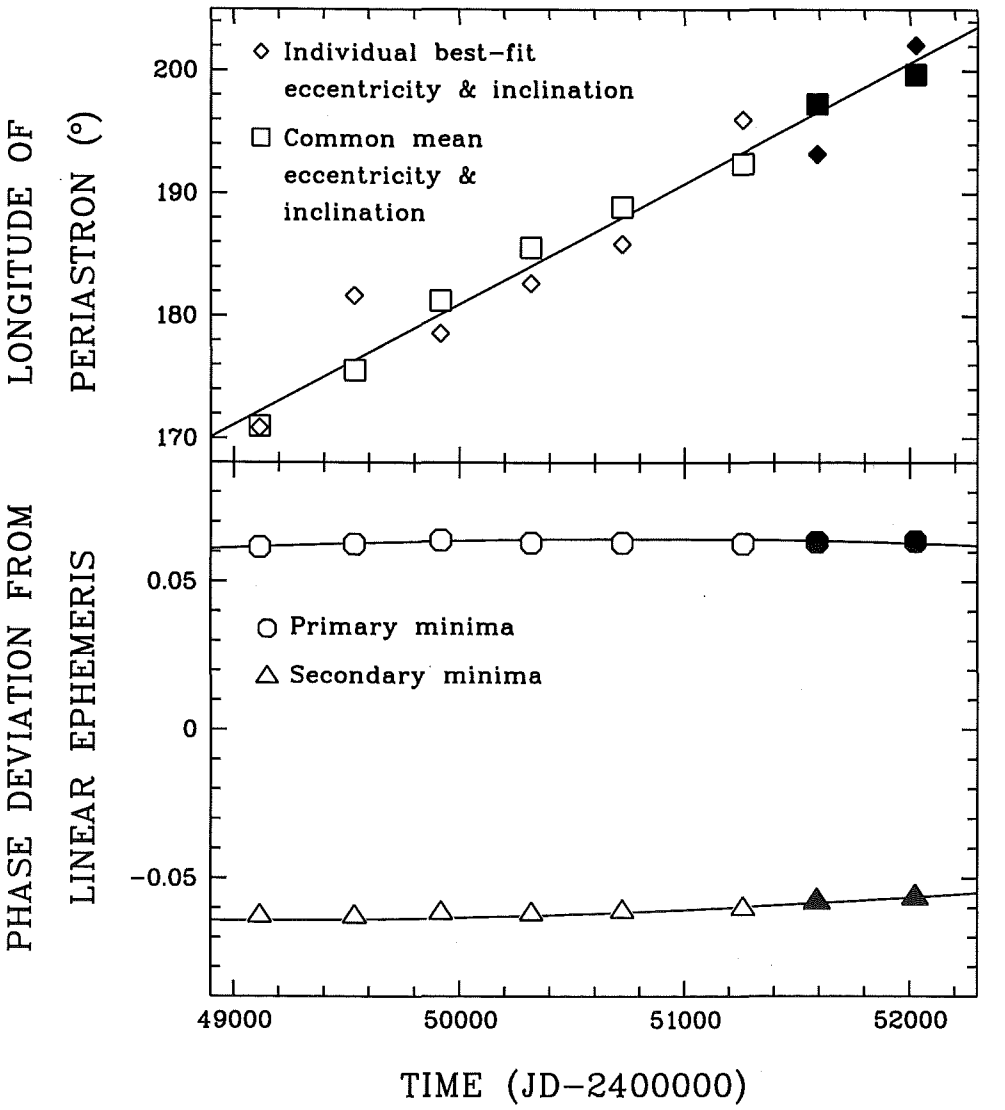

Figure 6.1: Apsidal motion analysis of MACHO*05:36:48.7−69:17:00. The combination of the MACHO and MJUO data was divided into yearly intervals. For each interval the longitude of periastron was calculated using *WD95*, upper graph. Values were calculated using an optimal eccentricity for each interval, ◇, while values using a common mean eccentricity are denoted by □. Filled symbols derive from the MJUO data, others from MACHO data. The fitted line gives an apsidal period of 100 ± 5 years. The lower graph presents the fit to the data in Table 6.1 and equation 6.12.

$j = 2$) eclipse in cycle E is given in equation 6.12 (reproduced from Gimenez & Garcia-Pelayo 1983 equation 20, with P_a substituted for P).

$$\begin{aligned}
T_{\mathrm{E,j}} &= T_0 + P_s E + (j-1)\frac{P_a}{2} + (2j-3)\frac{eP_a}{2\pi}\Bigg(\cot^2 i + 2 - \\
&- e^2\left[\frac{3}{4}\cot^2 i - \frac{1}{4}(2+\csc^2 i)\cot^2 i \csc^2 i + e^2\left(\frac{1}{8}\cot^2 i + \right.\right. \\
&+ \left.\left.\frac{1}{4}\cot^2 i \csc^2 i - \frac{1}{8}\cot^2 i \csc^6 i(2+\csc^2 i)\right)\right]\Bigg)\cos\omega + \\
&+ \frac{e^2 P_a}{4\pi}\left(\cot^2 i \csc^2 i + 2\cot^2 i + \frac{3}{2} + e^2\left[\frac{1}{4} - \cot^2 i + \right.\right. \\
&+ \left.\left.\frac{1}{2}\cot^2 i \csc^4 i(2+\csc^2 i)\right]\right)\sin 2\omega - \\
&- (2j-3)\frac{e^3 P_a}{8\pi}\left[(2+\csc^2 i)\cot^2 i \csc^2 i + 3\cot^2 i + \frac{4}{3} + \right. \\
&+ e^2\left(\frac{1}{2} - \frac{3}{4}\cot^2 i + \frac{3}{4}\cot^2 i \csc^4 i\,(2\csc^2 i + \right. \\
&+ \left.\left.\csc^4 i + 1)\right)\right]\cos 3\omega - \frac{e^4 P_a}{16\pi}\left(\frac{5}{4} + \cot^2 i\,(4 + 2\csc^4 i + \right. \\
&+ \left.3\csc^2 i + \csc^6 i)\right)\sin 4\omega + (2j-3)\frac{e^5 P_a}{32\pi}\left(\frac{6}{5} + \cot^2 i(5 + \right. \\
&+ \left.\csc^8 i + 2\csc^6 i + 3\csc^4 i + 4\csc^2 i)\right)\cos 5\omega
\end{aligned} \tag{6.12}$$

where T_0 is the initial primary minimum date for E=0, with the inclination and eccentricity denoted by i and e respectively. Calculated values of $T_{\mathrm{E},1}$ and $T_{\mathrm{E},2}$, as presented in Table 6.1 from the light curve analysis were fitted, Figure 6.1, to obtain values of T_0, P_a and P_s using the value of U determined from the periastron motion. The veering of the orbit gives, at this time, a side-on view of the orbit. This results in eclipse times that at present vary by only very small amounts from a linear ephemeris (Figure 6.1, lower panel).

Due to the apsidal motion, two different mean epochs for V_{J} and u/I_{C} were used in the light curve analysis with two independent solutions calculated for the respective bandpass. The small data span, with respect to the apsidal period, and with the current side-on viewing of the orbital plane, allowed a linear ephemeris based on T_0 and P_s to be used in the light curve analysis of the MJUO observations.

Due to the system's eccentricity, the axial rotation rate was synchronized to the value at periastron rather than the orbital value adopted when the orbit is circular.

6.5.1 Adjustments to parameters

Given the system most likely comprises of two similar early-B stars, the initial starting temperatures for the light curve analysis would be expected to fall in the range of 20 000 to 30 000 K. The adjustments were made in order to select appropriate values as explained in section 6.4. Initial tentative solutions for the system used a semi-major axis $\mathrm{a} = 20.00\,\mathrm{R}_\odot$. The solution was then scaled to give a maximum out of eclipse V_{J} luminosity of $\mathrm{M}_{V_{\mathrm{J}}} = -4.4$ mag.

Table 6.3: *WD95* fits for MACHO*05:36:48.7−69:17:00, V_J filter. $P_s = 3.853529$ d, $T_0 = 2451589.7409$, SMaxis $= 33.5\,R_\odot$, $e = 0.200$, $\omega = 196.6°$. Although not all figures are significant, they are presented to show differences in values, some due to numerical noise.

M_2/M_1	M_1 ($M_\odot$)	M_2 ($M_\odot$)	$T_{\rm eff,1}$ (K)	$T_{\rm eff,2}$ (K)	i (°)	$\overline{R1}/a$	$\overline{R2}/a$	L_1/L_2 V_J
0.7	20.03	14.02	22 500	20 995	85.836	0.213	0.157	2.064
0.7	20.03	14.02	30 000	26 490	85.201	0.209	0.164	1.827
0.7	20.03	14.02	37 500	34 795	86.008	0.212	0.156	2.051
0.9	17.92	16.13	22 500	20 904	84.183	0.193	0.186	1.197
0.9	17.92	16.13	30 000	26 514	84.292	0.196	0.182	1.306
0.9	17.92	16.13	37 500	34 621	84.485	0.198	0.179	1.379
1.1	16.21	17.84	22 500	20 981	84.258	0.178	0.198	0.906
1.1	16.21	17.84	30 000	26 848	84.317	0.177	0.198	0.888
1.1	16.21	17.84	37 500	34 812	84.341	0.182	0.195	0.973
1.3	14.80	19.25	22 500	20 965	84.304	0.173	0.203	0.821
1.3	14.80	19.25	30 000	26 803	84.323	0.173	0.203	0.815
1.3	14.80	19.25	37 500	34 788	84.421	0.173	0.202	0.820

Table 6.4: *WD95* fits for MACHO*05:36:48.7−69:17:00, u and I_C filter. $P_s = 3.853529$ d, $T_0 = 2452025.1908$, SMaxis $= 33.5\,R_\odot$, $e = 0.200$, $\omega = 200.9°$. Although not all figures are significant, they are presented to show differences in values, some due to numerical noise.

M_2/M_1	M_1 ($M_\odot$)	M_2 ($M_\odot$)	$T_{\rm eff,1}$ (K)	$T_{\rm eff,2}$ (K)	i (°)	$\overline{R1}/a$	$\overline{R2}/a$	L_1/L_2 u	I_C
0.7	20.03	14.02	22 500	20 708	85.366	0.212	0.160	2.011	1.974
0.7	20.03	14.02	30 000	26 011	85.552	0.215	0.158	2.131	2.006
0.7	20.03	14.02	37 500	34 766	85.499	0.212	0.159	2.022	1.951
0.9	17.92	16.13	22 500	20 541	85.245	0.212	0.161	1.997	1.967
0.9	17.92	16.13	30 000	25 487	85.345	0.212	0.159	2.027	2.023
0.9	17.92	16.13	37 500	34 282	85.360	0.213	0.160	2.027	1.942
1.1	16.21	17.84	22 500	20 328	84.570	0.204	0.171	1.652	1.620
1.1	16.21	17.84	30 000	25 226	84.636	0.205	0.169	1.694	1.687
1.1	16.21	17.84	37 500	34 024	84.663	0.205	0.170	1.687	1.610
1.3	14.80	19.25	22 500	20 454	84.004	0.190	0.189	1.172	1.147
1.3	14.80	19.25	30 000	25 464	84.056	0.191	0.188	1.195	1.185
1.3	14.80	19.25	37 500	34 087	84.126	0.192	0.186	1.241	1.186

Component stars were then be compared to Geneva models [136] and [95], for the LMC metallicity, $[m/\mathrm{H}] = -0.3$ (z=0.008). Here the solutions were expected to look like coeval Geneva models. Adjustments to q and $T_{\rm eff,1}$ gave the components masses on the theoretical HR diagram. Altering q has a relatively small effect on the effective temperatures, the individual masses M_1 and M_2 are changed more significantly. A solution can be found whereby the primary and secondary masses correspond to the Geneva evolutionary tracks and are also on (very close to) a single isochrone. Although the apparent magnitude was not known with any great accuracy, the solution does indicate an astrophysically plausible solution.

Separate solutions for the V_J bandpass and u/I_C bandpasses were calculated for various primary temperatures, $T_{\rm eff,1} = 37\,500$, 30 000 and 22 500 K for each mass ratio; 0.7, 0.9, 1.1 and 1.3. The results are presented in Table 6.3 for the V_J bandpass and Table 6.4 for the u/I_C bandpasses. The solutions are scaled to the value of semi-major axis finally adopted (a $= 33.5\,\mathrm{R}_\odot$). The addition of 3^{rd} light was not required in these solutions.

Table 6.5: An astrophysically plausible solution for MACHO*05:36:48.7–69:17:00

Mass ratio, q, (M_2/M_1)	0.7
M_1	$20\,M_\odot$
M_2	$14\,M_\odot$
$T_{\rm eff,1}$	33 500 K
$T_{\rm eff,2}$	29 500 K
Inclination, i, $\overline{\rm av}$ of individual $V_{\rm J}$ and $u/I_{\rm C}$	85.8°
Longitude of periastron, ω, $V_{\rm J}$	196.6°
Longitude of periastron, ω, $u/I_{\rm C}$	200.9°
Epoch $T_{1,\omega(V_{\rm J})}$ of longitude of periastron, ω, $V_{\rm J}$	2451589.7409
Epoch $T_{1,\omega(u,I_{\rm C})}$ of longitude of periastron, ω, $u/I_{\rm C}$	2452025.1908
Semi-major axis, a	$33.5\,R_\odot$
eccentricity, e	0.2
$\overline{R_1}/a$, $V_{\rm J}$	0.21
$\overline{R_2}/a$, $V_{\rm J}$	0.16
$\overline{R_1}$, $V_{\rm J}$	$7.0\,R_\odot$
$\overline{R_2}$, $V_{\rm J}$	$5.5\,R_\odot$
$\overline{R_1}/a$, $u/I_{\rm C}$	0.21
$\overline{R_2}/a$, $u/I_{\rm C}$	0.15
$\overline{R_1}$, $u/I_{\rm C}$	$7.1\,R_\odot$
$\overline{R_2}$, $u/I_{\rm C}$	$5.1\,R_\odot$
L_1/L_2 $V_{\rm J}$	1.9
L_1/L_2 u	2.1
L_1/L_2 $I_{\rm C}$	2.1

The solutions for the $V_{\rm J}$ bandpass tended to give values of $T_{\rm eff,2} \approx 400$ K higher than those for the $u/I_{\rm C}$ bandpasses, the exception being $M_2/M_1 = 0.9$, 1.1 and 1.3 for $T_{\rm eff,1} = 30\,000$ K where the difference is greater at $\approx 1\,000$ K, 1 500 K and 1 500 K respectively. The inclinations of the two solution sets generally agree within 0.3° except for the mass ratio of 0.9, where they differ by approximately 1°. The radii of the components are presented in terms of the components' separation, i.e. $\overline{R1}/a$ for the primary and $\overline{R2}/a$ for the secondary. The radii for the primary, are approximately $19\% \pm 2\%$ of the separation for $V_{\rm J}$ and $20\% \pm 1\%$ for $u/I_{\rm C}$ bandpasses, over all calculated mass ratios therefore giving agreement between the two solution sets. The secondary relative radius for $V_{\rm J}$ is $18.5\%^{+1.8\%}_{-2.9\%}$, with the results of $q = 0.7$ favouring a lower value. The $u/I_{\rm C}$ bandpasses give approximately $17.4\% \pm 1.5\%$. Difference between $\overline{R1}/a$ and $\overline{R2}/a$ were of the order of 10% for $q = 0.9$ and 1.1, increasing to approximately 25% for $q = 0.7$ and 1.3. The notable difference between the two being a large secondary for the $V_{\rm J}$ bandpass as $q = 1.1$ and 1.3 but $\overline{R1}/a$ always remains greater than $\overline{R2}/a$ for the ratio of $u/I_{\rm C}$ bandpasses solutions. For a given set of parameters, the WD95 code produced a particular radius ratio. But previous experience [123], has shown that there are likely to be almost equally good local minima with the inverse of this ratio. However no attempt was made to find them in this work. Spectroscopy is required to remove both these ambiguities, although is it expected that $R_1 > R_2$ since M1 is the more massive star.

The details of an astrophysically plausible solutions for the system is presented in Table 6.5, and plotted with the light curve in Figure 6.2 and by the components' positions in the HR diagram in Figure 6.3. The solution is a *possible* solution based on the photometric data, although the actual solution is expected to be close to this. The corresponding age is estimated to be 5 million years, as derived from the theoretical stellar models, Figure 6.3. The parameters were scaled to match the Geneva stellar evolutionary model solutions by a scaling factor of $\sqrt{2.80}$ with an increase in a from 20.00 to $33.5\,R_\odot$.

Table 6.6: *WD95* fits for MACHO*05:36:48.7−69:17:00, V_J filter near the possible solution. $P_s = 3.853529$ d, $T_0 = 2451589.7409$, SMaxis $= 33.5\,R_\odot$, $e = 0.200$, $\omega = 196.6°$. The possible solution parameters are given in Table 6.5. Although not all figures are significant, they are presented to show differences in values, some due to numerical noise.

M_2/M_1	M_1 ($M_\odot$)	M_2 ($M_\odot$)	$T_{\rm eff,1}$ (K)	$T_{\rm eff,2}$ (K)	i (°)	$\overline{R1}/a$	$\overline{R2}/a$	L_1/L_2 V_J
0.65	19.46	14.59	31 500	26 388	85.004	0.211	0.165	2.2112
0.65	19.46	14.59	33 500	28 338	84.870	0.210	0.166	1.8450
0.65	19.46	14.59	35 500	31 645	85.852	0.217	0.155	2.2381
0.70	20.03	14.02	31 500	26 404	85.409	0.213	0.160	2.0820
0.70	20.03	14.02	35 500	31 282	85.603	0.215	0.157	2.1548
0.75	19.46	14.59	31 500	26 046	84.478	0.205	0.173	1.6969
0.75	19.46	14.59	33 500	28 042	84.598	0.206	0.171	1.7050
0.75	19.46	14.59	35 500	29 500	84.856	0.211	0.163	2.1682

Table 6.7: *WD95* fits for MACHO*05:36:48.7−69:17:00, u and I_C filter near the possible solution. $P_s = 3.853529$ d, $T_0 = 2452045.1908$, SMaxis $= 33.5\,R_\odot$, $e = 0.200$, $\omega = 200.9°$. The possible solution parameters are given in Table 6.5. Although not all figures are significant, they are presented to show differences in values, some due to numerical noise.

M_2/M_1	M_1 ($M_\odot$)	M_2 ($M_\odot$)	$T_{\rm eff,1}$ (K)	$T_{\rm eff,2}$ (K)	i (°)	$\overline{R1}/a$	$\overline{R2}/a$	L_1/L_2 u	I_C
0.65	20.64	13.41	31 500	26 767	86.217	0.212	0.153	2.1699	2.1501
0.65	20.64	13.41	33 500	28 058	86.217	0.212	0.153	2.1984	2.1370
0.65	20.64	13.41	35 500	31 535	86.249	0.213	0.153	2.2140	2.1182
0.70	20.03	14.02	31 500	26 611	86.236	0.212	0.152	2.1878	2.1704
0.70	20.03	14.02	35 500	30 922	86.215	0.211	0.153	2.2088	2.1090
0.75	19.46	14.59	31 500	26 498	84.967	0.201	0.167	1.7209	1.6971
0.75	19.46	14.59	33 500	27 893	85.982	0.211	0.154	2.1552	2.0984
0.75	19.46	14.59	35 500	30 772	85.541	0.210	0.159	2.0437	1.9482

Several solutions were explored around the possible solution given in Table 6.5. Using the same semi-major axis of $33.5\,R_\odot$, solutions were obtained for mass ratios 0.05 above and below the possible solution, together with effective temperatures, namely $T_{\rm eff,1}$, 2 000 K above and below the possible solution. The numerical results are presented in Table 6.6 for the V_J bandpass and Table 6.7 for the u and I_C bandpasses.

As the solutions deviate from the possible solution, it becomes difficult to place both components on the same, or close to the same, isochrone, refer Figure 6.3 and on evolutionary tracks corresponding to each component's mass whilst maintaining the desired value of the absolute magnitude.

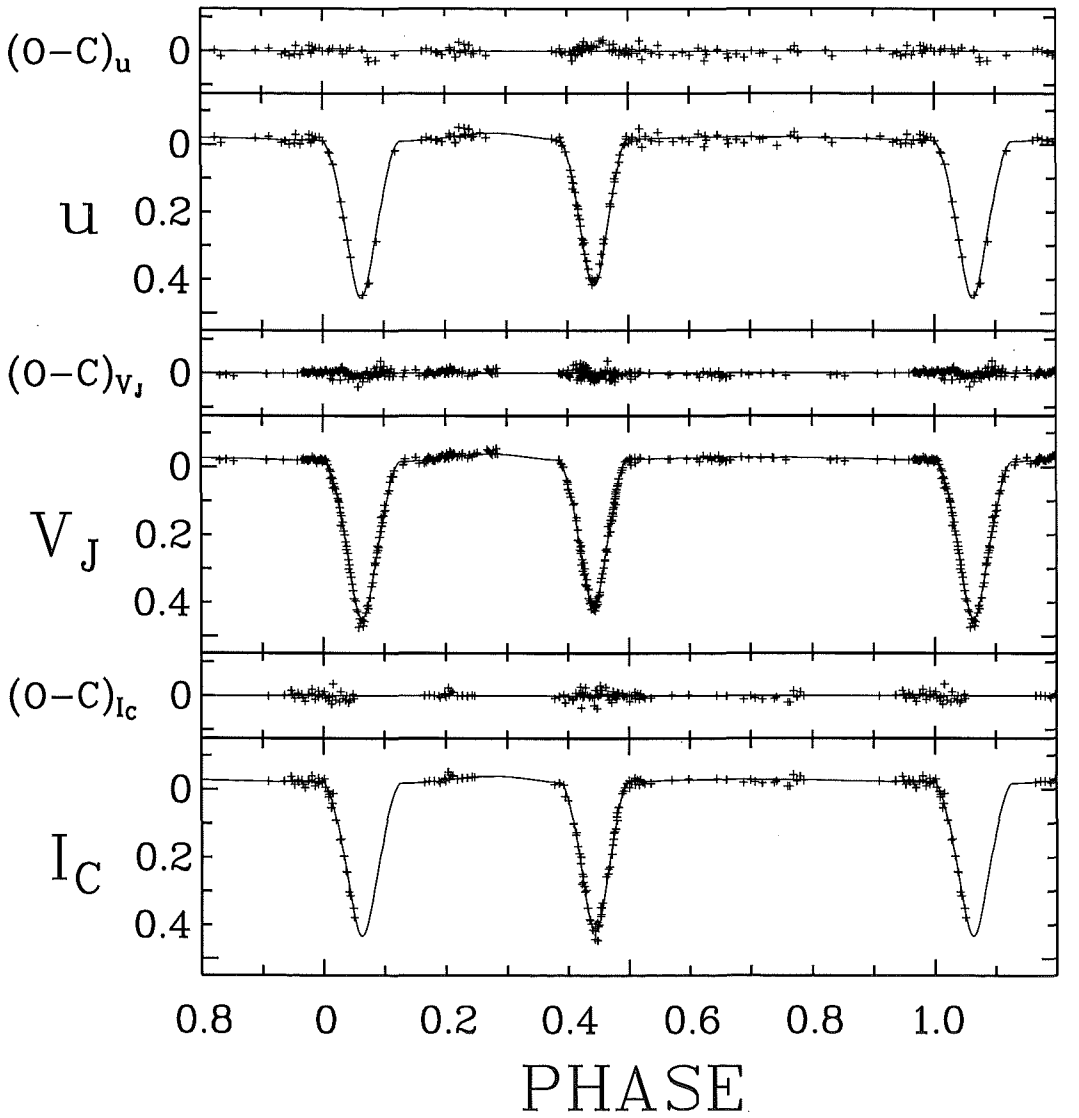

Figure 6.2: The preferred solution of MACHO*05:36:48.7−69:17:00. The most plausible light curve solution is for a mass ratio of $q = 0.7$ ($M_1 = 20\,\mathrm{M}_\odot$ and $M_2 = 14\,\mathrm{M}_\odot$) with $T_{\mathrm{eff},1} = 33\,500\,\mathrm{K}$ and $T_{\mathrm{eff},2} = 29\,500\,\mathrm{K}$.

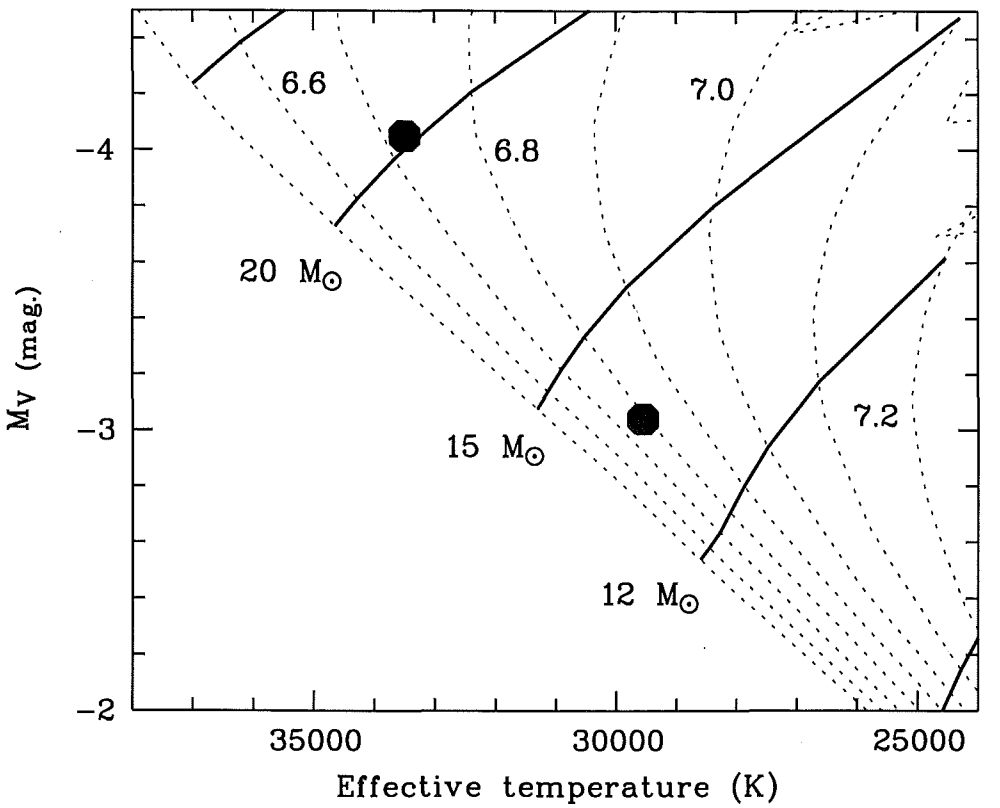

Figure 6.3: The two components of MACHO*05:36:48.7−69:17:00 are plotted as filled circles in the HR diagram. Heavy lines represent evolutionary tracks for z=0.008 calculated by the Geneva group at high mass loss rates [95] and are marked with the initial ZAMS masses. The conversion to absolute magnitudes is only approximate since it is based on normal-metallicity stars [136]. The corresponding isochrones are shown dashed, and are labelled with the $\log_{10}$ of the age. The primary and secondary components are plausibly not dissimilar from 20 and 14 $M_\odot$ solar mass stars of temperature 33 500 and 29 500 K respectively with an age of approximately 5 million years.

6.6 MOA J005018.4−723855

The light curve of the star gives the initial impression of a system with one evolved star therefore quite possibly a semi-detached system. The light curve exhibits an almost continuous variation throughout the period, figure 6.7. The shape out of eclipse is indicative of significant tidal distortions in at least one of the stars. Given the possible type of system, this is quite likely to be the case. The O'Connell effect is clearly seen: the out-of-eclipse light levels between primary and secondary eclipse are higher than between secondary and primary eclipse. Since the origin of this effect is unknown, it was not modelled in the *W95* fits.

The models indicate the secondary star is filling its Roche lobe and therefore the system has most likely undergone or is still undergoing mass transfer. Therefore the mass ratio is determined by the shape of the light curves and values of q need not necessarily be explored, however several models of various q were calculated in order to examine the parameter space.

Wellstein, Langer and Braun [167], examined the formation and mass exchange of contact binaries with primary masses of 12 to 25 $M_\odot$ and secondaries of 6 to 24 $M_\odot$. Wellstein et al. produced evolutionary tracks for a range of periods such as to develop case A mass transfer, i.e. mass overflow during the core hydrogen burning phase of the primary and case B mass transfer, after the core hydrogen burning phase. The results give insight into the possible bounds for the solution for MOA J005018.4−723855.

The diagram from Wellstein et al. (Figure 1), [167], representing the evolutionary tracks of a primary and secondary star in a case A mass transfer, is reproduced in Figure 6.4. Overlaid on this figure are the Geneva models of solar metallicity. The figure represents a binary system with initial masses of 12 $M_\odot$ for the primary (solid and dotted line) and 7.5 $M_\odot$ for the secondary star (dashed line). The start of the case A mass transfer is indicated as 1, the end by 2. The beginning of case AB mass transfer is indicated by 3, with the end indicated by 4. The letters A/a indicate the end of the central hydrogen burning in the primary/secondary. The end of the Helium burning in the primary/secondary is denoted by B/b. The supernova explosion of the secondary is indicated, c, at which time, the primary continues evolution along the dotted line. There are systematic differences between the Geneva model MS tracks and the Wellstein et al. model, the MS evolutionary tracks are misaligned presumably due to different input physics. During the rapid stage of case A mass transfer, section 1 to 2 on Figures 6.4 and 6.5 for both primary and secondary, the primary can become under-luminous and the secondary over-luminous for their mass due to the rapid mass transfer. The luminosities can deviate from the thermal equilibrium stage by up to factor of two.

To align the tracks, and aid in the interpretation, the Geneva model temperatures were reduced by 8% and the luminosities by 14%, Figure 6.5. We will see that the initial masses of the Wellstein et al. model are smaller than for MOA J005018.4−723855, however we can relate the evolutionary tracks to this system. In this semi-detached system, the mass ratio is set by the light curve and therefore a Geneva stellar evolutionary model for only one star was required. Additionally, the mass gainer star, may not look so different than a MS star. This is the constraint that will be used to obtain an astrophysically plausible solution for MOA J005018.4−723855.

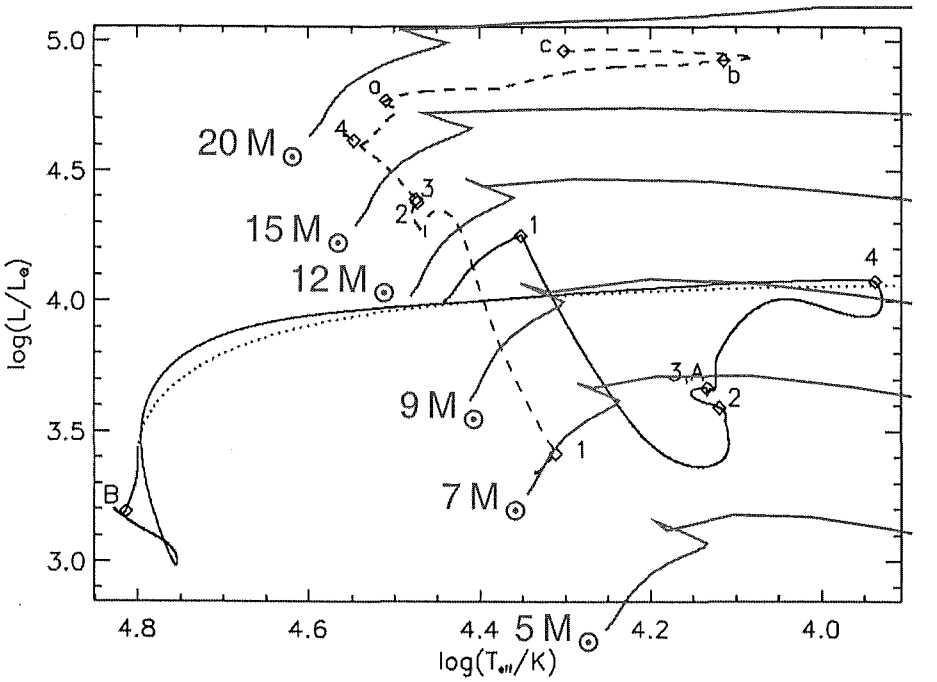

Figure 6.4: Evolutionary tracks of a primary and secondary star in a case A mass transfer, are reproduced from Wellstein et al., Figure 1 [167]. In this example the system has a period of 2.5 days with initial masses are 12 $M_\odot$ for the primary (solid and dotted line) and 7.5 $M_\odot$ for the secondary star (dashed line). Overlaid are the Geneva models of solar metallicity. An explanation of the stages of evolution is given in the text.

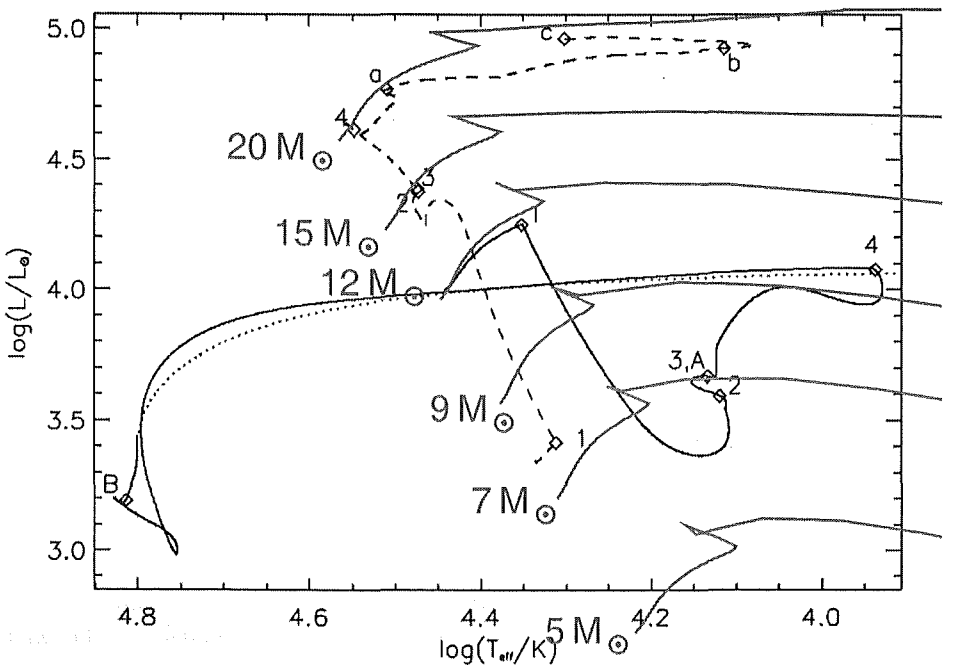

Figure 6.5: The MOA Geneva models have been adjusted by 8% in temperature and 14% in luminosity to align better with the Wellstein et al. model. The differences between the models most likely arise from different input physics.

6.6.1 Adjustments to parameters

A semi-detached system with the secondary filling its Roche lobe therefore gives the mass ratio for MOA J005018.4−723855. The system is scaled, as follows, in order for the primary to resemble a Geneva model. We required $M_{V_J} = -4.08$ mag. for this system, but $a = 15\,R_\odot$ gives $M_{V_J} = -3.41$ mag. Therefore the system from the *WD95* analysis needs to be brightened by 0.67 mag. or a factor of 1.859. This increases the $R_{1,2}/R_\odot$ and a for the $T_{\rm eff,1} = 29\,000$ K solution by a factor of $\sqrt{1.859}$. For a: 15.0 scales to $20.5\,R_\odot$, $R_1/R_\odot$: 4.35 to $5.9\,R_\odot$ and $R_2/R_\odot$: 6.26 to $8.5\,R_\odot$. The masses will increase by a factor of $1.859^{\frac{3}{2}}$, thereby giving M_1: 5.32 to $13.5\,M_\odot$ and M_2: 8.10 to $20.5\,M_\odot$.

Plotting the three solutions in the HR diagram, Figure 6.6, the parameters for $T_{\rm eff,1} = 29\,000$ K correspond to a $M_1 = 13.5\,M_\odot$ in the Geneva model for solar metallicity.

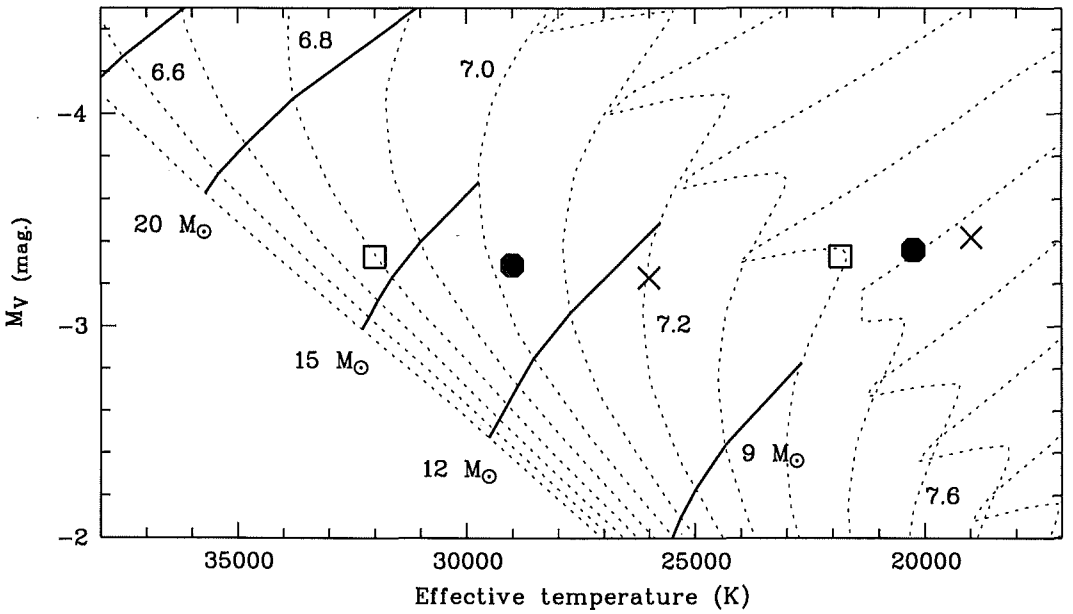

Figure 6.6: Solutions for MOA J005018.4−723855 in the HR diagram. The $T_{\rm eff,1} = 32\,000$, 29 000 and 26 000 K solutions (left group) are denoted by □, filled octagon and × respectively. The corresponding secondary effective temperatures, $T_{\rm eff,2} = 21\,803$, 20 246 and 18 978 K are denoted the by the same symbols (right group). The corresponding primary masses are 10.5, 13.5 and 15.4 $M_\odot$. The solution with $T_{\rm eff,1} = 29{,}000$ K has parameters for the primary which correspond to a Geneva model of the same mass.

The initial solutions were either acceptable in the u bandpass but not in the I_C bandpass and vice versa. This target is the one most affected by blending, therefore the addition of 3^{rd} light to the solution was considered. When allowed to adjust for third light, the *WD95* code adopted negative third light, which would suggest incorrect reference flux levels from the DAOPHOT II/ISIS-2.1 extraction of the reference images. However, it was thought more plausible that the relative amounts of third light were correct. The differences produced were adopted with zero u-filter third light under the assumption that any additional star was likely to be red. Nearby stars on the frames support the idea of a contribution from blended stars. Solutions were obtained with the 3^{rd} light parameter set as variable. The differences in 3^{rd} light between each bandpass, u, V_J and I_C, were noted. The parameter was set as a constant and the 3^{rd} light in each bandpass set to; $u = 0$, $V_J = 0.05$ and $I_C = 0.02$. The parameter space was examined by obtaining solutions for $T_{\rm eff,1} = 20\,000$, 25 000 and 35 000 K for each $q = 0.4$, 0.7, 1.0, 1.3. Sample solutions for these are presented in Table 6.8, with $a = 15.0$. The *WD95* was initially run was the assumption of a semi-detached binary, with star 1 filling its Roche lobe (`Mode 4`), however

the large and unstable oscillations in the solutions indicated the possibility of a semi-detached binary, with star 2 filling its Roche lobe (Mode 5) would be more preferable. Switching to the case of a semi-detached binary with the second star filling its Roche lobe, produced stable results.

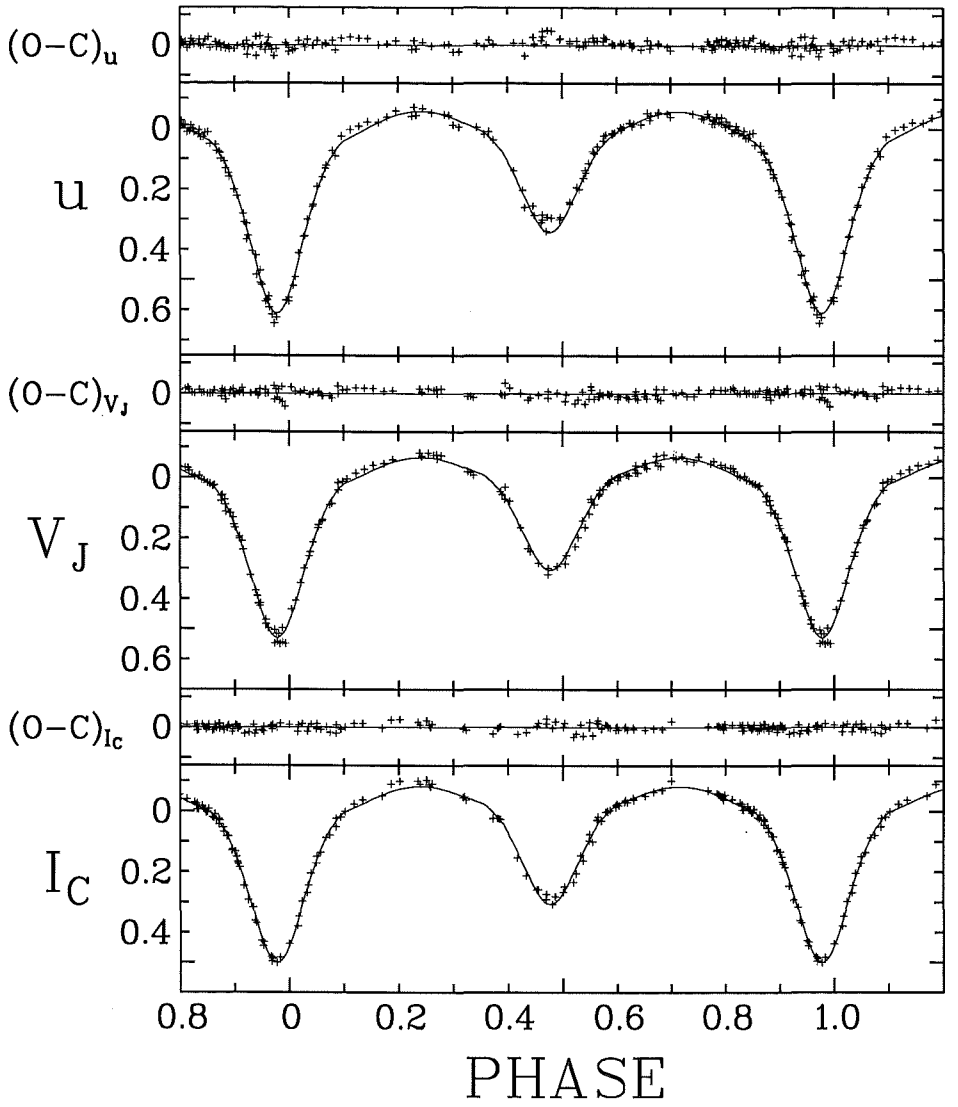

Figure 6.7: The preferred light curve solution of MOA J005018.4−723855. The most plausible light curve solution is for a mass ratio of q=1.5 ($M_1 = 13.5\,M_\odot$ and $M_2 = 20.5\,M_\odot$) with $T_{\rm eff,1} = 29\,000$ K and $T_{\rm eff,2} = 20\,246$ K.

The solutions for mass ratios 1.4 to 1.6 and $T_{\rm eff,1}$ in the range 26 000 to 32 000 K were explored in more detail as these solutions appeared the most relevant, since the *WD95* code yielded optimized values of q in this range. Setting $T_{\rm eff,1}$ to 26 000, 29 000 and 32 000 K while allowing the mass ratio, $T_{\rm eff,2}$, inclination and ω_1 to vary. The solutions tended to wander and therefore an average of ten solution were taken as the final solutions for each $T_{\rm eff,1}$, Table 6.11.

Solutions were calculated for a small parameter space around the possible solution with small adjustments to the mass ratios and the effective temperature $T_{1,\rm eff}$ made. Table 6.9 presents the results using $a = 20.50\,R_\odot$. The results give an indication of the range of the primary's

effective temperature for a given mass ratio and absolute magnitude.

Table 6.8: *WD95* fits for MOA J005018.4−723855, period = 1.83987 d, T_0=2452156.6570, SMaxis=15.0 $R_\odot$. Although not all figures are significant, they are presented to show differences in values, some due to numerical noise.

M_2/M_1	M_1 ($M_\odot$)	M_2 ($M_\odot$)	$T_{\rm eff,1}$ (K)	$T_{\rm eff,2}$ (K)	i (°)	$\overline{R_1/a}$	$\overline{R_2/a}$	L_1/L_2			3^{rd} light		
								u	$V_{\rm J}$	$I_{\rm C}$	u	$V_{\rm J}$	$I_{\rm C}$
0.4	9.59	3.83	20 000	14 896	82.137	0.425	0.303	3.927	3.648	3.233	0.0000	0.0500	0.0200
0.4	9.59	3.83	25 000	17 213	82.107	0.423	0.303	3.770	3.621	3.229	0.0000	0.0500	0.0200
0.4	9.59	3.83	30 000	18 860	81.734	0.419	0.302	3.524	3.524	3.136	0.0000	0.0500	0.0200
0.7	7.89	5.53	20 000	15 075	77.423	0.375	0.349	2.235	2.083	1.857	0.0000	0.0500	0.0200
0.7	7.89	5.53	25 000	17 669	77.557	0.526	0.349	2.050	1.973	1.778	0.0000	0.0500	0.0200
0.7	7.89	5.53	30 000	19 724	77.600	0.362	0.349	1.882	1.847	1.669	0.0000	0.0500	0.0200
1.0	6.71	6.71	20 000	15 320	76.605	0.339	0.380	1.478	1.382	1.242	0.0000	0.0500	0.0200
1.0	6.71	6.71	25 000	18 090	76.935	0.332	0.380	1.339	1.290	1.173	0.0000	0.0500	0.0200
1.0	6.71	6.71	30 000	20 224	77.052	0.331	0.380	1.272	1.250	1.139	0.0000	0.0500	0.0200
1.3	5.84	7.59	20 000	15 400	76.420	0.318	0.403	1.137	1.065	0.960	0.0000	0.0500	0.0200
1.3	5.84	7.59	25 000	18 157	76.718	0.314	0.403	1.051	1.015	0.924	0.0000	0.0500	0.0200
1.3	5.84	7.59	30 000	20 452	77.145	0.306	0.403	0.953	0.936	0.855	0.0000	0.0500	0.0200
1.6	5.16	8.26	20 000	15 584	77.005	0.296	0.422	0.874	0.820	0.743	0.0000	0.0500	0.0200
1.6	5.16	8.26	25 000	18 360	77.235	0.295	0.422	0.830	0.802	0.733	0.0000	0.0500	0.0200
1.6	5.16	8.26	30 000	20 713	77.735	0.290	0.422	0.763	0.749	0.688	0.0000	0.0500	0.0200

Table 6.9:]

WD95 fits for MOA J005018.4−723855, period = 1.83987 d, $T_0 = 2452156.6570$, SMaxis = 15.0 $R_\odot$. Although not all figures are significant, they are presented to show differences in values, some due to numerical noise.

M_2/M_1	M_1 ($M_\odot$)	M_2 ($M_\odot$)	$T_{\rm eff,1}$ (K)	$T_{\rm eff,2}$ (K)	i (°)	$\overline{R_1}/a$	$\overline{R_2}/a$	L_1/L_2			3^{rd} light		
								u	$V_{\rm J}$	$I_{\rm C}$	u	$V_{\rm J}$	$I_{\rm C}$
1.55	13.44	20.82	27 000	19 389	77.342	0.295	0.419	0.8299	0.8074	0.7424	0.0000	0.0500	0.0200
1.55	13.44	20.82	29 000	20 297	77.739	0.290	0.419	0.7825	0.7681	0.7077	0.0000	0.0500	0.0200
1.55	13.44	20.82	31 000	21 167	77.814	0.290	0.419	0.7691	0.7591	0.9659	0.0000	0.0500	0.0200
1.60	13.18	21.08	27 000	19 429	77.568	0.291	0.422	0.7924	0.7704	0.7088	0.0000	0.0500	0.0200
1.60	13.18	21.08	31 000	21 123	77.757	0.290	0.422	0.7583	0.7488	0.6861	0.0000	0.0500	0.0200
1.65	12.93	21.33	27 000	19 431	77.544	0.290	0.425	0.7755	0.7544	0.6941	0.0000	0.0500	0.0200
1.65	12.93	21.33	29 000	20 285	77.697	0.289	0.425	0.7531	0.7401	0.6818	0.0000	0.0500	0.0200
1.65	12.93	21.33	31 000	21 259	78.234	0.281	0.425	0.7027	0.6928	0.6362	0.0000	0.0500	0.0200

Table 6.10: An astrophysically plausible solution for MOA J005018.4−723855.

Mass ratio, q, (M_2/M_1)	1.5
M_1	$13.5\,M_\odot$
M_2	$20.5\,M_\odot$
$T_{\rm eff,1}$	29 000 K
$T_{\rm eff,2}$	20 000 K
Inclination, i	77.6°
Longitude of periastron	N/A
Semi-major axis, a	$20.5\,R_\odot$
eccentricity, e	0.0
$\overline{R_1}/a$	0.29
$\overline{R_2}/a$	0.42
L_1/L_2 u	0.8
L_1/L_2 $V_{\rm J}$	0.8
L_1/L_2 $I_{\rm C}$	0.7

Table 6.11 gives solutions for three different effective temperatures ($T_{\rm eff,1}$) 26 000 K, 29 000 K and 32 000 K. These are range over a slightly greater effective temperature than those in Table 6.9, but give a slightly clearer indication of the nearby solution space when plotted together. These are plotted in Figure 6.6 with their respective secondary components. The solution that best fits a Geneva model of solar metallicity is the $T_{\rm eff,1} = 29\,000$ K solution with the secondary effective temperature $T_{\rm eff,2}$ following from the primary value. The solution is presented in Table 6.10.

Table 6.11: *WD95* fits for MOA J005018.4−723855, period = 1.83987 d, $T_0 = 2452156.6570$, SMaxis=15.0 $R_\odot$. The preferred solution is with $T_{\rm eff,1} = 29\,000$ K. The output is from *WD95* and is not the true nature of the systems as adjustments to parameter values are required as discussed in section 6.6.1. Although not all figures are significant, they are presented to show differences in values, some due to numerical noise.

M_2/M_1	M_1	M_2	$T_{\rm eff,1}$	$T_{\rm eff,2}$	i	$\overline{R_1}/a$	$\overline{R_2}/a$	L_1/L_2			3^{rd} light		
	$(M_\odot)$	$(M_\odot)$	(K)	(K)	(°)			u	$V_{\rm J}$	$I_{\rm C}$	u	$V_{\rm J}$	$I_{\rm C}$
1.6585	5.05	8.37	26 000	18 978	77.539	0.295	0.425	0.8003	0.7788	0.7154	0.0000	0.0500	0.0200
1.5238	5.32	8.10	29 000	20 246	77.596	0.290	0.417	0.7870	0.7733	0.7111	0.0000	0.0500	0.0200
1.5092	5.35	8.07	32 000	21 803	77.855	0.289	0.417	0.7656	0.7537	0.6898	0.0000	0.0500	0.0200

6.7 MOA J005623.5−722123

Initial inspection of the light curves suggests a pair of similar stars Figure 6.8. The slight variations of the light curve out of eclipse may indicate slight tidal distortions of the components. The ingress and egress of the eclipse shoulders are of a similar level indicating no mass attenuation stream, therefore the solution will most probably consist of a detached system (almost semi-detached) with one component filling a significant amount of its Roche lobe.

A set of initial models were calculated in order to explore the possible solutions. A complicating factor was the incomplete phase coverage of all three bandpasses. Initially the solutions used a semi-major axis set to $20.0\,R_{\odot}$.

The initial $T_{\rm eff,1}$ was set at 20 000 K, 25 000 K and 28 000 K. The inclination of the model system fluctuated between 80.5° and 82.6°. The initial phasing indicated a circular orbit, therefore e was set to zero. However the initial fitting and setting of parameters, as mentioned above, did not provide a satisfactory fit and hinted at the possibility of a slight eccentricity. The eccentricity was allowed to vary and yielded a fit better for the secondary but worse for the primary. The eccentricity varied from 0 to 0.0058. The approach of allowing the eccentricity to vary was abandoned as it became apparent the 3^{rd} light was the dominant factor in the fitting. The eccentricity was set as a constant with a value of 0.

These initial solutions indicated 3^{rd} light was an issue in this case because the fit was either acceptable in the u bandpass but not the $I_{\rm C}$ bandpass, or vice versa. Therefore the 3^{rd} light parameter was set as variable and reasonable fits were achieved. The solutions had difficulty converging with the values of $T_{\rm eff,1,2}$ continuously varying. This was due to the amount of 3^{rd} light varying. The differences in 3^{rd} light between the u, $V_{\rm J}$ and $I_{\rm C}$ bandpasses were noted and the 3^{rd} light values were set as constant. The *WD95* code adopted negative third light, as was the case for MOA J005018.4−723855. Again this suggests incorrect reference flux levels from the DAOPHOT II/ISIS-2.1 extraction of the reference images. However, it was thought more plausible that the relative amounts of third light were correct. The differences produced were adopted with zero u-filter third light under the assumption that any additional star was likely to be red. Additionally, nearby blended stars are seen in the frames to support the idea of a contribution from another star.

A series of solutions were calculated for mass ratios of 0.7, 1.0 and 1.3. For each mass ratio $T_{\rm eff,1}$ was set constant at 15 000 K, 25 000 K and 35 000 K with the secondary, $T_{\rm eff,2}$, set as variable along with the surface potentials for both components. The inclination was allowed to vary, in order to fit to the u and $I_{\rm C}$ bandpasses. By doing so, the contributions in these bandpasses could be controlled as altering the inclination deepens or shallows the eclipse depths. Other parameters set constant were $\mathrm{SMaxis} = 20.0\,R_{\odot}$ and $e = 0$. The *WD95* code was set to calculate models for a detached binary system (`Mode 2`).

The relative eclipse depths of the secondary and primary vary from u, where the difference is greatest, to $I_{\rm C}$ where the primary is only slightly deeper than the secondary. This implies a cooler secondary. The effective temperatures are likely to be within a few hundred kelvin of each other. The series of solutions are given in Table 6.12.

The third light in the solutions were set constant at $u = 0.0000$, $V_{\rm J} = 0.0400$ and $I_{\rm C} = 0.1200$. The reference units of light are in fluxes, linear scale, with the reference frame level set to 1. Therefore the amount of 3^{rd} light, are equivalent to percentages of the reference frame flux, i.e. $u = 0\%$, $V = 4\%$ and $I_{\rm C} = 12\%$.

Table 6.12: *WD95* fits for MOA J005623.5−722123MOA73441, period = 2.3199 d, epoch = 2450681.9500, SMaxis = 20.0 $R_\odot$. Although not all figures are significant, they are presented to show differences in values, some due to numerical noise.

M_2/M_1	M_1	M_2	$T_{\rm eff,1}$	$T_{\rm eff,2}$	i	$\overline{R1}/a$	$\overline{R2}/a$	L_1/L_2			3^{rd} light		
	($M_\odot$)	($M_\odot$)	(K)	(K)	(°)			u	$V_{\rm J}$	$I_{\rm C}$	u	$V_{\rm J}$	$I_{\rm C}$
0.7	11.77	8.24	15 000	14 674	84.152	0.310	0.300	1.148	1.120	1.111	0.0000	0.0400	0.1200
0.7	11.77	8.24	25 000	24 832	84.124	0.301	0.313	0.982	0.956	0.956	0.0000	0.0400	0.1200
0.7	11.77	8.24	35 000	34 554	84.193	0.302	0.315	0.950	0.943	0.946	0.0000	0.0400	0.1200
1.0	10.00	10.00	15 000	14 756	84.831	0.275	0.335	0.721	0.706	0.700	0.0000	0.0400	0.1200
1.0	10.00	10.00	25 000	24 926	84.877	0.277	0.337	0.746	0.718	0.725	0.0000	0.0400	0.1200
1.0	10.00	10.00	35 000	34 375	84.290	0.294	0.329	0.828	0.822	0.822	0.0000	0.0400	0.1200
1.3	8.70	11.31	15 000	14 569	83.984	0.302	0.318	0.976	1.120	1.112	0.0000	0.0400	0.1200
1.3	8.70	11.31	25 000	23 663	84.045	0.301	0.321	0.932	0.940	0.928	0.0000	0.0400	0.1200
1.3	8.70	11.31	35 000	33 665	84.180	0.304	0.320	0.958	0.949	0.941	0.0000	0.0400	0.1200

The light curve for MOA J005623.5−722123 was initially phased using the MOA time-series photometric data whose analysis gave a period of 2.3195 ± 0.0001 days. The period was later revised with the data from the MJUO observations, with a new period determined, 2.3199 ± 0.0001 days. Several intermediate solutions displayed while converging during the light curve analysis which had inclinations near 90° and gave flat bottomed eclipses. These tended to be at the higher effective temperatures, around 35 000 K. These numerous solutions were due to the small number of data points around the minima of the primary and secondary, more so the primary. The phasing was then re-examined for both the MOA and MJUO data. Periods slightly higher than the original values were examined. A period of 2.32005 days gave a well phased light curve with the primary and secondary eclipse minima exhibiting flat bottomed eclipses. The uncertainties derived for the period in the previous two values of 2.3195 days and 2.3199 days were based on the the appearance of the phasing of the data. The addition of points, in particular around the minima, resulted in the a slight increase in the value of the period. The MACHO data for this region of the SMC was available on-line and was used to aid in the period refinement along with the initial analysis of using *WD95*. MACHO, MOA and MJUO data phased satisfactorily to this increased period. To obtain a more accurate value of the period, primarily from the MJUO data, more observations are needed especially around the eclipse minima. The light curve can be reasonably phased at any of the above periods, therefore some ambiguity exists but some values were able to be excluded with further analysis.

The solutions were re-determined using the same constant and variables set as in the previous solutions except with the data phased to the new period. The solutions are seen to be noticeably different for $q > 1.0$. The summary of the results is presented in Table 6.13.

Table 6.13: *WD95* fits for MOA J005623.5−722123, period = 2.32005 d, epoch = 2452150.5224, SMaxis = 20.0 $R_\odot$. Although not all figures are significant, they are presented to show differences in values, some due to numerical noise.

M_2/M_1	M_1 ($M_\odot$)	M_2 ($M_\odot$)	$T_{\rm eff,1}$ (K)	$T_{\rm eff,2}$ (K)	i (°)	$\overline{R_1}/a$	$\overline{R_2}/a$	L_1/L_2			3^{rd} light		
								u	$V_{\rm J}$	$I_{\rm C}$	u	$V_{\rm J}$	$I_{\rm C}$
0.7	11.77	8.24	15 000	14 674	84.152	0.314	0.303	1.1479	1.1201	1.1117	0.0000	0.0400	0.1200
0.7	11.77	8.24	25 000	24 748	84.165	0.305	0.310	1.0236	0.9992	0.9978	0.0000	0.0400	0.1200
0.7	11.77	8.24	35 000	34 499	84.214	0.302	0.301	0.9555	0.9475	0.9509	0.0000	0.0400	0.1200
1.0	10.00	10.00	15 000	14 740	88.102	0.255	0.341	0.5971	0.5750	0.5744	0.0000	0.0400	0.1200
1.0	10.00	10.00	25 000	25 090	87.926	0.257	0.340	0.6031	0.5841	0.5848	0.0000	0.0400	0.1200
1.0	10.00	10.00	35 000	34 749	89.000	0.259	0.341	0.5935	0.5891	0.5927	0.0000	0.0400	0.1200
1.3	8.70	11.31	15 000	14 742	88.707	0.297	0.392	0.6076	0.5937	0.5909	0.0000	0.0400	0.1200
1.3	8.70	11.31	25 000	24 601	87.618	0.265	0.347	0.6162	0.6057	0.6039	0.0000	0.0400	0.1200
1.3	8.70	11.31	35 000	34 340	87.640	0.267	0.349	0.6132	0.6083	0.6089	0.0000	0.0400	0.1200

Table 6.14: *WD95* fits for MOA J005623.5−722123, period = 2.32005 d, epoch = 2452150.5224, SMaxis = 22.65 $R_\odot$. Although not all figures are significant, they are presented to show differences in values, some due to numerical noise.

M_2/M_1	M_1	M_2	$T_{\rm eff,1}$	$T_{\rm eff,2}$	i	$\overline{R_1}/a$	$\overline{R_2}/a$	L_1/L_2			3^{rd} light		
	($M_\odot$)	($M_\odot$)	(K)	(K)	(°)			u	$V_{\rm J}$	$I_{\rm C}$	u	$V_{\rm J}$	$I_{\rm C}$
0.7	17.09	11.97	15000	14577	84.457	0.311	0.305	1.142	1.110	1.098	0.0000	0.0400	0.1200
0.7	17.09	11.97	25000	25330	88.131	0.247	0.326	0.616	0.588	0.590	0.0000	0.0400	0.1200
0.7	17.09	11.97	35000	34836	87.958	0.249	0.328	0.599	0.593	0.599	0.0000	0.0400	0.1200
1.0	14.53	14.53	15000	14788	89.122	0.255	0.340	0.593	0.572	0.572	0.0000	0.0400	0.1200
1.0	14.53	14.53	25000	25187	88.150	0.257	0.340	0.599	0.581	0.582	0.0000	0.0400	0.1200
1.0	14.53	14.53	35000	34831	88.916	0.259	0.341	0.591	0.587	0.591	0.0000	0.0400	0.1200
1.3	12.63	16.43	15000	14742	88.707	0.262	0.346	0.608	0.594	0.591	0.0000	0.0400	0.1200
1.3	12.63	16.43	25000	24621	87.768	0.264	0.347	0.610	0.600	0.598	0.0000	0.0400	0.1200
1.3	12.63	16.43	35000	34330	88.036	0.267	0.346	0.617	0.612	0.613	0.0000	0.0400	0.1200

The solution parameters from the *WD95* fitting for the shorter period, namely 2.3199 days, Table 6.12, gave solutions of effective temperatures for $T_{\rm eff,2}$ approximately 500 K less than $T_{\rm eff,1}$ in most cases, except for mass ratio $(M_2/M_1) = 1.3$, with $T_{\rm eff,1} = 25\,000$ K and 35 000 K where the difference was around 1 500 K. The inclination was in the range 84° to 84.9°. The longer period gave solutions, for the same mass ratios, of $T_{\rm eff,2}$ generally only a few 100 K less than the primary, overall the primary and secondary temperature are closer than in the small period case. The exception being the solution for $q = 1.0$, where $T_{\rm eff,2}$ was 187 K larger than $T_{\rm eff,1}$. The new period gave higher inclinations, 87.6 to 89.0°, the exception being $q = 0.7$. This implies we are observing this system's orbital plane nearly edge-on.

Solutions, were calculated, Table 6.13, given the convergence criterion, from the *WD95* analysis. Initially solutions were found with a period of 2.3199 days, Table 6.12, and the semi-major axis, SMaxis, set to 20.0 $R_\odot$. New solutions were calculated for the new period, 2.32005 days with the original SMaxis of 20.0 $R_\odot$, Table 6.13.

Geneva stellar evolution models over the expected mass range for $[m/{\rm H}] = -0.5$ (z=0.004) metallicity comparable to the SMC, together with isochrones were obtained. The solutions were plotted on these models and examined to give an astrophysically plausible solution i.e. one where the stars have a common age. The initial estimate of the absolute (out of eclipse) magnitude (15.1 mag.) from the light curves was used to scale the system, using the same principles as used for MACHO*05:36:48.7−69:17:00 in section 6.5.1. The result gave the system's semi-major axis, a, increasing from 15.0 to 22.65 $R_\odot$, refer Table 6.14. This enabled a pair of stars to be obtained that matched the Geneva stellar evolutionary models.

Comparing the two solution sets of Tables 6.13 and 6.14, period of 2.32005 days and SMaxis = 20.0 $R_\odot$ and 22.65 $R_\odot$ respectively, the main difference in the solutions are the values of the masses, both M_1 and M_2 (this would be expected from Kepler's third law). This is due to the different values of the semi-major axis, as this parameter scales the system. Other values such as temperature and inclination would therefore, in theory, be identical but are not due to numerical noise in the solutions/convergence criterion. However, both tables show reasonably similar results for a given mass ratio. Therefore, with respect to a given mass ratio, the individual masses can be adjusted to give a realistic system, whilst the temperatures and inclination vary by small amounts. This confirms the expected behaviour of the models.

The preferred solution, determined without spectroscopy or spectrophotometry, implies a system nearly edge on to the line of sight with two stars of approximate mass 13.5 and 15.5 $M_\odot$ for the primary and secondary respectively, Figure 6.8. The oddity of this system, derived from the *WD 95* modelling, is the primary is smaller and cooler on average than the secondary, yet has deeper primary eclipses. An explanation for this is presented in section 6.7.1. The parameters for this favoured solution are presented in Table 6.16, along with its position in the HR diagram in Figure 6.9. Several solutions were calculated around the preferred solution parameters, namely mass ratio and effective temperature with the semi-major axis set to 22.65 $R_\odot$. Presented in Table 6.15, the all give the secondary hotter, on average, than the primary.

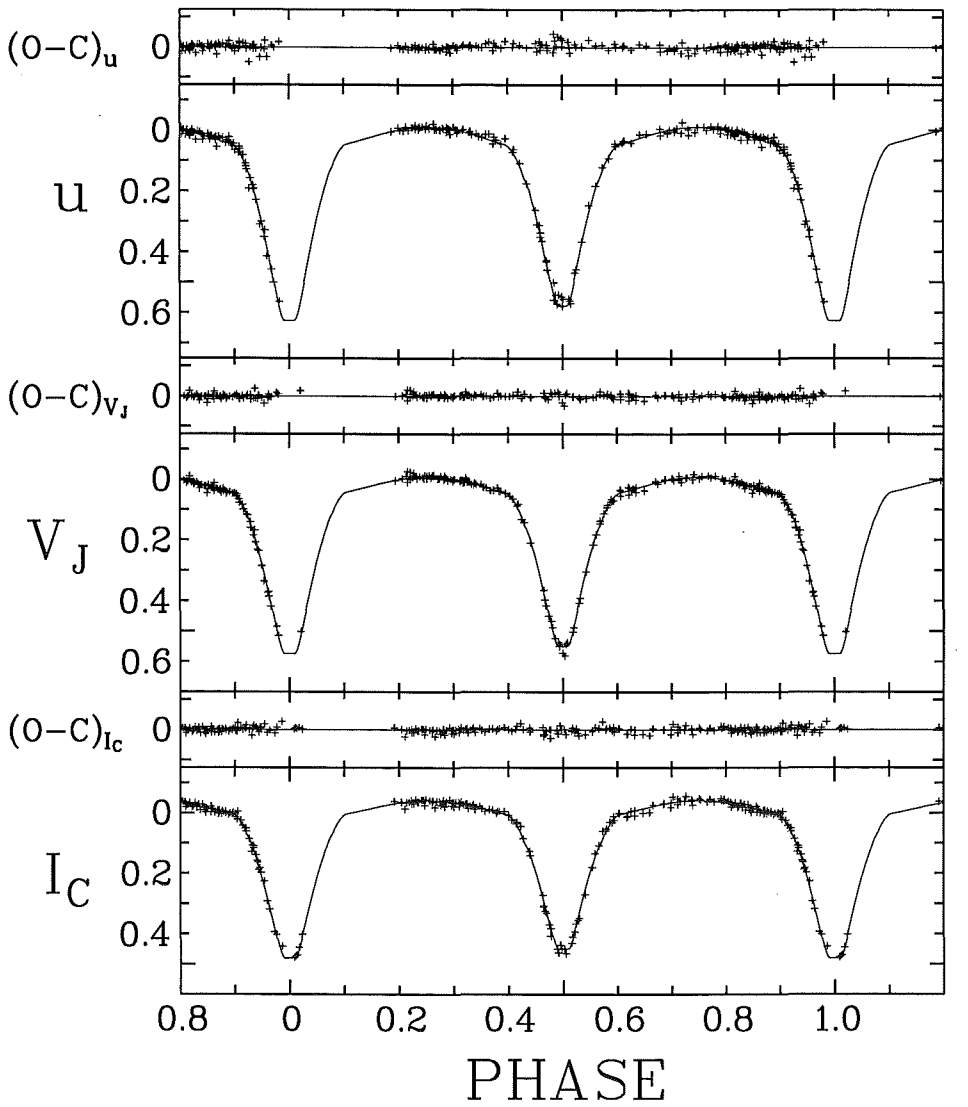

Figure 6.8: The preferred solution of MOA J005623.5−722123. The most plausible light curve solution is for a mass ratio of $q = 1.1$ ($M_1 = 15.5\,M_\odot$ and $M_2 = 13.5\,M_\odot$) with $T_{\rm eff,1} = 29\,000$ K and $T_{\rm eff,2} = 29\,350$ K.

Table 6.15: *WD95* fits for MOA J005623.5−722123, period = 2.32005 d, epoch = 2452150.5224, SMaxis = 22.65 $R_\odot$. Although not all figures are significant, they are presented to show differences in values, some due to numerical noise.

M_2/M_1	M_1	M_2	$T_{\rm eff,1}$	$T_{\rm eff,2}$	i	$\overline{R_1}/a$	$\overline{R_2}/a$	L_1/L_2			3^{rd} light		
	($M_\odot$)	($M_\odot$)	(K)	(K)	(°)			u	$V_{\rm J}$	$I_{\rm C}$	u	$V_{\rm J}$	$I_{\rm C}$
1.1	13.84	15.22	27 000	32 151	89.890	0.242	0.336	0.4690	0.4551	0.4755	0.0000	0.0400	0.1200
1.1	13.84	15.22	29 000	33 387	86.830	0.249	0.336	0.4948	0.4879	0.5125	0.0000	0.0400	0.1200
1.1	13.84	15.22	31 000	33 986	86.915	0.246	0.335	0.4977	0.4962	0.5157	0.0000	0.0400	0.1200
1.1481	13.53	15.53	27 000	31 977	88.737	0.245	0.338	0.4755	0.4619	0.4814	0.0000	0.0400	0.1200
1.1481	13.53	15.53	31 000	34 188	86.862	0.247	0.340	0.4798	0.4796	0.4988	0.0000	0.0400	0.1200
1.2	13.21	15.85	27 000	32 181	88.869	0.244	0.340	0.4626	0.4501	0.4704	0.0000	0.0400	0.1200
1.2	13.21	15.85	29 000	33 144	89.262	0.247	0.201	0.4957	0.4888	0.5111	0.0000	0.0400	0.1200
1.2	13.21	15.85	31 000	34 673	88.696	0.247	0.341	0.4628	0.4650	0.4843	0.0000	0.0400	0.1200

Table 6.16: An astrophysically plausible solution for MOA J005623.5−722123.

Mass ratio, q, (M_2/M_1)	1.1
M_1	$13.5\,M_\odot$
M_2	$15.5\,M_\odot$
$T_{\rm eff,1}$	29 000 K
$T_{\rm eff,2}$	29 350 K
Inclination, i	87.8°
Longitude of periastron	N/A
Semi-major axis, a	$22.7\,R_\odot$
eccentricity, e	0.0
$\overline{R_1}/a$	0.25
$\overline{R_2}/a$	0.34
L_1/L_2 u	0.6
L_1/L_2 $V_{\rm J}$	0.6
L_1/L_2 $I_{\rm C}$	0.6

6.7.1 MOA J005623.5−722123 geometry

An astrophysically plausible solution for MOA J005623.5−722123 based on the *WD95* analysis and fitting of the solution to the Geneva models, gives a secondary component slightly hotter than the primary. Both stars are early B stars and therefore we expect gravity brightening, so their atmospheres are hotter at the poles. The inclination of the system was determined to be 87.8° and an estimated semi-major axis of $22.65\,R_\odot$. The line of sight view, Figure 6.10, is given for the system with the centre of mass denoted by the small open circle. Total eclipses occur due to the high inclination, almost 90°; the poles are not noticeably displaced from the edge of the disc. In the primary eclipse, the larger secondary, (solid line) is totally eclipsing the primary (dashed line). In the secondary eclipse, the primary star's path cuts across the cooler central region of the secondary leaving the poles still visible. This therefore allows the secondary to have a higher average temperature than the primary yet a shallower eclipse depth.

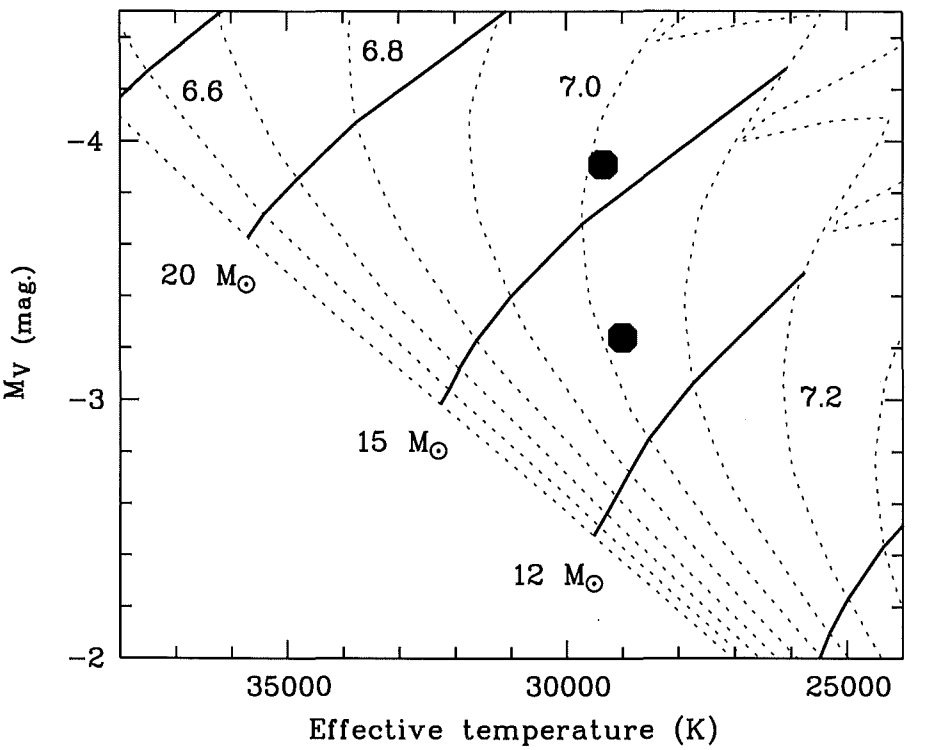

Figure 6.9: The two components of MOA J005623.5−722123 are plotted as filled circles in the HR diagram. Heavy lines represent evolutionary tracks for z = 0.004 calculated by the Geneva group at high mass loss rates [95] and are marked with the initial ZAMS masses. The conversion to absolute magnitude is only approximate since it is based on normal-metallicity stars [136]. The corresponding isochrones are shown dashed, and are labelled with the $\log_{10}$ of the age. The stars in MOA J005623.5−722123 are plausibly not dissimilar from $M_1 = 13.5$ and $M_2 = 15.5\,M_\odot$ stars of temperature $T_{\rm eff,1} = 29\,000$ and $T_{\rm eff,2} = 29\,400$ K and age 10 million years.

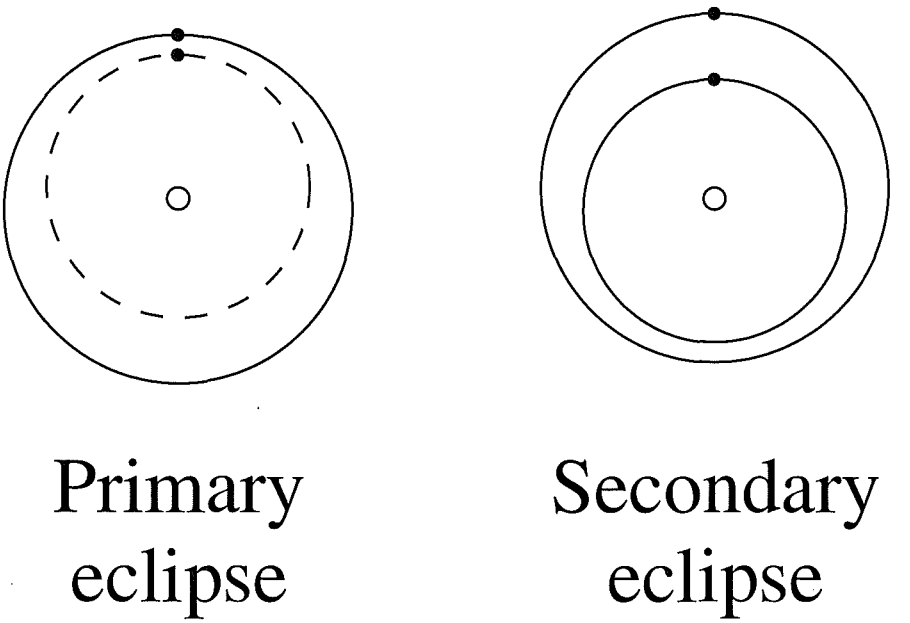

Figure 6.10: The preferred solution of MOA J005623.5−722123. The poles are expected to be hotter due to gravity brightening. Due to an inclination of nearly 90°, the polar regions are not noticeably displaced from the edge of the disk. As the secondary star eclipses the main disk (the cooler region) of the primary star the hotter poles are still visible. This would give the appearance of a higher average temperature for the secondary component, yet shallower eclipse depths.

6.8 Surface potentials and limiting lobes

The surface potentials and limiting lobes for each of the systems are presented in Figure 6.11. The Roche lobes for MACHO*05:36:48.7−69:17:00 do not touch. This because the elliptical orbit of the system and non-locking of tidal forces results in the non-synchronous rotation of the critical potential surfaces of each component. This gives a more complicated system and therefore the term limiting lobes instead of Roche lobes is preferred.

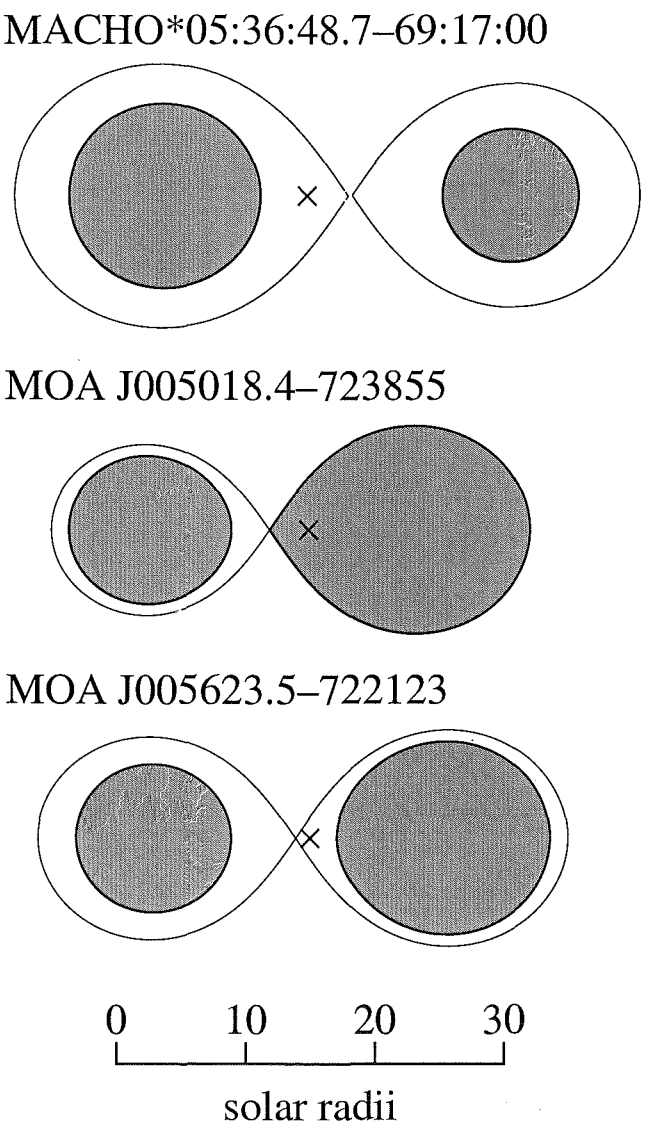

Figure 6.11: The stellar systems and limiting lobes for astrophysically plausible physical solutions for the three targets. The crosses (×) indicate the centre of gravity of each system.

Chapter 7

Conclusion

The goals of the initial thesis research proposal were to search for eclipsing binaries in the MOA SMC database; using these results, construct a catalogue of eclipsing binary stars in the SMC; select suitable candidates; make observations of them from MJUO and perform the subsequent reduction and analysis of the systems. All of these initial goals were achieved.

The coding and implementation of Grison's period detection algorithm successfully detected many thousands of variable stars in the SMC. These numbers were reduced to include only eclipsing binaries with the final number being 169. The completeness of the MOA catalogue was difficult to estimate. A total of 23 systems in the overlap region of the two MOA SMC fields, smc1 and smc2, were detected yet only 2 were detected in both fields. The detections common to the OGLE and MOA fields were cross-matched with 21 new detection identified within the common region. This indicated that neither catalogue is complete. Both databases initially used DoPhot for the data reductions. The problems of blending, especially in the crowded central regions would be expected to be a major issue. The re-reduction of the MOA data using image subtraction methods will undoubtedly yield a higher quality of extracted photometric data. This has been shown for the OGLE database (Galactic bulge data [117],[178],[179]), and will no-doubt apply to the MOA database too. The re-analysis of this data to detect eclipsing binaries would therefore be expected to yield higher numbers. A comparison of the systems common to both MOA fields would be expected to be greater, ideally 100%. A comparison of the eclipsing binary catalogues extracted from databases reduced using image subtraction should yield better agreement than current catalogues.

The MOA catalogue of eclipsing binaries in the SMC should provide several new targets for study from the MJUO site. Most other catalogues contain eclipsing binaries for which the majority of their data has been collected under, in terms of MJUO conditions, very good conditions. Comparison of the MOA catalogue with others containing the same systems should enable observers to better determine the feasibility of the planned study.

A MOA catalogue of eclipsing binaries in the LMC is currently in preparation. This will complement the SMC catalogue thereby enabling the selection of targets in both Clouds and thus make the most efficient use of telescope time. This catalogue is again based on DoPhot reduced photometry.

Two stars were selected from the MOA catalogue for follow-up photometric observations from MJUO using the 1-m McLellan Telescope. To fully utilize telescope time when the SMC is near lower culmination, a third target was selected from the MACHO catalogue of eclipsing binaries in the LMC. The Photometric Series 200 CCD system was used as the detector in combination with the CCD photometer head and $uV_{\rm J}I_{\rm C}$ filters. Differential photometry was extracted using Alard's difference imaging package ISIS-2.1. Altogether, some 1600 photometric measures were

obtained.

A partial analysis has been made of the three systems, MACHO*05:36:48.7−69:17:00 in the LMC, and MOA J005018.4−723855 and MOA J005623.5−722123 in the SMC. A full analysis requires spectroscopic radial velocities, not yet present for these targets, although they may be available for MACHO*05:36:48.7−69:17:00 in the near future due to the Villanova group's study of this target. The interest in this target is primarily due to its detached bright nature, but also its location, close to SN1987A, albeit that its depth is still undetermined. These analyses are the first to be determined for these systems. However masses, radii and temperatures have been estimated with the assumption that the distance to each system is equal to the respective mean galaxy distance. Solutions such as these based on solely photometric observations, are relatively sensitive to temperature and mass ratio. Therefore the solutions are termed astrophysically plausible, i.e. astrophysically such systems could exist, but they are not the definitive solutions for the target stars.

An astrophysically plausible solution for MACHO*05:36:48.7−69:17:00 was derived from Wilson-Devinney light curve analysis in conjunction with Geneva theoretical stellar evolution models. Initial inspection of the light curves clearly indicates an eccentric system with the *WD95* fits suggesting similar components, with the secondary a few thousand Kelvin cooler than the primary. Both components are well within their respective Roche lobes thereby categorizing the system as well detached, with masses typical of MS stars of their temperature and luminosity. The *WD95* fits calculated over a range of effective temperatures and mass ratios gave the same eccentricity, 0.200, with the inclination varying over a few degrees, 84° to 87°. The radius ratios for a given set of parameters by the *WD95* code are likely to be degenerate. Experience has shown that equally good local minima for R_1/R_2 and its inverse ratio most likely exist. This is typical for well detached systems where spectroscopy is not available. However no attempt was made to find them in this work. Analysis of the combined datasets from MJUO and MACHO, enabled the detection of apsidal motion in MACHO*05:36:48.7−69:17:00. The nature of this system opens the possibility for the study of stellar structure through observation and theoretical modelling once spectroscopic radial-velocities and spectrophotometry become available.

The semi-detached system of MOA J005018.4−723855 has one component filling its Roche lobe. Amounts of third light were required in the *WD95* fits, presumably due to the blending of the target with nearby stars, with the largest amount of third light in the I_C bandpass. This appears reasonable since most field stars are cooler than the B-stars which comprise this system. Light curve fitting was a balance between the I_C and u bandpasses with an O'Connell effect evident, but not modelled in the *WD95* fitting. The fits obtained for the light curve, particularly in the u bandpass, do not fit excellently. Furthermore, the solutions lie within a range of inclinations, which in-turn influences the eclipse fitting of the light curve. Together with the third light, it was not possible to obtain a good fit in all bandpasses simultaneously. The *WD95* fits indicated a secondary larger than the primary with case A mass transfer most likely occurring. Wellstein's theoretical evolutionary track models for mass transfer, Figures 6.4 and 6.5, show the mass donor can become cooler than the mass receptor as well as decrease rapidly in luminosity. This scenario ties in with the solution for this target. The mass-gaining primary was modelled as a Geneva MS star of SMC metallicity.

The properties of the components of MOA J005623.5−722123 compared to Geneva theoretical stellar evolution models together with the light curve, indicate a pair of similar stars. The *WD95* fits give a detached system with one component almost filling its Roche lobe with the masses indicative of MS stars of their age. More observations are required due to the minimal number of data points for the egress from primary eclipse in all bandpasses. The *WD95* solution included an allowance for third light, whose amount was averaged over a number of runs. Several

nearby, blended stars were identified on the reference frames. These appeared to be cooler red stars as one would expect for field stars. Therefore the third light was set to account for this. The solutions indicate a system nearly edge-on to the line of sight giving total eclipses. The solution gave a secondary component, on average, marginally hotter than the primary yet which exhibits shallower eclipses. Due to the high inclination and the components being hot B-stars that exhibit gravity brightening, the cooler secondary passes in-front of the cooler central disk region of the primary but the hotter outer regions of the disk of the primary are still seen.

The light curve analysis of the MJUO photometry obtained via image subtraction indicated precisions only slightly better than previous studies from MJUO. The estimation of third light on the reference frames was found to be difficult and also critical to the final result. Errors in third light estimation are compensated for in the *WD95* fits by the inclination, especially in the detached system, therefore making a precise estimation of the third light and inclination difficult due to their strong correlation. Furthermore, the accuracy of the reference frame levels was difficult to determine.

The current method employed to collect photometric data at MJUO is to observe one star at a time. The new MOA telescope, $f/2.5$, could be used, once available, for wide field observations of several systems at once. Ideally one would do standard calibrated photometry, such as Strömgren. Questions of phase coverage, filter size and linearity of the optical design to achieve high accuracy would however be issues.

All large telescopes have some type of high resolution spectrograph, however traditional methods of collecting spectroscopic data result in high telescope usage. The advent of multi-fibre instruments on a telescope such as 2dF on the 3.9 m AAT and more recently FLAMES on the VLT, dramatically reduces the required telescope time. Spectroscopy on an 8 m plus class of telescope such as VLT UT2 provides the most efficient use of telescope time. The number of known eclipsing binaries from the photometric studies shows that the density of known systems is sufficient to allow such an observing program. The argument by Wythie and Wilson that semi-detached systems should be used for distance scale determination adds to the number of possible systems to study. This in turn makes a project using a multi-fibre spectrograph even more warranted. The difficulty in obtaining time on these telescopes with these instruments is always a hurdle, however. The SALT project may make the use of a high resolution spectrograph, albeit not multi-fibre, possible for University of Canterbury astronomers in the near future.

Appendix A

ISIS-2.1

The description by Alard on how to run ISIS-2.1, is brief and only covers the main subroutines. A more detailed description is required however as there are many variable parameters in the configuration files but little explanation on what they do. The following therefore explains most of these parameters and how they affect the output of ISIS-2.1. It was found that the default settings are almost the optimal settings.

The tables below give the settings used for the MJUO reductions as well as the default settings for ISIS-2.1. These were used for all targets in both the LMC and SMC. The original CCD frame was 1024×1024 pixels but cropped to 570×570 pixels due to vignetting effects of the telescope's optical path. This therefore gave a small image size. The fields were moderately crowded as all targets were located near the central regions of their respective galaxies.

A note of caution: ISIS-2.1 overwrites *some* files, appends *some* and leave others if they exist, so it is most advantageous to remove all previous files from the working images directory, just leaving the images themselves prior to each run. This ensures a fresh start, otherwise the results can be very confusing especially when changes have been made.

Firstly, a brief description of the routines to be run is given. Details of the configuration files are given followed by a more in-depth description of the routines.

The ISIS-2.1 package installation creates two main working directories, in terms of use by the user, `register` and `images`. The `register` directory is used for the running of the program and is where the executable scripts are. The `images` directory contains the users images to be processed. The user can create multiple `register` directories as required and similarly for the images directory (customized names), though minor editing of some scripts as outlined below, is required. The order in which the routines are run from the current working register directory are:

- `interp.csh` - frame alignment
- `ref.csh` - construct reference image
- `subtract.csh` - subtract images
- `detect.csh` - detect variables on subtracted frames
- `find.csh` - find variable positions
- `phot.csh` - construct light curves of variables

These of course can be made into a script in the above order, but the file `phot.data` can be required to be edited prior to running the `phot.csh` script. Additionally, the value of the `SIG_THRESH` entry in the `process_config` file will most likely need to be changed.

A.1 ISIS configuration settings

The configuration files requiring setup are:

- `process_config`
- `default_config`
- `phot_config`

A.1.1 Process configuration file, `process_config`

These settings, Table A.1, supply ISIS-2.1 the paths for files and images. This can be edited to suit one's needs depending on directory structures. Contained in this configuration file are two important variables. Firstly `DEGREE` and secondly `SIG_THRESH`. The variable `DEGREE` is the degree of the polynomial of the astrometric transformation to the reference frame, used by `interp.csh`. `SIG_THRESH` sets the detection level above which a star is considered a variable as detected by `detect.csh`. Another variable in this configuration file, `COSMIC_THRESH`, sets the minimum level at which a pixel value can be considered to be affected by a cosmic ray. During the reduction of the MJUO data, the cosmic ray removal was performed by the MIDAS command `filter/cosmic` post dark-frame and flat-field correction and so `COSMIC_THRESH` was not tested. Two further variables `N_REJECT` and `MESH_SMOOTH` are associated with the cosmic ray removal or defect. These variables are used in the `detect.csh` routine which detects the variables in the frame. The value of `N_REJECT` specifies the n^{th} largest deviation less than the maximum of the absolute deviations of the pixel value in each of the subtracted frames. If this n^{th} deviation is less than half the maximum, the maximum is therefore most likely to be due to a cosmic ray or defect. The `MESH_SMOOTH` variable specifies the amount the image is smoothed during the variable detection process.

The remaining entries are locations of expected files and are explained in Table A.1.

A.1.2 Default configuration file, `default_config`

The configuration file `default_config`, Table A.2, contains the settings of parameters for the image subtraction process. In order to build a convolution kernel, local kernels are determined at several locations through the image; these location areas are term *stamps*, the number of which are denoted by the variables `nstamps_x` and `nstamps_y`. The program finds the brightest objects (not always stars) and places a stamp around them. The total number of stamps must be greater than 3 or 4 times $\frac{[(\texttt{deg\_spatial}+1)\times(\texttt{deg\_spatial}+2)]}{2}$ the spatial variation coefficients. The larger the image size and the greater the variation across the frame, the larger the number of stamps. In the case of the MJUO data using the cropped image size of 570 pixels square, the settings are given in Table A.2. If the image is larger than $1\,\mathrm{K}\times 1\,\mathrm{K}$, then the image can be divided into sub sections for processing, `sub_x` and `sub_y`. This helps to reduce processing time as matrices can become computationally large with large image sizes. Two variables are then set `half_mesh_size` and `half_stamp_size`. These are the half size of the kernel and half size of the stamps respectively. The half size of the kernel must be less than the half size of the stamp as the kernel is calculated in this area. Additionally, the half stamp size must

Table A.1: The settings used in the `process_config` file

Parameter	Value	Comment
IM_DIR	/astro6/macho565/ic/flat_fielded_images	Directory where the images are located
MRJ_DIR	/astro5/ISIS-2.1/package/	Installation directory
REFERENCE	/astro6/macho565/ic/flat_fielded_images/pf1961020.fits	Reference image for astrometry
REF_SUB	/astro6/macho565/ic/flat_fielded_images/ref.fits	Reference image for subtraction
INFILE	/astro5/ISIS-2.1/package/registermacho_ic/dates_macho565_ic	Dates of the frames
VARIABLES	/astro5/ISIS-2.1/package/registermacho_ic/phot.data	Coordinates of objects for which light curves will be made
DEGREE	1 (Default = 1)	Degree of the polynomial astrometric transform between frames
CONFIG_DIR	/astro5/ISIS-2.1/package/registermacho_ic	Where to find the configuration files
SIG_THRESH	2500 (Default = 2.0)	Value above which variable stars are detected in var.fits file
COSMIC_THRESH	1000.00 (Default = 1000.0)	Threshold pixel value for cosmic detection
REF_STACK	/astro6/macho565/ic/flat_fielded_images/pf1961020.fits	Used for bad pixel rejection
N_REJECT	2 (Default = 2)	N^{th} largest deviation for cosmic ray or defect removal
MESH_SMOOTH	1 (Default = 1)	Mesh smoothing parameter for cosmic ray or defect detection

Table A.2: The settings used in the `default_config file`. The critical parameters are `rad_phot` and `aper_phot`.

Parameter	Value	Default	Comment
`nstamps_x`	11	10	Number of stamps along x axis
`nstamps_y`	11	10	Number of stamps along y axis
`sub_x`	1	1	Number of sub_divisions of the image, x axis
`sub_y`	1	1	Number of sub_divisions of the image, y axis
`half_mesh_size`	9	9	Half kernel size
`half_stamp_size`	15	15	Half stamp size
`deg_bg`	1	3	Degree to fit differential background variations
`saturation`	65535.0	1000000.0	Degree to fit background variations
`pix_min`	5.0	5.0	Minimum value of the pixels to fit
`min_stamp_center`	130	130	Minimum value for object to enter kernel fit
`ngauss`	3	3	Number of Gaussians
`deg_gauss1`	6	6	Degree associated with 1^{st} Gaussian
`deg_gauss2`	4	4	Degree associated with 2^{nd} Gaussian
`deg_gauss3`	3	3	Degree associated with 3^{rd} Gaussian
`sigma_gauss1`	0.7	0.7	Sigma of 1^{st} Gaussian
`sigma_gauss2`	2.0	2.0	Sigma of 2^{nd} Gaussian
`sigma_gauss3`	6.0	4.0	Sigma of 3^{rd} Gaussian
`deg_spatial`	2	2	Degree of fit of the kernel spatial variations

be such that $2 \times$ `half_stamp_size` $\times$ `nstamps_x` $<$ image dimension in x and similarly for y. If the background in the images, more specifically the field, exhibits significant variation e.g. nebulosity, the `deg_bg` variable can be increased. This parameter specifies the degree of the polynomial modifying the Gaussian function which fits the background variations. This can therefore allow for a very complicated shape and of course variation between frames, however the larger the degree of the polynomial, the longer the processing time. A value of 1 for the `deg_bg` was found to be sufficient for all the reductions. The saturation level of the frame is set in the `saturation` variable. If there are any suspicions with regard to the linearity of the CCD detector as the counts approach the saturation level, the `saturation` variable should be set accordingly. The `pix_min` variable sets the minimum value a pixel must have before it is considered for the fitting procedure. The default value is acceptable. In the determination of the kernel, it is essential that the pixels within the stamp have no defects, i.e. cold pixels with negative values. To account for this possibility the variable `min_stamp_center`, the minimum value for an object to enter the kernel fit, is set. This can be adjusted to the background value, however very little difference is seen if the default value is used. The parameter `ngauss` gives the number of Gaussians used for the fit of the differential background variations and the spatial variations of the kernel. Here 3 is sufficient; increasing the number of Gaussians will increase processing time with little perceptible gain in quality. The `deg_gauss1,2,3` set the degree associated with the respective Gaussian and `sigma_gauss1,2,3` their sigma. The default settings are a reasonable start, although the `sigma_gauss3` may be varied by factors of order unity as this can improve the quality of the subtraction. The final variable, `deg_spatial` controls the degree of the polynomial used for the spatial variations i.e. the variations of the kernel coefficients as a function of position in the image, to modify the Gaussian functions for fitting the spatial variation of the kernel. A value of 2 was used for the MJUO data and performance was satisfactorily. Again, the higher the value, the longer the processing time. If the kernel size and stamp size are changed then the Gaussian sigma of the kernel expansion, `sigma_gauss1,2,3`, should be altered.

Table A.3: The settings used in the `phot_config` file. The critical parameters are `rad_phot` and `aper_phot`.

Parameter	Value	Default value
`sub_x`	1	1
`sub_y`	1	1
`rad1_bg`	15.0	15.0
`rad2_bg`	20.0	20.0
`nstars`	5	5
`mesh`	2	2
`saturation`	65535.0	1000000.0
`min`	5.0	5.0
`psf_width`	23	23
`rad_phot`	3.0	5.0
`nstar_max`	8	8
`rad_aper`	5	7.0
`nb_adu_el`	1.2	1
`rmax`	0.5	0.5
`first`	1	1
`keep`	5	5

A.1.3 Photometry configuration file, `phot_config`

The `phot_config` file, Table A.3, is used by `phot.csh`, for photometry extraction using PSF fitting. Again, the frame may be subdivided in x and y, (`sub_x` and `sub_x`) if required. This may be useful if it is desired to extract photometry of all the stars on the frame. The variables `rad1_bg` and `rad2_bg` refer to the fitting of the PSF to determine the background. An annulus (in units of pixels) is defined by `rad1_bg`, specifying the inner radius and `rad2_bg` the outer radius. Therefore the background is determined in the area enclosed by these two values. The default values of the variables `nstars`, `mesh`, `min`, `rmax`, `first` and `keep` were used. The exact definition of these was not entirely clear, however from the documentation provided with ISIS-2.1 and alteration of these variables, it was apparent that their default values were satisfactory. The same value of the `saturation` variable was used as in Table A.2. The `psf_width`, as the name suggests, is the PSF width variable. Various values were used, however the default value was preferred. The two variables `rad_phot` and `rad_aper` are the two most important variables of the photometry variables. Care must be taken to ensure the correct value of `rad_phot` is selected, refer Chapter 5, Figure 5.9. Too smaller a value and only a small amount of the profile is counted, too larger a value and the background starts to have an influence on the result. These parameters can have a significant effect on the light curve eclipse depths if they are not set correctly. The number of ADU per electron, `nb_adu_el` needs to be provided in the `phot_config` file.

A.1.4 Dates file

The dates file, Table A.4 files contains the name of the image to be reduced and the HMJD of the observation. In this work, the HMJD was calculated in MIDAS along with the dark and flat-field corrections. This file is used by ISIS-2.1 for processing all images. If an image is of poor quality its entry needs to be removed from this file to avoid future processing.

Table A.4: An extract from the `dates` file `dates_macho565_ic` for MACHO*05:36:48.7−69:17:00, I_C filter. The first column contains the image filenames that have been pre-processed with dark and flat fielding corrections and cosmic ray removal. Column 2 contains the HJD of mean observation less 2400000. The HMJD is report here as extracted from the FITS header. The rounding of the HMJD values to the relevant number of significant figures was performed at the light curve analysis stage.

Filename	HMJD
pf1295033.fits	51294.9735752
pf1295040.fits	51295.0796753
pf1295046.fits	51295.1584721
pf1295053.fits	51295.2587158
pf1404026.fits	51404.1778327

A.1.5 List of files used to construct the reference frame, `ref_list`

This file is located in the `register` directory and contains the list of files which will be used to construct the reference frame during the running of the `ref.csh` routine. The entries are in the form of a list of the file names. In order to ascertain the best seeing images, the seeing routine, `seeing.csh` can be used.

A.1.6 Determination of the seeing, `seeing.csh`

The `seeing.csh` routine in the ISIS-2.1 package, register directory, can be used to determine the values of the seeing in each frame. An example of the typical output is given in Table A.5. Note, the values reported are in units of pixels. The scaling factor, such as in Appendix C, equation C.3, is required to convert to units of arc seconds. If the seeing cannot be determined, the entries for the corresponding filename are blank. This will be the case for a very poor frame such as when cloud was present during the exposure. The routine is run independently of the image subtraction process, but requires the `dates` file for the list of images and configuration files. The seeing is given in units of pixels. The value of `rad_phot` and `rad_aper` need to be selected carefully. Images with very bad seeing, greater than ∼6 arc sec, will give very small seeing values if these two variables are not set large enough. However, setting them too large will mean too much background is taken into account in the better seeing frames. It is better to set these variables in relation to the better seeing frames. The very bad seeing frames give an excessively small seeing value, i.e. good seeing frame 3.2 pixels, very bad seeing frame 0.8 pixels. Therefore the incorrectly calculated seeing values are easily detected. These are best seen in a plot of seeing value versus HMJD.

A.2 Running ISIS-2.1

Once the configuration files have been set and the dates file constructed along with the list of files to use for the reference image construction, the image subtraction process can start. Details of running the processes and examples of processed image using the MJUO data are presented in Chapter 5 sections 5.1.3.2 to 5.1.7.

A.2.1 Production of files

Upon running, ISIS-2.1, many files are produced and written to the current working image directory, with the exception on one, `phot.data`. This is written to the current working (or

Table A.5: Sample of seeing values for observations of MOA J005018.4−723855, I_C filter. The first column is the filename. Second column the average (x, y) seeing. The third and fourth columns are the seeing in x and y respectively. The fifth column gives off-axis azimuthal angle of the PSF, measured with respect to the major axis of the profile. This is a type of *distortion* parameter with values near zero indicating a PSF with a nearly ideal Gaussian-like profile. The seeing values reported here, are as given by ISIS-2.1. The rounding of the seeing values to the relevant number of significant figures was performed at the light curve analysis stage.

File name	Average seeing	x seeing	y seeing	*distortion* parameter
pf2138014.fits	3.638211	3.708305	3.566740	11.484425
pf2138028.fits	3.431861	3.532478	3.328204	-7.203856
pf2138031.fits	3.788993	3.843998	3.733177	-6.136638
pf2138034.fits	4.112073	4.210808	4.010909	-8.582210
pf2138037.fits	4.500799	4.596265	4.403263	-2.678722
pf2138039.fits	4.880123	4.947107	4.812207	-1.917054
pf2138042.fits	4.365901	4.438579	4.291994	1.448883
pf2138045.fits	4.647453	4.715214	4.578689	-2.220129
pf2138047.fits	5.185666	5.392942	4.969753	-3.496966

register) directory, where ISIS-2.1 is generally run. Table A.6 shows the files produced at different stages of the reduction process. Again it is stressed that not all of the files are over written, some are merely appended therefore they should be removed prior to running ISIS-2.1 again.

Table A.6: Files produced when running ISIS-2.1. The * indicates the image filename as found in the `dates` file.

Routine	Files produced or rewritten

`interp.csh`	`bad.data`
	`bin.data`
	`coeff`
	`dayfile`
	`good.data`
	`interp_*`
	`log_interp2`
	`psf.data`
	`rad.data`
	`temp`
	`temp.fits`
	`toto`

`ref.csh`	`conv0r_interp_*`
	`convr_interp_*`
	`kc_0*`
	`kt_*`
	`ref.fits`

`subtract.csh`	`conv_*`
	`kc_0interp_*`
	`kt_*`
	`log_subtract`

`detect.csh`	`abs.fit` `var.fits`
`find.csh`	`toto` `phot.data`

`phot.csh`	`kernal.fits`
	`lc*.fits`
	`new_psf.fits`
	`psf.fits`
	`psf_table`
	`psf_file0.fits`

Appendix B

Transmission functions for the $uvbyV_{\rm J}I_{\rm C}$ MJUO photometric system

The response functions for the Strömgren *u,v,b,y* filters, Cousins $I_{\rm C}$ filter and Johnson $V_{\rm J}$ are given in tables B.1, B.2, B.3, B.4, B.5 and B.6 respectively. The data for the S200 SITe Si003ab CCD was supplied by Photometrics in the documentation for the S200 CCD system. This is presented on table B.7. Response curves for all filters and CCD are shown in Chapter 4, figure 4.3.

Table B.1: Data for the transmission function $T_{f_{MJUO,u}}$, for the Strömgren u filter used in the MJUO photometer head; data supplied by Omega Optical.

λ (nm)	$T_{f_{MJUO,u}}$ (Strömgren u filter)
310.00	0.0000
312.50	0.0080
315.00	0.0200
317.50	0.0500
320.00	0.0900
322.50	0.1450
325.00	0.2000
327.50	0.2600
330.00	0.3080
332.50	0.3600
335.00	0.4000
337.50	0.4350
340.00	0.4610
342.50	0.4780
345.00	0.4880
347.50	0.4900
350.00	0.4860
352.50	0.4800
355.00	0.4600
357.50	0.4300
360.00	0.3950
362.50	0.3500
365.00	0.2880
367.50	0.2200
370.00	0.1540
372.50	0.0950
375.00	0.0480
377.50	0.0200
380.00	0.0060
382.50	0.0010
385.00	0.0001
387.50	0.0000

Table B.2: Data for the transmission function $T_{f_{MJUO,v}}$, for the Strömgren v filter used in the MJUO photometer head; data supplied by Omega Optical.

λ (nm)	$T_{f_{MJUO,v}}$ (Strömgren v filter)
380	0.0000
385	0.0000
390	0.0062
395	0.0375
400	0.1937
405	0.4375
410	0.5093
415	0.4312
420	0.1750
425	0.0500
430	0.0125
435	0.0031
445	0.0000

Table B.3: Data for the transmission function $T_{f_{MJUO,b}}$, for the Strömgren b filter used in the MJUO photometer head; data supplied by Omega Optical.

λ (nm)	$T_{f_{MJUO,b}}$ (Strömgren b filter)
440	0.0000
445	0.0046
450	0.0343
455	0.1890
460	0.5796
465	0.7468
470	0.6000
475	0.2484
480	0.0718
485	0.0203
505	0.0000

Table B.4: Data for the transmission function $T_{f_{MJUO,y}}$, for the Strömgren y filter used in the MJUO photometer head; data supplied by Omega Optical.

λ (nm)	$T_{f_{MJUO,y}}$ (Strömgren y filter)
500	0.0000
515	0.0140
520	0.0343
525	0.0812
530	0.1718
535	0.3203
540	0.5875
545	0.6843
550	0.6125
555	0.4750
560	0.3031
565	0.1312
570	0.0843
575	0.0468
580	0.0265
585	0.0171
610	0.0000

Table B.5: Data for the transmission function $\mathrm{T}_{f_{\mathrm{MJUO},I_{\rm C}}}$, for the Cousins $I_{\rm C}$ filter used in the MJUO photometer head; data supplied by Omega Optical.

λ (nm)	$\mathrm{T}_{f_{\mathrm{MJUO},I_{\rm C}}}$ (Cousins $I_{\rm C}$ filter)
690.00	0.0000
710.00	0.0750
720.00	0.2625
730.00	0.5468
740.00	0.7281
750.00	0.8125
760.00	0.8359
770.00	0.8500
780.00	0.8656
790.00	0.8812
800.00	0.8781
810.00	0.8687
820.00	0.8562
830.00	0.8437
840.00	0.8437
850.00	0.8768
860.00	0.8015
870.00	0.4562
880.00	0.1875
890.00	0.0750
900.00	0.0343
940.00	0.0000

Table B.6: Data for the transmission function $\mathrm{T}_{f_{\mathrm{MJUO},V_{\rm J}}}$, for the Johnson $V_{\rm J}$ filter used in the MJUO photometer head; data supplied by J.D. Pritchard [123].

λ (nm)	$\mathrm{T}_{f_{\mathrm{MJUO},V_{\rm J}}}$ (Johnson $V_{\rm J}$ filter)
477.00	0.0000
484.00	0.2360
494.00	0.6420
505.00	0.7550
516.00	0.7900
527.00	0.7900
537.00	0.7680
548.00	0.7120
559.00	0.6340
570.00	0.5371
581.00	0.4237
591.00	0.3058
602.00	0.2024
613.00	0.1215
624.00	0.0587
634.00	0.0212
677.00	0.0000

Table B.7: The quantum efficiency, QE, of the S200 SITe Si003ab CCD as provided by the supplier, Photometrics.

λ (nm)	QE
240	0.30
260	0.27
280	0.25
300	0.26
320	0.34
340	0.38
360	0.42
380	0.46
400	0.47
450	0.51
500	0.68
550	0.70
600	0.72
650	0.72
700	0.71
750	0.61
800	0.53
850	0.43
900	0.34
950	0.22
1000	0.11

Appendix C

Photometric observations

Tables of CCD photometry acquired from MJUO for one LMC target, MACHO*05:36:48.7 −69:17:00 and two SMC targets, MOA J005018.4−723855 and MOA J005623.5−722123. The photometry is presented for the three bandpasses, Strömgren u (of the Strömgren *uvby* system), V_J and I_C (of the Johnson-Cousins $UBVRI$). Refer section 4.1.2, Table 4.1, Figure 4.3 and Appendix B for filter properties. A description of each column is given below.

Image: The name of the image as stored on the computer hard drive and CDROM archive. The name is slightly modified as some data acquisition programs used lower case, other upper case. All prefixes and suffixes were changed to lower case for the reduction process. During the pre-processing stage the prefix `p` was added to signify the image had been pre-processed. The letter `f` signifies that the ten-thousand JD digit is 5 (a=0, b=1, c=2, d=3, e=4, f=5). The name starts with a letter so MIDAS doesn't treat it as a number. The first group of four digits represents the mean Julian Date −2450000.0. The next three digits are a sequential file number beginning at 1 for each night's observations.

UTC date: The Universal Coordinated Time, UTC of the image acquisition. Here only the date portion of the UTC is presented.

Mean date: The Heliocentric Mean Julian Date as calculated by MIDAS from the time of mid-exposure as extracted from the FITS header. Again due to acquisition programs used, date formats varied in the raw science image FITS headers.

Orbital Phase: The calculated orbital phase of the system based on the period and ephemeris.

Flux difference: The flux presented as the difference of the target on the science frame relative to the flux of the target on the reference frame as calculated by ISIS-2.1.

δ **Flux difference:** Estimate of the uncertainty in the calculated flux difference. Note, the values presented are as derived by ISIS-2.1 and are only accurate to the hundreds digit. They are presented here in full rather than rounding each individual value to its respective uncertainty.

Norm. Light: The normalized light is calculated, equation C.1, with respect to the flux of the reference frame, since the science flux is a difference and doesn't need to be background corrected.

$$\text{Normalized light} = -\frac{(\text{science flux difference} - \text{background-corrected reference flux})}{\text{background-corrected reference flux}} \tag{C.1}$$

Note the negative sign which appears because an augmentation of light produces a *negative* flux difference with ISIS-2.1.

Quality Factor: The Quality factor flag of the photometry of the image as calculated by ISIS-2.1. This was one of the factors used to determine the exclusion of bad data points from the final light curve, although not completely reliable.

Seeing: The seeing as calculated from the seeing script in ISIS-2.1. The output gave the seeing values in the form of the mean Full-Width at Half Maximum, FWHM, in pixels, equation C.2. The seeing was determined by PSF fitting where σ_x and σ_y are the cross sections at FWHM.

$$\text{FWHM} = \sqrt{\sigma_x \sigma_y} \tag{C.2}$$

The mean FWHM value was then multiplied the image scale in equation C.3, to give units of arc seconds. The CCD detector pixels size is $24\,\mu$m square and the telescope focal length, 7.700 m.

$$\text{Image scale} = 24\,\mu m \times \frac{\frac{180}{\pi} \times 3600}{7.700} = 0.6429\,\text{arc sec/pixel} \tag{C.3}$$

Airmass: The airmass through which the target was observed. Calculated by MIDAS from the FITS header information.

LC analysis I = Included in the final light curve for analysis using the modified Wilson-Devinney code. **X** = eXcluded from the light curve analysis.

Comment: R = Indicating the reference frame, A = indicating the astrometric alignment frame. Some band passes used more than one image to construct the reference frame. The comment **CE** refers to computer/software errors that have resulted in the file name not remaining the same during the night's observations. This is seen when the frame name, HJD and UTC are compared.

C.1 MACHO*05:36:48.7−69:17:00 image subtraction photometry

C.1.1 MACHO*05:36:48.7−69:17:00 u filter, image subtraction photometry

Table C.1: MACHO*05:36:48.7−69:17:00 u filter, image subtraction photometry.

Image name	UTC	Mean date HJD−2400000.0	Orbital phase	Flux difference	δ Flux difference	Norm. light	Quality factor	Seeing (arc sec)	Airmass (χ)	LC analysis	Comment
pf1295027	26-Apr-1999	51294.9019	0.6095	−1200	658	1.008	0.41	4.8	1.5	I	
pf1295034	26-Apr-1999	51294.9893	0.6322	−1171	548	1.008	0.28	3.5	1.9	I	
pf1295041	26-Apr-1999	51295.0909	0.6586	−1189	348	1.008	0.15	2.7	2.4	I	
pf1295048	26-Apr-1999	51295.1864	0.6834	839	522	0.994	0.16	5.4	2.5	I	
pf1295054	26-Apr-1999	51295.2695	0.7049	−3763	795	1.026	0.44	3.3	2.2	I	
pf1404021	13-Aug-1999	51404.1051	0.9480	−2645	575	1.018	0.70	4.5	1.6	I	
pf1404027	13-Aug-1999	51404.1898	0.9700	−3209	549	1.022	0.77	3.6	1.3	I	
pf1405018	14-Aug-1999	51404.8151	0.1323	46343	306	0.684	0.99	4.7	2.4	I	
pf1405019	14-Aug-1999	51404.8382	0.1383	39245	292	0.731	1.00	0.6	2.4	X	
pf1405038	14-Aug-1999	51404.9932	0.1785	−2152	412	1.014	0.39	0.2	2.1	X	
pf1405039	14-Aug-1999	51405.0102	0.1829	−737	417	1.005	0.14	0.3	2.0	X	
pf1406038	15-Aug-1999	51406.1029	0.4664	16608	592	0.887	0.98	5.5	1.6	I	
pf1406043	15-Aug-1999	51406.1686	0.4835	35035	482	0.761	1.00	4.1	1.4	I	
pf1558013	14-Jan-2000	51557.9867	0.6865	−2957	727	1.020	0.71	5.0	1.1	I	
pf1558016	14-Jan-2000	51558.0283	0.7205	−668	703	1.005	0.25	5.4	1.1	I	
pf1558019	14-Jan-2000	51558.0687	0.7355	−1891	864	1.013	0.34	7.2	1.2	X	
pf1559013	15-Jan-2000	51558.9215	0.7612	49325	637	0.663	1.00	4.9	1.1	I	
pf1559016	15-Jan-2000	51558.9621	0.7793	46145	724	0.685	1.00	5.9	1.1	I	
pf1559019	15-Jan-2000	51559.0069	0.8020	34050	444	0.767	0.98	5.5	1.1	I	
pf1561013	17-Jan-2000	51560.9418	0.4644	−2288	673	1.016	0.61	3.8	1.1	I	
pf1561016	17-Jan-2000	51561.0420	0.4831	−4300	744	1.029	0.85	5.1	1.2	I	
pf1561019	17-Jan-2000	51561.0847	0.5137	−3578	666	1.024	0.78	5.4	1.2	I	
pf1725022	29-Jun-2000	51724.8297	0.5345	2469	700	0.983	0.58	3.6	1.9	I	
pf1725029	29-Jun-2000	51724.9753	0.5533	2342	701	1.003	0.33	8.0	1.9	X	

continued on next page

Table C.1: *continued*: MACHO*05:36:48.7−69:17:00 u filter, image subtraction photometry

Image name	UTC	Mean date HJD−2400000.0	Orbital phase	Flux difference	δ Flux difference	Norm. light	Quality factor	Seeing (arc sec)	Airmass (χ)	LC analysis	Comment
pf1725035	29-Jun-2000	51725.0741	0.5774	228	779	1.016	0.00	0.4	1.8	X	
pf1725042	29-Jun-2000	51725.1728	0.7223	−4282	668	1.029	0.81	5.4	1.8	I	
pf1727023	01-Jul-2000	51726.7938	0.7486	−1795	509	1.012	0.49	3.6	1.8	I	
pf1727030	01-Jul-2000	51726.9250	0.7743	−2068	515	1.014	0.47	4.7	2.4	I	
pf1727034	01-Jul-2000	51726.9828	0.4471	−1927	372	1.013	0.59	3.1	2.5	I	
pf1727040	01-Jul-2000	51727.0818	0.4584	−3118	391	1.021	0.88	3.0	2.2	I	
pf1727046	01-Jul-2000	51727.1516	0.4661	−2180	435	1.015	0.70	3.0	1.9	I	
pf1727052	01-Jul-2000	51727.2389	0.2203	461	469	0.997	0.27	3.2	1.5	I	
pf1730022	04-Jul-2000	51729.7915	0.2280	12292	590	0.916	0.96	5.0	1.8	I	
pf1730028	04-Jul-2000	51729.8638	0.2359	34859	523	0.762	0.99	5.3	2.2	I	
pf1730035	04-Jul-2000	51729.9817	0.2437	37825	393	0.742	0.99	4.0	2.5	I	
pf1730041	04-Jul-2000	51730.0618	0.4333	12914	545	0.912	0.97	5.4	2.3	I	
pf1730046	04-Jul-2000	51730.1341	0.4407	−491	524	1.003	0.13	4.5	1.9	I	
pf1730052	04-Jul-2000	51730.2269	0.4480	−2394	615	1.016	0.74	4.7	1.5	I	
pf1731022	05-Jul-2000	51730.7854	0.4555	−304	437	1.002	0.23	2.7	1.8	I	
pf1731029	05-Jul-2000	51730.8868	0.4631	−600	391	1.004	0.16	4.0	2.3	I	
pf1731035	05-Jul-2000	51730.9857	0.4707	−2016	423	1.014	0.40	3.7	2.5	I	
pf1957018	16-Feb-2001	51957.0830	0.4782	−1478	992	1.010	0.29	0.5	1.4	X	
pf1957021	16-Feb-2001	51957.1267	0.4855	3525	952	1.008	0.50	7.8	1.6	X	
pf1957024	16-Feb-2001	51957.1564	0.4950	9593	918	1.011	0.83	7.6	1.7	X	
pf1960028	16-Feb-2001	51960.0629	0.5026	−1760	638	1.012	0.58	5.7	1.4	I	
pf1960031	16-Feb-2001	51960.0925	0.5104	−2878	637	0.724	0.86	5.4	1.5	I	
pf1960034	16-Feb-2001	51960.1230	0.4463	−2186	506	1.015	0.78	3.7	1.6	I	
pf1960037	16-Feb-2001	51960.1530	0.4503	−1716	524	1.012	0.36	4.1	1.8	I	
pf1961013	20-Feb-2001	51960.8834	0.4754	−2352	485	1.016	0.87	2.5	1.1	I	
pf1961017	20-Feb-2001	51960.9119	0.4792	−1513	471	1.010	0.64	2.4	1.1	I	
pf1961019	20-Feb-2001	51960.9404	0.4944	−1101	449	1.008	0.70	2.2	1.2	I	R
pf1961022	20-Feb-2001	51960.9690	0.4982	2882	439	0.980	0.86	2.1	1.2	I	R,A

continued on next page

Table C.1: *continued*: MACHO*05:36:48.7−69:17:00 u filter, image subtraction photometry

Image name	UTC	Mean date HJD−2400000.0	Orbital phase	Flux difference	δ Flux difference	Norm. light	Quality factor	Seeing (arc sec)	Airmass (χ)	LC analysis	Comment
pf1961025	20-Feb-2001	51960.9982	0.4678	9872	439	0.933	0.98	2.5	1.3	I	
pf1961028	20-Feb-2001	51961.0275	0.4756	17886	463	0.878	0.99	3.1	1.3	I	
pf1961031	20-Feb-2001	51961.0566	0.4840	26963	499	0.816	0.99	3.8	1.4	I	
pf1961034	20-Feb-2001	51961.0848	0.4923	34343	514	0.765	1.00	5.3	1.5	I	
pf1961037	20-Feb-2001	51961.1214	0.4999	44712	472	0.695	1.00	5.1	1.7	I	
pf1961040	20-Feb-2001	51961.1506	0.5108	45283	467	0.791	1.00	4.5	1.8	I	
pf1961043	20-Feb-2001	51961.1805	0.5171	40359	514	0.763	0.99	0.7	1.9	X	
pf1988013	19-Mar-2001	51987.9082	0.5323	−2959	689	1.020	0.74	5.9	1.2	I	
pf1988014	19-Mar-2001	51987.9237	0.5445	445	701	0.997	0.08	6.3	1.3	I	
pf1989002	20-Mar-2001	51988.0204	0.5554	25640	381	0.825	0.99	2.7	1.5	I	
pf1989003	20-Mar-2001	51988.0349	0.4666	29131	361	0.801	1.00	2.6	1.6	I	
pf1989009	20-Mar-2001	51988.0938	0.4725	44688	344	0.695	1.00	3.1	1.9	I	
pf1989010	20-Mar-2001	51988.1084	0.4725	46458	340	0.683	1.00	3.2	1.9	I	
pf1992013	23-Mar-2001	51991.8446	0.4818	14654	507	0.900	0.98	3.1	1.1	I	
pf1992016	23-Mar-2001	51991.8749	0.4899	23566	595	0.839	0.99	4.7	1.2	I	
pf1992019	23-Mar-2001	51991.9070	0.4986	33548	543	0.771	1.00	4.7	1.2	I	
pf1992022	23-Mar-2001	51991.9391	0.5071	42162	408	0.712	1.00	3.2	1.3	I	
pf1992025	23-Mar-2001	51991.9683	0.5176	45725	397	0.688	1.00	3.8	1.4	I	
pf1992030	23-Mar-2001	51992.0102	0.5283	40692	460	0.722	1.00	4.1	1.6	I	
pf1992032	23-Mar-2001	51992.0345	0.5381	34640	472	0.763	1.00	4.2	1.6	I	
pf1992037	23-Mar-2001	51992.0931	0.5557	18187	398	0.876	0.98	3.1	1.9	I	
pf1992042	23-Mar-2001	51992.1404	0.5645	4042	458	0.972	0.73	4.0	2.2	I	
pf1992047	23-Mar-2001	51992.1823	0.0037	−2371	386	1.016	0.19	3.0	2.4	I	
pf2019013	19-Apr-2001	52018.8148	0.0122	14355	547	0.902	0.99	3.7	1.2	I	
pf2019014	19-Apr-2001	52018.8374	0.0213	22195	561	0.848	0.99	4.1	1.3	I	
pf2019018	19-Apr-2001	52018.8734	0.0431	33108	488	0.774	1.00	4.2	1.3	I	
pf2019021	19-Apr-2001	52018.9045	0.0476	39823	497	0.728	1.00	4.0	1.4	I	
pf2019024	19-Apr-2001	52018.9380	0.0782	44904	468	0.693	1.00	3.9	1.6	I	

continued on next page

Table C.1: *continued*: MACHO*05:36:48.7−69:17:00 u filter, image subtraction photometry

Image name	UTC	Mean date HJD−2400000.0	Orbital phase	Flux difference	δ Flux difference	Norm. light	Quality factor	Seeing (arc sec)	Airmass (χ)	LC analysis	Comment
pf2019027	19-Apr-2001	52018.9707	0.0911	44551	462	0.696	1.00	4.0	1.7	I	
pf2019030	19-Apr-2001	52019.0114	0.2457	33323	559	0.772	0.99	5.3	1.9	I	
pf2019033	19-Apr-2001	52019.0524	0.2536	22770	504	0.845	0.99	4.7	2.1	I	
pf2019036	19-Apr-2001	52019.0902	0.2657	10770	543	0.926	0.90	4.3	2.3	I	
pf2019039	19-Apr-2001	52019.1582	0.2739	3278	441	0.985	0.25	0.8	2.4	X	
pf2019042	19-Apr-2001	52019.1921	0.2909	−1341	623	1.009	0.22	6.8	2.5	I	
pf2021013	21-Apr-2001	52020.8847	0.3018	−133	679	1.001	0.08	6.2	1.4	I	
pf2021015	21-Apr-2001	52020.9174	0.5275	−638	676	1.004	0.22	5.7	1.5	I	
pf2021018	21-Apr-2001	52020.9525	0.5351	−218	698	1.001	0.09	6.3	1.6	I	
pf2021024	21-Apr-2001	52021.0201	0.5436	−750	591	1.005	0.22	4.9	1.9	I	
pf2021025	21-Apr-2001	52021.0362	0.5515	−2029	588	0.014	0.48	4.9	2.0	I	
pf2021026	21-Apr-2001	52021.0535	0.5591	−1477	618	1.004	0.31	0.3	2.1	X	
pf2021039	21-Apr-2001	52021.1717	0.5655	10144	540	1.003	0.89	0.3	2.5	X	
pf2021044	21-Apr-2001	52021.2215	0.5732	26410	537	0.820	0.99	5.9	2.5	I	
pf2022013	22-Apr-2001	52021.8170	0.5812	−1563	512	0.011	0.59	2.9	1.2	I	
pf2022016	22-Apr-2001	52021.8474	0.4749	−1119	532	1.008	0.30	3.2	1.3	I	
pf2022020	22-Apr-2001	52021.8941	0.4868	−3346	568	1.023	0.83	3.8	1.4	I	
pf2022023	22-Apr-2001	52021.9256	0.4985	−3420	540	1.023	0.78	3.7	1.5	I	
pf2022029	22-Apr-2001	52021.9913	0.5134	−4181	685	1.029	0.78	5.6	1.8	I	
pf2022032	22-Apr-2001	52022.0332	0.2676	−3040	577	1.021	0.57	5.0	2.0	I	
pf2023013	23-Apr-2001	52022.9032	0.2755	21896	674	0.850	0.99	5.7	1.5	I	
pf2023016	23-Apr-2001	52022.9323	0.2832	14141	484	0.903	0.98	3.5	1.6	I	
pf2023019	23-Apr-2001	52022.9651	0.2923	6864	515	0.953	0.92	4.0	1.7	I	
pf2023022	23-Apr-2001	52022.9954	0.3050	152	477	0.999	0.01	3.5	1.9	I	
pf2023025	23-Apr-2001	52023.0248	0.3158	−603	541	1.004	0.18	4.5	2.0	I	
pf2023028	23-Apr-2001	52023.0493	0.3255	−456	580	1.018	0.17	0.2	2.1	X	
pf2023031	23-Apr-2001	52023.0789	0.5552	−1405	487	1.010	0.25	4.2	2.3	I	
pf2023034	23-Apr-2001	52023.1098	0.5649	1009	458	0.993	0.23	4.0	2.4	I	

continued on next page

Table C.1: *continued*: MACHO*05:36:48.7−69:17:00 u filter, image subtraction photometry

Image name	UTC	Mean date HJD−2400000.0	Orbital phase	Flux difference	δ Flux difference	Norm. light	Quality factor	Seeing (arc sec)	Airmass (χ)	LC analysis	Comment
pf2046018	16-May-2001	52045.8215	0.5767	22547	366	0.846	0.99	2.6	1.4	I	
pf2046023	16-May-2001	52045.8672	0.5870	37827	376	0.742	1.00	3.2	1.6	I	
pf2046028	16-May-2001	52045.9125	0.5966	45255	438	0.691	1.00	4.3	1.8	I	
pf2046033	16-May-2001	52045.9700	0.6068	43536	296	0.660	0.97	0.5	2.0	X	
pf2206013	24-Oct-2001	52206.8707	0.8806	−3363	781	1.023	0.55	3.8	1.7	I	
pf2206015	24-Oct-2001	52206.9014	0.8914	−744	908	1.005	0.14	4.5	1.6	I	
pf2206017	24-Oct-2001	52206.9312	0.9019	−2918	976	1.012	0.55	4.8	1.5	I	
pf2206019	24-Oct-2001	52206.9661	0.1232	−3742	1148	1.026	0.72	4.9	1.4	I	
pf2206021	24-Oct-2001	52207.0152	0.1338	−4098	1205	1.028	0.81	5.0	1.3	I	
pf2206024	24-Oct-2001	52207.0565	0.1454	−4676	984	1.032	0.84	4.0	1.2	I	
pf2206026	24-Oct-2001	52207.0940	0.6475	−2718	1002	1.019	0.75	3.9	1.1	I	
pf2207017	25-Oct-2001	52207.9791	0.6735	−3320	1114	1.023	0.65	5.0	1.3	I	
pf2207019	25-Oct-2001	52208.0166	0.6846	−2991	1219	1.020	0.66	5.6	1.2	I	
pf2207021	25-Oct-2001	52208.0622	0.1768	−6475	1416	1.044	0.79	6.1	1.2	I	
pf2207023	25-Oct-2001	52208.1017	0.2146	−3337	1021	1.023	0.65	4.1	1.1	I	
pf2207025	25-Oct-2001	52208.1388	0.2402	−1638	1087	1.011	0.46	4.8	1.1	I	
pf2207027	25-Oct-2001	52208.1781	0.2658	−4900	1161	1.033	0.62	4.9	1.1	I	
pf2464023	08-Jul-2002	52464.1639	0.0357	−4020	741	1.027	0.56	3.8	1.8	I	
pf2464025	08-Jul-2002	52464.1844	0.0410	−3551	746	1.024	0.58	6.4	1.7	I	
pf2464027	08-Jul-2002	52464.2057	0.0466	−2916	723	1.020	0.55	6.5	1.6	I	
pf2464029	08-Jul-2002	52464.2427	0.0562	41	690	0.976	0.01	6.3	1.4	X	
pf2464031	08-Jul-2002	52464.2662	0.0623	316	741	0.979	0.06	7.0	1.3	X	
pf2464033	08-Jul-2002	52464.2880	0.0679	3073	636	0.979	0.55	6.3	1.3	I	
pf2465043	09-Jul-2002	52465.1083	0.2808	−6978	520	1.048	0.84	4.5	2.0	I	
pf2465046	09-Jul-2002	52465.1440	0.2901	−6618	482	1.045	0.91	4.1	1.8	I	
pf2465049	09-Jul-2002	52465.1738	0.2978	−6277	366	1.043	0.84	3.9	1.7	I	
pf2465052	09-Jul-2002	52465.2031	0.3054	−3206	471	1.022	0.83	3.8	1.6	I	
pf2467044	11-Jul-2002	52467.1801	0.8184	−622	720	1.004	0.15	1.1	1.6	X	

continued on next page

Table C.1: *continued*: MACHO*05:36:48.7−69:17:00 u filter, image subtraction photometry

Image name	UTC	Mean date HJD−2400000.0	Orbital phase	Flux difference	δ Flux difference	Norm. light	Quality factor	Seeing (arc sec)	Airmass (χ)	LC analysis	Comment
pf2467046	11-Jul-2002	52467.2033	0.8245	−3690	604	1.025	0.54	6.0	1.6	I	
pf2467048	11-Jul-2002	52467.2252	0.8302	−4959	483	1.034	0.67	5.4	1.5	I	
pf2467050	11-Jul-2002	52467.2473	0.8359	−2324	473	1.016	0.51	4.9	1.4	I	
pf2467052	11-Jul-2002	52467.2677	0.8412	−5533	420	1.037	0.79	0.4	1.3	X	
pf2467054	11-Jul-2002	52467.2880	0.8464	−2489	707	1.017	0.38	1.4	1.2	X	
pf2468014	12-Jul-2002	52467.8439	0.9907	−865	378	1.006	0.16	4.0	2.2	I	
pf2468016	12-Jul-2002	52467.8669	0.9967	−1397	414	1.010	0.32	6.8	2.3	I	
pf2468019	12-Jul-2002	52467.9086	0.0075	−1335	456	1.009	0.29	0.4	2.4	X	
pf2468021	12-Jul-2002	52467.9334	0.0139	−4039	453	1.028	0.73	4.5	2.5	I	
pf2468023	12-Jul-2002	52467.9536	0.0192	−3029	487	1.020	0.49	1.2	2.5	X	
pf2468025	12-Jul-2002	52467.9747	0.0246	−1839	469	1.013	0.30	4.9	2.5	I	
pf2468029	12-Jul-2002	52468.0174	0.0357	−2063	560	1.014	0.41	5.6	2.4	I	
pf2468031	12-Jul-2002	52468.0381	0.0411	−2238	552	1.015	0.40	5.9	2.3	I	
pf2468035	12-Jul-2002	52468.0841	0.0530	−2910	397	1.020	0.54	3.3	2.1	I	
pf2468037	12-Jul-2002	52468.1047	0.0584	−1442	461	1.010	0.43	3.0	2.0	I	
pf2468041	12-Jul-2002	52468.1471	0.0694	3351	479	0.977	0.70	3.8	1.8	I	
pf2468043	12-Jul-2002	52468.1680	0.0748	7685	541	0.948	0.92	4.6	1.7	I	
pf2468047	12-Jul-2002	52468.2156	0.0872	21188	518	0.855	0.99	5.6	1.5	I	
pf2468051	12-Jul-2002	52468.2568	0.0978	33613	438	0.770	1.00	3.8	1.4	I	
pf2468053	12-Jul-2002	52468.2772	0.1032	38802	477	0.735	1.00	4.3	1.3	I	

C.1.2 MACHO*05:36:48.7−69:17:00 V_J filter, image subtraction photometry

Table C.2: MACHO*05:36:48.7−69:17:00 V_J filter, image subtraction photometry.

Image name	UTC	Mean date HJD−2400000.0	Orbital phase	Flux difference	δ Flux difference	Norm. light	Quality factor	Seeing (arc sec)	Airmass (χ)	LC analysis	Comment
pf1295031	26-Apr-1999	51294.9547	0.6232	−13602	1133	1.021	0.82	4.5	1.7	I	
pf1295032	26-Apr-1999	51294.9662	0.6262	−14098	1093	1.022	0.80	3.9	1.8	I	
pf1295039	26-Apr-1999	51295.0731	0.6540	−14170	860	1.022	0.87	3.8	2.3	I	
pf1295045	26-Apr-1999	51295.1517	0.6744	−9523	311	1.015	0.53	3.1	2.5	I	
pf1295052	26-Apr-1999	51295.2526	0.7005	−15473	754	1.024	0.88	3.3	2.3	I	
pf1313007	13-May-1999	51313.0793	0.3266	−31518	631	1.048	0.72	4.4	2.5	I	
pf1313008	13-May-1999	51313.0871	0.3286	−29332	1219	1.045	0.65	6.2	2.5	I	
pf1313009	13-May-1999	51313.0949	0.3307	−26685	1267	1.041	0.84	5.6	2.5	I	
pf1313010	13-May-1999	51313.1024	0.3326	−24522	1229	1.038	0.90	5.8	2.5	I	
pf1313011	13-May-1999	51313.1103	0.3347	−22714	917	1.035	0.72	5.1	2.5	I	
pf1313012	13-May-1999	51313.1170	0.3364	−31158	1155	1.048	0.45	6.6	2.5	I	
pf1313013	13-May-1999	51313.1281	0.3393	−24710	1132	1.038	0.58	6.5	2.5	I	
pf1313015	13-May-1999	51313.1359	0.3413	−33559	648	1.051	0.76	4.7	2.5	I	
pf1313016	13-May-1999	51313.1432	0.3432	−23795	505	1.036	0.27	5.1	2.5	I	
pf1314006	14-May-1999	51313.8179	0.5183	145330	1212	0.777	0.94	6.6	1.4	I	
pf1314007	14-May-1999	51313.8546	0.5278	87745	1098	0.866	0.97	6.0	1.5	I	
pf1314008	14-May-1999	51313.8637	0.5302	88861	1059	0.864	0.94	6.4	1.5	I	
pf1314009	14-May-1999	51313.8706	0.5319	70636	1380	0.892	0.96	5.9	1.6	I	
pf1314010	14-May-1999	51313.8774	0.5337	59130	826	0.909	0.96	4.9	1.6	I	
pf1314011	14-May-1999	51313.8844	0.5355	45587	1393	0.930	0.88	6.4	1.6	I	
pf1314012	14-May-1999	51313.8912	0.5373	29648	1734	0.954	0.77	6.6	1.6	X	
pf1314013	14-May-1999	51313.8982	0.5391	33844	1560	0.948	0.91	6.2	1.6	X	
pf1314014	14-May-1999	51313.9049	0.5408	11125	1566	0.982	0.36	7.2	1.7	X	
pf1314015	14-May-1999	51313.9119	0.5427	6987	1608	0.989	0.26	6.9	1.7	X	
pf1314016	14-May-1999	51313.9188	0.5445	−4094	1323	1.006	0.16	6.5	1.7	X	
pf1314017	14-May-1999	51313.9256	0.5462	−15901	1637	1.024	0.63	6.9	1.8	X	

continued on next page

Table C.2: *continued*: MACHO*05:36:48.7−69:17:00 V_J filter, image subtraction photometry

Image name	UTC	Mean date HJD−2400000.0	Orbital phase	Flux difference	δ Flux difference	Norm. light	Quality factor	Seeing (arc sec)	Airmass (χ)	LC analysis	Comment
pf1314018	14-May-1999	51313.9325	0.5480	17	1721	1.000	0.01	6.6	1.8	X	
pf1314019	14-May-1999	51313.9394	0.5498	−22071	1942	1.033	0.64	7.6	1.8	X	
pf1314020	14-May-1999	51313.9462	0.5516	−10055	1770	1.015	0.37	7.2	1.9	X	
pf1314021	14-May-1999	51313.9532	0.5534	−14964	1977	1.023	0.54	7.0	1.9	X	
pf1314022	14-May-1999	51313.9644	0.5563	−17077	1912	1.026	0.44	7.7	1.9	X	
pf1314023	14-May-1999	51313.9711	0.5580	−22723	1957	1.034	0.80	6.9	2.0	X	
pf1314024	14-May-1999	51313.9778	0.5598	−16257	1975	1.024	0.58	6.9	2.0	X	
pf1314025	14-May-1999	51313.9886	0.5626	−19451	2026	1.029	0.66	7.0	2.1	X	
pf1314026	14-May-1999	51313.9952	0.5643	−31354	2111	1.048	0.68	7.4	2.1	X	
pf1314027	14-May-1999	51314.0019	0.5660	−23913	1958	1.036	0.55	7.6	2.1	X	
pf1314028	14-May-1999	51314.0101	0.5681	−17880	1923	1.027	0.38	7.9	2.2	X	
pf1314029	14-May-1999	51314.0170	0.5699	−17530	1661	1.026	0.44	7.6	2.2	X	
pf1314030	14-May-1999	51314.0239	0.5717	−18666	1522	1.028	0.41	7.8	2.2	X	
pf1314031	14-May-1999	51314.0341	0.5744	−12241	1828	1.018	0.42	7.7	2.3	X	
pf1314032	14-May-1999	51314.0422	0.5765	−10706	1898	1.016	0.38	7.6	2.3	X	
pf1314033	14-May-1999	51314.0543	0.5796	−10348	1885	1.015	0.30	7.9	2.4	X	
pf1314034	14-May-1999	51314.0629	0.5818	−1472	1730	1.002	0.06	8.0	2.4	X	
pf1314035	14-May-1999	51314.0702	0.5837	−10777	1266	1.016	0.34	8.0	2.4	X	
pf1314037	14-May-1999	51314.0874	0.5882	−5963	1526	1.009	0.22	7.8	2.4	X	
pf1314038	14-May-1999	51314.0998	0.5914	−12550	1756	1.019	0.24	7.9	2.5	X	
pf1314039	14-May-1999	51314.1066	0.5932	−2698	1566	1.004	0.07	8.2	2.5	X	
pf1314040	14-May-1999	51314.1144	0.5952	−25374	1996	1.038	0.48	7.9	2.5	X	
pf1314041	14-May-1999	51314.1223	0.5973	−7621	1494	1.011	0.27	8.0	2.5	X	
pf1314042	14-May-1999	51314.1320	0.5998	−30141	1851	1.046	0.26	8.1	2.5	X	
pf1314043	14-May-1999	51314.1405	0.6020	−3743	1107	1.005	0.17	7.9	2.4	X	
pf1314044	14-May-1999	51314.1477	0.6038	−16643	1593	1.025	0.29	8.2	2.4	X	
pf1314045	14-May-1999	51314.1646	0.6082	−23671	2033	1.036	0.35	8.1	2.4	X	
pf1314046	14-May-1999	51314.1713	0.6100	−4617	1309	1.007	0.13	8.3	2.4	X	

continued on next page

Table C.2: *continued*: MACHO*05:36:48.7−69:17:00 V_J filter, image subtraction photometry

Image name	UTC	Mean date HJD−2400000.0	Orbital phase	Flux difference	δ Flux difference	Norm. light	Quality factor	Seeing (arc sec)	Airmass (χ)	LC analysis	Comment
pf1314047	14-May-1999	51314.1781	0.6117	−11277	1850	1.017	0.30	7.8	2.3	X	
pf1314048	14-May-1999	51314.1861	0.6138	−9190	1866	1.014	0.26	7.8	2.3	X	
pf1314049	14-May-1999	51314.1952	0.6162	−23194	1902	1.035	0.59	7.5	2.3	X	
pf1314050	14-May-1999	51314.2022	0.6180	−15543	1764	1.023	0.39	7.8	2.2	X	
pf1314051	14-May-1999	51314.2119	0.6205	−12453	1984	1.019	0.45	7.6	2.2	X	
pf1314052	14-May-1999	51314.2188	0.6223	−19063	2003	1.029	0.65	7.4	2.2	X	
pf1314053	14-May-1999	51314.2255	0.6240	−25905	1828	1.039	0.64	7.3	2.1	X	
pf1314054	14-May-1999	51314.2322	0.6258	−17991	1876	1.027	0.48	7.5	2.1	X	
pf1314055	14-May-1999	51314.2390	0.6275	−20480	2056	1.031	0.45	7.7	2.1	X	
pf1314056	14-May-1999	51314.2522	0.6310	−22189	1935	1.034	0.58	7.6	2.0	X	
pf1314057	14-May-1999	51314.2588	0.6327	−16596	1997	1.025	0.63	7.1	2.0	X	
pf1314058	14-May-1999	51314.2657	0.6345	−24208	2155	1.037	0.56	7.4	1.9	X	
pf1314059	14-May-1999	51314.2755	0.6370	−11666	2664	1.017	0.41	7.5	1.9	X	
pf1314060	14-May-1999	51314.2848	0.6394	−11803	4580	1.018	0.17	7.6	1.8	X	
pf1215007	15-May-1999	51315.0997	0.8509	−22643	2109	1.034	0.60	7.3	2.5	X	CE
pf1215008	15-May-1999	51315.1072	0.8528	−24960	1979	1.038	0.79	6.9	2.5	X	CE
pf1215009	15-May-1999	51315.1140	0.8546	−9221	1883	1.014	0.49	6.7	2.5	X	CE
pf1215010	15-May-1999	51315.1207	0.8563	−27901	1878	1.042	0.87	6.6	2.5	X	CE
pf1215011	15-May-1999	51315.1284	0.8583	−23417	1810	1.035	0.85	6.5	2.5	X	CE
pf1215012	15-May-1999	51315.1350	0.8601	−20048	1983	1.030	0.76	7.0	2.5	X	CE
pf1215013	15-May-1999	51315.1420	0.8619	−31699	1906	1.048	0.84	6.8	2.4	X	CE
pf1215014	15-May-1999	51315.1486	0.8636	−25028	1974	1.038	0.80	6.8	2.3	X	CE
pf1215015	15-May-1999	51315.1555	0.8654	−29238	2078	1.044	0.68	7.1	2.3	X	CE
pf1215016	15-May-1999	51315.1694	0.8690	−29364	1987	1.045	0.74	7.1	2.3	X	CE
pf1215017	15-May-1999	51315.1800	0.8717	−17507	1923	1.026	0.77	6.9	2.3	X	CE
pf1215018	15-May-1999	51315.1884	0.8739	−29139	1943	1.044	0.77	6.8	2.3	X	CE
pf1215019	15-May-1999	51315.1949	0.8756	−18809	1828	1.028	0.71	6.7	2.3	X	CE
pf1215020	15-May-1999	51315.2020	0.8774	−25556	1785	1.039	0.84	6.5	2.2	X	CE

continued on next page

Table C.2: *continued*: MACHO*05:36:48.7−69:17:00 V_J filter, image subtraction photometry

Image name	UTC	Mean date HJD−2400000.0	Orbital phase	Flux difference	δ Flux difference	Norm. light	Quality factor	Seeing (arc sec)	Airmass (χ)	LC analysis	Comment
pf1215021	15-May-1999	51315.2086	0.8792	−19615	1788	1.030	0.80	6.5	2.2	X	CE
pf1215022	15-May-1999	51315.2152	0.8809	−19335	1657	1.029	0.82	6.0	2.2	X	CE
pf1215023	15-May-1999	51315.2221	0.8827	−19153	1647	1.029	0.81	6.1	2.1	X	CE
pf1215024	15-May-1999	51315.2288	0.8844	−21305	1702	1.032	0.77	6.3	2.1	X	CE
pf1215025	15-May-1999	51315.2368	0.8865	−20664	1450	1.031	0.86	5.5	2.1	X	CE
pf1215026	15-May-1999	51315.2649	0.8938	−5728	733	1.008	0.10	5.5	2.0	X	CE
pf1315036	16-May-1999	51315.7631	0.0231	−13106	1454	1.020	0.90	3.5	1.3	I	
pf1315037	16-May-1999	51315.7695	0.0247	−12613	1017	1.019	0.86	3.3	1.3	I	
pf1315038	16-May-1999	51315.7750	0.0262	−15925	797	1.024	0.90	3.2	1.3	I	
pf1315039	16-May-1999	51315.7800	0.0274	−11933	784	1.018	0.85	3.3	1.3	I	
pf1315040	16-May-1999	51315.7870	0.0293	−13751	884	1.021	0.91	3.7	1.3	I	
pf1315041	16-May-1999	51315.7940	0.0311	−12778	899	1.020	0.90	3.6	1.3	I	
pf1315042	16-May-1999	51315.7992	0.0324	−11061	991	1.017	0.58	4.5	1.4	I	
pf1315043	16-May-1999	51315.8048	0.0339	−13206	1107	1.020	0.81	4.3	1.4	I	
pf1315044	16-May-1999	51315.8106	0.0354	−12009	1121	1.018	0.76	4.4	1.4	I	
pf1315045	16-May-1999	51315.8178	0.0373	−13261	1045	1.020	0.76	4.0	1.4	I	
pf1315046	16-May-1999	51315.8283	0.0400	−18035	1039	1.028	0.90	4.0	1.4	I	
pf1315047	16-May-1999	51315.8340	0.0414	−13030	1018	1.020	0.82	4.0	1.4	I	
pf1315048	16-May-1999	51315.8412	0.0433	−16532	970	1.025	0.93	3.7	1.5	I	
pf1315049	16-May-1999	51315.8467	0.0448	−14441	1047	1.022	0.82	4.1	1.5	I	
pf1315050	16-May-1999	51315.8522	0.0462	−11011	903	1.017	0.84	3.9	1.5	I	
pf1315051	16-May-1999	51315.8582	0.0477	−7276	915	1.011	0.62	3.9	1.5	I	
pf1315052	16-May-1999	51315.8640	0.0492	−12670	894	1.019	0.81	3.8	1.5	I	
pf1315053	16-May-1999	51315.8695	0.0507	−11916	855	1.018	0.92	3.2	1.6	I	
pf1315054	16-May-1999	51315.8751	0.0521	−11903	848	1.018	0.87	3.6	1.6	I	
pf1315055	16-May-1999	51315.8807	0.0536	−15262	872	1.023	0.88	3.2	1.6	I	
pf1315056	16-May-1999	51315.8879	0.0554	−11316	896	1.017	0.86	4.2	1.6	I	
pf1315057	16-May-1999	51315.8944	0.0571	−8901	898	1.014	0.89	3.7	1.7	I	

continued on next page

Table C.2: *continued*: MACHO*05:36:48.7−69:17:00 V_J filter, image subtraction photometry

Image name	UTC	Mean date HJD−2400000.0	Orbital phase	Flux difference	δ Flux difference	Norm. light	Quality factor	Seeing (arc sec)	Airmass (χ)	LC analysis	Comment
pf1315058	16-May-1999	51315.8998	0.0585	−11672	868	1.018	0.77	3.7	1.7	I	
pf1315059	16-May-1999	51315.9054	0.0600	−11968	875	1.018	0.88	3.6	1.7	I	
pf1315060	16-May-1999	51315.9123	0.0618	−14359	847	1.022	0.90	3.8	1.8	I	
pf1315061	16-May-1999	51315.9200	0.0638	−10845	873	1.017	0.83	3.5	1.8	I	
pf1315062	16-May-1999	51315.9263	0.0654	−4204	898	1.006	0.53	4.0	1.8	I	
pf1315063	16-May-1999	51315.9378	0.0684	4120	962	0.994	0.44	3.9	1.9	I	
pf1315064	16-May-1999	51315.9434	0.0699	7253	958	0.989	0.70	4.0	1.9	I	
pf1315065	16-May-1999	51315.9524	0.0722	17528	983	0.973	0.87	4.0	2.0	I	
pf1315066	16-May-1999	51315.9580	0.0736	20199	963	0.969	0.87	3.9	2.0	I	
pf1315067	16-May-1999	51315.9636	0.0751	28728	987	0.956	0.94	4.1	2.0	I	
pf1315068	16-May-1999	51315.9693	0.0766	34507	924	0.947	0.97	4.3	2.0	I	
pf1315069	16-May-1999	51315.9748	0.0780	37410	848	0.943	0.99	3.5	2.1	I	
pf1315070	16-May-1999	51315.9819	0.0798	45385	839	0.930	0.97	4.1	2.1	I	
pf1315071	16-May-1999	51315.9873	0.0812	53711	824	0.918	0.99	4.1	2.1	I	
pf1315072	16-May-1999	51315.9927	0.0826	59271	828	0.909	0.99	4.2	2.2	I	
pf1315073	16-May-1999	51315.9982	0.0841	67841	832	0.896	0.99	3.5	2.2	I	
pf1316001	16-May-1999	51316.0037	0.0855	76459	795	0.883	1.00	3.2	2.2	I	CE
pf1316002	16-May-1999	51316.0093	0.0870	80820	808	0.876	1.00	3.7	2.2	I	CE
pf1316003	16-May-1999	51316.0182	0.0893	90734	839	0.861	1.00	3.6	2.3	I	CE
pf1316004	16-May-1999	51316.0238	0.0907	104378	822	0.840	1.00	3.6	2.3	I	CE
pf1316005	16-May-1999	51316.0298	0.0923	110020	790	0.832	1.00	3.8	2.3	I	CE
pf1316006	16-May-1999	51316.0365	0.0940	120270	878	0.816	1.00	4.0	2.4	I	CE
pf1316007	16-May-1999	51316.0427	0.0956	126207	873	0.807	1.00	4.0	2.4	I	CE
pf1316008	16-May-1999	51316.0488	0.0972	136169	883	0.791	1.00	4.4	2.4	I	CE
pf1316009	16-May-1999	51316.0543	0.0986	145262	919	0.778	1.00	4.3	2.4	I	CE
pf1316010	16-May-1999	51316.0600	0.1001	152391	920	0.767	1.00	4.3	2.4	I	CE
pf1316011	16-May-1999	51316.0655	0.1015	163012	913	0.750	1.00	4.4	2.5	I	CE
pf1316012	16-May-1999	51316.0717	0.1032	169216	933	0.741	1.00	4.4	2.5	I	CE

continued on next page

Table C.2: *continued*: MACHO*05:36:48.7−69:17:00 V_J filter, image subtraction photometry

Image name	UTC	Mean date HJD−2400000.0	Orbital phase	Flux difference	δ Flux difference	Norm. light	Quality factor	Seeing (arc sec)	Airmass (χ)	LC analysis	Comment
pf1316013	16-May-1999	51316.0777	0.1047	178393	994	0.727	1.00	4.8	2.5	I	CE
pf1316014	16-May-1999	51316.0839	0.1063	186382	1168	0.715	0.98	5.4	2.5	I	CE
pf1316015	16-May-1999	51316.0897	0.1078	196871	1020	0.698	0.99	4.8	2.5	I	CE
pf1316016	16-May-1999	51316.0986	0.1101	199357	1138	0.695	0.99	5.4	2.5	I	CE
pf1316017	16-May-1999	51316.1058	0.1120	210394	998	0.678	0.99	4.8	2.5	I	CE
pf1316018	16-May-1999	51316.1136	0.1140	212764	1246	0.674	0.96	5.8	2.5	I	CE
pf1316019	16-May-1999	51316.1195	0.1156	230949	1402	0.646	0.95	6.4	2.5	I	CE
pf1316020	16-May-1999	51316.1263	0.1173	221290	1278	0.661	0.97	6.0	2.5	I	CE
pf1316021	16-May-1999	51316.1331	0.1191	225882	1334	0.654	0.96	6.3	2.5	I	CE
pf1316022	16-May-1999	51316.1427	0.1216	222520	1557	0.659	0.90	6.9	2.5	I	CE
pf1316023	16-May-1999	51316.1484	0.1230	229458	1341	0.649	0.97	6.4	2.5	I	CE
pf1316024	16-May-1999	51316.1539	0.1245	224048	1306	0.657	0.98	6.4	2.5	I	CE
pf1316025	16-May-1999	51316.1798	0.1312	208611	1245	0.681	0.99	6.0	2.4	I	CE
pf1316026	16-May-1999	51316.1932	0.1347	195615	1334	0.700	0.98	6.2	2.3	I	CE
pf1316027	16-May-1999	51316.2009	0.1367	181498	1293	0.722	0.99	6.1	2.3	I	CE
pf1316028	16-May-1999	51316.2087	0.1387	176443	1337	0.730	0.97	6.1	2.2	I	CE
pf1316029	16-May-1999	51316.2142	0.1401	165173	1268	0.747	0.99	5.8	2.2	I	CE
pf1316030	16-May-1999	51316.2206	0.1418	149907	1383	0.770	0.96	6.2	2.2	I	CE
pf1316031	16-May-1999	51316.2266	0.1433	149717	1352	0.771	0.99	6.1	2.1	I	CE
pf1316032	16-May-1999	51316.2320	0.1448	142188	1340	0.782	0.99	6.1	2.1	I	CE
pf1316033	16-May-1999	51316.2375	0.1462	126086	1338	0.807	0.98	6.0	2.1	I	CE
pf1316034	16-May-1999	51316.2430	0.1476	126967	1348	0.806	0.96	5.9	2.1	I	CE
pf1316035	16-May-1999	51316.2520	0.1499	113145	1339	0.827	0.98	6.0	2.0	I	CE
pf1316036	16-May-1999	51316.2588	0.1517	104679	891	0.840	1.00	3.9	2.0	I	CE
pf1316037	16-May-1999	51316.2643	0.1531	96357	942	0.852	0.99	4.1	2.0	I	CE
pf1316038	16-May-1999	51316.2698	0.1545	91054	890	0.861	1.00	3.6	1.9	I	CE
pf1316039	16-May-1999	51316.2753	0.1560	80815	1091	0.876	0.99	4.0	1.9	I	CE
pf1316040	16-May-1999	51316.2811	0.1575	73743	1442	0.887	0.98	4.1	1.9	I	CE

continued on next page

Table C.2: *continued*: MACHO*05:36:48.7−69:17:00 V_J filter, image subtraction photometry

Image name	UTC	Mean date HJD−2400000.0	Orbital phase	Flux difference	δ Flux difference	Norm. light	Quality factor	Seeing (arc sec)	Airmass (χ)	LC analysis	Comment
pf1404025	13-Aug-1999	51404.1705	0.9650	−12778	1306	1.020	0.83	4.1	1.4	I	
pf1404031	13-Aug-1999	51404.2770	0.9926	−12462	1291	1.019	0.79	3.4	1.2	I	
pf1405016	14-Aug-1999	51404.7977	0.1278	214130	842	0.672	1.00	3.4	2.4	I	
pf1405017	14-Aug-1999	51404.8046	0.1295	205895	697	0.685	1.00	3.5	2.4	I	
pf1405021	14-Aug-1999	51404.8657	0.1454	135626	605	0.792	0.99	3.8	2.5	I	
pf1405022	14-Aug-1999	51404.8711	0.1468	132485	580	0.797	0.99	3.8	2.5	I	
pf1405023	14-Aug-1999	51404.8767	0.1483	128142	621	0.804	0.99	4.5	2.5	I	
pf1405025	14-Aug-1999	51404.8927	0.1524	83083	783	0.873	0.81	5.6	2.5	I	
pf1405026	14-Aug-1999	51404.9071	0.1561	81458	805	0.875	0.77	5.9	2.5	I	
pf1405027	14-Aug-1999	51404.9132	0.1577	63917	877	0.902	0.90	5.3	2.4	I	
pf1405028	14-Aug-1999	51404.9191	0.1593	72190	855	0.889	0.91	5.4	2.4	I	
pf1405029	14-Aug-1999	51404.9338	0.1631	45283	784	0.931	0.81	5.6	2.4	I	
pf1405030	14-Aug-1999	51404.9401	0.1647	8692	704	0.986	0.12	5.9	2.3	X	
pf1405031	14-Aug-1999	51404.9467	0.1664	40176	974	0.938	0.95	5.6	2.3	I	
pf1405032	14-Aug-1999	51404.9525	0.1679	25782	942	0.961	0.68	6.1	2.3	I	
pf1405033	14-Aug-1999	51404.9587	0.1695	16239	914	0.975	0.56	5.7	2.3	I	
pf1405035	14-Aug-1999	51404.9708	0.1727	16529	693	0.975	0.61	4.5	2.2	I	
pf1405036	14-Aug-1999	51404.9769	0.1742	6100	537	0.991	0.33	3.6	2.2	I	
pf1405041	14-Aug-1999	51405.0357	0.1895	−3746	673	1.006	0.29	3.6	1.9	I	
pf1405042	14-Aug-1999	51405.0417	0.1911	−9469	702	1.015	0.57	4.1	1.9	I	
pf1405043	14-Aug-1999	51405.0473	0.1925	−14761	466	1.023	0.44	3.8	1.8	I	
pf1405047	14-Aug-1999	51405.1141	0.2099	−17217	637	1.026	0.36	5.3	1.5	I	
pf1405048	14-Aug-1999	51405.1247	0.2126	−25992	714	1.039	0.59	5.1	1.5	X	
pf1405049	14-Aug-1999	51405.1365	0.2157	−6527	509	1.010	0.13	4.8	1.5	I	
pf1405052	14-Aug-1999	51405.1708	0.2246	−11091	999	1.017	0.76	4.3	1.4	I	
pf1405053	14-Aug-1999	51405.1772	0.2262	−11915	831	1.018	0.61	4.4	1.3	I	
pf1405054	14-Aug-1999	51405.1862	0.2286	−1306	916	1.002	0.04	5.5	1.3	X	
pf1405055	14-Aug-1999	51405.1920	0.2301	−18313	1060	1.028	0.72	5.5	1.3	I	

continued on next page

Table C.2: *continued*: MACHO*05:36:48.7−69:17:00 V_J filter, image subtraction photometry

Image name	UTC	Mean date HJD−2400000.0	Orbital phase	Flux difference	δ Flux difference	Norm. light	Quality factor	Seeing (arc sec)	Airmass (χ)	LC analysis	Comment
pf1406029	15-Aug-1999	51406.0272	0.4468	−6982	432	1.011	0.28	3.7	1.9	I	
pf1406030	15-Aug-1999	51406.0329	0.4483	−4313	423	1.007	0.15	3.6	1.9	I	
pf1406031	15-Aug-1999	51406.0397	0.4500	57	424	1.000	0.01	3.8	1.9	I	
pf1406032	15-Aug-1999	51406.0641	0.4564	23196	825	0.964	0.91	3.8	1.7	I	
pf1406033	15-Aug-1999	51406.0696	0.4578	29348	523	0.955	0.94	3.1	1.7	I	
pf1406034	15-Aug-1999	51406.0750	0.4592	38454	846	0.941	0.98	3.5	1.7	I	
pf1406035	15-Aug-1999	51406.0805	0.4606	44573	836	0.932	0.99	3.3	1.7	I	
pf1406036	15-Aug-1999	51406.0860	0.4621	50838	840	0.922	0.98	3.4	1.6	I	
pf1406040	15-Aug-1999	51406.1312	0.4738	117484	815	0.820	0.99	4.2	1.5	I	
pf1406041	15-Aug-1999	51406.1435	0.4770	131985	801	0.798	1.00	3.5	1.4	I	
pf1406049	15-Aug-1999	51406.2462	0.5036	198840	670	0.695	1.00	2.5	1.2	I	
pf1407006	16-Aug-1999	51407.0280	0.7065	−20548	1155	1.031	0.83	4.8	1.9	I	
pf1407007	16-Aug-1999	51407.0342	0.7081	−9941	966	1.015	0.58	4.9	1.9	I	
pf1407008	16-Aug-1999	51407.0397	0.7095	2745	651	0.995	0.05	5.0	1.8	X	
pf1407009	16-Aug-1999	51407.0455	0.7111	−12013	971	1.018	0.65	4.7	1.8	I	
pf1407010	16-Aug-1999	51407.0511	0.7125	−14248	1069	1.022	0.72	5.1	1.8	I	
pf1407011	16-Aug-1999	51407.0731	0.7182	−9734	1368	1.015	0.54	5.7	1.7	I	
pf1407012	16-Aug-1999	51407.0948	0.7239	−12337	931	1.019	0.65	5.0	1.6	I	
pf1407013	16-Aug-1999	51407.1004	0.7253	−11961	1322	1.018	0.67	5.5	1.6	I	
pf1490007	07-Nov-1999	51489.9585	0.2272	−8805	343	1.013	0.27	5.0	1.3	I	
pf1490008	07-Nov-1999	51489.9630	0.2283	−14513	1333	1.022	0.88	4.6	1.3	I	
pf1490009	07-Nov-1999	51489.9698	0.2301	−11594	1304	1.018	0.75	4.5	1.3	I	
pf1490010	07-Nov-1999	51489.9840	0.2338	−15513	1360	1.024	0.89	4.7	1.2	I	
pf1490011	07-Nov-1999	51489.9946	0.2365	−12205	1368	1.019	0.78	4.8	1.2	I	
pf1490012	07-Nov-1999	51490.0014	0.2383	−14185	1322	1.022	0.89	4.6	1.2	I	
pf1490013	07-Nov-1999	51490.0146	0.2417	−11278	1353	1.017	0.76	4.7	1.2	I	
pf1490014	07-Nov-1999	51490.0226	0.2438	−16193	1302	1.025	0.90	4.5	1.2	I	
pf1490015	07-Nov-1999	51490.0301	0.2458	−13730	1355	1.021	0.77	5.0	1.2	I	

continued on next page

Table C.2: *continued*: MACHO*05:36:48.7−69:17:00 V_J filter, image subtraction photometry

Image name	UTC	Mean date HJD−2400000.0	Orbital phase	Flux difference	δ Flux difference	Norm. light	Quality factor	Seeing (arc sec)	Airmass (χ)	LC analysis	Comment
pf1490016	07-Nov-1999	51490.0391	0.2481	−17855	1296	1.027	0.91	4.8	1.2	I	
pf1490017	07-Nov-1999	51490.0469	0.2501	−18086	1294	1.028	0.85	4.7	1.1	I	
pf1490018	07-Nov-1999	51490.0543	0.2520	−19596	1111	1.030	0.91	4.8	1.1	I	
pf1490019	07-Nov-1999	51490.0621	0.2540	−20751	795	1.032	0.71	4.7	1.1	I	
pf1490020	07-Nov-1999	51490.0715	0.2565	−14960	876	1.023	0.67	4.7	1.1	I	
pf1490021	07-Nov-1999	51490.0795	0.2586	−15930	728	1.024	0.57	4.7	1.1	I	
pf1490022	07-Nov-1999	51490.0862	0.2603	−18641	1034	1.029	0.83	4.3	1.1	I	
pf1490023	07-Nov-1999	51490.0929	0.2620	−18455	1256	1.028	0.92	4.3	1.1	I	
pf1490024	07-Nov-1999	51490.0997	0.2638	−19094	1225	1.029	0.79	5.6	1.1	I	
pf1490025	07-Nov-1999	51490.1069	0.2657	−28046	1189	1.043	0.96	4.6	1.1	I	
pf1490026	07-Nov-1999	51490.1164	0.2682	−23175	1373	1.035	0.93	5.0	1.1	I	
pf1490027	07-Nov-1999	51490.1230	0.2699	−20472	1271	1.031	0.89	4.7	1.1	I	
pf1490028	07-Nov-1999	51490.1296	0.2716	−24948	1317	1.038	0.93	4.8	1.1	I	
pf1490029	07-Nov-1999	51490.1370	0.2735	−23611	1317	1.036	0.96	4.4	1.1	I	
pf1490030	07-Nov-1999	51490.1664	0.2811	−21498	1896	1.033	0.85	5.0	1.1	I	
pf1491007	08-Nov-1999	51490.9271	0.4785	136514	1458	0.791	0.98	5.5	1.4	I	
pf1491008	08-Nov-1999	51490.9345	0.4804	152651	1436	0.766	0.98	5.3	1.4	I	
pf1491009	08-Nov-1999	51490.9418	0.4823	160538	1350	0.754	0.99	5.2	1.3	I	
pf1491010	08-Nov-1999	51490.9486	0.4841	165624	1235	0.746	1.00	4.8	1.3	I	
pf1491011	08-Nov-1999	51490.9565	0.4861	178646	1242	0.726	1.00	4.9	1.3	I	
pf1491012	08-Nov-1999	51490.9631	0.4879	181109	1294	0.723	1.00	5.2	1.3	I	
pf1491013	08-Nov-1999	51490.9789	0.4920	196297	1176	0.699	1.00	4.8	1.2	I	
pf1491014	08-Nov-1999	51490.9867	0.4940	202507	942	0.690	1.00	4.2	1.2	I	
pf1491015	08-Nov-1999	51490.9936	0.4958	209683	1357	0.678	0.99	5.4	1.2	I	
pf1491016	08-Nov-1999	51491.0015	0.4978	209148	1330	0.680	0.99	5.3	1.2	I	
pf1491017	08-Nov-1999	51491.0110	0.5003	210357	1426	0.678	0.98	5.6	1.2	I	
pf1491018	08-Nov-1999	51491.0189	0.5024	211162	1285	0.677	0.98	5.5	1.2	I	
pf1491019	08-Nov-1999	51491.0264	0.5043	205838	1084	0.685	0.99	5.2	1.2	I	

continued on next page

Table C.2: *continued*: MACHO*05:36:48.7−69:17:00 V_J filter, image subtraction photometry

Image name	UTC	Mean date HJD−2400000.0	Orbital phase	Flux difference	δ Flux difference	Norm. light	Quality factor	Seeing (arc sec)	Airmass (χ)	LC analysis	Comment
pf1491020	08-Nov-1999	51491.0331	0.5060	203619	1151	0.688	0.98	5.7	1.2	I	
pf1491021	08-Nov-1999	51491.0396	0.5077	161754	570	0.751	0.89	5.1	1.2	X	
pf1491022	08-Nov-1999	51491.0482	0.5100	188197	542	0.712	0.96	4.8	1.1	I	
pf1491023	08-Nov-1999	51491.0581	0.5125	170598	774	0.739	0.98	5.2	1.1	I	
pf1491024	08-Nov-1999	51491.0650	0.5143	164064	854	0.749	0.93	5.6	1.1	I	
pf1491025	08-Nov-1999	51491.0732	0.5164	156254	1198	0.761	0.98	5.6	1.1	I	
pf1491026	08-Nov-1999	51491.0797	0.5181	146577	1151	0.776	0.99	5.6	1.1	I	
pf1491027	08-Nov-1999	51491.0863	0.5198	131995	728	0.798	0.99	4.6	1.1	I	
pf1491028	08-Nov-1999	51491.0932	0.5216	134381	578	0.794	0.96	4.6	1.1	I	
pf1491029	08-Nov-1999	51491.1009	0.5236	96832	549	0.852	0.93	4.4	1.1	I	
pf1491030	08-Nov-1999	51491.1163	0.5276	91952	1162	0.859	0.99	4.5	1.1	I	
pf1491031	08-Nov-1999	51491.1236	0.5295	81156	1148	0.876	1.00	4.0	1.1	I	
pf1491032	08-Nov-1999	51491.1304	0.5313	75743	1149	0.884	1.00	4.4	1.1	I	
pf1491033	08-Nov-1999	51491.1371	0.5330	60204	885	0.908	0.99	3.9	1.1	I	
pf1491034	08-Nov-1999	51491.1437	0.5347	53334	1168	0.918	0.99	4.2	1.1	I	
pf1491035	08-Nov-1999	51491.1504	0.5365	42505	1068	0.935	0.98	3.8	1.1	I	
pf1491036	08-Nov-1999	51491.1578	0.5384	37794	1337	0.942	0.95	4.6	1.1	I	
pf1491037	08-Nov-1999	51491.1644	0.5401	30837	1299	0.953	0.96	4.0	1.1	I	
pf1491038	08-Nov-1999	51491.1709	0.5418	20101	1748	0.969	0.87	4.2	1.1	I	
pf1558015	14-Jan-2000	51558.0155	0.8881	−12236	1466	1.019	0.87	4.0	1.1	I	
pf1558018	14-Jan-2000	51558.0563	0.8987	−13534	1791	1.021	0.78	5.4	1.2	I	
pf1558021	14-Jan-2000	51558.1047	0.9113	−10453	2375	1.016	0.66	6.5	1.3	I	
pf1559015	15-Jan-2000	51558.9488	0.1303	204637	1448	0.687	0.99	4.5	1.1	I	
pf1559018	15-Jan-2000	51558.9943	0.1421	152862	1307	0.766	0.99	3.4	1.1	I	
pf1559020	15-Jan-2000	51559.0294	0.1512	104673	989	0.840	0.99	4.1	1.1	I	
pf1561015	17-Jan-2000	51561.0298	0.6703	−14449	1532	1.022	0.86	3.8	1.2	I	
pf1561018	17-Jan-2000	51561.0693	0.6806	−20047	1373	1.031	0.95	3.6	1.2	I	
pf1561020	17-Jan-2000	51561.0975	0.6879	−15193	1138	1.023	0.89	4.8	1.3	I	

continued on next page

Table C.2: *continued*: MACHO*05:36:48.7−69:17:00 V_J filter, image subtraction photometry

Image name	UTC	Mean date HJD−2400000.0	Orbital phase	Flux difference	δ Flux difference	Norm. light	Quality factor	Seeing (arc sec)	Airmass (χ)	LC analysis	Comment
pf1561021	17-Jan-2000	51561.1067	0.6903	−17358	1027	1.026	0.84	7.3	1.3	X	
pf1561022	17-Jan-2000	51561.1160	0.6927	−19034	872	1.029	0.70	5.7	1.3	I	
pf1561023	17-Jan-2000	51561.1248	0.6950	−11681	620	1.018	0.31	4.6	1.3	I	
pf1725027	29-Jun-2000	51724.9552	0.2094	−17724	2288	1.027	0.78	7.3	1.7	X	
pf1725033	29-Jun-2000	51725.0468	0.2331	−17867	2511	1.027	0.52	7.4	1.8	X	
pf1725040	29-Jun-2000	51725.1512	0.2602	−18002	1832	1.028	0.85	5.6	1.9	I	
pf1727028	01-Jul-2000	51726.8988	0.7137	−14712	1018	1.023	0.90	3.5	2.3	I	
pf1727038	01-Jul-2000	51727.0608	0.7558	−14840	1068	1.023	0.83	2.8	2.3	I	
pf1727044	01-Jul-2000	51727.1348	0.7750	−15647	1050	1.024	0.84	2.5	2.0	I	
pf1727050	01-Jul-2000	51727.2146	0.7957	−15614	1101	1.024	0.89	2.6	1.6	I	
pf1727056	01-Jul-2000	51727.2919	0.8157	−12568	1622	1.019	0.84	4.0	1.3	I	
pf1730026	04-Jul-2000	51729.8444	0.4781	126936	1373	0.806	1.00	4.4	2.1	I	
pf1730033	04-Jul-2000	51729.9643	0.5092	192307	1294	0.705	0.99	4.4	2.5	I	
pf1730039	04-Jul-2000	51730.0437	0.5298	87190	1355	0.866	0.99	4.5	2.4	I	
pf1730044	04-Jul-2000	51730.1062	0.5461	9570	1168	0.985	0.78	3.2	2.1	I	
pf1730050	04-Jul-2000	51730.2119	0.5735	−13551	1434	1.021	0.82	4.2	1.6	I	
pf1730058	04-Jul-2000	51730.2850	0.5925	−13795	1573	1.021	0.86	4.4	1.3	I	
pf1731027	04-Jul-2000	51730.8658	0.7432	−17689	1100	1.027	0.85	3.0	2.2	I	
pf1731039	04-Jul-2000	51731.0604	0.7937	−16231	1148	1.025	0.92	3.2	2.3	I	
pf1957027	16-Feb-2001	51957.1862	0.4738	68515	1849	0.894	0.76	6.4	1.8	X	
pf1957028	16-Feb-2001	51957.1950	0.4761	64935	2004	0.900	0.64	6.8	1.9	X	
pf1960030	19-Feb-2001	51960.0759	0.2237	−7492	1268	1.011	0.65	3.5	1.5	I	
pf1960033	19-Feb-2001	51960.1054	0.2314	−15713	1288	1.024	0.90	3.7	1.6	I	
pf1960036	19-Feb-2001	51960.1359	0.2393	−10896	1052	1.017	0.83	3.3	1.7	I	
pf1960039	19-Feb-2001	51960.1658	0.2471	−18188	1073	1.028	0.90	3.8	1.9	I	
pf1960040	19-Feb-2001	51960.1774	0.2501	−17533	1208	1.027	0.92	4.2	1.9	I	
pf1960041	19-Feb-2001	51960.1879	0.2528	−21297	1393	1.033	0.90	4.7	2.0	I	
pf1961018	20-Feb-2001	51960.9237	0.4437	−13395	963	1.021	0.94	2.2	1.1	I	

continued on next page

Table C.2: *continued*: MACHO*05:36:48.7−69:17:00 V_J filter, image subtraction photometry

Image name	UTC	Mean date HJD−2400000.0	Orbital phase	Flux difference	δ Flux difference	Norm. light	Quality factor	Seeing (arc sec)	Airmass (χ)	LC analysis	Comment
pf1961021	20-Feb-2001	51960.9522	0.4511	−23	931	1.000	0.06	2.0	1.2	I	R,A
pf1961024	20-Feb-2001	51960.9808	0.4586	25619	943	0.961	0.98	2.2	1.2	I	
pf1961027	20-Feb-2001	51961.0100	0.4661	63294	985	0.903	1.00	2.6	1.3	I	
pf1961030	20-Feb-2001	51961.0392	0.4737	102348	1004	0.843	1.00	2.7	1.4	I	
pf1961033	20-Feb-2001	51961.0684	0.4813	144835	1058	0.778	1.00	3.4	1.4	I	
pf1961036	20-Feb-2001	51961.0966	0.4886	179732	1167	0.725	1.00	4.2	1.6	I	
pf1961038	20-Feb-2001	51961.1332	0.4981	205011	1061	0.686	1.00	3.6	1.7	I	
pf1961042	20-Feb-2001	51961.1625	0.5057	200637	1311	0.693	0.99	4.6	1.9	I	
pf1988021	19-Mar-2001	51987.9911	0.4678	46126	1677	0.929	0.81	6.7	1.6	X	
pf1989006	19-Mar-2001	51988.0586	0.4853	157568	831	0.759	1.00	2.4	1.7	I	CE
pf1989007	19-Mar-2001	51988.0707	0.4884	172223	845	0.736	1.00	2.5	1.8	I	CE
pf1989008	19-Mar-2001	51988.0819	0.4913	184283	909	0.718	1.00	2.9	1.8	I	CE
pf1989011	19-Mar-2001	51988.1213	0.5016	206028	888	0.684	1.00	2.9	2.0	I	CE
pf1989012	19-Mar-2001	51988.1307	0.5040	203570	947	0.688	1.00	3.3	2.1	I	
pf1992015	23-Mar-2001	51991.8588	0.4715	88310	1059	0.865	1.00	2.8	1.2	I	
pf1992018	23-Mar-2001	51991.8892	0.4794	133089	1176	0.796	1.00	3.4	1.2	I	
pf1992024	23-Mar-2001	51991.9536	0.4961	201538	896	0.691	1.00	2.6	1.4	I	
pf1992027	23-Mar-2001	51991.9829	0.5037	203993	943	0.688	1.00	3.0	1.4	I	
pf1992029	23-Mar-2001	51991.9966	0.5072	193991	930	0.703	1.00	2.8	1.5	I	
pf1992034	23-Mar-2001	51992.0493	0.5209	130323	995	0.800	1.00	2.7	1.7	I	
pf1992039	23-Mar-2001	51992.1081	0.5362	49329	1067	0.924	0.99	3.1	2.0	I	
pf1992041	23-Mar-2001	51992.1219	0.5397	32805	1077	0.950	0.97	3.1	2.1	I	
pf1992044	23-Mar-2001	51992.1556	0.5485	397	1159	0.999	0.02	3.4	2.2	I	
pf1992046	23-Mar-2001	51992.1693	0.5520	−10124	1024	1.016	0.68	2.6	2.3	I	
pf1992049	23-Mar-2001	51992.1976	0.5594	−13371	968	1.020	0.91	2.4	2.4	I	
pf1992051	23-Mar-2001	51992.2114	0.5630	−14883	1024	1.023	0.87	2.7	2.5	I	
pf2019017	19-Apr-2001	52018.8538	0.4767	120298	1035	0.816	1.00	4.9	1.3	I	
pf2019020	19-Apr-2001	52018.8870	0.4854	164000	1427	0.749	1.00	3.8	1.4	I	

continued on next page

Table C.2: *continued*: MACHO*05:36:48.7−69:17:00 V_J filter, image subtraction photometry

Image name	UTC	Mean date HJD−2400000.0	Orbital phase	Flux difference	δ Flux difference	Norm. light	Quality factor	Seeing (arc sec)	Airmass (χ)	LC analysis	Comment
pf2019023	19-Apr-2001	52018.9201	0.4939	198892	1024	0.695	1.00	4.8	1.5	I	
pf2019026	19-Apr-2001	52018.9518	0.5022	204516	1020	0.687	1.00	5.6	1.6	I	
pf2019029	19-Apr-2001	52018.9889	0.5118	175336	1153	0.731	1.00	5.5	1.8	I	
pf2019032	19-Apr-2001	52019.0338	0.5234	111118	1277	0.830	1.00	5.6	2.0	I	
pf2019035	19-Apr-2001	52019.0697	0.5328	67564	1444	0.897	0.99	5.2	2.2	I	
pf2019038	19-Apr-2001	52019.1031	0.5414	27806	1388	0.957	0.96	4.9	2.3	I	
pf2019041	19-Apr-2001	52019.1744	0.5599	−16470	1756	1.025	0.86	5.5	2.5	I	
pf2019044	19-Apr-2001	52019.2065	0.5683	−16465	1831	1.025	0.83	6.1	2.5	I	
pf2019048	19-Apr-2001	52019.2426	0.5776	−16166	2111	1.025	0.71	6.2	2.4	I	
pf2019050	19-Apr-2001	52019.2589	0.5819	−1709	4269	1.002	0.04	7.2	2.4	X	
pf2021017	21-Apr-2001	52020.9317	0.0160	−12209	1450	1.019	0.85	5.4	1.6	I	
pf2021020	21-Apr-2001	52020.9681	0.0254	−13345	1570	1.020	0.80	5.4	1.7	I	
pf2021023	21-Apr-2001	52021.0027	0.0344	−10504	1446	1.016	0.71	5.4	1.9	I	
pf2021028	21-Apr-2001	52021.0697	0.0518	−11103	1303	1.017	0.75	5.3	2.2	I	
pf2021030	21-Apr-2001	52021.0877	0.0564	−14701	1577	1.023	0.83	5.6	2.3	I	
pf2021036	21-Apr-2001	52021.1397	0.0699	19999	1661	0.969	0.88	5.7	2.5	I	
pf2021038	21-Apr-2001	52021.1547	0.0738	36092	1770	0.945	0.89	5.3	2.5	I	
pf2021041	21-Apr-2001	52021.1857	0.0819	57085	2007	0.913	0.82	6.4	2.5	I	
pf2021043	21-Apr-2001	52021.2032	0.0864	95770	1590	0.853	0.99	5.4	2.4	I	
pf2021046	21-Apr-2001	52021.2376	0.0953	131424	1521	0.799	0.98	5.5	2.4	I	
pf2021048	21-Apr-2001	52021.2525	0.0992	158100	2116	0.758	0.99	6.1	2.4	I	
pf2022015	22-Apr-2001	52021.8303	0.2492	−15564	1096	1.024	0.95	4.3	1.3	I	
pf2022018	22-Apr-2001	52021.8614	0.2572	−16311	1153	1.025	0.95	4.1	1.3	I	
pf2022022	22-Apr-2001	52021.9082	0.2694	−18257	1141	1.028	0.94	4.3	1.5	I	
pf2022025	22-Apr-2001	52021.9389	0.2773	−18815	1212	1.029	0.94	4.2	1.6	I	
pf2022028	22-Apr-2001	52021.9715	0.2858	−24564	1290	1.038	0.96	5.2	1.7	I	
pf2022031	22-Apr-2001	52022.0155	0.2972	−21464	1357	1.033	0.94	5.2	1.9	I	
pf2022034	22-Apr-2001	52022.0473	0.3054	−24123	1295	1.037	0.95	5.2	2.1	I	

continued on next page

Table C.2: *continued*: MACHO*05:36:48.7−69:17:00 V_J filter, image subtraction photometry

Image name	UTC	Mean date HJD−2400000.0	Orbital phase	Flux difference	δ Flux difference	Norm. light	Quality factor	Seeing (arc sec)	Airmass (χ)	LC analysis	Comment
pf2023015	23-Apr-2001	52022.9174	0.5312	77723	823	0.881	0.98	4.9	1.5	I	
pf2023018	23-Apr-2001	52022.9464	0.5388	38642	586	0.941	0.99	3.3	1.6	I	
pf2023021	23-Apr-2001	52022.9797	0.5474	5081	1136	0.992	0.53	3.6	1.8	I	
pf2023024	23-Apr-2001	52023.0100	0.5553	−12371	1209	1.019	0.79	3.8	1.9	I	
pf2023027	23-Apr-2001	52023.0357	0.5620	−3888	496	1.006	0.16	4.3	2.1	I	
pf2023030	23-Apr-2001	52023.0638	0.5692	−8223	1246	1.013	0.78	4.8	2.2	I	
pf2023033	23-Apr-2001	52023.0934	0.5769	−16231	1304	1.025	0.86	5.1	2.3	I	
pf2045021	15-May-2001	52044.9934	0.2600	−24876	1740	1.038	0.96	5.5	2.1	I	
pf2045023	15-May-2001	52045.0081	0.2638	−15648	1777	1.024	0.84	5.5	2.2	I	
pf2045025	15-May-2001	52045.0232	0.2678	−25353	1976	1.039	0.87	5.9	2.3	I	
pf2045027	15-May-2001	52045.0380	0.2716	−21351	1822	1.033	0.41	6.1	2.4	I	
pf2046015	16-May-2001	52045.7944	0.4679	61787	978	0.905	1.00	3.3	1.3	I	
pf2046017	16-May-2001	52045.8094	0.4718	83747	917	0.872	1.00	3.2	1.4	I	
pf2046020	16-May-2001	52045.8396	0.4796	125646	890	0.808	1.00	3.2	1.5	I	
pf2046022	16-May-2001	52045.8551	0.4836	149629	877	0.771	1.00	3.0	1.5	I	
pf2046025	16-May-2001	52045.8853	0.4915	185120	994	0.716	1.00	4.0	1.6	I	
pf2046027	16-May-2001	52045.8999	0.4953	196439	839	0.699	1.00	4.4	1.7	I	
pf2046030	16-May-2001	52045.9303	0.5032	207471	1115	0.682	1.00	5.3	1.8	I	
pf2046032	16-May-2001	52045.9556	0.5097	191508	1029	0.707	1.00	4.5	2.0	I	
pf2046035	16-May-2001	52046.0231	0.5272	105387	851	0.839	1.00	3.6	2.3	I	
pf2046037	16-May-2001	52046.0400	0.5316	81328	1075	0.875	0.98	4.6	2.4	I	
pf2046039	16-May-2001	52046.0552	0.5356	62967	1212	0.904	0.96	5.2	2.4	I	
pf2465045	09-Jul-2002	52465.1255	0.2853	−19422	1226	1.030	0.90	4.1	1.9	I	
pf2465048	09-Jul-2002	52465.1612	0.2945	−16218	653	1.025	0.60	3.5	1.8	I	
pf2465051	09-Jul-2002	52465.1910	0.3023	−18856	776	1.029	0.78	3.6	1.6	I	
pf2465054	09-Jul-2002	52465.2209	0.3100	−25715	627	1.039	0.44	4.1	1.5	I	

C.1.3 MACHO*05:36:48.7−69:17:00 I_C filter, image subtraction photometry

Table C.3: MACHO*05:36:48.7−69:17:00 I_C filter, image subtraction photometry.

Image name	UTC	Mean date HJD−2400000.0	Orbital phase	Flux difference	δ Flux difference	Norm. light	Quality factor	Seeing (arc sec)	Airmass (χ)	LC analysis	Comment
pf1295033	26-Apr-1999	51294.9735	0.6281	−5906	1074	1.027	0.75	5.6	1.8	I	
pf1295040	26-Apr-1999	51295.0796	0.6557	−6430	765	1.029	0.80	2.3	2.3	I	
pf1295046	26-Apr-1999	51295.1585	0.6761	−11892	338	1.054	0.61	3.0	2.5	X	
pf1295053	26-Apr-1999	51295.2587	0.7021	−6488	914	1.029	0.88	2.7	2.3	I	
pf1404026	13-Aug-1999	51404.1778	0.9669	−5031	933	1.023	0.70	3.7	1.3	I	
pf1405024	14-Aug-1999	51404.8858	0.1506	3595	1034	0.983	0.15	6.2	2.5	X	
pf1406050	15-Aug-1999	51406.2527	0.5053	67174	693	0.697	1.00	3.6	1.2	I	
pf1406053	15-Aug-1999	51406.2732	0.5106	60709	846	0.726	1.00	2.8	1.1	I	
pf1406054	15-Aug-1999	51406.2786	0.5120	60787	1340	0.726	0.99	2.9	1.1	I	
pf1725028	29-Jun-2000	51724.9648	0.2118	−1210	1322	1.005	0.19	7.2	2.5	X	
pf1725034	29-Jun-2000	51725.0574	0.2359	158	1167	0.999	0.02	7.6	2.3	X	
pf1725041	29-Jun-2000	51725.1624	0.2631	−6408	1373	1.029	0.67	4.8	1.8	X	
pf1727029	01-Jul-2000	51726.9148	0.7179	−6004	1198	1.027	0.77	4.2	2.4	I	
pf1727039	01-Jul-2000	51727.0686	0.7578	−5898	796	1.027	0.84	2.6	2.3	I	
pf1727045	01-Jul-2000	51727.1408	0.7765	−3933	757	1.018	0.60	2.2	1.9	I	
pf1727051	01-Jul-2000	51727.2278	0.7991	−4966	712	1.022	0.76	2.2	1.6	I	
pf1727057	01-Jul-2000	51727.2995	0.8177	−1966	2316	1.009	0.23	4.5	1.3	I	
pf1730027	04-Jul-2000	51729.8510	0.4798	50090	1618	0.774	0.88	5.0	2.1	I	
pf1730034	04-Jul-2000	51729.9697	0.5106	64626	1159	0.708	0.98	4.3	2.5	I	
pf1730040	04-Jul-2000	51730.0515	0.5319	24474	1178	0.890	0.97	4.3	2.3	I	
pf1730045	04-Jul-2000	51730.1175	0.5490	752	1254	0.997	0.13	4.4	2.0	I	
pf1730051	04-Jul-2000	51730.2166	0.5747	−2879	1180	1.013	0.45	4.4	1.6	I	
pf1730059	04-Jul-2000	51730.2903	0.5938	−3817	1579	1.017	0.66	4.5	1.3	I	
pf1731028	05-Jul-2000	51730.8758	0.7458	−4312	736	1.019	0.67	2.1	2.3	I	
pf1731034	05-Jul-2000	51730.9479	0.7645	−4679	749	1.021	0.83	2.1	2.5	I	
pf1731040	05-Jul-2000	51731.0679	0.7956	−4155	809	1.019	0.65	3.1	2.3	I	

continued on next page

Table C.3: *continued*: MACHO*05:36:48.7−69:17:00 I_C filter, image subtraction photometry

Image name	UTC	Mean date HJD−2400000.0	Orbital phase	Flux difference	δ Flux difference	Norm. light	Quality factor	Seeing (arc sec)	Airmass (χ)	LC analysis	Comment
pf1957022	16-Feb-2001	51957.1365	0.4609	1926	875	0.991	0.35	7.3	1.6	X	
pf1957025	16-Feb-2001	51957.1661	0.4686	−1562	911	1.007	0.13	7.0	1.8	X	
pf1957029	16-Feb-2001	51957.1979	0.4769	882	891	0.996	0.07	6.9	1.9	X	
pf1960029	19-Feb-2001	51960.0726	0.2229	−4437	1012	1.020	0.66	3.7	1.5	I	
pf1960032	19-Feb-2001	51960.1022	0.2306	−5153	1078	1.023	0.66	4.3	1.6	I	
pf1960035	19-Feb-2001	51960.1327	0.2385	−5047	821	1.023	0.81	2.9	1.7	I	
pf1960038	19-Feb-2001	51960.1627	0.2463	−4999	835	1.023	0.75	3.1	1.8	I	
pf1960042	19-Feb-2001	51960.2003	0.2560	−6969	1260	1.031	0.70	4.4	2.0	I	
pf1961014	20-Feb-2001	51960.8931	0.4358	−3067	645	1.014	0.87	2.2	1.1	I	
pf1961016	20-Feb-2001	51960.9216	0.4432	−3858	614	1.017	0.94	1.9	1.1	I	R
pf1961020	20-Feb-2001	51960.9501	0.4506	−2917	598	1.013	0.79	1.7	1.2	I	R,A
pf1961023	20-Feb-2001	51960.9787	0.4580	6562	592	0.970	0.95	1.9	1.2	I	R
pf1961026	20-Feb-2001	51961.0079	0.4656	19625	638	0.911	0.99	2.1	1.3	I	
pf1961029	20-Feb-2001	51961.0371	0.4732	31595	656	0.857	1.00	2.2	1.4	I	
pf1961032	20-Feb-2001	51961.0663	0.4807	45445	787	0.795	1.00	3.4	1.4	I	
pf1961039	20-Feb-2001	51961.1311	0.4976	70386	790	0.682	1.00	3.5	1.7	I	
pf1961044	20-Feb-2001	51961.1902	0.5129	36221	1085	0.835	0.67	5.3	1.9	X	
pf1988015	19-Mar-2001	51987.9344	0.4531	4033	985	0.982	0.20	5.8	1.3	I	
pf1989004	20-Mar-2001	51988.0456	0.4819	49172	555	0.778	1.00	2.0	1.6	I	
pf1989005	20-Mar-2001	51988.0514	0.4834	51133	562	0.769	1.00	2.1	1.7	I	
pf1989013	20-Mar-2001	51988.1446	0.5076	68207	691	0.692	0.99	2.9	2.1	I	
pf1992014	23-Mar-2001	51991.8543	0.4703	24316	833	0.890	0.98	3.0	1.2	I	
pf1992017	23-Mar-2001	51991.8846	0.4782	36945	910	0.833	0.96	3.5	1.2	I	
pf1992020	23-Mar-2001	51991.9167	0.4865	53022	955	0.761	0.97	4.1	1.3	I	
pf1992023	23-Mar-2001	51991.9488	0.4948	67819	641	0.694	1.00	2.9	1.4	I	
pf1992026	23-Mar-2001	51991.9780	0.5024	67873	642	0.694	1.00	6.4	1.4	I	
pf1992028	23-Mar-2001	51991.9917	0.5060	68875	701	0.689	1.00	3.0	1.5	I	
pf1992031	23-Mar-2001	51992.0199	0.5133	58745	832	0.735	0.99	3.3	1.6	I	

continued on next page

Table C.3: *continued*: MACHO*05:36:48.7−69:17:00 I_C filter, image subtraction photometry

Image name	UTC	Mean date HJD−2400000.0	Orbital phase	Flux difference	δ Flux difference	Norm. light	Quality factor	Seeing (arc sec)	Airmass (χ)	LC analysis	Comment
pf1992033	23-Mar-2001	51992.0442	0.5196	46645	824	0.789	0.99	3.0	1.7	I	
pf1992035	23-Mar-2001	51992.0579	0.5231	42966	904	0.806	0.98	3.1	1.8	I	
pf1992038	23-Mar-2001	51992.1028	0.5348	22352	838	0.899	0.99	3.0	2.0	I	
pf1992040	23-Mar-2001	51992.1165	0.5384	13379	898	0.940	0.97	3.1	2.0	I	
pf1992043	23-Mar-2001	51992.1501	0.5471	2328	1020	0.989	0.41	3.5	2.2	I	
pf1992045	23-Mar-2001	51992.1638	0.5506	−1092	933	1.005	0.27	3.1	2.3	I	
pf1992048	23-Mar-2001	51992.1920	0.5579	−5425	823	1.024	0.72	2.6	2.4	I	
pf1992053	23-Mar-2001	51992.2292	0.5676	−7124	1005	1.032	0.65	3.0	2.5	I	
pf2019016	19-Apr-2001	52018.8499	0.4757	35239	864	0.841	0.99	3.9	1.3	I	
pf2019019	19-Apr-2001	52018.8842	0.4846	53710	751	0.758	1.00	3.0	1.4	I	
pf2019022	19-Apr-2001	52018.9148	0.4926	65919	767	0.702	1.00	3.3	1.5	I	
pf2019025	19-Apr-2001	52018.9489	0.5014	70902	793	0.680	1.00	3.5	1.6	I	
pf2019028	19-Apr-2001	52018.9861	0.5111	63773	877	0.712	1.00	3.4	1.8	I	
pf2019031	19-Apr-2001	52019.0303	0.5225	45174	1089	0.796	0.99	4.1	2.0	I	
pf2019034	19-Apr-2001	52019.0639	0.5313	27765	1038	0.875	0.98	3.9	2.1	I	
pf2019037	19-Apr-2001	52019.1007	0.5408	10329	1295	0.953	0.88	4.9	2.3	I	
pf2019040	19-Apr-2001	52019.1695	0.5587	−1247	1579	1.006	0.10	5.2	2.5	I	
pf2019043	19-Apr-2001	52019.2028	0.5673	−5881	1883	1.027	0.39	5.9	2.5	I	
pf2019045	19-Apr-2001	52019.2201	0.5718	−6191	2137	1.028	0.50	5.9	2.5	I	
pf2019047	19-Apr-2001	52019.2393	0.5768	−6138	2159	1.028	0.51	6.0	2.4	I	
pf2019049	19-Apr-2001	52019.2552	0.5809	−4427	2063	1.020	0.34	5.8	2.4	I	
pf2021014	21-Apr-2001	52020.8953	0.0065	−5286	1137	1.024	0.63	4.0	1.4	I	
pf2021016	21-Apr-2001	52020.9283	0.0151	−5915	1153	1.027	0.72	4.4	1.5	I	
pf2021019	21-Apr-2001	52020.9637	0.0242	−3132	1275	1.014	0.49	4.6	1.7	I	
pf2021022	21-Apr-2001	52020.9983	0.0332	−5436	1238	1.025	0.71	4.4	1.8	I	
pf2021027	21-Apr-2001	52021.0642	0.0503	−4869	1280	1.022	0.47	4.0	2.2	I	
pf2021029	21-Apr-2001	52021.0839	0.0554	−5387	1408	1.024	0.56	4.9	2.3	I	
pf2021035	21-Apr-2001	52021.1293	0.0672	2833	1495	0.987	0.35	4.7	2.4	I	

continued on next page

Table C.3: *continued*: MACHO*05:36:48.7−69:17:00 I_C filter, image subtraction photometry

Image name	UTC	Mean date HJD−2400000.0	Orbital phase	Flux difference	δ Flux difference	Norm. light	Quality factor	Seeing (arc sec)	Airmass (χ)	LC analysis	Comment
pf2021037	21-Apr-2001	52021.1522	0.0732	2354	1747	0.989	0.24	5.6	2.5	I	
pf2021040	21-Apr-2001	52021.1826	0.0811	2447	1216	0.988	0.20	6.6	2.5	X	
pf2021042	21-Apr-2001	52021.2005	0.0857	27797	1480	0.875	0.91	4.6	2.5	I	
pf2021045	21-Apr-2001	52021.2320	0.0939	44195	1526	0.800	0.95	4.9	2.4	I	
pf2021047	21-Apr-2001	52021.2499	0.0985	53809	1647	0.757	0.94	5.1	2.4	I	
pf2022014	22-Apr-2001	52021.8274	0.2484	−4043	793	1.018	0.82	2.6	1.2	I	
pf2022017	22-Apr-2001	52021.8586	0.2565	−6146	944	1.028	0.80	2.9	1.3	I	
pf2022021	22-Apr-2001	52021.9048	0.2685	−8187	885	1.037	0.89	2.9	1.5	I	
pf2022024	22-Apr-2001	52021.9362	0.2766	−6358	982	1.029	0.72	3.4	1.6	I	
pf2022027	22-Apr-2001	52021.9674	0.2847	−7055	1011	1.032	0.83	3.5	1.7	I	
pf2022033	22-Apr-2001	52022.0441	0.3046	−7596	1094	1.034	0.78	3.8	2.1	I	
pf2023014	23-Apr-2001	52022.9129	0.5301	30803	1112	0.861	0.97	4.0	1.5	I	
pf2023017	23-Apr-2001	52022.9420	0.5376	17672	905	0.920	0.98	3.3	1.6	I	
pf2023020	23-Apr-2001	52022.9751	0.5462	2136	930	0.990	0.43	3.5	1.8	I	
pf2023023	23-Apr-2001	52023.0054	0.5541	−3788	866	1.017	0.61	3.1	1.9	I	
pf2023026	23-Apr-2001	52023.0348	0.5617	−4565	1068	1.021	0.64	3.8	2.1	I	
pf2023029	23-Apr-2001	52023.0593	0.5681	−3269	1229	1.015	0.46	4.1	2.2	I	
pf2023032	23-Apr-2001	52023.0890	0.5758	−5386	1047	1.024	0.79	3.6	2.3	I	
pf2023035	23-Apr-2001	52023.1198	0.5838	−3716	1094	1.017	0.50	3.7	2.4	I	
pf2045020	15-May-2001	52044.9845	0.2577	−5252	1583	1.024	0.65	5.4	2.1	I	
pf2045022	15-May-2001	52044.9992	0.2615	−10649	1655	1.048	0.76	5.3	2.2	I	
pf2045024	15-May-2001	52045.0143	0.2654	−8908	1856	1.040	0.61	6.0	2.2	I	
pf2045026	15-May-2001	52045.0292	0.2693	−8391	1753	1.038	0.79	5.3	2.3	I	
pf2046014	16-May-2001	52045.7864	0.4658	19231	722	0.913	0.99	3.2	1.3	I	
pf2046016	16-May-2001	52045.8019	0.4698	25606	683	0.884	0.99	2.4	1.4	I	
pf2046019	16-May-2001	52045.8322	0.4777	40173	662	0.819	1.00	2.4	1.4	I	
pf2046021	16-May-2001	52045.8478	0.4817	46461	672	0.790	1.00	2.4	1.5	I	
pf2046024	16-May-2001	52045.8775	0.4894	60954	748	0.725	1.00	3.1	1.6	I	

continued on next page

Table C.3: *continued*: MACHO*05:36:48.7−69:17:00 I_C filter, image subtraction photometry

Image name	UTC	Mean date HJD−2400000.0	Orbital phase	Flux difference	δ Flux difference	Norm. light	Quality factor	Seeing (arc sec)	Airmass (χ)	LC analysis	Comment
pf2046026	16-May-2001	52045.8926	0.4934	66428	856	0.700	1.00	4.0	1.7	I	
pf2046029	16-May-2001	52045.9228	0.5012	74192	973	0.665	0.99	3.7	1.8	I	
pf2046031	16-May-2001	52045.9380	0.5051	74598	1045	0.663	0.97	4.2	1.9	I	
pf2046034	16-May-2001	52046.0157	0.5253	41828	996	0.811	0.97	3.8	2.3	I	
pf2046036	16-May-2001	52046.0305	0.5292	35590	1099	0.839	0.92	4.3	2.3	I	
pf2046038	16-May-2001	52046.0474	0.5335	23897	1401	0.892	0.91	4.5	2.4	I	
pf2046040	16-May-2001	52046.0626	0.5375	15706	1243	0.929	0.65	4.5	2.5	I	
pf2464024	08-Jul-2002	52464.1739	0.0383	−5768	1660	1.026	0.49	5.3	1.7	I	
pf2464026	08-Jul-2002	52464.1944	0.0437	−4732	1717	1.021	0.42	5.4	1.6	I	
pf2464028	08-Jul-2002	52464.2158	0.0492	−6747	1761	1.030	0.62	5.6	1.5	I	
pf2464030	08-Jul-2002	52464.2528	0.0588	−6363	1602	1.029	0.60	5.0	1.4	I	
pf2464032	08-Jul-2002	52464.2762	0.0649	1091	1904	0.995	0.11	5.5	1.3	I	
pf2464034	08-Jul-2002	52464.2980	0.0705	10709	1919	0.952	0.57	3.6	1.3	I	
pf2465047	09-Jul-2002	52465.1540	0.2927	−7141	949	1.032	0.82	3.4	1.8	I	
pf2465050	09-Jul-2002	52465.1838	0.3004	−7825	963	1.035	0.61	3.7	1.6	I	
pf2467045	11-Jul-2002	52467.1902	0.8211	−2012	1723	1.009	0.14	6.9	1.6	I	
pf2467047	11-Jul-2002	52467.2133	0.8271	−8997	1189	1.041	0.77	4.5	1.5	I	
pf2467049	11-Jul-2002	52467.2353	0.8328	−4994	879	1.023	0.54	3.6	1.4	I	
pf2467051	11-Jul-2002	52467.2573	0.8385	−8039	678	1.036	0.51	3.2	1.4	I	
pf2467053	11-Jul-2002	52467.2777	0.8438	−5719	861	1.026	0.59	3.6	1.3	I	
pf2468015	12-Jul-2002	52467.8539	0.9933	−5218	909	1.024	0.66	4.3	2.2	I	
pf2468018	12-Jul-2002	52467.8972	0.0045	−7871	1143	1.036	0.21	4.9	2.4	I	
pf2468020	12-Jul-2002	52467.9186	0.0101	−3075	957	1.014	0.42	3.7	2.5	I	
pf2468022	12-Jul-2002	52467.9434	0.0165	−4760	1070	1.021	0.64	3.8	2.5	I	
pf2468024	12-Jul-2002	52467.9636	0.0218	−5472	1152	1.025	0.65	4.3	2.5	I	
pf2468026	12-Jul-2002	52467.9847	0.0273	−1070	821	1.005	0.24	3.2	2.5	I	
pf2468028	12-Jul-2002	52468.0049	0.0325	−5033	1032	1.023	0.60	4.0	2.4	I	
pf2468030	12-Jul-2002	52468.0274	0.0383	−8258	1363	1.037	0.69	4.7	2.4	I	

continued on next page

Table C.3: *continued*: MACHO*05:36:48.7−69:17:00 I_C filter, image subtraction photometry

Image name	UTC	Mean date HJD−2400000.0	Orbital phase	Flux difference	δ Flux difference	Norm. light	Quality factor	Seeing (arc sec)	Airmass (χ)	LC analysis	Comment
pf2468032	12-Jul-2002	52468.0481	0.0437	−2137	1111	1.010	0.30	3.8	2.3	I	
pf2468034	12-Jul-2002	52468.0694	0.0492	−3239	837	1.015	0.63	3.1	2.2	I	
pf2468036	12-Jul-2002	52468.0941	0.0556	−4161	710	1.019	0.83	2.3	2.0	I	
pf2468038	12-Jul-2002	52468.1147	0.0610	−1363	739	1.006	0.30	2.4	1.9	I	
pf2468040	12-Jul-2002	52468.1351	0.0663	4386	839	0.980	0.69	2.7	1.8	I	
pf2468042	12-Jul-2002	52468.1571	0.0720	8131	1035	0.963	0.81	3.5	1.7	I	
pf2468044	12-Jul-2002	52468.1780	0.0774	17705	1092	0.920	0.92	4.3	1.6	I	
pf2468046	12-Jul-2002	52468.2017	0.0836	28221	926	0.873	0.99	3.4	1.5	I	
pf2468048	12-Jul-2002	52468.2257	0.0898	36604	864	0.835	0.99	3.2	1.5	I	
pf2468050	12-Jul-2002	52468.2464	0.0952	44500	701	0.799	1.00	3.2	1.4	I	
pf2468052	12-Jul-2002	52468.2668	0.1004	55498	655	0.749	1.00	2.4	1.3	I	
pf2468054	12-Jul-2002	52468.2873	0.1058	61141	816	0.724	1.00	3.1	1.3	I	
pf2468055	12-Jul-2002	52468.2938	0.1075	65173	962	0.706	1.00	3.2	1.3	I	

C.2 MOA J005018.4−723855 image subtraction photometry

C.2.1 MOA J005018.4−723855 u, image subtraction photometry

Table C.4: MOA J005018.4−723855 u filter, image subtraction photometry.

Image name	UTC	Mean date HJD−2400000.0	Orbital phase	Flux difference	δ Flux difference	Norm. light	Quality factor	Seeing (arc sec)	Airmass (χ)	LC analysis	Comment
pf1814026	26-Sep-2000	51814.0643	0.7718	−4382	666	1.040	0.94	4.6	1.1	I	
pf1814027	26-Sep-2000	51814.0794	0.7800	−3208	748	1.029	0.85	5.3	1.1	I	
pf1814028	26-Sep-2000	51814.0970	0.7895	−2517	830	1.023	0.77	5.8	1.1	I	
pf1814031	26-Sep-2000	51814.1278	0.8063	−1161	631	1.011	0.62	4.3	1.2	I	
pf1814034	26-Sep-2000	51814.1616	0.8247	72	648	0.999	0.08	4.5	1.2	I	
pf1814038	26-Sep-2000	51814.2015	0.8463	1398	666	0.987	0.57	5.0	1.3	I	
pf1815013	27-Sep-2000	51814.8991	0.2255	−4310	570	1.039	0.90	3.9	1.3	I	
pf1815014	27-Sep-2000	51814.9138	0.2335	−4658	573	1.042	0.97	3.9	1.2	I	
pf1815024	27-Sep-2000	51815.0088	0.2852	−4914	707	1.045	0.92	4.9	1.1	I	
pf1815025	27-Sep-2000	51815.0236	0.2932	−4649	728	1.042	0.89	5.1	1.1	I	
pf1815026	27-Sep-2000	51815.0382	0.3011	−1382	789	1.013	0.74	5.7	1.1	I	
pf1815027	27-Sep-2000	51815.0581	0.3120	−743	677	1.007	0.47	4.8	1.1	I	
pf1815034	27-Sep-2000	51815.1181	0.3445	−589	724	1.005	0.32	5.2	1.2	I	
pf1815035	27-Sep-2000	51815.1428	0.3580	1670	757	0.985	0.50	5.7	1.2	I	
pf1815036	27-Sep-2000	51815.1587	0.3666	801	743	0.993	0.44	5.5	1.2	I	
pf1815037	27-Sep-2000	51815.1732	0.3745	3597	737	0.967	0.80	5.6	1.2	I	
pf1818017	30-Sep-2000	51817.9626	0.8906	15028	745	0.864	0.99	6.0	1.2	I	
pf1818023	30-Sep-2000	51818.0216	0.9226	27674	713	0.749	1.00	5.9	1.1	I	
pf1818024	30-Sep-2000	51818.0532	0.9398	35241	732	0.681	1.00	6.4	1.1	I	
pf1818026	30-Sep-2000	51818.0917	0.9607	44844	609	0.594	1.00	5.5	1.2	I	
pf1818034	30-Sep-2000	51818.1628	0.9994	44270	488	0.599	1.00	5.6	1.2	I	
pf1847014	29-Oct-2000	51846.9245	0.6318	−1832	819	1.017	0.80	6.0	1.1	I	
pf1847017	29-Oct-2000	51846.9711	0.6572	−5587	696	1.051	0.78	6.7	1.1	I	
pf1871017	22-Nov-2000	51871.1183	0.7816	−1871	618	1.017	0.80	4.4	1.4	I	

continued on next page

Table C.4: *continued*: MOA J005018.4−723855 u filter, image subtraction photometry

Image name	UTC	Mean date HJD−2400000.0	Orbital phase	Flux difference	δ Flux difference	Norm. light	Quality factor	Seeing (arc sec)	Airmass (χ)	LC analysis	Comment
pf1873013	24-Nov-2000	51872.9209	0.7614	−3431	761	1.031	0.94	5.2	1.1	I	
pf1873024	24-Nov-2000	51873.0306	0.8210	−1114	698	1.010	0.57	5.1	1.3	I	
pf1873027	24-Nov-2000	51873.0576	0.8356	496	886	0.995	0.21	4.5	1.3	X	
pf1873034	24-Nov-2000	51873.1163	0.8675	7184	603	0.935	0.97	4.5	1.4	I	
pf1873035	24-Nov-2000	51873.1310	0.8755	9619	554	0.913	0.98	4.1	1.5	I	
pf1873036	24-Nov-2000	51873.1472	0.8843	12529	670	0.887	0.98	4.1	1.6	I	
pf1957014	16-Feb-2001	51957.0060	0.4630	27297	623	0.751	0.98	6.4	1.2	X	
pf1957015	16-Feb-2001	51957.0223	0.4718	29472	599	0.732	0.98	6.2	1.2	X	
pf1958013	17-Feb-2001	51957.8969	0.9472	38648	596	0.650	1.00	6.0	1.5	I	
pf1958016	17-Feb-2001	51957.9250	0.9625	44072	624	0.599	1.00	6.2	1.9	X	
pf1958020	17-Feb-2001	51957.9548	0.9787	44557	655	0.595	0.99	6.0	2.0	X	
pf1958022	17-Feb-2001	51957.9832	0.9941	49433	565	0.550	0.98	6.3	2.1	X	
pf1958025	17-Feb-2001	51958.0158	0.0118	29328	597	0.733	0.95	6.0	2.1	X	
pf1960013	19-Feb-2001	51959.8886	0.0297	30683	482	0.722	1.00	4.6	1.5	I	
pf1960016	19-Feb-2001	51959.9167	0.0450	22710	559	0.794	1.00	5.0	1.6	I	
pf1988034	20-Mar-2001	51988.8770	0.7854	−4330	453	1.039	0.91	3.1	1.7	I	R
pf1988035	20-Mar-2001	51988.8932	0.7942	−4055	431	1.037	0.83	2.9	1.8	I	R,A
pf1988036	20-Mar-2001	51988.9290	0.8137	1155	401	0.990	0.21	3.1	1.9	I	R
pf1988037	20-Mar-2001	51988.9415	0.8205	−190	414	1.001	0.21	3.1	1.9	I	R
pf2017014	17-Apr-2001	52016.8693	0.9997	45004	227	0.591	1.00	3.2	2.0	I	
pf2023036	23-Apr-2001	52023.1471	0.4118	13138	536	0.880	0.99	4.6	1.8	I	
pf2023038	23-Apr-2001	52023.1779	0.4285	18756	574	0.829	0.99	5.0	1.7	I	
pf2023041	23-Apr-2001	52023.2129	0.4475	23014	517	0.790	1.00	4.4	1.5	I	
pf2023044	23-Apr-2001	52023.2446	0.4647	25323	561	0.769	1.00	4.7	1.4	I	
pf2081017	20-Jun-2001	52080.8399	0.7688	−5366	284	1.048	0.78	4.5	2.2	I	
pf2081018	20-Jun-2001	52080.8572	0.7782	−2806	252	1.025	0.46	6.5	2.2	I	
pf2081022	20-Jun-2001	52080.9028	0.8029	−2720	208	1.025	0.42	3.9	2.1	I	
pf2081023	20-Jun-2001	52080.9686	0.8387	2795	364	0.975	0.55	3.8	1.8	I	

continued on next page

Table C.4: *continued*: MOA J005018.4−723855 u filter, image subtraction photometry

Image name	UTC	Mean date HJD−2400000.0	Orbital phase	Flux difference	δ Flux difference	Norm. light	Quality factor	Seeing (arc sec)	Airmass (χ)	LC analysis	Comment
pf2081026	20-Jun-2001	52080.9996	0.8556	5081	465	0.954	0.82	3.8	1.7	I	
pf2081029	20-Jun-2001	52081.0298	0.8720	7405	472	0.933	0.94	3.7	1.6	I	
pf2081032	20-Jun-2001	52081.1246	0.9235	31548	441	0.714	1.00	3.7	1.4	I	
pf2081035	20-Jun-2001	52081.1551	0.9401	39569	405	0.642	1.00	3.8	1.3	I	
pf2081038	20-Jun-2001	52081.1856	0.9567	45031	406	0.592	1.00	3.9	1.2	I	
pf2081041	20-Jun-2001	52081.2154	0.9729	49228	397	0.554	1.00	3.8	1.2	I	
pf2081044	20-Jun-2001	52081.2570	0.9955	44878	454	0.593	1.00	4.2	1.2	I	
pf2081045	20-Jun-2001	52081.2791	0.0075	41858	415	0.621	1.00	3.9	1.1	I	
pf2086013	25-Jun-2001	52085.9158	0.5276	17891	523	0.838	0.99	5.2	2.0	I	
pf2086016	25-Jun-2001	52085.9458	0.5439	13699	536	0.876	0.98	5.0	1.9	I	
pf2086019	25-Jun-2001	52085.9750	0.5598	7855	554	0.929	0.95	4.8	1.8	I	
pf2086022	25-Jun-2001	52086.0076	0.5775	2108	566	0.981	0.74	4.6	1.6	I	
pf2086025	25-Jun-2001	52086.0370	0.5935	1504	657	0.986	0.55	5.3	1.6	I	
pf2086028	25-Jun-2001	52086.0664	0.6094	−240	722	1.002	0.12	5.7	1.5	I	
pf2086031	25-Jun-2001	52086.0962	0.6256	−2111	670	1.019	0.62	5.1	1.4	I	
pf2086039	25-Jun-2001	52086.1662	0.6637	−4702	636	1.043	0.93	4.5	1.2	I	
pf2086042	25-Jun-2001	52086.2325	0.6998	−4242	729	1.038	0.88	5.4	1.2	I	
pf2138013	16-Aug-2001	52137.8252	0.7412	−5240	445	1.047	0.91	3.3	1.8	I	
pf2138016	16-Aug-2001	52137.8554	0.7576	−3822	451	1.035	0.76	3.4	1.7	I	
pf2138017	16-Aug-2001	52137.8908	0.7769	−1907	512	1.017	0.77	3.8	1.6	I	
pf2138018	16-Aug-2001	52137.9061	0.7852	−3765	492	1.034	0.88	3.5	1.5	I	
pf2138019	16-Aug-2001	52137.9217	0.7937	−1965	521	1.018	0.75	3.6	1.5	I	
pf2138020	16-Aug-2001	52137.9367	0.8018	−741	545	1.007	0.38	4.0	1.4	I	
pf2138021	16-Aug-2001	52137.9520	0.8102	−1341	529	1.012	0.64	3.7	1.4	I	
pf2138022	16-Aug-2001	52137.9670	0.8183	784	542	0.993	0.35	3.9	1.4	I	
pf2138023	16-Aug-2001	52137.9822	0.8265	1237	528	0.989	0.64	3.7	1.3	I	
pf2138024	16-Aug-2001	52137.9972	0.8347	1951	535	0.982	0.78	3.6	1.3	I	
pf2138025	16-Aug-2001	52138.0128	0.8432	2764	564	0.975	0.79	4.4	1.3	I	

continued on next page

Table C.4: *continued*: MOA J005018.4−723855 u filter, image subtraction photometry

Image name	UTC	Mean date HJD−2400000.0	Orbital phase	Flux difference	δ Flux difference	Norm. light	Quality factor	Seeing (arc sec)	Airmass (χ)	LC analysis	Comment
pf2138026	16-Aug-2001	52138.0289	0.8520	1183	542	0.989	0.57	3.6	1.2	I	
pf2138027	16-Aug-2001	52138.0541	0.8656	5259	500	0.952	0.89	3.2	1.2	I	
pf2138030	16-Aug-2001	52138.0833	0.8815	10387	478	0.906	0.98	3.1	1.2	I	R
pf2138033	16-Aug-2001	52138.1170	0.8998	18662	472	0.831	0.99	3.5	1.1	I	
pf2138036	16-Aug-2001	52138.1516	0.9187	27358	452	0.752	1.00	3.4	1.1	I	
pf2138041	16-Aug-2001	52138.2049	0.9476	41249	427	0.626	1.00	3.4	1.1	I	
pf2138044	16-Aug-2001	52138.2343	0.9636	46226	438	0.581	1.00	3.8	1.2	I	
pf2140023	18-Aug-2001	52139.9085	0.8735	7785	445	0.929	0.93	4.2	1.5	I	
pf2140026	18-Aug-2001	52139.9380	0.8896	13927	340	0.874	0.99	3.5	1.4	I	
pf2140029	18-Aug-2001	52139.9671	0.9054	20408	418	0.815	0.99	4.0	1.3	I	
pf2140030	18-Aug-2001	52139.9876	0.9165	25123	452	0.772	1.00	4.6	1.3	I	
pf2140031	18-Aug-2001	52140.0043	0.9256	30661	529	0.722	1.00	4.6	1.3	I	
pf2140032	18-Aug-2001	52140.0193	0.9337	34291	491	0.689	1.00	4.5	1.2	I	
pf2140035	18-Aug-2001	52140.0488	0.9498	41637	493	0.623	1.00	4.2	1.2	I	
pf2140036	18-Aug-2001	52140.0662	0.9592	44680	437	0.595	1.00	4.0	1.2	I	
pf2140037	18-Aug-2001	52140.0832	0.9685	47602	411	0.569	1.00	4.0	1.2	I	
pf2140038	18-Aug-2001	52140.0987	0.9769	48123	406	0.564	1.00	4.1	1.2	I	
pf2140041	18-Aug-2001	52140.1305	0.9942	44828	447	0.594	1.00	4.0	1.1	I	
pf2140044	18-Aug-2001	52140.1619	0.0113	40012	459	0.638	1.00	3.8	1.1	I	
pf2140049	18-Aug-2001	52140.1920	0.0276	30893	519	0.720	1.00	4.1	1.1	I	
pf2140050	18-Aug-2001	52140.2220	0.0440	23219	514	0.790	1.00	3.8	1.2	I	
pf2140053	18-Aug-2001	52140.2551	0.0619	15095	574	0.863	0.99	4.2	1.2	I	
pf2406013	11-May-2002	52405.8354	0.4093	5219	143	0.952	0.63	4.4	2.2	X	
pf2406016	11-May-2002	52405.8782	0.4325	23414	157	0.788	0.82	4.1	2.2	I	
pf2406019	11-May-2002	52405.9105	0.4501	25453	276	0.769	0.99	4.0	2.2	I	
pf2406021	11-May-2002	52405.9378	0.4649	26664	367	0.758	0.99	3.9	2.2	I	
pf2406024	11-May-2002	52405.9674	0.4810	26135	352	0.763	1.00	3.9	2.2	I	
pf2406027	11-May-2002	52405.9979	0.4976	25980	358	0.765	1.00	4.3	2.1	I	

continued on next page

Table C.4: *continued*: MOA J005018.4−723855 u filter, image subtraction photometry

Image name	UTC	Mean date HJD−2400000.0	Orbital phase	Flux difference	δ Flux difference	Norm. light	Quality factor	Seeing (arc sec)	Airmass (χ)	LC analysis	Comment
pf2406030	11-May-2002	52406.0296	0.5148	22492	330	0.796	0.99	4.2	2.0	I	
pf2406033	11-May-2002	52406.0759	0.5399	15293	412	0.861	0.99	4.1	1.9	I	
pf2406036	11-May-2002	52406.1079	0.5574	7198	330	0.935	0.84	4.5	1.7	I	
pf2406039	11-May-2002	52406.1373	0.5733	−2833	612	1.025	0.25	5.3	1.5	X	
pf2406042	11-May-2002	52406.1714	0.5919	1304	643	0.988	0.41	5.4	1.4	I	
pf2406045	11-May-2002	52406.2010	0.6079	−610	598	1.006	0.25	5.7	1.4	I	
pf2406048	11-May-2002	52406.2304	0.6239	−2198	587	1.020	0.61	5.5	1.9	I	
pf2408013	13-May-2002	52407.7937	0.4736	25920	640	0.765	0.98	6.7	2.1	I	
pf2408016	13-May-2002	52407.8345	0.4958	26536	537	0.760	0.99	5.8	2.2	I	
pf2408019	13-May-2002	52407.8684	0.5142	21962	499	0.801	1.00	5.3	2.2	I	
pf2408022	13-May-2002	52407.9010	0.5319	18441	503	0.833	0.99	5.4	2.2	I	
pf2408025	13-May-2002	52407.9331	0.5494	10874	503	0.901	0.97	5.1	2.2	I	
pf2408028	13-May-2002	52407.9623	0.5652	5666	523	0.949	0.95	5.3	2.2	I	
pf2408031	13-May-2002	52407.9916	0.5812	1829	550	0.983	0.64	5.3	2.1	I	
pf2408034	13-May-2002	52408.0207	0.5970	1154	588	0.990	0.41	5.6	2.0	I	
pf2408037	13-May-2002	52408.0498	0.6128	−798	535	1.007	0.31	4.8	1.9	I	
pf2408040	13-May-2002	52408.0798	0.6291	−1038	536	1.009	0.48	5.0	1.8	I	
pf2408043	13-May-2002	52408.1105	0.6458	−1663	551	1.015	0.69	4.7	1.7	I	
pf2408046	13-May-2002	52408.1400	0.6618	−3134	601	1.028	0.86	4.9	1.6	I	
pf2408049	13-May-2002	52408.1691	0.6776	−5856	569	1.053	0.93	4.5	1.5	I	
pf2408052	13-May-2002	52408.2002	0.6945	−5321	460	1.048	0.91	4.8	1.4	I	
pf2409013	14-May-2002	52408.7962	0.0185	34720	363	0.685	1.00	3.6	2.0	I	
pf2409016	14-May-2002	52408.8253	0.0343	26574	467	0.759	0.99	4.9	2.1	I	
pf2409019	14-May-2002	52408.8583	0.0523	17813	466	0.838	0.99	4.8	2.1	I	
pf2409022	14-May-2002	52408.8892	0.0690	11559	500	0.895	0.93	5.2	2.2	I	
pf2409025	14-May-2002	52408.9196	0.0856	8702	514	0.920	0.95	5.4	1.8	X	
pf2466015	10-Jul-2002	52465.9218	0.0672	12456	447	0.886	0.98	4.1	1.8	I	
pf2466017	10-Jul-2002	52465.9467	0.0807	7108	470	0.935	0.94	4.1	1.7	I	

continued on next page

Table C.4: *continued*: MOA J005018.4−723855 u filter, image subtraction photometry

Image name	UTC	Mean date HJD−2400000.0	Orbital phase	Flux difference	δ Flux difference	Norm. light	Quality factor	Seeing (arc sec)	Airmass (χ)	LC analysis	Comment
pf2466020	10-Jul-2002	52465.9760	0.0966	2438	514	0.977	0.81	4.4	1.6	I	
pf2466023	10-Jul-2002	52466.0057	0.1128	243	489	0.997	0.04	4.2	1.5	I	
pf2466026	10-Jul-2002	52466.0349	0.1287	−875	565	1.008	0.35	4.6	1.4	I	
pf2466029	10-Jul-2002	52466.0643	0.1447	−2327	581	1.021	0.78	4.7	1.4	I	
pf2466032	10-Jul-2002	52466.1008	0.1645	−2168	606	1.019	0.61	4.9	1.3	I	
pf2466035	10-Jul-2002	52466.1306	0.1807	−3950	614	1.035	0.90	4.7	1.2	I	
pf2466038	10-Jul-2002	52466.1597	0.1965	−6177	662	1.056	0.92	4.9	1.2	I	
pf2466044	10-Jul-2002	52466.2207	0.2296	−7517	593	1.068	0.93	4.8	1.1	I	
pf2466047	10-Jul-2002	52466.2498	0.2455	−7032	583	1.063	0.86	4.4	1.1	I	
pf2466050	10-Jul-2002	52466.2789	0.2613	−5538	539	1.050	0.94	4.4	1.1	I	
pf2467013	11-Jul-2002	52466.7976	0.5432	12960	477	0.882	0.95	6.0	2.2	I	
pf2467016	11-Jul-2002	52466.8268	0.5591	7719	367	0.929	0.86	5.2	2.1	I	
pf2467019	11-Jul-2002	52466.8582	0.5762	3738	483	0.966	0.62	6.0	2.0	I	
pf2467022	11-Jul-2002	52466.8876	0.5921	1738	637	0.984	0.39	6.5	1.9	I	
pf2467025	11-Jul-2002	52466.9180	0.6086	170	718	0.998	0.03	6.5	1.8	X	
pf2467028	11-Jul-2002	52466.9475	0.6247	1323	503	0.988	0.21	6.2	1.7	X	
pf2467036	11-Jul-2002	52467.0446	0.6775	−5245	521	1.047	0.70	6.5	1.4	X	
pf2467041	11-Jul-2002	52467.1462	0.7327	−1928	685	1.017	0.55	7.0	1.2	I	

C.2.2 MOA J005018.4−723855 V_J, image subtraction photometry

Table C.5: MOA J005018.4−723855 V_J filter, image subtraction photometry.

Image name	UTC	Mean date HJD−2400000.0	Orbital phase	Flux difference	δ Flux difference	Norm. light	Quality factor	Seeing (arc sec)	Airmass (χ)	LC analysis	Comment
pf1814030	26-Sep-2000	51814.1160	0.7999	−20092	1442	1.033	0.96	4.3	1.2	I	
pf1814033	26-Sep-2000	51814.1478	0.8172	−12196	1416	1.020	0.88	4.1	1.2	I	
pf1814036	26-Sep-2000	51814.1818	0.8356	−3225	1871	1.005	0.44	5.4	1.2	I	
pf1815016	27-Sep-2000	51814.9312	0.2430	−39853	1156	1.066	0.99	2.7	1.2	I	
pf1815021	27-Sep-2000	51814.9713	0.2648	−42190	1310	1.070	0.98	3.2	1.2	I	
pf1815022	27-Sep-2000	51814.9807	0.2699	−42902	1362	1.071	0.99	3.4	1.2	I	
pf1815023	27-Sep-2000	51814.9969	0.2787	−41288	1273	1.069	0.98	3.2	1.1	I	
pf1815031	27-Sep-2000	51815.0861	0.3272	−10963	1361	1.018	0.88	3.7	1.1	I	
pf1815032	27-Sep-2000	51815.0951	0.3320	−9357	1317	1.015	0.87	3.4	1.1	I	
pf1815033	27-Sep-2000	51815.1053	0.3376	−4873	1339	1.008	0.70	3.6	1.2	I	
pf1815041	27-Sep-2000	51815.2017	0.3900	29438	1571	0.951	0.93	4.6	1.3	I	
pf1815042	27-Sep-2000	51815.2104	0.3947	37030	1606	0.938	0.95	4.7	1.3	I	
pf1818014	30-Sep-2000	51817.9351	0.8756	40701	1754	0.932	0.82	5.6	1.2	I	
pf1818016	30-Sep-2000	51817.9504	0.8839	58733	1618	0.902	0.93	5.0	1.2	I	
pf1818019	30-Sep-2000	51817.9813	0.9007	83956	1487	0.860	0.98	4.6	1.2	I	
pf1818022	30-Sep-2000	51818.0093	0.9160	117267	1409	0.805	0.98	4.5	1.1	I	
pf1818029	30-Sep-2000	51818.1144	0.9731	236703	1187	0.606	0.97	4.4	1.2	I	
pf1818030	30-Sep-2000	51818.1234	0.9780	235047	1160	0.609	0.96	4.4	1.2	I	
pf1818031	30-Sep-2000	51818.1322	0.9827	237206	1132	0.605	0.96	4.5	1.2	I	
pf1818032	30-Sep-2000	51818.1413	0.9877	235913	1055	0.607	0.98	4.4	1.2	I	
pf1818033	30-Sep-2000	51818.1500	0.9924	236924	1076	0.605	0.98	4.7	1.2	I	
pf1818035	30-Sep-2000	51818.1848	0.0114	186455	1335	0.689	0.96	4.6	1.3	I	
pf1847016	29-Oct-2000	51846.9592	0.6507	−19884	1873	1.033	0.68	6.0	1.1	I	
pf1847021	29-Oct-2000	51847.0050	0.6756	−22464	1832	1.037	0.70	5.7	1.1	I	
pf1847022	29-Oct-2000	51847.0145	0.6808	−21572	1825	1.036	0.73	5.8	1.2	I	
pf1873015	24-Nov-2000	51872.9427	0.7732	−25994	1640	1.043	0.94	4.5	1.2	I	

continued on next page

Table C.5: *continued*: MOA J005018.4−723855 V_J filter, image subtraction photometry

Image name	UTC	Mean date HJD−2400000.0	Orbital phase	Flux difference	δ Flux difference	Norm. light	Quality factor	Seeing (arc sec)	Airmass (χ)	LC analysis	Comment
pf1873016	24-Nov-2000	51872.9528	0.7787	−30623	1430	1.051	0.98	3.8	1.2	I	
pf1873019	24-Nov-2000	51872.9766	0.7916	−24024	1525	1.040	0.94	4.3	1.2	I	
pf1873022	24-Nov-2000	51873.0101	0.8098	−17955	1466	1.030	0.96	4.0	1.2	I	
pf1873023	24-Nov-2000	51873.0188	0.8146	−17053	1441	1.028	0.95	4.0	1.2	I	
pf1873030	24-Nov-2000	51873.0847	0.8504	9803	1481	0.984	0.88	4.5	1.4	I	
pf1873031	24-Nov-2000	51873.0936	0.8552	12301	1523	0.980	0.91	4.7	1.4	I	
pf1958015	17-Feb-2001	51957.9134	0.9562	173695	1376	0.709	0.87	5.3	1.3	X	
pf1960015	19-Feb-2001	51959.9052	0.0387	120420	1150	0.799	0.99	3.6	1.5	I	
pf1960018	19-Feb-2001	51959.9333	0.0540	79838	1237	0.867	0.98	3.7	1.6	I	
pf1988038	20-Mar-2001	51988.9452	0.8225	−4272	976	1.007	0.93	2.4	2.0	I	R,A
pf1988039	20-Mar-2001	51988.9537	0.8271	−1324	1007	1.002	0.33	2.6	2.0	I	R
pf1988042	20-Mar-2001	51988.9764	0.8395	4173	1055	0.993	0.55	2.7	2.1	I	
pf1988043	20-Mar-2001	51988.9850	0.8441	5282	1035	0.991	0.82	2.7	2.1	I	R
pf1989023	21-Mar-2001	51989.0054	0.8552	11221	1082	0.981	0.93	2.9	2.1	I	
pf1989024	21-Mar-2001	51989.0139	0.8598	15113	1204	0.975	0.86	3.4	2.2	I	
pf1989028	21-Mar-2001	51989.0462	0.8774	30977	1471	0.948	0.95	4.3	2.2	I	
pf1989029	21-Mar-2001	51989.0548	0.8820	38901	1485	0.935	0.96	4.5	2.2	I	
pf1989032	21-Mar-2001	51989.0744	0.8927	60623	1439	0.899	0.98	4.6	2.2	I	
pf1989034	21-Mar-2001	51989.0829	0.8973	68048	1445	0.887	0.97	4.6	2.2	I	
pf1989036	21-Mar-2001	51989.1045	0.9090	97524	1720	0.838	0.95	5.1	2.2	I	
pf1989037	21-Mar-2001	51989.1130	0.9137	104628	1585	0.826	0.95	4.9	2.2	I	
pf1989040	21-Mar-2001	51989.1322	0.9241	67918	1602	0.886	0.59	6.2	2.2	X	
pf1989041	21-Mar-2001	51989.1407	0.9287	99167	1607	0.834	0.72	6.0	2.2	X	
pf1989044	21-Mar-2001	51989.1637	0.9413	180669	1003	0.699	1.00	3.5	2.0	I	
pf1989045	21-Mar-2001	51989.1723	0.9459	192966	1059	0.679	1.00	3.6	2.0	I	
pf1989048	21-Mar-2001	51989.1926	0.9569	214437	1001	0.643	1.00	3.5	1.9	I	
pf1989049	21-Mar-2001	51989.2011	0.9616	220015	969	0.634	1.00	3.4	1.9	I	
pf1989052	21-Mar-2001	51989.2273	0.9758	225963	1060	0.624	1.00	3.5	1.8	I	

continued on next page

Table C.5: *continued*: MOA J005018.4−723855 V_J filter, image subtraction photometry

Image name	UTC	Mean date HJD−2400000.0	Orbital phase	Flux difference	δ Flux difference	Norm. light	Quality factor	Seeing (arc sec)	Airmass (χ)	LC analysis	Comment
pf1989053	21-Mar-2001	51989.2358	0.9804	226020	1457	0.624	1.00	3.5	1.8	I	
pf2023040	23-Apr-2001	52023.1944	0.4375	115177	1126	0.808	1.00	3.3	1.6	I	
pf2023043	23-Apr-2001	52023.2295	0.4566	136371	1128	0.773	1.00	3.3	1.5	I	
pf2023046	23-Apr-2001	52023.2611	0.4738	151966	1632	0.747	0.98	4.2	1.4	I	
pf2086015	25-Jun-2001	52085.9330	0.5369	72402	1283	0.879	1.00	4.7	1.9	I	
pf2086018	25-Jun-2001	52085.9630	0.5533	41806	1269	0.930	0.99	4.3	1.8	I	
pf2086021	25-Jun-2001	52085.9922	0.5691	21490	1323	0.964	0.97	5.7	1.7	I	
pf2086024	25-Jun-2001	52086.0249	0.5869	8417	1336	0.986	0.84	5.5	1.6	I	
pf2086027	25-Jun-2001	52086.0542	0.6029	−1813	1549	1.003	0.22	5.1	1.5	I	
pf2086030	25-Jun-2001	52086.0836	0.6188	−4990	1794	1.008	0.56	5.4	1.4	I	
pf2086033	25-Jun-2001	52086.1134	0.6350	−22987	1263	1.038	0.95	4.3	1.3	I	
pf2086041	25-Jun-2001	52086.1834	0.6731	−40649	1395	1.068	0.97	4.2	1.2	I	
pf2086044	25-Jun-2001	52086.2498	0.7091	−35075	1676	1.058	0.88	5.0	1.1	I	
pf2138015	16-Aug-2001	52137.8434	0.7511	−39539	1060	1.066	0.99	2.9	1.7	I	
pf2138029	16-Aug-2001	52138.0713	0.8750	32077	1004	0.947	0.99	3.0	1.2	I	
pf2138032	16-Aug-2001	52138.1005	0.8909	61022	1040	0.898	1.00	3.3	1.2	I	
pf2138035	16-Aug-2001	52138.1342	0.9092	100770	986	0.832	1.00	3.2	1.1	I	
pf2138038	16-Aug-2001	52138.1719	0.9297	153224	1068	0.745	1.00	3.7	1.1	I	
pf2138040	16-Aug-2001	52138.1920	0.9406	180306	1015	0.700	1.00	3.6	1.1	I	
pf2138043	16-Aug-2001	52138.2221	0.9569	209720	950	0.651	1.00	3.4	1.2	I	
pf2138046	16-Aug-2001	52138.2515	0.9729	221524	773	0.631	1.00	4.0	1.2	I	
pf2140022	18-Aug-2001	52139.8893	0.8631	13661	1276	0.977	0.94	3.8	1.6	I	
pf2140025	18-Aug-2001	52139.9257	0.8829	46922	550	0.922	0.97	3.1	1.4	I	
pf2140028	18-Aug-2001	52139.9552	0.8989	79096	718	0.868	1.00	3.1	1.4	I	
pf2140034	18-Aug-2001	52140.0368	0.9433	189918	1051	0.684	1.00	3.5	1.2	I	
pf2140040	18-Aug-2001	52140.1174	0.9871	219603	791	0.634	1.00	2.9	1.1	I	
pf2140043	18-Aug-2001	52140.1477	0.0036	197275	910	0.671	1.00	2.9	1.1	I	
pf2140046	18-Aug-2001	52140.1791	0.0206	163750	1004	0.727	1.00	3.2	1.1	I	

continued on next page

Table C.5: *continued*: MOA J005018.4−723855 V_J filter, image subtraction photometry

Image name	UTC	Mean date HJD−2400000.0	Orbital phase	Flux difference	δ Flux difference	Norm. light	Quality factor	Seeing (arc sec)	Airmass (χ)	LC analysis	Comment
pf2140047	18-Aug-2001	52140.2092	0.0370	126298	1032	0.790	1.00	3.1	1.2	I	
pf2140052	18-Aug-2001	52140.2393	0.0533	84458	1004	0.859	1.00	2.7	1.2	I	
pf2196016	13-Oct-2001	52196.0491	0.3869	24258	647	0.960	0.91	3.9	1.1	I	
pf2196018	13-Oct-2001	52196.0646	0.3953	16823	526	0.972	0.40	4.4	1.2	I	
pf2196020	13-Oct-2001	52196.0797	0.4035	40499	816	0.933	0.90	4.7	1.2	I	
pf2406015	11-May-2002	52405.8619	0.4236	83794	275	0.860	0.94	2.3	2.1	I	
pf2406018	11-May-2002	52405.8956	0.4419	119765	434	0.801	0.99	2.8	2.2	I	
pf2406023	11-May-2002	52405.9552	0.4743	143403	918	0.761	1.00	2.9	2.2	I	
pf2406026	11-May-2002	52405.9847	0.4904	140752	736	0.766	1.00	3.0	2.1	I	
pf2406029	11-May-2002	52406.0152	0.5070	125148	979	0.792	1.00	3.2	2.1	I	
pf2406032	11-May-2002	52406.0549	0.5285	98713	1015	0.836	0.99	3.1	1.9	I	
pf2406035	11-May-2002	52406.0932	0.5493	61964	610	0.897	0.98	3.2	1.8	I	
pf2406038	11-May-2002	52406.1252	0.5668	31233	1013	0.948	0.94	3.4	1.7	I	
pf2406041	11-May-2002	52406.1546	0.5827	9673	999	0.984	0.85	3.6	1.6	I	
pf2406044	11-May-2002	52406.1887	0.6013	−439	1255	1.001	0.04	4.5	1.5	I	
pf2406047	11-May-2002	52406.2183	0.6174	−5987	1395	1.010	0.56	4.9	1.4	I	
pf2406050	11-May-2002	52406.2478	0.6334	−14738	1203	1.025	0.85	4.5	1.3	I	
pf2408015	13-May-2002	52407.8109	0.4829	98976	1548	0.834	0.73	3.8	2.1	X	
pf2408018	13-May-2002	52407.8517	0.5051	137157	1135	0.772	0.99	3.8	2.2	I	
pf2408021	13-May-2002	52407.8856	0.5235	112324	1172	0.813	0.99	3.8	2.2	I	
pf2408024	13-May-2002	52407.9182	0.5413	82990	1307	0.862	0.98	4.3	2.2	I	
pf2408027	13-May-2002	52407.9504	0.5588	46143	1231	0.923	0.98	4.0	2.2	I	
pf2408030	13-May-2002	52407.9795	0.5746	20229	1352	0.966	0.92	4.3	2.1	I	
pf2408033	13-May-2002	52408.0088	0.5905	1945	1336	0.997	0.13	4.1	2.1	I	
pf2408036	13-May-2002	52408.0379	0.6063	−2378	1233	1.004	0.39	3.8	2.0	I	
pf2408039	13-May-2002	52408.0670	0.6222	−4241	1179	1.007	0.59	3.5	1.9	I	
pf2408042	13-May-2002	52408.0971	0.6385	−9318	1182	1.016	0.74	3.4	1.8	I	
pf2408045	13-May-2002	52408.1278	0.6552	−17572	1205	1.029	0.93	3.5	1.6	I	

continued on next page

Table C.5: *continued*: MOA J005018.4−723855 V_J filter, image subtraction photometry

Image name	UTC	Mean date HJD−2400000.0	Orbital phase	Flux difference	δ Flux difference	Norm. light	Quality factor	Seeing (arc sec)	Airmass (χ)	LC analysis	Comment
pf2408048	13-May-2002	52408.1572	0.6712	−27998	1208	1.047	0.95	3.5	1.5	I	
pf2408051	13-May-2002	52408.1863	0.6870	−43151	960	1.072	0.98	3.6	1.5	I	
pf2408054	13-May-2002	52408.2174	0.7039	−38269	819	1.064	0.93	3.7	1.4	I	
pf2408057	13-May-2002	52408.2468	0.7198	−39953	585	1.067	0.95	3.5	1.3	I	
pf2408059	13-May-2002	52408.2631	0.7287	−31729	331	1.053	0.77	2.6	1.2	I	
pf2409015	14-May-2002	52408.8134	0.0278	143932	1056	0.760	1.00	3.6	2.1	I	
pf2409018	14-May-2002	52408.8425	0.0437	106470	1118	0.823	0.99	3.5	2.2	I	
pf2409021	14-May-2002	52408.8756	0.0616	71628	1159	0.881	0.99	3.7	2.2	I	
pf2409024	14-May-2002	52408.9064	0.0784	45094	1250	0.925	0.97	4.0	2.1	I	
pf2464014	08-Jul-2002	52463.8447	0.9383	173638	530	0.711	1.00	2.9	2.1	I	
pf2464016	08-Jul-2002	52463.8598	0.9465	189270	693	0.685	1.00	3.9	2.1	I	
pf2464017	08-Jul-2002	52463.8907	0.9633	321752	550	0.461	0.91	3.4	2.0	X	
pf2464020	08-Jul-2002	52464.1232	0.0896	8834	1460	0.985	0.42	5.1	1.9	I	
pf2464022	08-Jul-2002	52464.1391	0.0983	6893	1568	0.989	0.63	5.8	1.9	I	
pf2466014	10-Jul-2002	52465.9092	0.0603	73580	838	0.877	0.99	2.8	1.9	I	
pf2466016	10-Jul-2002	52465.9348	0.0742	46971	990	0.922	0.99	3.0	1.8	I	
pf2466019	10-Jul-2002	52465.9640	0.0901	22051	1016	0.963	0.96	3.2	1.7	I	
pf2466022	10-Jul-2002	52465.9932	0.1060	2465	1032	0.996	0.34	3.1	1.6	I	
pf2466025	10-Jul-2002	52466.0229	0.1222	−8157	1077	1.014	0.89	4.5	1.5	I	
pf2466028	10-Jul-2002	52466.0521	0.1380	−15121	1101	1.025	0.93	3.4	1.4	I	
pf2466031	10-Jul-2002	52466.0815	0.1540	−22644	1308	1.038	0.90	5.2	1.3	I	
pf2466034	10-Jul-2002	52466.1180	0.1738	−25649	1092	1.043	0.98	3.3	1.2	I	
pf2466037	10-Jul-2002	52466.1479	0.1901	−33281	1207	1.055	0.98	4.1	1.2	I	
pf2466046	10-Jul-2002	52466.2379	0.2390	−46484	1185	1.077	0.99	3.7	1.1	I	
pf2466049	10-Jul-2002	52466.2671	0.2549	−46052	1145	1.077	0.98	5.2	1.1	I	
pf2466052	10-Jul-2002	52466.2962	0.2707	−34722	1237	1.058	0.83	4.2	1.1	I	
pf2467015	11-Jul-2002	52466.8148	0.5526	36794	1163	0.939	0.77	4.6	2.2	I	
pf2467018	11-Jul-2002	52466.8440	0.5684	28304	997	0.953	0.92	4.2	2.1	I	

continued on next page

Table C.5: *continued*: MOA J005018.4−723855 V_J filter, image subtraction photometry

Image name	UTC	Mean date HJD−2400000.0	Orbital phase	Flux difference	δ Flux difference	Norm. light	Quality factor	Seeing (arc sec)	Airmass (χ)	LC analysis	Comment
pf2467021	11-Jul-2002	52466.8754	0.5855	7556	1420	0.987	0.62	4.8	2.0	I	
pf2467024	11-Jul-2002	52466.9049	0.6015	4579	1756	0.992	0.45	6.3	1.9	I	
pf2467030	11-Jul-2002	52466.9648	0.6341	−9375	1002	1.016	0.58	5.4	1.6	I	
pf2467032	11-Jul-2002	52466.9980	0.6521	−27181	924	1.045	0.82	5.6	1.5	I	
pf2467043	11-Jul-2002	52467.1635	0.7421	−29509	1541	1.049	0.83	6.0	1.2	I	

C.2.3 MOA J005018.4−723855 I_C, image subtraction photometry

Table C.6: MOA J005018.4−723855 I_C filter, image subtraction photometry.

Image name	UTC	Mean date HJD−2400000..0	Orbital phase	Flux difference	δ Flux difference	Norm. light	Quality factor	Seeing (arc sec)	Airmass (χ)	LC analysis	Comment
pf1814029	26-Sep-2000	51814.1073	0.7952	−9190	414	1.041	0.86	3.5	1.2	I	
pf1814032	26-Sep-2000	51814.1387	0.8122	−8245	426	1.037	0.84	3.6	1.2	I	
pf1814035	26-Sep-2000	51814.1730	0.8309	−5173	520	1.023	0.70	4.2	1.2	I	
pf1814037	26-Sep-2000	51814.1910	0.8406	−3556	476	1.016	0.64	4.0	1.3	I	
pf1814039	26-Sep-2000	51814.2123	0.8522	−1538	469	1.007	0.35	3.5	1.3	I	
pf1815015	27-Sep-2000	51814.9240	0.2391	19172	395	1.086	0.95	2.6	1.2	I	
pf1815018	27-Sep-2000	51814.9532	0.2549	18703	416	1.084	0.97	3.0	1.2	I	
pf1815019	27-Sep-2000	51814.9589	0.2580	17083	498	1.076	0.95	4.1	1.2	I	
pf1815020	27-Sep-2000	51814.9642	0.2609	19390	444	1.087	0.98	3.6	1.2	I	
pf1815028	27-Sep-2000	51815.0685	0.3176	−9635	442	1.043	0.91	3.7	1.1	I	
pf1815029	27-Sep-2000	51815.0737	0.3204	−9960	435	1.045	0.91	3.5	1.1	I	
pf1815030	27-Sep-2000	51815.0790	0.3233	−7649	440	1.034	0.79	3.5	1.1	I	
pf1815038	27-Sep-2000	51815.1843	0.3805	4444	521	0.980	0.54	4.4	1.2	I	
pf1815039	27-Sep-2000	51815.1895	0.3833	4887	551	0.978	0.70	4.8	1.3	I	
pf1815040	27-Sep-2000	51815.1947	0.3862	5227	562	0.977	0.69	5.0	1.3	I	
pf1818013	30-Sep-2000	51817.9271	0.8713	8691	462	0.961	0.90	4.4	1.2	I	
pf1818015	30-Sep-2000	51817.9432	0.8800	13353	489	0.940	0.76	5.0	1.2	I	
pf1818018	30-Sep-2000	51817.9726	0.8960	24211	472	0.892	0.97	4.8	1.2	I	
pf1818020	30-Sep-2000	51817.9917	0.9064	32574	437	0.854	0.99	4.4	1.1	I	
pf1818021	30-Sep-2000	51817.9973	0.9094	34511	431	0.846	0.99	4.3	1.1	I	
pf1818027	30-Sep-2000	51818.1019	0.9663	79252	428	0.645	1.00	4.5	1.2	I	
pf1818028	30-Sep-2000	51818.1073	0.9692	79719	432	0.643	1.00	4.6	1.2	I	
pf1847015	29-Oct-2000	51846.9345	0.6373	15317	521	1.069	0.94	4.8	1.1	I	
pf1847019	29-Oct-2000	51846.9892	0.6670	13365	583	1.060	0.90	5.7	1.1	I	
pf1847020	29-Oct-2000	51846.9970	0.6712	13024	601	1.058	0.87	6.0	1.1	I	
pf1847023	29-Oct-2000	51847.0217	0.6847	10701	624	1.048	0.84	6.3	1.2	I	

continued on next page

Table C.6: *continued*: MOA J005018.4−723855 I_C filter, image subtraction photometry

Image name	UTC	Mean date HJD−2400000.0	Orbital phase	Flux difference	δ Flux difference	Norm. light	Quality factor	Seeing (arc sec)	Airmass (χ)	LC analysis	Comment
pf1847024	29-Oct-2000	51847.0329	0.6908	15391	588	1.069	0.92	5.7	1.2	I	
pf1847025	29-Oct-2000	51847.0392	0.6942	13356	589	1.060	0.88	5.8	1.2	I	
pf1847026	29-Oct-2000	51847.0445	0.6971	10876	573	1.049	0.89	5.7	1.2	I	
pf1847027	29-Oct-2000	51847.0501	0.7001	13724	613	1.061	0.91	6.3	1.2	I	
pf1847028	29-Oct-2000	51847.0557	0.7032	15981	586	1.072	0.91	5.8	1.2	I	
pf1847029	29-Oct-2000	51847.0618	0.7065	16185	600	1.073	0.91	6.0	1.2	I	
pf1847030	29-Oct-2000	51847.0677	0.7097	12795	624	1.057	0.86	6.4	1.2	I	
pf1847031	29-Oct-2000	51847.0729	0.7125	10302	681	1.046	0.76	6.3	1.2	X	
pf1847032	29-Oct-2000	51847.0807	0.7167	−7750	656	1.035	0.71	6.7	1.3	X	
pf1847033	29-Oct-2000	51847.0875	0.7204	−5110	672	1.023	0.47	6.1	1.3	X	
pf1847034	29-Oct-2000	51847.0933	0.7236	−5223	664	1.023	0.46	6.4	1.3	X	
pf1847035	29-Oct-2000	51847.0985	0.7264	−5830	649	1.026	0.56	6.3	1.3	X	
pf1847036	29-Oct-2000	51847.1041	0.7295	12537	626	1.056	0.87	6.3	1.3	I	
pf1871018	22-Nov-2000	51871.1290	0.7874	12040	474	1.054	0.87	3.7	1.5	I	
pf1871019	22-Nov-2000	51871.1344	0.7903	10958	476	1.049	0.92	3.8	1.5	I	
pf1871020	22-Nov-2000	51871.1399	0.7933	10613	496	1.048	0.86	3.7	1.5	I	
pf1871021	22-Nov-2000	51871.1460	0.7966	−7951	589	1.036	0.74	3.9	1.5	I	
pf1873014	24-Nov-2000	51872.9336	0.7682	14612	450	1.065	0.97	3.9	1.1	I	
pf1873017	24-Nov-2000	51872.9634	0.7845	12372	442	1.055	0.95	3.5	1.2	I	
pf1873018	24-Nov-2000	51872.9687	0.7873	11456	496	1.051	0.94	4.3	1.2	I	
pf1873020	24-Nov-2000	51872.9838	0.7955	10413	494	1.047	0.92	4.4	1.2	I	
pf1873021	24-Nov-2000	51872.9898	0.7988	11393	467	1.051	0.92	3.9	1.2	I	
pf1873025	24-Nov-2000	51873.0412	0.8267	−6028	463	1.027	0.73	4.9	1.3	I	
pf1873026	24-Nov-2000	51873.0466	0.8296	−4091	507	1.018	0.62	4.7	1.3	I	
pf1873028	24-Nov-2000	51873.0710	0.8429	−1490	463	1.007	0.33	4.3	1.3	I	
pf1873029	24-Nov-2000	51873.0762	0.8457	−590	413	1.003	0.15	3.7	1.4	I	
pf1873032	24-Nov-2000	51873.1008	0.8591	4001	434	0.982	0.58	3.9	1.4	I	
pf1873033	24-Nov-2000	51873.1061	0.8620	4737	445	0.979	0.75	4.0	1.4	I	

continued on next page

Table C.6: *continued*: MOA J005018.4−723855 I_C filter, image subtraction photometry

Image name	UTC	Mean date HJD−2400000.0	Orbital phase	Flux difference	δ Flux difference	Norm. light	Quality factor	Seeing (arc sec)	Airmass (χ)	LC analysis	Comment
pf1957016	16-Feb-2001	51957.0343	0.4784	58575	657	0.738	0.97	6.5	2.0	I	
pf1957017	16-Feb-2001	51957.0397	0.4813	54524	715	0.753	0.95	6.8	2.0	X	
pf1958017	17-Feb-2001	51957.9348	0.9678	75453	603	0.659	0.97	6.6	2.0	X	
pf1958019	17-Feb-2001	51957.9645	0.9840	74791	624	0.662	0.95	7.0	2.1	X	
pf1960014	19-Feb-2001	51959.8983	0.0350	44566	404	0.800	0.99	3.6	1.5	I	
pf1960017	19-Feb-2001	51959.9265	0.0503	28435	449	0.873	0.98	4.1	1.6	I	
pf1988040	20-Mar-2001	51988.9606	0.8308	−1224	384	1.005	0.20	2.5	2.0	I	
pf1988041	20-Mar-2001	51988.9657	0.8336	−995	392	1.004	0.28	2.5	2.0	I	
pf1988044	20-Mar-2001	51988.9919	0.8478	844	417	0.996	0.21	2.8	2.1	I	
pf1988045	20-Mar-2001	51988.9969	0.8506	437	436	0.998	0.04	3.0	2.1	I	
pf1989026	21-Mar-2001	51989.0208	0.8636	2011	495	0.991	0.31	3.7	2.2	I	
pf1989025	21-Mar-2001	51989.0259	0.8663	5621	474	0.975	0.69	3.4	2.2	I	
pf1989027	21-Mar-2001	51989.0375	0.8726	6038	520	0.973	0.73	3.7	2.2	I	
pf1989030	21-Mar-2001	51989.0617	0.8858	16182	566	0.928	0.92	4.5	2.2	I	
pf1989031	21-Mar-2001	51989.0667	0.8885	16247	571	0.927	0.90	4.8	2.2	I	
pf1989033	21-Mar-2001	51989.0898	0.9011	25453	705	0.886	0.90	5.1	2.2	I	
pf1989035	21-Mar-2001	51989.0949	0.9038	28483	824	0.872	0.86	5.6	2.2	I	
pf1989038	21-Mar-2001	51989.1199	0.9174	44852	655	0.799	0.98	5.1	2.2	I	
pf1989046	21-Mar-2001	51989.1792	0.9496	72020	356	0.678	1.00	3.1	2.0	I	
pf1989047	21-Mar-2001	51989.1842	0.9524	74479	383	0.667	1.00	3.3	2.0	I	
pf1989050	21-Mar-2001	51989.2080	0.9653	83477	367	0.626	1.00	3.1	1.9	I	
pf1989051	21-Mar-2001	51989.2131	0.9681	81288	361	0.636	1.00	3.0	1.9	I	
pf2017016	17-Apr-2001	52016.8974	0.0150	65286	549	0.708	0.99	2.3	2.1	I	
pf2023037	23-Apr-2001	52023.1572	0.4173	29039	883	0.870	0.99	3.3	1.7	I	
pf2023039	23-Apr-2001	52023.1876	0.4338	39278	450	0.824	0.99	3.5	1.6	I	
pf2023042	23-Apr-2001	52023.2226	0.4528	46971	419	0.790	0.99	3.1	1.5	I	
pf2023045	23-Apr-2001	52023.2543	0.4700	51922	468	0.768	1.00	3.6	1.4	I	
pf2086014	25-Jun-2001	52085.9258	0.5331	27711	816	0.876	0.99	4.0	1.9	I	

continued on next page

Table C.6: *continued*: MOA J005018.4−723855 I_C filter, image subtraction photometry

Image name	UTC	Mean date HJD−2400000.0	Orbital phase	Flux difference	δ Flux difference	Norm. light	Quality factor	Seeing (arc sec)	Airmass (χ)	LC analysis	Comment
pf2086017	25-Jun-2001	52085.9558	0.5494	14840	870	0.934	0.94	4.1	1.8	I	
pf2086020	25-Jun-2001	52085.9850	0.5652	5326	869	0.976	0.67	3.7	1.7	I	
pf2086023	25-Jun-2001	52086.0177	0.5830	152	837	0.999	0.03	3.4	1.6	I	
pf2086026	25-Jun-2001	52086.0471	0.5990	−5123	946	1.023	0.72	4.6	1.5	I	
pf2086029	25-Jun-2001	52086.0764	0.6149	−7612	967	1.034	0.75	4.4	1.4	I	
pf2086032	25-Jun-2001	52086.1062	0.6311	13077	865	1.059	0.91	3.7	1.4	I	
pf2086040	25-Jun-2001	52086.1763	0.6692	21236	947	1.095	0.97	4.0	1.2	I	
pf2086043	25-Jun-2001	52086.2426	0.7052	19252	16	1.086	0.95	6.5	1.2	I	
pf2138014	16-Aug-2001	52137.8362	0.7472	21086	696	1.094	0.98	2.3	1.2	I	R
pf2138028	16-Aug-2001	52138.0641	0.8711	5107	655	0.977	0.93	2.2	1.2	I	R,A
pf2138031	16-Aug-2001	52138.0933	0.8870	16012	666	0.928	0.98	2.4	1.2	I	R
pf2138034	16-Aug-2001	52138.1271	0.9053	31513	682	0.859	0.99	2.6	1.1	I	
pf2138037	16-Aug-2001	52138.1647	0.9258	52348	658	0.766	0.99	2.9	1.1	I	
pf2138039	16-Aug-2001	52138.1848	0.9367	62706	698	0.719	1.00	3.1	1.1	I	
pf2138042	16-Aug-2001	52138.2149	0.9531	72853	681	0.674	1.00	2.8	1.2	I	
pf2138045	16-Aug-2001	52138.2443	0.9690	80102	627	0.641	1.00	3.0	1.2	I	
pf2138047	16-Aug-2001	52138.2592	0.9771	81829	647	0.634	1.00	3.3	1.2	I	
pf2140024	18-Aug-2001	52139.9186	0.8790	10597	508	0.953	0.76	2.7	1.5	I	
pf2140027	18-Aug-2001	52139.9480	0.8950	24908	569	0.888	0.97	2.6	1.4	I	
pf2140033	18-Aug-2001	52140.0296	0.9394	63862	726	0.714	1.00	3.0	1.2	I	
pf2140039	18-Aug-2001	52140.1102	0.9832	79632	570	0.644	1.00	2.5	1.1	I	
pf2140042	18-Aug-2001	52140.1406	0.9997	73574	660	0.671	1.00	3.0	1.1	I	
pf2140045	18-Aug-2001	52140.1719	0.0167	60596	738	0.729	1.00	3.2	1.1	I	
pf2140048	18-Aug-2001	52140.2020	0.0331	48551	704	0.783	1.00	3.0	1.1	I	
pf2140051	18-Aug-2001	52140.2321	0.0494	32309	681	0.855	0.99	3.4	1.2	I	
pf2140054	18-Aug-2001	52140.2652	0.0674	17027	871	0.924	0.97	3.5	1.2	I	
pf2196014	13-Oct-2001	52196.0226	0.3725	4617	545	0.979	0.19	3.9	1.1	I	
pf2196017	13-Oct-2001	52196.0574	0.3914	512	643	0.997	0.02	4.6	1.2	X	

continued on next page

Table C.6: *continued*: MOA J005018.4−723855 I_C filter, image subtraction photometry

Image name	UTC	Mean date HJD−2400000.0	Orbital phase	Flux difference	δ Flux difference	Norm. light	Quality factor	Seeing (arc sec)	Airmass (χ)	LC analysis	Comment
pf2406020	11-May-2002	52405.9207	0.4556	46845	642	0.790	0.99	3.8	2.2	I	
pf2406022	11-May-2002	52405.9480	0.4704	49333	773	0.779	0.99	3.6	2.2	I	
pf2406025	11-May-2002	52405.9776	0.4865	50473	707	0.774	0.96	4.0	2.2	I	
pf2406028	11-May-2002	52406.0081	0.5031	45252	790	0.797	0.99	3.5	2.1	I	
pf2406031	11-May-2002	52406.0477	0.5246	38090	757	0.829	0.98	3.4	2.0	I	
pf2406037	11-May-2002	52406.1181	0.5629	5693	730	0.975	0.48	3.2	1.7	I	
pf2406040	11-May-2002	52406.1475	0.5789	314	838	0.999	0.03	3.0	1.6	I	
pf2406043	11-May-2002	52406.1816	0.5974	−4317	986	1.019	0.50	2.7	1.5	I	
pf2406046	11-May-2002	52406.2111	0.6135	−6550	866	1.029	0.38	3.5	1.4	I	
pf2406049	11-May-2002	52406.2406	0.6295	−9169	815	1.041	0.70	3.7	1.3	I	
pf2408014	13-May-2002	52407.8037	0.4791	56641	383	0.746	0.98	4.5	2.0	I	
pf2408017	13-May-2002	52407.8445	0.5012	48203	993	0.784	0.99	2.8	2.1	I	
pf2408020	13-May-2002	52407.8784	0.5197	42833	984	0.808	0.99	4.8	2.2	I	
pf2408023	13-May-2002	52407.9111	0.5374	30693	46	0.863	0.97	4.6	2.2	I	
pf2408026	13-May-2002	52407.9432	0.5549	19428	971	0.913	0.95	2.9	2.2	I	
pf2408029	13-May-2002	52407.9723	0.5707	6135	920	0.973	0.77	3.1	2.2	I	
pf2408032	13-May-2002	52408.0017	0.5866	−717	45	1.003	0.12	3.2	2.1	I	
pf2408035	13-May-2002	52408.0307	0.6024	−4164	957	1.019	0.62	3.2	2.0	I	
pf2408038	13-May-2002	52408.0599	0.6183	−6283	948	1.028	0.74	3.4	1.9	I	
pf2408041	13-May-2002	52408.0899	0.6346	−6321	923	1.028	0.79	3.4	1.8	I	
pf2408044	13-May-2002	52408.1206	0.6513	10805	917	1.048	0.85	3.3	1.7	I	
pf2408047	13-May-2002	52408.1501	0.6673	13451	922	1.060	0.90	3.9	1.6	I	
pf2408050	13-May-2002	52408.1792	0.6831	14818	880	1.066	0.88	2.9	1.5	I	
pf2408053	13-May-2002	52408.2103	0.7000	21664	761	1.097	0.95	3.1	1.4	I	
pf2408056	13-May-2002	52408.2396	0.7160	21607	600	1.097	0.67	3.8	1.3	I	
pf2408058	13-May-2002	52408.2559	0.7248	21330	525	1.095	0.81	4.1	1.3	I	
pf2409014	14-May-2002	52408.8063	0.0240	53144	781	0.762	1.00	4.9	2.0	I	
pf2409017	14-May-2002	52408.8354	0.0398	38024	22	0.830	0.98	5.3	2.1	I	

continued on next page

Table C.6: *continued*: MOA J005018.4−723855 I_C filter, image subtraction photometry

Image name	UTC	Mean date HJD−2400000.0	Orbital phase	Flux difference	δ Flux difference	Norm. light	Quality factor	Seeing (arc sec)	Airmass (χ)	LC analysis	Comment
pf2409020	14-May-2002	52408.8684	0.0577	25887	24	0.884	0.98	5.5	2.2	I	
pf2409023	14-May-2002	52408.8992	0.0745	15429	93	0.930	0.89	5.5	2.2	X	
pf2464013	08-Jul-2002	52463.8376	0.9344	56059	857	0.749	0.99	2.8	2.1	I	
pf2464019	08-Jul-2002	52464.1160	0.0857	10130	147	0.955	0.85	3.0	1.3	I	
pf2464021	08-Jul-2002	52464.1319	0.0944	3779	94	0.983	0.55	2.9	1.2	I	
pf2466018	10-Jul-2002	52465.9568	0.0862	4712	840	0.979	0.62	3.2	1.7	I	
pf2466021	10-Jul-2002	52465.9861	0.1021	236	812	0.999	0.02	3.1	1.6	I	
pf2466024	10-Jul-2002	52466.0158	0.1183	−4898	792	1.022	0.75	3.4	1.5	I	
pf2466027	10-Jul-2002	52466.0450	0.1341	−7762	826	1.035	0.82	3.6	1.4	I	
pf2466030	10-Jul-2002	52466.0744	0.1501	14792	889	1.066	0.93	4.5	1.3	I	
pf2466033	10-Jul-2002	52466.1109	0.1700	10665	881	1.048	0.93	4.6	1.3	I	
pf2466036	10-Jul-2002	52466.1407	0.1862	19119	859	1.086	0.95	4.1	1.2	I	
pf2466039	10-Jul-2002	52466.1698	0.2020	21138	932	1.095	0.96	5.8	1.2	I	
pf2466045	10-Jul-2002	52466.2308	0.2351	21243	808	1.095	0.95	4.2	1.1	I	
pf2466048	10-Jul-2002	52466.2599	0.2510	22166	823	1.099	0.95	4.6	1.1	I	
pf2467014	11-Jul-2002	52466.8077	0.5487	18796	937	0.916	0.86	4.6	2.2	I	
pf2467017	11-Jul-2002	52466.8369	0.5645	3533	961	0.984	0.28	4.5	2.1	I	
pf2467020	11-Jul-2002	52466.8682	0.5816	−165	135	1.001	0.02	4.3	2.0	I	
pf2467023	11-Jul-2002	52466.8977	0.5976	−2859	322	1.013	0.31	4.8	1.9	I	
pf2467029	11-Jul-2002	52466.9576	0.6302	−8036	266	1.036	0.26	4.5	1.7	I	
pf2467042	11-Jul-2002	52467.1563	0.7382	12631	164	1.057	0.82	4.0	1.2	I	

C.3 MOA J005623.5−722123 image subtraction photometry

C.3.1 MOA J005623.5−722123 u, image subtraction photometry

Table C.7: MOA J005623.5−722123 u filter, image subtraction photometry.

Image name	UTC	Mean date HJD−2400000.0	Orbital phase	Flux difference	δ Flux difference	Norm. light	Quality factor	Seeing (arc sec)	Airmass (χ)	LC analysis	Comment
pf1814015	26-Sep-2000	51813.9024	0.9180	10662	615	0.934	0.90	5.2	1.3	I	
pf1814018	26-Sep-2000	51813.9511	0.9389	21835	575	0.865	0.99	4.7	1.2	I	
pf1814024	26-Sep-2000	51814.0133	0.9657	42254	548	0.739	1.00	4.8	1.1	I	
pf1817017	29-Sep-2000	51816.9903	0.2489	−1770	883	1.011	0.34	6.9	1.1	I	
pf1817025	29-Sep-2000	51817.0886	0.2913	−1270	711	1.008	0.34	6.1	1.1	I	
pf1817026	29-Sep-2000	51817.1055	0.2986	−1602	630	1.010	0.40	6.2	1.2	I	
pf1817027	29-Sep-2000	51817.1203	0.3050	1804	474	0.989	0.20	4.8	1.2	I	
pf1843013	25-Oct-2000	51843.0780	0.4934	64969	634	0.599	0.99	6.6	1.2	I	
pf1843014	25-Oct-2000	51843.0925	0.4996	66293	539	0.590	1.00	6.0	1.2	I	
pf1843020	25-Oct-2000	51843.1498	0.5243	66000	484	0.592	1.00	4.9	1.3	I	
pf1844013	26-Oct-2000	51843.9472	0.8680	2676	573	0.983	0.57	5.1	1.1	I	
pf1844014	26-Oct-2000	51843.9617	0.8743	3526	585	0.978	0.81	4.4	1.1	I	
pf1844019	26-Oct-2000	51844.0074	0.8940	6050	445	0.963	0.87	3.9	1.1	I	
pf1844020	26-Oct-2000	51844.0219	0.9002	5815	443	0.964	0.02	4.4	1.1	I	
pf1844025	26-Oct-2000	51844.0661	0.9193	8862	385	0.945	0.88	4.6	1.2	I	
pf1844026	26-Oct-2000	51844.0806	0.9255	11649	408	0.928	0.95	3.9	1.2	I	
pf1874013	25-Nov-2000	51873.9438	0.7973	−1956	627	1.012	0.62	4.8	1.1	I	
pf1874016	25-Nov-2000	51873.9771	0.8116	−1484	675	1.009	0.53	5.4	1.2	I	
pf1874019	25-Nov-2000	51874.0252	0.8324	−211	676	1.001	0.09	5.8	1.2	I	
pf1874022	25-Nov-2000	51874.0573	0.8462	892	703	0.994	0.18	6.3	1.3	I	
pf1874025	25-Nov-2000	51874.0918	0.8611	889	735	0.994	0.14	6.4	1.2	X	
pf1875028	26-Nov-2000	51874.9589	0.2349	−1329	503	1.008	0.59	3.4	1.2	I	
pf1875029	26-Nov-2000	51874.9735	0.2411	−2483	477	1.015	0.64	4.0	1.2	I	
pf1875030	26-Nov-2000	51874.9886	0.2477	−1465	504	1.009	0.50	4.0	1.2	I	

continued on next page

Table C.7: *continued*: MOA J005623.5−722123 u filter, image subtraction photometry

Image name	UTC	Mean date HJD−2400000.0	Orbital phase	Flux difference	δ Flux difference	Norm. light	Quality factor	Seeing (arc sec)	Airmass (χ)	LC analysis	Comment
pf1875035	26-Nov-2000	51875.0323	0.2665	−1330	572	1.008	0.28	5.3	1.3	I	
pf1875038	26-Nov-2000	51875.0897	0.2912	−2648	448	1.017	0.31	6.1	1.4	X	
pf1933019	23-Jan-2001	51933.0514	0.2742	−8393	846	1.054	0.68	6.2	1.8	X	
pf1933020	23-Jan-2001	51933.0666	0.2807	−6403	709	1.041	0.71	6.1	1.9	X	
pf1933021	23-Jan-2001	51933.1218	0.3045	−5339	601	1.034	0.69	6.3	2.0	X	
pf1933022	23-Jan-2001	51933.1368	0.3110	−1704	358	1.011	0.21	6.1	2.1	I	
pf1959015	18-Feb-2001	51958.9122	0.4208	9138	567	0.944	0.90	5.2	1.5	I	
pf1959021	18-Feb-2001	51959.0053	0.4609	34751	411	0.785	1.00	4.1	1.9	I	
pf1959024	18-Feb-2001	51959.0348	0.4737	46142	417	0.715	0.98	4.4	2.0	I	
pf1959025	18-Feb-2001	51959.0534	0.4817	53172	424	0.671	0.99	5.1	2.0	I	
pf1959028	18-Feb-2001	51959.0883	0.4967	63566	371	0.607	1.00	4.6	2.2	I	
pf1959031	18-Feb-2001	51959.1198	0.5103	64740	343	0.600	1.00	4.1	2.2	I	
pf1959034	18-Feb-2001	51959.1485	0.5227	65342	360	0.596	1.00	4.3	2.2	I	
pf1959037	18-Feb-2001	51959.1782	0.5355	55646	348	0.656	1.00	3.8	2.2	I	
pf1962013	21-Feb-2001	51961.8975	0.7076	−157	464	1.001	0.07	3.2	1.5	I	
pf1962016	21-Feb-2001	51961.9283	0.7209	−928	471	1.006	0.31	3.7	1.6	I	
pf1962019	21-Feb-2001	51961.9797	0.7430	2295	311	0.986	0.31	4.7	1.8	I	
pf1962024	21-Feb-2001	51962.1498	0.8163	545	564	0.997	0.03	6.0	2.2	I	
pf1962027	21-Feb-2001	51962.1779	0.8284	2746	579	0.983	0.49	6.1	2.2	I	
pf1991014	22-Mar-2001	51990.9106	0.2130	146	433	0.999	0.00	3.9	1.9	I	
pf1991015	22-Mar-2001	51990.9249	0.2191	329	431	0.998	0.16	3.8	1.9	I	
pf1991020	22-Mar-2001	51990.9753	0.2408	−1474	390	1.009	0.38	3.9	2.1	I	
pf1991021	22-Mar-2001	51990.9896	0.2470	−422	382	1.003	0.22	3.3	2.1	I	
pf1991024	22-Mar-2001	51991.0200	0.2601	−738	379	1.005	0.05	3.2	2.2	I	R
pf1991025	22-Mar-2001	51991.0343	0.2663	−1441	367	1.009	0.45	3.0	2.2	I	R
pf1991028	22-Mar-2001	51991.0656	0.2797	−462	388	1.003	0.44	3.4	2.2	I	
pf1991029	22-Mar-2001	51991.0799	0.2859	−491	383	1.003	0.22	3.6	2.2	I	
pf1991032	22-Mar-2001	51991.1081	0.2981	821	409	0.995	0.16	3.6	2.2	I	

continued on next page

Table C.7: *continued*: MOA J005623.5−722123 u filter, image subtraction photometry

Image name	UTC	Mean date HJD−2400000.0	Orbital phase	Flux difference	δ Flux difference	Norm. light	Quality factor	Seeing (arc sec)	Airmass (χ)	LC analysis	Comment
pf1991037	22-Mar-2001	51991.1530	0.3174	1101	431	0.993	0.24	4.0	2.1	I	
pf2017024	17-Apr-2001	52017.1015	0.5019	63574	214	0.607	1.00	2.7	2.0	I	
pf2018014	18-Apr-2001	52017.8567	0.8274	1304	406	0.992	0.26	3.1	1.9	I	
pf2018015	18-Apr-2001	52017.8735	0.8346	1028	367	0.994	0.38	3.2	2.0	I	
pf2018022	18-Apr-2001	52017.9481	0.8668	2757	409	0.983	0.60	3.7	2.2	I	
pf2018023	18-Apr-2001	52017.9673	0.8751	4613	425	0.971	0.77	4.1	2.2	I	
pf2018028	18-Apr-2001	52018.0257	0.9002	3210	410	0.980	0.59	3.7	2.2	I	
pf2018029	18-Apr-2001	52018.0459	0.9089	6361	434	0.961	0.88	4.1	2.2	I	
pf2018035	18-Apr-2001	52018.0968	0.9309	15413	428	0.905	0.96	4.1	2.0	I	
pf2018038	18-Apr-2001	52018.1314	0.9458	26147	469	0.838	0.99	4.7	1.9	I	
pf2018041	18-Apr-2001	52018.1631	0.9595	39065	541	0.759	0.99	5.8	1.8	I	
pf2045039	15-May-2001	52045.1861	0.6071	6494	657	0.960	0.85	5.3	1.4	I	
pf2045042	15-May-2001	52045.2213	0.6222	5311	795	0.967	0.71	6.4	1.4	I	
pf2083014	22-Jun-2001	52082.8107	0.8242	−785	543	1.005	0.17	6.3	2.2	X	
pf2083019	22-Jun-2001	52082.8722	0.8507	1955	520	0.988	0.38	5.9	2.1	I	
pf2083022	22-Jun-2001	52082.9020	0.8636	−2255	424	1.014	0.26	4.7	2.0	X	
pf2083025	22-Jun-2001	52082.9496	0.8841	4072	185	0.975	0.23	4.2	1.9	I	
pf2083028	22-Jun-2001	52082.9791	0.8968	4881	482	0.970	0.82	4.7	1.8	I	
pf2083031	22-Jun-2001	52083.0120	0.9110	9496	281	0.941	0.82	3.9	1.7	I	
pf2083034	22-Jun-2001	52083.0419	0.9238	4922	298	0.967	0.09	4.3	1.6	X	
pf2083036	22-Jun-2001	52083.0719	0.9368	26171	301	0.838	0.90	4.3	1.5	I	
pf2083040	22-Jun-2001	52083.1015	0.9495	30793	440	0.810	0.93	4.9	1.4	I	
pf2083043	22-Jun-2001	52083.1374	0.9650	44630	519	0.724	1.00	5.0	1.3	I	
pf2083046	22-Jun-2001	52083.1682	0.9783	55657	516	0.656	1.00	4.9	1.3	I	
pf2083049	22-Jun-2001	52083.1983	0.9913	65568	582	0.595	0.99	4.4	1.2	I	
pf2084013	23-Jun-2001	52083.8833	0.2865	−483	551	1.003	0.13	6.2	2.1	I	
pf2084016	23-Jun-2001	52083.9182	0.3016	−766	638	1.005	0.15	6.4	2.2	X	
pf2085013	24-Jun-2001	52084.8198	0.6902	−746	473	1.005	0.22	4.9	2.2	I	

continued on next page

Table C.7: *continued*: MOA J005623.5−722123 u filter, image subtraction photometry

Image name	UTC	Mean date HJD−2400000.0	Orbital phase	Flux difference	δ Flux difference	Norm. light	Quality factor	Seeing (arc sec)	Airmass (χ)	LC analysis	Comment
pf2085016	24-Jun-2001	52084.8507	0.7035	1529	509	0.991	0.08	5.6	2.2	I	
pf2085019	24-Jun-2001	52084.8806	0.7164	−181	560	1.001	0.09	6.1	2.1	I	
pf2085022	24-Jun-2001	52084.9150	0.7312	−4059	584	1.025	0.61	6.2	2.0	I	
pf2085028	24-Jun-2001	52084.9782	0.7585	−1576	496	1.010	0.52	4.4	1.8	I	
pf2085031	24-Jun-2001	52085.0078	0.7712	−1701	515	1.011	0.46	4.4	1.7	I	
pf2085034	24-Jun-2001	52085.0371	0.7838	−1944	542	1.012	0.62	4.6	1.6	I	
pf2085037	24-Jun-2001	52085.0664	0.7965	−1020	536	1.006	0.19	4.9	1.5	I	
pf2085040	24-Jun-2001	52085.0977	0.8100	−897	573	1.006	0.29	4.7	1.4	I	
pf2085043	24-Jun-2001	52085.1279	0.8230	−84	561	1.001	0.04	4.4	1.3	I	
pf2085046	24-Jun-2001	52085.1573	0.8356	1074	619	0.993	0.35	5.1	1.3	I	
pf2085049	24-Jun-2001	52085.1889	0.8493	1897	599	0.988	0.47	4.9	1.2	I	
pf2085052	24-Jun-2001	52085.2184	0.8620	1857	584	0.989	0.50	5.8	1.2	I	
pf2085055	24-Jun-2001	52085.2486	0.8750	3695	537	0.977	0.67	4.7	1.2	I	
pf2142013	20-Aug-2001	52141.8607	0.2762	−495	523	1.003	0.11	6.5	1.6	I	
pf2142016	20-Aug-2001	52141.8899	0.2888	1090	403	1.003	0.01	6.6	1.5	X	
pf2142019	20-Aug-2001	52141.9224	0.3028	−492	572	1.003	0.14	5.4	1.4	I	
pf2142022	20-Aug-2001	52141.9521	0.3156	−559	545	1.003	0.21	5.4	1.4	I	
pf2142025	20-Aug-2001	52141.9828	0.3289	−551	675	1.003	0.19	6.0	1.3	I	
pf2142028	20-Aug-2001	52142.0120	0.3414	417	648	0.997	0.09	5.5	1.2	I	
pf2142031	20-Aug-2001	52142.0607	0.3625	3251	664	0.980	0.43	5.7	1.2	I	
pf2142034	20-Aug-2001	52142.0917	0.3758	1777	561	0.989	0.55	4.4	1.2	I	
pf2142037	20-Aug-2001	52142.1214	0.3886	4668	568	0.971	0.78	4.4	1.1	I	
pf2142040	20-Aug-2001	52142.1602	0.4053	3965	560	0.975	0.85	4.3	1.1	I	
pf2142043	20-Aug-2001	52142.1923	0.4192	10302	568	0.936	0.95	4.6	1.1	I	
pf2142046	20-Aug-2001	52142.2221	0.4320	15416	525	0.905	0.98	4.1	1.2	I	
pf2142049	20-Aug-2001	52142.2514	0.4446	24229	516	0.850	0.99	4.3	1.2	I	
pf2170013	23-Aug-2001	52169.9538	0.3851	3203	698	0.980	0.62	6.1	1.2	I	
pf2170016	23-Aug-2001	52169.9831	0.3977	6546	747	0.960	0.75	6.7	1.2	I	

continued on next page

Table C.7: *continued*: MOA J005623.5−722123 u filter, image subtraction photometry

Image name	UTC	Mean date HJD−2400000.0	Orbital phase	Flux difference	δ Flux difference	Norm. light	Quality factor	Seeing (arc sec)	Airmass (χ)	LC analysis	Comment
pf2170019	23-Aug-2001	52170.0147	0.4113	7972	799	0.948	0.81	6.9	1.2	X	
pf2170022	23-Aug-2001	52170.0524	0.4276	12811	832	0.916	0.82	6.4	1.2	X	
pf2170025	23-Aug-2001	52170.0903	0.4439	17185	780	0.887	0.75	6.1	1.3	X	
pf2170028	23-Aug-2001	52170.1365	0.4638	40220	549	0.751	0.99	4.9	1.2	I	
pf2170029	23-Aug-2001	52170.1512	0.4702	43189	505	0.733	1.00	4.4	1.2	I	
pf2171013	18-Sep-2001	52170.8606	0.7759	−163	398	1.001	0.03	5.1	1.4	I	
pf2171016	18-Sep-2001	52170.8899	0.7885	−672	477	1.004	0.25	5.3	1.3	I	
pf2171019	18-Sep-2001	52170.9212	0.8020	−555	407	1.003	0.11	4.7	1.3	I	
pf2171022	18-Sep-2001	52170.9554	0.8168	−464	575	1.003	0.19	5.0	1.2	I	
pf2171025	18-Sep-2001	52170.9846	0.8294	757	591	0.995	0.21	5.0	1.2	I	
pf2171028	18-Sep-2001	52171.0141	0.8421	576	600	0.996	0.18	5.2	1.2	I	
pf2171031	18-Sep-2001	52171.0432	0.8546	2900	621	0.982	0.53	5.3	1.1	I	
pf2171034	18-Sep-2001	52171.0752	0.8684	2657	602	0.984	0.57	5.0	1.1	I	
pf2171037	18-Sep-2001	52171.1045	0.8811	3110	435	0.981	0.54	5.0	1.1	I	
pf2171040	18-Sep-2001	52171.1342	0.8938	6086	513	0.962	0.90	3.9	1.2	I	
pf2171043	18-Sep-2001	52171.1637	0.9066	7451	548	0.954	0.87	4.7	1.2	I	
pf2171046	18-Sep-2001	52171.1947	0.9199	10459	508	0.935	0.81	5.1	1.2	I	
pf2172013	19-Sep-2001	52171.8375	0.1970	702	366	0.996	0.11	3.6	1.5	I	
pf2172016	19-Sep-2001	52171.8670	0.2097	−1128	433	1.007	0.25	3.9	1.4	I	
pf2172019	19-Sep-2001	52171.8994	0.2237	−1656	382	1.010	0.63	3.2	1.3	I	
pf2172022	19-Sep-2001	52171.9286	0.2363	−1489	407	1.009	0.52	3.4	1.2	I	R
pf2172025	19-Sep-2001	52171.9587	0.2492	−1161	428	1.007	0.46	3.0	1.2	I	R
pf2172028	19-Sep-2001	52171.9879	0.2618	−2258	442	1.014	0.72	3.2	1.2	I	R
pf2172031	19-Sep-2001	52172.0171	0.2744	−3259	455	1.020	0.75	3.5	1.1	I	
pf2172034	19-Sep-2001	52172.0462	0.2870	−201	469	1.001	0.20	3.7	1.1	I	
pf2172037	19-Sep-2001	52172.0808	0.3018	−1333	449	1.008	0.55	3.0	1.1	I	R
pf2172040	19-Sep-2001	52172.1103	0.3146	−207	457	1.001	0.22	2.6	1.1	I	R
pf2172043	19-Sep-2001	52172.1397	0.3273	−141	443	1.001	0.01	2.9	1.2	I	R,A

continued on next page

Table C.7: *continued*: MOA J005623.5−722123 u filter, image subtraction photometry

Image name	UTC	Mean date HJD−2400000.0	Orbital phase	Flux difference	δ Flux difference	Norm. light	Quality factor	Seeing (arc sec)	Airmass (χ)	LC analysis	Comment
pf2172046	19-Sep-2001	52172.1688	0.3398	1015	403	0.994	0.38	3.1	1.2	I	R
pf2172049	19-Sep-2001	52172.1992	0.3529	1587	394	0.990	0.10	3.3	1.2	I	
pf2199013	16-Oct-2001	52198.8725	0.8498	1931	579	0.988	0.35	6.5	1.2	I	
pf2199016	16-Oct-2001	52198.9019	0.8625	3055	637	0.981	0.52	6.6	1.2	I	
pf2199019	16-Oct-2001	52198.9344	0.8764	3097	412	0.981	0.76	3.6	1.2	I	R
pf2199022	16-Oct-2001	52198.9639	0.8891	3702	485	0.977	0.90	3.2	1.1	I	R
pf2199025	16-Oct-2001	52198.9981	0.9039	6445	533	0.960	0.88	4.1	1.1	I	
pf2199028	16-Oct-2001	52199.0329	0.9189	7842	429	0.952	0.90	4.6	1.1	I	
pf2199031	16-Oct-2001	52199.0627	0.9317	18080	543	0.888	0.96	5.7	1.2	I	
pf2199034	16-Oct-2001	52199.0919	0.9443	26447	637	0.837	0.98	5.8	1.2	I	
pf2199037	16-Oct-2001	52199.1210	0.9569	40193	255	0.752	0.97	5.4	1.2	I	
pf2199040	16-Oct-2001	52199.1501	0.9694	51347	292	0.683	0.99	5.4	1.3	I	
pf2199043	16-Oct-2001	52199.1792	0.9820	59758	518	0.631	0.99	6.6	1.3	I	
pf2407013	12-May-2002	52406.7959	0.4700	44763	384	0.723	0.99	4.1	1.9	I	
pf2407016	12-May-2002	52406.8256	0.4828	55855	393	0.655	0.99	4.5	2.0	I	
pf2407019	12-May-2002	52406.8553	0.4956	65135	401	0.597	1.00	4.8	2.1	I	
pf2407022	12-May-2002	52406.8877	0.5096	66729	347	0.588	1.00	4.4	2.2	I	
pf2407025	12-May-2002	52407.0880	0.5959	13153	465	0.919	0.93	5.0	1.8	I	
pf2407028	12-May-2002	52407.1179	0.6088	7697	663	0.952	0.79	7.0	1.7	I	
pf2407031	12-May-2002	52407.1537	0.6242	5118	428	0.968	0.81	3.8	1.6	I	
pf2407034	12-May-2002	52407.1828	0.6368	6026	413	0.963	0.74	3.8	1.5	I	
pf2407037	12-May-2002	52407.2191	0.6524	2096	462	0.987	0.64	3.7	1.4	I	
pf2407040	12-May-2002	52407.2482	0.6649	1827	506	0.989	0.56	4.1	1.3	I	
pf2461016	05-Jul-2002	52460.9260	0.8014	1459	391	0.991	0.19	4.8	1.9	I	
pf2461019	05-Jul-2002	52460.9551	0.8140	2095	448	0.987	0.27	4.1	1.8	I	
pf2461022	05-Jul-2002	52460.9847	0.8267	2102	426	0.987	0.57	3.9	1.7	I	
pf2461025	05-Jul-2002	52461.0143	0.8395	4545	363	0.972	0.57	4.6	1.6	I	
pf2461028	05-Jul-2002	52461.0437	0.8521	4485	362	0.972	0.59	4.4	1.5	I	

continued on next page

Table C.7: *continued*: MOA J005623.5−722123 u filter, image subtraction photometry

Image name	UTC	Mean date HJD−2400000.0	Orbital phase	Flux difference	δ Flux difference	Norm. light	Quality factor	Seeing (arc sec)	Airmass (χ)	LC analysis	Comment
pf2461031	05-Jul-2002	52461.0730	0.8648	4436	436	0.973	0.76	4.8	1.4	I	
pf2461034	05-Jul-2002	52461.1031	0.8777	7981	571	0.951	0.94	4.9	1.3	I	
pf2461037	05-Jul-2002	52461.2273	0.9313	16697	599	0.897	0.97	5.1	1.1	I	
pf2461040	05-Jul-2002	52461.2565	0.9439	24745	551	0.847	0.99	5.3	1.1	I	
pf2462019	06-Jul-2002	52461.9179	0.2290	−142	591	1.001	0.09	6.5	1.9	I	
pf2462022	06-Jul-2002	52461.9470	0.2415	−694	620	1.004	0.17	6.1	1.8	I	
pf2462025	06-Jul-2002	52461.9763	0.2542	−1698	590	1.010	0.14	5.8	1.7	I	
pf2462028	06-Jul-2002	52462.0055	0.2667	−909	597	1.006	0.15	5.8	1.6	I	
pf2462031	06-Jul-2002	52462.0347	0.2793	−753	616	1.005	0.21	5.6	1.5	I	
pf2462034	06-Jul-2002	52462.0647	0.2922	−681	574	1.004	0.15	5.3	1.4	I	
pf2462037	06-Jul-2002	52462.0940	0.3048	−544	600	1.003	0.08	5.2	1.3	I	
pf2462040	06-Jul-2002	52462.1265	0.3189	−196	660	1.001	0.07	5.8	1.3	I	
pf2462043	06-Jul-2002	52462.1558	0.3315	1630	810	0.992	0.22	6.4	1.2	X	
pf2462046	06-Jul-2002	52462.1849	0.3441	1956	702	0.988	0.43	6.2	1.2	I	
pf2462049	06-Jul-2002	52462.2141	0.3566	2839	658	0.982	0.50	6.2	1.2	I	
pf2462052	06-Jul-2002	52462.2447	0.3698	1860	566	0.989	0.58	5.0	1.1	I	
pf2462055	06-Jul-2002	52462.2755	0.3831	6546	551	0.960	0.87	4.8	1.1	I	
pf2463015	07-Jul-2002	52462.7976	0.6081	7563	422	0.953	0.89	4.1	2.2	I	
pf2463018	07-Jul-2002	52462.8267	0.6207	6096	309	0.962	0.68	4.4	2.2	I	
pf2463027	07-Jul-2002	52462.9905	0.6913	2539	454	0.984	0.54	4.9	1.6	I	
pf2463030	07-Jul-2002	52463.0198	0.7039	989	469	0.994	0.20	4.7	1.5	I	
pf2463033	07-Jul-2002	52463.0488	0.7164	737	563	0.995	0.25	5.0	1.4	I	
pf2463036	07-Jul-2002	52463.0779	0.7289	1268	416	0.992	0.34	4.5	1.4	I	
pf2463039	07-Jul-2002	52463.1073	0.7416	−530	440	1.003	0.12	4.4	1.3	I	
pf2463042	07-Jul-2002	52463.1367	0.7543	904	233	0.994	0.04	3.8	1.2	I	
pf2463049	07-Jul-2002	52463.2899	0.8203	2077	557	0.987	0.43	3.5	1.1	I	
pf2465013	09-Jul-2002	52464.7935	0.4684	40459	368	0.750	1.00	4.2	2.2	I	
pf2465016	09-Jul-2002	52464.8227	0.4810	52693	362	0.674	1.00	4.4	2.2	I	

continued on next page

Table C.7: *continued*: MOA J005623.5−722123 u filter, image subtraction photometry

Image name	UTC	Mean date HJD−2400000.0	Orbital phase	Flux difference	δ Flux difference	Norm. light	Quality factor	Seeing (arc sec)	Airmass (χ)	LC analysis	Comment
pf2465019	09-Jul-2002	52464.8529	0.4940	59796	346	0.630	1.00	4.0	2.1	I	
pf2465022	09-Jul-2002	52464.8844	0.5076	64047	321	0.604	1.00	3.2	2.0	I	
pf2465025	09-Jul-2002	52464.9146	0.5206	64652	341	0.600	1.00	3.6	1.9	I	
pf2465028	09-Jul-2002	52464.9439	0.5332	56786	347	0.649	1.00	3.4	1.8	I	
pf2465031	09-Jul-2002	52464.9739	0.5462	46371	389	0.713	1.00	3.4	1.7	I	
pf2465034	09-Jul-2002	52465.0039	0.5591	32861	413	0.797	0.76	3.5	1.6	I	
pf2465037	09-Jul-2002	52465.0329	0.5716	25105	460	0.845	0.99	4.0	1.5	I	
pf2465040	09-Jul-2002	52465.0621	0.5842	17193	469	0.894	0.98	3.7	1.4	I	

C.3.2 MOA J005623.5−722123 V_J, image subtraction photometry

Table C.8: MOA J005623.5−722123 V_J filter, image subtraction photometry.

Image name	UTC	Mean date HJD−2400000.0	Orbital phase	Flux difference	δ Flux difference	Norm. light	Quality factor	Seeing (arc sec)	Airmass (χ)	LC analysis	Comment
pf1814017	26-Sep-2000	51813.9388	0.9337	55175	1349	0.897	1.00	3.8	1.2	I	
pf1814020	26-Sep-2000	51813.9730	0.9484	93076	2097	0.826	0.99	6.7	1.2	I	
pf1814025	26-Sep-2000	51814.0287	0.9724	154019	1189	0.711	1.00	3.6	1.1	I	
pf1817015	29-Sep-2000	51816.9682	0.2394	−5594	1767	1.010	0.68	5.3	1.2	I	
pf1817019	29-Sep-2000	51817.0203	0.2619	−870	2227	1.002	0.09	6.7	1.1	I	
pf1817020	29-Sep-2000	51817.0292	0.2657	−6329	2007	1.012	0.56	6.0	1.1	I	
pf1817021	29-Sep-2000	51817.0412	0.2709	−6381	2060	1.012	0.61	6.1	1.1	I	
pf1817030	29-Sep-2000	51817.1605	0.3223	1310	1022	0.998	0.18	3.9	1.2	I	
pf1817031	29-Sep-2000	51817.1736	0.3279	5632	792	0.989	0.23	4.7	1.2	I	
pf1817032	29-Sep-2000	51817.1847	0.3327	−2282	595	1.004	0.17	3.9	1.2	I	
pf1843017	26-Oct-2000	51843.1149	0.5093	218388	1677	0.591	1.00	5.8	1.3	I	
pf1843018	26-Oct-2000	51843.1236	0.5130	220886	1655	0.586	0.99	5.9	1.3	I	
pf1844017	26-Oct-2000	51843.9853	0.8845	16279	1256	0.969	0.97	3.6	1.1	I	
pf1844018	26-Oct-2000	51843.9957	0.8890	15325	1246	0.971	0.93	3.7	1.1	I	
pf1844023	26-Oct-2000	51844.0445	0.9100	22188	1001	0.958	0.97	2.7	1.2	I	
pf1844024	26-Oct-2000	51844.0533	0.9138	23547	959	0.956	0.94	3.0	1.2	I	
pf1844030	26-Oct-2000	51844.1306	0.9471	76523	675	0.857	1.00	3.1	1.3	I	
pf1874015	25-Nov-2000	51873.9653	0.8066	2076	1569	0.996	0.33	4.5	1.2	I	
pf1874018	25-Nov-2000	51874.0127	0.8270	−4926	1563	1.009	0.64	4.4	1.2	I	
pf1874021	25-Nov-2000	51874.0428	0.8400	4563	1598	0.991	0.63	4.7	1.3	I	
pf1874024	25-Nov-2000	51874.0801	0.8561	11503	1814	0.978	0.82	5.0	1.3	X	
pf1874027	25-Nov-2000	51874.1181	0.8725	6186	1619	0.988	0.48	5.8	1.5	I	
pf1875033	26-Nov-2000	51875.0119	0.2577	−6153	1199	1.012	0.77	3.2	1.2	I	
pf1875034	26-Nov-2000	51875.0206	0.2614	−6002	1292	1.011	0.70	3.8	1.2	I	
pf1875037	26-Nov-2000	51875.0749	0.2849	−1591	1632	1.003	0.18	5.5	1.4	I	
pf1875040	26-Nov-2000	51875.1076	0.2989	−11595	1403	1.021	0.30	8.3	1.4	X	

continued on next page

Table C.8: *continued*: MOA J005623.5−722123 V_J filter, image subtraction photometry

Image name	UTC	Mean date HJD−2400000.0	Orbital phase	Flux difference	δ Flux difference	Norm. light	Quality factor	Seeing (arc sec)	Airmass (χ)	LC analysis	Comment
pf1933013	23-Jan-2001	51932.9398	0.2261	4717	2318	0.991	0.45	6.9	1.4	I	
pf1933014	23-Jan-2001	51932.9516	0.2312	−11819	2150	1.022	0.86	6.3	1.4	I	
pf1933015	23-Jan-2001	51932.9659	0.2374	−10609	2258	1.020	0.73	6.6	1.5	I	
pf1933016	23-Jan-2001	51932.9758	0.2416	−5063	2141	1.009	0.35	6.9	1.5	I	
pf1959017	18-Feb-2001	51958.9287	0.4280	38688	1394	0.927	0.97	3.9	1.6	I	
pf1959030	18-Feb-2001	51959.1049	0.5039	210043	967	0.606	1.00	3.2	2.2	I	
pf1959033	18-Feb-2001	51959.1364	0.5175	208506	1061	0.609	1.00	3.7	2.2	I	
pf1959036	18-Feb-2001	51959.1650	0.5298	193031	915	0.638	1.00	2.8	2.2	I	
pf1959039	18-Feb-2001	51959.1948	0.5426	161352	1110	0.698	1.00	3.2	2.2	I	
pf1962015	21-Feb-2001	51961.9140	0.7147	1157	1098	0.998	0.25	2.8	1.6	I	
pf1962018	21-Feb-2001	51961.9449	0.7280	4468	755	0.992	0.34	4.4	1.7	I	
pf1962026	21-Feb-2001	51962.1663	0.8234	3564	1595	0.993	0.45	5.2	2.2	I	
pf1962029	21-Feb-2001	51962.1944	0.8356	7707	1608	0.986	0.75	4.8	2.2	I	
pf1991017	22-Mar-2001	51990.9414	0.2262	−12677	1144	1.024	0.31	2.9	2.0	I	
pf1991019	22-Mar-2001	51990.9632	0.2356	−2645	1169	1.005	0.56	3.2	2.0	I	
pf1991023	22-Mar-2001	51991.0061	0.2541	−2922	1079	1.005	0.48	2.8	2.2	I	
pf1991027	22-Mar-2001	51991.0508	0.2734	−4722	1011	1.009	0.66	2.4	2.2	I	R
pf1991031	22-Mar-2001	51991.0964	0.2930	295	1093	0.999	0.09	2.8	2.2	I	
pf1991034	22-Mar-2001	51991.1245	0.3052	−146	1110	1.000	0.02	2.8	2.2	I	
pf1991036	22-Mar-2001	51991.1382	0.3111	134	1192	1.000	0.09	3.2	2.1	I	
pf1991039	22-Mar-2001	51991.1694	0.3245	2213	1128	0.996	0.44	2.8	2.0	I	
pf1991041	22-Mar-2001	51991.1831	0.3304	4759	1133	0.991	0.70	2.9	2.0	I	
pf1991043	22-Mar-2001	51991.1980	0.3368	3787	1156	0.993	0.51	3.0	1.9	I	
pf1991045	22-Mar-2001	51991.2117	0.3427	7414	1103	0.986	0.87	2.6	1.9	I	
pf2017022	17-Apr-2001	52017.0753	0.4906	193020	799	0.638	1.00	2.2	2.1	I	R
pf2017023	17-Apr-2001	52017.0871	0.4957	203902	793	0.618	1.00	2.2	2.1	I	R
pf2018017	18-Apr-2001	52017.8951	0.8440	9886	1020	0.981	0.93	2.7	2.1	I	
pf2018019	18-Apr-2001	52017.9179	0.8538	10913	647	0.980	0.83	2.7	2.1	I	

continued on next page

Table C.8: *continued*: MOA J005623.5−722123 V_J filter, image subtraction photometry

Image name	UTC	Mean date HJD−2400000.0	Orbital phase	Flux difference	δ Flux difference	Norm. light	Quality factor	Seeing (arc sec)	Airmass (χ)	LC analysis	Comment
pf2018021	18-Apr-2001	52017.9359	0.8615	16122	1074	0.970	0.96	2.8	2.2	I	
pf2018025	18-Apr-2001	52017.9863	0.8833	18495	1147	0.965	0.98	3.0	2.2	I	
pf2018027	18-Apr-2001	52018.0123	0.8945	22428	1186	0.958	0.98	3.1	2.2	I	
pf2018031	18-Apr-2001	52018.0656	0.9175	31255	1184	0.941	0.94	3.0	2.1	I	
pf2018034	18-Apr-2001	52018.0814	0.9243	39737	1203	0.926	0.99	3.1	2.1	I	
pf2018037	18-Apr-2001	52018.1177	0.9399	73368	1390	0.862	1.00	4.1	2.0	I	
pf2018040	18-Apr-2001	52018.1505	0.9540	104167	1369	0.805	1.00	4.2	1.8	I	
pf2018043	18-Apr-2001	52018.1902	0.9712	155035	1235	0.709	1.00	5.2	1.7	I	
pf2045029	15-May-2001	52045.1047	0.5720	82234	1491	0.846	1.00	4.2	1.7	I	
pf2045031	15-May-2001	52045.1208	0.5789	63166	1408	0.882	1.00	3.9	1.7	I	
pf2045033	15-May-2001	52045.1369	0.5859	52547	1767	0.902	0.99	5.1	1.6	I	
pf2045035	15-May-2001	52045.1524	0.5926	39822	1757	0.925	0.98	5.0	1.6	I	
pf2045037	15-May-2001	52045.1681	0.5993	31417	1728	0.941	0.98	4.9	1.5	I	
pf2045041	15-May-2001	52045.2078	0.6164	18027	1756	0.966	0.93	4.8	1.4	I	
pf2045044	15-May-2001	52045.2407	0.6306	12432	1990	0.977	0.84	5.8	1.3	I	
pf2045046	15-May-2001	52045.2583	0.6382	15759	1769	0.970	0.92	5.0	1.3	I	
pf2045048	15-May-2001	52045.2731	0.6446	13006	1936	0.976	0.91	5.2	1.2	I	
pf2083015	22-Jun-2001	52082.8273	0.8314	4057	1668	0.992	0.47	5.4	2.2	I	
pf2083018	22-Jun-2001	52082.8600	0.8455	14438	1549	0.973	0.85	5.1	2.2	I	
pf2083024	22-Jun-2001	52082.9378	0.8790	15522	813	0.971	0.79	4.2	2.0	I	
pf2083027	22-Jun-2001	52082.9672	0.8917	17325	825	0.968	0.94	3.7	1.9	I	
pf2083030	22-Jun-2001	52083.0002	0.9059	22585	971	0.958	0.97	3.4	1.7	I	
pf2083033	22-Jun-2001	52083.0300	0.9188	36729	701	0.931	0.94	4.0	1.6	I	
pf2083037	22-Jun-2001	52083.0601	0.9317	54434	823	0.898	0.99	3.4	1.5	I	
pf2083039	22-Jun-2001	52083.0896	0.9445	83540	1279	0.843	1.00	4.3	1.4	I	
pf2083042	22-Jun-2001	52083.1256	0.9599	123220	1270	0.769	1.00	3.9	1.3	I	
pf2083045	22-Jun-2001	52083.1564	0.9732	159706	1281	0.701	1.00	4.2	1.3	I	
pf2083048	22-Jun-2001	52083.1865	0.9862	192006	1181	0.640	1.00	3.8	1.2	I	

continued on next page

Table C.8: *continued*: MOA J005623.5−722123 V_J filter, image subtraction photometry

Image name	UTC	Mean date HJD−2400000.0	Orbital phase	Flux difference	δ Flux difference	Norm. light	Quality factor	Seeing (arc sec)	Airmass (χ)	LC analysis	Comment
pf2083055	22-Jun-2001	52083.2881	0.0300	197223	1024	0.630	1.00	3.1	1.1	I	
pf2084015	23-Jun-2001	52083.9005	0.2940	−5978	2044	1.011	0.60	6.5	2.1	I	
pf2084018	23-Jun-2001	52083.9354	0.3090	996	1293	0.998	0.12	5.4	2.0	I	
pf2085015	24-Jun-2001	52084.8370	0.6976	482	1306	0.999	0.03	3.7	2.2	I	
pf2085018	24-Jun-2001	52084.8679	0.7109	−1087	1511	1.002	0.12	4.7	2.2	I	
pf2085021	24-Jun-2001	52084.8977	0.7238	−5631	1548	1.011	0.66	4.9	2.1	I	
pf2085024	24-Jun-2001	52084.9321	0.7386	−3100	1640	1.006	0.32	5.3	2.0	I	
pf2085025	24-Jun-2001	52084.9614	0.7512	−8533	1739	1.016	0.69	5.5	1.9	I	
pf2085030	24-Jun-2001	52084.9955	0.7659	−5099	1342	1.010	0.72	3.7	1.7	I	
pf2085033	24-Jun-2001	52085.0249	0.7786	−5841	1375	1.011	0.79	3.8	1.6	I	
pf2085036	24-Jun-2001	52085.0543	0.7913	−5506	1346	1.010	0.75	3.6	1.5	I	
pf2085039	24-Jun-2001	52085.0836	0.8039	−1241	1355	1.002	0.18	3.6	1.4	I	
pf2085042	24-Jun-2001	52085.1149	0.8174	2075	1270	0.996	0.46	3.2	1.4	I	
pf2085045	24-Jun-2001	52085.1451	0.8304	5430	1507	0.990	0.63	4.3	1.3	I	
pf2085048	24-Jun-2001	52085.1745	0.8431	7819	1293	0.985	0.91	3.4	1.2	I	
pf2085051	24-Jun-2001	52085.2061	0.8567	10834	1395	0.980	0.94	3.9	1.2	I	
pf2085054	24-Jun-2001	52085.2356	0.8694	14435	1232	0.973	0.94	3.3	1.2	I	
pf2085057	24-Jun-2001	52085.2657	0.8824	17218	862	0.968	0.88	4.0	1.1	I	
pf2085059	24-Jun-2001	52085.2818	0.8893	19527	1080	0.963	0.96	3.4	1.1	I	
pf2142018	20-Aug-2001	52141.9071	0.2962	−2817	1438	1.005	0.44	5.0	1.5	I	
pf2142021	20-Aug-2001	52141.9395	0.3102	125	1443	1.000	0.01	4.3	1.4	I	
pf2142024	20-Aug-2001	52141.9693	0.3231	1114	1656	0.998	0.22	5.0	1.3	I	
pf2142027	20-Aug-2001	52142.0000	0.3363	4082	1606	0.992	0.55	4.8	1.3	I	
pf2142030	20-Aug-2001	52142.0291	0.3489	6005	1602	0.989	0.74	4.8	1.2	I	
pf2142033	20-Aug-2001	52142.0779	0.3699	12731	1304	0.976	0.96	3.6	1.2	I	
pf2142036	20-Aug-2001	52142.1089	0.3832	17214	1270	0.968	0.96	3.4	1.1	I	
pf2142039	20-Aug-2001	52142.1386	0.3960	19027	1278	0.964	0.97	3.4	1.1	I	
pf2142042	20-Aug-2001	52142.1775	0.4128	26209	1252	0.951	0.98	3.3	1.1	I	

continued on next page

Table C.8: *continued*: MOA J005623.5−722123 V_J filter, image subtraction photometry

Image name	UTC	Mean date HJD−2400000.0	Orbital phase	Flux difference	δ Flux difference	Norm. light	Quality factor	Seeing (arc sec)	Airmass (χ)	LC analysis	Comment
pf2142045	20-Aug-2001	52142.2095	0.4266	41498	1274	0.922	0.99	3.5	1.1	I	
pf2142048	20-Aug-2001	52142.2393	0.4394	65301	1167	0.878	1.00	3.1	1.2	I	
pf2170015	23-Aug-2001	52169.9710	0.3925	19292	1655	0.964	0.97	5.2	1.2	I	
pf2170018	23-Aug-2001	52170.0003	0.4051	22348	1703	0.958	0.97	5.4	1.2	I	
pf2170021	23-Aug-2001	52170.0319	0.4188	30928	1869	0.942	0.97	5.9	1.1	I	
pf2170024	23-Aug-2001	52170.0695	0.4350	61080	1911	0.886	0.98	6.2	1.1	I	
pf2170027	23-Aug-2001	52170.1075	0.4513	93543	1918	0.825	0.98	6.4	1.1	I	
pf2170032	23-Aug-2001	52170.1738	0.4799	169683	1250	0.682	1.00	4.1	1.2	I	
pf2170033	23-Aug-2001	52170.1827	0.4838	180877	1176	0.661	1.00	3.8	1.2	I	
pf2171015	18-Sep-2001	52170.8778	0.7833	−2990	1144	1.006	0.31	4.3	1.4	I	
pf2171021	18-Sep-2001	52170.9384	0.8095	1235	1225	0.998	0.17	4.3	1.2	I	
pf2171024	18-Sep-2001	52170.9726	0.8242	3890	1618	0.993	0.57	4.9	1.2	I	
pf2171027	18-Sep-2001	52171.0018	0.8368	5949	1359	0.989	0.75	3.9	1.2	I	
pf2171030	18-Sep-2001	52171.0313	0.8495	9181	1325	0.983	0.86	3.8	1.1	I	
pf2171033	18-Sep-2001	52171.0604	0.8621	9130	1472	0.983	0.82	4.3	1.1	I	
pf2171036	18-Sep-2001	52171.0924	0.8759	14315	1330	0.973	0.93	3.7	1.1	I	
pf2171039	18-Sep-2001	52171.1217	0.8885	18916	1151	0.965	0.98	2.8	1.1	I	
pf2171042	18-Sep-2001	52171.1514	0.9013	20543	1233	0.961	0.98	3.3	1.2	I	
pf2171045	18-Sep-2001	52171.1808	0.9140	27384	1350	0.949	0.99	3.9	1.2	I	
pf2172015	19-Sep-2001	52171.8547	0.2044	2128	938	0.996	0.51	2.7	1.4	I	
pf2172018	19-Sep-2001	52171.8842	0.2172	−1212	861	1.002	0.34	2.5	1.3	I	
pf2172021	19-Sep-2001	52171.9166	0.2311	215	786	1.000	0.04	2.3	1.3	I	R
pf2172024	19-Sep-2001	52171.9458	0.2437	−1346	890	1.003	0.21	2.1	1.2	I	R,A
pf2172027	19-Sep-2001	52171.9759	0.2567	−1008	942	1.002	0.20	2.1	1.2	I	R
pf2172030	19-Sep-2001	52172.0051	0.2693	−3236	955	1.006	0.61	2.2	1.2	I	R
pf2172033	19-Sep-2001	52172.0343	0.2818	−1070	979	1.002	0.15	2.3	1.1	I	R
pf2172036	19-Sep-2001	52172.0634	0.2944	−1238	1085	1.002	0.25	2.7	1.1	I	
pf2172039	19-Sep-2001	52172.0980	0.3093	2458	968	0.995	0.61	2.2	1.1	I	R

continued on next page

Table C.8: *continued*: MOA J005623.5−722123 V_J filter, image subtraction photometry

Image name	UTC	Mean date HJD−2400000.0	Orbital phase	Flux difference	δ Flux difference	Norm. light	Quality factor	Seeing (arc sec)	Airmass (χ)	LC analysis	Comment
pf2172042	19-Sep-2001	52172.1275	0.3220	2687	942	0.995	0.39	2.1	1.1	I	R
pf2172045	19-Sep-2001	52172.1569	0.3347	4194	999	0.992	0.68	2.5	1.2	I	
pf2172048	19-Sep-2001	52172.1860	0.3472	8632	902	0.984	0.84	2.2	1.2	I	R
pf2172051	19-Sep-2001	52172.2164	0.3603	7935	963	0.985	0.76	2.7	1.3	I	
pf2172052	19-Sep-2001	52172.2284	0.3655	11774	976	0.978	0.82	2.5	1.3	I	
pf2199015	16-Oct-2001	52198.8897	0.8572	11015	1512	0.979	0.86	5.1	1.2	I	
pf2199018	16-Oct-2001	52198.9191	0.8699	13615	1495	0.974	0.91	5.2	1.2	I	
pf2199021	16-Oct-2001	52198.9516	0.8839	17690	859	0.967	0.96	2.3	1.1	I	
pf2199024	16-Oct-2001	52198.9810	0.8966	20515	1087	0.962	0.98	2.7	1.1	I	
pf2199027	16-Oct-2001	52199.0208	0.9137	26225	1199	0.951	0.99	3.3	1.1	I	
pf2199030	16-Oct-2001	52199.0501	0.9263	46490	1320	0.913	0.99	4.2	1.1	I	
pf2199033	16-Oct-2001	52199.0799	0.9392	72952	1576	0.863	0.99	5.9	1.2	I	
pf2199036	16-Oct-2001	52199.1090	0.9517	102446	1367	0.808	1.00	4.4	1.2	I	
pf2199039	16-Oct-2001	52199.1382	0.9643	141854	816	0.734	1.00	4.5	1.2	I	
pf2199042	16-Oct-2001	52199.1673	0.9769	170642	1073	0.680	1.00	4.5	1.3	I	
pf2199045	16-Oct-2001	52199.1964	0.9894	201329	1631	0.623	1.00	4.1	1.4	I	
pf2407015	12-May-2002	52406.8131	0.4774	163192	986	0.694	1.00	3.0	2.0	I	
pf2407021	12-May-2002	52406.8724	0.5030	211923	1034	0.603	1.00	3.6	2.2	I	
pf2407027	12-May-2002	52407.1052	0.6033	33185	1084	0.938	0.98	3.6	1.8	I	
pf2407030	12-May-2002	52407.1350	0.6162	25823	1757	0.952	0.93	5.5	1.6	I	
pf2407033	12-May-2002	52407.1708	0.6316	23980	1006	0.955	0.96	2.7	1.5	I	
pf2407036	12-May-2002	52407.2000	0.6442	20472	1047	0.962	0.96	2.7	1.4	I	
pf2407039	12-May-2002	52407.2363	0.6598	17868	1060	0.967	0.93	2.6	1.4	I	
pf2461018	05-Jul-2002	52460.9431	0.8088	1784	1188	0.997	0.38	3.3	1.8	I	
pf2461021	05-Jul-2002	52460.9723	0.8214	5790	1064	0.989	0.75	2.7	1.7	I	
pf2461024	05-Jul-2002	52461.0019	0.8342	6736	1049	0.987	0.66	3.1	1.6	I	
pf2461027	05-Jul-2002	52461.0315	0.8469	9638	848	0.982	0.65	3.8	1.5	I	
pf2461030	05-Jul-2002	52461.0608	0.8596	21884	646	0.959	0.89	3.7	1.4	I	

continued on next page

Table C.8: *continued*: MOA J005623.5−722123 V_J filter, image subtraction photometry

Image name	UTC	Mean date HJD−2400000.0	Orbital phase	Flux difference	δ Flux difference	Norm. light	Quality factor	Seeing (arc sec)	Airmass (χ)	LC analysis	Comment
pf2461033	05-Jul-2002	52461.0902	0.8722	18857	1258	0.966	0.97	3.4	1.3	I	
pf2461036	05-Jul-2002	52461.1202	0.8852	21101	1162	0.960	0.98	3.0	1.3	I	
pf2461039	05-Jul-2002	52461.2445	0.9387	64802	1035	0.879	1.00	3.8	1.1	I	
pf2462018	06-Jul-2002	52461.9059	0.2238	−5051	1474	1.009	0.50	5.7	1.9	I	
pf2462021	06-Jul-2002	52461.9351	0.2364	−6225	1836	1.012	0.64	5.7	1.8	I	
pf2462024	06-Jul-2002	52461.9642	0.2489	−3910	1704	1.007	0.53	5.2	1.7	I	
pf2462027	06-Jul-2002	52461.9935	0.2616	−3882	1650	1.007	0.55	5.0	1.6	I	
pf2462030	06-Jul-2002	52462.0227	0.2741	−6572	1687	1.012	0.75	5.0	1.5	I	
pf2462033	06-Jul-2002	52462.0519	0.2867	−4809	1480	1.009	0.59	4.2	1.4	I	
pf2462036	06-Jul-2002	52462.0819	0.2997	1683	1435	0.997	0.18	4.2	1.4	I	
pf2462039	06-Jul-2002	52462.1111	0.3123	−293	1308	1.001	0.12	3.5	1.3	I	
pf2462042	06-Jul-2002	52462.1437	0.3263	963	1695	0.998	0.13	5.1	1.2	I	
pf2462045	06-Jul-2002	52462.1730	0.3389	4866	1861	0.991	0.54	5.6	1.2	I	
pf2462048	06-Jul-2002	52462.2021	0.3515	7859	1520	0.985	0.75	4.6	1.2	I	
pf2462051	06-Jul-2002	52462.2313	0.3641	12202	1215	0.977	0.86	3.8	1.1	I	
pf2462054	06-Jul-2002	52462.2618	0.3772	17665	1032	0.967	0.92	3.5	1.1	I	
pf2462057	06-Jul-2002	52462.2927	0.3905	13770	1275	0.974	0.55	3.6	1.1	I	
pf2463013	07-Jul-2002	52462.7798	0.6005	34608	1198	0.935	0.99	3.5	2.2	I	
pf2463017	07-Jul-2002	52462.8148	0.6156	16701	1292	0.969	0.68	3.8	2.2	I	
pf2463021	07-Jul-2002	52462.8532	0.6321	13652	784	0.974	0.64	4.4	2.1	I	
pf2463022	07-Jul-2002	52462.8621	0.6359	17055	1313	0.968	0.92	4.8	2.1	I	
pf2463023	07-Jul-2002	52462.8730	0.6406	15339	1108	0.971	0.86	4.4	2.0	I	
pf2463025	07-Jul-2002	52462.9663	0.6809	3437	1414	0.994	0.39	4.8	1.7	I	
pf2463026	07-Jul-2002	52462.9756	0.6849	6825	1272	0.987	0.69	4.5	1.7	I	
pf2463029	07-Jul-2002	52463.0077	0.6987	302	1227	0.999	0.11	3.3	1.6	I	
pf2463032	07-Jul-2002	52463.0369	0.7113	−1577	1179	1.003	0.30	3.9	1.5	I	
pf2463035	07-Jul-2002	52463.0660	0.7238	151	1113	1.000	0.03	3.9	1.4	I	
pf2463038	07-Jul-2002	52463.0951	0.7364	−2155	1032	1.004	0.31	3.2	1.3	I	

continued on next page

Table C.8: *continued*: MOA J005623.5−722123 V_J filter, image subtraction photometry

Image name	UTC	Mean date HJD−2400000.0	Orbital phase	Flux difference	δ Flux difference	Norm. light	Quality factor	Seeing (arc sec)	Airmass (χ)	LC analysis	Comment
pf2463041	07-Jul-2002	52463.1245	0.7491	425	829	0.999	0.10	2.9	1.3	I	
pf2463044	07-Jul-2002	52463.1538	0.7617	−1770	637	1.003	0.18	3.2	1.2	I	
pf2465015	09-Jul-2002	52464.8106	0.4758	152089	1247	0.715	1.00	4.2	2.2	I	
pf2465018	09-Jul-2002	52464.8399	0.4884	186447	955	0.651	1.00	3.1	2.1	I	
pf2465021	09-Jul-2002	52464.8701	0.5014	207993	925	0.610	1.00	3.1	2.0	I	
pf2465024	09-Jul-2002	52464.9016	0.5150	209859	957	0.607	1.00	3.1	1.9	I	
pf2465027	09-Jul-2002	52464.9318	0.5280	197412	832	0.630	1.00	2.4	1.8	I	
pf2465030	09-Jul-2002	52464.9610	0.5406	166757	953	0.687	1.00	2.9	1.7	I	
pf2465033	09-Jul-2002	52464.9910	0.5536	130504	978	0.755	1.00	2.7	1.6	I	
pf2465036	09-Jul-2002	52465.0210	0.5665	96014	1057	0.820	1.00	2.9	1.5	I	
pf2465039	09-Jul-2002	52465.0501	0.5790	66999	1186	0.874	1.00	3.5	1.4	I	
pf2465042	09-Jul-2002	52465.0792	0.5916	43266	1098	0.919	1.00	2.8	1.3	I	

C.3.3 MOA J005623.5−722123 I_C, image subtraction photometry

Table C.9: MOA J005623.5−722123 I_C filter, image subtraction photometry.

Image name	UTC	Mean date HJD−2400000.0	Orbital phase	Flux difference	δ Flux difference	Norm. light	Quality factor	Seeing (arc sec)	Airmass (χ)	LC analysis	Comment
pf1814016	26-Sep-2000	51813.9311	0.9303	8993	809	0.954	0.93	3.1	1.2	I	
pf1814019	26-Sep-2000	51813.9619	0.9436	19837	1420	0.899	0.96	6.9	1.2	I	
pf1814021	26-Sep-2000	51813.9805	0.9516	27269	840	0.861	0.99	3.6	1.2	I	
pf1814022	26-Sep-2000	51813.9894	0.9554	30190	757	0.846	0.99	3.1	1.2	I	
pf1814023	26-Sep-2000	51813.9950	0.9579	32424	768	0.834	0.99	3.2	1.1	I	
pf1817014	29-Sep-2000	51816.9610	0.2363	-5530	1043	1.028	0.82	4.5	1.2	I	
pf1817016	29-Sep-2000	51816.9788	0.2440	-6548	1414	1.033	0.86	5.3	1.2	I	
pf1817018	29-Sep-2000	51817.0089	0.2569	-4749	1407	1.024	0.76	6.5	1.1	I	
pf1817022	29-Sep-2000	51817.0529	0.2759	-3337	1094	1.017	0.72	6.5	1.1	I	
pf1817024	29-Sep-2000	51817.0765	0.2861	-4672	1379	1.024	0.77	5.7	1.1	I	
pf1817028	29-Sep-2000	51817.1318	0.3099	-3866	702	1.020	0.49	4.0	1.2	I	
pf1817029	29-Sep-2000	51817.1401	0.3135	-6264	999	1.032	0.84	3.8	1.2	I	
pf1843015	25-Oct-2000	51843.1028	0.5040	64703	820	0.669	0.99	4.0	1.2	I	
pf1843016	25-Oct-2000	51843.1079	0.5063	66210	867	0.661	1.00	4.2	1.2	I	
pf1843021	25-Oct-2000	51843.1667	0.5316	59426	824	0.696	1.00	3.6	1.4	I	
pf1843022	25-Oct-2000	51843.1719	0.5338	55977	939	0.714	0.98	3.8	1.4	I	
pf1844015	26-Oct-2000	51843.9717	0.8786	-1506	837	1.008	0.45	3.5	1.1	I	
pf1844016	26-Oct-2000	51843.9781	0.8813	121	834	0.999	0.02	3.4	1.1	I	
pf1844021	26-Oct-2000	51844.0319	0.9045	687	640	0.996	0.18	2.6	1.2	I	
pf1844022	26-Oct-2000	51844.0371	0.9068	-131	622	1.001	0.14	2.5	1.2	I	
pf1844028	26-Oct-2000	51844.1183	0.9418	18483	651	0.905	0.98	2.6	1.3	I	
pf1844029	26-Oct-2000	51844.1236	0.9440	18770	627	0.904	0.98	2.5	1.3	I	
pf1874014	25-Nov-2000	51873.9539	0.8017	-7534	1445	1.039	0.85	5.9	1.2	I	
pf1874017	25-Nov-2000	51873.9956	0.8197	-5466	1093	1.028	0.81	4.3	1.2	I	
pf1874020	25-Nov-2000	51874.0358	0.8370	-5998	1053	1.031	0.82	4.8	1.3	I	
pf1874023	25-Nov-2000	51874.0674	0.8506	-5017	1167	1.026	0.76	5.8	1.3	I	

continued on next page

Table C.9: *continued*: MOA J005623.5−722123 I_C filter, image subtraction photometry

Image name	UTC	Mean date HJD−2400000.0	Orbital phase	Flux difference	δ Flux difference	Norm. light	Quality factor	Seeing (arc sec)	Airmass (χ)	LC analysis	Comment
pf1875031	26-Nov-2000	51874.9996	0.2524	-7904	829	1.040	0.91	3.0	1.2	I	
pf1875032	26-Nov-2000	51875.0049	0.2547	-8009	835	1.041	0.91	3.2	1.2	I	
pf1875036	26-Nov-2000	51875.0443	0.2717	-7373	909	1.038	0.89	4.2	1.3	I	
pf1959016	18-Feb-2001	51958.9220	0.4250	5585	1001	0.971	0.83	4.1	1.6	I	
pf1959029	18-Feb-2001	51959.0981	0.5010	67832	930	0.653	1.00	3.3	2.2	I	
pf1959032	18-Feb-2001	51959.1296	0.5145	68055	875	0.642	1.00	3.0	2.2	I	
pf1959035	18-Feb-2001	51959.1583	0.5269	61567	825	0.685	0.98	2.9	2.2	I	
pf1959038	18-Feb-2001	51959.1880	0.5397	53647	846	0.726	1.00	2.9	2.2	I	
pf1962014	21-Feb-2001	51961.9072	0.7118	-9883	768	1.051	0.96	2.8	1.6	I	
pf1962017	21-Feb-2001	51961.9381	0.7251	-7469	748	1.038	0.92	2.8	1.6	I	
pf1962020	21-Feb-2001	51961.9894	0.7472	-7281	844	1.037	0.81	3.7	1.9	I	
pf1962023	21-Feb-2001	51962.0200	0.7604	-8761	763	1.045	0.90	3.1	2.0	I	
pf1962025	21-Feb-2001	51962.1595	0.8205	-5276	1136	1.027	0.65	4.9	2.2	I	
pf1962028	21-Feb-2001	51962.1877	0.8326	-3987	1162	1.020	0.69	5.2	2.2	I	
pf1991016	22-Mar-2001	51990.9347	0.2233	-6280	791	1.032	0.92	2.6	1.9	I	
pf1991018	22-Mar-2001	51990.9564	0.2327	-7484	800	1.038	0.88	2.8	2.0	I	
pf1991022	22-Mar-2001	51990.9993	0.2512	-8004	698	1.041	0.94	2.4	2.1	I	
pf1991026	22-Mar-2001	51991.0440	0.2705	-6476	683	1.033	0.93	2.3	2.2	I	
pf1991030	22-Mar-2001	51991.0896	0.2901	-6866	743	1.035	0.93	2.6	2.2	I	
pf1991033	22-Mar-2001	51991.1178	0.3022	-7919	753	1.040	0.94	2.5	2.2	I	
pf1991035	22-Mar-2001	51991.1314	0.3081	-6090	818	1.031	0.81	2.9	2.1	I	
pf1991038	22-Mar-2001	51991.1627	0.3216	-5723	802	1.029	0.90	2.8	2.1	I	
pf1991040	22-Mar-2001	51991.1763	0.3275	-5007	824	1.026	0.84	2.9	2.0	I	
pf1991042	22-Mar-2001	51991.1913	0.3339	-5472	845	1.028	0.85	2.9	2.0	I	
pf1991044	22-Mar-2001	51991.2049	0.3398	-4240	795	1.022	0.81	2.7	1.9	I	
pf2017019	17-Apr-2001	52017.0487	0.4791	51298	572	0.738	1.00	2.0	2.2	I	R,A
pf2017020	17-Apr-2001	52017.0677	0.4873	57985	589	0.703	1.00	2.2	2.1	I	
pf2018016	18-Apr-2001	52017.8861	0.8401	-3301	726	1.017	0.80	2.3	2.0	I	

continued on next page

Table C.9: *continued*: MOA J005623.5−722123 I_C filter, image subtraction photometry

Image name	UTC	Mean date HJD−2400000.0	Orbital phase	Flux difference	δ Flux difference	Norm. light	Quality factor	Seeing (arc sec)	Airmass (χ)	LC analysis	Comment
pf2018020	18-Apr-2001	52017.9264	0.8574	-2861	611	1.015	0.45	2.5	2.2	I	
pf2018024	18-Apr-2001	52017.9778	0.8796	491	893	0.997	0.15	3.2	2.2	I	
pf2018026	18-Apr-2001	52017.9996	0.8890	-336	720	1.002	0.19	2.3	2.2	I	
pf2018030	18-Apr-2001	52018.0572	0.9138	3647	912	0.981	0.65	3.1	2.1	I	
pf2018032	18-Apr-2001	52018.0731	0.9207	4424	841	0.977	0.79	2.7	2.1	I	
pf2018036	18-Apr-2001	52018.1093	0.9363	14803	1099	0.924	0.94	3.9	2.0	I	
pf2018039	18-Apr-2001	52018.1423	0.9505	26477	1055	0.865	0.99	4.2	1.9	I	
pf2018042	18-Apr-2001	52018.1737	0.9640	36770	1169	0.812	0.97	4.7	1.7	I	
pf2045028	15-May-2001	52045.0969	0.5686	22738	1367	0.884	0.98	4.8	1.8	I	
pf2045030	15-May-2001	52045.1134	0.5757	18396	1102	0.906	0.97	3.6	1.7	I	
pf2045032	15-May-2001	52045.1288	0.5824	10598	1538	0.946	0.86	5.7	1.6	I	
pf2045034	15-May-2001	52045.1450	0.5893	9230	1380	0.953	0.80	5.3	1.6	I	
pf2045036	15-May-2001	52045.1605	0.5960	5465	1378	0.972	0.82	5.1	1.5	I	
pf2045038	15-May-2001	52045.1758	0.6026	2068	1129	0.989	0.41	4.4	1.5	I	
pf2045040	15-May-2001	52045.2005	0.6133	213	1095	0.999	0.04	4.3	1.4	I	
pf2045043	15-May-2001	52045.2318	0.6268	2393	1185	0.988	0.45	5.2	1.3	I	
pf2045045	15-May-2001	52045.2503	0.6347	-1214	1352	1.006	0.24	6.0	1.3	I	
pf2045047	15-May-2001	52045.2657	0.6414	-1466	1350	1.007	0.28	5.5	1.3	I	
pf2083013	22-Jun-2001	52082.8002	0.8197	-3582	1145	1.018	0.57	4.6	2.2	I	
pf2083020	22-Jun-2001	52082.8823	0.8551	-1616	1105	1.008	0.40	4.4	2.1	I	
pf2083023	22-Jun-2001	52082.9121	0.8679	-2662	861	1.014	0.53	3.7	2.1	I	
pf2083026	22-Jun-2001	52082.9597	0.8884	9541	724	0.950	0.53	4.2	1.9	X	
pf2083029	22-Jun-2001	52082.9891	0.9011	246	706	0.999	0.05	3.1	1.8	I	
pf2083032	22-Jun-2001	52083.0221	0.9153	-949	438	1.005	0.10	2.8	1.6	I	
pf2083035	22-Jun-2001	52083.0519	0.9282	8897	619	0.954	0.83	3.0	1.6	I	
pf2083038	22-Jun-2001	52083.0820	0.9411	21703	768	0.889	0.95	3.6	1.4	I	
pf2083041	22-Jun-2001	52083.1115	0.9539	31057	987	0.841	0.99	4.1	1.4	I	
pf2083044	22-Jun-2001	52083.1475	0.9694	45986	830	0.765	1.00	3.5	1.3	I	

continued on next page

Table C.9: *continued*: MOA J005623.5−722123 I_C filter, image subtraction photometry

Image name	UTC	Mean date HJD−2400000.0	Orbital phase	Flux difference	δ Flux difference	Norm. light	Quality factor	Seeing (arc sec)	Airmass (χ)	LC analysis	Comment
pf2083047	22-Jun-2001	52083.1783	0.9826	59380	799	0.696	1.00	3.4	1.2	I	
pf2083050	22-Jun-2001	52083.2083	0.9956	65273	791	0.666	0.99	3.0	1.2	I	
pf2083051	22-Jun-2001	52083.2603	0.0180	69483	865	0.645	1.00	3.4	1.1	I	
pf2083052	22-Jun-2001	52083.2658	0.0204	69073	730	0.647	1.00	3.1	1.1	I	
pf2083053	22-Jun-2001	52083.2713	0.0228	68607	646	0.649	1.00	2.6	1.1	I	
pf2083054	22-Jun-2001	52083.2809	0.0269	65672	634	0.664	1.00	2.6	1.1	I	
pf2083056	22-Jun-2001	52083.2965	0.0336	60441	845	0.691	1.00	2.9	1.1	I	
pf2084014	23-Jun-2001	52083.8934	0.2909	-5657	1161	1.029	0.75	4.9	2.1	I	
pf2084017	23-Jun-2001	52083.9283	0.3059	-4453	1058	1.023	0.63	5.6	2.0	I	
pf2085014	24-Jun-2001	52084.8299	0.6945	-5468	1056	1.028	0.86	3.9	2.2	I	
pf2085017	24-Jun-2001	52084.8608	0.7079	-3313	1124	1.017	0.65	4.7	2.2	I	
pf2085020	24-Jun-2001	52084.8906	0.7207	-8557	1204	1.044	0.91	4.9	2.1	I	
pf2085023	24-Jun-2001	52084.9250	0.7355	-10242	1249	1.052	0.80	5.6	2.0	I	
pf2085026	24-Jun-2001	52084.9543	0.7481	-4747	1234	1.024	0.65	5.7	1.9	I	
pf2085029	24-Jun-2001	52084.9883	0.7628	-8180	869	1.042	0.90	3.2	1.8	I	
pf2085032	24-Jun-2001	52085.0178	0.7755	-6760	901	1.035	0.87	3.6	1.6	I	
pf2085035	24-Jun-2001	52085.0472	0.7882	-6723	893	1.034	0.91	3.3	1.5	I	
pf2085038	24-Jun-2001	52085.0765	0.8008	-8684	955	1.044	0.91	3.5	1.4	I	
pf2085041	24-Jun-2001	52085.1078	0.8143	-7031	861	1.036	0.92	3.2	1.4	I	
pf2085044	24-Jun-2001	52085.1379	0.8273	-5881	927	1.030	0.89	3.4	1.3	I	
pf2085047	24-Jun-2001	52085.1673	0.8400	-3981	845	1.020	0.75	3.3	1.2	I	
pf2085050	24-Jun-2001	52085.1989	0.8536	-3260	906	1.017	0.68	3.7	1.2	I	
pf2085053	24-Jun-2001	52085.2285	0.8663	-3916	803	1.020	0.55	3.2	1.2	I	
pf2085056	24-Jun-2001	52085.2586	0.8793	-1201	672	1.006	0.15	3.7	1.1	I	
pf2085058	24-Jun-2001	52085.2747	0.8863	-1114	650	1.006	0.34	3.1	1.1	I	
pf2085060	24-Jun-2001	52085.2904	0.8930	-901	844	1.005	0.27	3.1	1.1	I	
pf2142017	20-Aug-2001	52141.9000	0.2932	-3917	1082	1.020	0.51	5.6	1.5	I	
pf2142020	20-Aug-2001	52141.9324	0.3072	-6488	926	1.033	0.88	4.1	1.4	I	

continued on next page

Table C.9: *continued*: MOA J005623.5−722123 I_C filter, image subtraction photometry

Image name	UTC	Mean date HJD−2400000.0	Orbital phase	Flux difference	δ Flux difference	Norm. light	Quality factor	Seeing (arc sec)	Airmass (χ)	LC analysis	Comment
pf2142023	20-Aug-2001	52141.9622	0.3200	-4123	964	1.021	0.72	5.2	1.4	I	
pf2142026	20-Aug-2001	52141.9929	0.3332	-4666	964	1.024	0.76	4.7	1.3	I	
pf2142029	20-Aug-2001	52142.0220	0.3458	-5071	963	1.026	0.79	4.4	1.2	I	
pf2142032	20-Aug-2001	52142.0708	0.3668	-1066	928	1.005	0.28	4.3	1.2	I	
pf2142035	20-Aug-2001	52142.1018	0.3801	-1816	808	1.009	0.63	3.1	1.1	I	
pf2142038	20-Aug-2001	52142.1315	0.3930	-939	860	1.005	0.31	3.3	1.1	I	
pf2142041	20-Aug-2001	52142.1704	0.4097	1290	796	0.993	0.31	3.0	1.1	I	
pf2142044	20-Aug-2001	52142.2024	0.4235	6441	777	0.967	0.93	3.1	1.1	I	
pf2142047	20-Aug-2001	52142.2321	0.4363	14706	740	0.925	0.98	2.9	1.2	I	
pf2142050	20-Aug-2001	52142.2615	0.4490	23752	810	0.879	0.99	3.2	1.2	I	
pf2170014	23-Aug-2001	52169.9639	0.3894	-879	1208	1.004	0.16	5.5	1.2	I	
pf2170017	23-Aug-2001	52169.9932	0.4021	-918	1361	1.005	0.22	5.7	1.2	I	
pf2170020	23-Aug-2001	52170.0248	0.4157	4137	1536	0.979	0.62	6.2	1.1	I	
pf2170023	23-Aug-2001	52170.0624	0.4319	7777	1471	0.960	0.78	6.2	1.1	I	
pf2170026	23-Aug-2001	52170.1004	0.4482	21481	1539	0.890	0.87	6.9	1.1	I	
pf2170030	23-Aug-2001	52170.1613	0.4745	48229	794	0.753	1.00	3.2	1.2	I	
pf2170031	23-Aug-2001	52170.1667	0.4768	50563	773	0.741	1.00	3.1	1.2	I	
pf2171014	18-Sep-2001	52170.8706	0.7803	-8237	849	1.042	0.71	4.1	1.4	I	
pf2171020	18-Sep-2001	52170.9313	0.8064	-8396	755	1.043	0.66	4.1	1.2	I	
pf2171023	18-Sep-2001	52170.9654	0.8211	-4967	881	1.025	0.82	3.8	1.2	I	
pf2171026	18-Sep-2001	52170.9947	0.8337	-4007	911	1.020	0.68	4.0	1.2	I	
pf2171029	18-Sep-2001	52171.0242	0.8464	-1775	906	1.009	0.53	4.2	1.1	I	
pf2171032	18-Sep-2001	52171.0533	0.8590	-2072	920	1.011	0.47	4.2	1.1	I	
pf2171035	18-Sep-2001	52171.0853	0.8728	-404	915	1.002	0.04	4.0	1.1	I	
pf2171038	18-Sep-2001	52171.1146	0.8854	431	818	0.998	0.05	3.2	1.1	I	
pf2171041	18-Sep-2001	52171.1443	0.8982	886	792	0.995	0.30	2.9	1.2	I	
pf2171044	18-Sep-2001	52171.1737	0.9109	2544	970	0.987	0.51	3.9	1.2	I	
pf2171047	18-Sep-2001	52171.2048	0.9243	7307	996	0.963	0.77	4.5	1.2	I	

continued on next page

Table C.9: *continued*: MOA J005623.5−722123 I_C filter, image subtraction photometry

Image name	UTC	Mean date HJD−2400000.0	Orbital phase	Flux difference	δ Flux difference	Norm. light	Quality factor	Seeing (arc sec)	Airmass (χ)	LC analysis	Comment
pf2171049	18-Sep-2001	52171.2193	0.9305	10633	1033	0.946	0.81	4.7	1.3	I	
pf2172014	19-Sep-2001	52171.8476	0.2014	-7042	654	1.036	0.85	2.7	1.4	I	
pf2172017	19-Sep-2001	52171.8771	0.2141	-6631	669	1.034	0.88	2.6	1.4	I	
pf2172020	19-Sep-2001	52171.9095	0.2280	-6539	586	1.033	0.88	2.4	1.3	I	
pf2172023	19-Sep-2001	52171.9387	0.2406	-8037	623	1.041	0.86	2.2	1.2	I	
pf2172029	19-Sep-2001	52171.9980	0.2662	-7428	634	1.038	0.87	2.2	1.2	I	
pf2172032	19-Sep-2001	52172.0272	0.2787	-7054	679	1.036	0.82	2.4	1.1	I	
pf2172035	19-Sep-2001	52172.0563	0.2913	-7580	709	1.039	0.93	2.6	1.1	I	
pf2172038	19-Sep-2001	52172.0908	0.3062	-6191	628	1.032	0.89	2.1	1.1	I	
pf2172041	19-Sep-2001	52172.1204	0.3189	-6566	627	1.034	0.87	2.1	1.1	I	
pf2172044	19-Sep-2001	52172.1498	0.3316	-5378	679	1.028	0.84	2.6	1.2	I	
pf2172047	19-Sep-2001	52172.1789	0.3442	-4644	606	1.024	0.84	2.1	1.2	I	
pf2172050	19-Sep-2001	52172.2093	0.3573	-4045	655	1.021	0.84	2.4	1.2	I	
pf2199014	16-Oct-2001	52198.8826	0.8541	-3257	1151	1.017	0.54	5.4	1.2	I	
pf2199017	16-Oct-2001	52198.9120	0.8668	-600	1160	1.003	0.16	5.6	1.2	I	
pf2199020	16-Oct-2001	52198.9445	0.8808	-1461	499	1.007	0.28	2.2	1.1	I	
pf2199023	16-Oct-2001	52198.9739	0.8935	0	569	1.000	0.04	2.0	1.1	I	
pf2199026	16-Oct-2001	52199.0137	0.9106	385	708	0.998	0.22	2.9	1.1	I	
pf2199035	16-Oct-2001	52199.1019	0.9487	23490	858	0.880	0.97	4.4	1.2	I	
pf2199041	16-Oct-2001	52199.1602	0.9738	49623	828	0.746	1.00	4.3	1.3	I	
pf2199044	16-Oct-2001	52199.1893	0.9863	60465	965	0.691	0.99	4.4	1.4	I	
pf2407014	12-May-2002	52406.8054	0.4741	48608	871	0.751	1.00	3.1	2.0	I	
pf2407017	12-May-2002	52406.8352	0.4869	61128	1011	0.687	1.00	3.7	2.1	I	
pf2407020	12-May-2002	52406.8648	0.4997	67666	946	0.654	1.00	3.5	2.2	I	
pf2407023	12-May-2002	52406.8972	0.5136	78077	676	0.597	0.97	3.1	2.3	X	
pf2407026	12-May-2002	52407.0975	0.6000	5578	890	0.971	0.78	3.4	1.8	I	
pf2407032	12-May-2002	52407.1632	0.6283	1917	731	0.990	0.47	2.7	1.6	I	
pf2407035	12-May-2002	52407.1923	0.6409	1710	708	0.991	0.36	2.7	1.5	I	

continued on next page

Table C.9: *continued*: MOA J005623.5−722123 I_C filter, image subtraction photometry

Image name	UTC	Mean date HJD−2400000.0	Orbital phase	Flux difference	δ Flux difference	Norm. light	Quality factor	Seeing (arc sec)	Airmass (χ)	LC analysis	Comment
pf2407038	12-May-2002	52407.2286	0.6565	100	722	0.999	0.04	2.7	1.4	I	
pf2407041	12-May-2002	52407.2577	0.6690	-261	796	1.001	0.01	3.0	1.3	I	
pf2407043	12-May-2002	52407.2722	0.6753	-4832	842	1.025	0.82	3.4	1.3	I	
pf2461017	05-Jul-2002	52460.9360	0.8057	-7454	865	1.038	0.89	3.0	1.8	I	
pf2461020	05-Jul-2002	52460.9652	0.8183	-6572	740	1.034	0.93	2.4	1.7	I	
pf2461023	05-Jul-2002	52460.9948	0.8311	-3522	890	1.018	0.57	3.3	1.6	I	
pf2461026	05-Jul-2002	52461.0244	0.8438	-5150	855	1.026	0.51	3.7	1.5	I	
pf2461029	05-Jul-2002	52461.0537	0.8565	-405	682	1.002	0.03	3.2	1.4	I	
pf2461032	05-Jul-2002	52461.0831	0.8691	-2223	1034	1.011	0.45	3.6	1.4	I	
pf2461035	05-Jul-2002	52461.1131	0.8821	-1626	1011	1.008	0.39	3.4	1.3	I	
pf2462017	06-Jul-2002	52461.8988	0.2207	-2450	1346	1.013	0.51	5.6	2.0	X	
pf2462020	06-Jul-2002	52461.9279	0.2333	-5514	1271	1.028	0.79	4.9	1.9	I	
pf2462023	06-Jul-2002	52461.9570	0.2458	-6751	1150	1.035	0.88	4.4	1.8	I	
pf2462026	06-Jul-2002	52461.9863	0.2585	-8076	1161	1.041	0.84	4.5	1.6	I	
pf2462029	06-Jul-2002	52462.0155	0.2710	-7005	1145	1.036	0.84	4.4	1.5	I	
pf2462032	06-Jul-2002	52462.0447	0.2836	-6798	1198	1.035	0.85	4.5	1.4	I	
pf2462035	06-Jul-2002	52462.0747	0.2966	-6695	1079	1.034	0.80	3.9	1.4	I	
pf2462038	06-Jul-2002	52462.1040	0.3092	-6321	1147	1.032	0.82	3.9	1.3	I	
pf2462041	06-Jul-2002	52462.1365	0.3232	-6577	1419	1.034	0.62	4.9	1.2	I	
pf2462044	06-Jul-2002	52462.1658	0.3358	-2868	1391	1.015	0.54	5.2	1.2	I	
pf2462047	06-Jul-2002	52462.1949	0.3484	-2085	1211	1.011	0.33	4.5	1.2	I	
pf2462050	06-Jul-2002	52462.2241	0.3610	-2727	1141	1.014	0.36	4.5	1.1	I	
pf2462053	06-Jul-2002	52462.2547	0.3741	-2164	934	1.011	0.41	3.5	1.1	I	
pf2462056	06-Jul-2002	52462.2855	0.3874	32	974	1.000	0.04	3.8	1.1	I	
pf2463014	07-Jul-2002	52462.7870	0.6035	4410	1048	0.977	0.75	3.2	2.2	I	
pf2463016	07-Jul-2002	52462.8075	0.6124	206	1098	0.999	0.04	3.4	2.2	I	
pf2463028	07-Jul-2002	52463.0005	0.6956	-5728	817	1.029	0.67	3.6	1.6	I	
pf2463031	07-Jul-2002	52463.0297	0.7082	-6393	866	1.033	0.78	3.4	1.5	I	

continued on next page

Table C.9: *continued*: MOA J005623.5−722123 I_C filter, image subtraction photometry

Image name	UTC	Mean date HJD−2400000.0	Orbital phase	Flux difference	δ Flux difference	Norm. light	Quality factor	Seeing (arc sec)	Airmass (χ)	LC analysis	Comment
pf2463034	07-Jul-2002	52463.0588	0.7207	-5040	1026	1.026	0.78	3.8	1.4	I	
pf2463037	07-Jul-2002	52463.0878	0.7332	-7212	877	1.037	0.81	3.7	1.3	I	
pf2463040	07-Jul-2002	52463.1172	0.7459	-8068	674	1.041	0.92	2.6	1.3	I	
pf2463043	07-Jul-2002	52463.1466	0.7585	2118	647	0.989	0.03	2.9	1.3	X	
pf2463050	07-Jul-2002	52463.2990	0.8242	-4683	854	1.024	0.75	2.2	1.1	I	
pf2465014	09-Jul-2002	52464.8035	0.4727	43339	1023	0.778	0.99	3.6	2.2	I	
pf2465017	09-Jul-2002	52464.8328	0.4854	56347	796	0.712	1.00	2.9	2.2	I	
pf2465020	09-Jul-2002	52464.8630	0.4984	66387	821	0.660	1.00	3.1	2.1	I	
pf2465023	09-Jul-2002	52464.8944	0.5119	66247	700	0.661	1.00	2.7	2.0	I	
pf2465026	09-Jul-2002	52464.9247	0.5250	64020	647	0.673	1.00	2.4	1.8	I	
pf2465029	09-Jul-2002	52464.9539	0.5376	54520	694	0.721	1.00	2.7	1.7	I	
pf2465032	09-Jul-2002	52464.9839	0.5505	43085	661	0.780	0.99	2.3	1.6	I	
pf2465035	09-Jul-2002	52465.0139	0.5634	29906	680	0.847	0.99	2.3	1.5	I	
pf2465038	09-Jul-2002	52465.0430	0.5759	18589	864	0.905	0.99	3.2	1.4	I	
pf2465041	09-Jul-2002	52465.0721	0.5885	10433	786	0.947	0.96	2.9	1.4	I	

Appendix D

Modified ISIS-2.1 script for flux extraction from a single target

The output from DAOPHOT II was used to create an image that contained only the target star, `refnosky.fits`. Every other pixel on the frame had on average a value of zero. Photometry was then performed on this frame using ISIS-2.1 but with a modified script. This is given below. The reference frame, (as specified in the `process_config` file) was also required. The photometry cannot be run directly as ISIS-2.1 requires several other files, which this script produces.

The script reads the parameters in the `process_config` file in order to extract directory locations and configuration files. The images **with** a background are dealt with first. A copy of the reference frame is then made which is used in subsequent scripts. The `mrj_phot` script is executed which produces an `interp` file from the reference frame. Next `Bphot` is executed. This produces the PSF from the reference frame as performed in the standard reduction process.

Next the images **without** a background are processed. The `refnosky` image is copied to two files, both required in the photometry extraction stage. The `detect` script is then run in order to detect the position of the target star on the `refnosky` image. This output data is required by the photometry script. The photometry extraction script is now run and the output in placed in the image location directory as specified in `process_config`. The file is `lc0.data`. This gives a dummy HJD, (value 1234), column1, the weighted flux and weight flux error columns 2 and 3, the flux and flux error columns 4 and 5 and the goodness factor column 6.

```
#! /bin/csh -f

set dir = 'grep IM_DIR process_config|awk 'print $2''
set dir_mrj = 'grep MRJ_DIR process_config|awk 'print $2''
set ref_file = 'grep REF_SUB process_config|awk 'print $2''
set date_file = 'grep INFILE process_config|awk 'print $2''
set phot_file = 'grep VARIABLES process_config|awk 'print $2''
set dir_config = 'grep CONFIG_DIR process_config|awk 'print $2''
set thresh = 'grep SIG_THRESH process_config|awk 'print $2''


set refnosky = refnosky.fits


cd $dir


#at this stage refPhot.fits has the sky still
cp $ref_file refPhot.fits
cp $ref_file interp_refPhot.fits
```

```
# you must have the one WITH sky
$dir_mrj"/bin/mrj_phot" interp_refPhot.fits interp_refPhot.fits -c $dir_config"/default_config"

$dir_mrj"/bin/Bphot" -i interp_refPhot.fits -c $dir_config"/phot_config"

# Use the one WITHOUT sky now
cp $refnosky conv_refPhot.fits
cp $refnosky interp_refPhot.fits

$dir_mrj"/bin/detect" -i interp_refPhot.fits -o $dir_config"/phot.data.singlestar" -r interp_refPhot.fits
-t $thresh -c $dir_config"/default_config"

$dir_mrj"/bin/Cphot" -i conv_refPhot.fits -j interp_refPhot.fits -o $dir_config"/phot.data.singlestar"
-e 1234 -c $dir_config"/default_config" -d $dir_config"/phot_config"
```

Appendix E

ST4 auto guider camera settings

The ST4 auto-guide is a small thermo-electrically cooled CCD camera located off-axis in the photometer head, refer Figure 4.1, connected via a RS-232 cable to the control box with alphanumeric displays, Figure E.1. The ST4 is positioned using the data acquisition interface `MOJO` via adjusts to the azimuth, `az` (0-370°) and radius, `ra` (6-220, digital readout) parameters, refer Figures 4.1 and 4.2. With the guide star on the ST4 CCD, the tracking is engaged and the ST4, via its control unit, will adjust the telescope's position in order to maintain the guide star at a fixed location.

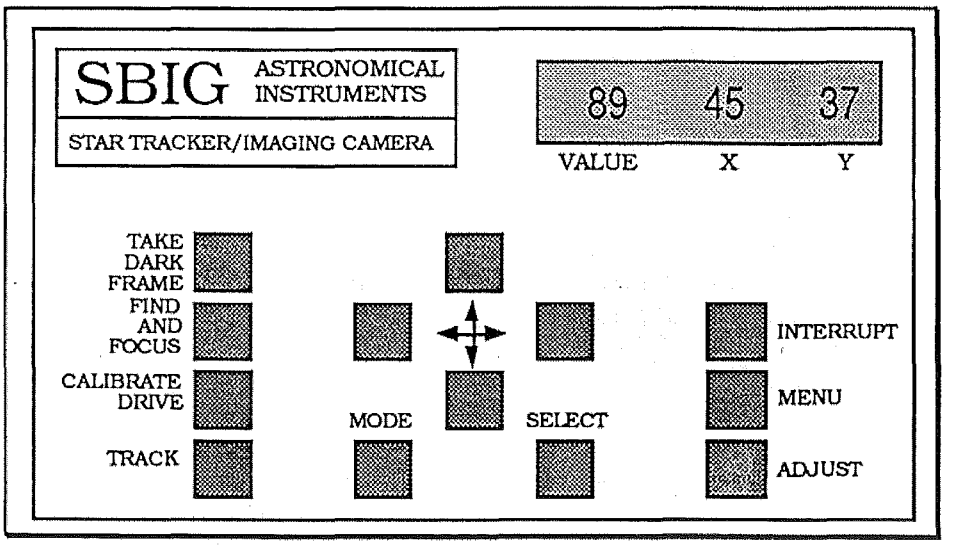

Figure E.1: The ST4 auto-guide control box that is connected via a RS-232 cable to the CCD. The camera unit can be controlled from this box, as was the case, or remotely if the camera and telescope orientations allow.

The use of the ST4 as a guide camera was conceived on the assumption that the x-axis of the ST4 CCD aligns with RA. However in the photometer head, the ST4 CCD orientation changes. This does not cause problems in practise if the chosen guide star is within 30° of the E-W line through the science target. Figure E.2 shows such a case where the selected guide star is not on the E-W line through the science target.

There are three ways to use the system.

1. Operate only from the ST4 control unit
2. Operate only via software

3. Operate image viewing via the software and tracking via the ST4 control unit

The third option was used with a laptop used to view the images. This enabled focusing of the guide star at the telescope as manual focusing is only possible with the focusing adjustment located in the photometer head, Figure 4.1. Additionally access to the photometer head, due to the telescope orientation, is often via a ladder with laptop in hand.

The settings used for the ST4 auto-guide camera are given in Table E.1. These were entered into the unit and differ from the default software settings. The settings where used for both the LMC and SMC as the declination change between targets was minimal. LMC $-69°\ 17'\ 00''$ and -72° 38′ 55″ for the SMC, a difference of 3° 21′ 55″. If the telescope is repositioned on a target where the change in declination is larger than 10°, then the tracking software and camera will need recalibration.

E.1 ST4 auto-guide settings

Table E.1: Settings for the ST4 auto-guide settings auto-guide unit. The default values are given along with customized setting used for guide stars when observing targets in the Magellanic Clouds.

Setting	Parameter	Range	Default	Target
EA	**E**xposure **A**djust time (sec)	0.1→20	1	10
b	**b**oost factor parameter	1,2,3,4	1	1
BA	**B**rightness **A**djust parameter	A or F	A	A
SA	**S**cintillation **A**djust Parameter	1→10	2	2
FL	**F**ocal **L**ength (inches)	S or L	S	S
C1	**C**alibrate **1** (drive time, sec, in R.A.)	1→40	5	6
C2	**C**alibrate **2** (drive time, sec, in Dec.)	1→40	5	3
H1	**H**ysteresis **1** (in the R.A. drive direction)	0→3.0	0	0
H2	**H**ysteresis **2** (in the Dec. drive direction)	0→3.0	0	0
AA	**A**veraging **A**djust	1→10	1	1
AL	**AL**arm cycles	1→10	1	1

The ST4 chip is 192 × 165 pixels, (x,y), with the position on the chip represented as a percentage of the pixel value in x and y, therefore the display value ranges from 0 to 99. Each pixel has 8 bits digitization, i.e. values from 0 to 255 and are also displayed as a percentage with 99 indicating a saturated pixel. Therefore on the display, 1 unit in $x = 1.92$ pixels, 1 unit in $y = 1.65$ pixels. This is due to the CCD pixels not being square, but 0.01375 mm in x, 0.016 mm in y giving a CCD chip area of 2.64 mm square. The CCD is thermo-electrically cooled to $-30°$ and the dark current will saturate the CCD after 5 minutes at this temperature.

E.2 Explanation of parameters

E.2.1 Exposure Adjust, EA

The exposure or integration time of the ST4 unit. The range is from 0.1 seconds to 20 seconds with the readout time being 0.14 seconds. However download time to a laptop is several seconds via the serial link. When using the 1 m telescope a guide star of about 11 to 12 magnitude can easily be used, therefore a large number of stars can be used as guide stars. Note that the CCD will easily saturate if brighter stars are used, i.e. those used with the previous Philips system.

The exposure time should be adjusted to give a value between 30 to 70. Preferably, **EA** is no longer than 10 seconds. The boost, *b*, maybe required to be increased if a reasonable value of the guide star is not measured. If dark frames are being subtracted from the images, then another dark frame **must** be taken if this parameter is adjusted.

E.2.2 Boost factor, b

The gain on the ST4 CCD chip. Settings options are 1,2,3 or 4. Increase gain for fainter guide stars. The ST4 has a coarse temperature regulator. Ambient temperature variations can cause problems with exposure > 5 seconds with the boost factor set at 4. If dark frames are being subtracted from the images, then another dark frame **must** be taken if this parameter is adjusted.

E.2.3 Brightness Adjust, BA

This has two settings **A**, average or **F**, faint. The average setting **A**, is mostly used with 1 pixel equal to 1 pixel. For faint objects the **F** setting can be used which sets 1 pixel equal to the sum of a 3×3 pixel box. Don't use **F**, faint mode, when the pixel value displayed is > 20 as this degrades the tracking performance due to saturation. If dark frames are being subtracted from the images, then another dark frame **must** be taken if this parameter is adjusted.

E.2.4 Scintillation Adjust, SA

This sets how many pixels the guide star is allowed to drift away from the preferred position before a correction takes place. The ST4 will notice any overshoot or under shooting and adjust the correction speeds to suit. It is recommended to increase the **SA** parameter if the focal length is greater than 3 metres. This is due to the greater tracking resolution in arc seconds. However the quality of the 1 metre telescope tracking allows the **SA** parameter to be set to 2 without tracking problems occurring. On nights of good seeing **SA** $= 2$ is large enough. In poor seeing the larger atmospheric scintillation means a larger value of **SA** maybe required, although at this stage, the quality of observations are very poor. Too low a value of **SA** may result in a tendency of the ST4 to *run away* from the guide star during tracking . If **SA** is set high, 10, it is most probable that the correction speed will not be readjusted automatically by the ST4.

E.2.5 Focal Length, FL

The two settings are **L**, long focal length > 1.250 m or **S**, short focal length < 1.250 m. The parameter controls the size of the track box. The **S** setting defines a 9×9 pixel box and the **L** setting a 33×33 pixel box. The accuracy of the telescope drive is the main influence on this parameter. The ST4 was built for small telescopes with varying drive errors. Due to the 1 metre telescope's good drives and torque motors, this parameter can be set to **S**.

E.2.6 Calibrate, C1 and C2

This sets the amount of time in seconds the ST4 will activate the relays in the calibrate mode. It is important to note that the chip x and y do not necessarily align with the R.A. and Dec. They should be set so the image moves tens of pixels during the calibrate process (this assumes **SA** $= 2$). The 1 metre telescope requires the time in the Dec. direction to be about half of

the R.A. time due to motor speeds. A typical setting is **C1** (R.A.) = 3 seconds, **C2** (Dec.) = 6 seconds. This gives a displayed move of ~18 in x, ~30 in y (corresponds to 34 and 50 pixels in x and y respectively). If these times are wrong, then at the end of the calibrate procedure the ST4 will display calibration errors E1 and possibly E2. The calibrate process starts with an exposure (time set by **EA**). The position and pixel value should be noted. The telescope then drives in the $+x$ (R.A.) for **C1** seconds, takes an exposure, then drives back in the $-x$ direction and takes an exposure. At this stage the pixel value and position should be similar to the starting position, within a few pixels. The relays are now activated driving in the $+y$ direction (Dec.) for **C2** seconds, an exposure taken, then back in the $-y$ direction, another exposure is taken. This is the end of the calibrate process and once again, the pixel value and position should be similar to that of the starting value. At this stage, if any errors occurred, error messages are displayed.

E.2.6.1 Errors in Calibrate mode

After the calibrate procedure is completed the errors E1 or E2 may appear. These are due to the change or lack of change of position of the guide star on the ST4 chip during the calibrate process. The Error E1 or E2 each have a sub code 1,2,3 or 4. The sub codes indicate the errors in the relays for direction: $+x$, $-x$, $+y$ and $-y$ respectively. E1 indicates that there was no perceptible movement of the star on the ST4 chip. E2 indicates that there was some movement, but it was less than 5 pixels, 2 to 3 display units. If the errors result at the end of the calibration process, the following could be the cause:

- **C1, C2** needs adjusting. Either the drive times are too high or too low. To determine the drive times and movement, view the read out during the calibration process as this will give the position of the star at the end of each activation of the relays. If the **value** parameter on the display dramatically falls away, then it is most likely that the star has moved off the chip. Therefore lower the driving time in the appropriate direction. If little change is noted the driving time in the appropriate direction needs to be increased.
- Check to see the telescope speed is set to 2.
- Check the focus to ensure the star shape is round.
- Check to see that there is only one bright star on the frame. If two or more stars of similar brightness are present, the unit will have difficulty distinguishing them. Also ensure a brighter star doesn't move into the CCD field of view during the calibration process.
- If the star is too close to the edge of the chip then it will move off during the calibrate process. Reposition the star nearer to the centre.
- If the CCD head isn't oriented properly. Generally this is not a problem until the path of the star across the chip during the calibration process, exceeds approximately 30° from the path expected by the control unit i.e. horizontal for R.A. or vertical for Dec. If this occurs, check the orientation of the ST4 in the photometer head. A white alignment dot on the rear edge on the ST4 unit should be horizontal to the bottom of the photometer head.

After the calibration process, the guide star is not positioned exactly back to its original starting position refer Figure E.2. The offset varies, but generally within 5 pixels, 3 display units, of the starting position.

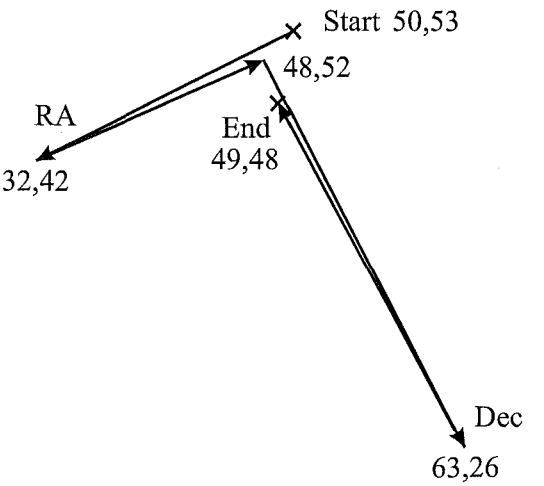

Figure E.2: The movement, in pixel coordinates, of the guide star is shown during the calibration process using ST4 with telescope speed = 2, **C1** = 3 and **C2** = 6. The start position is indicated with the telescope driven in declination and back to the start position, then in right ascension and back to the end position. Ideally the start position and end position should be the same, however slight errors in the telescope guiding result in these positions differing slightly.

E.2.7 Hysteresis (backlash) adjustment, x axis, H1

Sets the amount of extra time the telescope is driven for in order to allow for backlash. The parameter is the number of tenth-second increments added to the calculated move when the move direction is reversed from the previous one. This should be set as 0 on the 1 m due to the torque motors.

E.2.8 Hysteresis (backlash) adjustment, y axis, H2

The same as H1 but in the y direction.

E.2.9 Averaging Adjust, AA

This parameter sets the number of exposures the ST4 should average before making a correction. If exposure times are > 5 seconds, set **AA** = 1 (default). If exposure times are less than this, an average should be considered so that a correction is made every 5 seconds.

E.2.10 Alarm cycles, AL

If the ST4 is unable to locate the guide star, most likely due to cloud, an alarm will sound. This parameter sets the number, n, of unsuccessful cycles prior to the alarm being activated. The default value is satisfactory.

E.3 Settings for using the CCD track software to focus the guide star

The CCD track software, run via DOS, controls the ST4 box independent of the ST4 box settings. Running the software on a laptop enables the guide star to be focused more easily due the access to the focusing micrometer in the photometer head. The following hardware and software setting/functions enable the ST4 to be used to acquire images via the CCD track programme. A screen-shot of the CCD track software is shown in Figure E.3

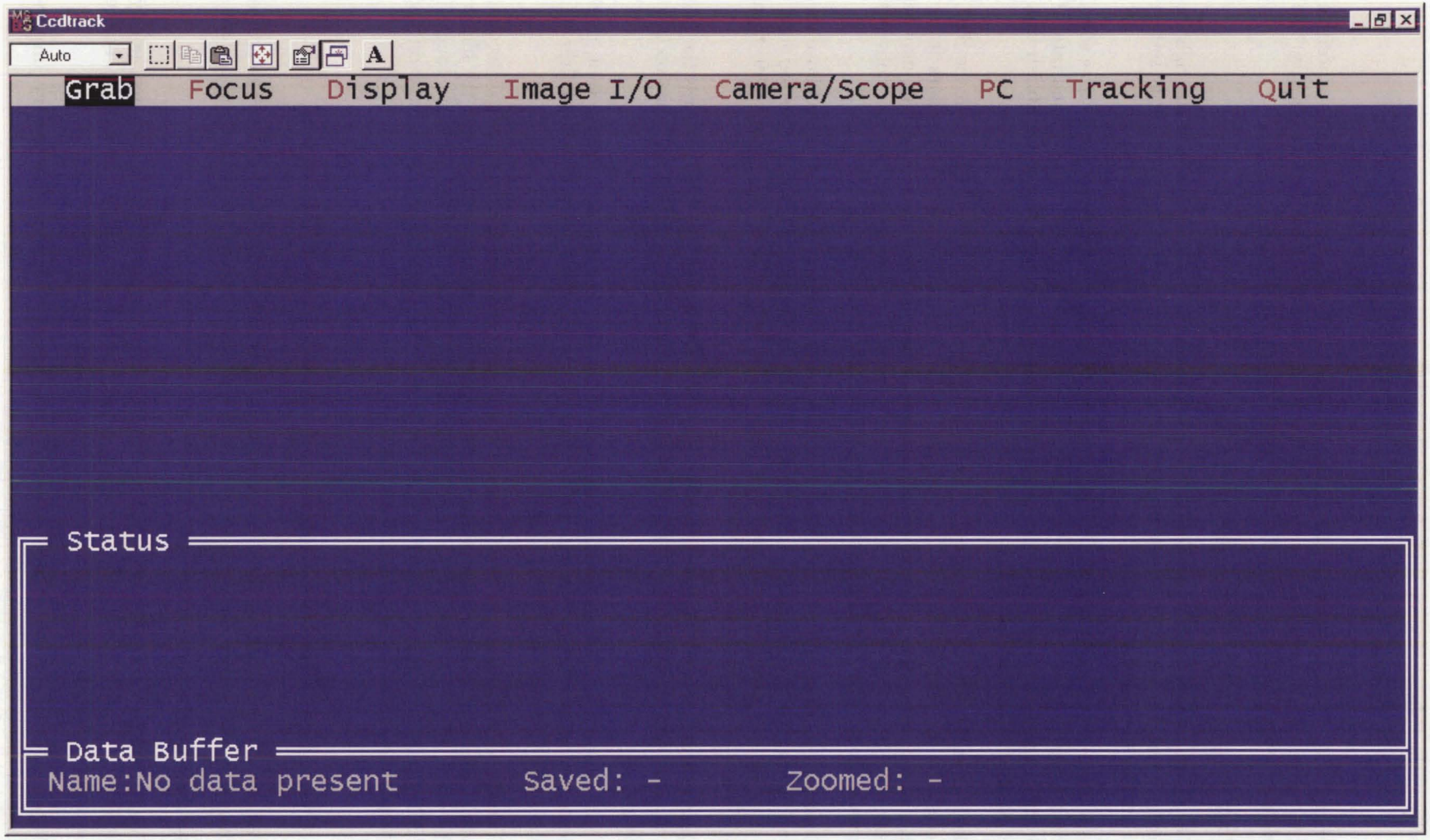

Figure E.3: Screen-shot of the CCD track software run via DOS. The program allows for the manual settings of the ST4 control box setup.

The correction calibration drive times can be calculated using the `CCD track` programme. Alternatively, the values given in Table E.1 can be used.

- Orientation - Forward polarity: the telescope drives in the negative direction for a positive track error. The star is to the right or below its desired position. Reverse polarity: the telescope drives in the positive direction for a positive track error.
- Pixel(1,1), upper left($-y$,$-x$) position; $-y \uparrow$, $+y \downarrow$, $-x \leftarrow$, $+x \rightarrow$
- Use the `Move` command to determine the orientation. If the star moves to the right or down, when the right ($+x$) or the up ($+y$) relays are activated, then the polarity setting needs to be Forward.
- Auto Baud - Use the auto baud setting. This sets the link speed and stores the value when the software is **first** run. Use the Establish link command to reset the auto baud rate. If the program is disconnected or shutdown from the ST4, you need to run **Establish link** to regain the highest baud rate.
- Dark Frames - You must **manually** cover the ST4 (end of the baffle tube on the ST4, access via the photometer head access panel) while the software is taking a dark frame as there is no shutter on the ST4 CCD. A glow in the top left corner pixel(1,1), may be noticed. This is due to heating from the array during readout and will be more obvious from readouts with actual images and longer integration times.
- Contrast - Background: any pixel below this is black. Range: range of values above the background which is displayed in grey scale. Values higher than the range + background, are considered saturated and shown as white i.e. If Background = 25, Range = 50, then < 25 black, 25 to 75 grey, > 75 white.
- Quarter frame mode - The user specifies $\frac{1}{4}$ of the CCD frame. The CCD records the full image but only downloads the $\frac{1}{4}$ specified, therefore reducing the image transmission time by $\frac{3}{4}$.
- Spot frame mode - This takes a full frame and locates and reports the brightest spot, then downloads a 33×27 pixel image. This is much faster than full frame download although it is best to use quarter frame as the area is user specified.
- Focusing - Set Background = 0, Range = 255; integrate with the **EA** time set to 1 second, adjust the focus based on the **value** figure displayed. The better the focus, the higher the value, also use a laptop to view the image. Ensure that the telescope is not touched during data recording as this will smear the image over several more pixels thus reducing the peak value. Good focus is essential for dimmer stars.

E.4 Operation from the instrument panel of the ST4 control unit

- Position the guide star in the centre (as close as possible) of the ST4 CCD. The coarse change in `r.a.` and `az.` in the photometer head can make centering the guide star difficult.
- Set the telescope speed to 2.
- Connect a laptop running CCDtrack to the ST4 with the guide star image continuously refreshed (Quarter Frame Mode is best, the user positions the initial boxed region before the refresh starts).
- Adjust the focus by using the micrometer so the image is circular. This is **very important**. If this is not done, tracking can be poor.

- Disconnect laptop and set the tracking parameter via the `menu` and `adjust` buttons on the box as given in Table E.1.
- Cover the ST4 baffle and press the `Take Dark Frame` button. The exposure time is that set in the previous step.
- Press the `Find and Focus`. The display should read the position (x, y) of the star and its value.
- Press the *Calibrate Drive* button. This will now drive in Declination $+y$,$-y$ and Right Ascension $+x$,$-x$. The star will return to nearly the same position. It is essential that **no** errors occur in the calibration process, otherwise the unit will not guide properly. The guide star does not have to be used for the calibration process, however the one selected must be close in declination as the R.A. correction speed is maximum near the equator and reduces toward the pole.
- Re-align the target at the optimum target position. Press the `Find and Focus` button to ensure the guide star is near the centre of the chip.
- Press the `Track` button. The unit will now track until the `Interrupt` button is pressed or the guide star is lost e.g. owing to cloud.

The ST4 constantly corrects the drive adjustment times to try to improve tracking. The visual x and y displays show the tracking error seen during each exposure in units of 0.2 pixels (i.e. a displayed y value of -3 indicates that the star moved 0.6 pixels in the $-y$ direction during the exposure). The number displayed after the **A** in the value location is the average error for the last 16 correction periods. If the star is lost during the tracking process, the unit will display the location of the brightest object in the field. It will activate the track lost relay for 1 second after 5 consecutive misses. The telescope will not be corrected again until the star reappears.

When moving to a new target of similar declination i.e. within 10°, simply position the guide star near the centre of the CCD and press `track`. Re-calibrate if repositioning the telescope $> 10°$ due to orientation and declination changes.

During the tracking process, if errors > 9 units (1.8 pixels) occur, an **E** is displayed due to the limits of the display screen on the ST4 control box. The **value** display gives an average error in the last 16 corrections denoted by an **A**. If the star value falls below half the initial value, it assumes that the star is lost and will not make any corrections. If it is lost for 4 cycles in a row, then the alarm relay is activated. If the star is regained (say due to a fast passing cloud), it will calculate the correction required and continue.

Appendix F

Grison algorithm C code

The period search algorithm developed by Grison [60] entitled *Automatic search for periodic light curves with any kind of shape in unevenly spaced data* was coded in C. This was used to detect the eclipsing binaries in the MOA catalogue. A flow diagram, Figure F.1, summarizes the C code written for this task. A separate program, incorporated into the period search code, was written and supplied by Dr I. Bond. This was used by MOA to extract the data from the MOA database. Some functions, where indicated, where sourced from Numerical Recipes in C, [172]. Additionally, the PostScript output file was written by Dr W. Tobin.

F.1 Flow diagram of the code

A flow diagram of the coded Grison algorithm is presented in Figure F.1 as an overview of the program structure.

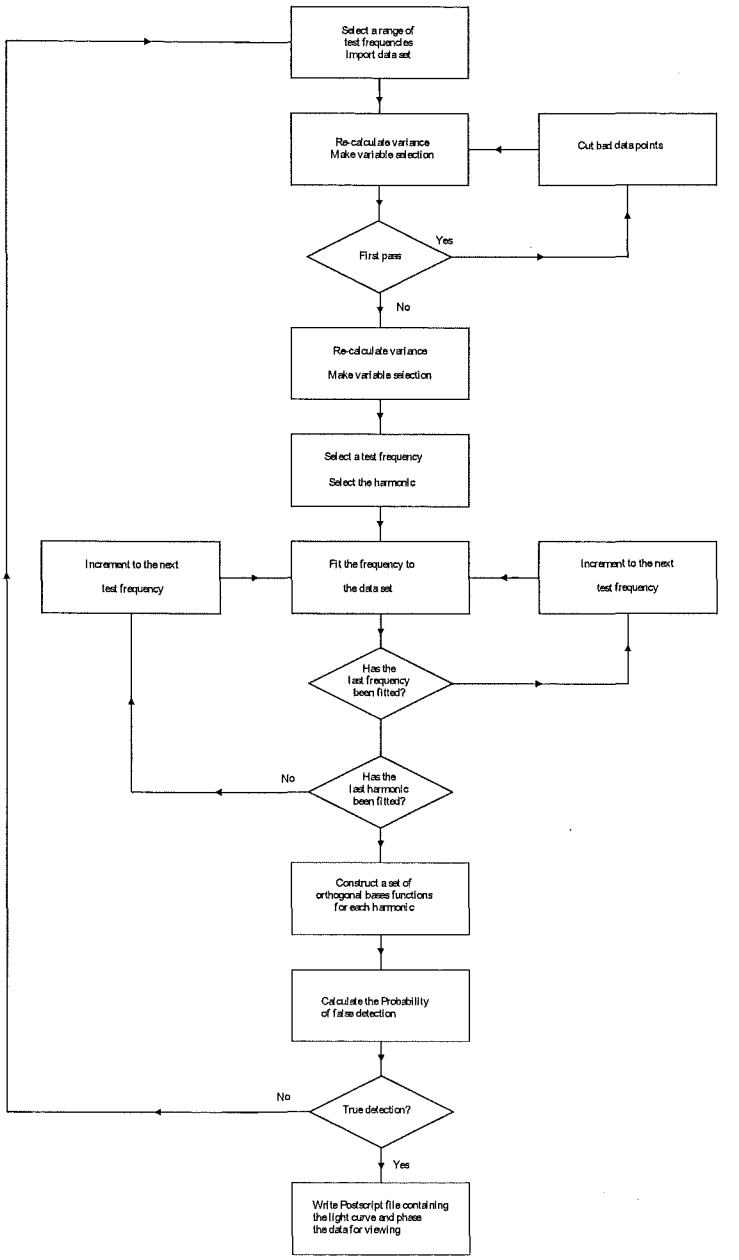

Figure F.1: Flow diagram of the coded Grison period search algorithm using the MOA SMC database as input.

F.2 The Grison code

A brief description of modified and written files is presented together with the respective C code for the mathematical working in Grison's paper.

F.2.1 Library files

In pgpf.h, a modified version of the one given by Numerical Recipes [119] nr.h, was used, nrgpb.h. Three functions were changed to use double instead of the default float. This was required for the accuracy in the calculation of the Periodogram. The changes made were as follows:

```
float betacf(float a, float b, float x); → double betacf(double a, double b, double
x);
float betai(float a, float b, float x); → double betai(double a, double b, double
x);
float gammln(float xx); → double gammln(double xx);
```

Another Numerical Recipes utility was used nrutil.h and nrutil.c. This was used to define the vector and matrices starting array indexing at 1 rather than the standard zero.

The initial input file containing the library files and set variables, as shown below:

```
#include <stddef.h>
#include <stdio.h>
#include <stdlib.h>
#include <math.h>
#include <time.h>
#include "pickup_std.inc"
#include "nrutil.h"
#include "nrgpb.h"
#include "nrutil.c"
#define NR_END 1
#define FREE_ARG char*
#define twopi 6.283153071795865
#define OFAC 5
#define HIFAC 2
#define n 1000
#define maxdata 3500
#define kmax 4
#define jmax 3                                        /* kmax-1 */
#define jmin 1
#define freqmin 1.0                                   /* 1 day (1/1) */
#define freqmax 0.05                                  /* 0.05 = 20 days (1/20) */
#define freq_change_min 2.5
#define wmin 1
#define wmax 7000
#define wscale_change 3000
#define wmax_3 wmax*3
#define JDoffset 2450500.0
#define Maxlinechar 120
double wt( double f, double t);
```

F.2.2 Implementation of the Grison algorithm, `findmoamcebs.c`

The main program `findmoamcebs.c`, to detect and extract eclipsing binaries from the MOA database.

/ Period search algorithm based on the P Grison mathematical code (A&A 289 no.2 pg404-410). The data is extracted from the photometric time series database provided by MOA. The stars that are detected as possible eclipsing binaries (although stars other than eclipsing binaries will be detected), are phased to the top three most probable periods detected. The output is in the form of a PostScript file that contains the raw photometirc data, periodogram, light curve phased to the top three most probable periods. NOTE: This program only uses the red bandpass data for the period searching as it was determined to be of slightly better quality */*

```
#include "pgpf.h"
#define SD_cut 1.8
#define datalength 200

main(int argc, char *argv[])
{
  void nerror();
  time_t now;
  FILE *fptr2;
  FILE *fptr3;
  FILE *fptr;
  int ID;                                          /* Requested star ID */
  int i=0;                                         /* Integer */
  int nred, nblue, nRB;                            /* Number of red and blue observations */
  int grp_no = 0;                                  /* database group number */
  char *field;                                     /* Observation field name */
  char dataname[30] = "";                          /* data field name */
  char fname1[30] = "";                            /* Star filename */
  char fname2[40] = "";                            /* Star filename */
  char fname3[40] = "";                            /* Star filename */
  char ch[5] = "";                                 /* Character to add ID number to filename */
  char lines[Maxlinechar];
  char *buffer1;
  char *buffer2;
  char *probptrs;
  time_t current = time(NULL);
  struct tm *ptr;
  char date_time[30];
  int m=0, e=0, p=0, pmax=4, pms=16, z=1, v;
  int total_pointsred, total_pointsblue, diff1, diff2, ndatapoints, indexred, indexblue,
newlimitr, newlimitb, pfd=0, max_num_files, max_numb_files;
  double I, J, Jtop, Jbottom, SDred, SDblue, minred, minblue, maxred, maxblue, meanred,
meanblue;
  double r1, r2, r3;
  double sumred, sumblue, magdiffred, magdiffblue, pfdmin, variable_cutr, variable_cutb;
  double totalsumred, totalsumblue, SD_cut_red_max, SD_cut_blue_max;
  double SD_cut_red_min, SD_cut_blue_min, probmax_1, probmax_2, probmax_3;
  double test, one_m_betai_result, pow_result, trial_Pkmax_value;
  int w, k, Nf, Nn, j, num, Nir, Nib, imin, debug, k_1, redint, blueint, nred_1;
```

```
  double redmean, totalr, bluemean, totalb, rxmax, rxmin, bxmin, bxmax, rxdif;
  double s2b, s2r, num_j, bxdif, *Pkmax, loghigh=0.0;
  double wprobmax11, wprobmax12, wprobmax13, wprobmax21, wprobmax22,
wprobmax23, wprobmax31, wprobmax32, wprobmax33;
  double sin(double x), cos(double x), sinkwt, coskwt;
  double a, b, q, Ni, *freq_period, period_1, period_2, period_3;
  int *probtestfreqmax, *testfreqmax;
  double *probmax, *probfalsedection, *log10_result, **pmsort, *pmsort1,*pmsort2,
*pmsort3, *pmsort4, *pmsortmax;
  dataset red[MAXOBS], blue[MAXOBS], RB[MAXOBS];
/* Define storage arrays */
  double *P, *sgnP, *redmagnew, *bluemagnew, *redmag, *bluemag, *redJD, *blueJD;
  double *weight, *deltared, *deltablue;
  double sum_apcbps, sum_apsbps, *Possible_period;
  double sin2wt, cos2wt, sum_sin2kwt, sum_cos2kwt;
  double tau, *testfreq, *Xr, *Xb;
  double betai_comp_x, *bluephase, *redphase, Nk, Dk;
  double sum_phicc, sum_phics, sum_phisc, sum_phiss, sum_phicksk;
  double sum_phic_itcoskwt, sum_phic_itsinkwt, sum_phis_itcoskwt, sum_phis_itsinkwt;
  double sum_phic_icostsq, sum_phic_isintsq;
  double **log10_Prob, **log10_Probsort;
  double sum_Xr_phic, sum_Xr_phis, sum_phic_sq, sum_phis_sq;
  double *NA, *NB, *DA, *DB, *Ac, *As, *Bc, *Bs;
  double **Periodogram, **Prob, A, B, **pi_sum, **sum_pi_sum, *freqpm;
  double alpha_cik, alpha_sik, beta_cik, beta_sik;
  double **phic, **phis, **probs;
  double **probmax1, **probmax2, **probmax3, *probmax_f, **prob_values;
  /* Assign names to vectors, 2-D and 3D arrays */
  freq_period = dvector(1,kmax);
  probfalsedection = dvector(1,kmax);
  log10_result = dvector(1,kmax);
  sgnP = dvector(1,maxdata);
  deltared = dvector(1,maxdata);
  deltablue = dvector(1,maxdata);
  P = dvector(1,maxdata);
  redmagnew = dvector(1,maxdata);
  bluemagnew = dvector(1,maxdata);
  weight = dvector(1,maxdata);
  Possible_period = dvector(1,kmax);
  Pkmax = dvector(1,kmax);
  probmax = dvector(1,kmax);
  testfreqmax = ivector(1,kmax);
  probtestfreqmax = ivector(1,kmax);
  buffer1 = cvector(1,Maxlinechar);
  buffer2 = cvector(1,Maxlinechar);
  redJD = dvector(1,maxdata);
  redmag = dvector(1,maxdata);
  blueJD = dvector(1,maxdata);
  bluemag = dvector(1,maxdata);
  testfreq = dvector(1,wmax);
  Xr = dvector(1,n);
  Xb = dvector(1,n);
  pmsort1 = dvector(1,pmax);
  pmsort2 = dvector(1,pmax);
  pmsort3 = dvector(1,pmax);
```

```
  pmsort4 = dvector(1,pmax);
  pmsortmax = dvector(1,pms);
  probs = dmatrix(1,4,1,wmax_3);
  prob_values = dmatrix(1,9,1,9);
  freqpm = dvector(1,wmax);
  bluephase = dvector(1,n);
  redphase = dvector(1,n);
  probmax1 = dmatrix(1,wmax_3,1,2);
  probmax2 = dmatrix(1,wmax,1,2);
  probmax3 = dmatrix(1,wmax,1,2);
  probmax_f = dvector(1,kmax);
  log10_Prob = dmatrix(1,kmax,1,wmax);
  log10_Probsort = dmatrix(1,kmax,1,wmax);
  Periodogram = dmatrix(1,kmax,1,wmax);
  pmsort = dmatrix(1,kmax,1,pmax);
  Prob = dmatrix(1,kmax,1,wmax);
  pi_sum = dmatrix(1,kmax,1,wmax);
  sum_pi_sum = dmatrix(1,kmax,1,wmax);
  NA = dvector(1,jmax);
  NB = dvector(1,jmax);
  DA = dvector(1,jmax);
  DB = dvector(1,jmax);
  Ac = dvector(1,jmax);
  As = dvector(1,jmax);
  Bc = dvector(1,jmax);
  Bs = dvector(1,jmax);
  phic = dmatrix(1,kmax,1,n);
  phis = dmatrix(1,kmax,1,n);

/*****************************************************************************/

debug=1;
if (debug == 1) printf("\nStarting Philip Grison period search\n\n");

/* Program line arguments */
/* NOTE: The program uses only the red bandpass data for the period searching */
if (argc ≠ 4) {
  printf("Usage:  findmcebs field-name ID_request max_num_files <
groupfilename\n");
  exit(0);
}

/* Read in the parameters */
field = &argv[1][0];
ID = atoi(argv[2]);
max_num_files = atoi(argv[3]);

/* Loop over the each star, calculate statistics to decide if to process further */
while (ID≤max_num_files) {
  fetch_star(ID, &nred, &red[0], &nblue, &blue[0]);
  nRB = make_CI(&RB[0], nred, &red[0], nblue, &blue[0]);
  totalr=totalb=meanred=meanblue=0.0;
  maxred=minred=red[0].mag;
  maxblue=minblue=blue[0].mag;
```

```
/* Adjust the matrices */
  for (i=0; i<nred; ++i){
    redmag[i+1]=red[i].mag;
    totalr += red[i].mag;
    redJD[i+1]=red[i].JD;
  }
  for (i=0; i<nblue; ++i){
    bluemag[i+1]=blue[i].mag;
    totalb += blue[i].mag;
    blueJD[i+1]=blue[i].JD;
  }

/* Calculate the mean of the raw data */
  meanred = totalr/nred;
  meanblue = totalb/nblue;

/* Calculate the Standard Deviation of the raw data */
  sumred=sumblue=0.0;
  for (i=1; i≤nred; ++i){
    sumred+=(redmag[i]-meanred)*(redmag[i]-meanred);
  }

  for (i=1; i≤nblue; ++i){
    sumblue+=(bluemag[i]-meanblue)*(bluemag[i]-meanblue);
  }

  totalsumred=(1.0/(nred-1.0))*sumred;
  totalsumblue=(1.0/(nblue-1.0))*sumblue;
  SDred=SD_cut*sqrt(totalsumred);
  SDblue=SD_cut*sqrt(totalsumblue);

/* Make the Standard Deviation cuts of the raw data */
/* Note: the magitudes are negative values */
  SD_cut_red_max=meanred-SDred;
  SD_cut_red_min=meanred+SDred;
  SD_cut_blue_max=meanblue-SDblue;
  SD_cut_blue_min=meanblue+SDblue;
  indexred=0;

  for (i=1; i≤nred; ++i){
    if (redmag[i] > SD_cut_red_max || redmag[i] < SD_cut_red_min)
redmagnew[i-indexred]=redmag[i];
    if (redmag[i] < SD_cut_red_max || redmag[i] > SD_cut_red_min)
    indexred+=1;
  }

  newlimitr=nred-indexred;

  indexblue=0;
  for (i=1; i≤nblue; ++i){
    if (bluemag[i] > SD_cut_blue_max || bluemag[i] < SD_cut_blue_min)
bluemagnew[i-indexblue]=bluemag[i];
    if (bluemag[i] < SD_cut_blue_max || bluemag[i] > SD_cut_blue_min)
    indexblue+=1;
  }
```

```
  newlimitb=nblue-indexblue;

/* Recalculate mean SD, min, max */
  maxred=minred=meanred;
  minblue=maxblue=meanblue;
  totalr=totalb=0.0;

  for (i=1; i≤newlimitr; ++i){
    totalr += redmagnew[i];
      if (redmagnew[i] > maxred) maxred=redmagnew[i];
      if (redmagnew[i] < minred) minred=redmagnew[i];
  }
  for (i=1; i≤newlimitb; ++i){
    totalb += bluemagnew[i];
      if (bluemagnew[i] > maxblue) maxblue=bluemagnew[i];
      if (bluemagnew[i] < minblue) minblue=bluemagnew[i];
  }

/* Calculate the new mean */
  meanred = totalr/newlimitr;
  meanblue = totalb/newlimitb;
  sumred=sumblue=totalsumred=totalsumblue=0.0;
  for (i=1; i≤newlimitr; ++i){
    sumred+=(redmagnew[i]-meanred)*(redmagnew[i]-meanred);
  }
  for (i=1; i≤newlimitb; ++i){
    sumblue+=(bluemagnew[i]-meanblue)*(bluemagnew[i]-meanblue);
  }
  totalsumred=(1.0/(newlimitr-1.0))*sumred;
  totalsumblue=(1.0/(newlimitb-1.0))*sumblue;
  SDred=sqrt(totalsumred);
  SDblue=sqrt(totalsumblue);
  magdiffred=maxred-minred;
  magdiffblue=maxblue-minblue;

/* Open and write to the statistics file */
  if (magdiffred≥0.25 && magdiffblue≥0.25 && nred>50 && nblue>50){
    printf("\n\nStar %d is being processed\n\n",ID);

/* Write the red bandpasss data to a file */
    totalr=s2r=redmean=0.0;
    rxmax=rxmin=red[0].JD-JDoffset;

    for (i=0; i<nred; ++i){
      redJD[i+1]=red[i].JD;
      redmag[i+1]=red[i].mag;
    }

    redJD[i]=redJD[i]-JDoffset;
    totalr += redmag[i];
    s2r+=redmag[i]*redmag[i];
    if (redJD[i] > rxmax) rxmax=redJD[i];
    if (redJD[i] < rxmin) rxmin=redJD[i];
    }
```

```
    redmean = totalr/nred;
    s2r = s2r/(nred - 1) - nred*redmean*redmean/(nred-1);
    rxdif=rxmax-rxmin;

/* Write the blue bandpass data to a file */
    totalb=s2b=bluemean=0.0;
    bxmax=bxmin=blue[i].JD-JDoffset;
    for (i=0; i<nblue; ++i){
      blueJD[i+1]=blue[i].JD;
      bluemag[i+1]=blue[i].mag;
    }

    for (i=1; i≤nblue; i++){
      blueJD[i]=blueJD[i]-JDoffset;
      totalb += bluemag[i];
      s2b+=bluemag[i]*bluemag[i];
      if (blueJD[i] > bxmax) bxmax=blueJD[i];
      if (blueJD[i] < bxmin) bxmin=blueJD[i];
    }
    bluemean = totalb/nblue;
    s2b = s2b/(nblue - 1) - nblue*bluemean*bluemean/(nblue-1);
    bxdif=bxmax-bxmin;

/* Find the deviation of the ordinate */
    if (nred == nblue){
      for (i=1; i≤nred; i++){
        Xr[i]=redmag[i] - redmean;
        Xb[i]=bluemag[i] - bluemean;
      }
    }
    if (nred ≠ nblue) {
      for (i=1; i≤nred; i++){
        Xr[i]=redmag[i] - redmean;
      }
    }
    if (nred ≠ nblue) {
      for (i=1; i≤nblue; i++){
        Xb[i]=bluemag[i] - bluemean;
      }
    }

/* Create test frequencies and fit harmonics*/
    Nir = nred*OFAC*HIFAC;
    Nib = nblue*OFAC*HIFAC;

    printf("Fitting the harmonics...\n\n");
    Ni=nred*OFAC*HIFAC;
    nred_1=(nred-1);
    a=(((double) nred_1)/2.0);
    for (k=1; k≤kmax; k++) {
      Pkmax[k]=0.;
      testfreqmax[k]=0;
      probmax[k]=1e-16;
      probtestfreqmax[k]=0;
    }
```

```
    for (w=wmin; w≤wmax; w++) {
      if (w≤wscale_change){
        testfreq[w]=freqmax+((w-1)*(freqmin-freqmax)/(wscale_change-wmin));
      }
      else{
      testfreq[w]=freq_change_min-((wmax-w-1)*(freq_change_min-freqmin)/(wmax-
wscale_change));
      }
      for (k=1; k≤kmax; k++){
        k_1=k-1;
        i=0;
        if (k==1){
          sum_phicksk=0.0;
          sin2wt = 0.0;
          cos2wt = 0.0;
          for (i=1; i≤nred; i++) {
            sin2wt += sin(2.0*wt(testfreq[w],redJD[i]));
            cos2wt += cos(2.0*wt(testfreq[w],redJD[i]));
          }
          tau = 0.5*atan2(sin2wt,cos2wt);
          for (i=1; i≤nred; i++) {
            phic[k][i] = cos((wt(testfreq[w],redJD[i])) - tau);
            phis[k][i] = sin((wt(testfreq[w],redJD[i])) - tau);
            sum_phicksk+=phic[k][i]*phis[k][i];
          }
          if (sum_phicksk>5.0e-8){
            printf("CAUTION: k==1 orthogonality functions summation checks are
not zero\n(sum_phicksk > 5.0e-8)\nRefer to code pgpf.c at line
450\nsum_phicksk[%d]=%e\n",w,sum_phicksk);
          }
        }

/* Calculate parameters Ac, As, Bc, Bs, DA, DB, NA, NB, N, D */
        if (k>1){
          for (j=jmin; j≤k_1; j++) {
            sum_phic_itcoskwt = 0.0;
            sum_phic_itsinkwt = 0.0;
            sum_phis_itcoskwt = 0.0;
            sum_phis_itsinkwt = 0.0;
            sum_phic_icostsq = 0.0;
            sum_phic_isintsq = 0.0;
            if ( j == jmin ) {
              Nk = 0.0;
              Dk = 0.0;
            }
            for (i=1; i≤nred; i++) {
              coskwt = cos(k*wt(testfreq[w],redJD[i]));
              sinkwt = sin(k*wt(testfreq[w],redJD[i]));
              sum_phic_itcoskwt += phic[j][i]*coskwt;
              sum_phic_itsinkwt += phic[j][i]*sinkwt;
              sum_phis_itcoskwt += phis[j][i]*coskwt;
              sum_phis_itsinkwt += phis[j][i]*sinkwt;
              sum_phic_icostsq += phic[j][i]*phic[j][i];
              sum_phic_isintsq += phis[j][i]*phis[j][i];
            }
```

```
            Ac[j] = sum_phic_itcoskwt/sum_phic_icostsq;
            As[j] = sum_phic_itsinkwt/sum_phic_icostsq;
            Bc[j] = sum_phis_itcoskwt/sum_phic_isintsq;
            Bs[j] = sum_phis_itsinkwt/sum_phic_isintsq;
            NA[j] = Ac[j]*As[j];
            NB[j] = Bc[j]*Bs[j];
            DA[j] = (As[j]*As[j] - Ac[j]*Ac[j])/2.0;
            DB[j] = (Bs[j]*Bs[j] - Bc[j]*Bc[j])/2.0;
            Nk += NA[j]*sum_phic_icostsq + NB[j]*sum_phic_isintsq;
            Dk += DA[j]*sum_phic_icostsq + DB[j]*sum_phic_isintsq;
          }
          sum_sin2kwt = -2.0*Nk;
          sum_cos2kwt = 2.0*Dk;
          for (i=1; i≤nred; i++) {
            sum_sin2kwt += (sin(2.0*k*wt(testfreq[w],redJD[i])));
            sum_cos2kwt += (cos(2.0*k*wt(testfreq[w],redJD[i])));
          }
          tau = 0.5*atan2(sum_sin2kwt,sum_cos2kwt);
          sum_phicksk=0.0;
          for (i=1; i≤nred; i++) {
            sum_apcbps = 0.0;
            sum_apsbps = 0.0;
            for (j=jmin; j≤k_1; j++) {
              alpha_cik = cos(tau)*Ac[j] + sin(tau)*As[j];
              alpha_sik = cos(tau)*As[j] - sin(tau)*Ac[j];
              beta_cik = cos(tau)*Bc[j] + sin(tau)*Bs[j];
              beta_sik = cos(tau)*Bs[j] - sin(tau)*Bc[j];
              sum_apcbps+=alpha_cik*phic[j][i] + beta_cik*phis[j][i];
              sum_apsbps+=alpha_sik*phic[j][i] + beta_sik*phis[j][i];
            }
            phic[k][i]=cos(k*wt(testfreq[w],redJD[i])-tau) - sum_apcbps;
            phis[k][i]=sin(k*wt(testfreq[w],redJD[i])-tau) - sum_apsbps;
            sum_phicksk+=phic[k][i]*phis[k][i];
          }
/* Orthogonality checks */
          if (sum_phicksk>5.0e-8) {
            printf("CAUTION: k==%d orthogonality functions summation checks are
not zero\n(sum_phicksk[%d]=%e > 5.0e-8)\nRefer to code findmcebs.c at line
603\n",k,w,sum_phicksk);
          }
          for (j=jmin; j≤k_1; j++) {
            sum_phicc=0.0;
            sum_phics=0.0;
            sum_phisc=0.0;
            sum_phiss=0.0;
            for (i=1; i≤nred; i++) {
              sum_phicc+=phic[j][i]*phic[k][i];
              sum_phics+=phic[j][i]*phis[k][i];
              sum_phisc+=phis[j][i]*phic[k][i];
              sum_phiss+=phis[j][i]*phis[k][i];
            }
            if (i≤nred){
              if (sum_phicc>5.0e-8){
                printf("CAUTION: orthogonality functions summation checks are
not zero\nSummed value of sum_phicc[%d] > 5.0e-8, sum_phicc[%d] = %e\nRefer to
```

```
code finmcebs.c at line 616\n",w,w, sum_phicc);
                }
              }
              if (i≤nred){
                if (sum_phics>5.0e-8){
                  printf("CAUTION: orthogonality functions summation checks are
not zero\nSummed value of sum_phics[%d] > 5.0e-8 sum_phics[%d] = %e\nRefer to
code findmcebs.c at line 617\n",w,w, sum_phics);
                }
              }
              if (i≤nred){
                if (sum_phisc>5.0e-8){
                  printf("CAUTION: orthogonality functions summation checks are
not zero\nSummed value of sum_phisc[%d] > 5.0e-8 sum_phisc[%d] = %e\nRefer to
code findmcebs.c at line 618\n",w,w, sum_phisc);
                  printf("phis[%d][%d][%d] = %e, phic[%d][%d][%d]=
%e\n\n",j,w,i,phis[j][i],j+1,w,i,phic[k][i]);
                }
              }
              if (i≤nred){
                if (sum_phiss>5.0e-8){
                  printf("CAUTION: orthogonality functions summation checks are
not zero\nSummed value of sum_phiss[%d] > 5.0e-8 sum_phiss[%d] = %e\nRefer to
code findmcebs.c at line 619\n",w,w, sum_phiss);
                }
              }
            }
          }
          sum_Xr_phic = 0.;
          sum_Xr_phis = 0.;
          sum_phic_sq = 0.;
          sum_phis_sq = 0.;
          for (i=1; i≤nred; i++) {
            sum_Xr_phic += (Xr[i]*phic[k][i]);
            sum_Xr_phis += (Xr[i]*phis[k][i]);
            sum_phic_sq += (phic[k][i]*phic[k][i]);
            sum_phis_sq += (phis[k][i]*phis[k][i]);
          }
          A = (sum_Xr_phic/sum_phic_sq);
          B = (sum_Xr_phis/sum_phis_sq);

/* Calculate Periodogram */
          pi_sum[k][w] = ((A*A)*sum_phic_sq) + ((B*B)*sum_phis_sq);
          sum_pi_sum[k][w]=pi_sum[k][w];
          if (k>1) sum_pi_sum[k][w]+=sum_pi_sum[k_1][w];
          Periodogram[k][w] = (1/(2*k*s2r))*sum_pi_sum[k][w];
          b=(double) k;
          trial_Pkmax_value=(Periodogram[k][w]/1.0);
          betai_comp_x=((double) nred_1)/(((double) nred_1) +
2.0*((double)k)*(double)trial_Pkmax_value);
          one_m_betai_result=(1-betai(a,b,betai_comp_x));
          pow_result=pow(one_m_betai_result,Ni);
          Prob[k][w]=1.0-pow_result;
          if(Prob[k][w]<1e-50){
            Prob[k][w]=1e-50;
```

```
      }
      log10_Prob[k][w]=log10(Prob[k][w]);
      log10_Probsort[k][w]=log10(Prob[k][w]);
      if (log10_Prob[k][w]<probmax[k]){
       probmax[k]=log10_Prob[k][w];
       probmax_f[k]=testfreq[w];
      }
      if (log10_Prob[k][w]<loghigh)
        loghigh=log10_Prob[k][w];
      if (Periodogram[k][w] ≥ Pkmax[k]){
        Pkmax[k]=Periodogram[k][w];
        testfreqmax[k]=w;
      }
    } /********** End of (k>1) loop **********/
  } /********** End of (w=wmin; w<=wmax; w++) loop **********/

  printf("\nFitting of harmonics completed\n\n");
  printf("Calculating periods and writing files ...\n\n");

  /* Calculate probability of false detection */
  m=1;
  prob_values[1][1]=probmax[1];
  prob_values[1][2]=probmax_f[1];
  prob_values[4][1]=probmax[2];
  prob_values[4][2]=probmax_f[2];
  prob_values[7][1]=probmax[3];
  prob_values[7][2]=probmax_f[3];
  while (m<3){
    for (w=wmin; w≤wmax; w++) {
      for (k=1; k≤3; k++){
        if (testfreq[w]>(probmax_f[k]-0.005) && (testfreq[w]<probmax_f[k]+0.005))
        log10_Probsort[k][w]=0.0;
      }
    }

    probmax[1]=probmax[2]=probmax[3]=probmax[4]=-0.001;

    for (w=wmin; w≤wmax; w++) {
      for (k=1; k≤3; k++){
        if (log10_Probsort[k][w]<probmax[k]){
          probmax[k]=log10_Probsort[k][w];
          probmax_f[k]=testfreq[w];
        }
      }
    }
    if (m==1){
      prob_values[2][1]=probmax[1];
      prob_values[2][2]=probmax_f[1];
      prob_values[5][1]=probmax[2];
      prob_values[5][2]=probmax_f[2];
      prob_values[8][1]=probmax[3];
      prob_values[8][2]=probmax_f[3];
    }
    if (m==2){
      prob_values[3][1]=probmax[1];
```

```
            prob_values[3][2]=probmax_f[1];
            prob_values[6][1]=probmax[2];
            prob_values[6][2]=probmax_f[2];
            prob_values[9][1]=probmax[3];
            prob_values[9][2]=probmax_f[3];
        }
        m++;
    }

    probmax[1]=probmax[2]=probmax[3]=probmax[4]=0.0;


    for(k=1; k≤9; ++k){
        if (prob_values[k][1]<probmax[1]){
            probmax[1]=prob_values[k][1];
            e=k;
            freq_period[1]=prob_values[k][2];
        }
    }

    prob_values[e][1]=0.0;

    for(k=1; k≤9; ++k){
        if (prob_values[k][1]<probmax[2] && (prob_values[k][2]<(freq_period[1]-0.005) ||
prob_values[k][2]>(freq_period[1]+0.005))){
            probmax[2]=prob_values[k][1];
            e=k;
            freq_period[2]=prob_values[k][2];
        }
    }

    prob_values[e][1]=0.0;

    for(k=1; k≤9; ++k){
        if (prob_values[k][1]<probmax[3] && (prob_values[k][2]<(freq_period[2]-0.005) ||
prob_values[k][2]>(freq_period[2]+0.005)) && (prob_values[k][2]<(freq_period[1]-0.005) ||
prob_values[k][2]>(freq_period[1]+0.005))){
            probmax[3]=prob_values[k][1];
            e=k;
            freq_period[3]=prob_values[k][2];
        }
    }

    for (k=1; k≤kmax; k++) {
        Possible_period[k]=1.0/testfreq[testfreqmax[k]];
        probfalsedection[k]=log10_Prob[k][testfreqmax[k]];
        if (k==1) pfdmin=probfalsedection[1];
        if (probfalsedection[k] ≤ pfdmin){
            pfd=k;
        }

/* Calculation of the three periods */
        if(k==4){
            period_1=1.0/freq_period[1];
            period_2=1.0/freq_period[2];
```

```
        period_3=1.0/freq_period[3];
        printf("freq_period_1=%e\n",freq_period[1]);
        printf("freq_period_2=%e\n",freq_period[2]);
        printf("freq_period_3=%e\n",freq_period[3]);
        printf("period_1=%f\n",period_1);
        printf("period_2=%f\n",period_2);
        printf("period_3=%f\n",period_3);
        printf("Star ID number=%d\n",ID);

/* Search for multiples of 1.5,2.0,3.0,1/1.5,1/2,1/3 with errors of +-0.003 */
        r1=period_1/period_2;
        r2=period_1/period_3;
        r3=period_2/period_3;
        printf("r1=%f\n",r1);
        printf("r2=%f\n",r2);
        printf("r3=%f\n",r3);
        probmax_1=probmax[1]*-1.0;
        probmax_2=probmax[2]*-1.0;
        probmax_3=probmax[3]*-1.0;
        if (
        ((period_1<0.99 || period_1>1.01) && (period_2<0.99 || period_2>1.01) &&
(period_3<0.99 || period_3>1.01)) &&
        ((r1>1.497 && r1<1.503) || (r1>1/1.503 && r1<1/1.497) || (r1>1.997 && r1<2.003)
|| (r1>1/2.003 && r1<1/1.997) || (r1>2.997 && r1<3.003) || (r1>1/3.003 && r1<1/2.997) ||
        (r2>1.497 && r2<1.503) || (r2>1/1.503 && r2<1/1.497) || (r2>1.997 && r2<2.003)
|| (r2>1/2.003 && r2<1/1.997) || (r2>2.997 && r2<3.003) || (r2>1/3.003 && r2<1/2.997) ||
        (r3>1.497 && r3<1.503) || (r3>1/1.503 && r3<1/1.497) || (r3>1.997 && r3<2.003)
|| (r3>1/2.003 && r3<1/1.997) || (r3>2.997 && r3<3.003) || (r3>1/3.003 && r3<1/2.997))
&&
        ((probmax_1>0.25) || (probmax_2>0.25) || (probmax_3>0.25))){
          printf("Probmax_1=%f\n",probmax_1);
          printf("Probmax_2=%f\n",probmax_2);
          printf("Probmax_3=%f\n",probmax_3);

/* Read in and redirect the first section of grison_analysis.ps file */
          for (i=1; i≤nred; i++){
            redJD[i]=redJD[i]+JDoffset;
          }
          for (i=1; i≤nblue; i++){
            blueJD[i]=blueJD[i]+JDoffset;
          }
          printf("setting the file names to open\n");
          sprintf(fname2,"grison_analysis_data%04d.ps",ID);
          sprintf(fname3,"grison_analysis.ps");
          sprintf(fname1,"starfile%04d.dat",ID);
/* Add the ID index to the filename */
          fptr = fopen(fname1,"w");          /* Open the file and write the data */
          fptr2=fopen(fname2,"w");
          fptr3=fopen(fname3,"r");
          strcpy(buffer1,"+-");
          printf("files opened, about to write\n");
          while (strncmp(buffer1,"%*",2) ≠ 0){
            fgets(buffer1, Maxlinechar, fptr3);
            fputs(buffer1,fptr2);
          }
```

```
            fprintf(fptr2, "/title {(Starfile%04d.dat)} def\n",ID);
            fprintf(fptr2, "/blueavmag { %f } def\n", bluemean);
            fprintf(fptr2, "/redavmag { %f } def\n", redmean);
            fprintf(fptr2, "/loghigh { %f } def\n", loghigh);
            fprintf(fptr2, "/Period1 { %f } def\n", period_1);
            fprintf(fptr2, "/Period2 { %f } def\n", period_2);
            fprintf(fptr2, "/Period3 { %f } def\n", period_3);
            fprintf(fptr2, "/no_frequencies { %d } def\n",wmax);
            ptr=localtime(&current);
            strftime(date_time, sizeof(date_time), "%A, %B %d, %Y", localtime(&current));
            fprintf(fptr2, "/date&time {(%d:%02d:%02d on %s)} def\n", ptr→tm_hour,
ptr→tm_min, ptr→tm_sec, date_time);
            loghigh=0.0;
            while (strncmp(buffer2,"%*",2) ≠ 0){
              fgets(buffer2, Maxlinechar, fptr3);
              fputs(buffer2,fptr2);
            }
            for (i=1; i≤nblue; i++){
              if (blueJD[i]≠0){
                fprintf(fptr2,"( %lf ) %010f b\n", blueJD[i], bluemag[i]);
               fprintf(fptr,"%lf %010f b\n", blueJD[i], bluemag[i]); }
              else{
                fprintf(fptr2,"%%A Julian date with the value of zero has been
encountered %lf %010f b\n", blueJD[i], bluemag[i]);
              }
            }
            for (i=1; i≤nred; i++){
              if (redJD[i]≠0){
                fprintf(fptr2,"( %lf ) %010f r\n", redJD[i], redmag[i]);
                fprintf(fptr,"%lf %010f r\n", redJD[i], redmag[i]); }
              else{
                fprintf(fptr2,"%%A Julian date with the value of zero has been
encountered %lf %010f r\n", redJD[i], redmag[i]);
              }
            }
            for (w=wmin; w≤wmax; w++){
             fprintf(fptr2,"%f %013e P1\n", testfreq[w],(log10_Prob[1][w]));
            }
            for (w=wmin; w≤wmax; w++){
             fprintf(fptr2,"%f %013e P2\n",testfreq[w],(log10_Prob[2][w]));
            }
            for (w=wmin; w≤wmax; w++){
             fprintf(fptr2,"%f %013e P3\n",testfreq[w],(log10_Prob[3][w]));
            }
            for (w=wmin; w≤wmax; w++){
             fprintf(fptr2,"%f %013e P4\n",testfreq[w],(log10_Prob[4][w]));
            }
            fprintf(fptr2,"showpage\n");
            strcpy(buffer2,"a");
            printf("Closing files\n");
            fclose(fptr3);
            fclose(fptr2);
            fclose(fptr);
          }  /* End of "if (...period criteria...)" condition */
        }  /* End of "if (k==4)" condition */
```

```
      fname1[0] = '\0';          /* Write the null character to the filename to reset it */
    }  /* End of "if(k=1; k<=kmax; k++)" condition */
  }  /* End of "if(magdiffred>=0.25 && magdiffblue>=0.25 && nred>50 && nblue>50)" condition */
 ID++;                                                    /* get next star to process */
}  /* End of "while (ID<=max_num_files)" condition */
}  /* End of "main(int argc, char *argv[])" */


/************************* FUNCTIONS ******************************/

double
wt(double f, double t)
{
  return(twopi*f*t);
}



double
betai(double a,double b,double x)
{
  //float betacf(),gammln();
  void nrerror();
  double bt;

  if (x < 0.0 || x > 1.0) nrerror("Bad x in routine betai");
  if (x == 0.0 || x == 1.0) bt=0.0;
  else
    bt=exp(gammln(a+b)-gammln(a)-gammln(b)+a*log(x)+b*log(1.0-x));
  if (x < (a+1.0)/(a+b+2.0))
    return bt*betacf(a,b,x)/a;
  else
    return 1.0-bt*betacf(b,a,1.0-x)/b;
}
/* (C) Copr. 1986-92 Numerical Recipes Software 51#. */



/* #define MAXIT 100 */
#define MAXIT 10000
#define EPS 3.0e-300
#define FPMIN 1.0e-350

double
betacf(double a,double b,double x)
{
  void nrerror();
  int m,m2;
  double aa,c,d,del,h,qab,qam,qap;

  qab=a+b;
  qap=a+1.0;
  qam=a-1.0;
  c=1.0;
```

```
  d=1.0-qab*x/qap;
  if (fabs(d) < FPMIN) d=FPMIN;
  d=1.0/d;
  h=d;

  for (m=1;m≤MAXIT;m++) {
    m2=2*m;
    aa=m*(b-m)*x/((qam+m2)*(a+m2));
    d=1.0+aa*d;
    if (fabs(d) < FPMIN) d=FPMIN;
    c=1.0+aa/c;
    if (fabs(c) < FPMIN) c=FPMIN;
    d=1.0/d;
    h *= d*c;
    aa = -(a+m)*(qab+m)*x/((a+m2)*(qap+m2));
    d=1.0+aa*d;
    if (fabs(d) < FPMIN) d=FPMIN;
    c=1.0+aa/c;
    if (fabs(c) < FPMIN) c=FPMIN;
    d=1.0/d;
    del=d*c;
    h *= del;
    if (fabs(del-1.0) < EPS) break;
  }
  if (m > MAXIT) nrerror("a or b too big, or MAXIT too small in betacf");
  return h;
}
#undef MAXIT
#undef EPS
#undef FPMIN
/* (C) Copr. 1986-92 Numerical Recipes Software 51#. */



double
gammln(double xx)
{
  double x,y,tmp,ser;
  static double cof[6]={76.18009172947146,-86.50532032941677,
                        24.01409824083091,-1.231739572450155,
                        0.1208650973866179e-2,-0.5395239384953e-5};
  int j;

  y=x=xx;
  tmp=x+5.5;
  tmp -= (x+0.5)*log(tmp);
  ser=1.000000000190015;
  for (j=0;j≤5;j++) ser += cof[j]/++y;
  return -tmp+log(2.5066282746310005*ser/x);
}
```

F.2.3 Graphical representation of the results, `grison_analysis_[ID. no.].ps`

This PostScript file presents the results graphically (Figure 3.2), for each possible eclipsing binary as determined by the `findmoamcebs.c` program. The ID. no. is assigned as the internal MOA catalogue number. The PostScript file can be viewed with `ghostview` or sent directly to a PostScript printer. Here is the skeleton code into which `findmoamcebs.c` writes. The photometric observations and log(probability of false detection) data from `findmoamcebs.c` are written at the end of this program. Shown are fives lines of sample data of the output per section.

```
%!PS-Adobe-2.0 EPSF-2.0
%%BoundingBox: 14 26 576 831
%
%%Pages: 2
%%EndComments
%%Page: 1 1
%
% PostScript output to display/print the results of the Grison analysis
% of the MOA 1996-97 observations of a single star.
%
%2000-Mar-05 Modifications by WT for 3 periods and phasing within
%2000-Mar-05 PostScript file itself
%2000-Mar-28 Frequencies up to 2.5 cycles/day

% scale coordinate system from points (1/72 inch) to millimetres
 72 25.4 div dup scale
% offset origin by 10 mm to right and upwards to avoid any areas that don't
% print
 10 10 translate

%2000-Mar-05
% rotate by 90 so as to become landscape
265 -5 translate 90 rotate
%2000-Mar-05

%2000-Mar-05
% Set line parameters
2 setlinejoin
0 setlinecap
2 setlinejoin
%2000-Mar-05

%*
%************************ To be written by c program ************************
% Define some parameters - will be written appropriately each time the file
% is written:
% /title {(The name of the star or other info)} def
% /blueavmag { -13.32 } def % will be rounded to nearest tenth
% /redavmag { -14.89 } def % will be rounded to nearest tenth
% /loghigh { -1790.3 } def % Need no longer be whole tenths. Note negative.
% /Period1 { 2.3456 } def % in days
% /Period2 { 2.3456 } def % in days
% /Period3 { 2.3456 } def % in days
% /no_frequencies { 3 } def % will really be 1000 or so.
```

```
% /date&time {(1999-Feb-02 10:00:00)} def
%*************************************************************************

%2000-Mar-05
% (2450567.123545) toModJD - sets real variable ModJD
/toModJD { /jd_string exch def
          0 1 jd_string length 1 sub { dup jd_string exch get 46 eq
                                        { /dec_point exch def } { pop } ifelse
                                        } for
          /mod_jd_string { (0000000000000000) } def
          dec_point 3 sub 1 jd_string length 1 sub { dup jd_string exch
          get exch dec_point sub 3 add exch mod_jd_string 3 1 roll put } for
          mod_jd_string cvr /ModJD exch def } def
%2000-Mar-05

% Define some more paramters - unlikely to be changed
 /titlesize { 6 } def
 /lhboxside { 20 } def
%2000-Mar-05
%180 changed to 160
 /rhboxside { 160 } def
%2000-Mar-05
 /photboxtop { 260 } def
 /photboxdepth { 25 } def
 /boxborderwidth { 0.3 } def
 /bigtick { 2.5 } def
 /smalltick { 1.3 } def
 /JDstart { 2450550 } def % Obviously just within precision
 /JDend { 2450810 } def % Obviously just within precision
%2000-Mar-05
 /JDModOffset { 2450000 } def
%2000-Mar-05
 /axislabelheight { 4 } def
 /no_tenths { 6 } def % Number of tenths of a magnitude plotted
                                % brigther and fainter than average
 /spotsize { 0.375 } def
 /probboxtop { photboxtop photboxdepth 2.75 mul sub } def
%2000-Mar-05
% 28 changed to 27
 /probboxdepth { 27 } def
%2000-Mar-05

% loghigh now set by calling program; loglow determined from loghigh
% /loglow { 0.1 } def % Must be whole tenths
% /loghigh { -1790.3 } def % Must be whole tenths
 /Flow { 0 } def % Must be whole tenths
%2000-Mar-28
 /Fintermediate { 1.0 } def % must be whole tenths, first 80% of scale
 /Fhigh { 2.5 } def % Must be whole tenths, remaining 20% of scale
%2000-Mar-28
 /phaseboxtop { photboxtop } def
 /phaselhboxside { 180 } def
 /phaserhboxside { 285 } def
 /phaseboxtranslate { -63 } def
 /PHstart { 0 } def
```

```
 /PHend { 2.0 } def
 /ylabeloffsetfactor { blueavmag 0 ge { 3.0 } { 3.3 } ifelse } def
                                        % 3.3 is good value if magnitudes negative
                                        % 3.0 is good value if magnitudes positive
%
 /str10 10 string def
% Title the plot
 /Helvetica findfont titlesize 1.5 mul scalefont setfont
 4 photboxtop titlesize 0.5 mul add moveto (MOA) show
 /Helvetica findfont titlesize scalefont setfont
%2000-Mar-05
% 2 changed to 2.3
 title dup stringwidth pop -2 div rhboxside 2.3 div add photboxtop 5 add
%2000-Mar-05
 moveto show


% Plot the observations - between JDs 2450550 and 2450810
 /xforJD { JDstart sub JDend JDstart sub div rhboxside lhboxside sub mul
           lhboxside add } def
%2000-Mar-05
 /xforModJD { JDstart JDModOffset sub sub JDend JDstart sub div rhboxside
              lhboxside sub mul lhboxside add } def
%2000-Mar-05
 /nearest_tenth { dup 0 ge { 0.05 add } {0.05 sub } ifelse
                  10 mul cvi 10 div } def
 /ymagincr { photboxdepth no_tenths div 2 div } def
% mag yformag --> ordinate corresponding to mag
 /blueyformag { blueavmag nearest_tenth sub photboxdepth mul no_tenths div
                -2 div 10 mul photboxtop add photboxdepth 0.5 mul sub } def
 /redyformag { redavmag nearest_tenth sub photboxdepth mul no_tenths div
               -2 div 10 mul photboxtop add photboxdepth 1.5 mul sub } def
 /bluebright { blueavmag nearest_tenth no_tenths 10 div sub } def
 /bluefaint { blueavmag nearest_tenth no_tenths 10 div add } def
 /redbright { redavmag nearest_tenth no_tenths 10 div sub } def
 /redfaint { redavmag nearest_tenth no_tenths 10 div add } def

 /obsbox { boxborderwidth setlinewidth
           newpath lhboxside photboxtop moveto rhboxside photboxtop lineto
                   rhboxside photboxtop photboxdepth 2 mul sub lineto
                   lhboxside photboxtop photboxdepth 2 mul sub lineto
                   closepath stroke
           newpath lhboxside photboxtop photboxdepth sub moveto
                   rhboxside photboxtop photboxdepth sub lineto stroke
            /Helvetica findfont axislabelheight scalefont setfont
           JDstart 10 JDend { xforJD dup photboxtop moveto
                                 dup photboxtop smalltick sub lineto stroke
                              dup photboxtop photboxdepth sub smalltick add moveto
                              dup photboxtop photboxdepth sub smalltick sub lineto
                                 stroke
                              dup photboxtop photboxdepth 2 mul sub smalltick add
                                 moveto
                                 photboxtop photboxdepth 2 mul sub lineto stroke
                            } for
         JDstart 10 sub 100 idiv 1 add 100 mul 100 JDend
```

```
                    { dup dup xforJD exch str10 cvs dup stringwidth
                      pop -2 div 3 -1 roll add photboxtop
                      photboxdepth 2 mul sub
                      axislabelheight 1.5 mul sub moveto show
                  xforJD dup photboxtop moveto
                  dup photboxtop bigtick sub lineto stroke
                  dup photboxtop photboxdepth sub bigtick add moveto
                  dup photboxtop photboxdepth sub bigtick sub lineto
                      stroke
                  dup photboxtop photboxdepth 2 mul sub bigtick add
                      moveto
                      photboxtop photboxdepth 2 mul sub lineto stroke
                  } for
  rhboxside 0.70 mul photboxtop photboxdepth 2 mul sub axislabelheight
                2 mul sub moveto (JULIAN DAY) show
              bluebright .1 bluefaint { dup lhboxside exch blueyformag moveto
                                        dup lhboxside smalltick add exch
                                        blueyformag lineto stroke
                                        dup rhboxside exch blueyformag moveto
                                            rhboxside smalltick sub exch
                                        blueyformag lineto stroke
                                      } for
              redbright .1 redfaint { dup lhboxside exch redyformag moveto
                                      dup lhboxside smalltick add exch
                                      redyformag lineto stroke
                                      dup rhboxside exch redyformag moveto
                                          rhboxside smalltick sub exch
                                      redyformag lineto stroke
                                    } for
bluebright 2 mul dup 0 ge { .999 add } if cvi
          2 div 0.5 bluefaint 2 mul dup 0 le { .999 sub } if
                              cvi 2 div
                  { dup lhboxside exch blueyformag moveto
                                      dup lhboxside bigtick add exch
                                      blueyformag lineto stroke
                                      dup rhboxside exch blueyformag moveto
                                      dup rhboxside bigtick sub exch
                                      blueyformag lineto stroke
                                      dup str10 cvs dup stringwidth pop
                                      lhboxside exch sub axislabelheight
                                      0.5 mul sub 3 -1 roll blueyformag
                                      axislabelheight 2 div sub moveto show
                  } for
redbright 2 mul dup 0 ge { .999 add } if cvi
          2 div 0.5 redfaint 2 mul dup 0 le { .999 sub } if
                                cvi 2 div
                  { dup lhboxside exch redyformag moveto
                                      dup lhboxside bigtick add exch
                                      redyformag lineto stroke
                                      dup rhboxside exch redyformag moveto
                                      dup rhboxside bigtick sub exch
                                      redyformag lineto stroke
                                      dup str10 cvs dup stringwidth pop
                                      lhboxside exch sub axislabelheight
                                      0.5 mul sub 3 -1 roll redyformag
```

```
                                        axislabelheight 2 div sub moveto show
                                    } for
      90 rotate
      photboxtop photboxdepth 2 div sub (Blue mag.) stringwidth pop
      2 div sub lhboxside axislabelheight ylabeloffsetfactor mul sub neg
      moveto (Blue mag.) show
      photboxtop photboxdepth 1.5 mul sub (Red mag.) stringwidth pop
      2 div sub lhboxside axislabelheight ylabeloffsetfactor mul sub neg
      moveto (Red mag.) show
     -90 rotate
          } def
%2000-Mar-05
/bplot { newpath blueyformag exch xforModJD exch spotsize 0 360 arc fill } def
/rplot { newpath redyformag exch xforModJD exch spotsize 0 360 arc fill } def
%2000-Mar-05

obsbox


% Now the four boxes for the probabilities of false detection.
% Plot from -log from loglow to loghigh in ordinate and
% from 0 to Fmax in abscissa
/xforF { dup Fintermediate le
          { Flow sub Fintermediate Flow sub div rhboxside lhboxside sub mul
            0.8 mul lhboxside add }
          { Fintermediate sub Fhigh Fintermediate sub div rhboxside lhboxside
            sub
            mul 0.2 mul lhboxside add rhboxside lhboxside sub 0.8 mul add }
          ifelse
        } def
% n logProb yforProb --> y where n is the k value of the
% probability 1,2,3 or 4
/yforProb { loglow sub loghigh loglow sub div probboxdepth mul exch
              probboxdepth neg mul exch add probboxtop add } def

lhboxside probboxtop moveto rhboxside probboxtop lineto
rhboxside probboxtop probboxdepth 4 mul sub lineto
lhboxside probboxtop probboxdepth 4 mul sub lineto
closepath stroke
lhboxside probboxtop probboxdepth 1 mul sub moveto
  rhboxside probboxtop probboxdepth 1 mul sub lineto stroke
lhboxside probboxtop probboxdepth 2 mul sub moveto
  rhboxside probboxtop probboxdepth 2 mul sub lineto stroke
lhboxside probboxtop probboxdepth 3 mul sub moveto
  rhboxside probboxtop probboxdepth 3 mul sub lineto stroke

%2000-Mar-28
Flow 0.1 Fintermediate 0.01 sub
                        { dup dup str10 cvs dup stringwidth pop -2 div 4 -1 roll
                          xforF add probboxtop probboxdepth 4 mul sub
                          axislabelheight 1.5 mul sub moveto show
                          xforF dup probboxtop moveto
                          dup probboxtop bigtick sub lineto stroke
                          dup probboxtop probboxdepth sub bigtick add moveto
                          dup probboxtop probboxdepth sub bigtick sub
```

```
                lineto stroke
                dup probboxtop probboxdepth 2 mul sub bigtick add
                moveto
                dup probboxtop probboxdepth 2 mul sub bigtick sub
                lineto stroke
                dup probboxtop probboxdepth 3 mul sub bigtick add
                moveto
                dup probboxtop probboxdepth 3 mul sub bigtick sub
                lineto stroke
                dup probboxtop probboxdepth 4 mul sub bigtick add
                moveto
                probboxtop probboxdepth 4 mul sub lineto stroke

        } for

Fintermediate 0.5 Fhigh 0.01 add
                { dup dup str10 cvs dup stringwidth pop -2 div 4 -1 roll
                  xforF add probboxtop probboxdepth 4 mul sub
                  axislabelheight 1.5 mul sub moveto show
                  xforF dup probboxtop moveto
                  dup probboxtop bigtick sub lineto stroke
                  dup probboxtop probboxdepth sub bigtick add moveto
                  dup probboxtop probboxdepth sub bigtick sub
                  lineto stroke
                  dup probboxtop probboxdepth 2 mul sub bigtick add
                  moveto
                  dup probboxtop probboxdepth 2 mul sub bigtick sub
                  lineto stroke
                  dup probboxtop probboxdepth 3 mul sub bigtick add
                  moveto
                  dup probboxtop probboxdepth 3 mul sub bigtick sub
                  lineto stroke
                  dup probboxtop probboxdepth 4 mul sub bigtick add
                  moveto
                  probboxtop probboxdepth 4 mul sub lineto stroke

        } for

 rhboxside 0.70 mul probboxtop probboxdepth 4 mul sub axislabelheight
                2.5 mul sub moveto (FREQUENCY (cycle/day)) show
Flow 0.01 Fintermediate { xforF dup probboxtop moveto
                dup probboxtop smalltick sub lineto stroke
                dup probboxtop probboxdepth sub smalltick add moveto
                dup probboxtop probboxdepth sub smalltick sub
                lineto stroke
                dup probboxtop probboxdepth 2 mul sub smalltick add
                moveto
                dup probboxtop probboxdepth 2 mul sub smalltick sub
                lineto stroke
                dup probboxtop probboxdepth 3 mul sub smalltick add
                moveto
                dup probboxtop probboxdepth 3 mul sub smalltick sub
                lineto stroke
                dup probboxtop probboxdepth 4 mul sub smalltick add
                moveto
```

```
                    probboxtop probboxdepth 4 mul sub lineto stroke
                } for
Fintermediate 0.1 Fhigh { xforF dup probboxtop moveto
                    dup probboxtop smalltick sub lineto stroke
                    dup probboxtop probboxdepth sub smalltick add moveto
                    dup probboxtop probboxdepth sub smalltick sub
                    lineto stroke
                    dup probboxtop probboxdepth 2 mul sub smalltick add
                    moveto
                    dup probboxtop probboxdepth 2 mul sub smalltick sub
                    lineto stroke
                    dup probboxtop probboxdepth 3 mul sub smalltick add
                    moveto
                    dup probboxtop probboxdepth 3 mul sub smalltick sub
                    lineto stroke
                    dup probboxtop probboxdepth 4 mul sub smalltick add
                    moveto
                    probboxtop probboxdepth 4 mul sub lineto stroke
                } for
%2000-Mar-28

%2000-Mar-05
% set tick mark intervals
/small_ti { -0.1 } def
/big_ti { -0.5 } def

loghigh -3 lt { /small_ti -0.5 def /big_ti -1 def } if
loghigh -10 lt { /small_ti -1.0 def /big_ti -5 def } if
loghigh -30 lt { /small_ti -5 def /big_ti -10 def } if
loghigh -100 lt { /small_ti -10 def /big_ti -50 def } if
loghigh -300 lt { /small_ti -50 def /big_ti -100 def } if
loghigh -1000 lt { /small_ti -100 def /big_ti -500 def } if
/loglow { small_ti neg } def

  0 small_ti loghigh { /temp exch def 1 1 4
                    { temp yforProb dup dup dup lhboxside exch moveto
                                lhboxside smalltick add exch lineto stroke
                                rhboxside smalltick sub exch moveto
                                rhboxside exch lineto stroke
                              } for
                    } for
  0 2 mul cvi 2 div big_ti loghigh { /temp exch def 1 1 4
                    { temp yforProb dup dup dup dup lhboxside exch moveto
                                lhboxside bigtick add exch lineto stroke
                                rhboxside bigtick sub exch moveto
                                rhboxside exch lineto stroke
                      temp str10 cvs dup stringwidth pop neg lhboxside
                      add axislabelheight 2 div sub 3 -1 roll
                      axislabelheight 2 div sub moveto show
                                } for
                     } for
%2000-Mar-05

    90 rotate
     probboxtop probboxdepth 2 div sub (log(Pr(1))) stringwidth pop
```

```
    2 div sub lhboxside axislabelheight ylabeloffsetfactor mul sub neg
    moveto (log(Pr(1))) show
    probboxtop probboxdepth 1.5 mul sub (log(Pr(2))) stringwidth pop
    2 div sub lhboxside axislabelheight ylabeloffsetfactor mul sub neg
    moveto (log(Pr(2))) show
    probboxtop probboxdepth 2.5 mul sub (log(Pr(3))) stringwidth pop
    2 div sub lhboxside axislabelheight ylabeloffsetfactor mul sub neg
    moveto (log(Pr(3))) show
    probboxtop probboxdepth 3.5 mul sub (log(Pr(4))) stringwidth pop
    2 div sub lhboxside axislabelheight ylabeloffsetfactor mul sub neg
    moveto (log(Pr(4))) show
  -90 rotate

%2000-Mar-05
% Indicate the 4 chosen frequencies
31 setdash
/Helvetica findfont axislabelheight 0.75 mul scalefont setfont
/clash2 { 1. Period1 div 1. Period2 div sub abs 0.1 lt { axislabelheight add }
          if } def
/clash3 { 1. Period1 div 1. Period3 div sub abs 0.1 lt
          1. Period2 div 1. Period3 div sub abs 0.1 lt or
          { axislabelheight add } if } def

1. Period1 div xforF dup probboxtop moveto probboxtop probboxdepth 4 mul sub
   lineto stroke
1. Period1 div xforF probboxtop axislabelheight 2 div add moveto
   Period1 str10 cvs dup stringwidth pop -2 div 0 rmoveto show

1. Period2 div xforF dup probboxtop moveto probboxtop probboxdepth 4 mul sub
   lineto stroke
1. Period2 div xforF probboxtop axislabelheight 2 div add clash2 moveto
   Period2 str10 cvs dup stringwidth pop -2 div 0 rmoveto show

1. Period3 div xforF dup probboxtop moveto probboxtop probboxdepth 4 mul sub
   lineto stroke
1. Period3 div xforF probboxtop axislabelheight 2 div add clash3 moveto
   Period3 str10 cvs dup stringwidth pop -2 div 0 rmoveto show

0 setdash
%2000-Mar05

% Now plot the probabilities of false detection
% frequency logprobability P1 etc


/P1count { 0 } def
/P1 { P1count 1 add /P1count exch def
      1 exch yforProb exch xforF exch
      P1count 1 eq { newpath moveto } { lineto } ifelse
      P1count no_frequencies eq { stroke } if
    } def
/P2count { 0 } def
/P2 { P2count 1 add /P2count exch def
      2 exch yforProb exch xforF exch
      P2count 1 eq { newpath moveto } { lineto } ifelse
```

```
        P2count no_frequencies eq { stroke } if
    } def
/P3count { 0 } def
/P3 { P3count 1 add /P3count exch def
        3 exch yforProb exch xforF exch
        P3count 1 eq { newpath moveto } { lineto } ifelse
        P3count no_frequencies eq { stroke } if
    } def
/P4count { 0 } def
/P4 { P4count 1 add /P4count exch def
        4 exch yforProb exch xforF exch
        P4count 1 eq { newpath moveto } { lineto } ifelse
        P4count no_frequencies eq { stroke } if
    } def

%2000-Mar-05
 /xforPH { PHstart sub PHend PHstart sub div phaserhboxside phaselhboxside
            sub mul phaselhboxside add } def
%2000-Mar-05
 /blueyforphase { blueavmag nearest_tenth sub photboxdepth mul no_tenths div
                  -2 div 10 mul phaseboxtop add photboxdepth 0.5 mul sub } def
 /redyforphase { redavmag nearest_tenth sub photboxdepth mul no_tenths div
                  -2 div 10 mul phaseboxtop add photboxdepth 1.5 mul sub } def
%2000-Mar-05
% phase mag bp/rp
/bp { newpath ModJD Period1 div dup truncate sub xforPH
            magnitude blueyforphase spotsize 0 360 arc fill
        newpath ModJD Period1 div dup truncate sub 1 add xforPH
            magnitude blueyforphase spotsize 0 360 arc fill
        newpath ModJD Period2 div dup truncate sub xforPH
            magnitude blueyforphase phaseboxtranslate add spotsize 0 360 arc fill
        newpath ModJD Period2 div dup truncate sub 1 add xforPH
            magnitude blueyforphase phaseboxtranslate add spotsize 0 360 arc fill
        newpath ModJD Period3 div dup truncate sub xforPH
            magnitude blueyforphase phaseboxtranslate 2 mul add
             spotsize 0 360 arc fill
        newpath ModJD Period3 div dup truncate sub 1 add xforPH
            magnitude blueyforphase phaseboxtranslate 2 mul add
             spotsize 0 360 arc fill
    } def
/rp { newpath ModJD Period1 div dup truncate sub xforPH
            magnitude redyforphase spotsize 0 360 arc fill
        newpath ModJD Period1 div dup truncate sub 1 add xforPH
            magnitude redyforphase spotsize 0 360 arc fill
        newpath ModJD Period2 div dup truncate sub xforPH
            magnitude redyforphase phaseboxtranslate add spotsize 0 360 arc fill
        newpath ModJD Period2 div dup truncate sub 1 add xforPH
            magnitude redyforphase phaseboxtranslate add spotsize 0 360 arc fill
        newpath ModJD Period3 div dup truncate sub xforPH
            magnitude redyforphase phaseboxtranslate 2 mul add
             spotsize 0 360 arc fill
        newpath ModJD Period3 div dup truncate sub 1 add xforPH
            magnitude redyforphase phaseboxtranslate 2 mul add
             spotsize 0 360 arc fill
    } def
```

```
%2000-Mar-05


%2000-Mar-05
/phasebox { boxborderwidth setlinewidth
            newpath phaselhboxside phaseboxtop moveto phaserhboxside
                    phaseboxtop lineto
                    phaserhboxside phaseboxtop photboxdepth 2 mul sub lineto
                    phaselhboxside phaseboxtop photboxdepth 2 mul sub lineto
                    closepath stroke
            newpath phaselhboxside phaseboxtop photboxdepth sub moveto
                    phaserhboxside phaseboxtop photboxdepth sub lineto stroke
             /Helvetica findfont axislabelheight scalefont setfont
            PHstart .1 PHend { xforPH dup phaseboxtop moveto
                                 dup phaseboxtop smalltick sub lineto stroke
                               dup phaseboxtop photboxdepth sub smalltick add moveto
                               dup phaseboxtop photboxdepth sub smalltick sub lineto
                                   stroke
                               dup phaseboxtop photboxdepth 2 mul sub smalltick add
                                   moveto
                                   phaseboxtop photboxdepth 2 mul sub lineto stroke
                              } for
          PHstart .05 sub cvi 2 idiv 2 mul .5 PHend
                              { dup dup xforPH exch str10 cvs dup stringwidth
                                pop -2 div 3 -1 roll add phaseboxtop
                                photboxdepth 2 mul sub
                                axislabelheight 1.5 mul sub moveto show
                               xforPH dup phaseboxtop moveto
                               dup phaseboxtop bigtick sub lineto stroke
                               dup phaseboxtop photboxdepth sub bigtick add moveto
                               dup phaseboxtop photboxdepth sub bigtick sub lineto
                                   stroke
                               dup phaseboxtop photboxdepth 2 mul sub bigtick add
                                   moveto
                                   phaseboxtop photboxdepth 2 mul sub lineto stroke
                              } for
  phaserhboxside 0.93 mul phaseboxtop photboxdepth 2 mul sub axislabelheight
                   2 mul sub moveto (PHASE) show
                 bluebright .1 bluefaint { dup phaselhboxside exch blueyforphase
                                             moveto
                                           dup phaselhboxside smalltick add exch
                                           blueyforphase lineto stroke
                                           dup phaserhboxside exch blueyforphase
                                           moveto phaserhboxside smalltick sub exch
                                           blueyforphase lineto stroke
                                         } for
                  redbright .1 redfaint { dup phaselhboxside exch redyforphase
                                            moveto
                                          dup phaselhboxside smalltick add exch
                                          redyforphase lineto stroke
                                          dup phaserhboxside exch redyforphase moveto
                                              phaserhboxside smalltick sub exch
                                          redyforphase lineto stroke
                                        } for
bluebright 2 mul dup 0 ge { .999 add } if
```

```
                cvi 2 div 0.5 bluefaint 2 mul dup 0 le { .999 sub } if
                        cvi 2 div
                            { dup phaselhboxside exch blueyforphase moveto
                                    dup phaselhboxside bigtick add exch
                                    blueyforphase lineto stroke
                                    dup phaserhboxside exch blueyforphase
                                    moveto dup phaserhboxside bigtick sub exch
                                    blueyforphase lineto stroke
                                    dup str10 cvs dup stringwidth pop
                                    phaselhboxside exch sub axislabelheight
                                    0.5 mul sub 3 -1 roll blueyforphase
                                    axislabelheight 2 div sub moveto show
                            } for
redbright 2 mul dup 0 ge { .999 add } if
                cvi 2 div 0.5 redfaint 2 mul dup 0 le { .999 sub } if
                            cvi 2 div
                            { dup phaselhboxside exch redyforphase moveto
                                    dup phaselhboxside bigtick add exch
                                    redyforphase lineto stroke
                                    dup phaserhboxside exch redyforphase moveto
                                    dup phaserhboxside bigtick sub exch
                                    redyforphase lineto stroke
                                    dup str10 cvs dup stringwidth pop
                                    phaselhboxside exch sub axislabelheight
                                    0.5 mul sub 3 -1 roll redyforphase
                                    axislabelheight 2 div sub moveto show
                            } for
        90 rotate
        phaseboxtop photboxdepth 2 div sub (Blue mag.) stringwidth pop
        2 div sub phaselhboxside axislabelheight ylabeloffsetfactor mul sub neg
        moveto (Blue mag.) show
        phaseboxtop photboxdepth 1.5 mul sub (Red mag.) stringwidth pop
        2 div sub phaselhboxside axislabelheight ylabeloffsetfactor mul sub neg
        moveto (Red mag.) show
       -90 rotate
            } def

/Helvetica findfont axislabelheight scalefont setfont

phasebox
phaselhboxside phaseboxtop axislabelheight 0.25 mul add moveto (Period = ) show
Period1 str10 cvs show ( day) show

0 phaseboxtranslate translate
phasebox
phaselhboxside phaseboxtop axislabelheight 0.25 mul add moveto (Period = ) show
Period2 str10 cvs show ( day) show

0 phaseboxtranslate translate
phasebox
phaselhboxside phaseboxtop axislabelheight 0.25 mul add moveto (Period = ) show
Period3 str10 cvs show ( day) show

0 phaseboxtranslate -2 mul translate
%2000-Mar-05
```

```
%2000-Mar-05
% Commands for reading, phasing and plottign the photometry
/b { /magnitude exch def toModJD ModJD magnitude bplot bp } def
/r { /magnitude exch def toModJD ModJD magnitude rplot rp } def
%2000-Mar-05

%2000-Mar-05
/Helvetica findfont axislabelheight 0.75 mul scalefont setfont
date&time dup stringwidth pop neg rhboxside add photboxtop
    axislabelheight 0.60 mul add moveto show
%2000-Mar-05

% Insert photometric observations and log(probs false detection)
% here. The log(probs false detection) are plotted at a
% joined line, so must be sorted in frequency order.

%************************ To be written by c program ***********************
%*
( 2450569.930359 ) -10.635000 b
( 2450569.938171 ) -10.640000 b
( 2450570.168461 ) -10.761000 b
( 2450570.176296 ) -10.759000 b
( 2450570.929699 ) -10.707000 b
.
.
.
( 2450569.926458 ) -10.178000 r
( 2450569.934259 ) -10.187000 r
( 2450570.164549 ) -10.292000 r
( 2450570.172373 ) -10.290000 r
( 2450570.925787 ) -10.224000 r
.
.
.
0.050000 -8.559785e-11 P1
0.050272 -4.922258e-05 P1
0.050543 -2.664672e-02 P1
0.050815 -2.849585e-01 P1
0.051086 -7.794274e-01 P1
.
.
.
0.050000 00.000000e+00 P2
0.050272 00.000000e+00 P2
0.050543 -7.571570e-09 P2
0.050815 -2.064583e-03 P2
0.051086 -1.149607e-01 P2
.
.
.
0.050000 00.000000e+00 P3
0.050272 00.000000e+00 P3
0.050543 -3.004603e-11 P3
0.050815 -9.221222e-05 P3
```

```
0.051086 -3.354796e-02 P3
.
.
.
0.050000 00.000000e+00 P4
0.050272 00.000000e+00 P4
0.050543 -1.276389e-11 P4
0.050815 -3.128789e-04 P4
0.051086 -3.287783e-02 P4
.
.
.
showpage
```

Appendix G

MOA catalogue of eclipsing binary stars in the SMC paper

The paper as it appeared in Monthly Notices of the Royal Astronomical Society **331** 609-614 (2002) is followed by Figures 2–35 and the full versions of Tables 1 and 2 which were not published on paper but were made available electronically from the Centre de Données astronomiques de Strasbourg.

Mon. Not. R. Astron. Soc. **331**, 609–614 (2002)

The MOA catalogue of eclipsing binary stars in the Small Magellanic Cloud

G. Bayne,[1] W. Tobin,[1★] J. D. Pritchard,[1] I. Bond,[1,2] K. R. Pollard,[1] S. C. Besier,[1] S. Noda,[3] T. Sumi,[3] T. Yanagisawa,[3] M. Sekiguchi,[4] M. Honda,[4] Y. Muraki,[3] M. Takeuti,[5] J. B. Hearnshaw,[1] P. M. Kilmartin,[1] R. J. Dodd,[2,6,7] D. J. Sullivan[7] and P. C. M. Yock[2]

[1]*Mount John University Observatory and Department of Physics and Astronomy, University of Canterbury, Private Bag 4800, Christchurch, New Zealand*
[2]*Science Faculty, University of Auckland, Private Bag 92019, Auckland, New Zealand*
[3]*Solar Terrestrial Environment Laboratory, Nagoya University, Nagoya 464, Japan*
[4]*Institute of Cosmic Ray Research, University of Tokyo, Tanashi, Tokyo 188, Japan*
[5]*Tohoku University Astronomical Institute, Sendai 980, Japan*
[6]*Carter National Observatory, PO Box 2909, Wellington, New Zealand*
[7]*School of Chemical and Physical Sciences, Victoria University of Wellington, PO Box 600, Wellington, New Zealand*

Accepted 2001 November 19. Received 2001 November 16; in original form 2001 May 30

ABSTRACT

We present a catalogue of 167 eclipsing binary stars in the Small Magellanic Cloud (SMC) derived from the data base of time-series photometry for 400 000 SMC stars acquired by the Microlensing Observations in Astrophysics (MOA) project during 1997. We print coordinates, ephemerides, magnitudes and light curves for the 35 new detections; similar data and finding charts are available electronically for the whole catalogue. The majority of periods lie within the range 0.4 to 20 d; six systems are possibly eccentric while 14 are probably or certainly so. The majority of the newly identified systems lie in the outer regions of the SMC.

Key words: gravitational lensing – catalogues – binaries: eclipsing – Magellanic Clouds.

1 INTRODUCTION

Studies of extragalactic eclipsing binary stars are currently of interest for two reasons. First, if the observational material is of sufficient quality, they permit high-accuracy testing of models of stellar evolution calculated for metallicities other than those found in our own Galaxy (e.g. Claret 1999; Ribas et al. 2000). Secondly, they yield direct distances, which hold the promise of being important calibrators in the extragalactic distance scale, although observational and analytical uncertainties still need to be reduced (e.g. compare Guinan et al. 1998, Nelson et al. 2000 and Groenewegen & Salaris 2001). Detecting eclipsing binaries is an essential prerequisite to selecting interesting systems for detailed study. In this paper we present a catalogue of eclipsing binary systems detected in the Small Magellanic Cloud (SMC) via the data base of time-sequence photometry gathered by the Microlensing Observations in Astrophysics (MOA) project (e.g. Hearnshaw et al. 2000). Earlier catalogues of SMC eclipsing binaries have been published from Córdoba Observatory [e.g. Dartayet & Landi Dessy 1952 (five systems)], Harvard College Observatory [e.g. Gaposchkin 1965; Gaposhkin 1977 (33 systems)] and by the OGLE microlensing project [Udalski et al. 1998 (1459 systems)]. Of the 167 systems that we found from the MOA observations, 35 are new detections.

We note that the EROS and MACHO microlensing projects have recently published catalogues of eclipsing binaries in the Large Magellanic Cloud (Grison et al. 1995, Alcock et al. 1997). Eclipsing binaries are also being discovered in M31 and M33 by the DIRECT project (Mochejska et al. 1999, 2001, and references therein).

2 OBSERVATIONS AND REDUCTIONS

The MOA observations were conducted at the Mount John University Observatory using the 61-cm Boller and Chivens Cassegrain reflector with a new secondary mirror and correcting lenses giving an overall *f*/6.25 focal ratio (e.g. Pennycook 1998). The MOACAM1 CCD camera was used, which consisted of nine Texas Instruments TC215 CCD chips each comprising 1000 × 1018 12 × 12 μm pixels. The chips were arranged in a 3 × 3 spaced array separated by 800 and 812 pixel widths in right ascension and declination respectively. Each pixel corresponded to a 0.645-arcsec square, and a full, filled field of 0°.97 × 0°.98 was obtained by offsetting the telescope in a four-step cyclic motion for successive exposures. A mosaic of the field therefore comprised 36 individual CCD frames.

Two bandpasses were used: a blue one corresponding to ~390–610 nm, and a red one from ~610 nm out to the limit of the

★E-mail: w.tobin@phys.canterbury.ac.nz

quantum efficiency of the chips at about 1 μm. Individual exposures typically lasted 5 min, and because of the southerly latitude of the Observatory (44°S) observations were possible over all the fortnights straddling new Moon between 1997 May and December. Two fields were surveyed, located as shown in Fig. 1. As with most surveys made primarily for microlensing purposes, the placements centred on the densest star fields, rather than regions where follow-up spectroscopy would be easier. Seeing was typically a few arcseconds. The acquired images were passed to a Sun computer for processing. After correcting for the instrumental effects of dark current and flat-fielding, the CCD frames were analysed using the DOPHOT photometry software in the fixed position warm-start mode (Schechter, Mateo & Saha 1993).

The templates for the warm starts were constructed by selecting all frames in the best seeing observations for a given field. These frames were then reduced using DOPHOT without the warm starts to resolve as many individual stars as possible. Using the overlap between adjoining frames, a mosaic of star positions across the field was constructed. After eliminating double counting in the overlapping regions, an internal catalogue of star positions across the field was constructed.

All individual observation frames were then analysed individually by first matching to the coordinate system in the catalogue. Star positions from the catalogue were then extracted and transformed to local CCD coordinates to produce an input list for the fixed position warm starts. The subsequent photometry was normalized to a common internal scale using constant stars and renormalization techniques similar to those of Honeycutt (1992). The quality of the photometry depends on the brightness of the star and the extent to which its field is crowded. The blue and red magnitudes B_M and R_M reported here have been converted from the MOA instrumental scale to the scale of the *Hubble Space Telescope* Guide Star Catalogue (GSC) using the transformation determined by Muraki et al. (1999):

$$B_M = B_{MOA}^{instr} + 24.82^{+0.18}_{-0.27}$$

$$R_M = R_{MOA}^{instr} + 25.10^{+0.26}_{-0.36}.$$

As the errors indicate, this calibration is uncertain at the 0.2–0.4 mag level, but such an uncertainty is of little consequence for the selection of targets for further observation. However the transformations to Johnson colours published by Reid, Dodd & Sullivan (1998) are considerably more accurate and are useful for determining the likely colours of the catalogue stars. Expressed in terms of the B_M and R_M presented here, these transformations are

$$(B-V)_{Johnson} = \underset{\pm 0.006}{0.646} + \underset{\pm 0.010}{1.036} \times (B_M - R_M),$$

$$(R-I)_{Johnson} = \underset{\pm 0.006}{0.321} + \underset{\pm 0.010}{0.612} \times (B_M - R_M).$$

The internal catalogue positions were transformed to J2000 equatorial coordinates through comparison with GSC positions. Comparison with 31 stars in common with the Magellanic Catalogue of Stars (MACS: Tucholke, de Boer & Seitter 1996) reveals rms uncertainties of 0.11 s in right ascension and 0.6 arcsec in declination.

3 FINDING ECLIPSING BINARIES

The reductions yielded photometric time sequences containing typically 90–100 data points in each colour for some 400 000 stars in the SMC. To find the eclipsing binaries among these systems we proceeded as follows. We used only the red time sequences, which to visual inspection were generally of marginally higher quality. They were first cleaned of outlying and therefore probably unreliable measurements by deleting all points more than 4.0 standard deviations from the mean. We then applied Grison's algorithm (Grison 1994) for the detection of periodic variables to every star. This algorithm fits a sinusoidal variation and its harmonics to the observed time sequences and exhibits enhanced sensitivity to periodic variables with markedly non-sinusoidal light curves such as eclipsing binary systems and some Cepheid variables. For each period tested, it produces the probability that

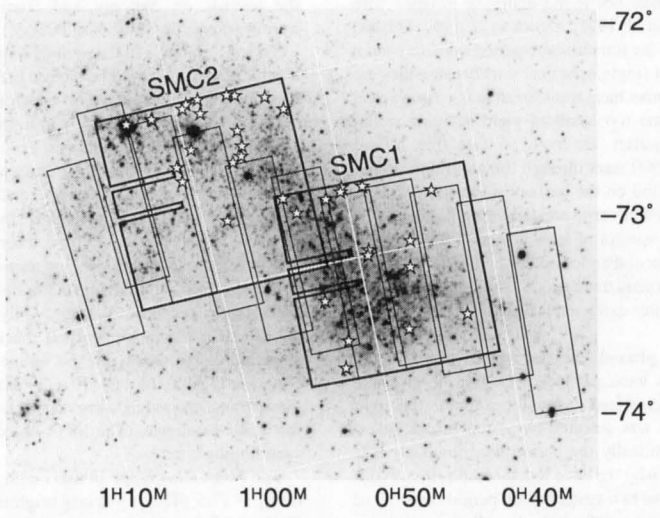

Figure 1. Location of the two fields SMC1 and SMC2 surveyed by MOA in 1997 superimposed on the photograph of the Small Magellanic Cloud taken from the Canterbury Sky Atlas (Doughty, Shane & Wood 1972). Stars indicate the locations of the 35 newly identified eclipsing binary systems. Also outlined are the 11 OGLE search fields and a J2000 coordinate grid.

Table 1. The MOA catalogue of eclipsing binary stars in the SMC. Only a sample of the catalogue is published in the printed journal; the full catalogue is available electronically in the online version of the journal on *Synergy*, and on the CDS data base.

Designation and coordinates (J2000) Name MOA J	Extra digit§	B_M R_M (max.)	Period (days)	Primary Epoch HJD −245 0680	OGLE name Remarks
00 42 25.5	6	16.88	1.3368	0.655	SMC_SC3 8986
−73 29 29	*.8*	*17.50*	±0.0002	±0.007	
00 43 06.1	2	16.83	21.25	1.166	SMC_SC3 28139
−73 11 04	*.5*	*17.01*	±0.05	±0.005	
00 43 10.8	3	15.96	7.903	1.959	
−73 23 39	*.7*	*15.60*	±0.003	±0.006	
00 43 42.0	2	16.42	1.56853	1.540	SMC_SC3 71563
−73 20 44	*.3*	*16.98*	±0.00007	±0.002	
00 44 06.9	2	17.42	2.43682	0.914	
−72 43 32	*.8*	*17.96*	±0.00003	±0.001	
00 44 08.7	4	13.39	6.052	0.336	SMC_SC3 139376
−73 14 17	*.6*	*14.12*	±0.002	±0.005	*probably eccentric*
00 44 08.8	7	17.05	0.8601	0.566	SMC_SC3 139681
−73 15 25	*.7*	*17.42*	±0.0002	±0.008	
00 44 11.6	6	15.86	11.85	0.046	SMC_SC3 134555
−73 17 37	*.6*	*16.22*	±0.01	±0.003	
00 44 22.0	7	15.59	0.84545	0.19	SMC_SC3 139427
−73 14 49	*.2*	*16.23*	±0.00004	±0.02	

§ IAU-approved designations are formed from coordinates truncated to the level at which there is no ambiguity between sources. The extra digit column provides additional significant figures (e.g. for spacecraft pointing). For example, the system MOA J004310.8−732339 has J2000 coordinated $00^h43^m10^s.83$, $-73°23'39''.7$.

that period will falsely be recognized as significant. The method works well when there are of the order of 150 data points (Beaulieu, private communication). We tested 500 evenly spaced frequencies between periods of 0.4 and 1.0 d, and 3000 evenly spaced frequencies between periods of 1.0 and 20 d. These period-search limits are somewhat arbitrary, but were selected so as not to compromise our ultimate goal of accurate stellar parameters and their interpretation. The 0.4-d limit was chosen because other searches in both Clouds have not found eclipsing binaries with such short periods (Grison et al. 1995; Alcock et al. 1997; Udalski et al. 1998), and in any case the stars in short-period systems cannot be compared with models of single, spherical stars because they are significantly distorted and may have transferred mass. Above 20 d the stellar velocities become too small to yield accurate stellar parameters. Desktop computers are now so fast that it was practicable to pass all 400 000 stars through the algorithm, rather than just a subsample selected on the basis of a variability index. The periods were extracted that corresponded to the three deepest but separate minima in the spectra of false detection probabilities corresponding to the first, second and third harmonics of the tested frequencies. For some 5000 stars there was a simple ratio (1:2, 1:3, 1:4, 2:3, etc.) between the three extracted periods, revealing the star as a periodic variable.

The photometry was phased on the three periods and corresponding light curves were produced. Certain or probable eclipsing systems were recognized manually amongst the light curves. The correct period was selected by visual inspection of these phased curves. Occasionally the period was obviously half the correct period, which is why we have found some systems with periods greater than 20 d. The two systems with periods over 100 d presented for inspection because of whole-day aliasing but were easily recognized as periodic from the time sequences themselves. Designations were assigned based on the J2000 equatorial coordinates of each system according to the IAU-recommended form MOA JHHMMSS.S−ddmmss (IAU 2000).

4 RESULTS

The MOA catalogue containing 167 eclipsing binaries in the SMC is listed in Table 1 [only a sample is given in the printed journal; the full catalogue is available electronically in the on-line version of the journal on *Synergy* and from the Centre de Données astronomiques de Strasbourg (CDS)[1]].

The uncertainties in the periods were determined by seeing how much each period could be altered before the resulting light curve was obviously degraded. The epoch uncertainty for each system derives from the formal errors in fitting Gaussian functions to the central parts of the two eclipses. For systems with similar eclipse depths it was often rather arbitrary which one we chose as the primary. Possibly and probably eccentric systems were identified when the fit to the secondary eclipse implied an epoch that differed from the value determined from the primary alone by more than two or three standard deviations respectively. Table 2 lists epochs of the secondary minima for six possibly eccentric and 14 probably or certainly eccentric systems. Only a sample of the table is published in the paper journal; the full version of the table is available electronically in the online version of the journal on *Synergy*. Figs 2–18 and 19–35 (available electronically only) present blue and red light curves and finding charts respectively for the whole catalogue. (The MOA object is located at the centre of each finding chart.)

The MOA stars range in maximum brightness from $B_M \sim 12.5$ to $B_M \sim 17.5$. (This is ~2 mag brighter than the OGLE catalogue.) Only 22 systems have periods shorter than 1 d; 114 have periods

[1] ftp://cdsarc.u-strasbg.fr/MNRAS

Table 2. Times of secondary minimum for eccentric systems. Only a sample of the table is published in the printed journal; the full table is available electronically in the online version of the journal on *Synergy*, and on the CDS data base.

MOA name	Secondary Epoch HJD −245 0680	OGLE name	Remarks
MOA J004408.7−731417	3.505 ±0.005	SMC_SC3 139376	probably eccentric
MOA J004659.0−731457	0.547 ±0.004	SMC_SC4 113885	eccentric
MOA J004940.5−730023	5.690 ±0.002	SMC_SC5 129441	eccentric
MOA J005128.0−731517	2.134 ±0.005	SMC_SC6 17345	eccentric
MOA J005134.7−724546	1.074 ±0.002		eccentric

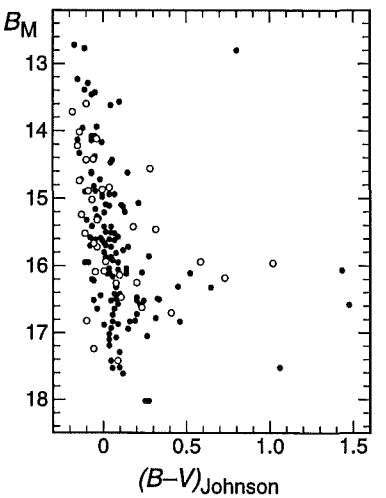

Figure 36. Colour–magnitude diagram for the 167 stars in the MOA catalogue. The 35 new identifications are plotted as open circles.

between 1 and 3.5 d; 23 have periods between 3.5 and 9 d; and eight have longer periods. Fig. 36 presents the colour–magnitude diagram. Most systems have $(B-V)_{\rm Johnson}$ colours within 0.2 mag of zero; only four are redder than $(B-V)_{\rm Johnson}=1$.

The MOA catalogue contains 35 systems (21 per cent) that do not appear in the OGLE, Harvard or Córdoba lists. Table 3 and Fig. 37, both included in the printed journal, present data and light curves for these newly identified systems, which are also plotted on the sky image in Fig. 1. Most are seen to lie outside the region surveyed by OGLE, but 14 fall within it. Taking OGLE systems in the common area brighter at maximum than the MOA faint limit of ~17.5, we find 514 OGLE systems of which 384 are not in our catalogue, i.e. 130 systems are common to both catalogues. Two of our systems, MOA J005329.1−723853 and 005434.6−724051, which lie in the overlap region between the SMC1 and SMC2 fields, were identified independently in each field, but 21 other systems were only found in one of the two fields. We conclude that the MOA catalogue is far from complete, but nevertheless in the common area has revealed that ~10 per cent of its contents were not identified by OGLE. The different number of detections may in part be due to the different typical seeing in the two surveys, but it is impossible to make any definitive statement without an excessively time-consuming investigation.

Readers should be aware of other limitations of the MOA catalogue. The choice of the primary minimum is always uncertain when the two minima are of very similar depth. The star MOA J010225.5−720745 is listed in the OGLE catalogue with a period 4/3 bigger than the one that we have found. Our observations certainly phase better with our period, but the eclipses are not well-sampled and we suspect that the OGLE period is correct. In addition, we caution that some of the stars in the MOA catalogue may not be eclipsing binaries, for the following reasons.

(i) Eclipsing contact or low-inclination ellipsoidal systems are present down to low amplitudes (MOA J005258.0−723704, 005417.1−723750, 010042.4−722457 and 010136.8−720415). However, at low amplitudes, where pulsational instabilities might be present (Waelkens 1991; Dziembowski, Moskalik & Pamyatnykh 1993) and/or at poorer signal-to-noise ratio, some doubt must remain concerning the true nature of the systems.

(ii) Systems with periods greater than about 30 d and unequal eclipses could possibly be RV Tauri stars (MOA J004828.9−731234, 004928.4−724942, 005947.8−724426 and 010459.6−725026), but the characteristic colour changes and phase lags seem absent and the stars are a little faint.

(iii) On the basis of the light curves alone, several systems with relatively noisy photometry and/or sinusoidal light variations could possibly be confused with Cepheid variables (of half the catalogued period) pulsating in the fundamental or first harmonic [MOA J004613.2−725755 ($P=3.7$ d), 004634.0−730600 ($P=3.7$ d), 005124.5−724014 ($P=0.57$ d), 005227.9−724135 ($P=0.83$ d), 005300.1−731123 ($P=0.72$ d), 005412.7−724207 ($P=0.50$ d), 005552.0−720229 ($P=1.3$ d), 005615.6−721324 ($P=1.3$ d), 005936.1−721557 ($P=1.9$ d) and 010321.3−720538 ($P=2.2$ d)]. These are mostly systems with short periods, and short-period Cepheids are well known in the SMC (Payne-Gaposchkin & Gaposchkin 1966). However, the Cepheid period–luminosity relation indicates that all these systems are far too bright to be Cepheids in the SMC, with the exception of the two 3.7/1.85-d systems MOA J004613.2−725755 and 004634.0−730600.

ACKNOWLEDGMENTS

GB, WT, JDP, IB, KRP, RJD and the MOA collaboration thank

Table 3. The 35 new systems identified in the MOA catalogue of eclipsing binary stars in the SMC. This table is also available in ASCII and PostScript formats in the online version of the journal on *Synergy*.

Designation and coordinates (J2000) Name MOA J	Extra digit§	B_M R_M (max.)	Period (d)	Primary Epoch HJD −245 0680	Remarks	Designation and coordinates (J2000) Name MOA J	Extra digit§	B_M R_M (max.)	Period (d)	Primary Epoch HJD −245 0680	Remarks
00 43 10.8	3	15.96	7.903	1.959		00 55 52.0	0	15.24	1.2704	0.839	
−73 23 39	*.7*	*15.60*	±0.003	±0.006		*−72 02 29*	*.3*	*15.99*	±0.0002	±0.009	
00 44 06.9	2	17.42	2.43682	0.914		00 56 11.6	1	13.72	4.482	1.770	eccentric
−72 43 32	*.8*	*17.96*	±0.00003	±0.001		*−72 18 24*	*.2*	*14.52*	±0.002	±0.004	
00 46 13.2	2	15.94	3.712	1.86	Cepheid?	00 56 15.6	1	15.94	1.3182	0.407	
−72 57 55	*.4*	*16.00*	±0.001	±0.01		*−72 13 24*	*.8*	*16.55*	±0.0001	±0.008	
00 46 34.0	4	16.18	3.7015	1.30	Cepheid?	00 56 23.5	9	14.02	2.3195	1.936	
−73 06 00	*.3*	*16.10*	±0.0002	±0.02		*−72 21 23*	*.7*	*14.78*	±0.0001	±0.003	
00 47 29.5	9	14.42	1.12508	0.41		00 56 24.2	1	14.74	1.6202	1.580	
−73 25 01	*.9*	*15.10*	±0.00005	±0.01		*−72 01 44*	*.9*	*15.50*	±0.0002	±0.003	
00 48 45.3	9	16.82	0.91365	0.819		00 57 03.0	3	16.08	1.5837	1.042	
−72 38 29	*.3*	*17.54*	±0.00004	±0.006		*−72 22 46*	*.3*	*16.70*	±0.0001	±0.004	
00 49 13.2	1	16.26	0.98910	0.968		00 58 21.3	7	15.52	3.111	1.873	probably
−72 58 23	*.3*	*16.81*	±0.00005	±0.008		*−72 01 07*	*.2*	*16.25*	±0.002	±0.005	eccentric
00 49 20.2	5	16.70	1.05780	0.211		00 58 22.3	5	16.25	1.05184	0.626	
−73 00 01	*.5*	*16.93*	±0.00002	±0.004		*−72 40 09*	*.0*	*16.68*	±0.00002	±0.004	
00 50 10.4	3	15.72	2.0739	0.38		00 58 24.4	0	14.89	1.47120	0.938	
−72 37 36	*.3*	*16.38*	±0.0002	±0.02		*−72 05 32*	*.5*	*15.60*	±0.00003	±0.003	
00 50 18.4	0	14.12	1.8399	1.084		00 59 11.4	3	17.24	1.29380	0.380	
−72 38 55	*.2*	*14.78*	±0.0002	±0.006		*−72 01 47*	*.6*	*17.92*	±0.00003	±0.003	
00 51 24.5	3	14.87	0.56565	0.03		00 59 30.2	7	15.32	3.3070	2.768	
−72 40 14	*.6*	*15.50*	±0.00008	±0.01		*−72 02 53*	*.1*	*15.98*	±0.0005	±0.008	
00 51 57.8	5	16.47	1.5422	1.190		00 59 36.1	5	13.60	1.9496	0.47	
−73 24 58	*.0*	*16.99*	±0.0002	±0.004		*−72 15 57*	*.3*	*14.32*	±0.0003	±0.01	
00 52 34.6	3	16.62	3.373	0.422	possibly	01 00 42.4	7	14.56	1.5953	0.589	
−73 33 05	*.0*	*17.02*	±0.001	±0.007	eccentric	*−72 24 57*	*.1*	*14.91*	±0.0002	±0.009	
00 52 53.3	3	15.67	1.53890	0.764		01 00 50.8	6	16.14	1.4868	1.398	
−72 09 50	*.4*	*16.35*	±0.00003	±0.006		*−72 20 17*	*.8*	*16.67*	±0.0001	±0.005	
00 53 00.1	6	14.22	0.72149	0.23		01 01 36.8	5	15.42	1.6766	0.755	
−73 11 23	*.1*	*14.99*	±0.00002	±0.01		*−72 04 15*	*.0*	*15.87*	±0.0003	±0.009	
00 53 34.4	9	15.02	0.80633	0.75		01 01 40.0	9	14.84	5.275	0.446	
−72 42 31	*.6*	*15.71*	±0.00002	±0.01		*−72 03 44*	*.2*	*15.43*	±0.002	±0.003	
00 53 55.9	1	16.09	2.2199	1.202		01 03 22.6	9	14.43	3.477	3.167	
−72 04 58	*.9*	*16.76*	±0.0002	±0.005		*−72 03 22*	*.0*	*15.15*	±0.001	±0.004	
00 54 17.1	7	15.46	1.1007	1.07							
−72 37 10	*.7*	*15.78*	±0.0001	±0.02							

§IAU-approved designations are formed from coordinates truncated to the level at which there is no ambiguity between sources. The extra digit column provides additional significant figures (e.g. for spacecraft pointing). For example, the system MOA J004310.8 − 732339 has J2000 coordinates $00^h43^m10^s.83$, $-73°23'39''.7$.

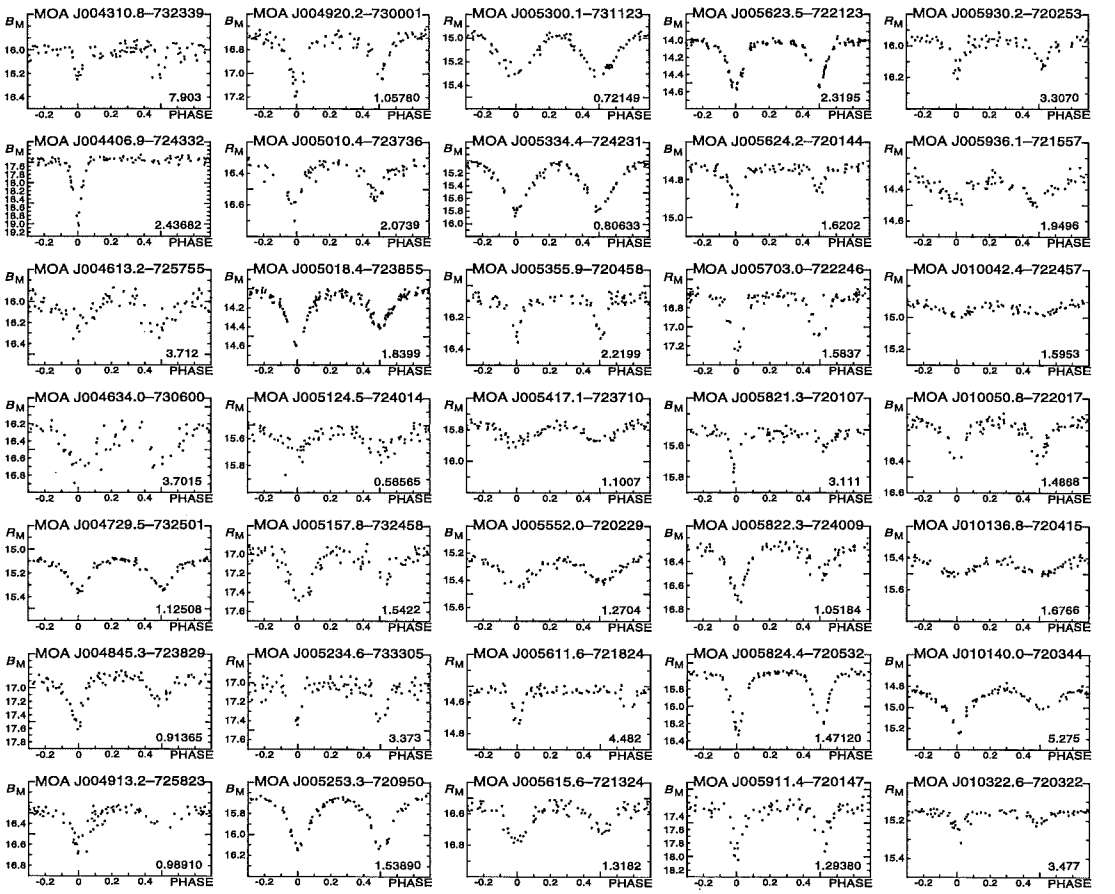

Figure 37. Light curves for the 35 new eclipsing systems in the SMC identified in our catalogue. Systems are presented down the columns in right-ascension order. The light curves are phased from −0.3 to 0.8 in order to make visual inspection easier. Note that the vertical scales are different on each light curve as the depth of the eclipses varies from 0.2 to 1.1 mag. The blue or red light curve is presented according to which one appears less noisy. The period in days is marked at the lower right of each light curve.

New Zealand's Marsden Fund for curiosity-driven scientific research for financial support.

REFERENCES

Alcock C. et al., 1997, AJ, 114, 326
Claret A., 1999, A&A, 352, 163
Dartayet M., Landi Dessy J., 1952, ApJ, 115, 279
Doughty N. A., Shane C. D., Wood F. B., 1972, The Mount John University Observatory Photographic Sky Survey and the Canterbury Sky Atlas (Australis). Department of Physics, University of Canterbury, Christchurch
Dziembowski W. A., Moskalik P., Pamyatnykh A. A., 1993, MNRAS, 265, 588
Gaposchkin S., 1965, Kleine Veröff. Remeis-Sternw. Bamberg, IV, No.40, 66
Gaposhkin S. I., 1977, Smithson. Astrophys. Obs. Spec. Rep., No. 380
Grison P., 1994, A&A, 289, 404
Grison P. et al., 1995, A&AS, 109, 447
Groenewegen M. A. T., Salaris M., 2001, A&A, 366, 752
Guinan E. F. et al., 1998, ApJ, 509, 21
Hearnshaw J. B. et al., 2000, in Szabados L., Kurtz D. W., eds, Proc. IAU Symp. 176, The Impact of Large-Scale Surveys on Pulsating Star Research. Astron. Soc. Pac., San Francisco, p. 31
Honeycutt R. K., 1992, PASP, 104, 435
IAU, 2000, IAU Recommendations for Nomenclature, http://vizier.u-strasbg.fr/iau-spec.htx
Mochejska B. J., Kaluzny J., Stanek K. Z., Krockenberger M., Sasselow D. D., 1999, ApJ, 118, 2211
Mochejska B. J., Kaluzny J., Stanek K. Z., Sasselow D. D., Szentgyorgyi A. H., 2001, ApJ, 121, 2032 (Erratum, ApJ, 121, 3284)
Muraki Y. et al., 1999, Prog. Theor. Phys. Suppl., No. 133, 233
Nelson C. A., Cook K. H., Popowski P., Alves D. R., 2000, AJ, 119, 1205
Payne-Gaposchkin C., Gaposchkin S., 1966, Smithson. Contrib. Astrophys., 9, 1
Pennycook G. S., 1998, MSc thesis, University of Auckland
Reid M., Dodd R. J., Sullivan D. J., 1998, Aust. J. Astron., 7, 79
Ribas I. et al., 2000, ApJ, 528, 692
Schechter P. L., Mateo M., Saha A., 1993, PASP, 105, 1342
Tucholke H.-J., de Boer K. S., Seitter W. C., 1996, A&AS, 119, 91
Udalski A., Soszyński I., Szymański M., Kubiak M., Pietrzyński G., Woźniak P., Żebruń K., 1998, Acta Astron., 48, 563
Waelkens A. J., 1991, A&A, 246, 453

This paper has been typeset from a TEX/LATEX file prepared by the authors.

Bayne *et al.*, The MOA Catalogue of Eclipsing Binary Stars in the SMC. Fig 2

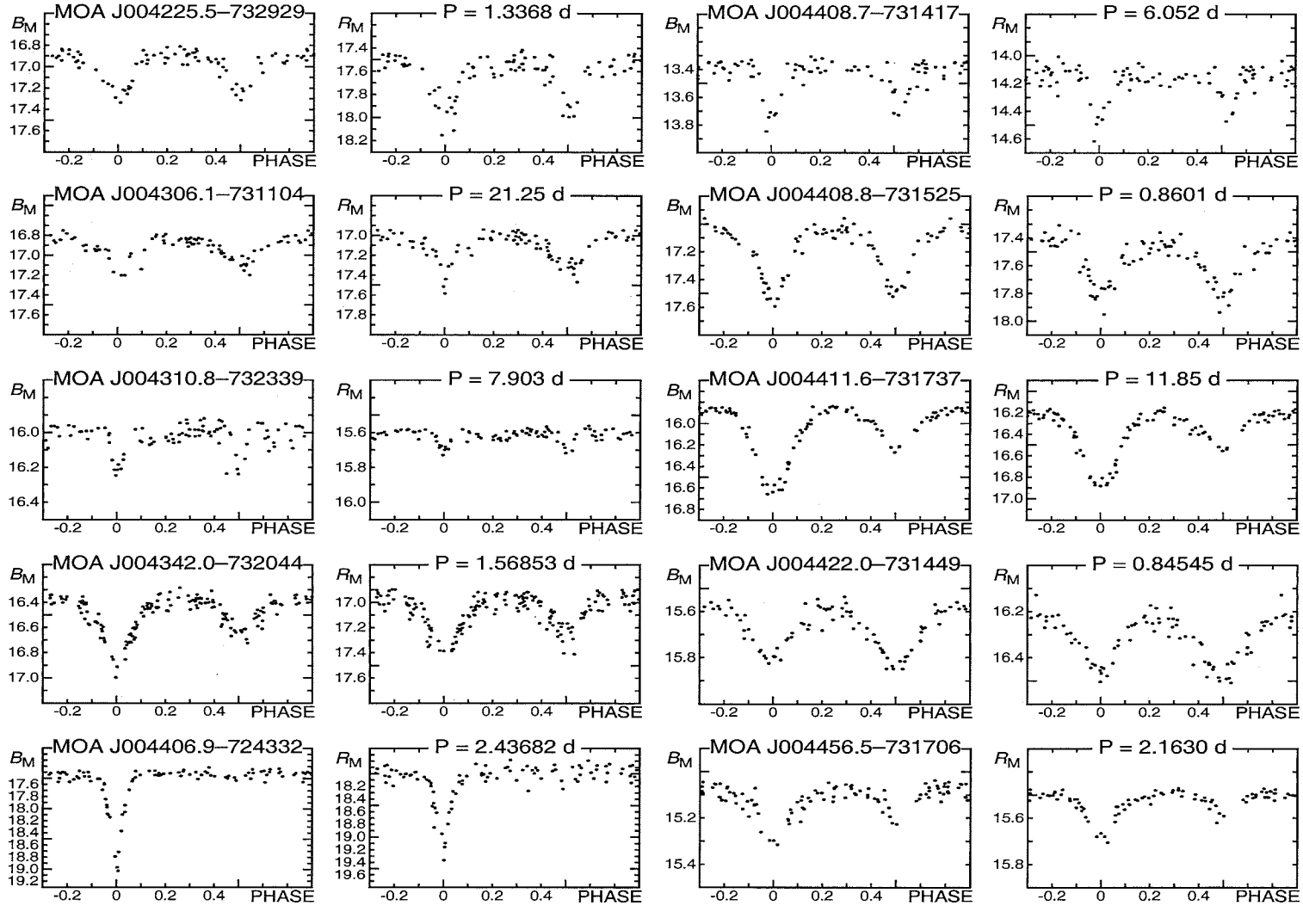

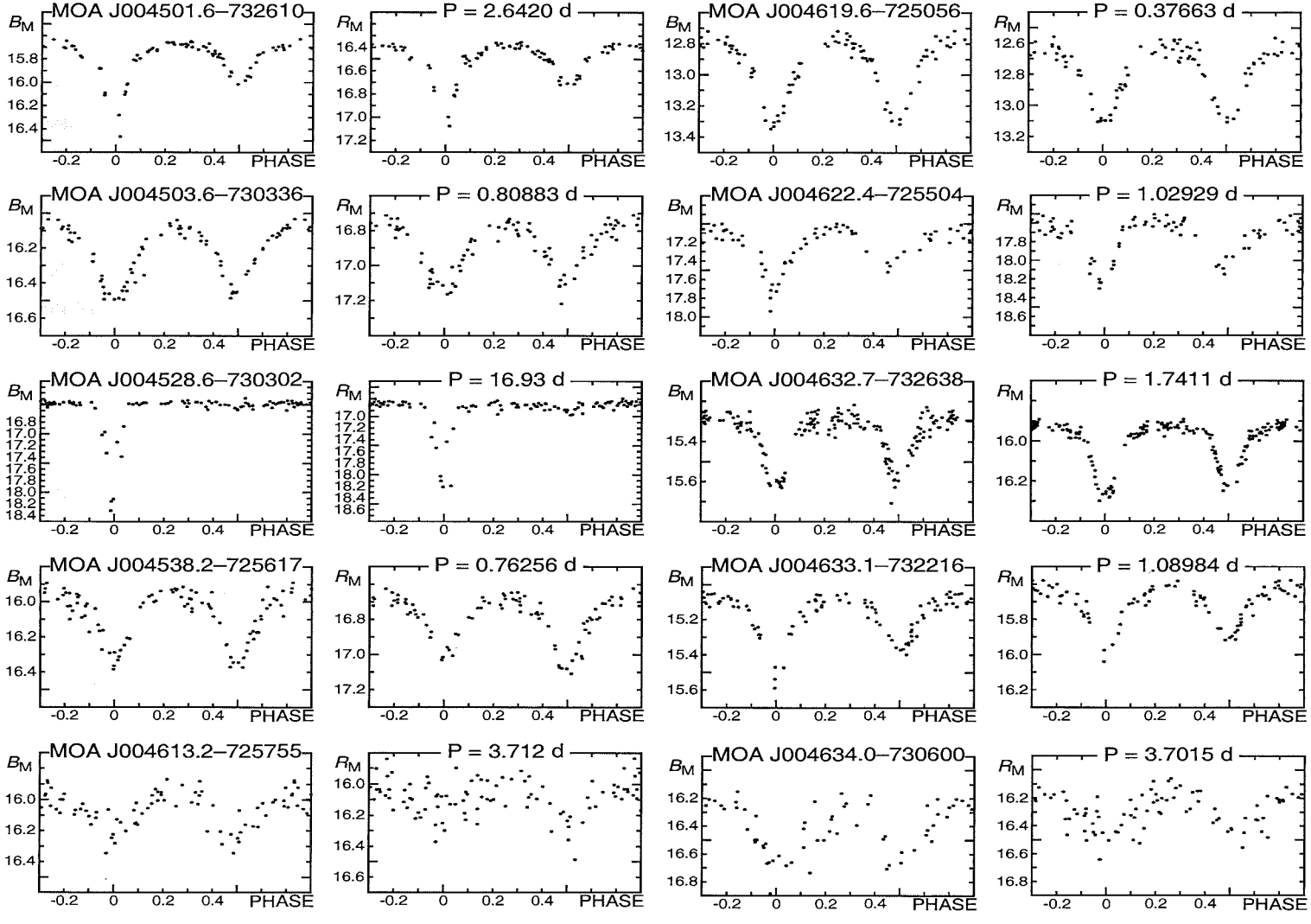
MOA J004501.6–732610
P = 2.6420 d
MOA J004619.6–725056
P = 0.37663 d
MOA J004503.6–730336
P = 0.80883 d
MOA J004622.4–725504
P = 1.02929 d
MOA J004528.6–730302
P = 16.93 d
MOA J004632.7–732638
P = 1.7411 d
MOA J004538.2–725617
P = 0.76256 d
MOA J004633.1–732216
P = 1.08984 d
MOA J004613.2–725755
P = 3.712 d
MOA J004634.0–730600
P = 3.7015 d
BM
RM
PHASE

Bayne *et al.*, The MOA Catalogue of Eclipsing Binary Stars in the SMC. Fig 4

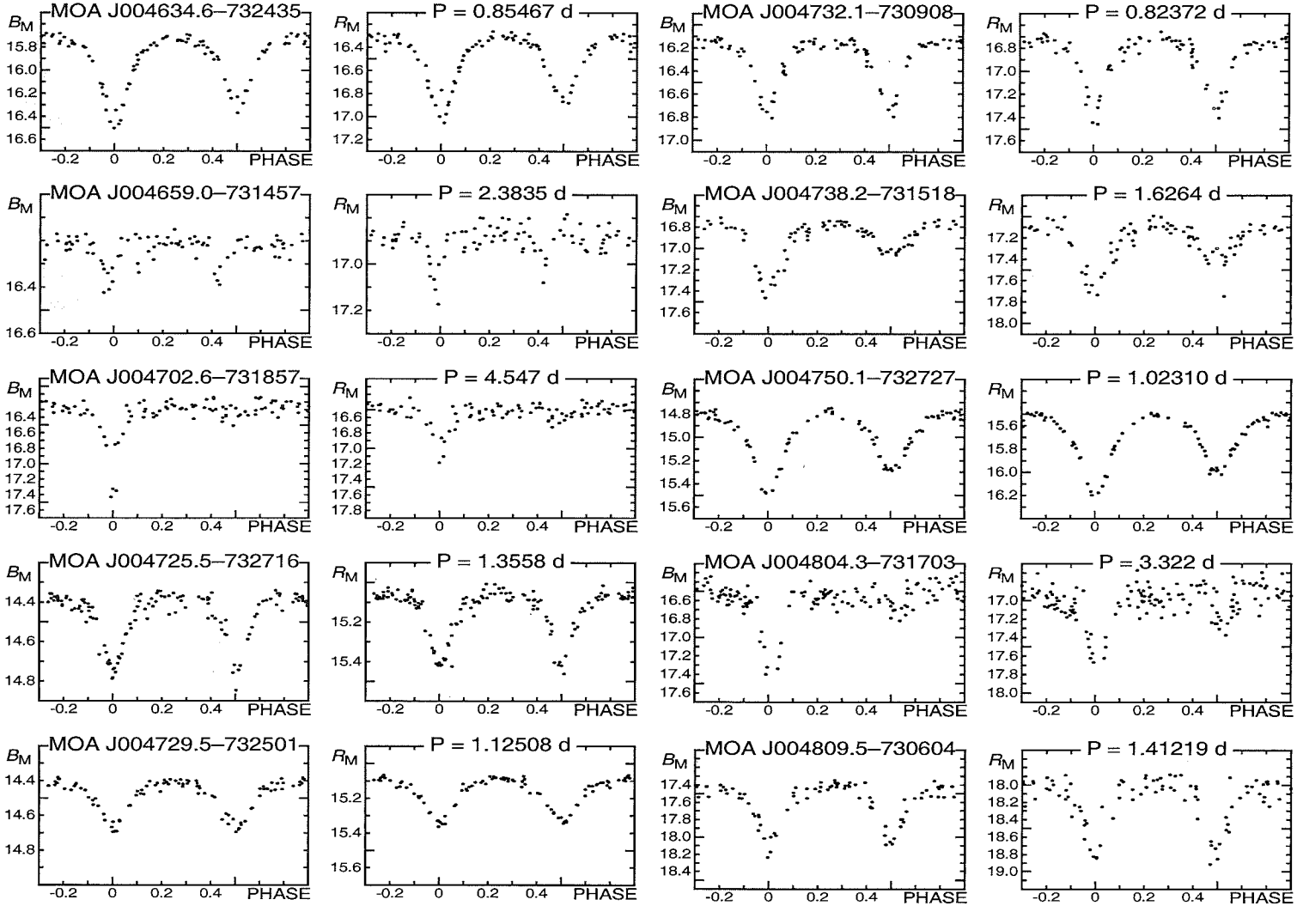

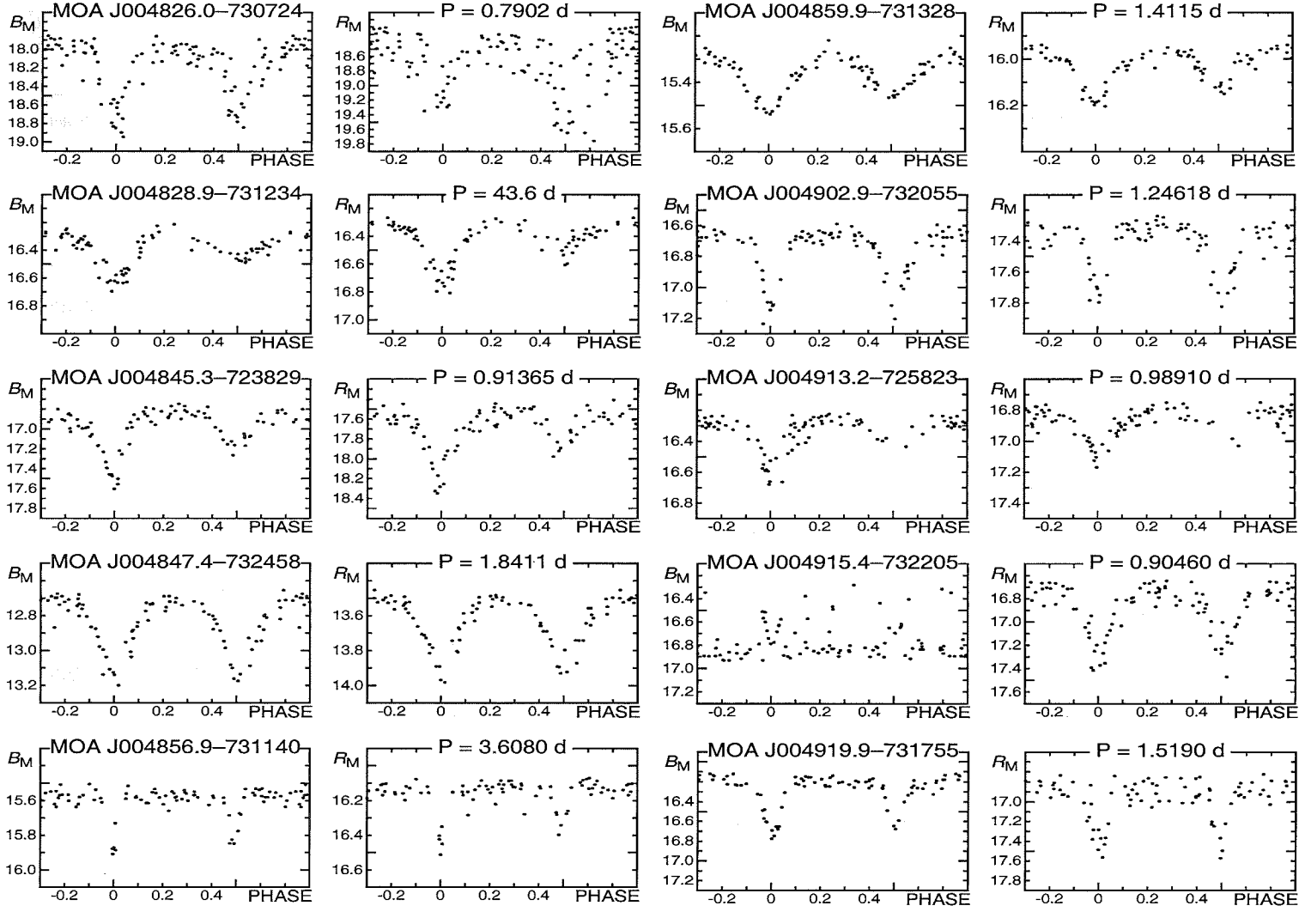
MOA J004826.0–730724
P = 0.7902 d
MOA J004859.9–731328
P = 1.4115 d
MOA J004828.9–731234
P = 43.6 d
MOA J004902.9–732055
P = 1.24618 d
MOA J004845.3–723829
P = 0.91365 d
MOA J004913.2–725823
P = 0.98910 d
MOA J004847.4–732458
P = 1.8411 d
MOA J004915.4–732205
P = 0.90460 d
MOA J004856.9–731140
P = 3.6080 d
MOA J004919.9–731755
P = 1.5190 d
PHASE

Bayne *et al.*, The MOA Catalogue of Eclipsing Binary Stars in the SMC. Fig 6

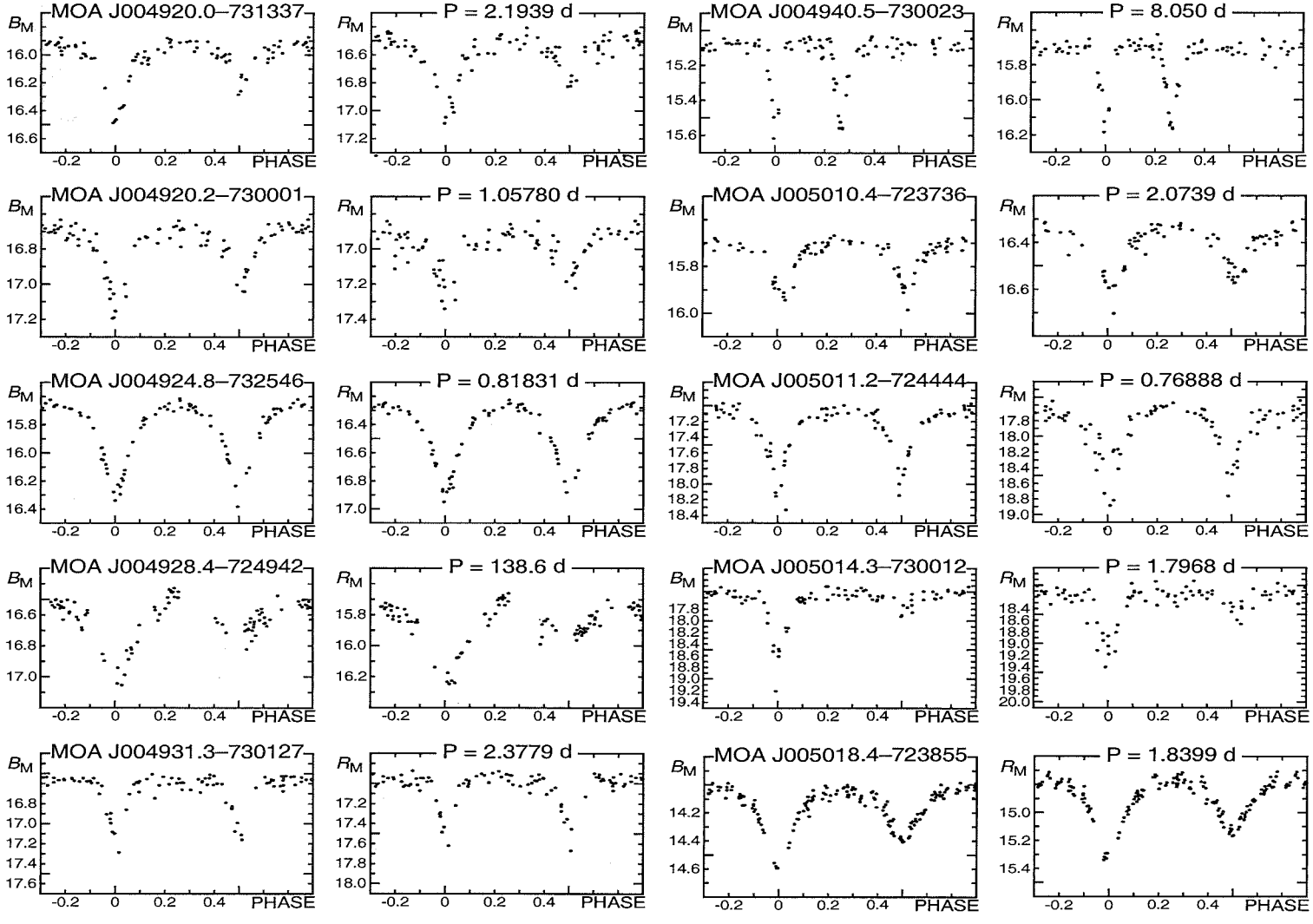

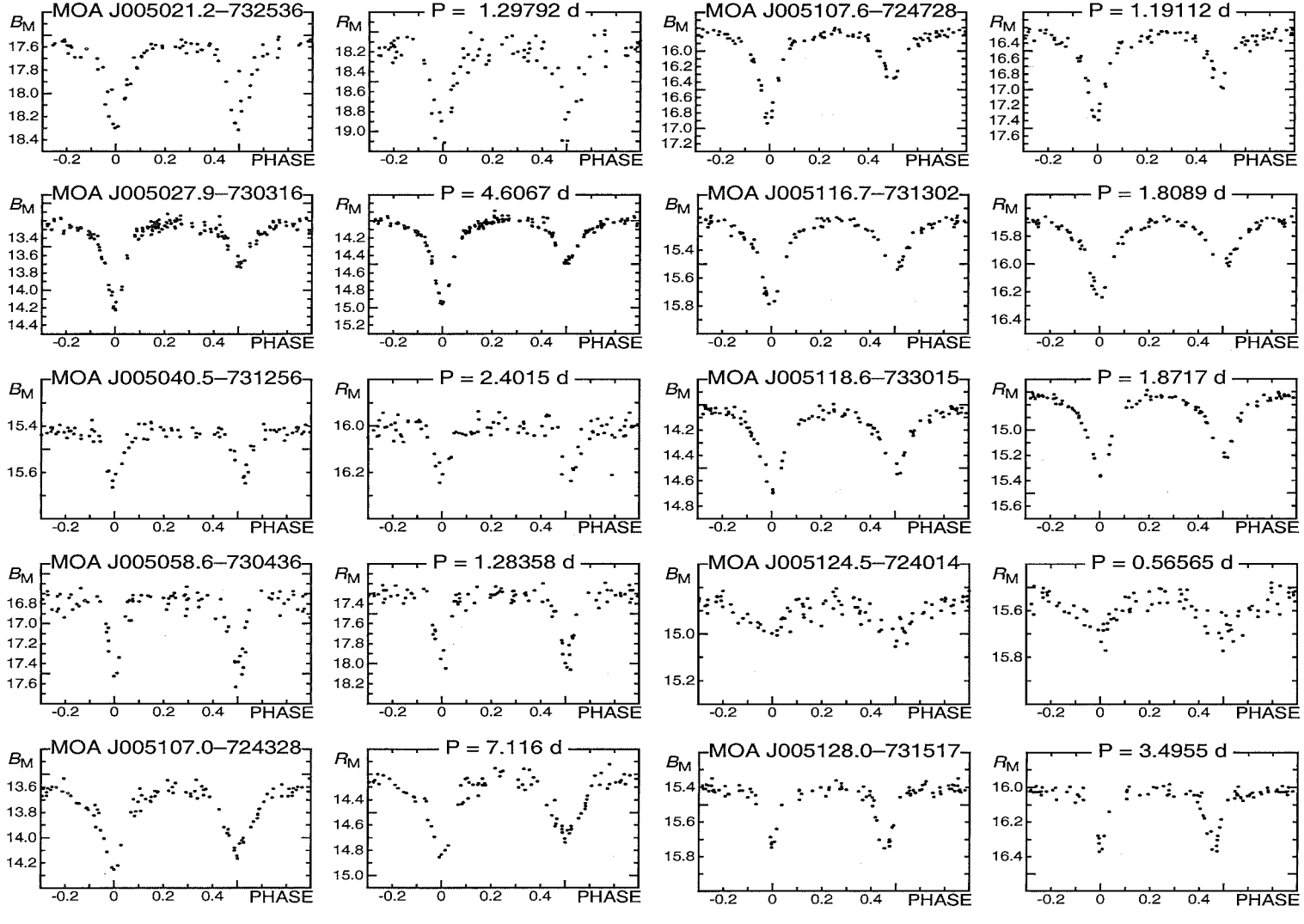
MOA J005021.2–732536
P = 1.29792 d
MOA J005107.6–724728
P = 1.19112 d
MOA J005027.9–730316
P = 4.6067 d
MOA J005116.7–731302
P = 1.8089 d
MOA J005040.5–731256
P = 2.4015 d
MOA J005118.6–733015
P = 1.8717 d
MOA J005058.6–730436
P = 1.28358 d
MOA J005124.5–724014
P = 0.56565 d
MOA J005107.0–724328
P = 7.116 d
MOA J005128.0–731517
P = 3.4955 d
PHASE

Bayne *et al.*, The MOA Catalogue of Eclipsing Binary Stars in the SMC. Fig 8

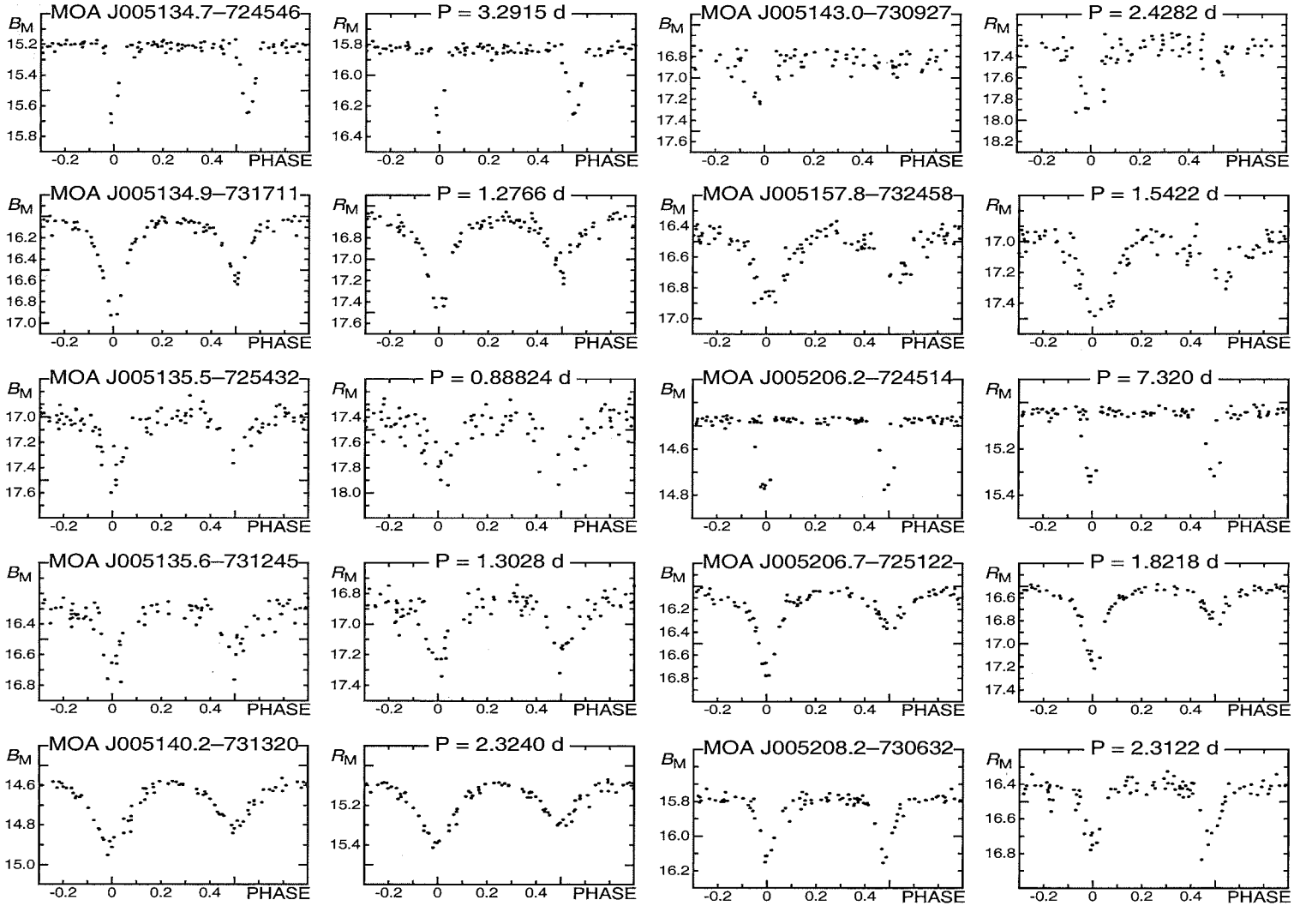

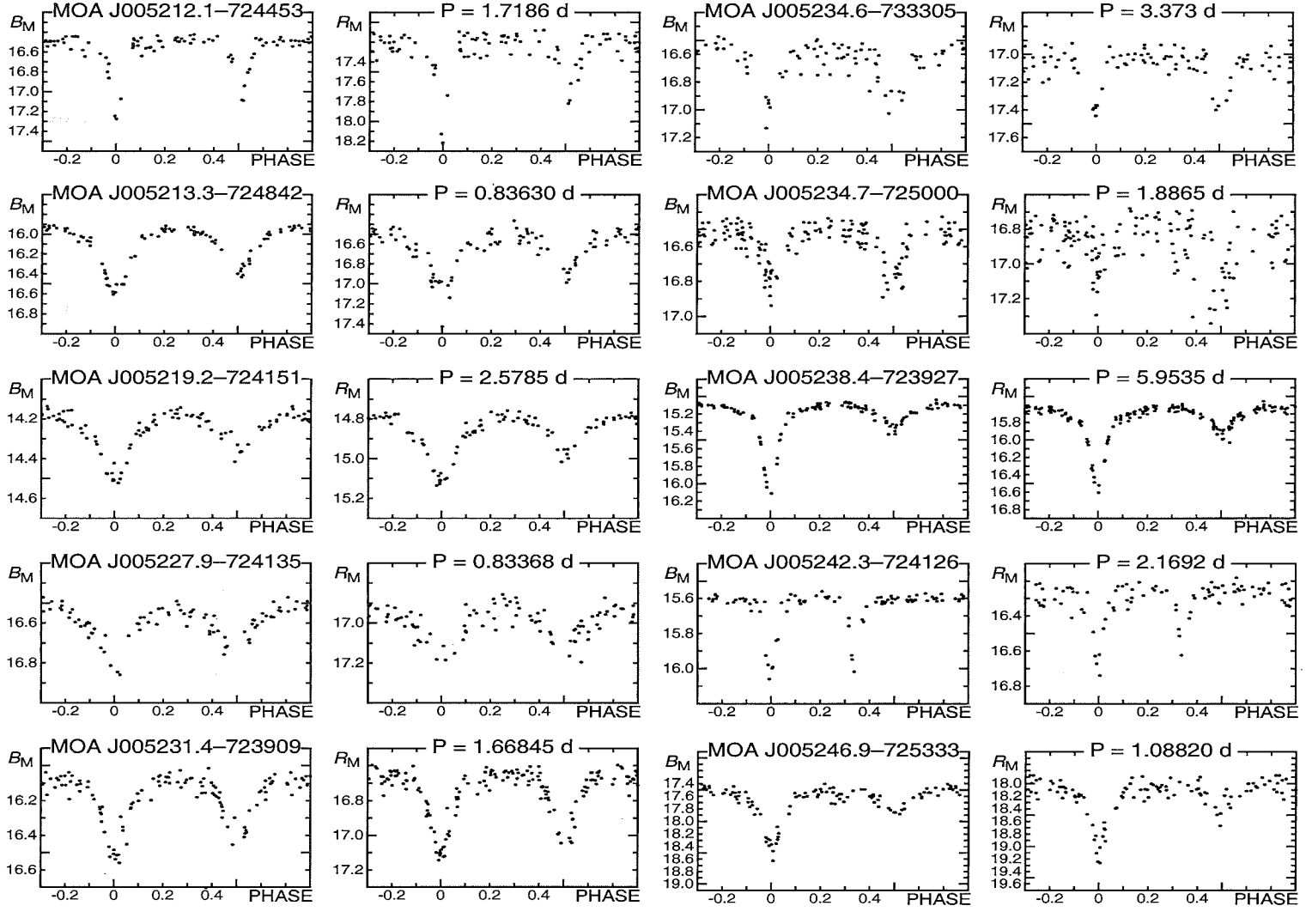
MOA J005212.1–724453
P = 1.7186 d
MOA J005234.6–733305
P = 3.373 d
MOA J005213.3–724842
P = 0.83630 d
MOA J005234.7–725000
P = 1.8865 d
MOA J005219.2–724151
P = 2.5785 d
MOA J005238.4–723927
P = 5.9535 d
MOA J005227.9–724135
P = 0.83368 d
MOA J005242.3–724126
P = 2.1692 d
MOA J005231.4–723909
P = 1.66845 d
MOA J005246.9–725333
P = 1.08820 d
B_M
R_M
PHASE

Bayne *et al.*, The MOA Catalogue of Eclipsing Binary Stars in the SMC. Fig 10

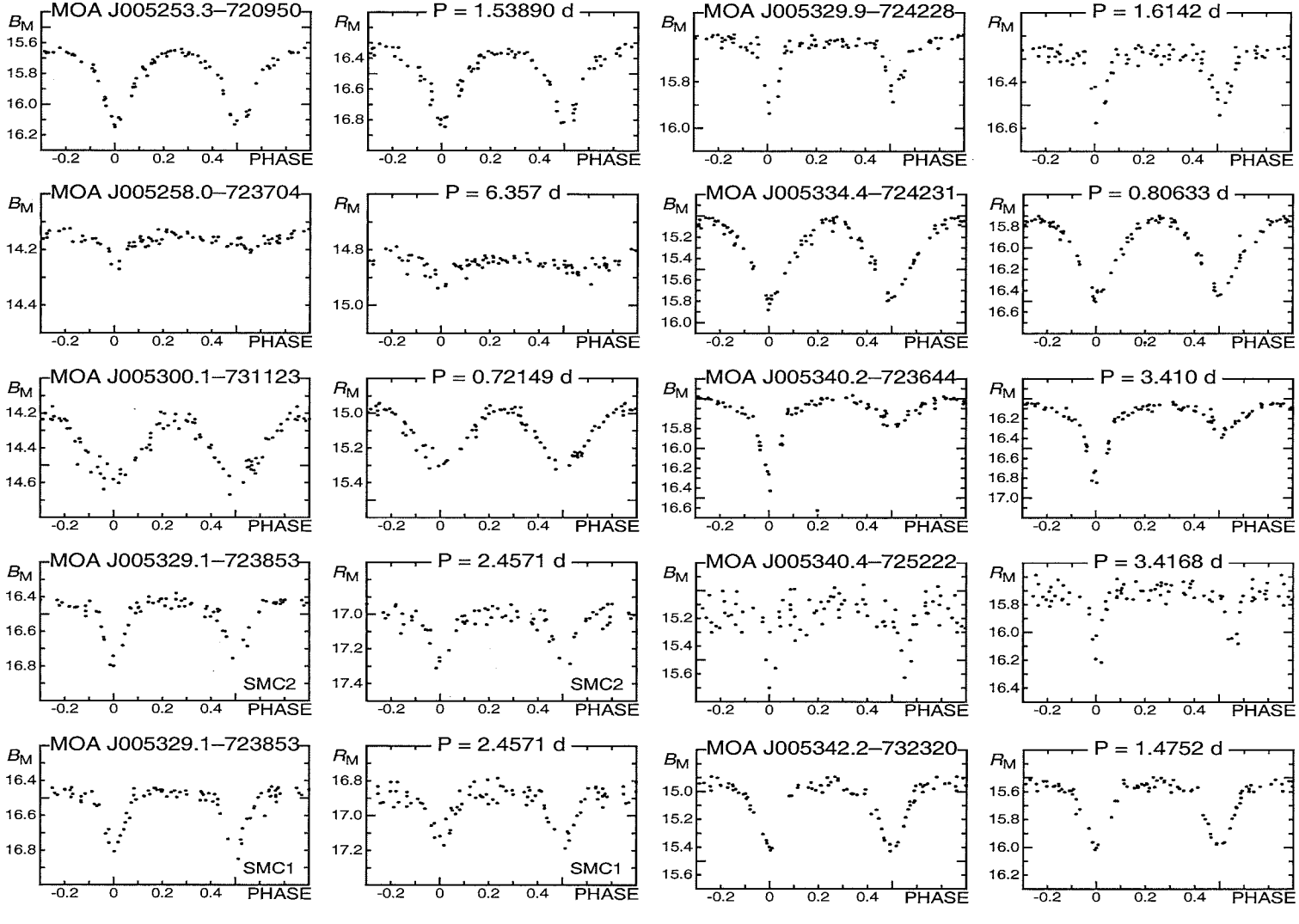

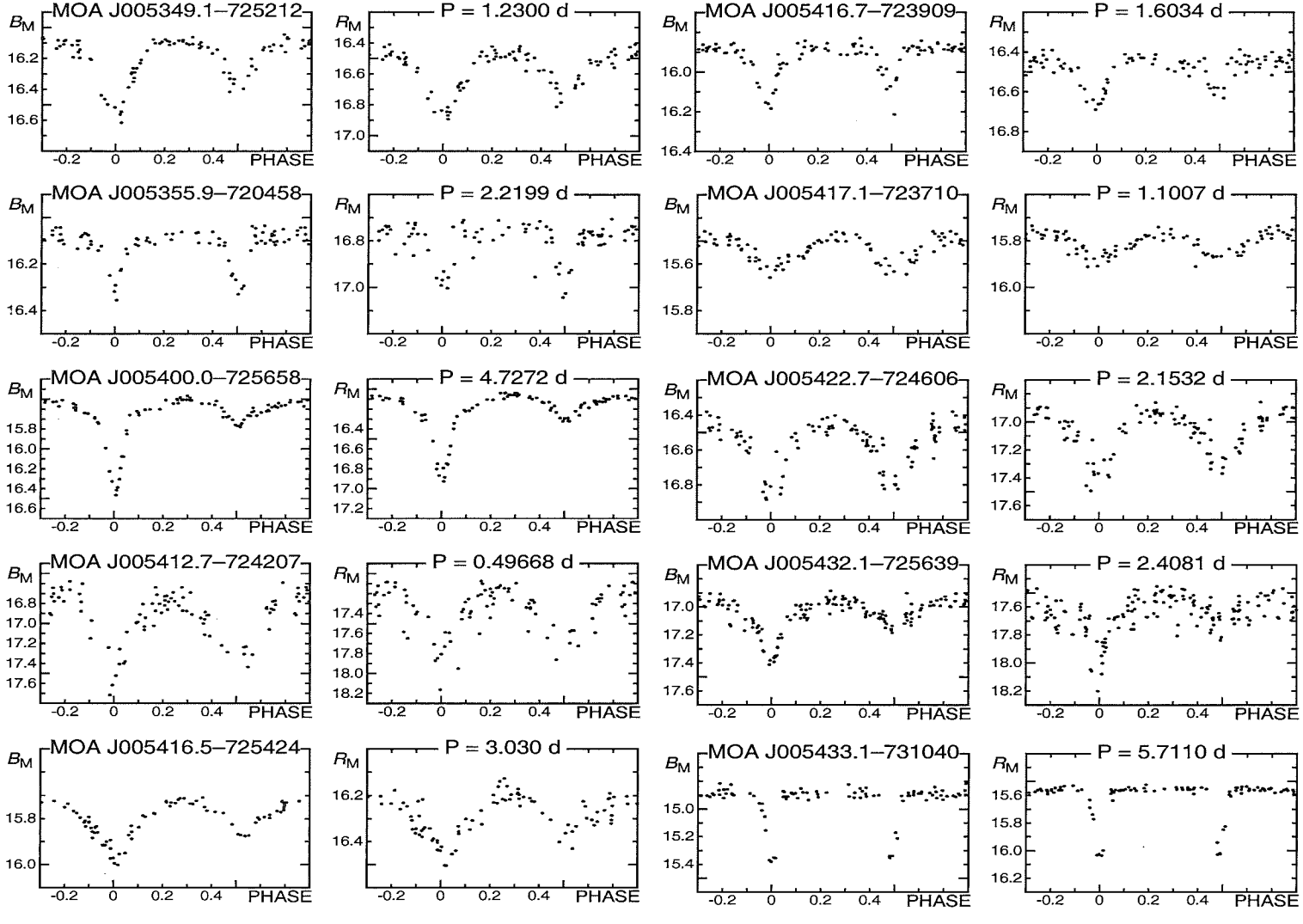
MOA J005349.1–725212
P = 1.2300 d
MOA J005416.7–723909
P = 1.6034 d
MOA J005355.9–720458
P = 2.2199 d
MOA J005417.1–723710
P = 1.1007 d
MOA J005400.0–725658
P = 4.7272 d
MOA J005422.7–724606
P = 2.1532 d
MOA J005412.7–724207
P = 0.49668 d
MOA J005432.1–725639
P = 2.4081 d
MOA J005416.5–725424
P = 3.030 d
MOA J005433.1–731040
P = 5.7110 d
B_M
R_M
PHASE

Bayne *et al.*, The MOA Catalogue of Eclipsing Binary Stars in the SMC. Fig 12

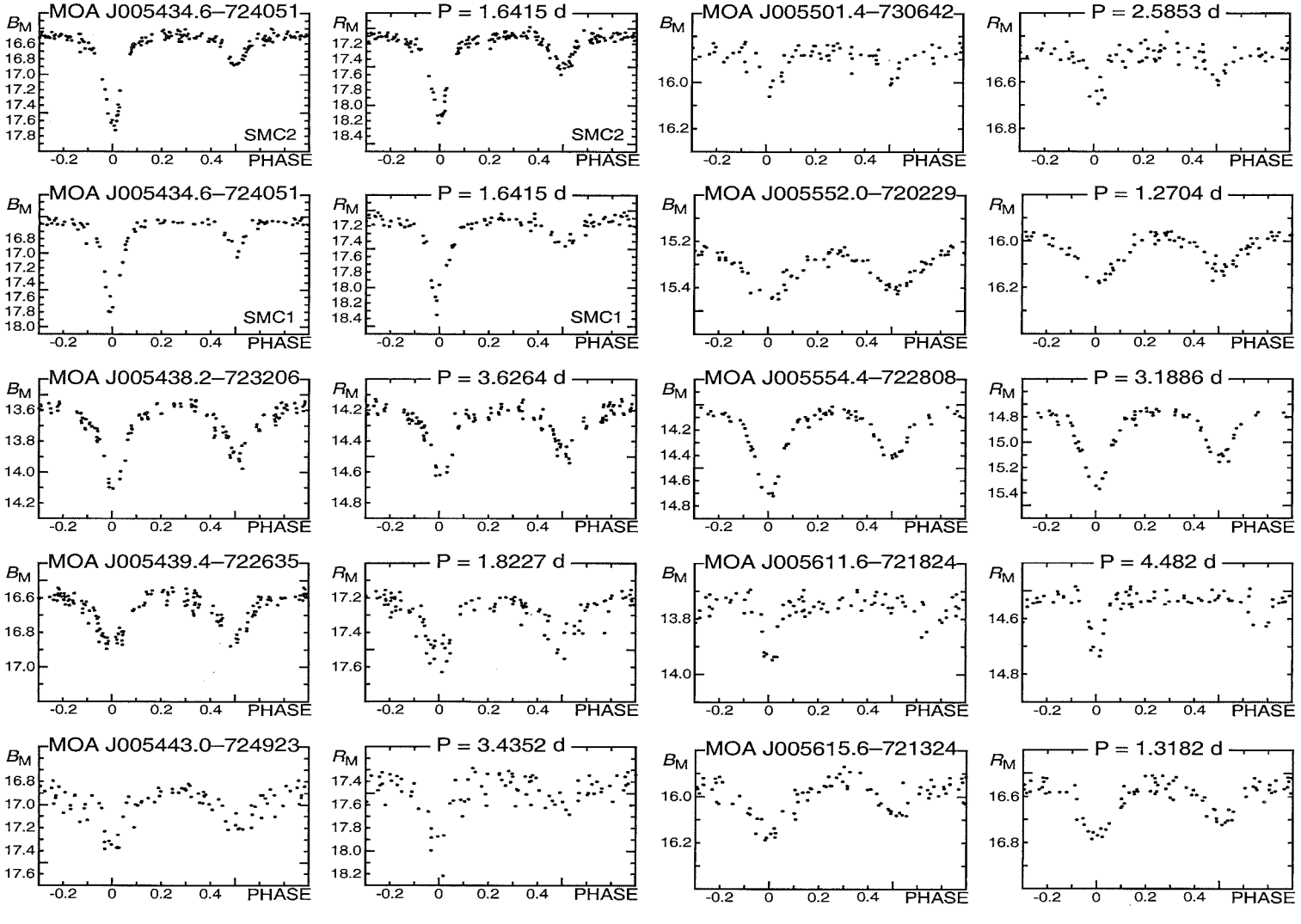

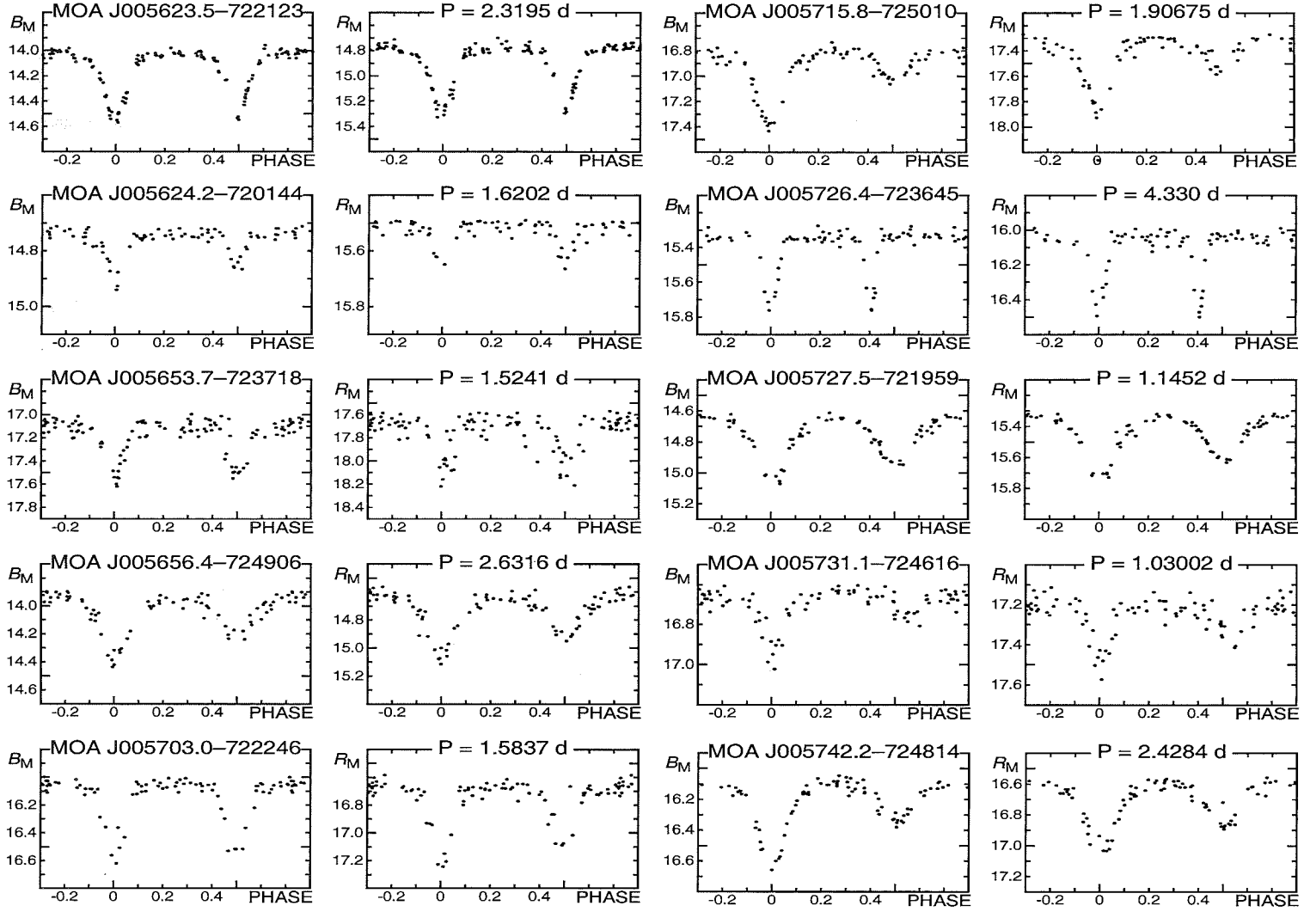
MOA J005623.5–722123
P = 2.3195 d
MOA J005715.8–725010
P = 1.90675 d
MOA J005624.2–720144
P = 1.6202 d
MOA J005726.4–723645
P = 4.330 d
MOA J005653.7–723718
P = 1.5241 d
MOA J005727.5–721959
P = 1.1452 d
MOA J005656.4–724906
P = 2.6316 d
MOA J005731.1–724616
P = 1.03002 d
MOA J005703.0–722246
P = 1.5837 d
MOA J005742.2–724814
P = 2.4284 d
PHASE

Bayne *et al.*, The MOA Catalogue of Eclipsing Binary Stars in the SMC. Fig 14

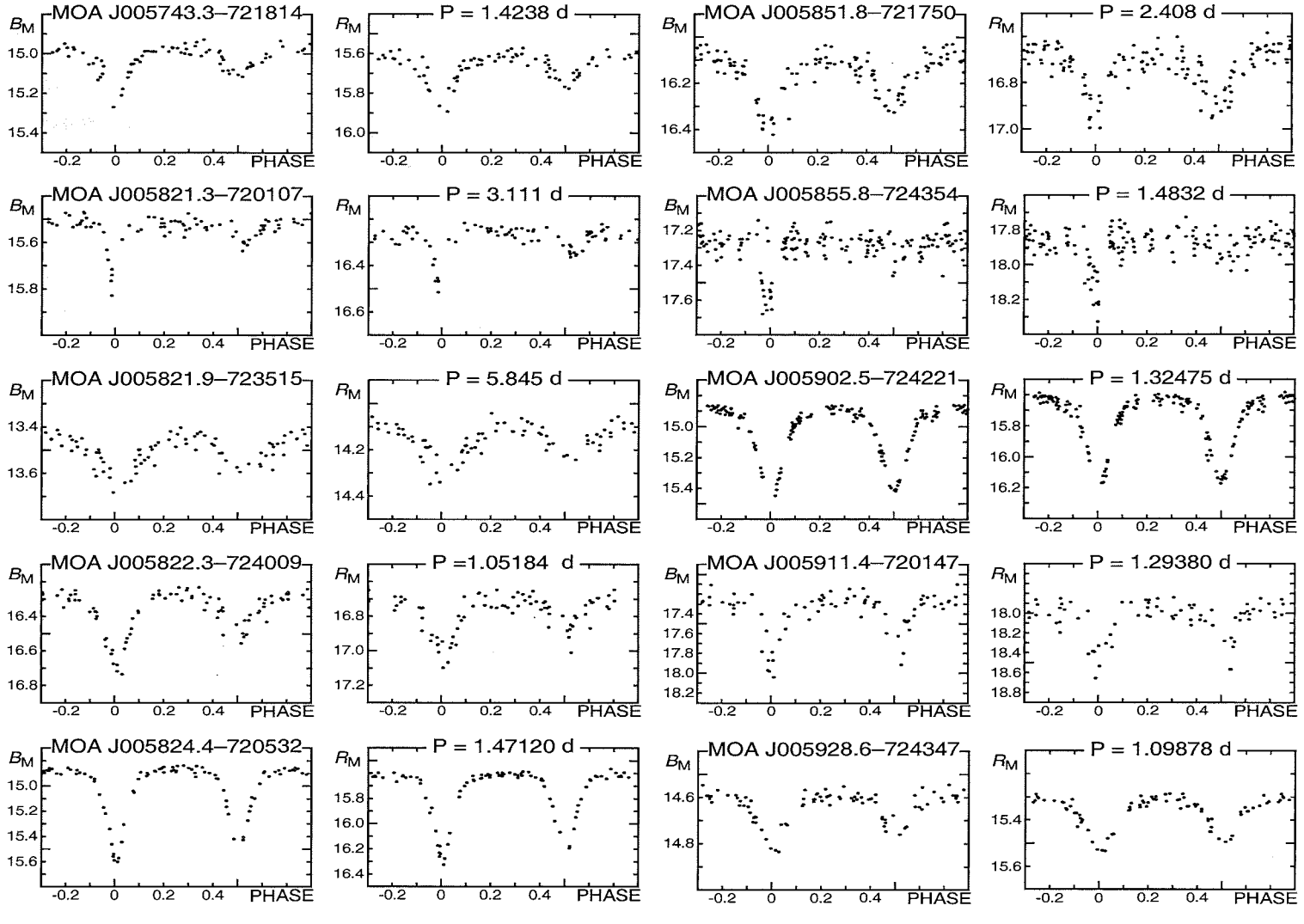

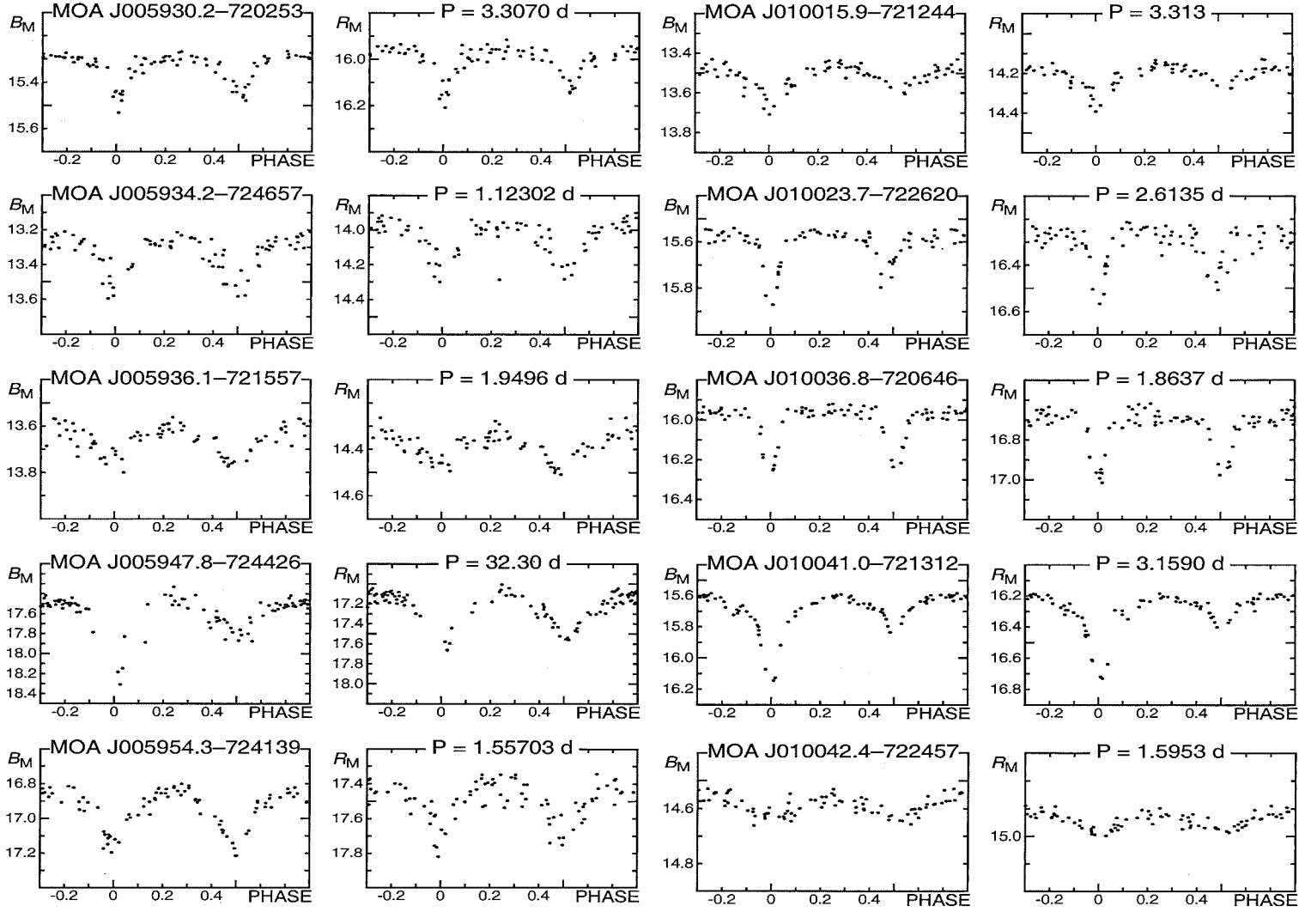
MOA J005930.2–720253
P = 3.3070 d
MOA J010015.9–721244
P = 3.313
MOA J005934.2–724657
P = 1.12302 d
MOA J010023.7–722620
P = 2.6135 d
MOA J005936.1–721557
P = 1.9496 d
MOA J010036.8–720646
P = 1.8637 d
MOA J005947.8–724426
P = 32.30 d
MOA J010041.0–721312
P = 3.1590 d
MOA J005954.3–724139
P = 1.55703 d
MOA J010042.4–722457
P = 1.5953 d
B_M
R_M
PHASE

Bayne *et al.*, The MOA Catalogue of Eclipsing Binary Stars in the SMC. Fig 16

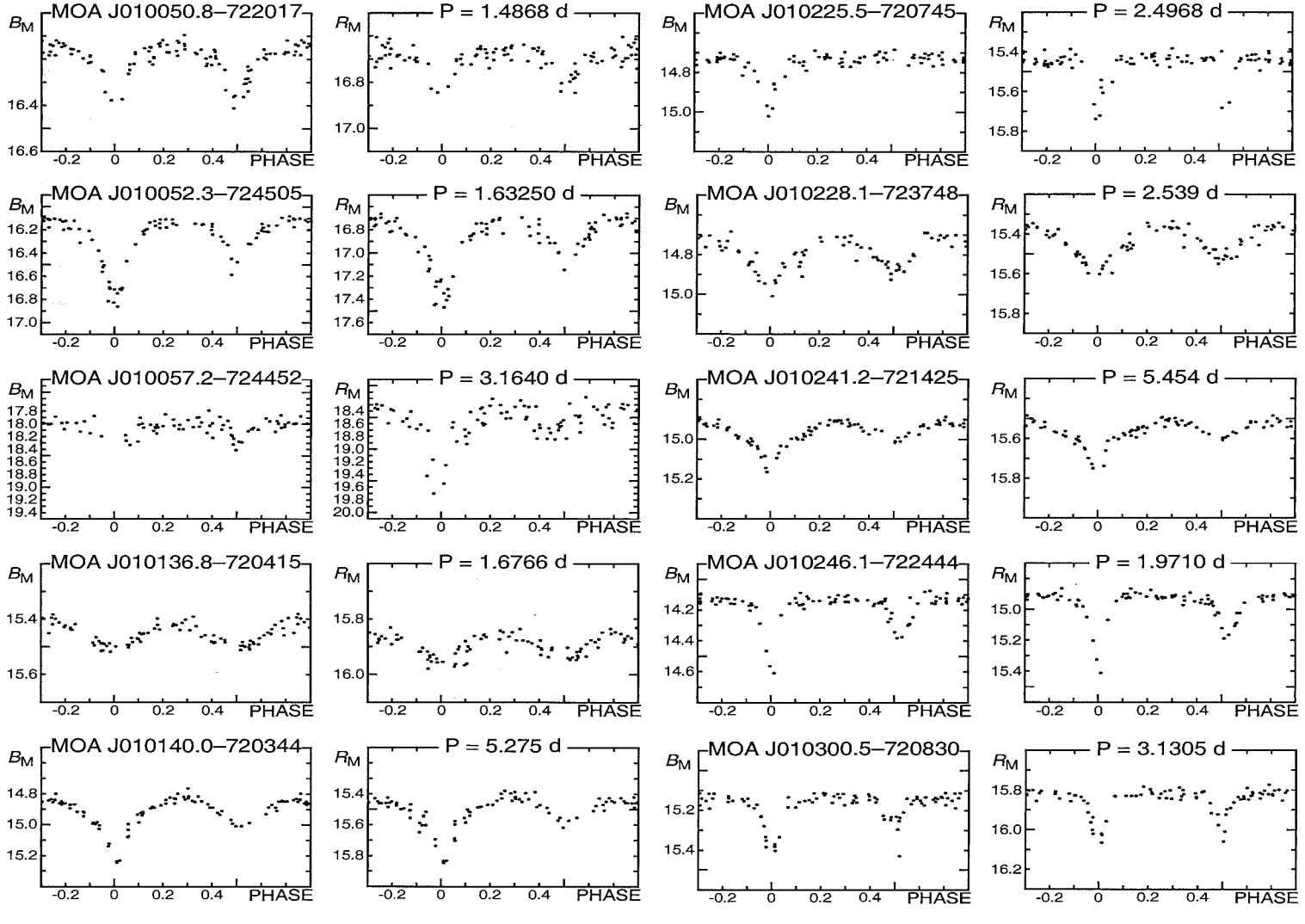

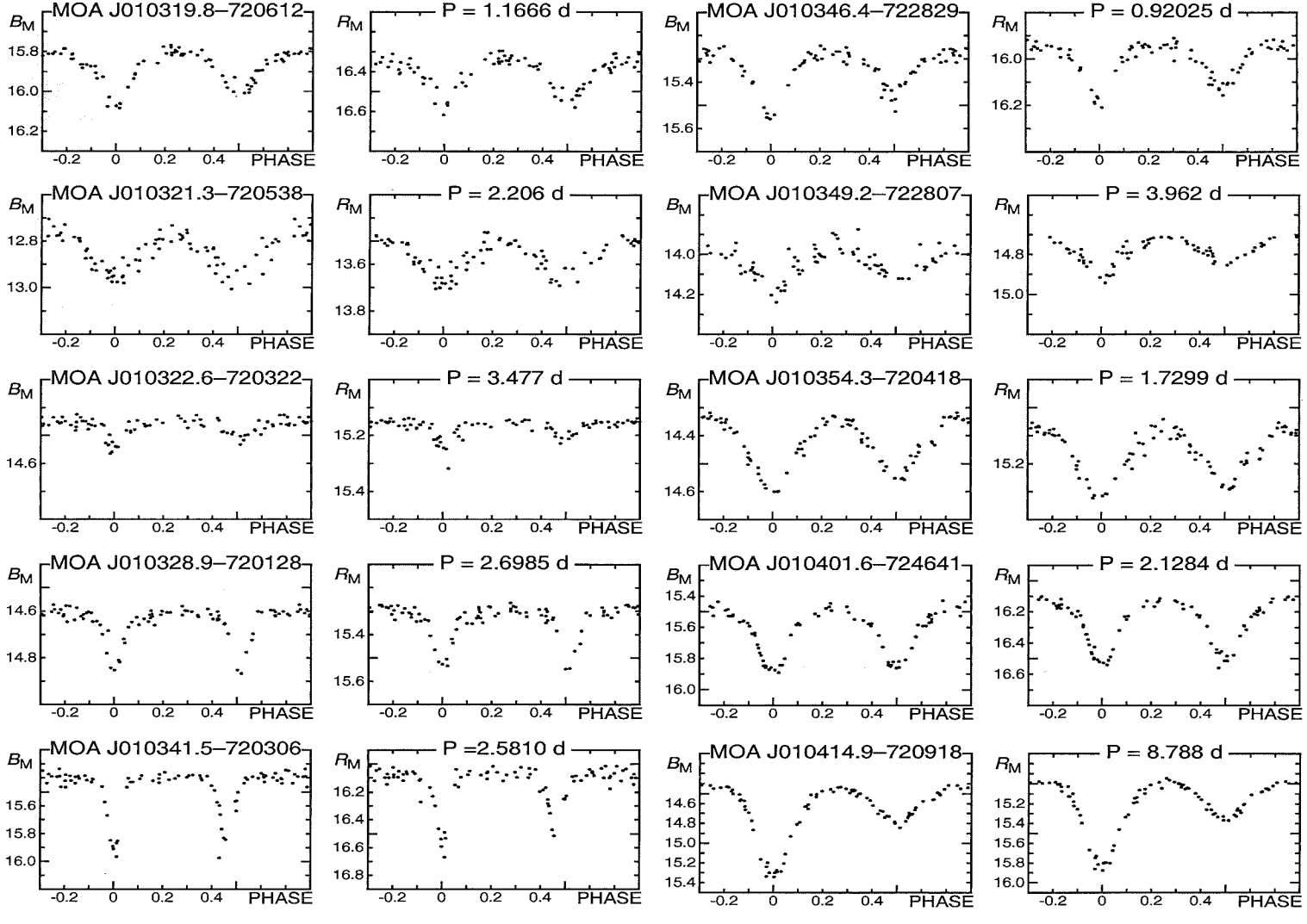
MOA J010319.8–720612
P = 1.1666 d
MOA J010346.4–722829
P = 0.92025 d
MOA J010321.3–720538
P = 2.206 d
MOA J010349.2–722807
P = 3.962 d
MOA J010322.6–720322
P = 3.477 d
MOA J010354.3–720418
P = 1.7299 d
MOA J010328.9–720128
P = 2.6985 d
MOA J010401.6–724641
P = 2.1284 d
MOA J010341.5–720306
P =2.5810 d
MOA J010414.9–720918
P = 8.788 d
PHASE

Bayne *et al.*, The MOA Catalogue of Eclipsing Binary Stars in the SMC. Fig 18

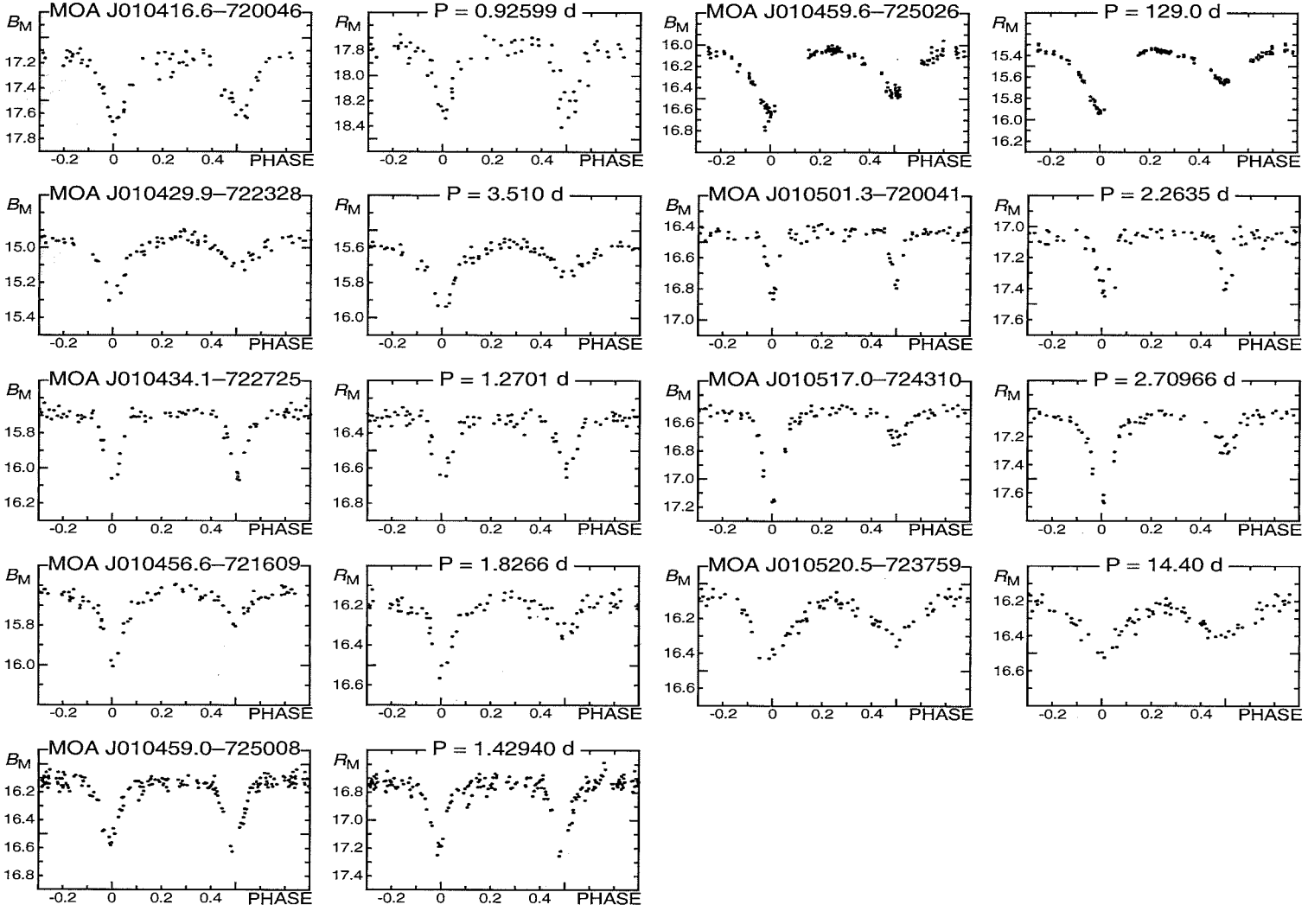

Bayne *et al.*, The MOA Catalogue of Eclipsing Binary Stars in the SMC. Fig 19

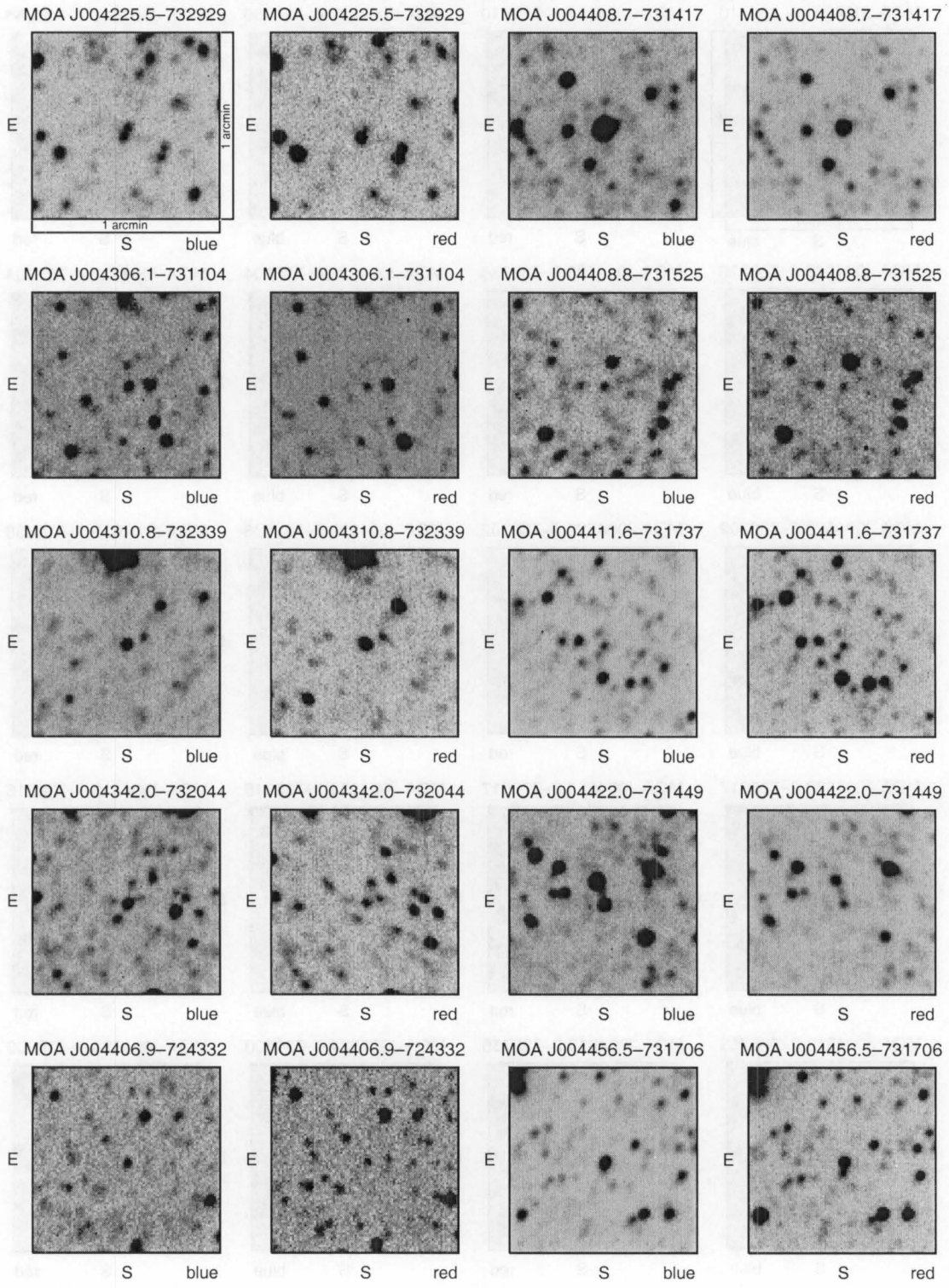

Bayne *et al.*, The MOA Catalogue of Eclipsing Binary Stars in the SMC. Fig 20

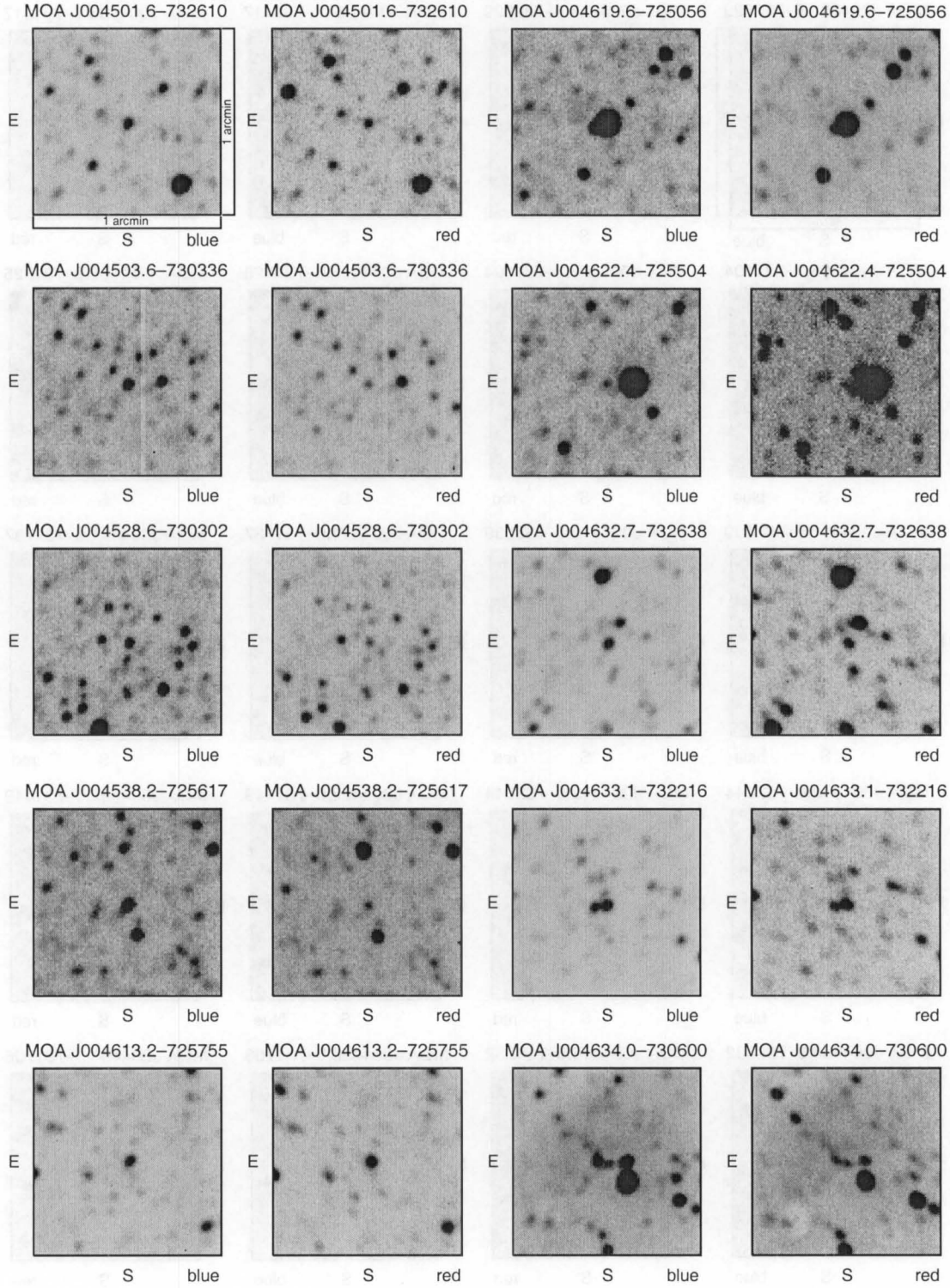

Bayne *et al.*, The MOA Catalogue of Eclipsing Binary Stars in the SMC. Fig 21

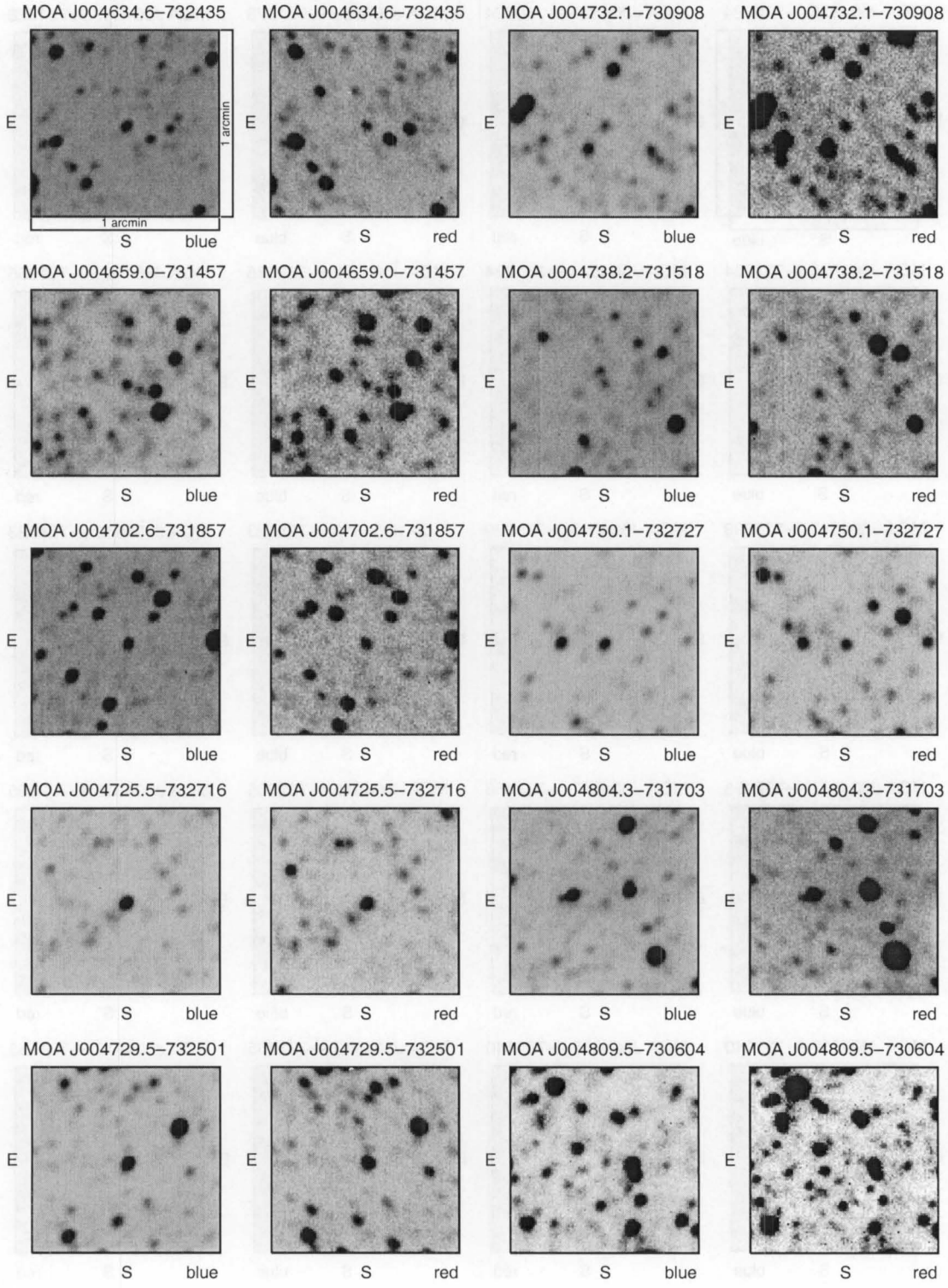

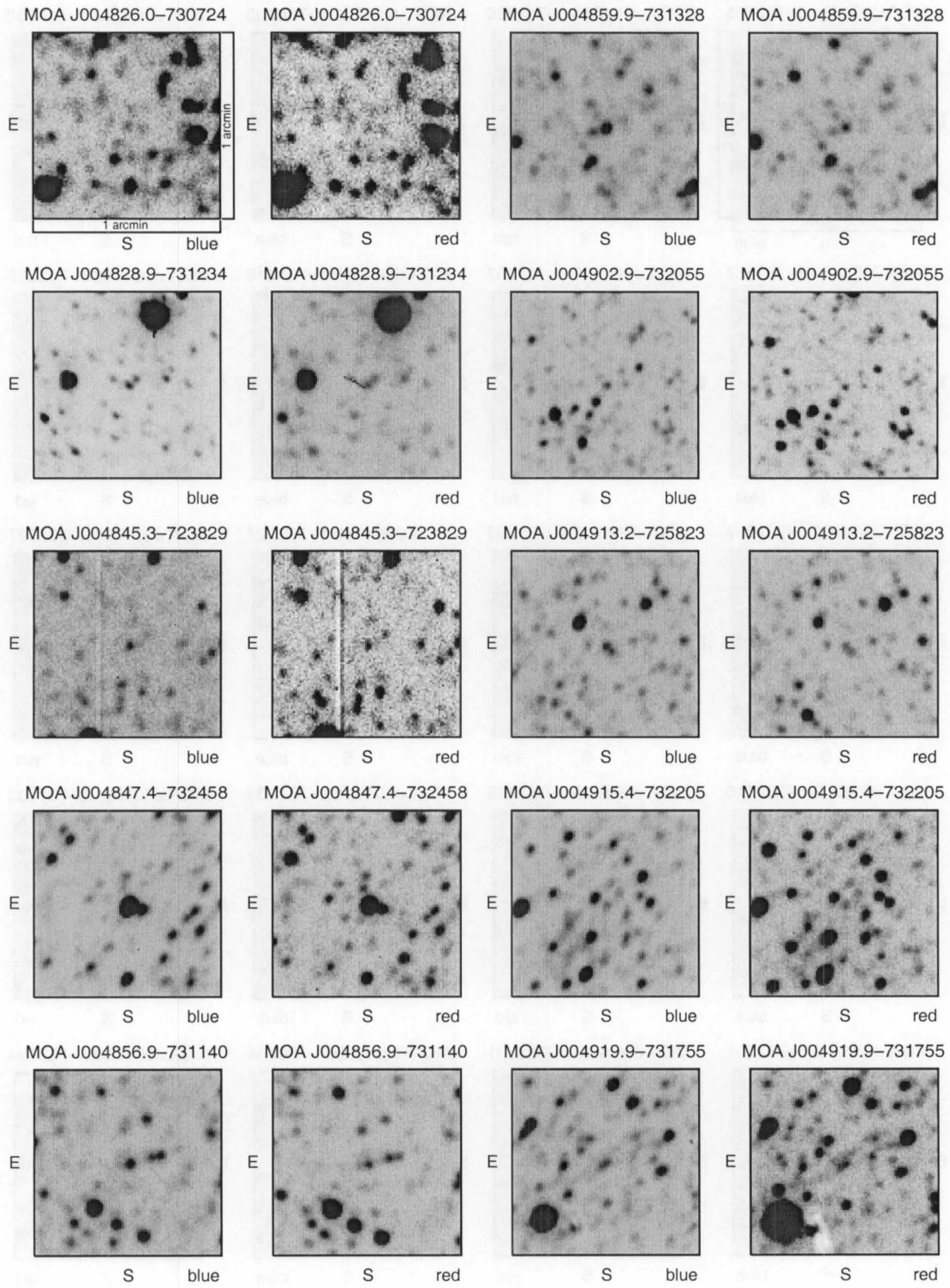
Bayne *et al.*, The MOA Catalogue of Eclipsing Binary Stars in the SMC. Fig 22
MOA J004826.0–730724
MOA J004826.0–730724
MOA J004859.9–731328
MOA J004859.9–731328
1 arcmin
1 arcmin
E
S
blue
red
MOA J004828.9–731234
MOA J004828.9–731234
MOA J004902.9–732055
MOA J004902.9–732055
MOA J004845.3–723829
MOA J004845.3–723829
MOA J004913.2–725823
MOA J004913.2–725823
MOA J004847.4–732458
MOA J004847.4–732458
MOA J004915.4–732205
MOA J004915.4–732205
MOA J004856.9–731140
MOA J004856.9–731140
MOA J004919.9–731755
MOA J004919.9–731755

Bayne *et al.*, The MOA Catalogue of Eclipsing Binary Stars in the SMC. Fig 23

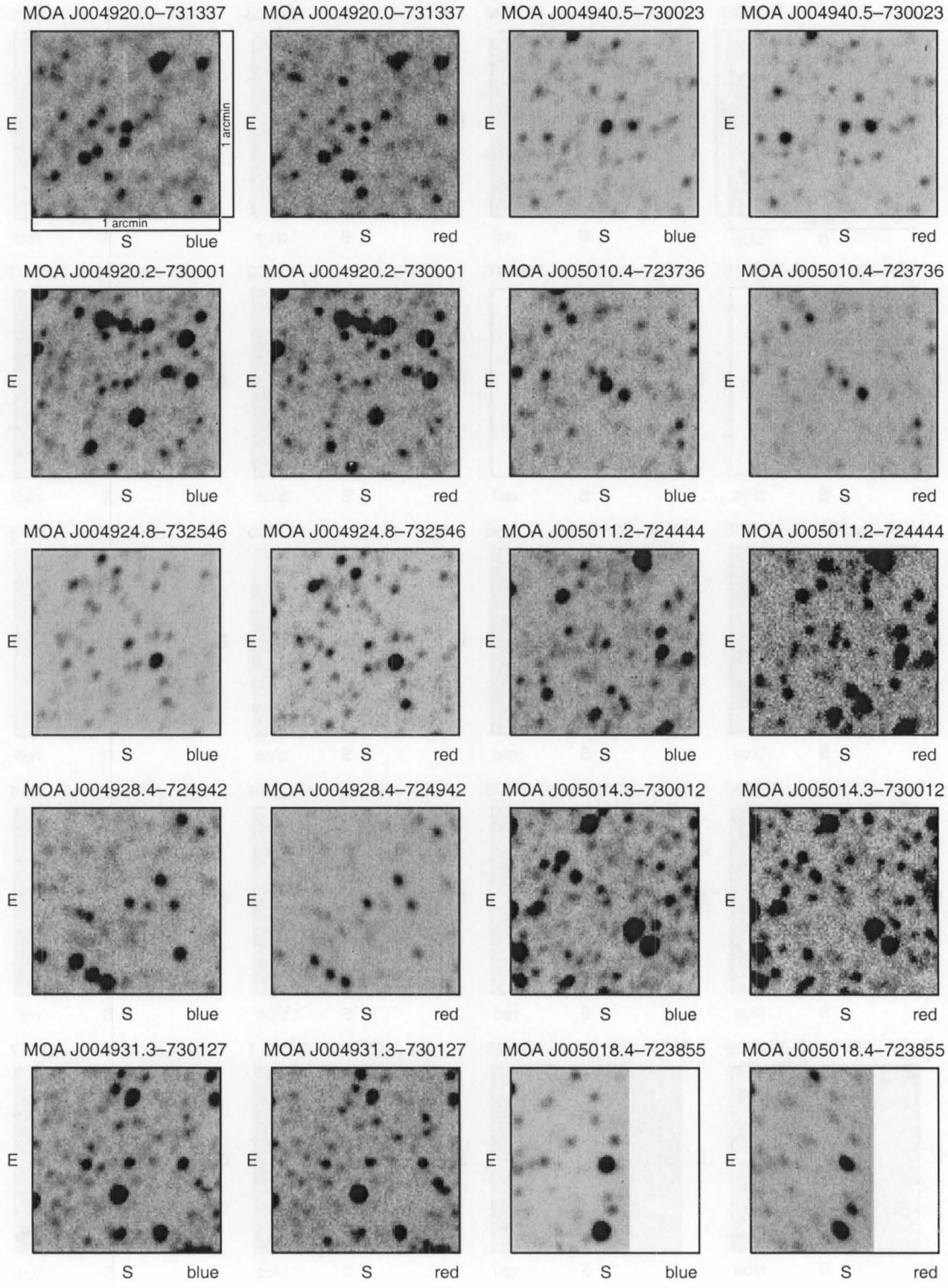

Bayne *et al.*, The MOA Catalogue of Eclipsing Binary Stars in the SMC. Fig 24

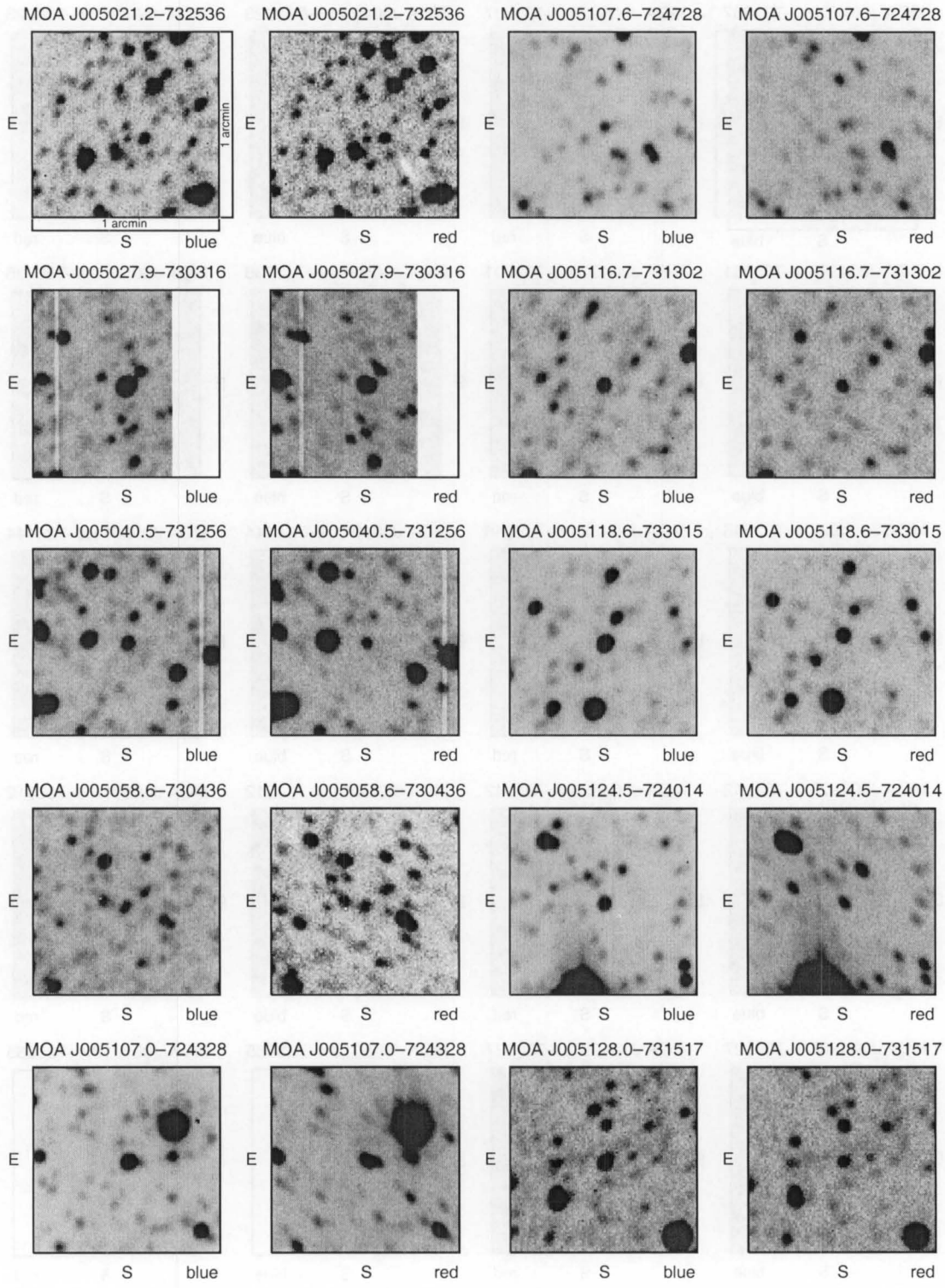

Bayne *et al.*, The MOA Catalogue of Eclipsing Binary Stars in the SMC. Fig 25

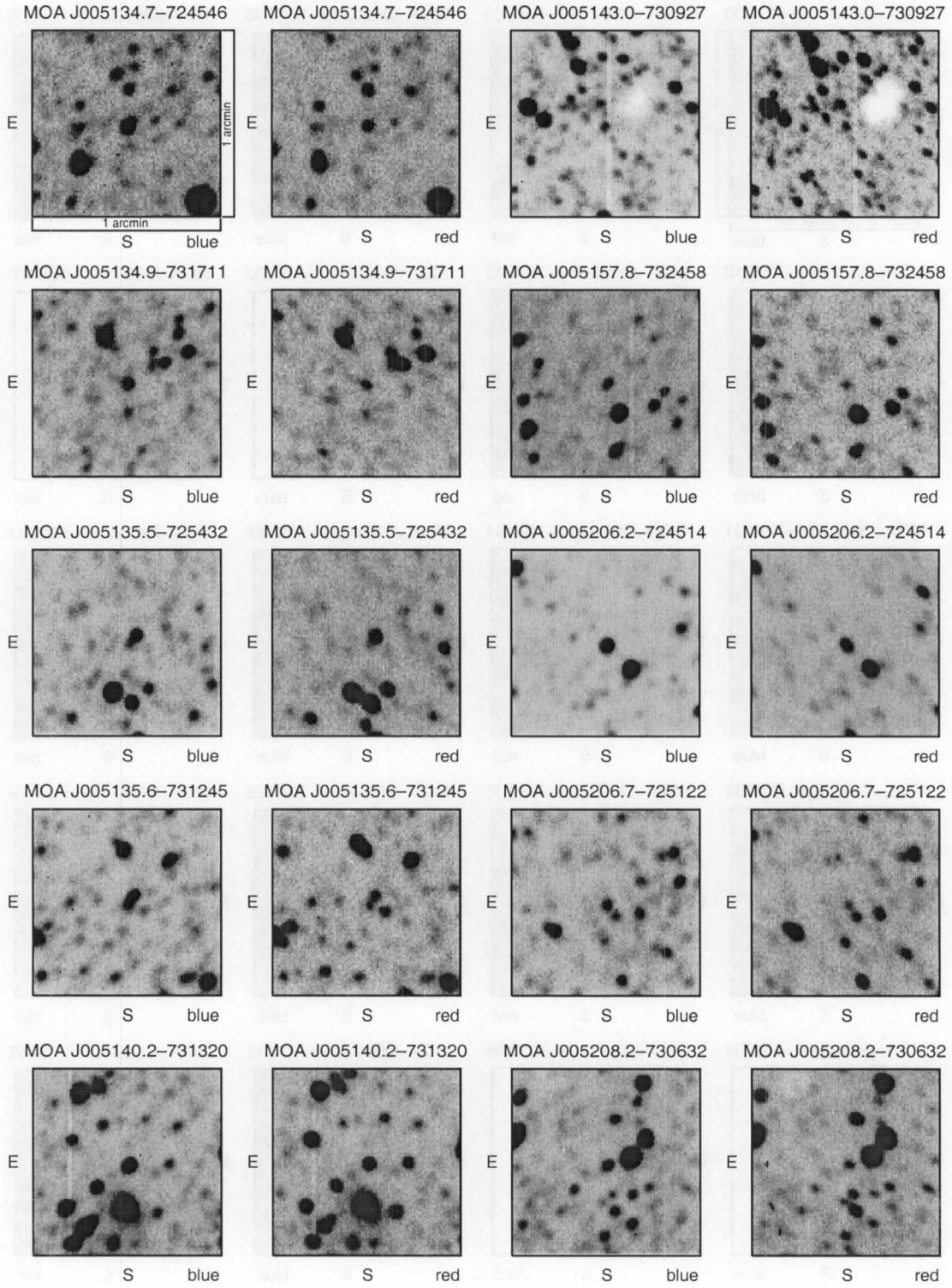

Bayne *et al.*, The MOA Catalogue of Eclipsing Binary Stars in the SMC. Fig26

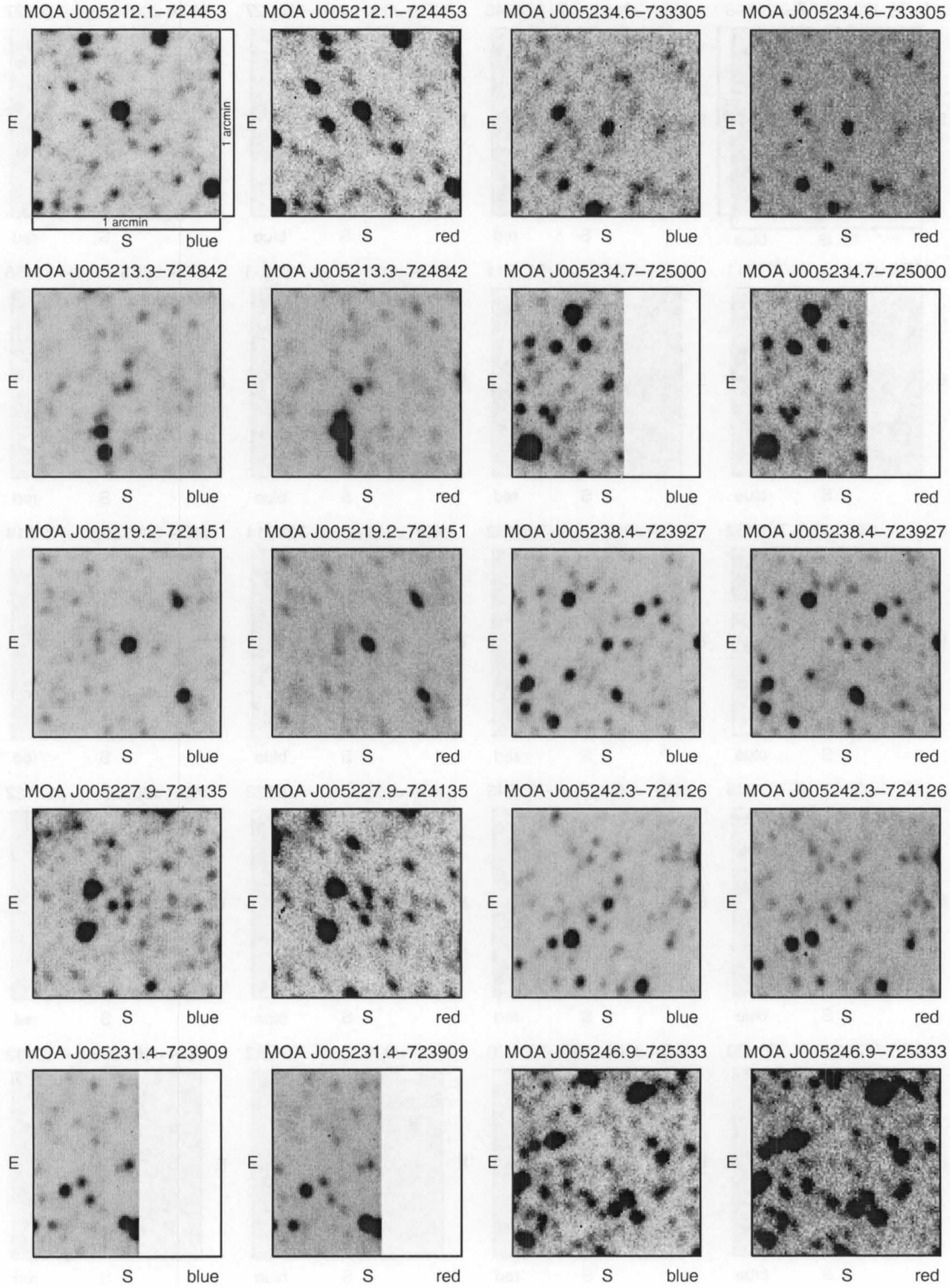

Bayne *et al.*, The MOA Catalogue of Eclipsing Binary Stars in the SMC. Fig 27

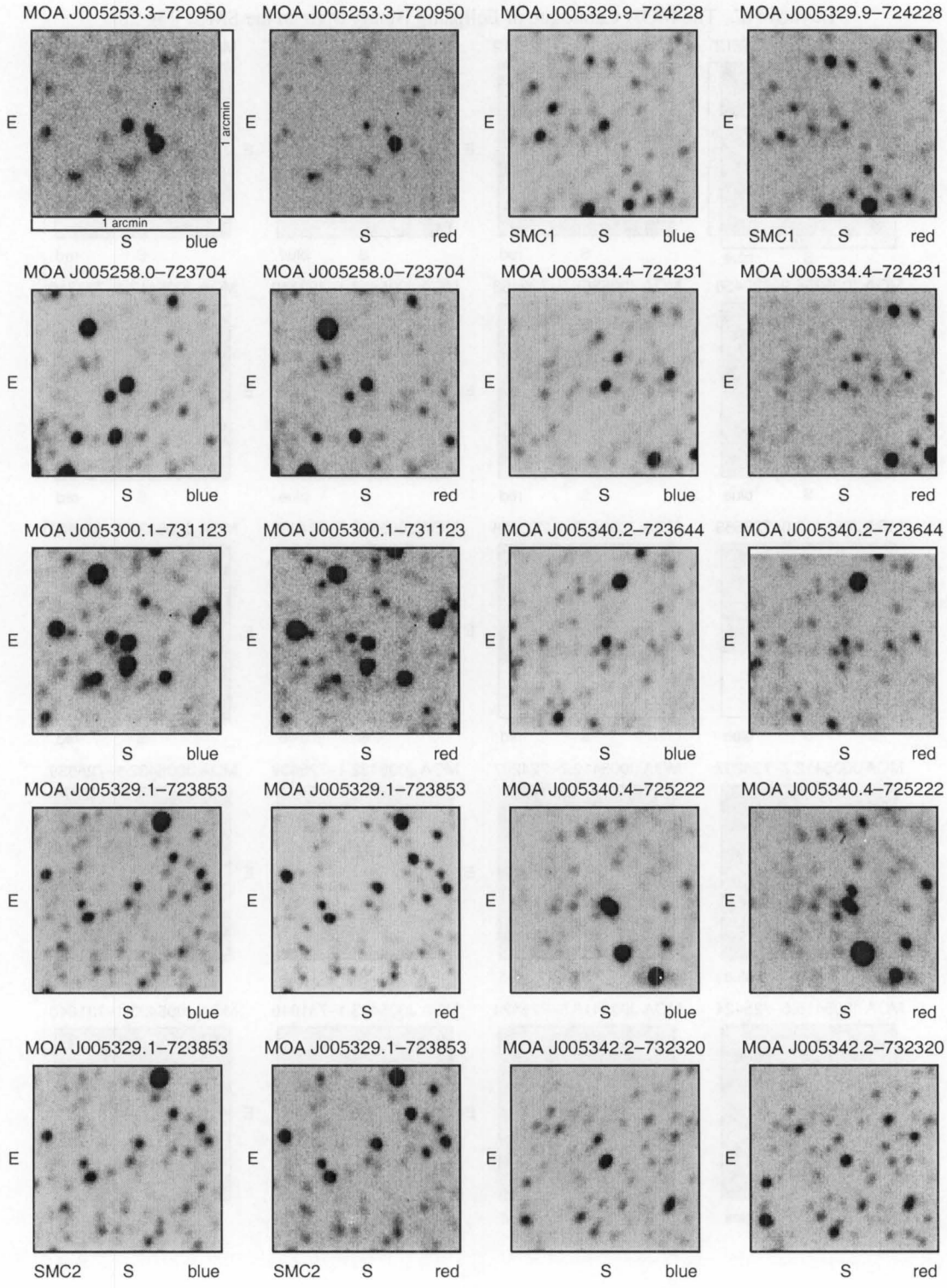

Bayne *et al.*, The MOA Catalogue of Eclipsing Binary Stars in the SMC. Fig 28

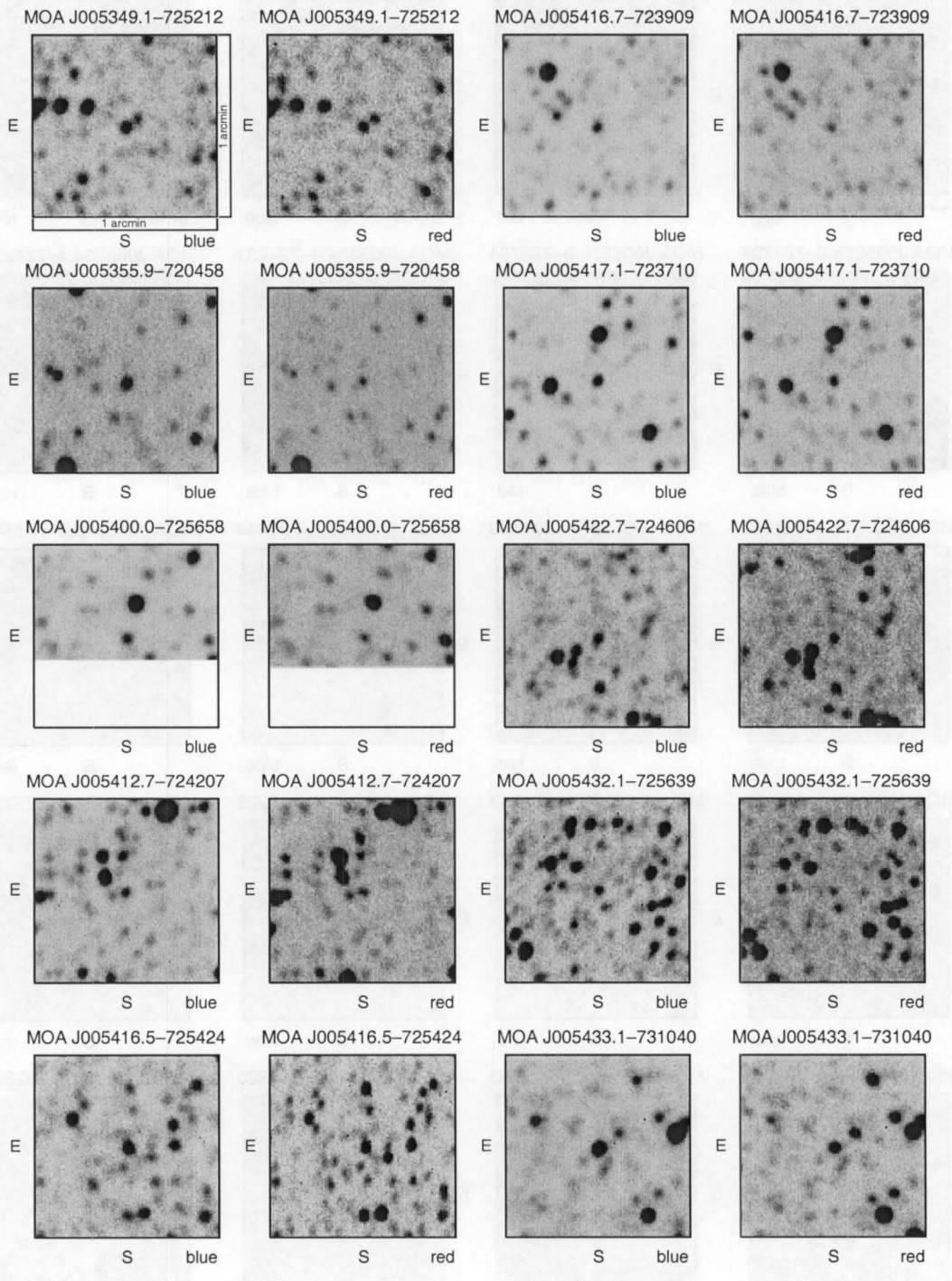

Bayne *et al.*, The MOA Catalogue of Eclipsing Binary Stars in the SMC. Fig 29

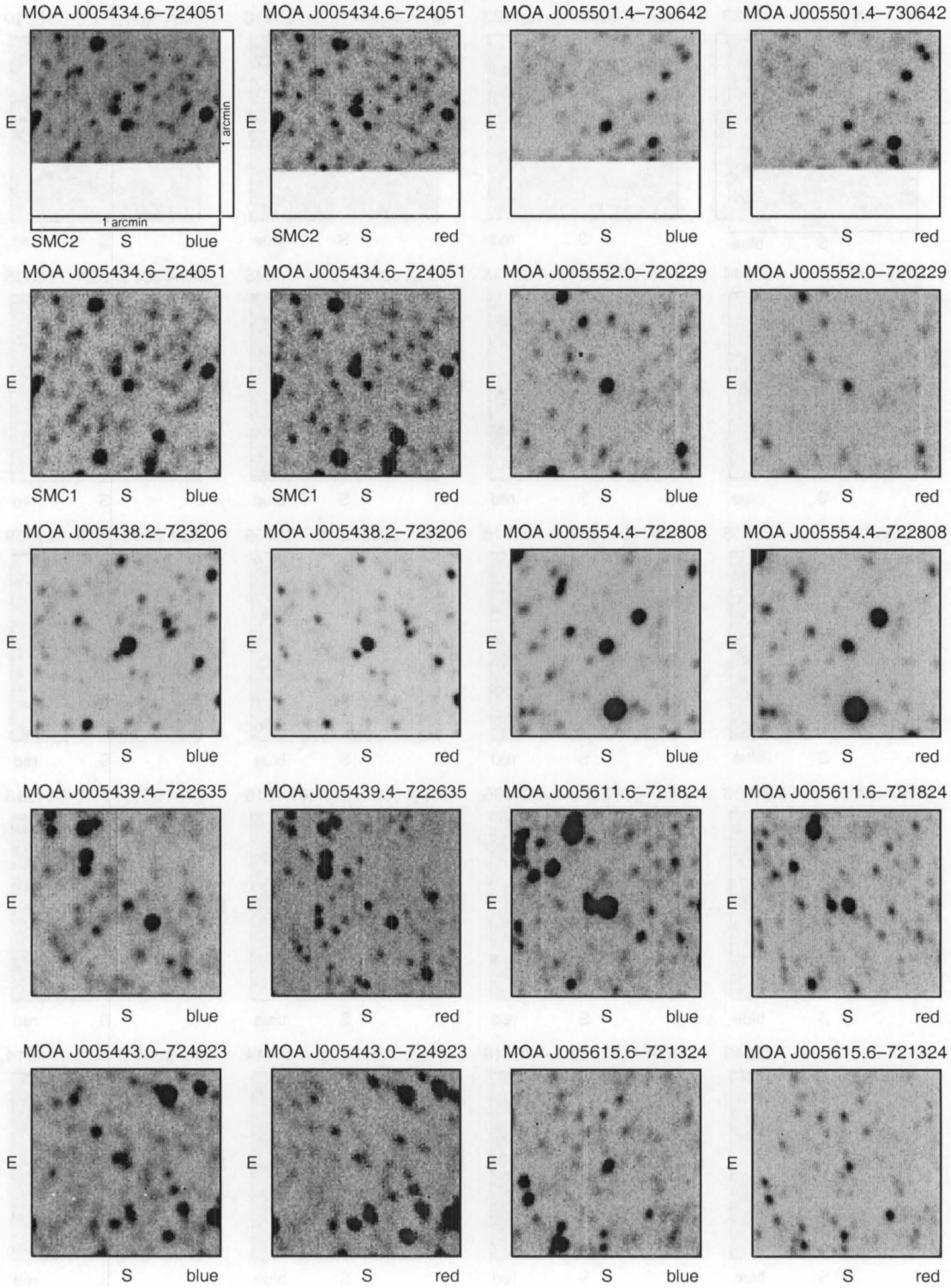

Bayne *et al.*, The MOA Catalogue of Eclipsing Binary Stars in the SMC. Fig 30

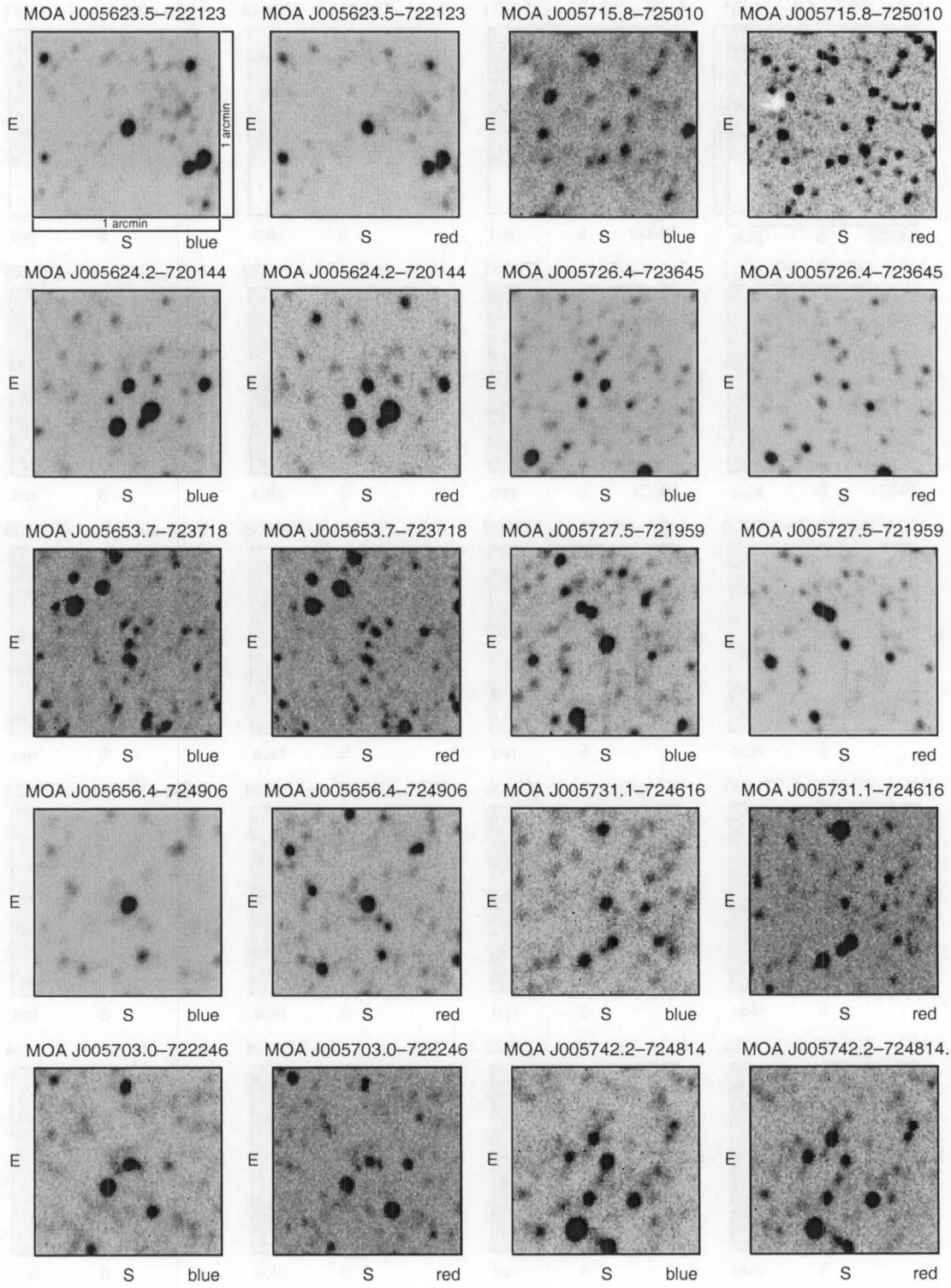

Bayne *et al.*, The MOA Catalogue of Eclipsing Binary Stars in the SMC. Fig 31

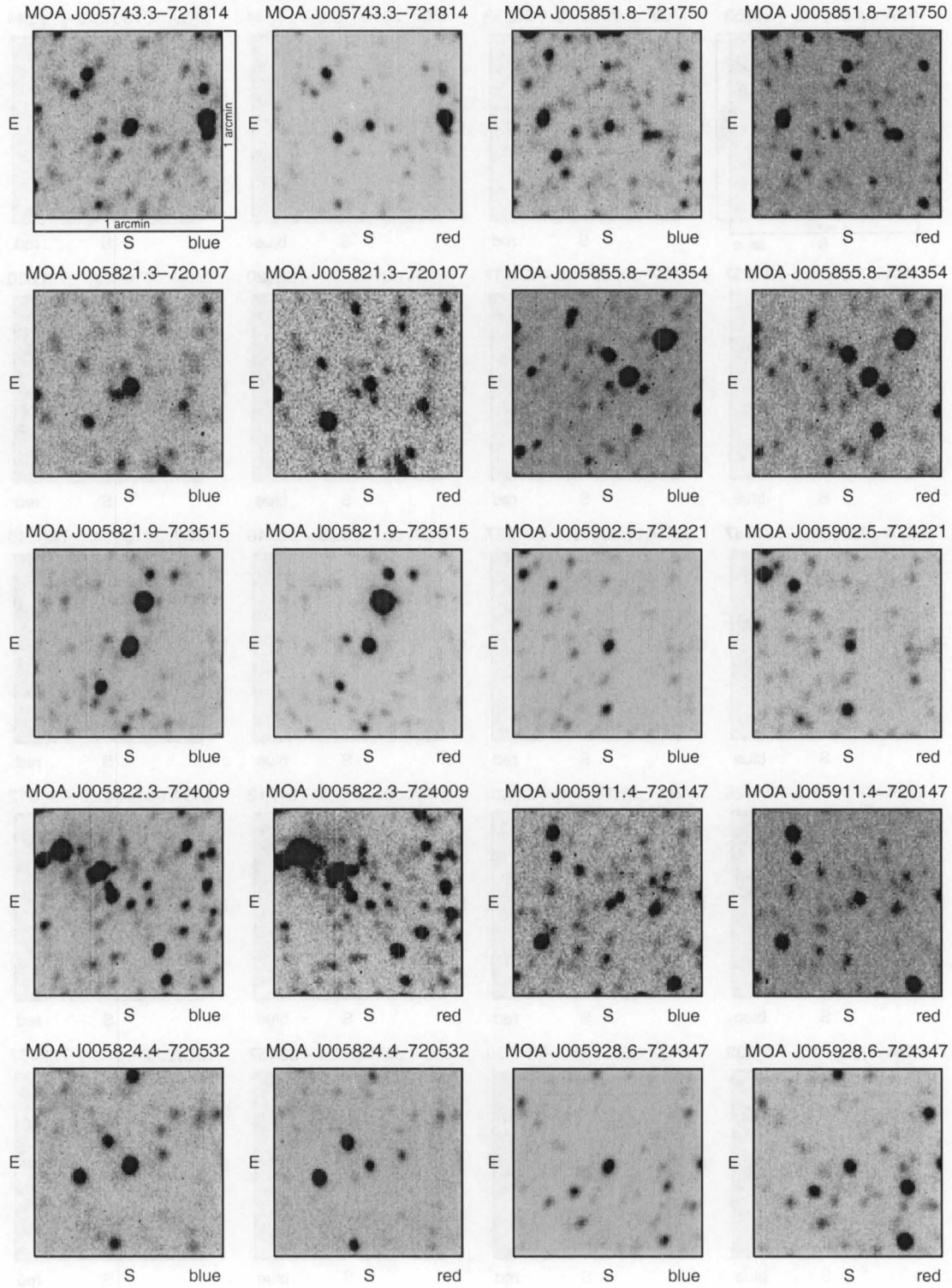

Bayne *et al.*, The MOA Catalogue of Eclipsing Binary Stars in the SMC. Fig 32

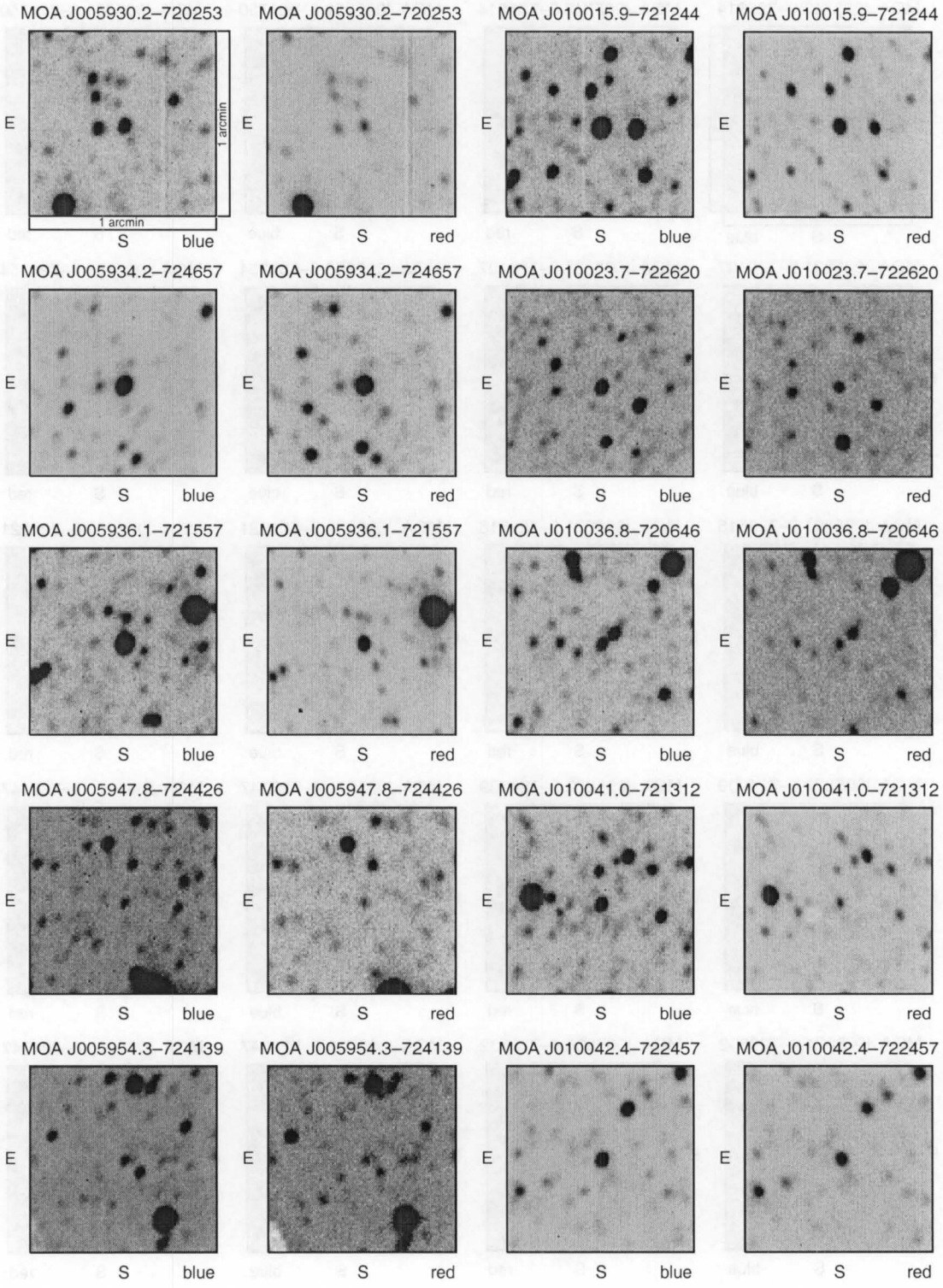

Bayne *et al.*, The MOA Catalogue of Eclipsing Binary Stars in the SMC. Fig 33

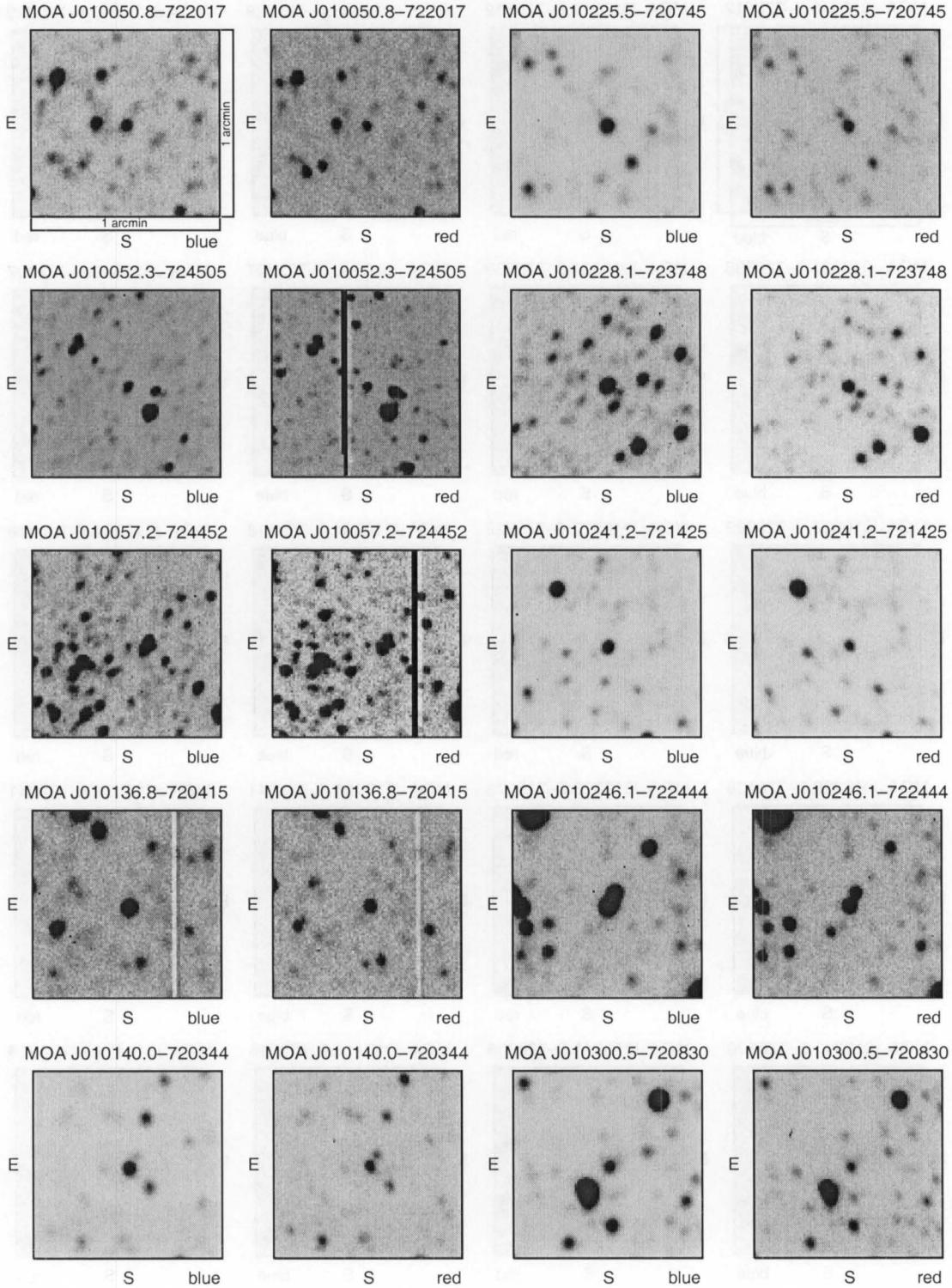

Bayne *et al.*, The MOA Catalogue of Eclipsing Binary Stars in the SMC. Fig 34

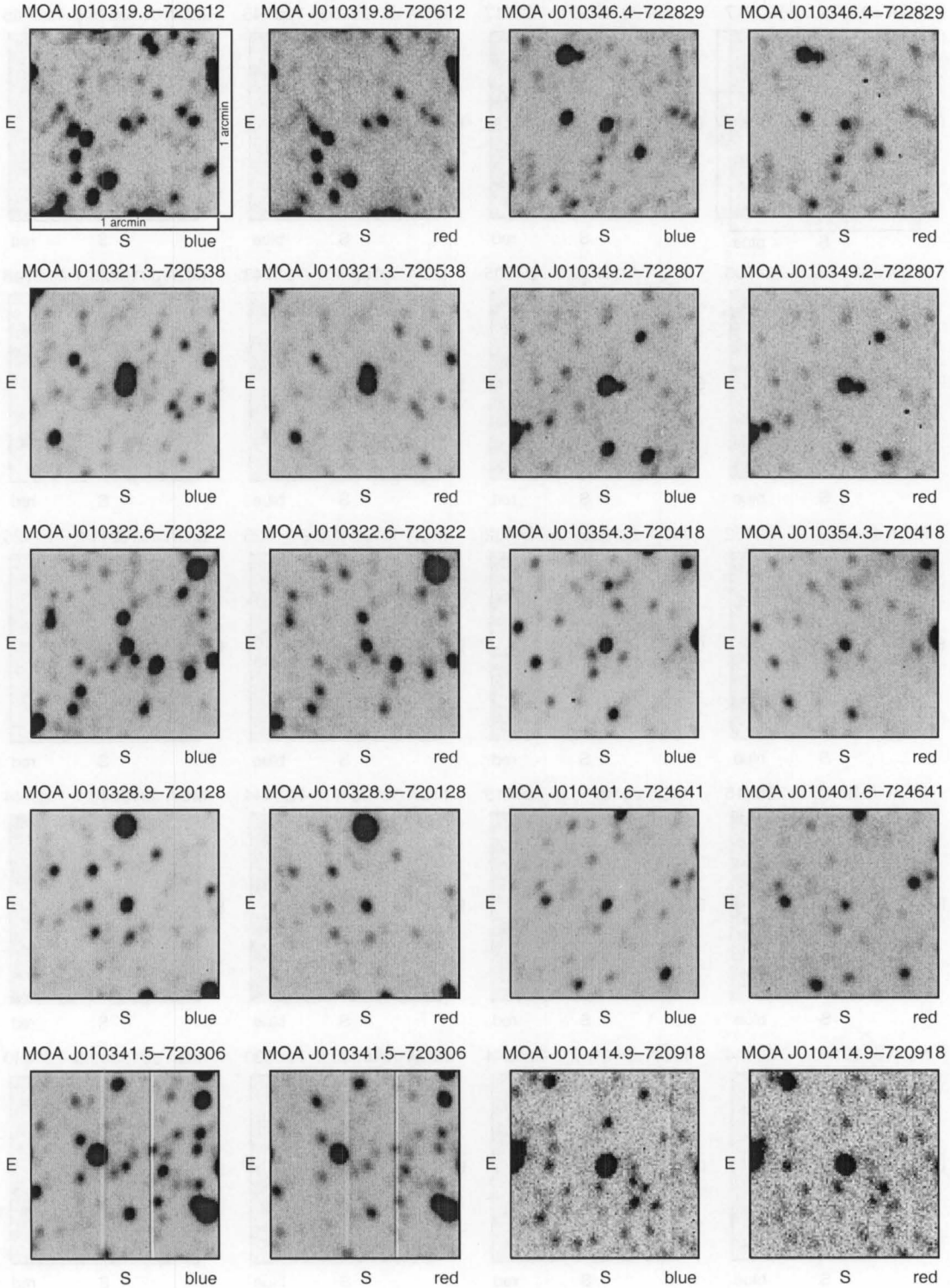

Bayne *et al.*, The MOA Catalogue of Eclipsing Binary Stars in the SMC. Fig 35

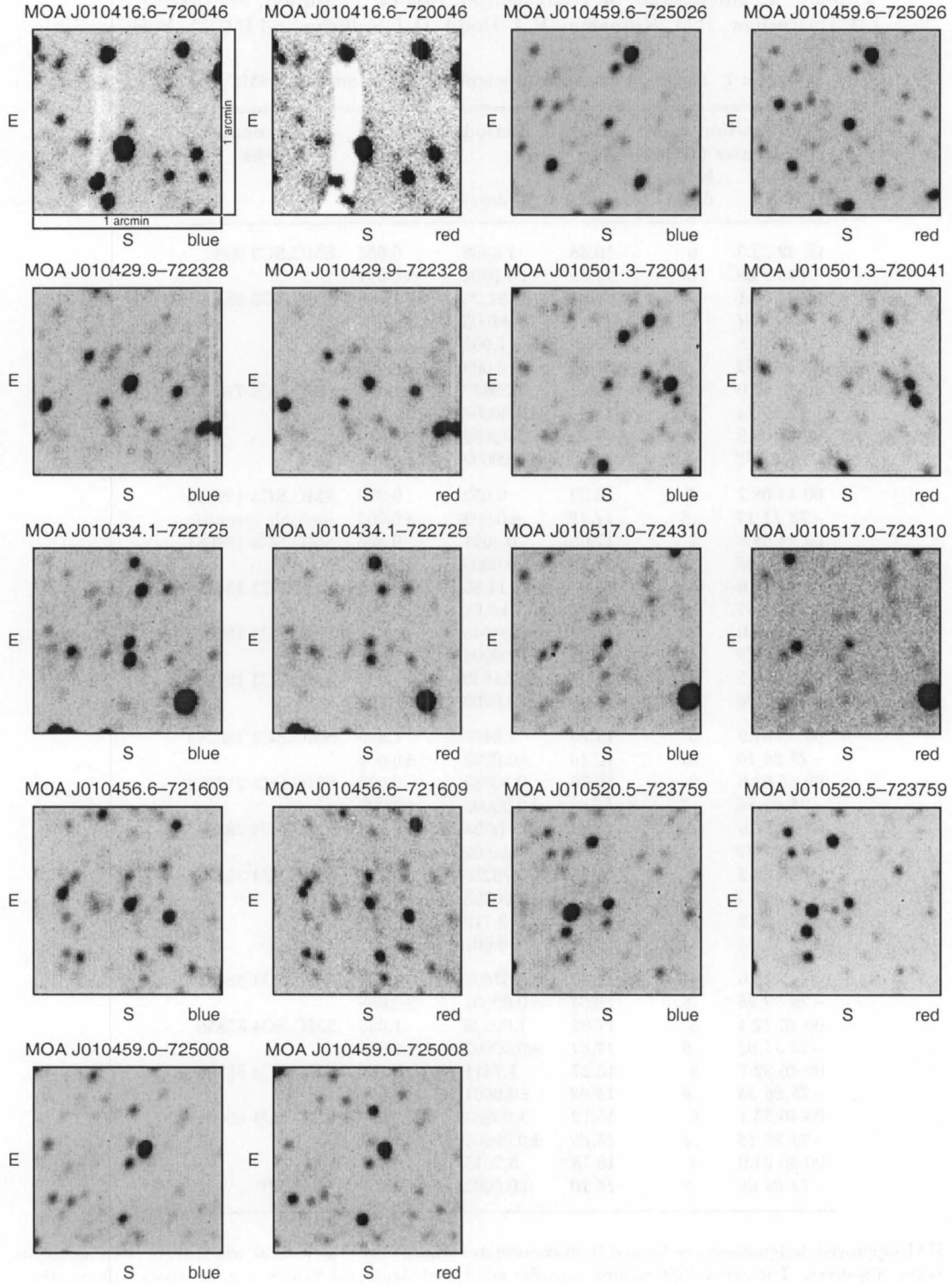

MOA catalogue of eclipsing binary stars in the Small Magellanic Cloud

G. Bayne, W. Tobin, J.D. Pritchard, I. Bond, K.R. Pollard, S.C. Besier, S. Noda, T. Sumi, T. Yanagisawa, M. Sekiguchi, M. Honda, Y. Muraki, M. Takeuti, J.B. Hearnshaw, P.M. Kilmartin, R.J. Dodd, D.J. Sullivan and P.C.M. Yock

Table 1. The MOA catalogue of eclipsing binary stars in the SMC.

Designation and coordinates (J2000) Name MOA J	Extra digit§	B_M R_M (max.)	**Period** (days)	**Primary Epoch** HJD −2450680	**OGLE name** *Remarks*
00 42 25.5	6	16.88	1.3368	0.655	SMC_SC3 8986
−73 29 29	*.8*	*17.50*	±0.0002	±0.007	
00 43 06.1	2	16.83	21.25	1.166	SMC_SC3 28139
−73 11 04	*.5*	*17.01*	±0.05	±0.005	
00 43 10.8	3	15.96	7.903	1.959	
−73 23 39	*.7*	*15.60*	±0.003	±0.006	
00 43 42.0	2	16.42	1.56853	1.540	SMC_SC3 71563
−73 20 44	*.3*	*16.98*	±0.00007	±0.002	
00 44 06.9	2	17.42	2.43682	0.914	
−72 43 32	.8	*17.96*	±0.00003	±0.001	
00 44 08.7	4	13.39	6.052	0.336	SMC_SC3 139376
−73 14 17	*.6*	*14.12*	±0.002	±0.005	*probably eccentric*
00 44 08.8	7	17.05	0.8601	0.566	SMC_SC3 139681
−73 15 25	*.7*	*17.42*	±0.0002	±0.008	
00 44 11.6	6	15.86	11.85	0.046	SMC_SC3 134555
−73 17 37	*.6*	*16.22*	±0.01	±0.003	
00 44 22.0	7	15.59	0.84545	0.19	SMC_SC3 139427
−73 14 49	*.2*	*16.23*	±0.00004	±0.02	
00 44 56.5	3	15.07	2.1630	0.53	SMC_SC3 197942
−73 17 06	*.6*	*15.49*	±0.0003	±0.02	
00 45 01.6	3	15.70	2.6420	1.025	SMC_SC3 189215
−73 26 10	*.6*	*16.40*	±0.0003	±0.002	
00 45 03.6	9	16.06	0.80883	0.092	SMC_SC3 217672
−73 03 36	*.7*	*16.60*	±0.00002	±0.006	
00 45 28.6	4	16.49	16.93	16.119	SMC_SC4 29281
−73 03 02	*.2*	*16.80*	±0.02	±0.002	
00 45 38.2	5	15.95	0.76256	0.759	SMC_SC4 35694
−72 56 17	*.9*	*16.68*	±0.00003	±0.009	
00 46 13.2	2	15.94	3.712	1.86	
−72 57 55	*.4*	*16.00*	±0.001	±0.01	*Cepheid?*
00 46 19.6	5	12.80	0.37663	0.375	SMC_SC4 88435
−72 50 56	*.6*	*12.65*	±0.00001	±0.008	
00 46 22.4	5	17.02	1.02929	1.055	SMC_SC4 85856
−72 55 04	*.6*	*17.61*	±0.00002	±0.006	
00 46 32.7	8	15.27	1.7411	0.581	SMC_SC4 53898
−73 26 38	*.6*	*15.93*	±0.0001	±0.004	
00 46 33.1	6	15.12	1.08984	0.47	SMC_SC4 56804
−73 22 16	*.4*	*15.63*	±0.00005	±0.01	
00 46 34.0	4	16.18	3.7015	1.30	
−73 06 00	*.3*	*16.10*	±0.0002	±0.02	*Cepheid?*

§IAU-approved designations are formed from coordinates truncated to the level at which there is no ambiguity between sources. The extra digit column provides additional significant figures (e.g. for spacecraft pointing). For example, the system MOA J004310.8−732339 has J2000 coordinates $00^h43^m10^s.83$, $-73°23'39''.7$

Table 1 (continued).

Designation and coordinates (J2000) Name MOA J	Extra digit	B_M R_M (max.)	**Period** (days)	**Primary Epoch** HJD −2450680	**OGLE name** *Remarks*
00 46 34.6	5	15.72	0.85467	0.345	SMC_SC4 56829
−73 24 35	*.9*	*16.30*	±0.00003	±0.003	
00 46 59.0	8	16.22	2.3835	1.592	SMC_SC4 113885
−73 14 57	*.6*	*16.90*	±0.0004	±0.004	*eccentric*
00 47 02.6	7	16.31	4.547	3.363	SMC_SC4 111053
−73 18 57	*.3*	*16.50*	±0.001	±0.003	
00 47 25.5	1	14.38	1.3558	0.224	SMC_SC4 103706
−73 27 16	*.1*	*15.05*	±0.0001	±0.003	
00 47 29.5	9	14.42	1.12508	0.41	
−73 25 01	*.9*	*15.05*	±0.00005	±0.01	
00 47 32.1	4	16.16	0.82372	0.412	SMC_SC4 121084
−73 09 08	*.8*	*16.73*	±0.00002	±0.005	
00 47 38.2	3	16.78	1.6264	0.095	SMC_SC4 113857
−73 15 18	*.9*	*17.10*	±0.0002	±0.005	
00 47 50.1	2	14.82	1.02310	0.830	SMC_SC4 153178
−73 27 27	*.5*	*15.50*	±0.00007	±0.006	
00 48 04.3	7	16.52	3.322	1.881	SMC_SC4 163724
−73 17 03	*.5*	*16.95*	±0.005	±0.002	
00 48 09.5	0	17.42	1.41219	0.735	SMC_SC4 175831
−73 06 04	*.4*	*18.00*	±0.00005	±0.006	
00 48 26.0	0	18.02	0.7902	0.005	SMC_SC5 39026
−73 07 24	*.7*	*18.40*	±0.0005	±0.006	
00 48 28.9	3	16.32	43.6	30.434	SMC_SC5 26819
−73 12 34	*.9*	*16.32*	±0.1	±0.004	
00 48 45.3	9	16.82	0.91365	0.819	
−72 38 29	*.3*	*17.54*	±0.00004	±0.006	
00 48 47.4	7	12.72	1.8411	0.515	SMC_SC5 11416
−73 24 58	*.5*	*13.51*	±0.0002	±0.005	
00 48 56.9	3	15.57	3.6080	1.176	SMC_SC5 32412
−73 11 40	*.0*	*16.11*	±0.0005	±0.001	
00 48 59.9	2	15.29	1.4115	0.563	SMC_SC5 26631
−73 13 28	*.9*	*15.95*	±0.0005	±0.007	
00 49 02.9	7	16.64	1.24618	0.412	SMC_SC5 16658
−73 20 55	*.7*	*17.30*	±0.00008	±0.005	
00 49 13.2	1	16.26	0.98910	0.968	
−72 58 23	*.3*	*16.81*	±0.00005	±0.008	
00 49 15.4	0	?	0.90460	0.570	SMC_SC5 95337
−73 22 05	*.5*	*16.71*	±0.00005	±0.005	B_M *unreliable*
00 49 19.9	1	16.20	1.5190	1.345	SMC_SC5 100485
−73 17 55	*.5*	*16.89*	±0.0003	±0.003	
00 49 20.0	5	15.92	2.1939	0.389	SMC_SC5 106039
−73 13 37	*.4*	*16.49*	±0.0002	±0.003	
00 49 20.2	5	16.70	1.05780	0.211	
−73 00 01	*.5*	*16.93*	±0.00002	±0.004	
00 49 24.8	3	15.66	0.81831	0.280	SMC_SC5 90597
−73 25 46	*.6*	*16.28*	±0.00003	±0.005	
00 49 28.4	4	16.58	138.6	94.420	SMC_SC5 145588
−72 49 42	*.5*	*15.78*	±0.4	±0.006	
00 49 31.3	0	16.58	2.3779	1.349	SMC_SC5 129722
−73 01 27	*.2*	*16.99*	±0.0001	±0.005	

Table 1 (continued).

Designation and coordinates (J2000) Name MOA J	Extra digit	**B_M** ***R_M*** (max.)	**Period** (days)	**Primary Epoch** HJD −2450680	**OGLE name** ***Remarks***
00 49 40.5	7	15.09	8.050	3.545	SMC_SC5 129441
−73 00 23	*.3*	*15.70*	±0.001	±0.002	*eccentric*
00 50 10.4	3	15.72	2.0739	0.38	
−72 37 36	*.3*	*16.38*	±0.0002	±0.02	
00 50 11.2	7	17.10	0.76888	0.152	SMC_SC5 230776
−72 44 44	*.2*	*17.69*	±0.00005	±0.003	
00 50 14.3	3	17.53	1.7968	0.055	SMC_SC5 208422
−73 00 12	*.6*	*18.10*	±0.0002	±0.001	
00 50 18.4	0	14.12	1.8399	1.084	
−72 38 55	*.2*	*14.78*	±0.0002	±0.006	
00 50 21.2	9	17.61	1.29792	1.449	SMC_SC5 170506
−73 25 36	*.7*	*18.12*	±0.00005	±0.004	
00 50 27.9	1	13.23	4.6067	0.064	SMC_SC5 202153
−73 03 16	*.9*	*14.00*	±0.0002	±0.003	
00 50 40.5	2	15.42	2.4015	2.268	SMC_SC5 185154
−73 12 56	*.2*	*16.00*	±0.0005	±0.006	
00 50 58.6	6	16.73	1.28358	0.648	SMC_SC5 283079
−73 04 36	*.7*	*17.30*	±0.00004	±0.004	
00 51 07.0	9	13.62	7.116	4.229	SMC_SC5 316708
−72 43 28	*.2*	*14.20*	±0.001	±0.009	
00 51 07.6	8	15.77	1.19112	0.021	SMC_SC5 311526
−72 47 28	*.7*	*16.28*	±0.00002	±0.005	
00 51 16.7	3	15.20	1.8089	0.363	SMC_SC5 266015
−73 13 02	*.4*	*15.70*	±0.0001	±0.006	
00 51 18.6	9	14.08	1.8717	0.953	SMC_SC5 243188
−73 30 15	*.7*	*14.75*	±0.0002	±0.004	
00 51 24.5	3	14.87	0.56565	0.03	
−72 40 14	*.6*	*15.50*	±0.00008	±0.01	
00 51 28.0	1	15.42	3.4955	0.538	SMC_SC6 17345
−73 15 17	*.9*	*16.04*	±0.0003	±0.005	*eccentric*
00 51 34.7	9	15.21	3.2915	2.501	SMC_SC5 311566
−72 45 46	*.1*	*15.83*	±0.0005	±0.002	*eccentric*
00 51 34.9	6	16.04	1.2766	0.732	SMC_SC6 11806
−73 17 11	*.6*	*16.63*	±0.0001	±0.006	
00 51 35.5	4	16.94	0.88824	0.599	SMC_SC6 55836
−72 54 32	*.9*	*17.42*	±0.00004	±0.004	
00 51 35.6	8	16.32	1.3028	0.485	SMC_SC6 22883
−73 12 45	*.4*	*16.87*	±0.0001	±0.005	
00 51 40.2	4	14.62	2.3240	0.856	SMC_SC6 17316
−73 13 20	*.7*	*15.10*	±0.0005	±0.007	
00 51 43.0	0	16.82	2.4282	0.10	SMC_SC6 23618
−73 09 27	*.7*	*17.26*	±0.0002	±0.01	
00 51 57.8	5	16.47	1.5422	1.190	
−73 24 58	*.0*	*16.99*	±0.0002	±0.004	
00 52 06.2	1	14.47	7.320	3.039	SMC_SC6 67221
−72 45 14	*.3*	*15.05*	±0.002	±0.002	
00 52 06.7	0	16.04	1.8218	1.487	SMC_SC6 61502
−72 51 22	*.0*	*16.53*	±0.0001	±0.003	
00 52 08.2	0	15.80	2.3122	2.215	SMC_SC6 29212
−73 06 32	*.2*	*16.42*	±0.0005	±0.007	*possibly eccentric*

Table 1 (continued).

Designation and coordinates (J2000) Name MOA J	Extra digit	B_M R_M (max.)	**Period** (days)	**Primary Epoch** HJD −2450680	**OGLE name** ***Remarks***
00 52 12.1	0	16.51	1.7186	1.228	SMC_SC6 67902
−72 44 53	*.3*	*17.19*	±0.0001	±0.003	
00 52 13.3	2	15.95	0.83630	0.318	SMC_SC6 61653
−72 48 42	*.4*	*16.49*	±0.00003	±0.003	
00 52 19.2	8	14.17	2.5785	1.387	SMC_SC6 158118
−72 41 51	*.2*	*14.80*	±0.0005	±0.004	
00 52 27.9	3	16.52	0.83368	0.59	SMC_SC6 158653
−72 41 35	*.1*	*16.91*	±0.00005	±0.01	
00 52 31.4	1	16.12	1.66845	1.233	SMC_SC6 163076
−72 39 09	*.0*	*16.65*	±0.00005	±0.003	
00 52 34.6	3	16.62	3.373	0.422	*possibly eccentric*
−73 33 05	*.0*	*17.02*	±0.001	±0.007	
00 52 34.7	0	16.50	1.8865	0.679	SMC_SC6 148139
−72 50 00	*.2*	*16.80*	±0.0001	±0.005	
00 52 38.4	3	15.10	5.9535	1.252	SMC_SC6 162962
−72 39 27	*.7*	*15.62*	±0.0008	±0.001	
00 52 42.3	3	15.61	2.1692	1.119	SMC_SC6 158178
−72 41 26	*.7*	*16.28*	±0.0001	±0.002	*eccentric*
00 52 46.9	8	17.52	1.08820	0.066	SMC_SC6 142123
−72 53 33	*.6*	*18.05*	±0.00005	±0.004	*possibly eccentric*
00 52 53.3	3	15.67	1.53890	0.764	
−72 09 50	*.4*	*16.35*	±0.00003	±0.006	
00 52 58.0	9	14.14	6.357	2.064	SMC_SC6 167473
−72 37 04	*.0*	*14.83*	±0.002	±0.007	*probably eccentric*
00 53 00.1	6	14.22	0.72149	0.23	
−73 11 23	*.1*	*14.99*	±0.00002	±0.01	
00 53 29.1	3	16.47	2.4571	1.08	SMC_SC6 242137
−72 38 53	*.2*	*16.90*	±0.0001	±0.01	*detected SMC1 & SMC2*
00 53 29.9	2	15.62	1.6142	0.037	
−72 42 28	*.9*	*16.25*	±0.0004	±0.006	SMC_SC6 237514
00 53 34.4	9	15.02	0.80633	0.75	
−72 42 31	*.6*	*15.71*	±0.00002	±0.01	
00 53 40.2	9	15.51	3.410	0.675	SMC_SC6 246676
−72 36 44	*.3*	*16.09*	±0.002	±0.006	
00 53 40.4	3	15.11	3.4168	1.965	SMC_SC6 221543
−72 52 22	*.1*	*15.70*	±0.0005	±0.004	*eccentric*
00 53 42.2	9	14.94	1.4752	0.33	SMC_SC6 180084
−73 23 20	*.1*	*15.53*	±0.0001	±0.01	
00 53 49.1	6	16.10	1.2300	1.138	SMC_SC6 296901
−72 52 12	*.4*	*16.50*	±0.0001	±0.007	
00 53 55.9	1	16.09	2.2199	1.202	
−72 04 58	*.9*	*16.76*	±0.0002	±0.005	
00 54 00.0	0	15.52	4.7272	0.413	SMC_SC6 291695
−72 56 58	*.0*	*16.08*	±0.0007	±0.002	
00 54 12.7	1	16.72	0.49668	0.01	SMC_SC6 311582
−72 42 07	*.8*	*17.15*	±0.00001	±0.02	
00 54 16.5	9	15.72	3.030	1.272	SMC_SC6 296738
−72 54 24	*.0*	*16.20*	±0.002	±0.004	
00 54 16.7	8	15.87	1.6034	0.976	SMC_SC6 315786
−72 39 09	*.3*	*16.45*	±0.0001	±0.005	

Table 1 (continued).

Designation and coordinates (J2000) Name MOA J	Extra digit	B_M R_M (max.)	**Period** (days)	**Primary Epoch** HJD −2450680	**OGLE name** *Remarks*
00 54 17.1	7	15.46	1.1007	1.07	
−72 37 10	*.7*	*15.78*	±0.0001	±0.02	
00 54 22.7	1	16.42	2.1532	1.030	SMC_SC6 306609
−72 46 06	*.3*	*16.95*	±0.0002	±0.006	
00 54 32.1	3	16.93	2.4081	0.937	SMC_SC7 32419
−72 56 39	*.3*	*17.51*	±0.0002	±0.002	
00 54 33.1	1	14.89	5.7110	0.577	SMC_SC7 13487
−73 10 40	*.1*	*15.56*	±0.0005	±0.005	
00 54 34.6	1	16.52	1.6415	1.586	SMC_SC6 315873
−72 40 51	*.0*	*17.10*	±0.0001	±0.006	*detected SMC1 & SMC2*
00 54 38.2	6	13.57	3.6264	0.234	SMC_SC7 66175
−72 32 06	*.0*	*14.10*	±0.0003	±0.003	
00 54 39.4	5	16.57	1.8227	1.743	SMC_SC7 70994
−72 26 35	*.8*	*17.11*	±0.0001	±0.003	
00 54 43.0	8	16.87	3.4352	0.460	SMC_SC7 42474
−72 49 23	*.7*	*17.41*	±0.0005	±0.006	
00 55 01.4	0	15.87	2.5853	0.95	SMC_SC7 18319
−73 06 42	*.7*	*16.48*	±0.0005	±0.02	
00 55 52.0	0	15.24	1.2704	0.839	
−72 02 29	*.3*	*15.99*	±0.0002	±0.009	
00 55 54.4	8	14.08	3.1886	2.069	SMC_SC7 142073
−72 28 08	*.3*	*14.77.*	±0.0001	±0.003	
00 56 11.6	1	13.72	4.482	1.770	
−72 18 24	*.2*	*14.52*	±0.002	±0.004	*eccentric*
00 56 15.6	1	15.94	1.3182	0.407	
−72 13 24	*.8*	*16.55*	±0.0001	±0.008	
00 56 23.5	9	14.02	2.3195	1.936	
−72 21 23	*.7*	*14.78*	±0.0001	±0.003	
00 56 24.2	1	14.74	1.6202	1.580	
−72 01 44	*.9*	*15.50*	±0.0002	±0.003	
00 56 53.7	3	17.07	1.5241	0.156	SMC_SC7 255917
−72 37 18	*.5*	*17.62*	±0.0001	±0.005	
00 56 56.4	5	13.94	2.6316	0.093	SMC_SC7 243913
−72 49 06	*.1*	*14.60*	±0.0002	±0.008	
00 57 03.0	3	16.08	1.5837	1.042	
−72 22 46	*.3*	*16.70*	±0.0001	±0.004	
00 57 15.8	0	16.83	1.90675	0.689	SMC_SC7 240244
−72 50 10	*.2*	*17.30*	±0.00006	±0.003	
00 57 26.4	0	15.32	4.330	2.345	SMC_SC8 30634
−72 36 45	*.5*	*16.04*	±0.002	±0.002	*eccentric*
00 57 27.5	5	14.63	1.1452	1.030	SMC_SC8 49526
−72 19 59	*.5*	*15.32*	±0.0001	±0.006	
00 57 31.1	6	16.64	1.03002	0.352	SMC_SC8 22435
−72 46 16	*.6*	*17.20*	±0.00004	±0.003	*possibly eccentric*
00 57 42.2	0	16.11	2.4284	0.172	SMC_SC8 18970
−72 48 14	*.4*	*16.60*	±0.0001	±0.003	
00 57 43.3	2	14.98	1.4238	0.545	SMC_SC8 52831
−72 18 14	*.3*	*15.61*	±0.0002	±0.003	
00 58 21.3	7	15.52	3.111	1.873	*probably eccentric*
−72 01 07	*.2*	*16.25*	±0.002	±0.005	

Table 1 (continued).

Designation and coordinates (J2000) Name MOA J	Extra digit	**B_M** ***R_M*** (max.)	**Period** (days)	**Primary Epoch** HJD −2450680	**OGLE name** ***Remarks***
00 58 21.9	9	13.43	5.845	2.31	SMC_SC8 90965
−72 35 15	*.8*	*14.10*	±0.002	±0.01	
00 58 22.3	5	16.25	1.05184	0.626	
−72 40 09	*.0*	*16.68*	±0.00002	±0.004	
00 58 24.4	0	14.89	1.47120	0.938	
−72 05 32	*.5*	*15.60*	±0.00003	±0.003	
00 58 51.8	0	16.10	2.408	2.362	SMC_SC8 107328
−72 17 50	*.8*	*16.69*	±0.001	±0.004	
00 58 55.8	4	17.29	1.4832	1.621	SMC_SC8 79914
−72 43 54	*.8*	*17.82*	±0.0001	±0.004	
00 59 02.5	2	14.90	1.32475	0.372	SMC_SC8 135992
−72 42 21	*.1*	*15.63*	±0.00002	±0.003	
00 59 11.4	3	17.24	1.29380	0.380	
−72 01 47	*.6*	*17.92*	±0.00003	±0.003	
00 59 28.6	3	14.61	1.09878	0.594	SMC_SC8 132613
−72 43 47	*.0*	*15.30*	±0.00004	±0.004	
00 59 30.2	7	15.32	3.3070	2.768	
−72 02 53	*.1*	*15.98*	±0.0005	±0.008	
00 59 34.2	2	13.29	1.12302	0.325	SMC_SC8 129157
−72 46 57	*.4*	*14.00*	±0.00002	±0.008	
00 59 36.1	5	13.60	1.9496	0.47	
−72 15 57	*.3*	*14.32*	±0.0003	±0.01	
00 59 47.8	1	17.52	32.30	28.92	SMC_SC8 183352
−72 44 26	*.4*	*17.12*	±0.03	±0.02	
00 59 54.3	5	16.83	1.55703	0.416	SMC_SC8 186844
−72 41 39	*.4*	*17.40*	±0.00002	±0.008	
01 00 15.9	7	13.46	3.313	0.243	SMC_SC8 209964
−72 12 44	*.7*	*14.15*	±0.002	±0.008	
01 00 23.7	3	15.58	2.6135	0.246	SMC_SC9 30310
−72 26 20	*.1*	*16.28*	±0.0003	±0.004	*probably eccentric*
01 00 36.8	0	15.95	1.8637	0.803	SMC_SC9 47495
−72 06 46	*.8*	*16.66*	±0.0002	±0.005	
01 00 41.0	8	15.61	3.1590	0.751	SMC_SC9 41849
−72 13 12	*.1*	*16.20*	±0.0007	±0.002	
01 00 42.4	7	14.56	1.5953	0.589	
−72 24 57	*.1*	*14.91*	±0.0002	±0.009	
01 00 50.8	6	16.14	1.4868	1.398	
−72 20 17	*.8*	*16.67*	±0.0001	±0.005	
01 00 52.3	3	16.12	1.63250	0.988	SMC_SC9 13423
−72 45 05	*.6*	*16.61*	±0.00004	±0.002	*possibly eccentric*
01 00 57.2	9	18.02	3.1640	1.568	SMC_SC9 14011
−72 44 52	*.6*	*18.38*	±0.0003	±0.004	
01 01 36.8	5	15.42	1.6766	0.755	
−72 04 15	*.0*	*15.87*	±0.0003	±0.009	
01 01 40.0	9	14.84	5.275	0.446	
−72 03 44	*.2*	*15.43*	±0.002	±0.003	
01 02 25.5	6	14.72	2.4968	1.443	SMC_SC9 134245
−72 07 45	*.0*	*15.47*	±0.0004	±0.005	*(3/4)P*
01 02 28.1	3	14.72	2.539	1.611	SMC_SC9 111281
−72 37 48	*.6*	*15.36*	±0.001	±0.009	

Table 1 (continued).

Designation and coordinates (J2000) Name MOA J	Extra digit	**B_M** ***R_M*** (max.)	**Period** (days)	**Primary Epoch** HJD −2450680	**OGLE name** ***Remarks***
01 02 41.2	6	14.94	5.454	3.754	SMC_SC9 129557
−72 14 25	*.5*	*15.50*	±0.001	±0.005	
01 02 46.1	8	14.13	1.9710	0.747	SMC_SC9 163575
−72 24 44	*.0*	*14.90*	±0.0004	±0.003	*probably eccentric*
01 03 00.5	7	15.16	3.1305	1.821	SMC_SC9 173156
−72 08 30	*.1*	*15.83*	±0.0007	±0.004	
01 03 19.8	8	15.81	1.1666	1.158	SMC_SC9 175441
−72 06 12	*.1*	*16.36*	±0.0001	±0.008	
01 03 21.3	3	12.77	2.206	0.300	SMC_SC10 33878
−72 05 38	*.2*	*13.50*	±0.001	±0.009	
01 03 22.6	9	14.43	3.477	3.167	
−72 03 22	*.0*	*15.15*	±0.001	±0.004	
01 03 28.9	0	14.62	2.6985	0.690	SMC_SC10 37156
−72 01 28	*.3*	*15.31*	±0.0002	±0.003	*possibly eccentric*
01 03 41.5	5	15.41	2.5810	2.257	SMC_SC10 37223
−72 03 06	*.8*	*16.10*	±0.0002	±0.008	*eccentric*
01 03 46.4	4	15.30	0.92025	0.549	SMC_SC10 17256
−72 28 29	*.8*	*15.95*	±0.00007	±0.007	
01 03 49.2	2	13.96	3.962	0.426	SMC_SC10 19653
−72 28 07	*.0*	*14.70*	±0.003	±0.007	
01 03 54.3	1	14.33	1.7299	0.157	SMC_SC10 33925
−72 04 18	*.3*	*15.09*	±0.0002	±0.007	
01 04 01.6	1	15.50	2.1284	1.78	SMC_SC10 3097
−72 46 41	*.7*	*16.11*	±0.0002	±0.01	
01 04 14.9	5	14.43	8.788	1.495	SMC_SC10 70439
−72 09 18	*.7*	*15.00*	±0.005	±0.005	
01 04 16.6	1	17.19	0.92599	0.364	SMC_SC10 75073
−72 00 46	*.1*	*17.78*	±0.00003	±0.005	
01 04 29.9	9	14.94	3.510	1.577	SMC_SC10 61625
−72 23 28	*.7*	*15.57*	±0.001	±0.005	
01 04 34.1	1	15.70	1.2701	0.542	SMC_SC10 59402
−72 27 25	*.7*	*16.31*	±0.0003	±0.006	
01 04 56.6	4	15.62	1.8266	1.879	SMC_SC10 100613
−72 16 09	*.9*	*16.18*	±0.0002	±0.004	
01 04 59.0	9	16.12	1.42940	1.408	SMC_SC10 78731
−72 50 08	*.2*	*16.72*	±0.00005	±0.003	
01 04 59.6	7	16.07	129.0	118.18	SMC_SC10 78655
−72 50 26	*.2*	*15.31*	±0.2	±0.01	
01 05 01.3	7	16.44	2.2635	0.677	SMC_SC10 108195
−72 00 41	*.1*	*17.08*	±0.0003	±0.003	
01 05 17.0	7	16.50	2.70966	0.040	SMC_SC10 83754
−72 43 10	*.4*	*17.05*	±0.00002	±0.002	
01 05 20.5	4	16.11	14.40	5.398	SMC_SC10 88122
−72 37 59	*.5*	*16.23*	±0.02	±0.007	

MOA catalogue of eclipsing binary stars in the Small Magellanic Cloud

G. Bayne, W. Tobin, J.D. Pritchard, I. Bond, K.R. Pollard, S.C. Besier, S. Noda, T. Sumi, T. Yanagisawa, M. Sekiguchi, M. Honda, Y. Muraki, M. Takeuti, J.B. Hearnshaw, P.M. Kilmartin, R.J. Dodd, D.J. Sullivan and P.C.M. Yock

Table 2. Times of secondary minimum for eccentric systems.

MOA name	**Secondary Epoch** HJD −2450600	**OGLE name**	**Remarks**
MOA J004408.7−731417	3.505 ±0.005	SMC_SC3 139376	probably eccentric
MOA J004659.0−731457	0.547 ±0.004	SMC_SC4 113885	eccentric
MOA J004940.5−730023	5.690 ±0.002	SMC_SC5 129441	eccentric
MOA J005128.0−731517	2.134 ±0.005	SMC_SC6 17345	eccentric
MOA J005134.7−724546	1.074 ±0.002		eccentric
MOA J005208.2−730632	1.740 ±0.007	SMC_SC6 29212	possibly eccentric
MOA J005234.6−733305	2.176 ±0.007	SMC_SC5 311566	possibly eccentric
MOA J005242.3−724126	1.866 ±0.002	SMC_SC6 158178	eccentric
MOA J005246.9−725333	0.594 ±0.004	SMC_SC6 142123	possibly eccentric
MOA J005258.0−723704	5.705 ±0.007	SMC_SC6 167473	probably eccentric
MOA J005340.4−725222	0.443 ±0.004	SMC_SC6 221543	eccentric
MOA J005611.6−721824	0.281 ±0.004		eccentric
MOA J005726.4−723645	4.088 ±0.002	SMC_SC8 30634	eccentric
MOA J005731.1−724616	0.925 ±0.003	SMC_SC8 22435	possibly eccentric
MOA J005821.3−720107	0.430 ±0.005		probably eccentric
MOA J010023.7−722620	1.466 ±0.004	SMC_SC9 30310	probably eccentric
MOA J010052.3−724505	0.150 ±0.002	SMC_SC9 13423	possibly eccentric
MOA J010246.1−722444	1.775 ±0.003	SMC_SC9 163575	probably eccentric
MOA J010328.9−720128	2.074 ±0.003	SMC_SC10 37156	possibly eccentric
MOA J010341.5−720306	0.852 ±0.008	SMC_SC10 37223	eccentric

Appendix H

CCD Photometry of variable stars in the Magellanic Clouds VII paper

This paper has been accepted for publication in the Monthly Notices of the Royal Astronomical Society. The three tables following the paper, contain the photometric observations and will be available electronically from the Centre de Données astronomiques de Strasbourg.

Mon. Not. R. Astron. Soc. **000**, 1–7 (2004) Printed 5 December 2003 (MN LATEX style file v2.2)

CCD photometry of variable stars in the Magellanic Clouds – VII. The eclipsing binaries MACHO*05:36:48.7−69:17:00 in the LMC and MOA J005018.4−723855 & J005623.5−722123 in the SMC

G.P. Bayne,[1] W. Tobin,[1] J.D. Pritchard,[2] K.R. Pollard[1] and M.D. Albrow[1]
[1]*Mount John University Observatory and Department of Physics & Astronomy, University of Canterbury, Private Bag 4800, Christchurch, New Zealand*
[2]*European Southern Observatory, Casilla 19001, Santiago 19, Chile*

Accepted 2003 December ??. Received 2003 October 22

ABSTRACT
Using improved techniques, we have obtained CCD $uV_{\rm J}I_{\rm C}$ photometry for three eclipsing binary stars in the Magellanic Clouds and made preliminary analyses of the light curves. MACHO*05:36:48.7−69:17:00 in the LMC is a detached, eccentric system. Apsidal motion is detected with period 100 ± 5 yr. The radii of the component stars are less than a fifth of their orbital separation and their masses are plausibly ∼14 and ∼20 $M_\odot$. Similar masses may also characterize the components of MOA J005018.4−723855 in the SMC, but here the more massive star is cooler, fills its Roche lobe, and is probably in an early stage of case A mass transfer. MOA J005623.5−722123 in the SMC is detached with a nearly edge-on orbit. The masses are plausibly ∼14 and ∼16 $M_\odot$. Because of polar gravity brightening, the star occulted at the shallower eclipse may actually have the higher mean effective temperature by a marginal amount.

Key words: binaries: eclipsing – stars: early-type – stars: fundamental parameters – stars: individual: MACHO*05:36:48.7−69:17:00, MOA J005018.4−723855, MOA J005623.5−722123 – Magellanic Clouds

1 INTRODUCTION

In this paper we present light curves and provide preliminary analyses for a further three eclipsing binary stars in the Magellanic Clouds. This work continues the campaign of improved CCD photometry that is underway at the Mount John University Observatory, Lake Tekapo, New Zealand (MJUO), and which has as its ultimate goal the determination of accurate fundamental parameters and distances for stars in the Magellanic Clouds, as has been described in previous papers in this series (e.g. Pritchard et al. 1998a,b [Papers V & VI]). Improvements in our observing and reduction procedures include a new CCD system, uv flat-fielding with a uv-reflective dome screen, autoguiding, and difference-imaging photometric reductions.

One target is in the Large Magellanic Cloud (LMC); it is MACHO*05:36:48.7−69:17:00, and was selected from the catalogue of LMC eclipsing binaries published by the MACHO project (Alcock et al. 1997) on account of its deep, well-separated eclipses and relative brightness. These properties should indicate component stars whose fundamental parameters can be compared stringently with theoretical models of low-metallicity spherical stars, though Wyithe & Wilson (2002) have recently argued that semi-detached systems hold advantages as far as being a standard candle is concerned, and systems of all types have been used in the new determination of the distance of the Small Magellanic Cloud (SMC) by Harries, Hilditch & Howarth (2003).

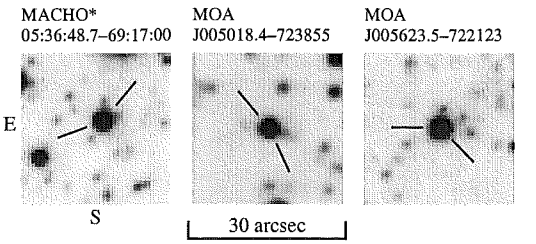

Figure 1. The immediate fields of the three targets. Negative representations of the $I_{\rm C}$ reference images, for which the FWHM seeing is about 2 arcsec.

MACHO*05:36:48.7−69:17:00 is an eccentric system and we have detected apsidal motion in it, opening the prospect, ultimately, of tests of the stars' interior structure as well as their exterior properties.

The other targets are in the SMC and were selected from the catalogue of SMC eclipsing binaries published by the MOA group (Bayne et al. 2002).[1] They also are bright, and have relatively-well separated eclipses, but their orbits are circular. They

[1] We note the $0^{\rm h}40^{\rm m}$ grid line in Fig. 1 of this paper is misplaced.

Table 1. (extract) Photometry of MACHO*05:36:48.7−69:17:00. The columns are Heliocentric Julian Day of mid exposure, normalized light, airmass (X) and FWHM seeing in arcsec (σ). The full table appears in *Synergy*, along with Tables 2 and 3. The data are also available in machine-readable form from the CDS in Strasbourg.

HJD −2450000	Norm. light	X	σ "	HJD −2450000	Norm. light	X	σ "	HJD −2450000	Norm. light	X	σ "	HJD −2450000	Norm. light	X	σ "	HJD −2450000	Norm. light	X	σ "	HJD −2450000	Norm. light	X	σ "
												u											
1294.9019	1.008	1.5	4.8	1726.7938	1.012	1.8	3.6	1960.9119	1.010	1.1	2.4	1992.0102	0.722	1.6	4.1	2021.2215	0.820	2.5	5.9	2206.9661	1.026	1.4	4.9	2467.2473	1.016	1.4	4.9
1294.9893	1.008	1.9	3.5	1726.9250	1.014	2.4	4.7	1960.9404	1.008	1.2	2.2	1992.0345	0.763	1.6	4.2	2021.8170	1.011	1.2	2.9	2207.0152	1.028	1.3	5.0	2467.8439	1.006	2.2	4.0
1295.0909	1.008	2.4	2.7	1726.9828	1.013	2.5	3.1	1960.9690	0.980	1.2	2.1	1992.0931	0.876	1.9	3.1	2021.8474	1.008	1.3	3.2	2207.0565	1.032	1.2	4.0	2467.8669	1.010	2.3	6.8
1295.1864	0.994	2.5	5.4	1727.0818	1.021	2.2	3.0	1960.9982	0.933	1.3	2.5	1992.1404	0.972	2.2	4.0	2021.8941	1.023	1.4	3.8	2207.0940	1.019	1.1	3.9	2467.9334	1.028	2.5	4.6
1295.2695	1.026	2.2	3.3	1727.1516	1.015	1.9	3.0	1961.0275	0.878	1.3	3.1	1992.1823	1.016	2.4	3.0	2021.9256	1.023	1.5	3.7	2207.9791	1.023	1.3	5.0	2467.9747	1.013	2.5	4.9
1404.1051	1.018	1.6	4.5	1727.2389	0.997	1.5	3.2	1961.0566	0.816	1.4	3.8	2018.8148	0.902	1.2	3.7	2021.9913	1.029	1.8	5.6	2208.0166	1.020	1.2	5.6	2468.0174	1.014	2.4	5.6
1404.1898	1.022	1.3	3.6	1729.7915	0.916	1.8	5.0	1961.0848	0.765	1.5	5.3	2018.8374	0.848	1.3	4.1	2022.0332	1.021	2.0	5.0	2208.0622	1.044	1.2	6.1	2468.0381	1.015	2.3	5.9
1404.8151	0.684	2.4	4.7	1729.8638	0.762	2.2	5.3	1961.1214	0.695	1.7	5.1	2018.8734	0.774	1.3	4.2	2022.9032	0.850	1.5	5.7	2208.1017	1.023	1.1	4.1	2468.0841	1.020	2.1	3.3
1406.1029	0.887	1.6	5.5	1729.9817	0.742	2.5	4.0	1961.1506	0.691	1.8	4.5	2018.9045	0.728	1.4	4.0	2022.9323	0.903	1.6	3.5	2208.1388	1.011	1.1	4.8	2468.1047	1.010	2.0	3.0
1406.1686	0.761	1.4	4.1	1730.0618	0.912	2.3	5.4	1987.9082	1.020	1.2	5.9	2018.9380	0.693	1.6	3.9	2022.9651	0.953	1.7	4.0	2208.1781	1.033	1.1	4.9	2468.1471	0.977	1.8	3.8
1557.9867	1.020	1.1	5.0	1730.1341	1.003	1.9	4.5	1987.9237	0.997	1.3	6.3	2018.9707	0.696	1.7	4.0	2022.9954	0.999	1.9	3.5	2464.1639	1.027	1.8	3.8	2468.1680	0.948	1.7	4.6
1558.0283	1.005	1.1	5.4	1730.2269	1.016	1.5	4.7	1988.0204	0.825	1.5	2.7	2019.0114	0.772	1.9	5.3	2023.0248	1.004	2.0	4.5	2464.1844	1.024	1.7	6.4	2468.2156	0.855	1.5	5.6
1558.9215	0.663	1.1	4.9	1730.7854	1.002	1.8	2.7	1988.0349	0.801	1.6	2.6	2019.0524	0.845	2.1	4.7	2023.0789	1.010	2.3	4.2	2464.2057	1.020	1.6	6.5	2468.2568	0.770	1.4	3.8
1558.9621	0.685	1.1	5.9	1730.8868	1.004	2.3	4.0	1988.0938	0.695	1.9	3.1	2019.0902	0.926	2.3	4.3	2023.1098	0.993	2.4	4.0	2464.2880	0.979	1.3	6.3	2468.2772	0.735	1.3	4.3
1559.0069	0.767	1.1	5.5	1730.9857	1.014	2.5	3.7	1988.1084	0.683	1.9	3.2	2019.1921	1.009	2.5	6.8	2045.8215	0.846	1.4	2.6	2465.1083	1.048	2.0	4.5				
1560.9418	1.016	1.1	3.8	1960.0629	1.012	1.4	5.7	1991.8446	0.900	1.1	3.1	2020.8847	1.001	1.4	6.2	2045.8672	0.742	1.6	3.2	2465.1440	1.045	1.8	4.1				
1561.0420	1.029	1.2	5.1	1960.0925	1.020	1.5	5.4	1991.8749	0.839	1.2	4.7	2020.9174	1.004	1.5	5.7	2045.9125	0.691	1.8	4.3	2465.1738	1.043	1.7	3.9				
1561.0847	1.024	1.2	5.4	1960.1230	1.015	1.6	3.7	1991.9070	0.771	1.2	4.7	2020.9525	1.001	1.6	6.3	2206.8707	1.023	1.7	3.8	2465.2031	1.022	1.6	3.8				
1724.8297	0.983	1.9	3.6	1960.1530	1.012	1.8	4.1	1991.9391	0.712	1.3	3.2	2021.0201	1.005	1.9	4.9	2206.9014	1.005	1.6	4.5	2467.2033	1.025	1.6	6.0				
1725.1728	1.029	1.8	5.4	1960.8834	1.016	1.1	2.5	1991.9683	0.688	1.4	3.8	2021.0362	1.014	2.0	4.9	2206.9312	1.020	1.5	4.8	2467.2252	1.034	1.5	5.4				
												V_J											
1294.9547	1.021	1.7	4.5	1315.9123	1.022	1.8	3.8	1316.2266	0.771	2.1	6.1	1406.1435	0.798	1.4	3.5	1491.0189	0.677	1.2	5.5	1731.0604	1.025	2.3	3.2	2020.9317	1.019	1.6	5.4
1294.9662	1.022	1.8	3.9	1315.9200	1.017	1.8	3.5	1316.2320	0.782	2.1	6.1	1406.2462	0.695	1.2	2.5	1491.0264	0.685	1.2	5.2	1960.0759	1.011	1.5	3.5	2020.9681	1.020	1.7	5.4
1295.0731	1.022	2.3	3.8	1315.9263	1.006	1.8	4.0	1316.2375	0.807	2.1	6.0	1407.0280	1.031	1.9	4.8	1491.0331	0.688	1.2	5.7	1960.1054	1.024	1.6	3.7	2021.0027	1.016	1.9	5.4
...																											

are MOA J005018.4−723855 and MOA J005623.5−722123. The fields for all three targets are shown in Fig. 1

Photometric time sequences obtained by the MACHO project between 1992 August and 2000 January are available on-line for all three targets. We have used these data to refine ephemerides and as a check of our own photometry, which we now present.

2 INSTRUMENTATION, OBSERVATIONS AND REDUCTIONS

Observations were made between 1999 April and 2002 July using the McLellan Cassegrain 1-m telescope at MJUO in its f/7.7 configuration in conjunction with the CCD photometer head (Tobin et al. 1993). The detector was the Photometrics Series 200 cryogenic CCD system (Barnes et al. 2000) which incorporates a Grade 1 SITe 003AB chip with an array of 1024×1024 pixels. The 24-μm pixel size projects to 0.64 arcsec on the sky, though with the 25-mm square filters for which the photometer head was designed, the total useful field is only 6.1×6.1 arcmin (570×570 pixels). The system suffers less from a.c. pickup and has lower base-level noise than the one used in previous papers in this series. The thinned, back-illuminated, MPP chip is almost twice as sensitive as the previous one, with a quantum efficiency in excess of 70% between 600 and 700nm. It has improved charge-transfer efficiency and is overcoated with Metachrome II for uv response. Observations were mostly made with a gain of ∼0.8 ADU/e$^-$.

Observations were made in Strömgren u, Johnson V_J and Cousins I_C filters (Paper V, Fig. 1). The plasticized wooden screen previously employed for flat-fielding calibrations was replaced by a silica textile SORICSCREEN (McCall & Siegmund 1994) whose enhanced uv reflectivity reduced the time required for u flat-field calibrations from about 45 to 5 minutes. Although sharpened annuli in the telescope baffles have greatly reduced the amount of scattered light at the focal plane, targets were always placed at a fixed location on the detector in order to eliminate the effect of any systematic errors in the flat-field correction (e.g. Grundahl & Sørensen 1996). Image compactness and symmetry were improved when manual offset-guiding was superseded by autoguiding via an ST4 system from the Santa Barbara Instruments Group.

In eclipsing-binary and other fields, astronomers have traditionally acquired what Woźniak (2000) has characterized as d.c. flux signals, i.e. photometry which may be absolute or relative, and perhaps expressed in magnitudes, but which at heart is reported on a linear flux scale with a zero-point corresponding to no light. Woźniak, however, has argued eloquently in favour of a.c. signals, i.e. ones in which the flux changes relative to some reference frame are measured, pointing out that in crowded fields determination of the true zero point of flux is extremely difficult. The a.c. or difference imaging approach is embodied in software packages such as DIA (Woźniak 2000) or ISIS (Alard & Lupton 1998, Alard 2000a).

Experiments with Mt John observations of the eclipsing binary EROS1044 in a crowded field have shown that difference imaging can produce much more consistent photometry than PSF fitting (Alard 2000b). We therefore used Alard's ISIS-2.1 software to reduce our observations, constructing reference images from our best-seeing images. Although a.c. variations may be sufficient for purely light-curve analysis of our stars, it is certainly important to estimate the d.c. level from which the variations are measured for distance-indicator work. The imperative is to ensure that the a.c. and d.c. fluxes are measured in the same way. To obtain the reference-level fluxes we used DAOPHOT-II (Stetson 1987) on our reference images to produce two further images in each bandpass. The first had all identified stars subtracted while the second had all but the target subtracted. The two were subtracted to yield an image with only the target and zero background. ISIS aperture photometry was then extracted from this image in the same way as for the difference measures.

Our photometry is listed in Tables 1-3 (available in the electronic version of this paper on *Synergy*) and is plotted in phased form in Figs 3-5. An extract of Table 1 is printed here. The data are also available in machine-readable form from the Centre des

Table 4. Typical exposure durations and achieved precisions.

	u	V_J	I_C
Typical exposure time (s)	1200	700	400
Number of observations			
MACHO*05:36:48.7−69:17:00	134	308	142
MOA J005018.4−723855	141	138	149
MOA J005623.5−722123	186	204	206
R.m.s. precisions† (mag.)			
MACHO*05:36:48.7−69:17:00	0.013	0.010	0.011
MOA J005018.4−723855	0.016	0.013	0.013
MOA J005623.5−722123	0.012	0.008	0.009

† With respect to Wilson-code solutions. For MOA J005018.4−723855, the solution included a hot spot to model the O'Connell effect.

Données astronomiques de Strasbourg (CDS)[2]. Observations for which the FWHM seeing exceeded 7 arcsec or for which results were markedly deviant have been excluded. To emphasize the novel way in which the photometry has been obtained, we report it as light (i.e. on a linear flux scale) rather than magnitudes, normalized to the reference-image fluxes. The photon-counting uncertainties in our reference-level fluxes are in the 0.2-0.4 per cent range, and we do not report them individually since other uncertainties are clearly greater. Comparison of our V_J and I_C light curves with the roughly-equivalent MACHO B_M and R_M photometry, which was extracted on a PSF-fitting basis, shows that some of our eclipses are at most a few percent deeper. There is some evidence in our light curves for similar differences between the photometry from different nights. In Table 4 we report the photometric precision achieved based on the r.m.s. deviations with respect to light-curve fits. The number of observations and typical observing times are also listed.

In Papers V and VI of this series we attempted absolute (calibrated) photometry of those papers' target stars, with disappointing results. In one case, the there was a 0.07 magnitude difference between V magnitudes obtained using V and y filters. Part of the difficulty is that the McLellan Telescope does not point accurately and target acquisition is time-consuming. It is therefore not possible to acquire the dense series of measurements of standard stars which are essential for the accurate characterization of atmospheric extinction and its variation through the night. We therefore did not attempt calibrated photometry in this paper. (Differential photometry in filters that avoid discontinities such as the Balmer jump, such as we present here, is of course insensitive to atmospheric extinction.) However, we have endeavoured to obtain some indication of the absolute level of our photometry. We have extracted instrumental colour-magnitude diagrams from our reference frames. These show the red-giant clump. From the difference between our targets' magnitudes and those of the clump, and calibrated clump magnitudes of V_J∼19.2 and ∼19.4 derived from OGLE colour-magnitude diagrams for the LMC and SMC respectively, we estimate that at maximum light the magnitudes of our targets are approximately as follows: MACHO*05:36:47.7−69:17:00, $V_J \sim 14.5$; MOA J005018.4−723855, $V_J \sim 14.9$; and MOA J005623.5−722123, $V_J \sim 15.1$.

[2] ftp://cdsarc.u-strasbg.fr/MNRAS

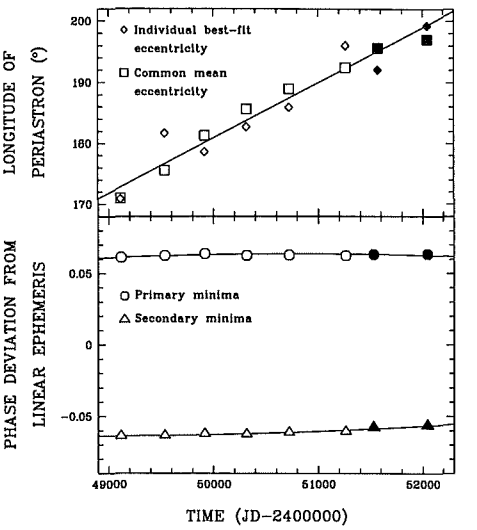

Figure 2. Apsidal motion analysis of MACHO*05:36:48.7−69:17:00. The upper graph shows values of the longitude of periastron obtained through Wilson-code light-curve analysis when observations are divided into roughly year-long spans. The lozenges (◇) indicate values obtained when the eccentricity is optimized for each individual span, while results obtained with a common mean eccentricity are indicated by squares. Open symbols indicate MACHO data while filled symbols indicate data from this paper. The line is the adopted fit to the common-eccentricity measurements and indicates an apsidal period of 100±5 yr. The lower graph shows the fit to the ephemeris defined by the values in Table 5 and Eq. 20 of Giménez & Garcia-Pelayo (1983). The only parameters adjusted to make this fit were T_0 and P_s.

3 ANALYSIS

3.1 Ephemerides

The unevenly spaced eclipses of different width clearly reveal that MACHO*05:36:48.7−69:17:00 is in an eccentric orbit. In Table 5 we report times of representative primary and secondary minima, T_1 and T_2, derived by fitting synthetic light curves to our observations, as detailed below. Two values are given since the mean epoch of the V_J observations is some 440 days earlier than for those in u and I_C. We also report times of minima derived from splitting the MACHO observations of this star into six roughly year-long intervals.

Corresponding longitudes of periastron, ω, are plotted in Fig. 2 along with the adopted regression line, from which we derive an apsidal period of 100±5 yr. Using in addition the eccentricity, e, and inclination, i, determined from our light curves solutions, we have determined the epoch, T_0, and the sidereal and anomalistic periods, P_s and P_a, by fitting the observed times of minima with Eq. 20 of Giménez & Garcia-Pelayo (1983). The fit, which is insensitive to i, is shown in Fig. 2. Because the orbit is currently long-side on, the deviations of the eclipse times from a linear ephemeris hardly change. The values of T_0, the corresponding longitude of periastron, ω_0, and P_s and P_a are reported in Table 5. The full ephemeris for MACHO*05:36:48.7−69:17:00 is given by Eq. 20 of Giménez & Garcia-Pelayo substituting these numerical values;

Table 5. Times of minima and non-linear ephemeris for MACHO*05:36:48.7−69:17:00.

	T_1	T_2
Representative minima		
From MACHO observations	HJD 2449115.7687	HJD 2449117.2161
	2449535.8072	2449537.2500
	2449917.3118	2449918.7542
	2450318.0755	2450319.5201
	2450722.6960	2450724.1438
	2451262.1891	2451263.6416
From Mt John V_J	2451589.7409	2451591.2003
From Mt John u, I_C	2452025.1908	2452026.6548
Ephemeris		
Epoch, T_0		HJD 2452024.946 ±0.002
Sidereal period, P_s		3.853529 d ±0.000005
Anomalistic period, P_a		3.853935 d ±0.000005
Apsidal period, U	36 600 d ±1 700	100 yr ±5
Longitude of periastron, ω, at T_0		200.9° ±1.2
Rate of advance of periastron, $\dot{\omega}$		3.6°/yr ±0.2

however, the light curves plotted in this paper, light-curve analyses, etc., all use a simpler, linear ephemeris based on T_0 and P_s.

Light curve analyses shows no observable eccentricity for the two MOA targets. Improved ephemerides for them at the epoch of the new observations were obtained via phasing and light-curve fitting of our and the MACHO observations. (The MOA photometry added no additional constraint.) These ephemerides are

— for MOA J005018.4−723855:

Time of primary minimum = HJD 2452156.6598 ± 0.0003 + 1.839870 ± 0.000005 × E,

— for MOA J005623.5−722123:

Time of primary minimum = HJD 2452150.5222 ± 0.0003 + 2.32005 ± 0.00002 × E.

3.2 Light-curve analysis

The nature of our three targets cannot be determined definitively without (i) ultraviolet-visible spectrophotometry to constrain the temperatures and reddenings, and (ii) radial velocity curves to constrain the masses. Our light-curve analysis therefore aims only to determine approximate properties of our targets' component stars.

To analyse our light curves we have used the Differential Corrections (DC) program of the Wilson code (Wilson 1994), which can treat several light curves simultaneously. Its detailed treatment of the surfaces of the stars using the Roche potential model allows accurate modelling of detached, semi-detached and even contact systems. We have used a modified version of the code which incorporates Kurucz model atmospheres (Kurucz 1993) in addition to the black-body and Carbon-Gingerich atmosphere approximations of the standard version of the code. Our modified version is derived from the atmosphere subroutine (ATM) of the Calgary group (Milone, priv. comm.). The ATM subroutine interpolates the Kurucz atmosphere models at the local temperature for each grid element on the surface of the model stars whilst adopting the global mean gravity of the star. We have extended the ATM routine to interpolate the Kurucz atmosphere models at the local temperature *and* gravity for each grid element, and to interpolate within tabulated values of the ratios of the flux at the emergent angle relative to the normal emergent flux (thereby eliminating the limb-darkening approximation) for each grid element. We adopted Kurucz atmospheres with abundance $[m/\mathrm{H}] = -0.3$ and -0.5 for the LMC and SMC respectively. The apparent magnitudes of our targets indicate early B stars, so gravity-darkening exponents and bolometric albedos were set to theoretical values for radiative envelopes and we typically computed fits for effective temperatures of the primary, $T_{\mathrm{eff},1}$, across the range 20 000–35 000 K. The axial rotation rate was set equal to the orbital value except for the eccentric target, where it was synchronized to the value at periastron.

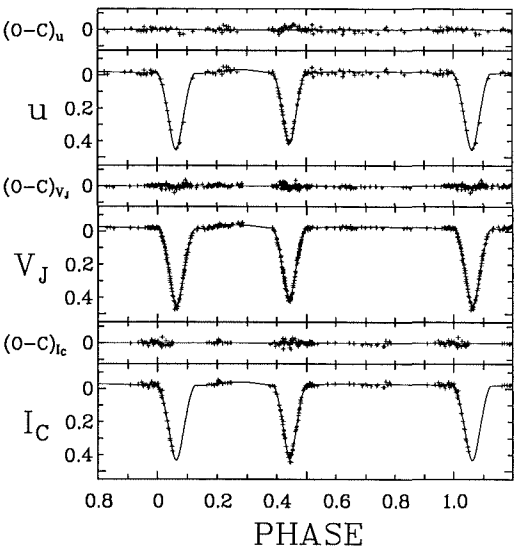

Figure 3. A Wilson-code fit to the light curves of MACHO* 05:36:47.7−69:17:00 phased according to the linear ephemeris derived in Section 3.1. The slightly earlier mean epoch of the V_J photometry compared to the u & I_C measures has been allowed for approximately by averaging separate solutions. The particular solution plotted here, which is probably representative of the true nature of the system, corresponds to components that match Geneva evolutionary models for LMC stars with $M_1 = 20\,\mathrm{M}_\odot$, $M_2 = 14\,\mathrm{M}_\odot$ and common age 5×10^6 yr. The semi-major axis $a = 33.5\,\mathrm{R}_\odot$, the mean radii are $\overline{R_1}/a = 0.22$ and $\overline{R_2}/a = 0.16$, and the inclination $i = 85\overset{\circ}{.}8$. The photometry is plotted as crosses and the model fits as lines for the three bandpasses. The ordinate scales are in magnitudes. No third light has been invoked. The (Observed−Calculated) deviations from the fit are also shown.

The light curves of MACHO*05:36:48.7−69:17:00 indicate a well-detached, eccentric system. The similar eclipse depths suggest stars of roughly similar temperature and therefore, for coeval components, similar mass.

We were able to obtain satisfactory Wilson-code fits over a range of input parameters. We found that irrespective of the values adopted for the mass ratio, $q = M_2/M_1$, and the effective temperature of the primary star, the eccentricity was given by $e = 0.200 \pm 0.001$ while the inclination, i, ranged from 84 to 87°.

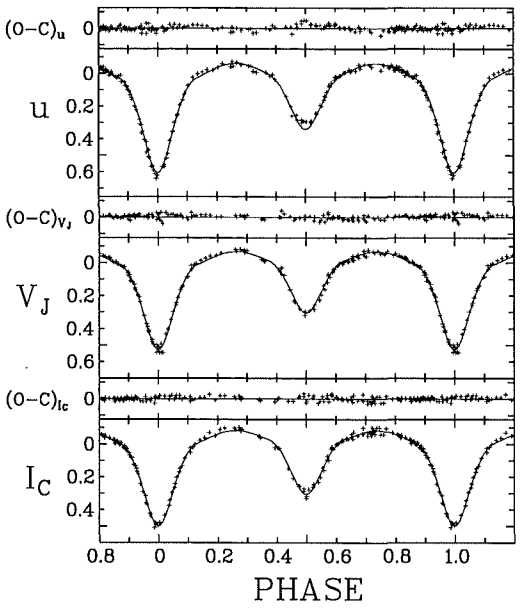

Figure 4. Wilson-code fit to the light curves of MOA J005018.4−723855. The system is semi-detached with the secondary filling its Roche lobe. The solution shown corresponds to a primary similar to a Geneva model star with parameters: $M_1 = 13.5\,M_\odot$, $T_{\rm eff,1} = 29\,000$ K, $\overline{R_1} = 5.9\,R_\odot$. Other parameters of the solution are $M_2 = 20.5\,M_\odot$, $T_{\rm eff,2} = 20\,000$ K, $\overline{R_2} = 8.5\,R_\odot$, $a = 20.5\,R_\odot$ and $i = 77\overset{\circ}{.}6$. The photometry is plotted as crosses and the model fits as lines. The ordinate scales are in magnitudes. The deviations from the fit are also plotted. For the V_J and I_C bandpasses 5 and 2 per cent of third light relative to the reference level has been necessary, but the fit is not perfect. In particular, the unexplained O'Connell effect is clearly present (the flux level between primary and secondary eclipse is higher than between secondary and primary eclipse) and the eclipses in u do not fit well.

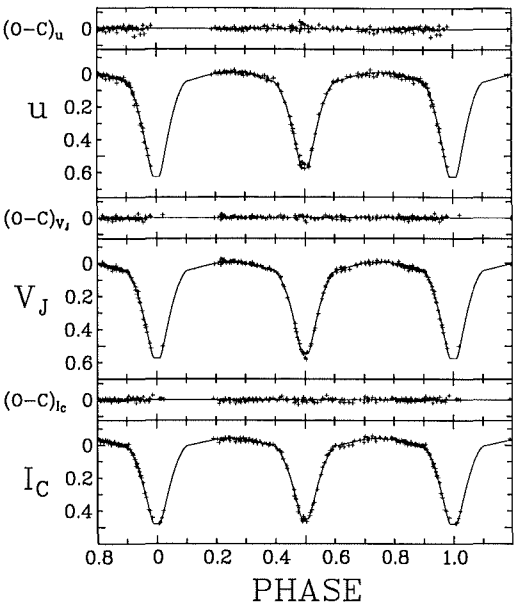

Figure 5. Wilson-code fit to the light curves of MOA J005623.5−722123 corresponding to a pair of Geneva evolutionary models with age 10×10^6 yr. The parameters are: $M_1 = 13.5\,M_\odot$, $T_{\rm eff,1} = 29\,000$ K, $\overline{R_1} = 5.8\,R_\odot$, $M_2 = 15.5\,M_\odot$, $T_{\rm eff,2} = 29\,350$ K, $\overline{R_2} = 7.8\,R_\odot$, $a = 22.5\,R_\odot$, $i = 87\overset{\circ}{.}8$. The marginally-hotter secondary, despite the shallower secondary eclipse, is due to gravity brightening at the pole and the near edge-on orbital inclination. The photometry is plotted as crosses and the model fits as lines. The ordinate scales are in magnitudes. For the V_J and I_C bandpasses 4 and 12 per cent of third light relative to the reference level has been necesssary. The deviations from the fit are also shown.

The primary is 10-15 per cent hotter than the secondary. As is usual for detached, eccentric sytems, we found that solutions existed at both a particular radius ratio R_1/R_2 and its inverse, and more solutions may exist (*four* sets were found for the system HV 982 [Paper VI]). Spectroscopy is needed to remove this ambiguity: presumably R_1 will turn out to be larger than R_2, but in either case, the radii are about one-fifth of the separation between the stars, differing between themselves by about 2-4 percent if $q = 1$, rising to 10 percent if $q = 0.8$ or 1.2, and 40 percent if $q = 0.7$.

To gain further insight into the likely nature of the component stars, we searched for solutions for which their total light corresponds to the estimated maximum-light V_J magnitude of the system, assuming a distance modulus of 18.5 and a representative reddening of $E(B-V) = 0.13$ (Westerlund 1997). We also required that the mass and effective temperature of the individual stars matched those of theoretical stellar models of identical age calculated for LMC metallicity by the Geneva group (Schaerer et al. 1993; Meynet et al. 1994). We found a match for $M_1 = 20\,M_\odot$, $M_2 = 14\,M_\odot$, $T_{\rm eff,1} = 33\,500$ K, $T_{\rm eff,2} = 29\,500$ K corresponding to an age of about 5 million years. The system is sketched in Fig. 6 while the fit to the photometry is indicated in Fig. 3 along with other details of the solution. Though the solution is only indicative, we would not expect the true parameters of the stars to be grossly different.

Light-curve analysis shows that MOA J005018.4−723855 is a semi-detached system with the secondary filling its Roche lobe. Fig. 4 shows a Wilson fit to our photometry. There is clear evidence in all three bandpasses of a small O'Connell effect (a brighter maximum between the primary and secondary eclipses than between the secondary and primary eclipses). The physical origin of this effect is unknown and so is not modelled.

To obtain the best fits elsewhere in the light curves, the Differential Corrections part of the Wilson code formally required the *subtraction* of several per cent of the reference-level light from the solutions in all bandpasses (i.e. negative 'third' light), suggesting that the reference flux levels are too low by the same amount. Such a large error seems unlikely, even though MOA J005018.4−723855 is our target that is most affected by blending (Fig. 1, where the star to the south west is closer and relatively brighter than any of the neighbours of the other targets). Further, the amount of third light is highly correlated with the inclination, making it difficult to estimate. We adopted the *relative* amounts of third light between the bandpasses indicated by the Wilson code, but set the third light in u to zero, since this bandpass would seem least likely to be contaminated given the low uv flux of most field stars. The third light was therefore set to 5 and 2 per cent in V_J and I_C respectively. Never-

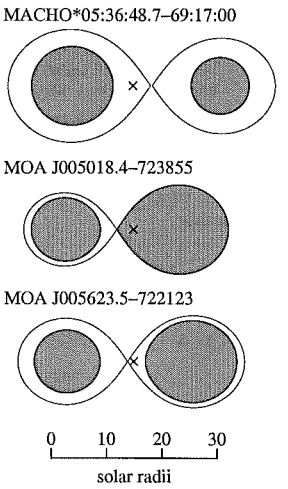

Figure 6. Schematics of the surface potentials and limiting lobes for the likely nature of the three target stars, as discussed in the text. The sketches are made in the planes perpendicular to the orbits and are aligned on the systems' centres of gravity, which are marked with crosses (×). Within each system, the relative dimensions are well-determined by the light-curve analysis, but the absolute sizes, which are based on solutions that match Geneva evolutionary models and the observed maximum brightnesses, should only be considered indicative. For MACHO*05:36:48.7−69:17:00, the system is shown at periastron; the limiting lobes do not quite touch because the stars' rotation is presumed synchronised there rather than with their orbital motion.

theless, the fit to the eclipses was not always perfect, particularly in the u light curve.

The derived mass ratios and inclinations lie in the ranges $q =$ 1.4-1.6 and $i =$ 73-78°. The secondary has a temperature 20-30 per cent lower than the primary, but its radius is larger, being approximately 40 per cent of the orbital separation, whereas the primary's radius is about 30 per cent of the orbital separation.

Given the short period and the larger, more massive secondary, the system is presumably undergoing case A mass transfer (transfer during the main-sequence evolution of the initially more-massive star). The theoretical evolutionary tracks for case A mass transfer printed in Fig. 1 of Wellstein, Langer & Braun (2001) and Figs 3-8 of Nelson & Eggleton (2001) certainly show that the mass donor can rapidly lose luminosity and become cooler than the mass receptor, as appears to be the case for MOA J005018.4−723855. We compared Geneva single-star evolutionary tracks for solar metallicity (Schaller et al. 1992; Meynet et al. 1994) with the Wellstein et al. Fig 1 tracks. These latter refer to a system that initially has 12 and 7.5 $M_\odot$ stars in a 2.5-d orbit and so is not grossly dissimilar to what we deduce below for MOA J005018.4−723855. After making a systematic shift to align the pre-mass-exchange tracks (presumably needed because of different input physics), we found that the Wellstein et al. mass receptor star has the same temperature, luminosity and therefore radius at the begining and end of the Case A and AB mass-transfer episodes as Geneva models of the same mass (but different age); i.e., the mass receptor mimics a normal main-sequence star at these points. However Wellstein et al. note that during the rapid initial phase of transfer the mass gainer can be overluminous for its mass by a factor of two. (De Loore & Vanbeveren [1994] have calculated that the mass receiver can also be overluminous during Case B mass transfer.) Given the uncertainties in our estimate for the out-of-eclipse apparent magnitudes, a factor of two is not enormously significant. We have estimated the physical nature of the stars in MOA J005018.4−723855 by requiring the primary to have properties corresponding to a Geneva SMC main-sequence model (Charbonnel et al. 1993; Meynet et al. 1994) and the system light to correspond to the estimated apparent magnitude adopting an SMC distance modulus and reddening of 18.9 and 0.09 respectively (Westerlund 1997). (For this system we need fit only one component to an evolutionary model because the photometric solution provides the mass ratio.) We found $M_1 = 13.5\,M_\odot$, $M_2 = 20.5\,M_\odot$, $T_{\rm eff,1} = 29\,000$ K, $T_{\rm eff,2} = 20\,000$ K. The system is sketched in Fig. 6 while the fit to the photometry is indicated in Fig. 4 along with other details of the solution. The donor star is still more massive than the receptor, and with a lower limit to its initial mass of 20.5 $M_\odot$ would indeed fill and overflow the current Roche lobe during its hydrogen-burning phase. If the primary is hotter than 29 000 K, the masses and sizes of the stars and their orbit will be correspondingly less, and vice versa.

Analysis of the light curves of MOA J005623.5−722123 shows that the system is detached. The similar eclipse depths indicate similar temperatures for the component stars, and by extension stars that are generally similar. The same remarks concerning third light apply as for MOA J005018.4−723855: we adopted 4 percent third light in $V_{\rm J}$ and 12 per cent in $I_{\rm C}$. We were able to obtain Wilson-code fits over a range of mass ratios and temperatures. In Fig. 5 we show the solution that corresponds to a pair of Geneva models of age 10×10^6 yr such as to produce the observed apparent magnitude at maximum light. Corresponding parameters are $M_1 = 13.5\,M_\odot$, $T_{\rm eff,1} = 29\,000$ K $M_2 = 15.5\,M_\odot$, $T_{\rm eff,2} = 29\,350$ K and $i = 87\overset{\circ}{.}8$. Once again, these parameters should only be considered indicative. The eclipses appear to be total. It is interesting that the secondary is marginally hotter than the primary despite the secondary eclipse being shallower. Experiments with the Wilson code indicated that this is because of gravity darkening and the nearly edge-on orbital inclination. The secondary's poles are hotter than its equator, but it is its cooler equator that is occulted during secondary eclipse, resulting in a shallower depth despite the hemisphere-averaged effective temperature being hotter.

4 CONCLUSIONS

We have presented $uV_{\rm J}I_{\rm C}$ CCD photomtery for three eclipsing binary systems in the Magellanic Clouds. The photometry was extracted using difference imaging. Like the stars in earlier papers in this series, our targets do not suffer especially from blending, so it is perhaps not surprising that the precision achieved is only marginally better than previously where profile-fitting photometry was employed. The systems were selected as possibly well-detached and of interest for tests of stellar evolution models at low metallicity and as distance indicators. The use of difference imaging has clairified, in our minds at least, the importance–and difficulty–of estimating third light and/or the reference level accurately, since level errors can be compensated by an altered inclination in the light-curve fits of detached systems. Detached systems are essential for testing evolutionary models, while for distance indicators, it is beyond doubt that the flux levels must be estimated correctly. The most appropriate type of eclipsing binary for use as distance indicators is an item of current debate (Wyithe & Wilson

2002), and Graczyk (2003) has claimed that an advantage of systems exhibiting proximity effects is that in them third light can be estimated accurately.

Additional observations are needed before accurate fundamental parameters can be determined for our target stars. High-resolution time-series spectroscopy with 8-m class telescopes is needed to set linear dimensions via radial-velocity curves, while ultraviolet-visible spectrophotometry is required to derive interstellar extinction and stellar surface radiative-flux distributions. It will then be possible to obtain distances to each system through comparison of the flux outside the terrestrial atmosphere with the luminosities of the component stars.

5 ACKNOWLEDGMENTS

We thank: The MACHO project for the on-line availability of their observations; Drs I. Bond and S. Besier for useful discussions; Dr R. Wilson for providing his synthetic light-curve codes; and Dr E.F. Milone for providing his ATM subroutine to incorporate Kurucz models into the Wilson code.

GPB would like to acknowledge financial support provided by the Dennis William Moore and Marsden Funds.

REFERENCES

Alard C., 2000a, A&AS, 144, 363
Alard C., 2000b, in Szabados L., Kurtz, D., eds, Iau Coll. 176, The Impact of Large-Scale Surveys on Pulsating Star Research, ASP Conf. Ser. 203, San Francisco, p. 50
Alard C., Lupton R.H., 2000, ApJ, 503, 325
Alcock C. et al., 1997, AJ, 114, 326
Barnes S.I. et al., 2002, Southern Stars, 39, 1
Bayne G. et al., 2002, MNRAS, 331, 609
Charbonnel C., Meynet G., Maeder A., Schaller G., Schaerer D., 1993, A&AS, 101, 415
Giménez A., Garcia-Pelayo J., 1983, ApSS, 92, 203
Graczyk D., 2003, MNRAS, 342, 1334
Grundahl, F., Sørensen, A.N., 1996, A&AS, 116, 367
Harries, T.J., Hilditch R.W., Howarth, I.D., 2003, MNRAS, 339, 157
Kurucz R., 1993, in Milone E., ed, Light Curve Modeling of Eclipsing Binary Stars. Springer-Verlag, New York, p. 93
de Loore C., Vanbeveren D., 1994, A&AS, 103, 67
McCall, S.H.C.P., Siegmund, W.A., 1994, Proc. Soc. Photo-Optical Instrumentation Engineers, 2198, 1385
Meynet G., Maeder A., Schaller G., Schaerer D., Charbonnel C., 1994, A&AS, 103, 97
Nelson C.A., Eggleton P.P., 2001, ApJ, 552, 664
Pritchard J.D., Tobin W., Clark M., Guinan E.F., 1998a, MNRAS, 297, 278 (Paper V)
Pritchard J.D., Tobin W., Clark M., Guinan E.F., 1998b, MNRAS, 299, 1087 (Paper VI)
Schaller G., Schaerer D., Meynet G., Maeder A., A&AS, 96, 269
Schaerer D., Meynet G., Maeder A., Schaller G., 1993, A&AS, 98, 523
Stetson P.B., 1987, PASP, 99, 191
Tobin W., Kershaw G.M., Ritchie R.A., Ma L., Graham G.J., Hemmingsen S.B., 1993, in Elliott I., Butler C.J., eds, Poster Papers on Stellar Photometry. Dublin Institute for Advanced Studies, Dublin, p. 153
Wellstein S., Langer N., Braun H., 2001, A&A, 369, 939
Westerlund B.E., 1997, The Magellanic Clouds. Cambridge University Press, Cambridge
Wilson R.E., 1994, PASP, 106, 921
Wyithe J.S.B., Wilson, R.E., 2002, ApJ, 571, 293
Woźniak, P.R., 2000, Acta Astronomica, 50, 421

This paper has been typeset from a TEX/ LATEX file prepared by the author.

CCD photometry of variable stars in the Magellanic Clouds – VII. The eclipsing binaries MACHO*05:36:48.7−69:17:00 in the LMC and MOA J005018.4−723855 & J005623.5−722123 in the SMC

G.P. Bayne, W. Tobin, J.D. Pritchard, K.R. Pollard and M.D. Albrow

Table 1. Photometry of MACHO*05:36:48.7−69:17:00. The columns are Heliocentric Julian Day of mid exposure, normalized light, airmass (X) and FWHM seeing in arcsec (σ).

HJD −2450000	Norm. light	X	σ "	HJD −2450000	Norm. light	X	σ "	HJD −2450000	Norm. light	X	σ "	HJD −2450000	Norm. light	X	σ "	HJD −2450000	Norm. light	X	σ "	HJD −2450000	Norm. light	X	σ "
												u											
1294.9019	1.008	1.5	4.8	1726.7938	1.012	1.8	3.6	1960.9119	1.010	1.1	2.4	1992.0102	0.722	1.6	4.1	2021.2215	0.820	2.5	5.9	2206.9661	1.026	1.4	4.9	2467.2473	1.016	1.4	4.9
1294.9893	1.008	1.9	3.5	1726.9250	1.014	2.4	4.7	1960.9404	1.008	1.2	2.2	1992.0345	0.763	1.6	4.2	2021.8170	1.011	1.2	2.9	2207.0152	1.028	1.3	5.0	2467.8439	1.006	2.2	4.0
1295.0909	1.008	2.4	2.7	1726.9828	1.013	2.5	3.1	1960.9690	0.980	1.2	2.1	1992.0931	0.876	1.9	3.1	2021.8474	1.008	1.3	3.2	2207.0565	1.032	1.2	4.0	2467.8669	1.010	2.3	6.8
1295.1864	0.994	2.5	5.4	1727.0818	1.021	2.2	3.0	1960.9982	0.933	1.3	2.5	1992.1404	0.972	2.2	4.0	2021.8941	1.023	1.4	3.8	2207.0940	1.019	1.1	3.9	2467.9334	1.028	2.5	4.6
1295.2695	1.026	2.2	3.3	1727.1516	1.015	1.9	3.0	1961.0275	0.878	1.3	3.1	1992.1823	1.016	2.4	3.0	2021.9256	1.023	1.5	3.7	2207.9791	1.023	1.3	5.0	2467.9747	1.013	2.5	4.9
1404.1051	1.018	1.6	4.5	1727.2389	0.997	1.5	3.2	1961.0566	0.816	1.4	3.8	2018.8148	0.902	1.2	3.7	2021.9913	1.029	1.8	5.6	2208.0166	1.020	1.2	5.6	2468.0174	1.014	2.4	5.6
1404.1898	1.022	1.3	3.6	1729.7915	0.916	1.8	5.0	1961.0848	0.765	1.5	5.3	2018.8374	0.848	1.3	4.1	2022.0332	1.021	2.0	5.0	2208.0622	1.044	1.2	6.1	2468.0381	1.015	2.3	5.9
1404.8151	0.684	2.4	4.7	1729.8638	0.762	2.2	5.3	1961.1214	0.695	1.7	5.1	2018.8734	0.774	1.3	4.2	2022.9032	0.850	1.5	5.7	2208.1017	1.023	1.1	4.1	2468.0841	1.020	2.1	3.3
1406.1029	0.887	1.6	5.5	1729.9817	0.742	2.5	4.0	1961.1506	0.691	1.8	4.5	2018.9045	0.728	1.4	4.0	2022.9323	0.903	1.6	3.5	2208.1388	1.011	1.1	4.8	2468.1047	1.010	2.0	3.0
1406.1686	0.761	1.4	4.1	1730.0618	0.912	2.3	5.4	1987.9082	1.020	1.2	5.9	2018.9380	0.693	1.6	3.9	2022.9651	0.953	1.7	4.0	2208.1781	1.033	1.1	4.9	2468.1471	0.977	1.8	3.8
1557.9867	1.020	1.1	5.0	1730.1341	1.003	1.9	4.5	1987.9237	0.997	1.3	6.3	2018.9707	0.696	1.7	4.0	2022.9954	0.999	1.9	3.5	2464.1639	1.027	1.8	3.8	2468.1680	0.948	1.7	4.6
1558.0283	1.005	1.1	5.4	1730.2269	1.016	1.5	4.7	1988.0204	0.825	1.5	2.7	2019.0114	0.772	1.9	5.3	2023.0248	1.004	2.0	4.5	2464.1844	1.024	1.7	6.4	2468.2156	0.855	1.5	5.6
1558.9215	0.663	1.1	4.9	1730.7854	1.002	1.8	2.7	1988.0349	0.801	1.6	2.6	2019.0524	0.845	2.1	4.7	2023.0789	1.010	2.3	4.2	2464.2057	1.020	1.6	6.5	2468.2568	0.770	1.4	3.8
1558.9621	0.685	1.1	5.9	1730.8868	1.004	2.3	4.0	1988.0938	0.695	1.9	3.1	2019.0902	0.926	2.3	4.3	2023.1098	0.993	2.4	4.0	2464.2880	0.979	1.3	6.3	2468.2772	0.735	1.3	4.3
1559.0069	0.767	1.1	5.5	1730.9857	1.014	2.5	3.7	1988.1084	0.683	1.9	3.2	2019.1921	1.009	2.5	6.8	2045.8215	0.846	1.4	2.6	2465.1083	1.048	2.0	4.5				
1560.9418	1.016	1.1	3.8	1960.0629	1.012	1.4	5.7	1991.8446	0.900	1.1	3.1	2020.8847	1.001	1.4	6.2	2045.8672	0.742	1.6	3.2	2465.1440	1.045	1.8	4.1				
1561.0420	1.029	1.2	5.1	1960.0925	1.020	1.5	5.4	1991.8749	0.839	1.2	4.7	2020.9174	1.004	1.5	5.7	2045.9125	0.691	1.8	4.3	2465.1738	1.043	1.7	3.9				
1561.0847	1.024	1.2	5.4	1960.1230	1.015	1.6	3.7	1991.9070	0.771	1.2	4.7	2020.9525	1.001	1.6	6.3	2206.8707	1.023	1.7	3.8	2465.2031	1.022	1.6	3.8				
1724.8297	0.983	1.9	3.6	1960.1530	1.012	1.8	4.1	1991.9391	0.712	1.3	3.2	2021.0201	1.005	1.9	4.9	2206.9014	1.005	1.6	4.5	2467.2033	1.025	1.6	6.0				
1725.1728	1.029	1.8	5.4	1960.8834	1.016	1.1	2.5	1991.9683	0.688	1.4	3.8	2021.0362	1.014	2.0	4.9	2206.9312	1.020	1.5	4.8	2467.2252	1.034	1.5	5.4				
												V_J											
1294.9547	1.021	1.7	4.5	1315.9123	1.022	1.8	3.8	1316.2266	0.771	2.1	6.1	1406.1435	0.798	1.4	3.5	1491.0189	0.677	1.2	5.5	1731.0604	1.025	2.3	3.2	2020.9317	1.019	1.6	5.4
1294.9662	1.022	1.8	3.9	1315.9200	1.017	1.8	3.5	1316.2320	0.782	2.1	6.1	1406.2462	0.695	1.2	2.5	1491.0264	0.685	1.2	5.2	1960.0759	1.011	1.5	3.5	2020.9681	1.020	1.7	5.4
1295.0731	1.022	2.3	3.8	1315.9263	1.006	1.8	4.0	1316.2375	0.807	2.1	6.0	1407.0280	1.031	1.9	4.8	1491.0331	0.688	1.2	5.7	1960.1054	1.024	1.6	3.7	2021.0027	1.016	1.9	5.4
1295.1517	1.015	2.5	3.1	1315.9378	0.994	1.9	3.9	1316.2430	0.806	2.1	5.9	1407.0342	1.015	1.9	4.9	1491.0482	0.712	1.1	4.8	1960.1359	1.017	1.7	3.3	2021.0697	1.017	2.2	5.3
1295.2526	1.024	2.3	3.3	1315.9434	0.989	1.9	4.0	1316.2520	0.827	2.0	6.0	1407.0455	1.018	1.8	4.7	1491.0581	0.739	1.1	5.2	1960.1658	1.028	1.9	3.8	2021.0877	1.023	2.3	5.6
1313.0793	1.048	2.5	4.4	1315.9524	0.973	2.0	4.0	1316.2588	0.840	2.0	3.9	1407.0511	1.022	1.8	5.1	1491.0650	0.749	1.1	5.6	1960.1774	1.027	1.9	4.2	2021.1397	0.969	2.5	5.7
1313.0871	1.045	2.5	6.2	1315.9580	0.969	2.0	3.9	1316.2643	0.852	2.0	4.1	1407.0731	1.015	1.7	5.7	1491.0732	0.761	1.1	5.6	1960.1879	1.033	2.0	4.7	2021.1547	0.945	2.5	5.3
1313.0949	1.041	2.5	5.6	1315.9636	0.956	2.0	4.1	1316.2698	0.861	1.9	3.6	1407.0948	1.019	1.6	5.0	1491.0797	0.776	1.1	5.6	1960.9237	1.021	1.1	2.2	2021.1857	0.913	2.5	6.4
1313.1024	1.038	2.5	5.8	1315.9693	0.947	2.0	4.3	1316.2753	0.876	1.9	4.0	1407.1004	1.018	1.6	5.5	1491.0863	0.798	1.1	4.6	1960.9522	1.000	1.2	2.0	2021.2032	0.853	2.5	5.4
1313.1103	1.035	2.5	5.1	1315.9748	0.943	2.1	3.5	1316.2811	0.887	1.9	4.1	1489.9585	1.013	1.3	5.0	1491.0932	0.794	1.1	4.6	1960.9808	0.961	1.2	2.2	2021.2376	0.799	2.4	5.5
1313.1170	1.048	2.5	6.6	1315.9819	0.930	2.1	4.1	1404.1705	1.020	1.4	4.1	1489.9630	1.022	1.3	4.6	1491.1009	0.852	1.1	4.4	1961.0100	0.903	1.3	2.6	2021.2525	0.758	2.4	6.1
1313.1281	1.038	2.5	6.5	1315.9873	0.918	2.1	4.1	1404.2770	1.019	1.2	3.4	1489.9698	1.018	1.3	4.5	1491.1163	0.859	1.1	4.5	1961.0392	0.843	1.4	2.7	2021.8303	1.024	1.3	4.3
1313.1359	1.051	2.5	4.7	1315.9927	0.909	2.2	4.2	1404.7977	0.672	2.4	3.4	1489.9840	1.024	1.2	4.7	1491.1236	0.876	1.1	4.0	1961.0684	0.778	1.4	3.4	2021.8614	1.025	1.3	4.1
1313.1432	1.036	2.5	5.1	1315.9982	0.896	2.2	3.5	1404.8046	0.685	2.4	3.5	1489.9946	1.019	1.2	4.8	1491.1304	0.884	1.1	4.4	1961.0966	0.725	1.6	4.2	2021.9082	1.028	1.5	4.3
1313.8179	0.777	1.4	6.6	1316.0037	0.883	2.2	3.2	1404.8657	0.792	2.5	3.8	1490.0014	1.022	1.2	4.6	1491.1371	0.908	1.1	3.9	1961.1332	0.686	1.7	3.6	2021.9389	1.029	1.6	4.2
1313.8546	0.866	1.5	6.0	1316.0093	0.876	2.2	3.7	1404.8711	0.797	2.5	3.8	1490.0146	1.017	1.2	4.7	1491.1437	0.918	1.1	4.2	1961.1625	0.693	1.9	4.6	2021.9715	1.038	1.7	5.2
1313.8637	0.864	1.5	6.4	1316.0182	0.861	2.3	3.6	1404.8767	0.804	2.5	4.5	1490.0226	1.025	1.2	4.5	1491.1504	0.935	1.1	3.8	1988.0586	0.759	1.7	2.4	2022.0155	1.033	1.9	5.2
1313.8706	0.892	1.6	5.9	1316.0238	0.840	2.3	3.6	1404.8927	0.873	2.5	5.6	1490.0301	1.021	1.2	5.0	1491.1578	0.942	1.1	4.6	1988.0707	0.736	1.8	2.5	2022.0473	1.037	2.1	5.2
1313.8774	0.909	1.6	4.9	1316.0298	0.832	2.3	3.8	1404.9071	0.875	2.5	5.9	1490.0391	1.027	1.2	4.8	1491.1644	0.953	1.1	4.0	1988.0819	0.718	1.8	2.9	2022.9174	0.881	1.5	4.9
1313.8844	0.930	1.6	6.4	1316.0365	0.816	2.4	4.0	1404.9132	0.902	2.4	5.3	1490.0469	1.028	1.1	4.7	1491.1709	0.969	1.1	4.2	1988.1213	0.684	2.0	2.9	2022.9464	0.941	1.6	3.3
1315.7631	1.020	1.3	3.5	1316.0427	0.807	2.4	4.0	1404.9191	0.889	2.4	5.4	1490.0543	1.030	1.1	4.8	1558.0155	1.019	1.1	4.0	1988.1307	0.688	2.1	3.3	2022.9797	0.992	1.8	3.6
1315.7695	1.019	1.3	3.3	1316.0488	0.791	2.4	4.4	1404.9338	0.931	2.4	5.6	1490.0621	1.032	1.1	4.7	1558.0563	1.021	1.2	5.4	1991.8588	0.865	1.2	2.8	2023.0100	1.019	1.9	3.8
1315.7750	1.024	1.3	3.2	1316.0543	0.778	2.4	4.3	1404.9467	0.938	2.3	5.6	1490.0715	1.023	1.1	4.7	1558.1047	1.016	1.3	6.5	1991.8892	0.796	1.2	3.4	2023.0357	1.006	2.1	4.3
1315.7800	1.018	1.3	3.3	1316.0600	0.767	2.4	4.3	1404.9525	0.961	2.3	6.1	1490.0795	1.024	1.1	4.7	1558.9488	0.687	1.1	4.5	1991.9536	0.691	1.4	2.6	2023.0638	1.013	2.2	4.8
1315.7870	1.021	1.3	3.7	1316.0655	0.750	2.5	4.4	1404.9587	0.975	2.3	5.7	1490.0862	1.029	1.1	4.3	1558.9943	0.766	1.1	3.4	1991.9829	0.688	1.4	3.0	2023.0934	1.025	2.3	5.1
1315.7940	1.020	1.3	3.6	1316.0717	0.741	2.5	4.4	1404.9708	0.975	2.2	4.5	1490.0929	1.028	1.1	4.3	1559.0294	0.840	1.1	4.1	1991.9966	0.703	1.5	2.8	2044.9934	1.038	2.1	5.5
1315.7992	1.017	1.4	4.5	1316.0777	0.727	2.5	4.8	1404.9769	0.991	2.2	3.6	1490.0997	1.029	1.1	5.6	1561.0298	1.022	1.2	3.8	1992.0493	0.800	1.7	2.7	2045.0081	1.024	2.2	5.5
1315.8048	1.020	1.4	4.3	1316.0839	0.715	2.5	5.4	1405.0357	1.006	1.9	3.6	1490.1069	1.043	1.1	4.6	1561.0693	1.031	1.2	3.6	1992.1081	0.924	2.0	3.1	2045.0232	1.039	2.3	5.9
1315.8106	1.018	1.4	4.4	1316.0896	0.698	2.5	4.9	1405.0417	1.015	1.9	4.1	1490.1164	1.035	1.1	5.0	1561.0975	1.023	1.3	4.8	1992.1219	0.950	2.1	3.1	2045.0380	1.033	2.4	6.1
1315.8178	1.020	1.4	4.0	1316.0986	0.695	2.5	5.4	1405.0473	1.023	1.8	3.8	1490.1230	1.031	1.1	4.7	1561.1160	1.029	1.3	5.7	1992.1556	0.999	2.2	3.4	2045.7944	0.905	1.3	3.3
1315.8283	1.028	1.4	4.0	1316.1058	0.678	2.5	4.8	1405.1141	1.026	1.5	5.3	1490.1296	1.038	1.1	4.8	1561.1248	1.018	1.3	4.6	1992.1693	1.016	2.3	2.6	2045.8094	0.872	1.4	3.2
1315.8340	1.020	1.4	4.0	1316.1136	0.674	2.5	5.8	1405.1365	1.010	1.5	4.8	1490.1370	1.036	1.1	4.4	1725.1512	1.028	1.9	5.6	1992.1976	1.020	2.4	2.4	2045.8396	0.808	1.5	3.2
1315.8412	1.025	1.5	3.7	1316.1195	0.646	2.5	6.4	1405.1708	1.017	1.4	4.3	1490.1664	1.033	1.1	5.0	1726.8988	1.023	2.3	3.5	1992.2114	1.023	2.5	2.7	2045.8551	0.771	1.5	3.0
1315.8467	1.022	1.5	4.1	1316.1263	0.661	2.5	6.0	1405.1772	1.018	1.3	4.4	1490.9271	0.791	1.4	5.5	1727.0608	1.023	2.3	2.8	2018.8538	0.816	1.3	4.9	2045.8853	0.716	1.6	4.0
1315.8522	1.017	1.5	3.9	1316.1331	0.654	2.5	6.3	1405.1920	1.028	1.3	5.5	1490.9345	0.766	1.4	5.3	1727.1348	1.024	2.0	2.5	2018.8870	0.749	1.4	3.8	2045.8999	0.699	1.7	4.4
1315.8582	1.011	1.5	3.9	1316.1427	0.659	2.5	6.9	1406.0272	1.011	1.9	3.7	1490.9418	0.754	1.3	5.2	1727.2146	1.024	1.6	2.6	2018.9201	0.695	1.5	4.8	2045.9303	0.682	1.8	5.3
1315.8640	1.019	1.6	3.8	1316.1484	0.649	2.5	6.4	1406.0329	1.007	1.9	3.6	1490.9486	0.746	1.3	4.8	1727.2919	1.019	1.3	4.0	2018.9518	0.687	1.6	5.6	2045.9556	0.707	2.0	4.5
1315.8695	1.018	1.6	3.2	1316.1539	0.657	2.5	6.4	1406.0397	1.000	1.9	3.8	1490.9565	0.726	1.3	4.9	1729.8444	0.806	2.1	4.4	2018.9889	0.731	1.8	5.5	2046.0231	0.839	2.3	3.6
1315.8751	1.018	1.6	3.6	1316.1798	0.681	2.4	6.0	1406.0641	0.964	1.7	3.8	1490.9631	0.723	1.3	5.2	1729.9643	0.705	2.5	4.4	2019.0338	0.830	2.0	5.6	2046.0400	0.875	2.4	4.6
1315.8807	1.023	1.6	3.2	1316.1932	0.700	2.3	6.2	1406.0696	0.955	1.7	3.1	1490.9789	0.699	1.2	4.8	1730.0437	0.866	2.4	4.5	2019.0697	0.897	2.2	5.2	2046.0552	0.904	2.4	5.2
1315.8879	1.017	1.6	4.2	1316.2009	0.722	2.3	6.1	1406.0750	0.941	1.7	3.5	1490.9867	0.690	1.2	4.2	1730.1062	0.985	2.1	3.2	2019.1031	0.957	2.3	4.9	2465.1255	1.030	1.9	4.1
1315.8944	1.014	1.7	3.7	1316.2087	0.730	2.2	6.1	1406.0805	0.932	1.7	3.3	1490.9936	0.679	1.2	5.4	1730.2119	1.021	1.6	4.2	2019.1744	1.025	2.5	5.5	2465.1612	1.025	1.8	3.5
1315.8998	1.018	1.7	3.7	1316.2142	0.747	2.2	5.8	1406.0860	0.922	1.6	3.4	1491.0015	0.680	1.2	5.3	1730.2850	1.021	1.3	4.4	2019.2065	1.025	2.5	6.1	2465.1910	1.029	1.6	3.6
1315.9054	1.018	1.7	3.6	1316.2206	0.770	2.2	6.2	1406.1312	0.820	1.5	4.2	1491.0110	0.678	1.2	5.6	1730.8658	1.027	2.2	3.0	2019.2426	1.025	2.4	6.2	2465.2209	1.039	1.5	4.1
												I_C											
1294.9735	1.027	1.8	5.6	1731.0679	1.019	2.3	3.1	1991.9488	0.694	1.4	2.9	2019.2028	1.027	2.5	5.9	2022.9129	0.861	1.5	4.0	2046.0305	0.839	2.3	4.3	2467.9847	1.005	2.5	3.2
1295.0796	1.029	2.3	2.3	1960.0726	1.020	1.5	3.7	1991.9780	0.694	1.4	6.4	2019.2201	1.028	2.5	5.9	2022.9420	0.920	1.6	3.3	2046.0474	0.892	2.4	4.5	2468.0049	1.023	2.4	4.0
1295.2587	1.029	2.3	2.7	1960.1022	1.023	1.6	4.3	1991.9917	0.689	1.5	3.0	2019.2393	1.028	2.4	6.0	2022.9751	0.990	1.8	3.5	2046.0626	0.929	2.5	4.5	2468.0274	1.037	2.4	4.7
1404.1778	1.023	1.3	3.7	1960.1327	1.023	1.7	2.9	1992.0199	0.735	1.6	3.3	2019.2552	1.020	2.4	5.8	2023.0054	1.017	1.9	3.1	2464.1739	1.026	1.7	5.3	2468.0481	1.010	2.3	3.8
1406.2527	0.697	1.2	3.6	1960.1627	1.023	1.8	3.1	1992.0442	0.789	1.7	3.0	2020.8953	1.024	1.4	4.0	2023.0348	1.021	2.1	3.8	2464.1944	1.021	1.6	5.4	2468.0694	1.015	2.2	3.1
1406.2732	0.726	1.1	2.8	1960.2003	1.031	2.0	4.4	1992.0579	0.806	1.8	3.1	2020.9283	1.027	1.5	4.4	2023.0593	1.015	2.2	4.1	2464.2157	1.030	1.5	5.6	2468.0941	1.019	2.0	2.3
1406.2786	0.726	1.1	2.9	1960.8931	1.014	1.1	2.2	1992.1028	0.899	2.0	3.0	2020.9637	1.014	1.7	4.6	2023.0890	1.024	2.3	3.6	2464.2528	1.029	1.4	5.0	2468.1147	1.006	1.9	2.4
1725.1624	1.029	1.9	4.8	1960.9216	1.017	1.1	1.9	1992.1165	0.940	2.0	3.1	2020.9983	1.025	1.8	4.4	2023.1198	1.017	2.4	3.7	2464.2762	0.995	1.3	5.5	2468.1351	0.980	1.8	2.7
1726.9148	1.027	2.4	4.2	1960.9501	1.013	1.2	1.7	1992.1501	0.989	2.2	3.5	2021.0642	1.022	2.2	4.0	2044.9845	1.024	2.1	5.4	2464.2980	0.952	1.3	3.6	2468.1571	0.963	1.7	3.5
1727.0686	1.027	2.3	2.6	1960.9787	0.970	1.2	1.9	1992.1638	1.005	2.3	3.1	2021.0839	1.024	2.3	4.9	2044.9992	1.048	2.2	5.3	2465.1540	1.032	1.8	3.4	2468.1780	0.920	1.6	4.3
1727.1408	1.018	1.9	2.2	1961.0079	0.911	1.3	2.1	1992.1920	1.024	2.4	2.6	2021.1293	0.987	2.4	4.7	2045.0143	1.040	2.2	6.0	2465.1838	1.035	1.6	3.7	2468.2017	0.873	1.5	3.4
1727.2278	1.022	1.6	2.2	1961.0371	0.857	1.4	2.2	1992.2292	1.032	2.5	3.0	2021.1522	0.989	2.5	5.6	2045.0292	1.038	2.3	5.3	2467.1902	1.009	1.6	6.9	2468.2257	0.835	1.5	3.2
1727.2995	1.009	1.3	4.5	1961.0663	0.795	1.4	3.4	2018.8499	0.841	1.3	3.9	2021.2005	0.875	2.5	4.6	2045.7864	0.913	1.3	3.2	2467.2133	1.041	1.5	4.5	2468.2464	0.799	1.4	3.2
1729.8510	0.774	2.1	5.0	1961.1311	0.682	1.7	3.5	2018.8842	0.758	1.4	3.0	2021.2320	0.800	2.4	4.9	2045.8019	0.884	1.4	2.4	2467.2353	1.023	1.4	3.6	2468.2668	0.749	1.3	2.4
1729.9697	0.708	2.5	4.3	1987.9344	0.982	1.3	5.8	2018.9148	0.702	1.5	3.3	2021.2499	0.757	2.4	5.1	2045.8322	0.819	1.4	2.4	2467.2573	1.036	1.4	3.2	2468.2873	0.724	1.3	3.1
1730.0515	0.890	2.3	4.3	1988.0456	0.778	1.6	2.0	2018.9489	0.680	1.6	3.5	2021.8274	1.018	1.2	2.6	2045.8478	0.790	1.5	2.4	2467.2777	1.026	1.3	3.6	2468.2938	0.706	1.3	3.2
1730.1175	0.997	2.0	4.4	1988.0514	0.769	1.7	2.1	2018.9861	0.712	1.8	3.4	2021.8586	1.028	1.3	2.9	2045.8775	0.725	1.6	3.1	2467.8539	1.024	2.2	4.3				
1730.2166	1.013	1.6	4.4	1988.1446	0.692	2.1	2.9	2019.0303	0.796	2.0	4.1	2021.9048	1.037	1.5	2.9	2045.8926	0.700	1.7	4.0	2467.8972	1.036	2.4	4.9				
1730.2903	1.017	1.3	4.5	1991.8543	0.890	1.2	3.0	2019.0639	0.875	2.1	3.9	2021.9362	1.029	1.6	3.4	2045.9228	0.665	1.8	3.7	2467.9186	1.014	2.5	3.7				
1730.8758	1.019	2.3	2.1	1991.8846	0.833	1.2	3.5	2019.1007	0.953	2.3	4.9	2021.9674	1.032	1.7	3.5	2045.9380	0.663	1.9	4.2	2467.9434	1.021	2.5	3.8				
1730.9479	1.021	2.5	2.1	1991.9167	0.761	1.3	4.1	2019.1695	1.006	2.5	5.2	2022.0441	1.034	2.1	3.8	2046.0157	0.811	2.3	3.8	2467.9636	1.025	2.5	4.3				

CCD photometry of variable stars in the Magellanic Clouds – VII. The eclipsing binaries MACHO*05:36:48.7−69:17:00 in the LMC and MOA J005018.4−723855 & J005623.5−722123 in the SMC

G.P. Bayne, W. Tobin, J.D. Pritchard, K.R. Pollard and M.D. Albrow

Table 2. Photometry of MOA J005018.4−723855. The columns are Heliocentric Julian Day of mid exposure, normalized light, airmass (X) and FWHM seeing in arcsec (σ).

HJD −2450000	Norm. light	X	σ "	HJD −2450000	Norm. light	X	σ "	HJD −2450000	Norm. light	X	σ "	HJD −2450000	Norm. light	X	σ "	HJD −2450000	Norm. light	X	σ "	HJD −2450000	Norm. light	X	σ "
												u											
1814.0643	1.040	1.1	4.6	1846.9245	1.017	1.1	6.0	2080.8572	1.025	2.2	6.5	2137.8554	1.035	1.7	3.4	2140.0043	0.722	1.3	4.6	2406.2304	1.020	1.4	5.5	2465.9760	0.978	1.6	4.4
1814.0794	1.029	1.1	5.3	1846.9711	1.051	1.1	6.7	2080.9028	1.025	2.1	3.9	2137.8908	1.017	1.6	3.8	2140.0193	0.689	1.2	4.5	2407.7937	0.765	1.9	6.7	2466.0057	0.998	1.5	4.2
1814.0970	1.023	1.1	5.8	1871.1183	1.017	1.4	4.4	2080.9686	0.975	1.8	3.8	2137.9061	1.034	1.5	3.5	2140.0488	0.623	1.2	4.2	2407.8345	0.760	2.1	5.8	2466.0349	1.008	1.4	4.6
1814.1278	1.011	1.2	4.3	1872.9209	1.031	1.1	5.2	2080.9996	0.954	1.7	3.8	2137.9217	1.018	1.5	3.6	2140.0662	0.595	1.2	4.0	2407.8684	0.801	2.2	5.3	2466.0643	1.021	1.4	4.7
1814.1616	0.999	1.2	4.5	1873.0306	1.010	1.3	5.1	2081.0298	0.933	1.6	3.7	2137.9367	1.007	1.4	4.0	2140.0832	0.569	1.2	4.0	2407.9010	0.833	2.2	5.4	2466.1008	1.020	1.3	4.9
1814.2015	0.987	1.3	5.0	1873.1163	0.935	1.4	4.5	2081.1246	0.714	1.4	3.7	2137.9520	1.012	1.4	3.7	2140.0987	0.564	1.2	4.1	2407.9331	0.901	2.2	5.1	2466.1306	1.036	1.2	4.7
1814.8991	1.039	1.3	3.9	1873.1310	0.913	1.5	4.1	2081.1551	0.642	1.3	3.8	2137.9670	0.993	1.4	3.9	2140.1305	0.594	1.1	4.0	2407.9623	0.949	2.2	5.3	2466.1597	1.056	1.2	4.9
1814.9138	1.042	1.2	3.9	1873.1472	0.887	1.6	4.1	2081.1856	0.592	1.2	3.9	2137.9822	0.989	1.3	3.7	2140.1619	0.638	1.1	3.8	2407.9916	0.983	2.1	5.3	2466.2207	1.068	1.1	4.8
1815.0088	1.045	1.1	4.9	1957.8969	0.650	1.5	6.0	2081.2154	0.554	1.2	3.8	2137.9972	0.982	1.3	3.6	2140.1920	0.720	1.1	4.1	2408.0207	0.990	2.0	5.6	2466.2498	1.064	1.1	4.4
1815.0236	1.042	1.1	5.1	1959.8886	0.722	1.5	4.6	2081.2570	0.593	1.2	4.2	2138.0128	0.975	1.3	4.4	2140.2220	0.790	1.2	3.8	2408.0498	1.007	1.9	4.8	2466.2789	1.050	1.1	4.4
1815.0382	1.013	1.1	5.7	1959.9167	0.794	1.6	5.0	2081.2791	0.621	1.1	3.9	2138.0289	0.989	1.2	3.6	2140.2551	0.863	1.2	4.2	2408.0798	1.009	1.8	5.0	2466.7976	0.883	2.2	6.0
1815.0581	1.007	1.1	4.8	1988.8770	1.039	1.7	3.1	2085.9158	0.838	2.0	5.2	2138.0541	0.952	1.2	3.2	2405.8782	0.788	2.2	4.1	2408.1105	1.015	1.7	4.7	2466.8268	0.930	2.1	5.2
1815.1181	1.005	1.2	5.2	1988.8932	1.037	1.8	2.9	2085.9458	0.876	1.9	5.0	2138.0833	0.906	1.2	3.1	2405.9105	0.769	2.2	4.0	2408.1400	1.028	1.6	4.9	2466.8582	0.966	2.0	6.0
1815.1428	0.985	1.2	5.7	1988.9290	0.990	1.9	3.1	2085.9750	0.929	1.8	4.8	2138.1170	0.831	1.1	3.5	2405.9378	0.758	2.2	3.9	2408.1691	1.053	1.5	4.5	2466.8876	0.984	1.9	6.5
1815.1587	0.993	1.2	5.5	1988.9415	1.002	1.9	3.1	2086.0076	0.981	1.6	4.6	2138.1516	0.752	1.1	3.4	2405.9674	0.763	2.2	3.9	2408.2002	1.048	1.4	4.8	2467.1462	1.017	1.2	7.0
1815.1732	0.967	1.2	5.6	2016.8693	0.592	2.0	3.2	2086.0370	0.986	1.6	5.3	2138.2049	0.626	1.1	3.4	2405.9979	0.765	2.1	4.3	2408.7962	0.685	2.0	3.6				
1817.9626	0.864	1.2	6.0	2023.1471	0.881	1.8	4.6	2086.0664	1.002	1.5	5.7	2138.2343	0.581	1.2	3.8	2406.0296	0.796	2.0	4.2	2408.8253	0.759	2.1	4.9				
1818.0216	0.749	1.1	5.9	2023.1779	0.830	1.7	5.0	2086.0962	1.019	1.4	5.1	2139.9085	0.929	1.5	4.2	2406.0759	0.861	1.9	4.1	2408.8583	0.839	2.1	4.8				
1818.0532	0.681	1.1	6.4	2023.2129	0.792	1.5	4.4	2086.1662	1.043	1.2	4.5	2139.9380	0.874	1.4	3.5	2406.1079	0.935	1.7	4.5	2408.8892	0.895	2.2	5.2				
1818.0917	0.594	1.2	5.5	2023.2446	0.771	1.4	4.7	2086.2325	1.038	1.2	5.4	2139.9671	0.815	1.3	4.0	2406.1714	0.988	1.5	5.4	2465.9218	0.887	1.8	4.1				
1818.1628	0.599	1.2	5.6	2080.8399	1.049	2.2	4.5	2137.8252	1.047	1.8	3.3	2139.9876	0.772	1.3	4.4	2406.2010	1.006	1.4	5.7	2465.9467	0.936	1.7	4.1				
												V_J											
1814.1160	1.033	1.2	4.3	1818.1500	0.605	1.2	4.7	1989.0462	0.948	2.2	4.3	2086.0836	1.008	1.4	5.4	2140.2393	0.859	1.2	2.7	2407.9795	0.966	2.1	4.3	2465.9348	0.922	1.8	3.0
1814.1478	1.020	1.2	4.1	1818.1848	0.689	1.3	4.6	1989.0548	0.935	2.2	4.5	2086.1134	1.038	1.3	4.3	2196.0491	0.960	1.1	3.9	2408.0088	0.997	2.1	4.1	2465.9640	0.963	1.7	3.2
1814.1818	1.005	1.2	5.4	1846.9592	1.033	1.1	6.0	1989.0744	0.899	2.2	4.6	2086.1834	1.068	1.2	4.2	2196.0646	0.972	1.2	4.4	2408.0379	1.004	2.0	3.8	2465.9932	0.996	1.6	3.1
1814.9312	1.066	1.2	2.7	1847.0050	1.037	1.1	5.7	1989.0829	0.887	2.2	4.6	2086.2498	1.058	1.1	5.0	2196.0797	0.933	1.2	4.7	2408.0670	1.007	1.9	3.5	2466.0229	1.014	1.5	4.5
1814.9713	1.070	1.2	3.2	1847.0145	1.036	1.2	5.8	1989.1045	0.838	2.2	5.1	2137.8434	1.066	1.7	2.9	2405.8619	0.860	2.1	2.3	2408.0971	1.016	1.8	3.4	2466.0521	1.025	1.4	3.4
1814.9807	1.071	1.2	3.4	1872.9427	1.043	1.2	4.5	1989.1130	0.826	2.2	4.9	2138.0713	0.947	1.2	3.0	2405.8956	0.801	2.2	2.8	2408.1278	1.029	1.6	3.5	2466.0815	1.038	1.3	5.2
1814.9969	1.069	1.1	3.2	1872.9528	1.051	1.2	3.8	1989.1637	0.699	2.0	3.5	2138.1005	0.898	1.2	3.3	2405.9552	0.761	2.2	2.9	2408.1572	1.047	1.5	3.5	2466.1180	1.043	1.2	3.3
1815.0861	1.018	1.1	3.7	1872.9766	1.040	1.2	4.3	1989.1723	0.679	2.0	3.6	2138.1342	0.832	1.1	3.2	2405.9847	0.766	2.1	3.0	2408.1863	1.072	1.5	3.6	2466.1479	1.055	1.2	4.1
1815.0951	1.016	1.1	3.4	1873.0101	1.030	1.2	4.0	1989.1926	0.643	1.9	3.5	2138.1719	0.745	1.1	3.7	2406.0152	0.792	2.1	3.2	2408.2174	1.064	1.4	3.7	2466.2379	1.077	1.1	3.7
1815.1053	1.008	1.2	3.6	1873.0188	1.028	1.2	4.0	1989.2011	0.634	1.9	3.4	2138.1920	0.700	1.1	3.6	2406.0549	0.836	1.9	3.1	2408.2468	1.067	1.3	3.5	2466.2671	1.077	1.1	5.2
1815.2017	0.951	1.3	4.6	1873.0847	0.984	1.4	4.5	1989.2273	0.624	1.8	3.5	2138.2221	0.651	1.2	3.4	2406.0932	0.897	1.8	3.2	2408.2631	1.053	1.3	2.6	2466.2962	1.058	1.1	4.2
1815.2104	0.938	1.3	4.7	1873.0936	0.980	1.4	4.7	1989.2358	0.624	1.8	3.5	2138.2515	0.631	1.2	4.0	2406.1252	0.948	1.7	3.4	2408.8134	0.760	2.0	3.6	2466.8148	0.939	2.2	4.6
1817.9351	0.932	1.2	5.6	1959.9052	0.799	1.5	3.6	2023.1944	0.808	1.6	3.3	2139.8893	0.977	1.6	3.8	2406.1546	0.984	1.6	3.6	2408.8425	0.823	2.1	3.5	2466.8440	0.953	2.1	4.2
1817.9504	0.902	1.2	5.0	1959.9333	0.867	1.6	3.7	2023.2295	0.773	1.5	3.3	2139.9257	0.922	1.4	3.1	2406.1887	1.001	1.5	4.5	2408.8756	0.881	2.2	3.7	2466.8754	0.987	2.0	4.8
1817.9813	0.860	1.2	4.6	1988.9452	1.007	2.0	2.4	2023.2611	0.747	1.4	4.2	2139.9552	0.868	1.4	3.1	2406.2183	1.010	1.4	4.9	2408.9064	0.925	2.2	4.0	2466.9049	0.992	1.9	6.3
1818.0093	0.805	1.1	4.5	1988.9537	1.002	2.0	2.6	2085.9330	0.879	1.9	4.7	2140.0368	0.684	1.2	3.5	2406.2478	1.025	1.3	4.5	2463.8447	0.711	2.1	2.9	2466.9648	1.016	1.6	5.4
1818.1144	0.606	1.2	4.4	1988.9764	0.993	2.1	2.7	2085.9630	0.930	1.8	4.3	2140.1174	0.634	1.1	2.9	2407.8517	0.772	2.1	3.8	2463.8598	0.685	2.1	3.9	2466.9980	1.045	1.5	5.6
1818.1234	0.609	1.2	4.4	1988.9850	0.991	2.1	2.7	2085.9922	0.964	1.7	5.7	2140.1477	0.671	1.1	2.9	2407.8856	0.813	2.2	3.8	2464.1232	0.985	1.2	5.1	2467.1635	1.049	1.2	6.0
1818.1322	0.605	1.2	4.5	1989.0054	0.981	2.1	2.9	2086.0249	0.986	1.6	5.5	2140.1791	0.727	1.1	3.2	2407.9182	0.862	2.2	4.3	2464.1391	0.989	1.2	5.8				
1818.1413	0.607	1.2	4.4	1989.0139	0.975	2.2	3.4	2086.0542	1.003	1.5	5.1	2140.2092	0.790	1.2	3.1	2407.9504	0.923	2.2	4.0	2465.9092	0.877	1.9	2.8				
												I_C											
1814.1073	1.041	1.2	3.5	1846.9345	1.069	1.1	4.8	1873.0466	1.018	1.3	4.7	1989.2080	0.626	1.9	3.1	2138.2149	0.674	1.2	2.8	2406.2406	1.041	1.3	3.7	2464.1319	0.983	1.2	2.9
1814.1387	1.037	1.2	3.6	1846.9802	1.060	1.1	5.7	1873.0710	1.007	1.3	4.3	1989.2131	0.636	1.9	3.0	2138.2443	0.641	1.2	3.0	2407.8037	0.746	2.0	4.5	2465.9568	0.979	1.7	3.2
1814.1730	1.023	1.2	4.2	1846.9970	1.058	1.1	6.0	1873.0762	1.003	1.4	3.7	2016.8974	0.708	2.1	2.3	2138.2592	0.634	1.2	3.3	2407.8445	0.784	2.1	2.8	2465.9861	0.999	1.6	3.1
1814.1910	1.016	1.3	4.0	1847.0217	1.048	1.2	6.3	1873.1008	0.983	1.4	3.9	2023.1572	0.870	1.7	3.3	2139.9186	0.953	1.5	2.7	2407.8784	0.808	2.2	4.8	2466.0158	1.022	1.5	3.4
1814.2123	1.007	1.3	3.5	1847.0329	1.069	1.2	5.7	1873.1061	0.979	1.4	4.0	2023.1876	0.824	1.6	3.5	2139.9480	0.888	1.4	2.6	2407.9111	0.863	2.2	4.6	2466.0450	1.035	1.4	3.6
1814.9240	1.086	1.2	2.6	1847.0392	1.060	1.2	5.8	1957.0343	0.738	2.0	6.5	2023.2226	0.790	1.5	3.1	2140.0296	0.714	1.2	3.0	2407.9432	0.913	2.2	2.9	2466.0744	1.066	1.3	4.5
1814.9532	1.084	1.2	3.0	1847.0445	1.049	1.2	5.7	1959.8983	0.800	1.5	3.6	2023.2543	0.768	1.4	3.6	2140.1102	0.644	1.1	2.5	2407.9723	0.973	2.2	3.1	2466.1109	1.048	1.3	4.6
1814.9589	1.076	1.2	4.1	1847.0501	1.061	1.2	6.3	1959.9265	0.873	1.6	4.1	2085.9258	0.876	1.9	4.0	2140.1406	0.671	1.1	3.0	2408.0017	1.003	2.1	3.2	2466.1407	1.086	1.2	4.1
1814.9642	1.087	1.2	3.6	1847.0557	1.072	1.2	5.8	1988.9606	1.005	2.0	2.5	2085.9558	0.934	1.8	4.1	2140.1719	0.729	1.1	3.2	2408.0307	1.019	2.0	3.2	2466.1698	1.095	1.2	5.8
1815.0685	1.043	1.1	3.7	1847.0618	1.072	1.2	6.0	1988.9657	1.004	2.0	2.5	2085.9850	0.976	1.7	3.7	2140.2020	0.783	1.1	3.0	2408.0599	1.028	1.9	3.4	2466.2308	1.095	1.1	4.2
1815.0737	1.045	1.1	3.5	1847.0677	1.057	1.2	6.4	1988.9919	0.996	2.1	2.8	2086.0177	0.999	1.6	3.4	2140.2321	0.855	1.2	3.4	2408.0899	1.028	1.8	3.4	2466.2599	1.099	1.1	4.6
1815.0790	1.034	1.1	3.5	1847.1041	1.056	1.3	6.3	1988.9969	0.998	2.1	3.0	2086.0471	1.023	1.5	4.6	2140.2652	0.924	1.2	3.5	2408.1206	1.048	1.7	3.3	2466.8077	0.916	2.2	4.6
1815.1843	0.980	1.2	4.4	1871.1290	1.054	1.5	3.7	1989.0208	0.991	2.2	3.7	2086.0764	1.034	1.4	4.4	2196.0226	0.979	1.1	3.9	2408.1501	1.060	1.6	3.9	2466.8369	0.984	2.1	4.5
1815.1895	0.978	1.3	4.8	1871.1344	1.049	1.5	3.8	1989.0259	0.975	2.2	3.4	2086.1062	1.059	1.4	3.7	2405.9207	0.790	2.2	3.8	2408.1792	1.066	1.5	2.9	2466.8682	1.001	2.0	4.3
1815.1947	0.977	1.3	5.0	1871.1399	1.048	1.5	3.7	1989.0375	0.973	2.2	3.7	2086.1763	1.095	1.2	4.0	2405.9480	0.779	2.2	3.6	2408.2102	1.097	1.4	3.1	2466.8977	1.013	1.9	4.8
1817.9271	0.961	1.2	4.4	1871.1460	1.036	1.5	3.9	1989.0617	0.928	2.2	4.5	2086.2426	1.086	1.2	6.5	2405.9776	0.774	2.2	4.0	2408.2396	1.097	1.3	3.8	2466.9576	1.036	1.7	4.5
1817.9432	0.940	1.2	5.0	1872.9336	1.065	1.1	3.9	1989.0667	0.927	2.2	4.8	2137.8362	1.094	1.8	2.3	2406.0081	0.797	2.1	3.5	2408.2559	1.095	1.3	4.1	2467.1563	1.057	1.2	4.0
1817.9726	0.892	1.2	4.8	1872.9634	1.055	1.2	3.5	1989.0898	0.886	2.2	5.1	2138.0641	0.977	1.2	2.2	2406.0477	0.829	2.0	3.4	2408.8063	0.762	2.0	4.9				
1817.9917	0.854	1.1	4.4	1872.9687	1.051	1.2	4.3	1989.0949	0.872	2.2	5.6	2138.0933	0.928	1.2	2.4	2406.1181	0.975	1.7	3.2	2408.8354	0.830	2.1	5.3				
1817.9973	0.846	1.1	4.3	1872.9838	1.047	1.2	4.4	1989.1199	0.799	2.2	5.1	2138.1271	0.859	1.1	2.6	2406.1475	0.999	1.6	3.0	2408.8684	0.884	2.2	5.5				
1818.1019	0.645	1.2	4.5	1872.9898	1.051	1.2	3.9	1989.1792	0.678	2.0	3.1	2138.1647	0.766	1.1	2.9	2406.1816	1.019	1.5	2.7	2463.8376	0.749	2.1	2.8				
1818.1073	0.643	1.2	4.6	1873.0412	1.027	1.3	4.9	1989.1842	0.667	2.0	3.3	2138.1848	0.719	1.1	3.1	2406.2111	1.029	1.4	3.5	2464.1160	0.955	1.3	3.0				

CCD photometry of variable stars in the Magellanic Clouds – VII. The eclipsing binaries MACHO*05:36:48.7−69:17:00 in the LMC and MOA J005018.4−723855 & J005623.5−722123 in the SMC

G.P. Bayne, W. Tobin, J.D. Pritchard, K.R. Pollard and M.D. Albrow

Table 3. Photometry of MOA J005623.5−722123. The columns are Heliocentric Julian Day of mid exposure, normalized light, airmass (X) and FWHM seeing in arcsec (σ).

HJD −2450000	Norm. light	X	σ "	HJD −2450000	Norm. light	X	σ "	HJD −2450000	Norm. light	X	σ "	HJD −2450000	Norm. light	X	σ "	HJD −2450000	Norm. light	X	σ "	HJD −2450000	Norm. light	X	σ "
												u											
1813.9024	0.934	1.3	5.2	1959.0348	0.715	2.0	4.4	2018.0459	0.961	2.2	4.1	2085.1889	0.988	1.2	4.9	2171.1045	0.981	1.1	5.0	2199.1792	0.631	1.3	6.6	2462.1265	1.001	1.3	5.8
1813.9511	0.865	1.2	4.7	1959.0534	0.671	2.0	5.1	2018.0968	0.905	2.0	4.1	2085.2184	0.989	1.2	5.8	2171.1342	0.962	1.2	3.9	2406.7959	0.723	1.9	4.1	2462.1849	0.988	1.2	6.2
1814.0133	0.739	1.1	4.8	1959.0883	0.607	2.2	4.6	2018.1314	0.838	1.9	4.7	2085.2486	0.977	1.2	4.7	2171.1637	0.954	1.2	4.7	2406.8256	0.655	2.0	4.5	2462.2141	0.982	1.2	6.2
1816.9903	1.011	1.1	6.9	1959.1198	0.600	2.2	4.1	2018.1631	0.759	1.8	5.8	2141.8607	1.003	1.6	6.5	2171.1947	0.935	1.2	5.1	2406.8553	0.597	2.1	4.8	2462.2447	0.989	1.1	5.0
1817.0886	1.008	1.1	6.1	1959.1485	0.596	2.2	4.3	2045.1861	0.960	1.4	5.3	2141.9224	1.003	1.4	5.4	2171.8375	0.996	1.5	3.6	2406.8877	0.588	2.2	4.4	2462.2755	0.960	1.1	4.8
1817.1055	1.010	1.2	6.2	1959.1782	0.656	2.2	3.8	2045.2213	0.967	1.4	6.4	2141.9521	1.003	1.4	5.4	2171.8670	1.007	1.4	3.9	2407.0880	0.919	1.8	5.0	2462.7976	0.953	2.2	4.1
1817.1203	0.989	1.2	4.8	1961.8975	1.001	1.5	3.2	2082.8722	0.988	2.2	5.9	2141.9828	1.003	1.3	6.0	2171.8994	1.010	1.3	3.2	2407.1179	0.952	1.7	7.0	2462.8267	0.962	2.2	4.4
1843.0780	0.599	1.2	6.6	1961.9283	1.006	1.6	3.7	2082.9496	0.975	1.9	4.2	2142.0120	0.997	1.2	5.5	2171.9286	1.009	1.2	3.4	2407.1537	0.968	1.6	3.8	2462.9905	0.984	1.6	4.9
1843.0925	0.590	1.2	6.0	1961.9797	0.986	1.8	4.7	2082.9791	0.970	1.8	4.7	2142.0607	0.980	1.2	5.7	2171.9587	1.007	1.2	3.0	2407.1828	0.963	1.5	3.8	2463.0198	0.994	1.5	4.7
1843.1498	0.592	1.3	4.9	1962.1498	0.997	2.2	6.0	2083.0120	0.941	1.7	3.9	2142.0917	0.989	1.2	4.4	2171.9879	1.014	1.2	3.2	2407.2191	0.987	1.4	3.7	2463.0488	0.995	1.4	5.0
1843.9472	0.983	1.1	5.1	1962.1779	0.983	2.2	6.1	2083.0719	0.838	1.5	4.3	2142.1214	0.971	1.1	4.4	2172.0171	1.020	1.1	3.5	2407.2482	0.989	1.3	4.1	2463.0779	0.992	1.4	4.5
1843.9617	0.978	1.1	4.4	1990.9106	0.999	1.9	3.9	2083.1015	0.810	1.4	4.9	2142.1602	0.975	1.1	4.3	2172.0462	1.001	1.1	3.7	2460.9260	0.991	1.9	4.8	2463.1073	1.003	1.3	4.4
1844.0074	0.963	1.1	3.9	1990.9249	0.998	1.9	3.8	2083.1374	0.724	1.3	5.0	2142.1923	0.936	1.1	4.6	2172.0808	1.008	1.1	3.0	2460.9551	0.987	1.8	4.1	2463.1367	0.994	1.2	3.8
1844.0219	0.964	1.1	4.4	1990.9753	1.009	2.1	3.9	2083.1682	0.656	1.3	4.9	2142.2221	0.905	1.2	4.1	2172.1103	1.001	1.1	2.6	2460.9847	0.987	1.7	3.9	2463.2899	0.987	1.1	3.5
1844.0661	0.945	1.2	4.6	1990.9896	1.003	2.1	3.3	2083.1983	0.595	1.2	4.4	2142.2514	0.850	1.2	4.3	2172.1397	1.001	1.2	2.9	2461.0143	0.972	1.6	4.6	2464.7935	0.750	2.2	4.2
1844.0806	0.928	1.2	3.9	1991.0200	1.005	2.2	3.2	2083.8833	1.003	2.1	6.2	2169.9538	0.980	1.2	6.1	2172.1688	0.994	1.2	3.1	2461.0437	0.972	1.5	4.4	2464.8227	0.674	2.2	4.4
1873.9438	1.012	1.1	4.8	1991.0343	1.009	2.2	3.0	2084.8198	1.005	2.2	4.9	2169.9831	0.960	1.2	6.7	2172.1992	0.990	1.2	3.3	2461.0730	0.973	1.4	4.8	2464.8529	0.630	2.1	4.0
1873.9771	1.009	1.2	5.4	1991.0656	1.003	2.2	3.4	2084.8507	0.991	2.2	5.6	2170.1365	0.751	1.2	4.9	2198.8725	0.988	1.2	6.5	2461.1031	0.951	1.3	4.9	2464.8844	0.604	2.0	3.2
1874.0252	1.001	1.2	5.8	1991.0799	1.003	2.2	3.6	2084.8806	1.001	2.1	6.1	2170.1512	0.733	1.2	4.4	2198.9019	0.981	1.2	6.6	2461.2273	0.897	1.1	5.1	2464.9146	0.600	1.9	3.6
1874.0573	0.994	1.3	6.3	1991.1081	0.995	2.2	3.6	2084.9150	1.025	2.0	6.2	2170.8606	1.001	1.4	5.1	2198.9344	0.981	1.2	3.6	2461.2565	0.847	1.1	5.3	2464.9439	0.649	1.8	3.4
1874.9589	1.008	1.2	3.4	1991.1530	0.993	2.1	4.0	2084.9782	1.010	1.8	4.4	2170.8899	1.004	1.3	5.3	2198.9639	0.977	1.1	3.2	2461.9179	1.001	1.9	6.5	2464.9739	0.713	1.7	3.4
1874.9735	1.015	1.2	4.0	2017.1015	0.607	2.0	2.7	2085.0078	1.011	1.7	4.4	2170.9212	1.003	1.3	4.7	2198.9981	0.960	1.1	4.1	2461.9470	1.004	1.8	6.1	2465.0039	0.797	1.6	3.5
1874.9886	1.009	1.2	4.0	2017.8567	0.992	1.9	3.1	2085.0371	1.012	1.6	4.6	2170.9554	1.003	1.2	5.0	2199.0329	0.952	1.1	4.6	2461.9763	1.010	1.7	5.8	2465.0329	0.845	1.5	4.0
1875.0323	1.008	1.3	5.3	2017.8735	0.994	2.0	3.2	2085.0664	1.006	1.5	4.9	2170.9846	0.995	1.2	5.0	2199.0627	0.888	1.2	5.7	2462.0055	1.006	1.6	5.8	2465.0621	0.894	1.4	3.7
1933.1368	1.011	2.1	6.1	2017.9481	0.983	2.2	3.7	2085.0977	1.006	1.4	4.7	2171.0141	0.996	1.2	5.2	2199.0919	0.837	1.2	5.8	2462.0347	1.005	1.5	5.6				
1958.9122	0.944	1.5	5.2	2017.9673	0.971	2.2	4.1	2085.1279	1.001	1.3	4.4	2171.0432	0.982	1.1	5.3	2199.1210	0.752	1.2	5.4	2462.0647	1.004	1.4	5.3				
1959.0053	0.785	1.9	4.1	2018.0257	0.980	2.2	3.7	2085.1573	0.993	1.3	5.1	2171.0752	0.984	1.1	5.0	2199.1501	0.683	1.3	5.4	2462.0940	1.003	1.3	5.2				
												V_J											
1813.9388	0.897	1.2	3.8	1959.1364	0.609	2.2	3.7	2045.1047	0.846	1.7	4.2	2085.0543	1.010	1.5	3.6	2171.0018	0.989	1.2	3.9	2199.1673	0.680	1.3	4.5	2462.2927	0.974	1.1	3.6
1813.9730	0.826	1.2	6.7	1959.1650	0.638	2.2	2.8	2045.1208	0.882	1.7	3.9	2085.0836	1.002	1.4	3.6	2171.0313	0.983	1.1	3.8	2199.1964	0.623	1.4	4.1	2462.7798	0.935	2.2	3.5
1814.0287	0.711	1.1	3.6	1959.1948	0.698	2.2	3.2	2045.1369	0.902	1.6	5.1	2085.1149	0.996	1.4	3.2	2171.0604	0.983	1.1	4.3	2406.8131	0.694	2.0	3.0	2462.8148	0.969	2.2	3.8
1816.9682	1.010	1.2	5.3	1961.9140	0.998	1.6	2.8	2045.1524	0.925	1.6	5.0	2085.1451	0.990	1.3	4.3	2171.0924	0.973	1.1	3.7	2406.8724	0.603	2.2	3.6	2462.8532	0.974	2.1	4.4
1817.0203	1.002	1.1	6.7	1961.9449	0.992	1.7	4.4	2045.1681	0.941	1.5	4.9	2085.1745	0.985	1.2	3.4	2171.1217	0.965	1.1	2.8	2407.1052	0.938	1.8	3.6	2462.8621	0.968	2.1	4.8
1817.0292	1.012	1.1	6.0	1962.1663	0.993	2.2	5.2	2045.2078	0.966	1.4	4.8	2085.2061	0.980	1.2	3.9	2171.1514	0.961	1.2	3.3	2407.1350	0.952	1.6	5.5	2462.8730	0.971	2.0	4.4
1817.0412	1.012	1.1	6.1	1962.1944	0.986	2.2	4.8	2045.2407	0.977	1.3	5.8	2085.2356	0.973	1.2	3.3	2171.1808	0.949	1.2	3.9	2407.1708	0.955	1.5	2.7	2462.9663	0.994	1.7	4.8
1817.1605	0.998	1.2	3.9	1990.9414	1.024	2.0	2.9	2045.2583	0.970	1.3	5.0	2085.2657	0.968	1.1	4.0	2171.8547	0.996	1.4	2.7	2407.2000	0.962	1.4	2.7	2462.9756	0.987	1.7	4.5
1817.1736	0.989	1.2	4.7	1990.9632	1.005	2.0	3.2	2045.2731	0.976	1.2	5.2	2085.2818	0.963	1.1	3.4	2171.8842	1.002	1.3	2.5	2407.2363	0.967	1.4	2.6	2463.0077	0.999	1.6	3.3
1817.1847	1.004	1.2	3.9	1991.0061	1.005	2.2	2.8	2082.8273	0.992	2.2	5.4	2141.9071	1.005	1.5	5.0	2171.9166	1.000	1.3	2.3	2460.9431	0.997	1.8	3.3	2463.0369	1.003	1.5	3.9
1843.1149	0.591	1.3	5.8	1991.0508	1.009	2.2	2.4	2082.8600	0.973	2.2	5.1	2141.9395	1.000	1.4	4.3	2171.9458	1.003	1.2	2.1	2460.9723	0.989	1.7	2.7	2463.0660	1.000	1.4	3.9
1843.1236	0.586	1.3	5.9	1991.0964	0.999	2.2	2.8	2082.9378	0.971	2.0	4.2	2141.9693	0.998	1.3	5.0	2171.9759	1.002	1.2	2.1	2461.0019	0.987	1.6	3.1	2463.0951	1.004	1.3	3.2
1843.9853	0.969	1.1	3.6	1991.1245	1.000	2.2	2.8	2082.9672	0.968	1.9	3.7	2142.0000	0.992	1.3	4.8	2172.0051	1.006	1.2	2.2	2461.0315	0.982	1.5	3.8	2463.1245	0.999	1.3	2.9
1843.9957	0.971	1.1	3.7	1991.1382	1.000	2.1	3.2	2083.0002	0.958	1.7	3.4	2142.0291	0.989	1.2	4.8	2172.0343	1.002	1.1	2.3	2461.0608	0.959	1.4	3.7	2463.1538	1.003	1.2	3.2
1844.0445	0.958	1.2	2.7	1991.1694	0.996	2.0	2.8	2083.0300	0.931	1.6	4.0	2142.0779	0.976	1.2	3.6	2172.0634	1.002	1.1	2.7	2461.0902	0.965	1.3	3.4	2464.8106	0.715	2.2	4.2
1844.0533	0.956	1.2	3.0	1991.1831	0.991	2.0	2.9	2083.0601	0.898	1.5	3.4	2142.1089	0.968	1.1	3.4	2172.0980	0.995	1.1	2.2	2461.1202	0.960	1.3	3.0	2464.8399	0.651	2.1	3.1
1844.1306	0.857	1.3	3.1	1991.1980	0.993	1.9	3.0	2083.0896	0.843	1.4	4.3	2142.1386	0.964	1.1	3.4	2172.1275	0.995	1.1	2.1	2461.2445	0.879	1.1	3.8	2464.8701	0.610	2.0	3.1
1873.9653	0.996	1.2	4.5	1991.2117	0.986	1.9	2.6	2083.1256	0.769	1.3	3.9	2142.1775	0.951	1.1	3.3	2172.1569	0.992	1.2	2.5	2461.9059	1.009	1.9	5.7	2464.9016	0.607	1.9	3.1
1874.0127	1.009	1.2	4.4	2017.0753	0.638	2.1	2.2	2083.1564	0.701	1.3	4.2	2142.2095	0.922	1.1	3.5	2172.1860	0.984	1.2	2.2	2461.9351	1.012	1.8	5.7	2464.9318	0.630	1.8	2.4
1874.0428	0.991	1.3	4.7	2017.0871	0.618	2.1	2.2	2083.1865	0.640	1.2	3.8	2142.2393	0.878	1.2	3.1	2172.2164	0.985	1.3	2.7	2461.9642	1.007	1.7	5.2	2464.9610	0.687	1.7	2.9
1874.1181	0.988	1.5	5.8	2017.8951	0.981	2.1	2.7	2083.2881	0.630	1.1	3.1	2169.9710	0.964	1.2	5.2	2172.2284	0.978	1.3	2.5	2461.9935	1.007	1.6	5.0	2464.9910	0.755	1.6	2.7
1875.0119	1.012	1.2	3.2	2017.9179	0.980	2.1	2.7	2083.9005	1.011	2.1	6.5	2170.0003	0.958	1.2	5.4	2198.8897	0.979	1.2	5.1	2462.0227	1.012	1.5	5.0	2465.0210	0.820	1.5	2.9
1875.0206	1.011	1.2	3.8	2017.9359	0.970	2.2	2.8	2083.9354	0.998	2.0	5.4	2170.0319	0.942	1.1	5.9	2198.9191	0.974	1.2	5.2	2462.0519	1.009	1.4	4.2	2465.0501	0.874	1.4	3.5
1875.0749	1.003	1.4	5.5	2017.9863	0.965	2.2	3.0	2084.8370	0.999	2.2	3.7	2170.0695	0.886	1.1	6.2	2198.9516	0.967	1.1	2.3	2462.0819	0.997	1.4	4.2	2465.0792	0.919	1.3	2.8
1932.9398	0.991	1.4	6.9	2018.0123	0.958	2.2	3.1	2084.8679	1.002	2.2	4.7	2170.1075	0.825	1.1	6.4	2198.9810	0.962	1.1	2.7	2462.1111	1.001	1.3	3.5				
1932.9516	1.022	1.4	6.3	2018.0656	0.941	2.1	3.0	2084.8977	1.011	2.1	4.9	2170.1738	0.682	1.2	4.1	2199.0208	0.951	1.1	3.3	2462.1437	0.998	1.2	5.1				
1932.9659	1.020	1.5	6.6	2018.0814	0.926	2.1	3.1	2084.9321	1.006	2.0	5.3	2170.1827	0.661	1.2	3.8	2199.0501	0.913	1.1	4.2	2462.1730	0.991	1.2	5.6				
1932.9758	1.009	1.5	6.9	2018.1177	0.862	2.0	4.1	2084.9614	1.016	1.9	5.5	2170.8778	1.006	1.4	4.3	2199.0799	0.863	1.2	5.9	2462.2021	0.985	1.2	4.6				
1958.9287	0.927	1.6	3.9	2018.1505	0.805	1.8	4.2	2084.9955	1.010	1.7	3.7	2170.9384	0.998	1.2	4.3	2199.1090	0.808	1.2	4.4	2462.2313	0.977	1.1	3.8				
1959.1049	0.606	2.2	3.2	2018.1902	0.709	1.7	5.2	2085.0249	1.011	1.6	3.8	2170.9726	0.993	1.2	4.9	2199.1382	0.734	1.2	4.5	2462.2618	0.967	1.1	3.5				
												I_C											
1813.9311	0.954	1.2	3.1	1959.0981	0.653	2.2	3.3	2018.1423	0.865	1.9	4.2	2084.8299	1.028	2.2	3.9	2169.9932	1.005	1.2	5.7	2198.8826	1.017	1.2	5.4	2462.0747	1.034	1.4	3.9
1813.9619	0.899	1.2	6.9	1959.1296	0.652	2.2	3.0	2018.1737	0.812	1.7	4.7	2084.8608	1.017	2.2	4.7	2170.0248	0.979	1.1	6.2	2198.9120	1.003	1.2	5.6	2462.1040	1.032	1.3	3.9
1813.9805	0.861	1.2	3.6	1959.1583	0.685	2.2	2.9	2045.0969	0.884	1.8	4.8	2084.8906	1.044	2.1	4.9	2170.0624	0.960	1.1	6.2	2198.9445	1.007	1.1	2.2	2462.1365	1.034	1.2	4.9
1813.9894	0.846	1.2	3.1	1959.1880	0.726	2.2	2.9	2045.1134	0.906	1.7	3.6	2084.9250	1.052	2.0	5.6	2170.1004	0.890	1.1	6.9	2198.9739	1.000	1.1	2.0	2462.1658	1.015	1.2	5.2
1813.9950	0.834	1.1	3.2	1961.9072	1.051	1.6	2.8	2045.1288	0.946	1.6	5.7	2084.9543	1.024	1.9	5.7	2170.1613	0.753	1.2	3.2	2199.0137	0.998	1.1	2.9	2462.1949	1.011	1.2	4.5
1816.9610	1.028	1.2	4.5	1961.9381	1.038	1.6	2.8	2045.1450	0.953	1.6	5.3	2084.9883	1.042	1.8	3.2	2170.1667	0.741	1.2	3.1	2199.1019	0.880	1.2	4.4	2462.2241	1.014	1.1	4.5
1816.9788	1.033	1.2	5.3	1961.9894	1.037	1.9	3.7	2045.1605	0.972	1.5	5.1	2085.0178	1.035	1.6	3.6	2170.8706	1.042	1.4	4.1	2199.1602	0.746	1.3	4.3	2462.2547	1.011	1.1	3.5
1817.0089	1.024	1.1	6.5	1962.0200	1.045	2.0	3.1	2045.1758	0.989	1.5	4.4	2085.0472	1.034	1.5	3.3	2170.9313	1.043	1.2	4.1	2199.1893	0.691	1.4	4.4	2462.2855	1.000	1.1	3.8
1817.0529	1.017	1.1	6.5	1962.1595	1.027	2.2	4.9	2045.2005	0.999	1.4	4.3	2085.0765	1.044	1.4	3.5	2170.9654	1.025	1.2	3.8	2406.8054	0.751	2.0	3.1	2462.7870	0.977	2.2	3.2
1817.0765	1.024	1.1	5.7	1962.1877	1.020	2.2	5.2	2045.2318	0.988	1.3	5.2	2085.1078	1.036	1.4	3.2	2170.9947	1.020	1.2	4.0	2406.8352	0.687	2.1	3.7	2462.8075	0.999	2.2	3.4
1817.1318	1.020	1.2	4.0	1990.9347	1.032	1.9	2.6	2045.2503	1.006	1.3	6.0	2085.1379	1.030	1.3	3.4	2171.0242	1.009	1.1	4.2	2406.8648	0.654	2.2	3.5	2463.0005	1.029	1.6	3.6
1817.1401	1.032	1.2	3.8	1990.9564	1.038	2.0	2.8	2045.2657	1.007	1.3	5.5	2085.1673	1.020	1.2	3.3	2171.0533	1.011	1.1	4.2	2407.0975	0.971	1.8	3.4	2463.0297	1.033	1.5	3.4
1843.1028	0.669	1.2	4.0	1990.9993	1.041	2.1	2.4	2082.8002	1.018	2.2	4.6	2085.1989	1.017	1.2	3.7	2171.0853	1.002	1.1	4.0	2407.1632	0.990	1.6	2.7	2463.0588	1.026	1.4	3.8
1843.1079	0.661	1.2	4.2	1991.0440	1.033	2.2	2.3	2082.8823	1.008	2.1	4.4	2085.2285	1.020	1.2	3.2	2171.1146	0.998	1.1	3.2	2407.1923	0.991	1.5	2.7	2463.0878	1.037	1.3	3.7
1843.1667	0.696	1.4	3.6	1991.0896	1.035	2.2	2.6	2082.9121	1.014	2.1	3.7	2085.2586	1.006	1.1	3.7	2171.1443	0.995	1.2	2.9	2407.2286	0.999	1.4	2.7	2463.1172	1.041	1.3	2.6
1843.1719	0.714	1.4	3.8	1991.1178	1.040	2.2	2.5	2082.9891	0.999	1.8	3.1	2085.2747	1.006	1.1	3.1	2171.1737	0.987	1.2	3.9	2407.2577	1.001	1.3	3.0	2463.2990	1.024	1.1	2.2
1843.9717	1.008	1.1	3.5	1991.1314	1.031	2.1	2.9	2083.0221	1.005	1.6	2.8	2085.2904	1.005	1.1	3.1	2171.2048	0.963	1.2	4.5	2407.2722	1.025	1.3	3.4	2464.8035	0.778	2.2	3.6
1843.9781	0.999	1.1	3.4	1991.1627	1.029	2.1	2.8	2083.0519	0.954	1.6	3.0	2141.9000	1.020	1.5	5.6	2171.2193	0.946	1.3	4.7	2460.9360	1.038	1.8	3.0	2464.8328	0.712	2.2	2.9
1844.0319	0.996	1.2	2.6	1991.1763	1.026	2.0	2.9	2083.0820	0.889	1.4	3.6	2141.9324	1.033	1.4	4.1	2171.8476	1.036	1.4	2.7	2460.9652	1.034	1.7	2.4	2464.8630	0.660	2.1	3.1
1844.0371	1.001	1.2	2.5	1991.1913	1.028	2.0	2.9	2083.1115	0.841	1.4	4.1	2141.9622	1.021	1.4	5.2	2171.8771	1.034	1.4	2.6	2460.9948	1.018	1.6	3.3	2464.8944	0.661	2.0	2.7
1844.1183	0.905	1.3	2.6	1991.2049	1.022	1.9	2.7	2083.1475	0.765	1.3	3.5	2141.9929	1.024	1.3	4.7	2171.9095	1.033	1.3	2.4	2461.0244	1.026	1.5	3.7	2464.9247	0.673	1.8	2.4
1844.1236	0.904	1.3	2.5	2017.0487	0.738	2.2	2.0	2083.1783	0.696	1.2	3.4	2142.0220	1.026	1.2	4.4	2171.9387	1.041	1.2	2.2	2461.0537	1.002	1.4	3.2	2464.9539	0.721	1.7	2.7
1873.9539	1.039	1.2	5.9	2017.0677	0.703	2.1	2.2	2083.2083	0.666	1.2	3.0	2142.0708	1.005	1.2	4.3	2171.9980	1.038	1.2	2.2	2461.0831	1.011	1.4	3.6	2464.9839	0.780	1.6	2.3
1873.9956	1.028	1.2	4.3	2017.8861	1.017	2.0	2.3	2083.2603	0.645	1.1	3.4	2142.1018	1.009	1.1	3.1	2172.0272	1.036	1.1	2.4	2461.1131	1.008	1.3	3.4	2465.0139	0.847	1.5	2.3
1874.0358	1.031	1.3	4.8	2017.9264	1.015	2.2	2.5	2083.2658	0.647	1.1	3.1	2142.1315	1.005	1.1	3.3	2172.0563	1.039	1.1	2.6	2461.8988	1.013	2.0	5.6	2465.0430	0.905	1.4	3.2
1874.0674	1.026	1.3	5.8	2017.9778	0.997	2.2	3.2	2083.2713	0.649	1.1	2.6	2142.1704	0.993	1.1	3.0	2172.0908	1.032	1.1	2.1	2461.9279	1.028	1.9	4.9	2465.0721	0.947	1.4	2.9
1874.9996	1.040	1.2	3.0	2017.9996	1.002	2.2	2.3	2083.2809	0.664	1.1	2.6	2142.2024	0.967	1.1	3.1	2172.1204	1.034	1.1	2.1	2461.9570	1.035	1.8	4.4				
1875.0049	1.041	1.2	3.2	2018.0572	0.981	2.1	3.1	2083.2965	0.691	1.1	2.9	2142.2321	0.925	1.2	2.9	2172.1498	1.028	1.2	2.6	2461.9863	1.041	1.6	4.5				
1875.0443

Appendix I

Glossary

AGAPE	Andromeda Galaxy and Amplified Pixels Experiment
A_V	Interstellar extinction in V
arcsec	Seconds of arc, used as a unit for the value of the seeing
AU	Astronomical Unit; 1 AU $= 1.496 \times 10^{11}$ m
b	Strömgren b filter
BC	Bolometric Correction
CCD	Charged Coupled Device
DIA	Difference Imaging Analysis
DSS	Digital Sky Survey
DUO	Disk Unseen Objects
EB	Eclipsing Binary
EROS	Expérience de Recherche d'Objets Sombres
ESO	European Southern Observatory
FWHM	Full-Width at Half Maximum
GHRS	Goddard High Resolution Spectrograph
H_2	Molecular hydrogen
HI	Neutral hydrogen
HII	Ionized hydrogen
HJD	Heliocentric Julian Date
HMJD	Heliocentric Mean Julian Date
HR	Hertzsprung Russell
HST	Hubble Space Telescope
IAP	Institut d'Astrophysique de Paris
IAU	International Astronomical Union
I_C	Cousins I filter
ISIS	Data reduction package based on a image subtraction method
ISM	Interstellar Medium
IUE	International Ultraviolet Explorer (NASA, UK and ESA)
JD	Julian date
$L_\odot$	Solar Luminosity $= 3.82 \times 10^{26}$ Js^{-1}
LMC	Large Magellanic Cloud
$M_\odot$	Solar Mass $= 1.99 \times 10^{30}$ kg
$M_{bol\odot}$	Solar bolometric magnitude $= 4.6$ mag.
MACHO	MAssive Compact Halo Objects
MCEB	Magellanic Cloud Eclipsing Binary
MJUO	Mount John University Observatory
MNRAS	Monthly Notices of the Royal Astronomical Society
MOA	Microlensing Observations in Astrophysics
OGLE	Optical Gravitational Lensing Experiment
PSF	Point Spread Function

$R_\odot$	Solar Radius $= 6.96 \times 10^8$ m
SMC	Small Magellanic Cloud
SWPLD	Short Wavelength Primary Low Dispersion
TAMS	Terminal-Age Main Sequence
u	Str¨omgren u filter
UV	Ultra Violet
UVES	Ultra Violet Echelle Spectrograph
v	Strömgren v filter
V_J	Johnson V filter
VLT	Very Large Telescope
WD95	Wilson and Devinney software package, modified 1995 version, for computing eclipsing binary light curves
y	Strömgren y filter
ZAMS	Zero Age Main Sequence

Bibliography

[1] C. Akerlof, C. Alcock, R. Allsman, T. Axelrod, D. P. Bennett, K. H. Cook, K. Freeman, K. Griest, S. Marshall, H.-S. Park, S. Perlmutter, B. Peterson, P. Quinn, J. Reimann, A. Rodgers, C. W. Stubbs and W. Sutherland, *Application of cubic splines to the spectral analysis of unequally spaced data*, **APJ**, **436**, 787–794, December 1994.

[2] C. Alard, *Image subtraction using a space-varying kernel*, **AAPS**, **144**, 363–370, June 2000.

[3] C. Alard and R. H. Lupton, *A Method for Optimal Image Subtraction*, **APJ**, **503**, 325–+, August 1998.

[4] C. Alcock, *Orbital Elements of MACHO Project Eclipsing Binary Stars*, *Extragalactic Binaries, 25th meeting of the IAU, Joint Discussion 13, 18 July 2003, Sydney, Australia*, **13**, 2003.

[5] C. Alcock, R. A. Allsman, D. Alves, T. S. Axelrod, A. C. Becker, D. P. Bennett, K. H. Cook, K. C. Freeman, K. Griest, C. H. S. Lacy, M. J. Lehner, S. L. Marshall, D. Minniti, B. A. Peterson, M. R. Pratt, P. J. Quinn, A. W. Rodgers, C. W. Stubbs, W. Sutherland and D. L. Welch, *The MACHO Project LMC Variable Star Inventory. V. Classification and Orbits of 611 Eclipsing Binary Stars*, **AJ**, **114**, 326+, July 1997.

[6] C. Alcock, R. A. Allsman, D. R. Alves, T. S. Axelrod, A. C. Becker, D. P. Bennett, K. H. Cook, N. Dalal, A. J. Drake, K. C. Freeman, M. Geha, K. Griest, M. J. Lehner, S. L. Marshall, D. Minniti, C. A. Nelson, B. A. Peterson, P. Popowski, M. R. Pratt, P. J. Quinn, C. W. Stubbs, W. Sutherland, A. B. Tomaney, T. Vandehei and D. Welch, *The MACHO Project: Microlensing Results from 5.7 Years of Large Magellanic Cloud Observations*, **APJ**, **542**, 281–307, October 2000.

[7] C. Alcock, R. A. Allsman, D. R. Alves, T. S. Axelrod, A. C. Becker, D. P. Bennett, K. H. Cook, A. J. Drake, K. C. Freeman, M. Geha, K. Griest, M. J. Lehner, S. L. Marshall, D. Minniti, C. A. Nelson, B. A. Peterson, P. Popowski, M. R. Pratt, P. J. Quinn, C. W. Stubbs, W. Sutherland, A. B. Tomaney, T. Vandehei and D. L. Welch, *The MACHO Project: Microlensing Optical Depth toward the Galactic Bulge from Difference Image Analysis*, **APJ**, **541**, 734–766, October 2000.

[8] D. R. Alves, M. Rejkuba, D. Minniti and K. H. Cook, *K-Band Red Clump Distance to the Large Magellanic Cloud*, **APJL**, **573**, L51–L54, July 2002.

[9] M. Arnaud, E. Aubourg, P. Bareyre, S. Brehin, R. Caridroit, J. de Kat, G. Dispau, K. Djidi, M. Gros and M. Lachieze-Rey, *A 20 sq CM CCD mosaic camera for a dark matter search. Part 1: Mechanics, optics and cryogeny*, *Experimental Astronomy*, **4**, 265–278, 1994.

[10] M. Arnaud, E. Aubourg, P. Bareyre, S. Brehin, R. Caridroit, J. de Kat, G. Dispau, K. Djidi, M. Gros and M. Lachieze-Rey, *A 20 sq CM CCD mosaic camera for a dark matter search. Part 2: Electronics, data acquisition and performance*, *Experimental Astronomy*, **4**, 279–296, 1994.

[11] Y. Avni, *The eclipse duration of the X-ray pulsar 3U 0900-40*, **APJ**, **209**, 574–577, October 1976.

[12] L. M. Barge, I. Ribas, F. P. Maloney, L. E. DeWarf, E. L. Fitzpatrick and E. F. Guinan, *The LMC Eclipsing Binary HV2241: Fundamental Properties and Evolution*, *Bulletin of the American Astronomical Society*, **202**, 806–+, May 2003.

[13] A.H Batten, *Binary and Multiple Systems of Stars*, Pergamon Press, Oxford, Washington, Toronto, —c1973, 1973.

[14] G. Bayne, W. Tobin, J. D. Pritchard, I. Bond, K. R. Pollard, S. C. Besier, S. Noda, T. Sumi, T. Yanagisawa, M. Sekiguchi, M. Honda, Y. Muraki, M. Takeuti, J. B. Hearnshaw, P. M. Kilmartin, R. J. Dodd, D. J. Sullivan and P. C. M. Yock, *The MOA catalogue of eclipsing binary stars in the Small Magellanic Cloud*, **MNRAS**, **331**, 609+, April 2002.

[15] J. P. Beaulieu, P. Grison, W. Tobin, J. D. Pritchard, R. Ferlet, F. Lepeintre, A. Vidal-Madjar, E. Maurice, L. Prevot, C. Gry, J. Guibert, O. Moreau, F. Tajhamady, E. Aubourg, P. Bareyre, C. Coutures, M. Gros, B. Laurent, M. Lachieze-Rey, E. Lesquoy, C. Magneville, A. Milsztajn, L. Moscoso, F. Queinnec, C. Renault, J. Rich, M. Spiro, L. Vigroux, S. Zylberajch, R. Ansari, F. Cavalier and M. Moniez, *EROS variable stars: fundamental-mode and first-overtone Cepheids in the bar of the Large Magellanic Cloud.*, **AAP**, **303**, 137+, November 1995.

[16] J. P. Beaulieu, P. Grison, W. Tobin, J. D. Pritchard, R. Ferlet, F. Lepeintre, A. Vidal-Madjar, E. Maurice, L. Prevot, C. Gry, J. Guibert, O. Moreau, F. Tajhamady, E. Aubourg, P. Bareyre, C. Coutures, M. Gros, B. Laurent, M. Lachieze-Rey, E. Lesquoy, C. Magneville, A. Milsztajn, L. Moscoso, F. Queinnec, C. Renault, J. Rich, M. Spiro, L. Vigroux, S. Zylberajch, R. Ansari, F. Cavalier and M. Moniez, *EROS Variables: Cepheids in the bar of LMC (Beaulieu+ 1995)*, *VizieR Online Data Catalog*, **330**, 30137+, November 1995.

[17] S. A. Bell, R. W. Hilditch, A. P. Reynolds, G. Hill and J. V. Clausen, *Eclipsing binaries in the Magellanic Clouds. I - Absolute dimensions and distance modulus for HV 2226 in the Small Magellanic Cloud*, **MNRAS**, **250**, 119–126, May 1991.

[18] S. A. Bell, G. Hill, R. W. Hilditch, J. V. Clausen and A. P. Reynolds, *Eclipsing Binaries in the Magellanic Clouds - Part Two - Absolute Dimensions and Distance Modulus for HV:5936 in the Large Magellanic Cloud*, **MNRAS**, **265**, 1047–+, December 1993.

[19] G. F. Benedict, B. E. McArthur, L. W. Fredrick, T. E. Harrison, J. Lee, C. L. Slesnick, J. Rhee, R. J. Patterson, E. Nelan, W. H. Jefferys, W. van Altena, P. J. Shelus, O. G. Franz, L. H. Wasserman, P. D. Hemenway, R. L. Duncombe, D. Story, A. L. Whipple and A. J. Bradley, *Astrometry with the Hubble Space Telescope: A Parallax of the Fundamental Distance Calibrator RR Lyrae*, **AJ**, **123**, 473–484, January 2002.

[20] M. S. Bessell, *Concerning the reddening of the Magellanic Clouds*, **AAP**, **242**, L17–L20, February 1991.

[21] L. Blitz, J. Binney, K. Y. Lo, J. Bally and P. T. P. Ho, *The centre of the Milky Way*, **NAT**, **361**, 417–424, February 1993.

[22] I. Bond, *Time Critical Analysis by Image Subtraction*, in *ASP Conf. Ser. 216: Astronomical Data Analysis Software and Systems IX*, 555–+, 2000.

[23] D. H. Bradstreet, L. E. Dewarf, E. F. Guinan, F. P. Maloney and P. A. Maurone, *Eclipsing Binaries in the Magellanic Clouds: Laboratories for Stellar Structure and Evolution*, *Bulletin of the American Astronomical Society*, **26**, 1463–+, December 1994.

[24] D. A. H. Buckley, *M.Sc. Thesis*, Master's thesis, Department of Physics, University of Canterbury, Christchurch, New Zealand, 1982.

[25] P. R. Bxevington, *Data reduction and error analysis for the physical sciences*, New York: McGraw-Hill, 1969, 1969.

[26] C. R. Chambliss, *The eclipsing binary system BV 419*, **AJ**, **72**, 512–+, May 1967.

[27] C. R. Chambliss, *The eclipsing binary system BV 430*, **AJ**, **72**, 518–+, May 1967.

[28] C. Charbonnel, G. Meynet, A. Maeder, G. Schaller and D. Schaerer, *Grids of Stellar Models - Part Three - from 0.8 to 120-SOLAR-MASSES at Z=0.004*, **AAPS**, **101**, 415–+, October 1993.

[29] A. Claret, A. Gimenez and N. C. S. Cunha, *Circularization and synchronization times in the main sequence of detached eclipsing binaries.I. Using the formalism by Tassoul.*, **AAP**, **299**, 724–+, July 1995.

[30] J. V. Clausen, J. Storm, S. S. Larsen and A. Giménez, *Eclipsing binaries in the Magellanic Clouds. uvby CCD light curves and photometric analyses for HV 982 (LMC), HV 12578 (LMC), HV 1433 (SMC), and HV 11284 (SMC)*, **AAP**, **402**, 509–530, May 2003.

[31] A. A. Cole, *Age, Metallicity, and the Distance to the Magellanic Clouds from Red Clump Stars*, **APJL**, **500**, L137+, June 1998.

[32] K. H. Cook, *Binary Star Research Using the MACHO Database, Extragalactic Binaries, 25th meeting of the IAU, Joint Discussion 13, 18 July 2003, Sydney, Australia*, **13**, 2003.

[33] A. P. S. Crotts, *M31 - A unique laboratory for gravitational microlensing*, **APJL**, **399**, L43–L46, November 1992.

[34] A. P. S. Crotts and A. B. Tomaney, *Results from a Survey of Gravitational Microlensing toward M31*, **APJL**, **473**, L87+, December 1996.

[35] T. J. Davidge, *UBV photometry of eclipsing binaries in the LMC*, **AJ**, **94**, 1169–1177, November 1987.

[36] T. J. Davidge, *UBV photometry of eclipsing binaries in the SMC*, **AJ**, **95**, 731–738, March 1988.

[37] T. J. Davidge and E. F. Milone, *A study of the O'Connell effect in the light curves of eclipsing binaries*, **APJS**, **55**, 571–584, August 1984.

[38] K. S. de Boer, H.-J. Tucholke and W. C. Seitter, *The Magellanic Catalogue of Stars - MACS.*, *The Messenger*, **81**, 20–22, 1995.

[39] T. J. Deeming, *Fourier analysis with unequally-spaced data*, **APSS**, **36**, 137–158, August 1975.

[40] L. Di Fabrizio, G. Clementini, M. Marconi, E. Carretta, I. I. Ivans, A. Bragaglia, S. Di Tomaso, R. Merighi, H. A. Smith, C. Sneden and M. Tosi, *Anomalous RR Lyrae stars(?): CM Leonis*, **MNRAS**, **336**, 841–850, November 2002.

[41] S. P. R. Duncan, W. Tobin, R. D. Watson and A. C. Gilmore, *CCD Photometry of Variable Stars in the Magellanic Clouds - Part Four - the Eclipsing Binary HV:1761 and Nearby Field Variables*, **MNRAS**, **265**, 189–+, November 1993.

[42] F. W. Dyson, *On the opportunity afforded by the eclipse of 1919 May 29 of verifying Einstein's theory of gravitation*, **MNRAS**, **77**, 445+, March 1917.

[43] J. Evershed, *The Einstein effect and the eclipse of 1919 May 29* , *The Observatory*, **40**, 269–270, July 1917.

[44] M. J. Feast, *Stellar Candles for the extragalactic Distance Scale Workshop, December 2002, Concepcion, Chile*, To be published in Springer Lecture Notes in Physics Series. Editors will be W. Gieren and D. Alloin.

[45] M. W. Feast, *The Magellanic Clouds and the Extragalactic Distance Scale*, in *ASP Conf. Ser. 4: The Extragalactic Distance Scale*, 9–, 1988.

[46] M. W. Feast, I. S. Glass, P. A. Whitelock and R. M. Catchpole, *A period-luminosity-colour relation for Mira variables*, **MNRAS**, **241**, 375–392, November 1989.

[47] S. Ferraz-Mello, *Estimation of Periods from Unequally Spaced Observations*, **AJ**, **86**, 619+, April 1981.

[48] E. L. Fitzpatrick, I. Ribas, E. F. Guinan, L. E. DeWarf, F. P. Maloney and D. Massa, *Fundamental Properties and Distances of the Large Magellanic Cloud from Eclipsing Binaries. II. HV 982*, **APJ**, **564**, 260–273, January 2002.

[49] E. L. Fitzpatrick, I. Ribas, E. F. Guinan, L. E. DeWarf, F. P. Maloney and D. L. Massa, *The Distance to the Large Magellanic Cloud from Eclipsing Binaries*, *Bulletin of the American Astronomical Society*, **32**, 716–+, May 2000.

[50] E. L. Fitzpatrick, I. Ribas, E. F. Guinan, F. P. Maloney and A. Claret, *Fundamental Properties of the LMC Eclipsing Binary HV5936*, *Bulletin of the American Astronomical Society*, **201**, 405–+, December 2002.

[51] E. L. Fitzpatrick, I. Ribas, E. F. Guinan, F. P. Maloney and A. Claret, *Fundamental Properties and Distances of Large Magellanic Cloud Eclipsing Binaries. IV. HV 5936*, **APJ**, **587**, 685–700, April 2003.

[52] G. Foster, *Wavelets for period analysis of unevenly sampled time series*, **AJ**, **112**, 1709+, October 1996.

[53] W. L. Freedman, B. F. Madore, B. K. Gibson, L. Ferrarese, D. D. Kelson, S. Sakai, J. R. Mould, R. C. Kennicutt, H. C. Ford, J. A. Graham, J. P. Huchra, S. M. G. Hughes, G. D. Illingworth, L. M. Macri and P. B. Stetson, *Final Results from the Hubble Space Telescope Key Project to Measure the Hubble Constant*, **APJ**, **553**, 47–72, May 2001.

[54] C. H. P. Gaposchkin and S. Gaposchkin, *Variable stars in the Small Magellanic Cloud*, Washington, Smithsonian Institution; [for sale by the Superintendent of Documents, U.S. Govt. Print. Off.] 1966., 1966.

[55] S. I. Gaposhkin, *The Large Magellanic Cloud: its Topography of 1830 Variable Stars*, *SAO Special Report*, **310**, March 1970.

[56] S. I. Gaposhkin, *One Hundred and Eight Eclipsing Variables in the Magellanic Clouds*, *SAO Special Report*, **380**, September 1977.

[57] A. Gimenez and J. M. Garcia-Pelayo, *A new method for the analysis of apsidal motions in eclipsing binaries*, **APSS**, **92**, 203–222, May 1983.

[58] D. Graczyk, *Light-curve solutions for bright detached eclipsing binaries in the Small Magellanic Cloud: absolute dimensions and distance indicators*, **MNRAS**, **342**, 1334–1348, July 2003.

[59] J. A. Graham, *Distance indicators in the Magellanic Clouds*, *Highlights in Astronomy*, **6**, 209–216, 1983.

[60] P. Grison, *Automatic search for periodic light curves with any kind of shape in unevenly spaced data*, **AAP**, **289**, 404–410, September 1994.

[61] P. Grison, J.-P. Beaulieu, J. D. Pritchard, W. Tobin, R. Ferlet, A. Vidal-Madjar, J. Guibert, C. Alard, O. Moreau, F. Tajahmady, E. Maurice, L. Prevot, C. Gry, E. Aubourg, P. Bareyre, S. Brehin, M. Gros, M. Lachieze-Rey, B. Laurent, E. Lesquoy, C. Magneville, A. Milsztajn, L. Moscoso, F. Queinnec, C. Renault, J. Rich, M. Spiro, L. Vigroux, S. Zylberajch, R. Ansari, F. Cavalier and M. Moniez, *EROS catalogue of eclipsing binary stars in the bar of the Large Magellanic Cloud.*, **AAPS**, **109**, 447–469, March 1995.

[62] P. Grison, J.-P. Beaulieu, J. D. Pritchard, W. Tobin, R. Ferlet, A. Vidal-Madjar, J. Guibert, C. Alard, O. Moreau, F. Tajahmady, E. Maurice, L. Prevot, C. Gry, E. Aubourg, P. Bareyre, S. Brehin, M. Gros, M. Lachieze-Rey, B. Laurent, E. Lesquoy, C. Magneville, A. Milsztajn, L. Moscoso, F. Queinnec, C. Renault, J. Rich, M. Spiro, L. Vigroux, S. Zylberajch, R. Ansari, F. Cavalier and M. Moniez, *Eclipsing binaries EROS catalogue (Grison+, 1995), VizieR Online Data Catalog*, **410**, 90447+, October 1994.

[63] M. A. T. Groenewegen and M. Salaris, *The LMC eclipsing binary HV 2274 revisited*, **AAP**, **366**, 752–764, February 2001.

[64] E. F. Guinan, *Multiband photoelectric photometry of the eclipsing binary R Canis Majoris*, **AJ**, **82**, 51–66, January 1977.

[65] E. F. Guinan, D. H. Bradstreet and L. E. Dewarf, *Eclipsing Binaries in the Magellanic Clouds*, in *ASP Conf. Ser. 90: The Origins, Evolution, and Destinies of Binary Stars in Clusters*, 196–+, 1996.

[66] E. F. Guinan, L. E. Dewarf, F. P. Maloney, E. L. Fitzpatrick, P. A. Maurone, D. H. Bradstreet, I. Ribas and A. Gimenez, *HST and IUE Studies of Eclipsing Binaries in the Magellanic Clouds: Fundamental Properties and Distances*, *Bulletin of the American Astronomical Society*, **29**, 1209–+, December 1997.

[67] E. F. Guinan, E. L. Fitzpatrick, L. E. Dewarf, F. P. Maloney, P. A. Maurone, I. Ribas, J. D. Pritchard, D. H. Bradstreet and A. Giménez, *The Distance to the Large Magellanic Cloud from the Eclipsing Binary HV 2274*, **APJL**, **509**, L21–L24, December 1998.

[68] E. F. Guinan, I. Ribas, E. L. Fitzpatrick and J. D. Pritchard, *Ultraviolet Studies of Eclipsing Binaries in the Magellanic Clouds: Fundamental Properties and Distances*, in *ESA SP-413: Ultraviolet Astrophysics Beyond the IUE Final Archive*, 315–+, 1998.

[69] A. F. Gulliver, G. Hill and S. J. Adelman, *Vega: A rapidly rotating pole-on star*, **APJL**, **429**, L81–L84, July 1994.

[70] R. Haefner, K. P. Simon and A. Fiedler, *Empirical masses and radii for the luminous binary Sk-67 deg 105 in the LMC*, **AAP**, **288**, L9–L12, August 1994.

[71] T. J. Harries, R. W. Hilditch and I. D. Howarth, *Ten eclipsing binaries in the Small Magellanic Cloud: fundamental parameters and Cloud distance*, **MNRAS**, **339**, 157–172, February 2003.

[72] R. W. Hilditch, *Binary Stars in Local Group Galaxies*, in *ASP Conf. Ser. 90: The Origins, Evolution, and Destinies of Binary Stars in Clusters*, 207–+, 1996.

[73] R.W Hilditch, *An Introduction to Close Binary Stars*, CUP, —c2001, 2001.

[74] G. Hill, *Description of an Eclipsing Binary Light Curve Computer Code with Application to Y-Sextus and the W-Ursae Code of Rucinski*, *Publications of the Dominion Astrophysical Observatory Victoria*, **15**, 297–+, 1979.

[75] G. Hill and J. B. Hutchings, *The Synthesis of Close-Binary Light Curves. I. The Reflection Effect and Distortion in Algol*, **APJ**, **162**, 265–+, October 1970.

[76] J. V. Hindman, *Notes on the structure of the SMC as observed in 21-cm line radiation from neutral hydrogen*, in *IAU Symp. 20: The Galaxy and the Magellanic Clouds*, 255–+, 1964.

[77] J. V. Hindman, *A high resolution study of the distribution and motions of neutral hydrogen in the Small Cloud of Magellan.*, *Australian Journal of Physics*, **20**, 147–171, 1967.

[78] R. K. Honeycutt, *CCD ensemble photometry on an inhomogeneous set of exposures*, **PASP**, **104**, 435–440, June 1992.

[79] G. H. Jacoby, editor, *CCDs in astronomy; Proceedings of the Conference, Tucson, AZ, Sept. 6-8, 1989*, 1990.

[80] K. S. Jensen, J. V. Clausen and A. Gimenez, *CCD photometry in the fields of six eclipsing binaries in the Large and Small Magellanic Clouds. I - Light curves of the binaries - Standard V, B-V data and variability study for 161 selected stars in the fields*, **AAPS**, **74**, 331–350, August 1988.

[81] Y. W. Kang, E. F. Dewarf, L. E. Guinan and P. A. Maurone, *Far Ultraviolet Observations of Large Magellanic Cloud Eclipsing Binaries Found from the Eros Program.*, in *Variables Stars and the Astrophysical Returns of the Microlensing Surveys*, 423–+, 1997.

[82] Z. Kopal, *The classification of close binary systems*, *Annales d'Astrophysique*, **18**, 379–+, January 1955.

[83] R. P. Kudritzki, F. Bresolin and N. Przybilla, *A New Extragalactic Distance Determination Method Using the Flux-weighted Gravity of Late B and Early A Supergiants*, **APJL**, **582**, L83–L86, January 2003.

[84] H. S. Leavitt, *Ten variable stars of the Algol type*, *Annals of Harvard College Observatory*, **60**, 109–146, 1908.

[85] K.-C. Leung, *Photoelectric investigation of BV 544.*, **AJ**, **79**, 852–857, August 1974.

[86] N. R. Lomb, *Least-squares frequency analysis of unequally spaced data*, **APSS**, **39**, 447–462, February 1976.

[87] M. Loudon and E. Budding, *Photometric analysis of two eclipsing binaries in the Magellanic Clouds*, **APSS**, **201**, 287–295, March 1993.

[88] L. B. Lucy, *The Light Curves of W Ursae Majoris Stars*, **APJ**, **153**, 877–+, September 1968.

[89] L. B. Lucy, *The Structure of Contact Binaries*, **APJ**, **151**, 1123–+, March 1968.

[90] F. P. Maloney, E. L. Fitzpatrick, E. F. Guinan, L. E. Dewarf, D. H. Bradstreet, I. Ribas and A. Gimenez, *Eclipsing Binary Systems in the Magellanic Clouds: HV2226 and HV2241*, *Bulletin of the American Astronomical Society*, **30**, 1402–+, December 1998.

[91] F. P. Maloney, I. Ribas, E. L. Fitzpatrick, E. F. Guinan, L. E. DeWarf, J. E. Castora and J. F. Sepinsky, *Accurate Distance to the Large Magellanic Cloud: Analysis of the Eclipsing Binary LMC EROS 1044*, *Bulletin of the American Astronomical Society*, **33**, 787–+, May 2001.

[92] N. Martin, E. Maurice and J. Lequeux, *The structure of the Small Magellanic Cloud*, **AAP**, **215**, 219–242, May 1989.

[93] M. Mateo and P. L. Schechter, *The Dophot Two-Dimensional Photometry Program*, in *1st. ESO/ST-ECF Data Analysis Workshop, Proceedings, held in Garching, F.R.G., April 17-19, 1989. Editors, P.J. Grosbol, F. Murtagh, R.H. Warmels; Publisher, European Southern Observatory, Garching bei Munchen, F.R.G., 1989. ISBN # 3-923524-32-3. LC # QB51.3. E43 E86. P. 69, 1989*, 69–+, 1989.

[94] D. S. Mathewson, V. L. Ford and N. Visvanathan, *The structure of the Small Magellanic Cloud. II*, **APJ**, **333**, 617–643, October 1988.

[95] G. Meynet, A. Maeder, G. Schaller, D. Schaerer and C. Charbonnel, *Grids of massive stars with high mass loss rates. V. From 12 to 120 M_{sun}_ at Z=0.001, 0.004, 0.008, 0.020 and 0.040*, **AAPS**, **103**, 97–105, January 1994.

[96] E. Milone, editor, *Light curve modeling of eclisping binary stars*, Springer-Verlag, 1993.

[97] S. W. Mochnacki, *PhD. Thesis*, Master's thesis, Department of Physics, University of Canterbury, Christchurch, New Zealand, 1971.

[98] S. W. Mochnacki and N. A. Doughty, *A model for the totally eclipsing W UMa system AW UMa.*, **MNRAS**, **156**, 51–+, 1972.

[99] S. W. Mochnacki and N. A. Doughty, *Models for five W UMa systems.*, **MNRAS**, **156**, 243–+, 1972.

[100] Y. Muraki, T. Sumi, F. Abe, I. Bond, B. Carter, R. Dodd, M. Fujimoto, J. Hearnshaw, M. Honda, J. Jugaku, S. Kabe, Y. Kato, M. Kobayashi, B. Koribalski, P. Kilmartin, K. Masuda, Y. Matsubara, T. Nakamura, S. Noda, G. Pennycook, N. Rattenbury, M. Reid, T. Saito, H. Sato, S. Sato, M. Sekiguchi, D. Sullivan, M. Takeuti, Y. Watase, T. Yanagisawa, Yock P. and M. Yoshizawa, *Search for Machos by the MOA collaboration*, *Progress in Theoretical Physics Supplement*, **133**, 233–246, 1999.

[101] B. Nelson and W. D. Davis, *Eclipsing-Binary Solutions by Sequential Optimization of the Parameters*, **APJ**, **174**, 617–+, June 1972.

[102] V. S. Niemela and L. P. Bassino, *Studies of binary stars in the Magellanic Clouds. 2: Spectroscopic orbits of four massive eclipsing binaries*, **APJ**, **437**, 332–337, December 1994.

[103] V. S. Niemela and N. I. Morrell, *Studies of binary stars in the Magellanic Clouds. I - NS 105-67: A massive double-lined O-type binary in the Large Magellanic Cloud*, **APJ**, **310**, 715–718, November 1986.

[104] V. S. Niemela and N. I. Morrell, *Massive Binary Stars in the Magellanic Clouds*, in *IAU Symp. 190: New Views of the Magellanic Clouds*, 181–+, 1999.

[105] S. Noda, M. Takeuti, F. Abe, I. A. Bond, R. J. Dodd, J. B. Hearnshaw, M. Honda, M. Honma, J. Jugaku, S. Kabe, Y. Kan-ya, Y. Kato, P. M. Kilmartin, Y. Matsubara, K. Masuda, Y. Muraki, T. Nakamura, G. R. Nankivell, C. Noguchi, K. Ohnishi, M. Reid, N. J. Rattenbury, T. Saito, H. Sato, M. Sekiguchi, J. Skuljan, D. J. Sullivan, T. Sumi, Y. Watase, S. Wilkinson, R. Yamada, T. Yanagisawa, P. C. M. Yock and M. Yoshizawa, *Study of variable stars in the MOA data base: long-period red variables in the Large Magellanic Cloud* , **MNRAS**, **330**, 137–152, February 2002.

[106] D. J. K. O'Connell, *The so-called periastron effect in eclipsing binaries (summary)*, **MNRAS**, **111**, 642–+, 1951.

[107] J. A. Orosz and P. H. Hauschildt, *The use of the NextGen model atmospheres for cool giants in a light curve synthesis code*, **AAP**, **364**, 265–281, December 2000.

[108] P. G. Ostrov, *Fundamental parameters for the eclipsing binary AzV 73 in the Small Magellanic Cloud*, **AAP**, **380**, 258–263, December 2001.

[109] P. G. Ostrov, *Orbital solution for the MACHO*05:34:41.3-69:31:39 O3If*+O6:V eclipsing binary system in the Large Magellanic Cloud*, **MNRAS**, **321**, L25–L28, February 2001.

[110] P. G. Ostrov and E. Lapasset, *The O4f + O6V eclipsing binary system Sk-67°105 in the Large Magellanic Cloud*, **MNRAS**, **338**, 141–146, January 2003.

[111] P. G. Ostrov, N. I. Morrell and E. Lapasset, *Investigation of the Magellanic eclipsing binary HV 2241*, **AAP**, **377**, 972–980, October 2001.

[112] B. Paczynski, *Gravitational microlensing by the galactic halo*, **APJ**, **304**, 1–5, May 1986.

[113] B. E. J. Pagel, *Stellar vs. interstellar abundances in the Magellanic clouds*, in *New Aspects of Magellanic Cloud Research*, 330–336, 1993.

[114] S. Palen and J. C. Armstrong, *Searching the MaCHO Database for Tertiary Companions to Eclipsing Binaries*, *American Astronomical Society Meeting*, **203**, –+, December 2003.

[115] C. H. Payne-Gaposchkin, *The variable stars of the Large Magellanic Cloud*, Smithsonian Contributions to Astrophysics, Washington: Smithsonian Institution Press, —c1971, 1971.

[116] A. C. Phillips and L. E. Davis, *Registering, PSF-Matching and Intensity-Matching Images in IRAF*, in *ASP Conf. Ser. 77: Astronomical Data Analysis Software and Systems IV*, 297–+, 1995.

[117] A. Pigulski, Z. Kolaczkowski and G. Kopacki, *Reanalysis of the OGLE-I Observations with the Image Subtraction Method. I.Galactic Bar Fields MM1-A, MM1-B, MM7-A, and MM7-B*, *Acta Astronomica*, **53**, 27–50, March 2003.

[118] W. H. Press and G. B. Rybicki, *Fast algorithm for spectral analysis of unevenly sampled data*, **APJ**, **338**, 277–280, March 1989.

[119] W. H. Press, S. A. Teukolsky, W. T. Vetterling and B. P. Flannery, *Numerical recipes in C. The art of scientific computing*, Cambridge: University Press, —c1992, 2nd ed., 1992.

[120] J. D. Pritchard, W. Tobin and M. Clark, *HV982 A Magellanic Cloud Eclipsing Binary Star System*, *Experimental Astronomy*, **5**, 43–+, 1994.

[121] J. D. Pritchard, W. Tobin, M. Clark and E. F. Guinan, *CCD photometry of variable stars in the Magellanic Clouds - V. The eclipsing binaries HV1620 and HV2241*, **MNRAS**, **297**, 278–290, June 1998.

[122] J. D. Pritchard, W. Tobin, M. Clark and E. F. Guinan, *CCD photometry of variable stars in the Magellanic Clouds - VI. The eclipsing binary HV982 in the Large Magellanic Cloud*, **MNRAS**, **299**, 1087–1096, October 1998.

[123] J.D. Pritchard, *CCD photometry of eclipsing binary star systems in the Large and Small Magellanic Clouds*, Ph.D. thesis, Department of Physics, University of Canterbury, Christchurch, New Zealand, 1998.

[124] M Reid, R. J. Dodd and D. J. Sullivan, *Synthetic magnitudes and colours.*, *Australian Journal of Astronomy*, **7**, 79–+, 1998.

[125] J. D. Reimann, *Frequency Estimation Using Unequally-Spaced Astronomical Data.*, *Ph.D. Thesis*, January 1994.

[126] I. Ribas, E. L. Fitzpatrick, F. P. Maloney, E. F. Guinan and A. Udalski, *Fundamental Properties and Distances of Large Magellanic Cloud Eclipsing Binaries. III. EROS 1044*, **APJ**, **574**, 771–782, August 2002.

[127] I. Ribas, E. F. Guinan, E. L. Fitzpatrick, L. E. DeWarf, F. P. Maloney, P. A. Maurone, D. H. Bradstreet, Á. Giménez and J. D. Pritchard, *The Large Magellanic Cloud Eclipsing Binary HV 2274: Fundamental Properties and Comparison with Evolutionary Models*, **APJ**, **528**, 692–701, January 2000.

[128] D. H. Roberts, J. Lehar and J. W. Dreher, *Time Series Analysis with Clean - Part One - Derivation of a Spectrum*, **AJ**, **93**, 968+, April 1987.

[129] H. N. Russell, *Idealized Models and Rectified Light-Curves for Eclipsing Variables.*, **APJ**, **108**, 388–+, November 1948.

[130] H. N. Russell, *Preliminary Solutions for Eclipsing Binaries from Accurate Observations.*, **APJ**, **108**, 53–+, July 1948.

[131] A. Saha, A. Sandage, G. A. Tammann, L. Labhardt, F. D. Macchetto and N. Panagia, *Cepheid Calibration of the Peak Brightness of Type IA Supernovae. IX. SN 1989B in NGC 3627*, **APJ**, **522**, 802–838, September 1999.

[132] C. Salyk and K. A. G. Olsen, *A Warp in the Large Magellanic Cloud Disk?*, *Bulletin of the American Astronomical Society*, **34**, 1115–+, December 2002.

[133] N. N. Samus', V. P. Goranskii, O. V. Durlevich, A. V. Zharova, E. V. Kazarovets, E. N. Pastukhova, M. L. Hazen and T. M. Tsvetkova, *An Electronic Version of Volume I of the General Catalogue of Variable Stars with Improved Coordinates*, *Astronomy Letters*, **28**, 174–181, March 2002.

[134] J. D. Scargle, *Studies in astronomical time series analysis. II - Statistical aspects of spectral analysis of unevenly spaced data*, **APJ**, **263**, 835–853, December 1982.

[135] J.D Scargle, *Application of time series analysis in Astronomy and Meteorolgy*, Smithsonian Contributions to Astrophysics, Washington: Smithsonian Institution Press, —c1971, 1971.

[136] D. Schaerer, G. Meynet, A. Maeder and G. Schaller, *Grids of stellar models. II - From 0.8 to 120 solar masses at Z = 0.008*, **AAPS**, **98**, 523–527, May 1993.

[137] P. L. Schechter, M. Mateo and A. Saha, *DOPHOT, a CCD photometry program: Description and tests*, **PASP**, **105**, 1342–1353, November 1993.

[138] A. Schwarzenberg-Czerny, *On the advantage of using analysis of variance for period search*, **MNRAS**, **241**, 153–165, November 1989.

[139] A. Schwarzenberg-Czerny, *The Correct Probability Distribution for the Phase Dispersion Minimization Periodogram*, **APJ**, **489**, 941+, November 1997.

[140] A. Schwarzenberg-Czerny, *Optimum Period Search: Quantitative Analysis*, **APJ**, **516**, 315–323, May 1999.

[141] L. Staveley-Smith, R. J. Sault, D. McConnell, M. J. Kesteven, D. Hatzidimitriou, K. C. Freeman and M. A. Dopita, *An HI Mosaic of the Small Magellanic Cloud*, *Publications of the Astronomical Society of Australia*, **12**, 13–+, April 1995.

[142] P. B. Stetson, *DAOPHOT - A computer program for crowded-field stellar photometry*, **PASP**, **99**, 191–222, March 1987.

[143] P. B. Stetson, *Some factors affecting the accuracy of stellar photometry with CCDs (And some ways of dealing with them*, in *Highlights of Astronomy*, Kluwer Academic Publishers, Dordrecht, 1989.

[144] P. B. Stetson, *More Experiments with DAOPHOT II and WF/PC Images*, in *ASP Conf. Ser. 25: Astronomical Data Analysis Software and Systems I*, 297–+, 1992.

[145] P. B. Stetson, *The center of the core-cusp globular cluster M15: CFHT and HST Observations, ALLFRAME reductions*, **PASP**, **106**, 250–280, March 1994.

[146] P. B. Stetson, L. E. Davis and D. R. Crabtree, *Future development of the DAOPHOT crowded-field photometry package*, in *ASP Conf. Ser. 8: CCDs in astronomy*, 289–304, 1990.

[147] K. Szatmary, J. Vinko and J. Gal, *Application of wavelet analysis in variable star research. I. Properties of the wavelet map of simulated variable star light curves.*, **AAPS**, **108**, 377–394, December 1994.

[148] K. I. Tanaka, *The Magellanic Stream and the Interacting Galaxies*, **PASJ**, **33**, 247–+, 1981.

[149] W. Tobin, *The Mt-John CCD System - Status and First Scientific Results*, *Proceedings of the Astronomical Society of Australia*, **9**, 164–+, 1991.

[150] W. Tobin, S. P. R. Duncan, S. R. D. West and A. C. Gilmore, *CCD photometry of variable stars in the Magellanic Clouds. III - The eclipsing binary HV 12484*, **MNRAS**, **260**, 777–781, February 1993.

[151] W. Tobin and G. M. Evans, *Stars in a cluster: MT John University Observatory*, Christchurch: University of Canterbury, Dept. of Physics and Astronomy, —c1996, edited by Tobin, William; Evans, G.M., 1996.

[152] W. Tobin, A. C. Gilmore, A. Wadsworth and S. R. D. West, *First CCD Observations of Magellanic Cloud Variable Stars from the MT John University Observatory, New Zealand*, in *IAU Symp. 148: The Magellanic Clouds*, 381–+, 1991.

[153] W. Tobin, G. M. Kershaw, R. A. Ritchie, L. Ma, G. J. Graham and S. B. Hemmingsen, *A CCD Photometer Head*, in *Poster Papers on Stellar Photometry, Poster Proceedings of the IAU Colloquium No. 136 held in Dublin, Ireland, 4-7 August, 1992. Edited by I. Elliott, and C. J. Butler, p.153*, 153–+, 1993.

[154] A. B. Tomaney and A. P. S. Crotts, *Expanding the Realm of Microlensing Surveys with Difference Image Photometry*, **AJ**, **112**, 2872–+, December 1996.

[155] B. A. Twarog, B. J. Anthony-Twarog and A. R. Bricker, *Zeroing the Stellar Isochrone Scale: The Red Giant Clump Luminosity at Intermediate Metallicity*, **AJ**, **117**, 1816–1826, April 1999.

[156] A. Udalski, *The Optical Gravitational Lensing Experiment: Red Clump Stars as a Distance Indicator*, **APJL**, **531**, L25–L28, March 2000.

[157] A. Udalski, M. Kubiak and M. Szymanski, *Optical Gravitational Lensing Experiment. OGLE-2 – the Second Phase of the OGLE Project*, *Acta Astronomica*, **47**, 319–344, July 1997.

[158] A. Udalski, G. Pietrzyński, P. Woźniak, M. Szymański, M. Kubiak and K. Żebruń , *The Optical Gravitational Lensing Experiment: Short Distance Scaleto the Large Magellanic Cloud*, **APJL**, **509**, L25–L28, December 1998.

[159] A. Udalski, I. Soszynski, M. Szymanski, M. Kubiak, G. Pietrzynski, P. Wozniak and K. Zebrun, *The Optical Gravitational Lensing Experiment. Eclipsing Binary Stars in the Small Magellanic Cloud*, *Acta Astronomica*, **48**, 563–651, December 1998.

[160] A. Udalski, M. Szymanski, J. Kaluzny, M. Kubiak, W. Krzeminski, M. Mateo, G. W. Preston and B. Paczynski, *The optical gravitational lensing experiment. Discovery of the first candidate microlensing event in the direction of the Galactic Bulge*, *Acta Astronomica*, **43**, 289–294, July 1993.

[161] A. Udalski, M. Szymanski, J. Kaluzny, M. Kubiak, M. Mateo, W. Krzeminski and B. Paczynski, *The Optical Gravitational Lensing Experiment. The Early Warning System: Real Time Microlensing*, *Acta Astronomica*, **44**, 227–234, July 1994.

[162] A. Udalski, M. Szymanski, M. Kubiak, G. Pietrzynski, I. Soszynski, P. Wozniak and K. Zebrun, *The Optical Gravitational Lensing Experiment. BVI Maps of Dense Stellar Regions. II. The Large Magellanic Cloud*, *Acta Astronomica*, **50**, 307–335, September 2000.

[163] A. Udalski, M. Szymanski, M. Kubiak, G. Pietrzynski, P. Wozniak and K. Zebrun, *The Optical Gravitational Lensing Experiment. BVI Maps of Dense Stellar Regions. I. The Small Magellanic Cloud*, *Acta Astronomica*, **48**, 147–174, April 1998.

[164] A. Udalski, M. Szymanski, S. Mao, R. di Stefano, J. Kaluzny, M. Kubiak, M. Mateo and W. Krzeminski, *The optical gravitational lensing experiment: OGLE no. 7: Binary microlens or a new unusual variable?*, **APJL**, **436**, L103–L106, December 1994.

[165] D. Walsh, R. F. Carswell and R. J. Weymann, *0957 + 561 A, B - Twin quasistellar objects or gravitational lens*, **NAT**, **279**, 381–384, May 1979.

[166] R. D. Watson, S. R. D. West, W. Tobin and A. C. Gilmore, *CCD photometry of variable stars in the Magellanic Clouds. II - The eclipsing binary HV 2274*, **MNRAS**, **258**, 527–532, October 1992.

[167] S. Wellstein, N. Langer and H. Braun, *Formation of contact in massive close binaries*, **AAP**, **369**, 939–959, April 2001.

[168] S. R. D. West, W. Tobin and A. C. Gilmore, *CCD photometry of variable stars in the Magellanic Clouds. I - The eclipsing binaries HV 2208 and HV 12634*, **MNRAS**, **254**, 419–426, February 1992.

[169] B. E. Westerlund, *The Magellanic Clouds*, Cambridge University Press,, January 1997.

[170] R. E. Wilson, *Eccentric orbit generalization and simultaneous solution of binary star light and velocity curves*, **APJ**, **234**, 1054–1066, December 1979.

[171] R. E. Wilson, *Accuracy and efficiency in the binary star reflection effect*, **APJ**, **356**, 613–622, June 1990.

[172] R. E. Wilson, *Binary-star light curve models*, **PASP**, **106**, 921–941, September 1994.

[173] R. E. Wilson and P. Biermann, *TX CANCRI - Which component is hotter*, **AAP**, **48**, 349–357, May 1976.

[174] R. E. Wilson and E. J. Devinney, *Realization of Accurate Close-Binary Light Curves: Application to MR Cygni*, **APJ**, **166**, 605–+, June 1971.

[175] R. E. Wilson and S. Sofia, *Effects of tidal distortion on binary-star velocity curves and ellipsoidal variation*, **APJ**, **203**, 182–186, January 1976.

[176] R. E. Wilson and D. Terrell, *Simultaneous Solutions of X-ray Binary Parameters*, *Bulletin of the American Astronomical Society*, **24**, 1169–+, September 1992.

[177] D. B. Wood, *An analytic model of eclipsing binary star systems.*, **AJ**, **76**, 701–+, October 1971.

[178] P. R. Wozniak, A. Udalski, M. Szymanski, M. Kubiak, G. Pietrzynski, I. Soszynski and K. Zebrun, *Difference Image Analysis of the OGLE-II Bulge Data. II. Microlensing Events*, *Acta Astronomica*, **51**, 175–219, September 2001.

[179] P. R. Wozniak, A. Udalski, M. Szymanski, M. Kubiak, G. Pietrzynski, I. Soszynski and K. Zebrun, *Difference Image Analysis of the OGLE-II Bulge Data. III. Catalog of 200000 Candidate Variable Stars*, *Acta Astronomica*, **52**, 129–142, June 2002.

[180] J. S. B. Wyithe and R. E. Wilson, *Photometric Solutions for Semidetached Eclipsing Binaries: Selection of Distance Indicators in the Small Magellanic Cloud*, **APJ**, **571**, 293–319, May 2002.

[181] L. Wyrzykowski, A. Udalski, M. Kubiak, M. Szymanski, K. Zebrun, I. Soszynski, P. R. Wozniak, G. Pietrzynski and O. Szewczyk, *The Optical Gravitational Lensing Experiment. Eclipsing Binary Stars in the Large Magellanic Cloud*, *Acta Astronomica*, **53**, 1–25, March 2003.

[182] L. Wyrzykowski, A. Udalski, M. Kubiak, M. Szymanski, K. Zebrun, I. Soszynski, P. R. Wozniak, G. Pietrzynski and O. Szewczyk, *The Optical Gravitational Lensing Experiment. Eclipsing Binary Stars in the Large Magellanic Cloud*, *ArXiv Astrophysics e-prints*, April 2003.

[183] K. Zebrun, I. Soszynski and P. R. Wozniak, *The Optical Gravitational Lensing Experiment. Difference Image Analysis of LMC and SMC Data. The Method*, *Acta Astronomica*, **51**, 303–316, December 2001.

[184] K. Zebrun, I. Soszynski, P. R. Wozniak, A. Udalski, M. Kubiak, M. Szymanski, G. Pietrzynski, O. Szewczyk and L. Wyrzykowski, *The Optical Gravitational Lensing Experiment. Difference Image Analysis of LMC and SMC Data. The Catalog*, *Acta Astronomica*, **51**, 317–329, December 2001.